AN ASYMPTOTIC, HOMOGENIZED, ANISOTROPIC, MULTIGROUP DIFFUSION APPROXIMATION TO THE NEUTRON TRANSPORT EQUATION

by

Travis John Trahan

A dissertation submitted in partial fulfillment
of the requirements for the degree of
Doctor of Philosophy
(Nuclear Engineering and Radiological Sciences)
in The University of Michigan
2014

Doctoral Committee:

Professor Edward W. Larsen, Chair
Professor Thomas J. Downar
Professor William R. Martin
Professor Peter S. Smereka

For Alexis,
whose endless patience, support, and love made all of this possible.

ACKNOWLEDGEMENTS

This work would not have been possible without the help of countless individuals, only a small subset of whom I am able to give the thanks they deserve. First, thank you to my advisor, Prof. Ed Larsen, who has been a constant source of ideas and solutions to problems encountered along the way. I would also like to thank the other members of my committee for their suggestions, all of which have served to improve both my own understanding and the quality of this thesis.

This work could not have been completed without funding from the Department of Energy Computational Science Graduate Fellowship, grant number DE-FG02-97ER25308, and the support of the Krell Institute and its staff. The allotment of CPU hours used for some of these calculations was provided by the Consortium for Advanced Simulation of Light Water Reactors, an Energy Innovation Hub for Modeling and Simulations of Nuclear Reactors under U.S. Department of Energy Contract No. DE-AC05-00OR22725. This research used resources of the Oak Ridge Leadership Computing Facility at the Oak Ridge National Laboratory, which is supported by the Office of Science of the U.S. Department of Energy under Contract No. DE-AC05-00OR22725.

Thank you to Prof. Tom Downar for allowing me the use of his computers, and to the MPACT team for me to implement my work into their code. In particular, thank you to Ben Collins, Brendan Kochunas, Shane Stimpson, and Mitch Young for answering so many of my questions, to Brendan Kochunas for running large jobs on

the Titan supercomputer, and especially to Tommy Saller, whose help implementing and debugging the method saved me months of work and frustration.

Thanks to all of my friends, but particularly to the gentlemen of 144 Hill St: Andrew J. Hall, Andrew J. Pavlou, Brendan J. Kochunas, Christopher J. Perfetti, Eric, J. Baker, Piotr J. Starakiewicz, Randall J. Beaman, and Timothy J. Watson. Living with you gentlemen, there was never a dull moment, and those were easily the best years of my life.

I would like to thank my family (Cookie, Chuck, Mike, and Catherine) for putting an emphasis on my education from an early age, and for giving me the support and resources to have made it this far. Most importantly, thank you to Alexis for tolerating me on my bad days, and for all the little favors you've done to help keep my life in order while I completed this work.

TABLE OF CONTENTS

LIST OF FIGURES

Figure

LIST OF TABLES

Table

LIST OF APPENDICES

Appendix

ABSTRACT

An Asymptotic Homogenized, Anisotropic Diffusion Approximation to the Neutron Transport Equation

by
Travis John Trahan

Chair: Edward Larsen

Due to its relatively low computational cost, the neutron diffusion approximation remains one of the most commonly-used computational tools for reactor analysis. Although diffusion requires more approximations than higher-order "transport" methods such as SN and Monte Carlo, the computational cost of these methods prohibits their widespread general use. It has long been known that diffusion is *anisotropic* in heterogeneous reactors, i.e., neutrons diffuse more rapidly in some directions than others. While in many reactors the anisotropic diffusion effects are negligible, in lattices containing voided or optically-thin channels these effects are significant. It is therefore desirable that the homogenized diffusion coefficient be a tensor.

In this thesis, a multigroup, homogenized, anisotropic diffusion equation is derived asymptotically from the exact Boltzmann transport equation for large, 3-D, multiplying systems with a periodic lattice structure. The primary mathematical assumption is that the system is a large, periodic lattice, and that the length scale of a lattice element is small relative to the total system size. The leading-order term

of the asymptotic flux has a standard form, i.e., it is the product of a homogenized diffusion solution and a transport solution for an infinite, periodic system. The first-order correction term significantly improves the accuracy of the reconstructed fluxes.

The goal of this research is to derive a complete homogenized, multigroup diffusion theory using rigorous mathematical analyses, rather than using ad hoc approximations, as have typically been done previously. Specifically, we use an asymptotic method to derive the homogenized diffusion equation, and we use a variational analysis to obtain "Marshak"- and "variational"-like boundary conditions specifically for lattice geometries, and interface conditions that include flux and current discontinuity factors.

We also provide extensive numerical simulations that demonstrate the high accuracy of the asymptotic method. Our results indicate that when the assumptions of the asymptotic analysis are met, the use of the asymptotic diffusion coefficient can lead to significantly improved estimates of the reactor eigenvalue and the neutron flux, otherwise it is comparable in accuracy. The asymptotic flux reconstruction is significantly more accurate than the standard flux reconstruction, especially near the outer regions of the reactor core.

CHAPTER I

Introduction

In this chapter, we motivate the derivation of an asymptotic diffusion approximation to the neutron transport equation. Also, we outline the remainder of this dissertation, in which the diffusion approximation is presented and tested.

1.1 Motivation

A key element of nuclear reactor design is the determination of the neutron flux. Reactor power, fuel utilization, and temperature distribution are all intimately related to the neutron flux. These quantities must be known to verify the safe operation of the reactor and determine the optimum design and placement of fuel for best economic performance [1].

Many of the operational limits of a reactor are determined by local quantities. For example, the reactor must be operated such that the temperature of the hottest fuel pin never exceeds the melting point of the fuel. Similar limits are placed on the peak cladding temperatures and peak heat fluxes on pin surfaces [2, 3, 4]. This means that we must know the flux (and therefore power and, indirectly, temperature) of every pin. If we can improve the accuracy of the pin-level solution, then we can operate the reactor closer to its safety limits, i.e., at a higher power. In this event, the reactor can more efficiently generate more electricity without compromising safety. If we

also wish to better predict fuel performance and material damage over long times, it becomes necessary to know the intra-pin fluxes with reasonable accuracy.

In a large reactor, we may then need to know the intra-pin fluxes for over 50,000 fuel pins [1, 5]. If we assume 50,000 fuel pins divided into roughly 100 radial mesh and 400 axial mesh cells, and we wish to model on the order of 200 angles and 100 energy groups, then the system contains between 10^{13} and 10^{14} unknowns. These estimates are conservative, and in reality the total number of unknowns could be even higher. In reactor accident analysis or fuel depletion studies, it may also be necessary to simulate hundreds of time steps.

Many methods exist for calculating the neutron flux, but they generally fall into two categories [1, 6, 7]. The first, *transport methods*, are based on solving the Boltzmann transport equation and in principle are capable of obtaining the true neutron flux to an arbitrary accuracy. These methods include the discrete ordinates approximation, the spherical harmonics approximation, the method of characteristics, and Monte Carlo simulations.

The second class of methods, *diffusion*, do not solve the neutron transport equation. Instead, they solve a related, approximate equation having no angular dependence. The absence of the angular variable means that (i) there are roughly 2 orders of magnitude fewer unknowns to solve for, and (ii) the algorithms needed to solve the equation are much simpler and less expensive.

Some government research laboratories have access to large, peta-scale computers and are actively researching ways to simulate whole reactor cores using fine-grid transport theory. Active projects include the development of the MC-21 code at Knolls Atomic Power Laboratory/Bettis Atomic Power Laboratory, which uses Monte Carlo, and the Consortium for Advanced Simulation of Light Water Reactors

(CASL) at Oak Ridge National Laboratory, which is studying a variety of methods [8, 9, 10, 11, 12, 13, 14, 15, 16, 17]. Other research is focused on "2D/1D" methods that combine transport and diffusion methods by dividing reactor cores into several radial planes, solving the 2D transport equation on each plane, and coupling the planes together with an axial diffusion calculation [18, 19].

However, most industrial companies responsible for the design and operation of reactors in use today do not have access to the same level of supercomputing resources. For this reason, neutron diffusion theory remains one of the most commonly-used tools for calculating the neutron flux. Although diffusion requires more approximations than higher-order transport methods, the computational cost of the more sophisticated methods prohibits their widespread use [20].

Because so many reactor calculations must be performed in industry, including modeling many time steps for depletion studies and accident analysis for a large number of fuel loading patterns, modeling a reactor using a fine spatial grid, even with diffusion, is often impractical. Reactor design may require tens of thousands of full core calculations per cycle of operation [20]. For this reason, neutron interaction cross sections and diffusion coefficients are often *homogenized* over subregions of the reactor (e.g., over each fuel assembly). The (approximate) homogenization process makes it possible to solve the diffusion equation on a coarse mesh, thereby reducing the number of unknowns in the system and enabling calculations to be performed as much as 100 times faster [20]. Assembly homogenization techniques are discussed in papers by Koebke, Smith, and Sanchez [21, 22, 23]. The homogenized diffusion equation is typically solved using a coarse-grid "nodal" method, of which four of the more common variations are the Nodal Expansion Method (NEM), Analytic Nodal Method (ANM), Analytic Function Expansion Nodal Method (AFEN), and

Semi-Analytic Nodal Method (SANM) [24, 25, 26, 27].

The derivation of homogenized cross sections is straightforward, and the definitions are unique. However, no theoretically-unique way to define homogenized diffusion coefficients has been published [6, 21, 22]. The "standard" definition of the space-dependent diffusion coefficient, assuming for now that scattering is isotropic and considering only one energy group, is defined locally by $1/3\Sigma_t$, where Σ_t is the total cross section. The homogenized diffusion coefficient can be defined many ways, so long as the definition reduces to $1/3\Sigma_t$ for a homogeneous medium. It is desirable to have an unambiguous, mathematically rigorous definition of the homogenized diffusion coefficient.

An issue that arises in homogenized diffusion theory is that there are an insufficient number of degrees of freedom to simultaneously preserve the coarse-mesh volume-average fluxes and the surface-average neutron currents. For this reason, *discontinuity factors* are often introduced into the equations. These factors allow the diffusion flux to be discontinuous between coarse regions, and to preserve the volume-average flux and the surface-average currents. However, the definitions of these factors are heuristic. They are typically obtained by performing transport and diffusion calculations for a subdomain within the reactor (either a single assembly or a multi-assembly "colorset"), and then defining the factors that make the diffusion solution match the transport solution at assembly interfaces [21, 22]. Discontinuity factors have also been defined to preserve assembly partial currents in low-order (e.g., diffusion) operators [23].

There is no universal way to choose the subdomains that are used to define the discontinuity factors, so the definition of these factors is not unique. One can define discontinuity factors based on single lattice calculations with 0 net current boundary

conditions [22]. This method is inexpensive, since it requires no additional lattice calculations, but it is not accurate when neighboring fuel assemblies have significantly different compositions, as in Mixed Oxide (MOX) fuel reactors [28]. One could instead define discontinuity factors based on "colorset" calculations involving multiple assembly types with 0 net current along the outer boundary of the set. This method is more accurate, but it requires lattice calculations for every possible combination of neighboring lattices [28]. In this thesis, we develop a rigorous mathematical, rather than heuristic, derivation that yields unambiguous discontinuity factors. The new discontinuity factors do not require additional lattice calculations (e.g. colorset calculations), but they do use information obtained from lattice calculations for neighboring lattices to improve the quality of the discontinuity factors.

Finally, it has long been known that in heterogeneous reactors, diffusion is anisotropic [29, 30, 31, 32, 33, 34, 35, 36, 37]. While in many reactors the anisotropic diffusion effects are small, in lattices containing voided or optically-thin channels, such as Very High Temperature Reactors (VHTRs), these effects are significant [29, 30, 35, 36, 37]. In such reactors, neutron diffusion is greater in directions parallel to the optically-thin channels than in the transverse directions. It is therefore desirable that the homogenized diffusion coefficient be a tensor, rather than a (standard) scalar. A diffusion tensor for fine-mesh diffusion calculations has been derived already by Larsen and Trahan [35, 37]. In the present work we use an asymptotic analysis to systematically derive a homogenized diffusion equation with an anisotropic diffusion tensor.

The overall purpose of this thesis is to develop a "complete", mathematically rigorous diffusion theory for reactor analysis, including appropriate discontinuity factors and boundary conditions. The new theory yields unambiguously-defined ho-

mogenized parameters, and an anisotropic diffusion tensor. It also provides a means of accurately calculating detailed pin fluxes from the solution of the homogenized diffusion equation. Numerical tests demonstrate the superiority of the asymptotic method relative to other methods.

1.2 Historical Review of Homogenized Diffusion Approximations

Here we review some of the many homogenized diffusion approximations developed in the past. The most relevant of these are presented with more mathematical detail in the next chapter.

The standard space-dependent diffusion coefficient is simply defined $1/(3\Sigma_{tr})$ at every point, where Σ_{tr} is the transport cross section (see Section 2.2.1). Homogenized cross sections can be unambiguously defined as the flux-volume-weighted average of a cross section in the homogenization region. However, there has been no unique, mathematically derived definition of the homogenized diffusion coefficient [6, 21, 22].

A simple definition of the homogenized diffusion coefficient is to calculate the flux-volume-weighted homogenized transport cross section $\overline{\Sigma_{tr}}$ and then calculate the homogenized diffusion coefficient using the formula: $\overline{D} = 1/(3\overline{\Sigma_{tr}})$. Another possibility is to calculate $\overline{D}$ from the flux-volume-weighted homogenized inverse transport cross section: $\overline{D} = (1/3)(\overline{1/\Sigma_{tr}})$. These simple definitions are "arbitrary" according to Cho [6]. Nevertheless, they are used to calculate diffusion coefficients in many codes, including the Serpent continuous-energy Monte Carlo reactor physics burnup calculation code [38].

Since the diffusion coefficient describes neutron leakage, one can also make a case for calculating the diffusion coefficient from the current-volume-weighted, rather than flux-volume-weighted, transport cross section [39]. Many neutron transport codes

do not calculate region-average currents for every region, and so this method is less common than using flux-volume-weighted transport cross sections.

Another method makes use of the relationship between the diffusion length and diffusion coefficient. The diffusion length is proportional to the straight-line distance between the point at which a neutron is born and the point at which it is removed, either by absorption or changing energy [40, 41]. The Monte Carlo code Serpent can tally this quantity and use it to generate multigroup diffusion coefficients [38].

The buckling (B_N) method assumes that for a large, homogeneous system, the spatial dependence of the neutron flux is separable from its angle and energy dependencies. Thus, a "critical" energy spectrum exists at all points in the reactor. In the B_1 approximation, it is furthermore assumed that scattering is linearly anisotropic. Multigroup, homogenized cross sections and diffusion coefficients can be generated from the critical energy spectrum. For more information on the B_1 method, we refer the reader to the course notes of Joo and Lee and the text by Stamm'ler [42, 43, 39]. This method is available in the DRAGON neutron transport code and the Serpent Monte Carlo code [44, 45, 38].

Two similar methods based on the buckling approach assume that the flux in a periodic system is the product of a periodic function of space, angle, and energy and a slowly-varying (buckled) amplitude function of space. The Benoist diffusion coefficients are derived to optimally estimate leakage in such a system [29, 30, 31], while the Deniz-Gelbard diffusion coefficients optimally estimate the reactor multiplication factor in the buckled, periodic system [46, 31]. The Benoist diffusion coefficients are implemented in the TIBERE module of the DRAGON code [45]. We know of no publicly distributed code that calculates and utilizes the Deniz-Gelbard diffusion coefficients.

In 1975, Larsen showed that a homogenized diffusion equation can be obtained through an asymptotic analysis of the Boltzmann transport equation [32]. In order to make the solution $O(1)$ in magnitude, this analysis assumed that sources (including the fission source) are small in terms of the spatial asymptotic scaling parameter. The asymptotic analysis presented in this thesis makes no assumptions about the size of the fission source. Therefore, the analysis in this thesis is more general than the earlier analysis by Larsen; it does not assume that the fission term is small.

A related asymptotic analysis performed by Zhang et al. in 1997 assumed an embedded lattice structure in which many pin-cells are arrayed in a lattice within each assembly, and many assemblies are arrayed in a lattice within the core [47]. This approach leads to *three* different length scales, not two, and the asymptotic analysis is much more complicated. Also, this analysis was performed only for monoenergetic problems, and it only considered the leading-order term in the asymptotic expansion.

We note that asymptotic analyses have been applied numerous times to problems of radiation transport, and that the validity of this technique has been demonstrated via formal mathematical proofs. Some examples of the formal application of asymptotic analysis to problems of radiation transport are: (i) the work of Habetler and Matkowsky [48], who asymptotically derived the diffusion equation for homogeneous, monoenergetic, planar-geometry systems, (ii) the works of Papanicolaou [49] and Bensoussan, Lions, and Papanicolaou [50], who proved the validity of the asymptotic approach for homogeneous and periodic media respectively, and (iii) the work of Dumas and Golse [51], who studied the asymptotic limit of the transport equation for problems in which individual material regions are small relative to the mean free path of particles in a material (which is not typically the case in nuclear reactor cores).

An analytic relationship exists between the asymptotic diffusion approximation derived by Larsen and the Benoist and Deniz-Gelbard diffusion approximations [52, 53]. Although numerical results have demonstrated that these various diffusion approximations yield different diffusion coefficients [31, 33, 54], and some studies have presented limited comparisons between the Benoist method and standard method [55, 45], we know of no comprehensive study prior to our own that compares the eigenvalues, power distributions, and *reconstructed fluxes* yielded by the various diffusion approximations for realistic test problems [56]. The relationship between these methods is discussed in detail, and several numerical comparisons are made in later chapters.

The original 1975 work by Larsen included only leading order terms and thus, the resulting angular flux had $O(\epsilon)$ error. Also, appropriate boundary conditions and discontinuity factors were not derived. The diffusion equation obtained in that work was monoenergetic, and it was not understood at the time how to extend the work to obtain a multigroup diffusion equation.

In this thesis, we extend the original asymptotic analysis by including a first-order $O(\epsilon)$ correction term in the angular flux. The result is a method with $O(\epsilon^2)$ error. Furthermore, a multigroup diffusion equation has been derived, along with boundary and interface (discontinuity factor) conditions. The new theory derived in this thesis yields a homogenized, multigroup diffusion equation with an unambiguously defined, anisotropic diffusion tensor, discontinuity factors, and boundary conditions.

1.3 Overview of This Thesis

In this section we outline the remainder of this thesis. We note that numerous papers have used formal mathematical proofs to show that the application of asymp-

totic analysis to problems of radiation transport is valid [48, 49, 50, 51]. This thesis uses asymptotic analysis in the same vein as those previous works, but is written with less mathematical formalism and does not contain any proofs.

Chapter II summarizes existing transport and diffusion methodologies. Several transport methods are briefly presented, as they are used both for the generation of homogenized diffusion parameters and for reference solutions. The standard multigroup diffusion equation is derived, and shortcomings of this equation are discussed. The three diffusion approximations that we measure our own against are presented with limited mathematical detail.

Chapter III contains a detailed derivation of the monoenergetic asymptotic diffusion approximation. We consider the continuous energy neutron transport equation in the limit of a large periodic system in which the size of individual lattice elements is small. The analysis yields a monoenergetic diffusion equation with a non-standard diffusion coefficient.

We continue in Chapter IV by deriving a multigroup asymptotic diffusion approximation. The same asymptotic scaling is applied to the multigroup diffusion equation with to-be-determined diffusion coefficients. Again, a monoenergetic diffusion equation is obtained, and the multigroup diffusion coefficients are chosen such that this monoenergetic asymptotic diffusion equation matches the one obtained in Chapter III from the analysis of the continuous energy transport equation.

In Chapter V, boundary and interface conditions for the multigroup diffusion approximation are discussed, and a variational analysis is used to obtain novel boundary and interface conditions that include discontinuity factors. The functional in the variational analysis is designed to "optimally" estimate the reactor multiplication factor. We also define discontinuity factors that make certain angular moments of

the reconstructed flux continuous across interfaces. Unlike standard discontinuity factors, our discontinuity factors allow both the diffusion flux *and* current to be discontinuous.

All aspects of the asymptotic/variational diffusion approximation are summarized and pieced together, and the implementation of the method is discussed in Chapter VI.

Numerical results demonstrating the effectiveness of the asymptotic diffusion coefficient, asymptotic flux reconstruction, variational boundary conditions, and our non-standard discontinuity factors are presented in Chapters VII-X. The results show that the asymptotic diffusion coefficient can give more accurate solutions compared to other commonly-used diffusion coefficients for truly periodic systems, but for realistic pressurized light water reactor systems (without voided channels) the asymptotic coefficient performs similarly to the other diffusion coefficients. However, there is a clear benefit to using the asymptotic anisotropic diffusion coefficient in simulations of reactors with long streaming channels (e.g., VHTRs). The asymptotic flux reconstruction yields more accurate intra-pin fluxes than the standard method of flux reconstruction. The variational boundary conditions are a function of an adjustable parameter α, and give better estimates of the reactor multiplication factor in most cases. However, the value of α that gives the best estimate of the reactor multiplication factor and the value of α that gives the most accurate assembly powers are typically different. It remains unclear how to systematically choose the optimal value of α. Our discontinuity factors in many cases improve the estimate of the reactor multiplication factor, but reduce the accuracy of the assembly powers. This seemingly paradoxical result, though disappointing, is consistent with an earlier study performed by Cheng et al. [57]. The variationally-derived discontinuity factors typi-

cally yield the most accurate value of the reactor multiplication factor relative to all other discontinuity factors studied.

In Chapter XI, the asymptotic diffusion approximation with and without discontinuity factors is compared to existing diffusion methodologies for two realistic Pressurized Water Reactor (PWR) problems. The results indicate that for realistic PWR systems, which contain no large voided channels, the methods tend to perform similarly.

The final Chapter XII summarizes our work and numerical results, and discusses related, ongoing, and possible future work.

CHAPTER II

Overview of Existing Methodologies

In this chapter, we briefly describe the most commonly used transport methodologies (Sections 2.1). We then describe the typical *three-step* process for modeling reactors using homogenized diffusion theory (Section 2.2), and some prominent existing homogenized diffusion approximations (Section 2.3).

2.1 Transport Methodologies

Here, we briefly summarize the most commonly used computational methodologies for solving the neutron transport equation. Because these methods have no direct connection to our work, the exact mathematical representations of the methods are not presented here. They are simply described in words in order to familiarize the reader with related terms that appear later in this work.

All transport methods are capable of obtaining an arbitrarily accurate solution to the Boltzmann transport equation [1, 7]:

$$\begin{aligned}(2.1)\qquad &\boldsymbol{\Omega}\cdot\nabla\psi(\boldsymbol{x},\boldsymbol{\Omega},E)+\Sigma_t(\boldsymbol{x},E)\psi(\boldsymbol{x},\boldsymbol{\Omega},E)\\ &\quad=\int_0^\infty\int_{4\pi}\Sigma_s(\boldsymbol{x},\boldsymbol{\Omega}'\cdot\boldsymbol{\Omega},E'\to E)\psi(\boldsymbol{x},\boldsymbol{\Omega}',E')\,\mathrm{d}\Omega'\,\mathrm{d}E'\\ &\qquad+(1-\rho)\,\frac{\chi(\boldsymbol{x},E)}{4\pi}\int_0^\infty\int_{4\pi}\nu\Sigma_f(\boldsymbol{x},E')\psi(\boldsymbol{x},\boldsymbol{\Omega}',E')\,\mathrm{d}\Omega'\,\mathrm{d}E'\,.\end{aligned}$$

In Eq. (2.1), ψ = angular neutron flux, $\Sigma_{t,s,f}$ = macroscopic total, scattering, and fission cross sections respectively, ν = average number of neutrons born per fission, χ = the normalized energy spectrum of neutrons born from fission, and ρ = reactivity. The reactivity is related to the reactor multiplication factor or reactor eigenvalue, k, by $(1 - \rho) = 1/k$. The terms on the left side of the equation represent neutron loss terms due to leakage and collisions respectively. The terms on the right side of the equation represent neutron source terms due to inscattering and fission respectively. In this work we deal only with steady-state eigenvalue problems, and so time dependence is not included in Eq. (2.1).

2.1.1 Discrete Ordinates, S_N

The discrete ordinates (S_N) approximation solves the Boltzmann transport equation for a set of discrete directions of neutron flight. The subscript N refers to the number of polar angles used in the approximation. There are many ways to choose the set of angles and corresponding weights, but in all cases this quadrature set is chosen to yield an accurate approximation of the angular integrals in the transport equation. If an infinite number of angles are included, then the solution will be exact.

The discrete ordinates equations must be solved on a spatial mesh (i.e., a rectilinear, cylindrical, or spherical grid), rather than the explicit geometry of the system. The discrete ordinates equations are solved using two nested iteration loops. The inner iteration is performed by "sweeping" across the mesh along the discrete angles and then updating the within-group scalar flux. Sweeps are performed until the scalar flux converges, at which point the inner iteration loop is terminated. The scattering and fission sources are then updated, and a new set of sweeps (inner iterations) is performed. Each update of the scattering and fission sources constitutes an outer iteration, and these outer iterations continue until the scattering and fission

sources converge. For more information on the discrete ordinates approximation, see Chapters 3 and 4 in the textbook by E. E. Lewis and W. F. Miller [7], Chapter 3 of the textbook by Pomraning [58], or the course notes by Larsen [59].

2.1.2 Spherical Harmonics, $\mathbf{P_N}$

In the spherical harmonics (P_N) approximation, the angular flux is expanded in a series of spherical harmonics functions:

$$\psi(\boldsymbol{x}, \boldsymbol{\Omega}, E) = \sum_{n=0}^{N} \sum_{m=-n}^{n} \psi_{n,m}(\boldsymbol{x}, E) Y_n^m(\boldsymbol{\Omega}) \,, \tag{2.2}$$

where:

$$\psi_{n,m}(\boldsymbol{x}, E) = \int_{4\pi} \psi(\boldsymbol{x}, \boldsymbol{\Omega}, E) \overline{Y_n^m}(\boldsymbol{\Omega}) \, \mathrm{d}\Omega \,. \tag{2.3}$$

Here $Y_n^m(\boldsymbol{\Omega})$ are the spherical harmonics functions, and the overbar denotes their complex conjugates. In this method, one does not solve for the neutron flux directly using the Boltzmann equation. Rather, spherical harmonic moments of the Boltzmann equation are taken and the resulting equations are solved for the spherical harmonics moments of the neutron flux, $\psi_{n,m}$.

The subscript N in P_N indicates the truncation point of the flux expansion. If an infinite number of terms are included in the expansion, then the exact flux can be obtained. The zeroth and first spherical harmonic moments have simple physical interpretations: the zeroth moment is the *scalar flux*, and the first moments are the components of the *neutron current* (to within a normalization constant). The P_1 approximation, which assumes that the flux is a linear function of angle, is the standard diffusion approximation. This indicates that the diffusion approximation should be accurate for systems in which the flux is nearly linear in angle. The P_N method is discussed in more detail elsewhere [7, 58, 59, 60].

2.1.3 Method of Characteristics (MOC)

As with the S_N method, the method of characteristics (MOC) solves the transport equation for a specified, discrete set of directions. In MOC, many rays parallel to the discrete directions are overlaid on the geometry, and the average flux for each ray segment (characteristic line) is calculated analytically. Unlike S_N, the MOC method of ray-tracing enables the use of an irregular spatial mesh that can contain any number of shapes. Thus, any geometry can be modeled explicitly without approximation. Like S_N, an inner loop sweeps across the system to obtain a converged neutron flux, and an outer loop updates scattering and fission sources until they converge. Then the cell-average flux is calculated for each spatial region using the average fluxes for each ray passing through the cell. See the reports by Cho and Kochunas for more on the Method of Characteristics [6, 15].

2.1.4 Monte Carlo (MC)

Monte Carlo (MC) methods use pseudo-random number generators to simulate random neutron histories. The pseudo-random numbers determine the outcomes of various random events in the history of each neutron. If a sufficiently large number of histories are simulated and tallied, then the correct average behavior of the system is obtained. No physical approximations need be made, and no discretization errors occur. However, because of the random behavior of the particles, there is a statistical error associated with Monte Carlo results. The statistical error decreases as $CN^{-1/2}$, where N is the number of particle histories contributing to that tally and C is a problem-dependent constant. This represents a slow decrease in the error, and thus it is common to employ variance reduction techniques to further reduce statistical error. Although variance reduction techniques do not alter the $N^{-1/2}$ rate of convergence,

they can drastically reduce the magnitude of C. Monte Carlo methods and variance reduction techniques are discussed in more detail by Lewis [7].

2.2 Diffusion Theory

2.2.1 Continuous Energy Diffusion Theory

As mentioned in Section 2.1.2, the standard diffusion approximation is obtained by applying the P_1 approximation to the Boltzmann equation (i.e., by assuming that the flux is a linear function of angle). One must also make an additional assumption that anisotropic scattering does not alter the energy of the scattered neutron. In practice, this last approximation is applied by setting the within group anisotropic scattering cross section equal to the integral of the anisotropic scattering cross section over all outgoing energies (see Eq. (2.6) below). The out-of-group anisotropic scattering cross sections are then assumed to be 0. With this additional approximation, we obtain the continuous energy diffusion equation [60]:

$$
\begin{aligned}
(2.4) \qquad & -\nabla \cdot D(\boldsymbol{x}, E)\nabla\phi(\boldsymbol{x}, E) + \Sigma_t(\boldsymbol{x}, E)\phi(\boldsymbol{x}, E) \\
& = \int_0^\infty \Sigma_{s,0}(\boldsymbol{x}, E' \to E)\phi(\boldsymbol{x}, E')\,\mathrm{d}E' \\
& \quad + (1-\rho)\chi(E)\int_0^\infty \nu\Sigma_f(\boldsymbol{x}, E')\phi(\boldsymbol{x}, E')\,\mathrm{d}E' \,.
\end{aligned}
$$

Here we have defined the diffusion coefficient D:

$$
(2.5) \qquad D(\boldsymbol{x}, E) = \frac{1}{3\Sigma_{tr}(\boldsymbol{x}, E)} \,,
$$

where the transport cross section, Σ_{tr}, is defined:

$$
(2.6) \qquad \Sigma_{tr}(\boldsymbol{x}, E) = \Sigma_t(\boldsymbol{x}, E) - \int_0^\infty \Sigma_{s,1}(\boldsymbol{x}, E \to E')\,\mathrm{d}E' \,.
$$

Equations (2.4) and (2.6) have also made use of the scattering cross section mo-

ments defined by:

$$\Sigma_{s,n}(\boldsymbol{x}, E' \to E) = \int_{-1}^{1} P_n(\mu_0)\Sigma_s(\boldsymbol{x}, \mu_0, E' \to E)\,\mathrm{d}\mu_0\,, \tag{2.7}$$

where $\mu_0 = \boldsymbol{\Omega}' \cdot \boldsymbol{\Omega}$. Also, in the above equations the scalar flux, ϕ, is the integral of the angular flux, ψ, over all angles:

$$\phi(\boldsymbol{x}, E) = \int_{4\pi} \psi(\boldsymbol{x}, \boldsymbol{\Omega}E)\,\mathrm{d}\Omega \tag{2.8}$$

2.2.2 Multigroup Homogenized Parameters

Equation (2.4) is somewhat problematic to solve. First, the equation must be discretized in space and energy in order to be numerically solvable. Second, solving this equation on a fine mesh is often too expensive to be practical (see Section 1.1). In addition, the assumption that the flux is nearly linear in angle is not appropriate near material boundaries, where boundary layer effects yield a more complex flux behavior. Therefore, for reactor calculations it is desirable to define multigroup (as opposed to continuous energy) cross sections and diffusion coefficients and then solve the multigroup diffusion equation on a coarse mesh using spatially homogenized parameters. The homogenization process reduces the number of unknowns in the system and better accounts for boundary layer effects.

Homogenized, multigroup parameters are defined to preserve important heterogeneous quantities. Preserving local quantities is impossible when homogenizing, so it is typically chosen to preserve group-averaged spatial integrals over the homogenized regions. The quantities of greatest interest are the region-averaged reaction rates, surface-averaged currents, and the reactor multiplication factor [21, 22]. The first two requirements can be expressed as follows:

$$\int_{V_i}\int_{E_g}^{E_{g-1}} \overline{\Sigma_{r,g,i}}\phi_g(\boldsymbol{x})\,\mathrm{d}E'\,\mathrm{d}V = \int_{V_i}\int_{E_g}^{E_{g-1}} \Sigma_r(\boldsymbol{x}, E')\phi_{het}(\boldsymbol{x}, E')\,\mathrm{d}E'\,\mathrm{d}V\,, \tag{2.9}$$

$$\int_{S_i^k}\int_{E_g}^{E_{g-1}} \boldsymbol{n}_k \cdot \boldsymbol{J}_g(\boldsymbol{x})\,\mathrm{d}E'\,\mathrm{d}S = \int_{S_i^k}\int_{E_g}^{E_{g-1}} \boldsymbol{n}_k \cdot \boldsymbol{J}_{het}(\boldsymbol{x},E')\,\mathrm{d}E'\,\mathrm{d}S\,, \tag{2.10}$$

where V_i is the volume of the homogenized region i, S_i^k is the k-th surface of homogenized region i, $\boldsymbol{n}_k$ is the unit normal vector to that surface, r is the reaction type (e.g. t, s, a, or f), and g is the energy group index. Each energy group is assumed to be bounded by energies E_g and E_{g-1}. $\phi_g(\boldsymbol{x})$ is the scalar flux from the multigroup homogenized diffusion problem, and $\phi_{het}(\boldsymbol{x},E')$ is the scalar flux from the heterogeneous problem. Similarly, $\boldsymbol{J}(\boldsymbol{x})$ is the current from the multigroup homogenized diffusion problem, while $\boldsymbol{J}_{het}(\boldsymbol{x},E')$ is the current from the heterogeneous problem.

Thus, the exact homogenized cross sections are defined by:

$$\overline{\Sigma_{r,g,i}} = \frac{\displaystyle\int_{V_i}\int_{E_g}^{E_{g-1}} \Sigma_r(\boldsymbol{x},E')\phi_{het}(\boldsymbol{x},E')\,\mathrm{d}E'\,\mathrm{d}V}{\displaystyle\int_{V_i}\phi_g(\boldsymbol{x})\,\mathrm{d}V}\,. \tag{2.11}$$

In the diffusion approximation, we write:

$$\boldsymbol{J}_g(\boldsymbol{x}) = -\overline{D_g}\nabla\phi_g(\boldsymbol{x}) \tag{2.12}$$

and so the homogenized diffusion coefficient is defined:

$$\overline{D_{g,i,k}} = \frac{\displaystyle\int_{S_i^k}\int_{E_g}^{E_{g-1}} \boldsymbol{n}_k \cdot \boldsymbol{J}_{het}(\boldsymbol{x},E')\,\mathrm{d}E'\,\mathrm{d}S}{\displaystyle\int_{S_i^k}\boldsymbol{n}_k\cdot\nabla\phi_g(\boldsymbol{x})\,\mathrm{d}S}\,. \tag{2.13}$$

An obvious problem with Eqs. (2.11) and (2.13) is that the scalar fluxes are not known *a priori*. Therefore, approximate fluxes must be used instead. The most commonly used approach is to solve the heterogeneous problem (using one of the aforementioned transport methods) with a zero net current boundary condition on each face. This is equivalent to assuming that the homogenized region is part of an infinite lattice, and the approximation is accurate in the inner regions of the reactor.

The heterogeneous calculation is often referred to as the lattice calculation. The lattice flux, $\phi_{lat}(\boldsymbol{x})$, is then used in place of $\phi_{het}(\boldsymbol{x})$ and $\phi(\boldsymbol{x})$ in Eq. (2.11) to yield:

$$\overline{\Sigma_{r,i}} = \frac{\int_{V_i}\int_{E_g}^{E_{g-1}} \Sigma_r(\boldsymbol{x}, E')\phi_{lat}(\boldsymbol{x}, E')\,\mathrm{d}E'\,\mathrm{d}V}{\int_{V_i}\int_{E_g}^{E_{g-1}} \phi_{lat}(\boldsymbol{x}, E')\,\mathrm{d}E'\,\mathrm{d}V}\,. \tag{2.14}$$

This definition preserves the reaction rates exactly if the homogenized region is truly part of an infinite lattice.

Another issue with Eq. (2.13) is that the homogenized diffusion coefficient does not have a unique definition within the homogenized volume, but rather a value specific to each face of the region [6, 21, 22]. Thus, the definition of the homogenized diffusion coefficient is ambiguous. Instead of this definition of $\overline{D}$, many other approximations are widely used. It is generally agreed that any expression for the homogenized diffusion coefficient should reduce to the P_1 diffusion coefficient, $D = 1/3\Sigma_{tr}$, in the limit of a monoenergetic, homogeneous medium. Beyond this, the definitions are chosen primarily by experience. Some of the more well known homogenized diffusion coefficients are discussed later, in Section 2.3.

2.2.3 A Multigroup Homogenized Diffusion Equation

We now *hypothesize* the form of the multigroup, homogenized diffusion equation for lattice systems. We begin by considering the transport equation (Eq. (2.1)) in an infinite lattice. We operate on this equation by $\int_{V_i}\int_{E_g}^{E_{g-1}}\int_{4\pi}(\cdot)\mathrm{d}\Omega\,\mathrm{d}E\,\mathrm{d}V$. Since

the lattice system is periodic, the leakage term vanishes, leaving us with:

$$\begin{aligned}(2.15)\quad &\int_{V_i}\int_{E_g}^{E_{g-1}} \Sigma_t(\boldsymbol{x},E)\phi_{lat}(\boldsymbol{x},E)\,\mathrm{d}E\,\mathrm{d}V \\ &\quad=\sum_{g'=1}^{G}\int_{V_i}\int_{E_g}^{E_{g-1}}\int_{E'_g}^{E_{g'-1}} \Sigma_{s,0}(\boldsymbol{x},E'\to E)\phi_{lat}(\boldsymbol{x},\boldsymbol{\Omega}',E')\,\mathrm{d}E'\,\mathrm{d}E\,\mathrm{d}V \\ &\qquad+(1-\rho_0)\int_{V_i}\int_{E_g}^{E_{g-1}}\chi(\boldsymbol{x},E)\int_0^{\infty}\nu\Sigma_f(\boldsymbol{x},E')\phi_{lat}(\boldsymbol{x},\boldsymbol{\Omega}',E')\,\mathrm{d}E'\,\mathrm{d}E\,\mathrm{d}V\,,\end{aligned}$$

where ρ_0 is the reactivity for the infinite lattice.

If we define the volume-average multigroup flux and multigroup cross sections by:

$$\boxed{\overline{\phi_g}=\frac{1}{V_i}\int_{V_i}\int_{E_g}^{E_{g-1}}\phi_{lat}(\boldsymbol{x},E)\,\mathrm{d}E\,\mathrm{d}V\,,} \tag{2.16}$$

$$\boxed{\overline{\Sigma_{t,g}}=\frac{\displaystyle\int_{V_i}\int_{E_g}^{E_{g-1}}\Sigma_t(\boldsymbol{x},E)\phi_{lat}(\boldsymbol{x},E)\,\mathrm{d}E\,\mathrm{d}V}{\displaystyle\int_{V_i}\int_{E_g}^{E_{g-1}}\phi_{lat}(\boldsymbol{x},E)\,\mathrm{d}E\,\mathrm{d}V}\,,} \tag{2.17}$$

$$\boxed{\overline{\Sigma_{s,0,g'\to g}}=\frac{\displaystyle\int_{V_i}\int_{E_g}^{E_{g-1}}\int_{E'_g}^{E_{g'-1}}\Sigma_s(\boldsymbol{x},E'\to E)\phi_{lat}(\boldsymbol{x},E')\,\mathrm{d}E'\,\mathrm{d}E\,\mathrm{d}V}{\displaystyle\int_{V_i}\int_{E_{g'}}^{E_{g'-1}}\phi_{lat}(\boldsymbol{x},E')\,\mathrm{d}E'\,\mathrm{d}V}\,,} \tag{2.18}$$

$$\boxed{\overline{\nu\Sigma_{f,g}}=\frac{\displaystyle\int_{V_i}\int_{E_g}^{E_{g-1}}\nu\Sigma_f(\boldsymbol{x},E)\phi_{lat}(\boldsymbol{x},E)\,\mathrm{d}E\,\mathrm{d}V}{\displaystyle\int_{V_i}\int_{E_g}^{E_{g-1}}\phi_{lat}(\boldsymbol{x},E)\,\mathrm{d}E\,\mathrm{d}V}\,,} \tag{2.19}$$

$$\boxed{\overline{\chi_g}=\frac{\displaystyle\int_{V_i}\int_{E_g}^{E_{g-1}}\chi(\boldsymbol{x},E)\int_0^{\infty}\nu\Sigma_f(\boldsymbol{x},E')\phi_{lat}(\boldsymbol{x},E')\,\mathrm{d}E'\,\mathrm{d}E\,\mathrm{d}V}{\displaystyle\int_{V_i}\int_0^{\infty}\nu\Sigma_f(\boldsymbol{x},E')\phi_{lat}(\boldsymbol{x},E')\,\mathrm{d}E'\,\mathrm{d}V}\,,} \tag{2.20}$$

then we can rewrite Eq. (2.15) as:

$$\overline{\Sigma_{t,g}}\,\overline{\phi_g} = \sum_{g'=1}^{G} \overline{\Sigma_{s,0,g'\to g}}\,\overline{\phi'_g} + (1-\rho_0)\,\overline{\chi_g} \sum_{g'=1}^{G} \overline{\nu\Sigma_{f,g'}}\,\overline{\phi'_g}\,, \qquad 1 \le g \le G\,. \tag{2.21}$$

This system of equations is *exact* for an infinite lattice.

Comparing Eqs. (2.21) and (2.4), we now *hypothesize* that for a large but finite lattice, the multigroup diffusion equation should be of the form:

$$\boxed{\begin{aligned} &-\nabla\cdot\overline{D_g}\cdot\nabla\phi_g(\boldsymbol{x}) + \overline{\Sigma_{t,g}}\phi_g(\boldsymbol{x}) \\ &\quad = \sum_{g'=1}^{G} \overline{\Sigma_{s,0,g'\to g}}\phi_{g'}(\boldsymbol{x}) + (1-\rho)\,\overline{\chi_g} \sum_{g'=1}^{G} \overline{\nu\Sigma_{f,g'}}\phi_{g'}(\boldsymbol{x})\,, \qquad 1 \le g \le G\,. \end{aligned}} \tag{2.22}$$

The homogenized cross sections obtained in this analysis (Eqs. (2.17)-(2.19)) are exactly those prescribed by the discussion in Section 2.2.2 (Eq. (2.14)). Thus, these homogenized cross sections attempt to preserve reaction rates, and indeed do so in the limit of an infinite lattice. However, the multigroup, homogenized diffusion coefficients, $\overline{D_g}$ in Eq. (2.22) have not yet been defined, and will be the primary subject of Section 2.3 and Chapters III and IV.

2.2.4 Reactor Analysis Using Multigroup Homogenized Diffusion

As discussed in Section 1.1, it is desirable to obtain the detailed neutron flux at the pin level, but the solution of the homogenized diffusion equation does not contain that information. A three-step process is typically applied in order to obtain pin fluxes from a diffusion calculation [21]:

1. Perform a lattice calculation for each homogenization region using transport theory (solve Eq. (2.1)). The lattice solution is used to generate appropriate homogenized parameters. The homogenized cross sections are defined by Eqs. (2.17)-(2.20). There are many possible definitions of the homogenized diffusion coefficient, some of which will be discussed in the next section.

2. Perform a diffusion calculation using the homogenized parameters (solve Eq. (2.22)). Typically this is done using a nodal diffusion method [24, 25, 27].

3. Assume that the pin flux has the local shape of the lattice solution, but has the global gradient of the diffusion solution. Then the pin fluxes are reconstructed using the following equation:

$$\phi_{het}(\boldsymbol{x}) = \phi_{lat}(\boldsymbol{x})\phi(\boldsymbol{x})\,. \tag{2.23}$$

2.3 Existing Homogenized Diffusion Methodologies

Next, we discuss several homogenized diffusion approximations that have been applied in the past.

2.3.1 Standard Diffusion Theory

As mentioned previously, the definition of a homogenized diffusion coefficient is ambiguous. Some common definitions discussed in Section 1.2 are based on: flux-volume weighting of the transport cross section, Σ_{tr}, flux-volume weighting of $1/\Sigma_{tr}$, or current-volume weighting of Σ_{tr}.

Experience has shown that first flux-volume weighting the transport cross section in space, and then flux-volume weighting the inverse of the resulting homogenized, continuous energy or fine group transport cross section in energy works well for multigroup reactor analysis [61]. Thus, from this point on we define the *standard* homogenized diffusion coefficient by:

$$\boxed{\overline{D_g} = \frac{1}{3}\frac{\displaystyle\int_{E_g}^{E_{g-1}} \frac{1}{\overline{\overline{\Sigma_{tr}(E)}}} \int_{V_i} \phi_{lat}(\boldsymbol{x}, E)\,\mathrm{d}V\,\mathrm{d}E}{\displaystyle\int_{E_g}^{E_{g-1}} \int_{V_i} \phi_{lat}(\boldsymbol{x}, E)\,\mathrm{d}V\,\mathrm{d}E}\,,} \tag{2.24}$$

where the homogenized, continuous energy transport cross section is defined by:

$$\boxed{\overline{\Sigma_{tr}(E)} = \frac{\displaystyle\int_{V_i} \Sigma_{tr}(\boldsymbol{x}, E)\phi_{lat}(\boldsymbol{x}, E)\,\mathrm{d}V}{\displaystyle\int_{V_i} \phi_{lat}(\boldsymbol{x}, E)\,\mathrm{d}V}}. \tag{2.25}$$

The standard diffusion coefficient of Eq. (2.24) can be formally derived by replacing the spatially dependent cross sections with flux-volume weighted cross sections (Eq. (2.14)) in the transport equation (Eq. (2.1)). We then apply the P_1 approximation to the homogenized equation and integrate the resulting homogenized, continuous energy diffusion equation over each energy group.

Although widely used, this diffusion approximation has a limited theoretical basis. There is no mathematical justification for simply rewriting the transport equation with homogenized cross sections in place of the spatially dependent cross sections. By applying the P_1 approximation to an already homogenized transport equation, many transport effects are neglected. For example, the resulting *isotropic* diffusion coefficient cannot capture the *anisotropic* diffusion effects that occur in heterogeneous systems.

Nevertheless, the standard diffusion coefficient, as well as the diffusion coefficients discussed in Section 1.2 are accurate for typical light water reactors, and all have found widespread use in reactor analysis.

2.3.2 Deniz-Gelbard Diffusion Theory

Another well known homogenized diffusion coefficient has been proposed by Deniz and Gelbard [31, 46]. We present an abbreviated derivation for the case of monoenergetic neutrons and isotropic scattering and then simply state the result for the general case.

Deniz and Gelbard assume from the start that the neutron flux is composed of

an amplitude function with a small buckling, $\boldsymbol{B}^2 \ll 1$, superimposed on a periodic function. Thus, the solution to Eq. (2.1) has the form:

$$\psi(\boldsymbol{x}, \boldsymbol{\Omega}) = \text{Real}[f(\boldsymbol{x}, \boldsymbol{\Omega}) \exp(i\boldsymbol{B} \cdot \boldsymbol{x})] \,, \tag{2.26}$$

where $f(\boldsymbol{x}, \boldsymbol{\Omega})$ is periodic in $\boldsymbol{x}$ and complex. The "buckling" term $\exp(i\boldsymbol{B} \cdot \boldsymbol{x})$ is not periodic. We define the real and imaginary components of f as:

$$R(\boldsymbol{x}, \boldsymbol{\Omega}) = \text{Real}[f(\boldsymbol{x}, \boldsymbol{\Omega})] \,, \tag{2.27}$$

$$I(\boldsymbol{x}, \boldsymbol{\Omega}) = \text{Imag}[f(\boldsymbol{x}, \boldsymbol{\Omega})] \,. \tag{2.28}$$

Introducing Eqs. (2.26)-(2.28) into Eq. (2.1) (considering only an infinite periodic lattice) and equating the real and imaginary components, we get:

(2.29)

$$\begin{aligned} &\boldsymbol{\Omega} \cdot \nabla R(\boldsymbol{x}, \boldsymbol{\Omega}) + \Sigma_t(\boldsymbol{x}) R(\boldsymbol{x}, \boldsymbol{\Omega}) \\ &\quad = \frac{\Sigma_s(\boldsymbol{x})}{4\pi} \int_{4\pi} R(\boldsymbol{x}, \boldsymbol{\Omega}') \, \mathrm{d}\Omega' + (1-\rho) \frac{\nu\Sigma_f(\boldsymbol{x})}{4\pi} \int_{4\pi} R(\boldsymbol{x}, \boldsymbol{\Omega}') \, \mathrm{d}\Omega' + (\boldsymbol{\Omega} \cdot \boldsymbol{B}) I(\boldsymbol{x}, \boldsymbol{\Omega}) \,, \end{aligned}$$

(2.30)

$$\begin{aligned} &\boldsymbol{\Omega} \cdot \nabla I(\boldsymbol{x}, \boldsymbol{\Omega}) + \Sigma_t(\boldsymbol{x}) I(\boldsymbol{x}, \boldsymbol{\Omega}) \\ &\quad = \frac{\Sigma_s(\boldsymbol{x})}{4\pi} \int_{4\pi} I(\boldsymbol{x}, \boldsymbol{\Omega}') \, \mathrm{d}\Omega' + (1-\rho) \frac{\nu\Sigma_f(\boldsymbol{x})}{4\pi} \int_{4\pi} I(\boldsymbol{x}, \boldsymbol{\Omega}') \, \mathrm{d}\Omega' - (\boldsymbol{\Omega} \cdot \boldsymbol{B}) R(\boldsymbol{x}, \boldsymbol{\Omega}) \,. \end{aligned}$$

Deniz and Gelbard then consider the term $(\boldsymbol{\Omega} \cdot \boldsymbol{B}) I(\boldsymbol{x}, \boldsymbol{\Omega})$ in Eq. (2.29) as a perturbation term to the following unperturbed problems:

$$\begin{aligned} &\boldsymbol{\Omega} \cdot \nabla R(\boldsymbol{x}, \boldsymbol{\Omega}) + \Sigma_t(\boldsymbol{x}) R(\boldsymbol{x}, \boldsymbol{\Omega}) \\ &\qquad = \frac{\Sigma_s(\boldsymbol{x})}{4\pi} \int_{4\pi} R(\boldsymbol{x}, \boldsymbol{\Omega}') \, \mathrm{d}\Omega' + (1-\rho_0) \frac{\nu\Sigma_f(\boldsymbol{x})}{4\pi} \int_{4\pi} R(\boldsymbol{x}, \boldsymbol{\Omega}') \, \mathrm{d}\Omega' \,, \end{aligned} \tag{2.31}$$

$$\boldsymbol{\Omega}\cdot\nabla I(\boldsymbol{x},\boldsymbol{\Omega})+\Sigma_t(\boldsymbol{x})I(\boldsymbol{x},\boldsymbol{\Omega})=\frac{\Sigma_s(\boldsymbol{x})}{4\pi}\int_{4\pi}I(\boldsymbol{x},\boldsymbol{\Omega}')\,\mathrm{d}\Omega' + (1-\rho_0)\,\frac{\nu\Sigma_f(\boldsymbol{x})}{4\pi}\int_{4\pi}I(\boldsymbol{x},\boldsymbol{\Omega}')\,\mathrm{d}\Omega'-(\boldsymbol{\Omega}\cdot\boldsymbol{B})R(\boldsymbol{x},\boldsymbol{\Omega})\,. \tag{2.32}$$

From Eq. (2.31) we see that R is actually the infinite lattice angular flux, ψ_{lat}, which can be obtained by a standard lattice calculation.

If one defines the functions $I_i(\boldsymbol{x},\boldsymbol{\Omega})$ by the equations:

$$\boldsymbol{\Omega}\cdot\nabla I_i(\boldsymbol{x},\boldsymbol{\Omega})+\Sigma_t(\boldsymbol{x})I_i(\boldsymbol{x},\boldsymbol{\Omega})=\frac{\Sigma_s(\boldsymbol{x})}{4\pi}\int_{4\pi}I_i(\boldsymbol{x},\boldsymbol{\Omega}')\,\mathrm{d}\Omega' + (1-\rho_0)\,\frac{\nu\Sigma_f(\boldsymbol{x})}{4\pi}\int_{4\pi}I_i(\boldsymbol{x},\boldsymbol{\Omega}')\,\mathrm{d}\Omega'-\Omega_i R(\boldsymbol{x},\boldsymbol{\Omega})\,,\qquad i=1,2,3\,, \tag{2.33}$$

then $I=B_1I_1+B_2I_2+B_3I_3=\boldsymbol{B}\cdot\boldsymbol{I}$.

Deniz and Gelbard now seek a diffusion approximation that will preserve the eigenvalue of the true system. Using perturbation theory and their unperturbed equations, they find that if one solves the diffusion Eq. (2.22), where the homogenized cross sections are given by Eqs. (2.17)-(2.19) and the homogenized diffusion tensor is defined by:

$$D_{ij}=-4\pi\frac{\displaystyle\int_{cell}\int_{4\pi}\Omega_i R(\boldsymbol{x},-\boldsymbol{\Omega})I_j(\boldsymbol{x},\boldsymbol{\Omega})\,\mathrm{d}\Omega\,\mathrm{d}V}{\displaystyle\int_{cell}\phi^*_{lat}(\boldsymbol{x})\nu\Sigma_f(\boldsymbol{x})\phi_{lat}(\boldsymbol{x})\,\mathrm{d}V}\,\frac{\displaystyle\int_{cell}\nu\Sigma_f(\boldsymbol{x})\phi_{lat}(\boldsymbol{x})\,\mathrm{d}V}{\displaystyle\int_{cell}\phi_{lat}(\boldsymbol{x})\,\mathrm{d}V}\,, \tag{2.34}$$

$$i,j=1,2,3\,,$$

then the eigenvalue of the lattice system will be preserved to $O(\boldsymbol{B}^2)$. In Eq. (2.34), we have used a forward and adjoint lattice scalar flux, ϕ_{lat} and ϕ^*_{lat} respectively, that are defined as follows.

$$\phi_{lat}(\boldsymbol{x})=\int_{4\pi}R(\boldsymbol{x},\boldsymbol{\Omega})\,\mathrm{d}\Omega\,, \tag{2.35}$$

$$\phi^*_{lat}(\boldsymbol{x})=\int_{4\pi}R^*(\boldsymbol{x},\boldsymbol{\Omega})\,\mathrm{d}\Omega\,. \tag{2.36}$$

The function R^* is the solution to the adjoint infinite lattice transport equation. The adjoint equation is defined in Section 3.3. The adjoint eigenfunction, R^*, can be considered an importance function. Note that for this monoenergetic case, $\phi_{lat} = \phi^*_{lat}$, but this is not generally true for energy dependent problems.

The multigroup Deniz-Gelbard diffusion coefficient is not derived here (see the paper by Gelbard [31]), but it can be written:

(2.37)

$$\overline{\boldsymbol{D}_{g,ij}} = 4\pi \frac{\displaystyle\sum_{g=1}^{G} \overline{\nu\Sigma}_{f,g}\overline{R}_g \sum_{g'=1}^{G} \overline{\chi}_{g'}\overline{R}^*_{g'}}{\displaystyle\int_{cell}\left(\int_0^\infty \phi^*_{lat}(\boldsymbol{x},E)\chi(\boldsymbol{x},E)\,\mathrm{d}E\right)\left(\int_0^\infty \nu\Sigma_f(\boldsymbol{x},E)\phi_{lat}(\boldsymbol{x},E)\,\mathrm{d}E\right)\,\mathrm{d}V} \times \frac{\displaystyle\int_{cell}\int_{E_g}^{E_{g-1}}\int_{4\pi} \boldsymbol{\Omega}_i R^*(\boldsymbol{x},\boldsymbol{\Omega},E) I_j(\boldsymbol{x},\boldsymbol{\Omega},E)\,\mathrm{d}\Omega\,\mathrm{d}E\,\mathrm{d}V}{\overline{R}^*_g\overline{R}_g}, \quad 1 \le g \le G,$$

where the homogeneous forward and adjoint multigroup fluxes, $\overline{R}_g$ and $\overline{R}^*_g$ respectively, are the solution to the infinite lattice multigroup transport equation (Eq. (2.21)) and its adjoint (the transpose of the $G \times G$ operator).

The process for obtaining pin fluxes is now slightly more complex than the process used in standard diffusion, but it is quite similar.

1. Perform a lattice calculation for each homogenization region using transport theory (solve Eq. (2.31)). If the problem is energy dependent, then an adjoint calculation is also necessary. An additional, *fixed source* lattice calculation must also be solved using transport theory (solve Eq. (2.33)). The homogenized diffusion coefficient and cross sections are now calculated using Eqs. (2.37) and (2.17)-(2.19) respectively.
2. Perform a diffusion calculation using the homogenized parameters (solve Eq. (2.22)). We note that the scalar diffusion coefficient has been replaced by a

diffusion tensor.

3. Reconstruct the pin flux using Eq. (2.26). We note that the real component of the amplitude function, $\exp(i\boldsymbol{B}\cdot\boldsymbol{x})$, which behaves as $\cos(\boldsymbol{B}\cdot\boldsymbol{x})$, is analogous to the scalar flux from the diffusion solution. The imaginary component of the amplitude function, which behaves as $\sin(\boldsymbol{B}\cdot\boldsymbol{x})$, is analogous to the gradient of the scalar flux from the diffusion solution. Then Eq. (2.26) gives:

$$\begin{aligned}\psi(\boldsymbol{x},\boldsymbol{\Omega}) &= R(\boldsymbol{x},\boldsymbol{\Omega})\cos(\boldsymbol{B}\cdot\boldsymbol{x}) - \boldsymbol{I}(\boldsymbol{x},\boldsymbol{\Omega})\cdot\boldsymbol{B}\sin(\boldsymbol{B}\cdot\boldsymbol{x})\,,\\ &= R(\boldsymbol{x},\boldsymbol{\Omega})\phi(\boldsymbol{x}) - \boldsymbol{I}(\boldsymbol{x},\boldsymbol{\Omega})\cdot\nabla\phi(\boldsymbol{x})\,.\end{aligned} \tag{2.38}$$

Integrating Eq. (2.38) over all angles gives an equation for the reconstructed scalar flux with two terms:

$$\phi_{het}(\boldsymbol{x}) = \phi_{lat}(\boldsymbol{x})\phi(\boldsymbol{x}) - \left[\int_{4\pi}\boldsymbol{I}(\boldsymbol{x},\boldsymbol{\Omega})\,\mathrm{d}\Omega\right]\cdot\nabla\phi(\boldsymbol{x})\,. \tag{2.39}$$

The first term is standard flux reconstruction, Eq. (2.23). The second term is a correction term, the meaning of which will become more clear in the next chapter. In common practice, the correction term is not used.

It is shown in Chapters III and IV that although the derivations are different, the Deniz-Gelbard diffusion approximation and our asymptotic diffusion approximation are the same. However, we are unaware of the Deniz-Gelbard method's application in commercial reactor design. Furthermore, the method as presented first by Deniz and Gelbard predated the use of discontinuity factors, and so the previous work did not include any discussion of them.

2.3.3 Benoist Diffusion Theory

We now discuss the well-known Benoist diffusion theory [29, 30]. Again, we only present an abbreviated derivation for the case of monoenergetic neutrons and

isotropic scattering, and then we state the general result. The Benoist approximation begins with the same assumed form of the angular flux as Deniz and Gelbard [29, 30, 31], so we begin with Eqs. (2.26)-(2.30). Benoist then performs a power series expansion of R and I in the components of $\boldsymbol{B}$:

$$R(\boldsymbol{x},\boldsymbol{\Omega}) = \sum_{i,j,k}^{\infty} B_1^i B_2^j B_3^k R^{(i,j,k)}(\boldsymbol{x},\boldsymbol{\Omega})\,, \tag{2.40}$$

$$I(\boldsymbol{x},\boldsymbol{\Omega}) = \sum_{i,j,k}^{\infty} B_1^i B_2^j B_3^k I^{(i,j,k)}(\boldsymbol{x},\boldsymbol{\Omega})\,. \tag{2.41}$$

Benoist asserts that $I^{(0,0,0)} = R^{(1,0,0)} = R^{(0,1,0)} = R^{(0,0,1)} = 0$, and so the leading order terms satisfy:

(2.42)

$$\begin{aligned}&\boldsymbol{\Omega}\cdot\nabla R^{(0,0,0)}(\boldsymbol{x},\boldsymbol{\Omega}) + \Sigma_t(\boldsymbol{x}) R^{(0,0,0)}(\boldsymbol{x},\boldsymbol{\Omega})\\ &\quad = \frac{\Sigma_s(\boldsymbol{x})}{4\pi}\int_{4\pi} R^{(0,0,0)}(\boldsymbol{x},\boldsymbol{\Omega}')\,\mathrm{d}\Omega' + (1-\rho_0)\,\frac{\nu\Sigma_f(\boldsymbol{x})}{4\pi}\int_{4\pi} R^{(0,0,0)}(\boldsymbol{x},\boldsymbol{\Omega}')\,\mathrm{d}\Omega'\,,\end{aligned}$$

$$\begin{aligned}\boldsymbol{\Omega}\cdot\nabla I_i(\boldsymbol{x},\boldsymbol{\Omega}) + \Sigma_t(\boldsymbol{x}) I_i(\boldsymbol{x},\boldsymbol{\Omega}) &= \frac{\Sigma_s(\boldsymbol{x})}{4\pi}\int_{4\pi} I_i(\boldsymbol{x},\boldsymbol{\Omega}')\,\mathrm{d}\Omega'\\ &\quad + (1-\rho_0)\,\frac{\nu\Sigma_f(\boldsymbol{x})}{4\pi}\int_{4\pi} I_i(\boldsymbol{x},\boldsymbol{\Omega}')\,\mathrm{d}\Omega' - \Omega_i R^{(0,0,0)}\,,\qquad i=1,2,3\,,\end{aligned} \tag{2.43}$$

where for simplicity of notation, one can write $I^{(1,0,0)} = I_1$, $I^{(0,1,0)} = I_2$, and $I^{(0,0,1)} = I_3$. We note that Eqs. (2.42) and (2.43) are exactly Eqs. (2.31) and (2.33).

With $O(\boldsymbol{B}^2)$ error, the angular neutron flux is given by:

$$\psi(\boldsymbol{x},\boldsymbol{\Omega}) = R^{(0,0,0)}\cos(\boldsymbol{B}\cdot\boldsymbol{x}) - (B_1 I_1 + B_2 I_2 + B_3 I_3)\sin(\boldsymbol{B}\cdot\boldsymbol{x})\,. \tag{2.44}$$

This angular flux reconstruction is identical to the Deniz-Gelbard formula, Eq. (2.38).

Benoist now chooses to preserve the leakage from each lattice cell with $O(\boldsymbol{B}^2)$ error, and he arrives at the following definition for the diffusion tensor:

$$D_{ii} = \frac{\displaystyle\int_{cell} J_{1,ii}(\boldsymbol{x})\,\mathrm{d}V + \int_{cell}(x_i - x_{i,0})\frac{\partial}{\partial x_i}J_{1,ii}(\boldsymbol{x})\,\mathrm{d}V}{\displaystyle\int_{cell}\phi_{lat}(\boldsymbol{x})\,\mathrm{d}V}\,, \tag{2.45}$$

$$D_{ij} = 0\,, \qquad i \neq j\,,$$

$$i = 1,2,3 \quad j = 1,2,3\,.$$

Here,

$$J_{1,ij}(\boldsymbol{x}) = \begin{cases} -\int_{4\pi} \Omega_i I_j(\boldsymbol{x}, \boldsymbol{\Omega})\, \mathrm{d}\Omega & i = j \\ 0 & i \neq j \end{cases} \qquad i = 1,2,3 \quad j = 1,2,3\,, \tag{2.46}$$

is the current in Eq. (2.43), and $x_{i,0}$ is i-th coordinate of the center of the lattice element.

The multigroup Benoist diffusion tensor is given by:

(2.47)

$$\boxed{D_{ii} = \frac{\displaystyle\int_{cell}\int_{E_g}^{E_{g-1}} J_{1,ii}(\boldsymbol{x}, E)\, \mathrm{d}E\, \mathrm{d}V + \int_{cell}\int_{E_g}^{E_{g-1}} (x_i - x_{i,0}) \frac{\partial}{\partial x_i} J_{1,ii}(\boldsymbol{x}, E)\, \mathrm{d}E\, \mathrm{d}V}{\displaystyle\int_{cell}\int_{E_g}^{E_{g-1}} \phi_{lat}(\boldsymbol{x}, E)\, \mathrm{d}E\, \mathrm{d}V}\,,}$$

$$\boxed{D_{ij} = 0\,, \qquad i \neq j\,,}$$

$$\boxed{i = 1,2,3 \quad j = 1,2,3\,.}$$

The Benoist diffusion coefficients have the undesirable property that both the homogenized cross sections and diffusion tensor are multiple-valued; there are multiple ways to define a lattice element, and each yields different values for the homogenized cross sections and diffusion tensor. For simplicity and consistency with common practice, one can require that the homogenized cross sections be buckling-independent. In this case they are uniquely defined as the standard flux weighted cross sections of Eqs. (2.17)-(2.19). The second integral in the numerator of Eq. (2.47) can be considered a correction term and is often neglected, in which case the diffusion tensor is uniquely defined. The resulting "uncorrected" Benoist diffusion coefficient always lies between the two uncorrected values [31]. According to Gelbard, there is no

theoretical reason to believe that any one of the possible definitions of the Benoist coefficient will be best for all problems [31].

The expression for the "corrected" Benoist diffusion coefficient can be rewritten as a surface integral:

$$D_{ii} = \frac{\int_{x_{k,min}}^{x_{k,max}} \int_{x_{j,min}}^{x_{j,max}} \int_{E_g}^{E_{g-1}} J_{1,ii}(x_{i,min}, x_j, x_k, E)\, \mathrm{d}E\, \mathrm{d}x_j\, \mathrm{d}x_k}{\int_{cell} \int_{E_g}^{E_{g-1}} \phi_{lat}(\boldsymbol{x}, E)\, \mathrm{d}E\, \mathrm{d}V}\,, \tag{2.48}$$

$$D_{ij} = 0\,, \qquad i \neq j\,,$$

$$i = 1, 2, 3 \quad j = 1, 2, 3\,,$$

where x_i, x_j, and x_k are the components of $\boldsymbol{x}$ and the min and max subscripts indicate the boundaries of the homogenization cell. We note that the function $J_{1,ii}$ is evaluated at the boundary of the lattice cell, and because the cell structure is periodic, one could choose to do this at either $x_{i,min}$ or $x_{i,max}$.

The Benoist method is applied in exactly the same manner as the Deniz-Gelbard method (see Section 2.3.2). The only difference is that Eq. (2.45) defines the diffusion coefficient. We now have a more concrete interpretation of the second term in the flux reconstruction (Eq. (2.44)): the second term is $O(\boldsymbol{B})$, and the error in the flux reconstruction is $O(\boldsymbol{B}^2)$. If the buckling $\boldsymbol{B}^2$ is small (i.e., if the reactor is large, and the global curvature of the solution is small), this reconstruction should be accurate.

As noted by Gelbard, the Benoist method, which preserves leakage rates, may yield more accurate fluxes than the Deniz-Gelbard method, which preserves the eigenvalue [31]. Conversely, one might expect that the Deniz-Gelbard method will yield a better estimate of the reactor eigenvalue.

In this thesis, numerical test problems are used in Chapters VII and XI to compare the accuracies of these existing methodologies to the accuracy of the asymptotic

diffusion approximation.

CHAPTER III

Asymptotic Diffusion Analysis of the Continuous Energy Transport Equation

In this chapter, we apply an asymptotic analysis to the Boltzmann transport equation for a large lattice system to obtain a homogenized diffusion equation. This analysis assumes an unperturbed system that is an infinite, periodic lattice. The lattice is perturbed to be finite, but sufficiently large that the system is asymptotic with respect to the dimensionless parameter ϵ, defined as the ratio of the characteristic length of a single lattice element to the characteristic length of the reactor. The analysis makes it possible to reconstruct the angular flux with $O(\epsilon^2)$ error.

3.1 Asymptotic Expansion of the Continuous Energy Transport Equation

The starting point for the derivation of the asymptotic diffusion approximation is the Boltzmann transport equation for neutrons in a multiplying system:

$$\begin{aligned}(3.1)\qquad &\boldsymbol{\Omega}\cdot\nabla\psi(\boldsymbol{x},\boldsymbol{\Omega},E)+\Sigma_t(\boldsymbol{x},E)\psi(\boldsymbol{x},\boldsymbol{\Omega},E)\\ &\quad=\int_0^\infty\int_{4\pi}\Sigma_s(\boldsymbol{x},\boldsymbol{\Omega}'\cdot\boldsymbol{\Omega},E'\to E)\psi(\boldsymbol{x},\boldsymbol{\Omega}',E')\,\mathrm{d}\Omega'\,\mathrm{d}E'\\ &\qquad+(1-\rho)\,\frac{\chi(\boldsymbol{x},E)}{4\pi}\int_0^\infty\int_{4\pi}\nu\Sigma_f(\boldsymbol{x},E')\psi(\boldsymbol{x},\boldsymbol{\Omega}',E')\,\mathrm{d}\Omega'\,\mathrm{d}E'\,.\end{aligned}$$

First, we define an unperturbed system to be an infinite, periodic lattice. The perturbed system is large but finite, resulting in a small change to the eigenvalue.

The perturbation parameter, ϵ, is defined to be the ratio of the characteristic length of a lattice element, l_c, to the characteristic length of the reactor, L_c. Thus, $\epsilon = l_c/L_c$, which is assumed to be small, and the reactor system is asymptotic with respect to ϵ. We assume that both the macroscopic cross sections and the characteristic length of a lattice element are $O(1)$.

One expects that the neutron flux will, to leading order, be composed of a "slowly varying" amplitude component and a "rapidly varying" periodic component. Therefore, we define two spatial variables:

$$\boldsymbol{y} = \boldsymbol{x} = \text{“fast”, periodic spatial variable}\,, \tag{3.2a}$$

$$\boldsymbol{z} = \epsilon\boldsymbol{x} = \text{“slow”, non-periodic spatial variable}\,. \tag{3.2b}$$

Note that over a single cell, $\boldsymbol{y} = O(1)$, and over the entire reactor, $\boldsymbol{z} = O(1)$.

The system is assumed to have a periodic or "lattice" spatial structure, and so we write:

$$\Sigma_r(\boldsymbol{x}, E) = \Sigma_r(\boldsymbol{y}, E)\,, \qquad r = t, s, f\,. \tag{3.3a}$$

We furthermore assume that each lattice element is symmetric about its center. The angular flux can be written in terms of the fast and slow spatial variables:

$$\psi(\boldsymbol{x}, \boldsymbol{\Omega}, E) = \Psi(\boldsymbol{y}, \boldsymbol{z}, \boldsymbol{\Omega}, E)\,. \tag{3.3b}$$

The scaled spatial variables $\boldsymbol{y}$ and $\boldsymbol{z}$ are treated as independent. Thus, Ψ is a periodic function of $\boldsymbol{y}$, but not of $\boldsymbol{z}$. Also, we note that the gradient operator in the scaled system is:

$$\nabla\psi(\boldsymbol{x}, \boldsymbol{\Omega}, E) = \nabla_y\Psi(\boldsymbol{y}, \boldsymbol{z}, \boldsymbol{\Omega}, E) + \epsilon\nabla_z\Psi(\boldsymbol{y}, \boldsymbol{z}, \boldsymbol{\Omega}, E)\,. \tag{3.4}$$

The angular flux and reactivity are now expanded in powers of ϵ:

$$\Psi(\boldsymbol{y},\boldsymbol{z},\boldsymbol{\Omega},E)=\Psi_0(\boldsymbol{y},\boldsymbol{z},\boldsymbol{\Omega},E)+\epsilon\Psi_1(\boldsymbol{y},\boldsymbol{z},\boldsymbol{\Omega},E)+\epsilon^2\Psi_2(\boldsymbol{y},\boldsymbol{z},\boldsymbol{\Omega},E)+\cdots\,, \tag{3.5a}$$

$$\rho=\rho_0+\epsilon\rho_1+\epsilon^2\rho_2\,. \tag{3.5b}$$

The angular flux is represented by an infinite power series expansion, while the reactivity is represented by a quadratic power series expansion. The quadratic power series expansion is the simplest expansion that yields a systematically derived diffusion approximation. Higher order terms can be included in the expansion of the reactivity, but their inclusion ultimately has no effect on the diffusion approximation derived here.

Introducing Eqs. (3.3a)-(3.4) into Eq. (3.1), we obtain:

(3.6)

$$\begin{aligned}
&[\boldsymbol{\Omega}\cdot[\epsilon\nabla_z+\nabla_y]+\Sigma_t(\boldsymbol{y},E)]\\
&\qquad\times\left[\Psi_0(\boldsymbol{y},\boldsymbol{z},\boldsymbol{\Omega},E)+\epsilon\Psi_1(\boldsymbol{y},\boldsymbol{z},\boldsymbol{\Omega},E)+\epsilon^2\Psi_2(\boldsymbol{y},\boldsymbol{z},\boldsymbol{\Omega},E)+\cdots\right]\\
&=\int_0^\infty\int_{4\pi}\Sigma_s(\boldsymbol{y},\boldsymbol{\Omega}'\cdot\boldsymbol{\Omega},E'\to E)\\
&\qquad\times\left[\Psi_0(\boldsymbol{y},\boldsymbol{z},\boldsymbol{\Omega}',E')+\epsilon\Psi_1(\boldsymbol{y},\boldsymbol{z},\boldsymbol{\Omega}',E')+\epsilon^2\Psi_2(\boldsymbol{y},\boldsymbol{z},\boldsymbol{\Omega}',E')+\cdots\right]\,\mathrm{d}\Omega'\,\mathrm{d}E'\\
&\quad+\left(1-\rho_0-\epsilon\rho_1-\epsilon^2\rho_2\right)\frac{\chi(\boldsymbol{y},E)}{4\pi}\int_0^\infty\int_{4\pi}\nu\Sigma_f(\boldsymbol{y},E')\\
&\qquad\times\left[\Psi_0(\boldsymbol{y},\boldsymbol{z},\boldsymbol{\Omega}',E')+\epsilon\Psi_1(\boldsymbol{y},\boldsymbol{z},\boldsymbol{\Omega}',E')+\epsilon^2\Psi_2(\boldsymbol{y},\boldsymbol{z},\boldsymbol{\Omega}',E')+\cdots\right]\,\mathrm{d}\Omega'\,\mathrm{d}E'\,.
\end{aligned}$$

Now we equate the coefficients of different powers of epsilon. The first four equa-

tions in the series are:

(3.7)

$$\begin{aligned}\epsilon^0: \qquad & L\Psi_0(\boldsymbol{y},\boldsymbol{z},\boldsymbol{\Omega},E)\\ &= \boldsymbol{\Omega}\cdot\nabla_y\Psi_0(\boldsymbol{y},\boldsymbol{z},\boldsymbol{\Omega},E)+\Sigma_t(\boldsymbol{y},E)\Psi_0(\boldsymbol{y},\boldsymbol{z},\boldsymbol{\Omega},E)\\ &\quad -\int_0^\infty\int_{4\pi}\Sigma_s(\boldsymbol{y},\boldsymbol{\Omega}'\cdot\boldsymbol{\Omega},E'\to E)\Psi_0(\boldsymbol{y},\boldsymbol{z},\boldsymbol{\Omega}',E')\,\mathrm{d}\Omega'\,\mathrm{d}E'\\ &\quad -(1-\rho_0)\,\frac{\chi(\boldsymbol{y},E)}{4\pi}\int_0^\infty\int_{4\pi}\nu\Sigma_f(\boldsymbol{y},E')\Psi_0(\boldsymbol{y},\boldsymbol{z},\boldsymbol{\Omega}',E')\,\mathrm{d}\Omega'\,\mathrm{d}E'\,,\\ &= 0\,,\end{aligned}$$

(3.8) $$\begin{aligned}\epsilon^1: \qquad & L\Psi_1(\boldsymbol{y},\boldsymbol{z},\boldsymbol{\Omega},E)\\ &= -\boldsymbol{\Omega}\cdot\nabla_z\Psi_0(\boldsymbol{y},\boldsymbol{z},\boldsymbol{\Omega},E)\\ &\quad -\rho_1\frac{\chi(\boldsymbol{y},E)}{4\pi}\int_0^\infty\int_{4\pi}\nu\Sigma_f(\boldsymbol{y},E')\Psi_0(\boldsymbol{y},\boldsymbol{z},\boldsymbol{\Omega}',E')\,\mathrm{d}\Omega'\,\mathrm{d}E'\,,\end{aligned}$$

(3.9) $$\begin{aligned}\epsilon^2: \qquad & L\Psi_2(\boldsymbol{y},\boldsymbol{z},\boldsymbol{\Omega},E)\\ &= -\boldsymbol{\Omega}\cdot\nabla_z\Psi_1(\boldsymbol{y},\boldsymbol{z},\boldsymbol{\Omega},E)\\ &\quad -\rho_1\frac{\chi(\boldsymbol{y},E)}{4\pi}\int_0^\infty\int_{4\pi}\nu\Sigma_f(\boldsymbol{y},E')\Psi_1(\boldsymbol{y},\boldsymbol{z},\boldsymbol{\Omega}',E')\,\mathrm{d}\Omega'\,\mathrm{d}E'\\ &\quad -\rho_2\frac{\chi(\boldsymbol{y},E)}{4\pi}\int_0^\infty\int_{4\pi}\nu\Sigma_f(\boldsymbol{y},E')\Psi_0(\boldsymbol{y},\boldsymbol{z},\boldsymbol{\Omega}',E')\,\mathrm{d}\Omega'\,\mathrm{d}E'\,,\end{aligned}$$

(3.10) $$\begin{aligned}\epsilon^3: \qquad & L\Psi_3(\boldsymbol{y},\boldsymbol{z},\boldsymbol{\Omega},E)\\ &= -\boldsymbol{\Omega}\cdot\nabla_z\Psi_2(\boldsymbol{y},\boldsymbol{z},\boldsymbol{\Omega},E)\\ &\quad -\rho_1\frac{\chi(\boldsymbol{y},E)}{4\pi}\int_0^\infty\int_{4\pi}\nu\Sigma_f(\boldsymbol{y},E')\Psi_2(\boldsymbol{y},\boldsymbol{z},\boldsymbol{\Omega}',E')\,\mathrm{d}\Omega'\,\mathrm{d}E'\\ &\quad -\rho_2\frac{\chi(\boldsymbol{y},E)}{4\pi}\int_0^\infty\int_{4\pi}\nu\Sigma_f(\boldsymbol{y},E')\Psi_1(\boldsymbol{y},\boldsymbol{z},\boldsymbol{\Omega}',E')\,\mathrm{d}\Omega'\,\mathrm{d}E'\,.\end{aligned}$$

We now discuss an important property of the operator L. Suppose that $g(\boldsymbol{y},\boldsymbol{\Omega},E)$ is a symmetric function of $(\boldsymbol{y},\boldsymbol{\Omega})$:

(3.11a) $$g(\boldsymbol{y},\boldsymbol{\Omega},E)=g(-\boldsymbol{y},-\boldsymbol{\Omega},E)\,.$$

Then:

$$\begin{aligned}\boldsymbol{\Omega}\cdot\nabla_y g(\boldsymbol{y},\boldsymbol{\Omega},E) &= \boldsymbol{\Omega}\cdot\nabla_y\big[g(-\boldsymbol{y},-\boldsymbol{\Omega},E)\big]\,,\\ &= \boldsymbol{\Omega}\cdot\nabla_y g(-\boldsymbol{y},-\boldsymbol{\Omega},E)(-1)\,,\\ &= -\boldsymbol{\Omega}\cdot\nabla_y g(-\boldsymbol{y},-\boldsymbol{\Omega},E)\,.\end{aligned}$$

Thus, $\boldsymbol{\Omega}\cdot\nabla_y g$ is also symmetric. From Eq. (3.7), it follows that Lg is symmetric:

$$Lg(\boldsymbol{y},\boldsymbol{\Omega},E) = Lg(-\boldsymbol{y},-\boldsymbol{\Omega},E)\,. \tag{3.11b}$$

Similarly, if $h(\boldsymbol{y},\boldsymbol{\Omega},E)$ is an antisymmetric function of $(\boldsymbol{y},\boldsymbol{\Omega})$:

$$h(\boldsymbol{y},\boldsymbol{\Omega},E) = -h(-\boldsymbol{y},-\boldsymbol{\Omega},E)\,, \tag{3.12a}$$

then Lh is also antisymmetric:

$$Lh(\boldsymbol{y},\boldsymbol{\Omega},E) = -Lh(-\boldsymbol{y},-\boldsymbol{\Omega},E)\,. \tag{3.12b}$$

Thus, the operator L preserves the symmetry or antisymmetry of the functions on which it operates.

3.2 Solution of the Zeroth-Order Equation

The operator L defined by Eq. (3.7) operates only on the periodic variable $\boldsymbol{y}$ and the angular variable $\boldsymbol{\Omega}$. Thus, L has periodic boundary conditions. If one defines the lattice appropriately, the periodic boundaries become reflecting boundaries. Then with ρ_0 chosen to be the reactivity for the infinite periodic system, with eigenfunction $f_0(\boldsymbol{y},\boldsymbol{\Omega},E)$, the general solution of Eq. (3.7) is:

$$\boxed{\Psi_0(\boldsymbol{y},\boldsymbol{z},\boldsymbol{\Omega},E) = f_0(\boldsymbol{y},\boldsymbol{\Omega},E)A_0(\boldsymbol{z})\,,} \tag{3.13}$$

where $A_0(\boldsymbol{z})$ is unspecified. Thus, as might be expected, the leading-order neutron flux is the product of a "slowly-varying" amplitude component, $A_0(\boldsymbol{z})$, and a

"rapidly varying" periodic component, $f_0(\boldsymbol{y}, \boldsymbol{\Omega}, E)$. Since the lattice cells are defined to be symmetric in $(\boldsymbol{y})$ about their centers, the lattice eigenfunction $f_0(\boldsymbol{y}, \boldsymbol{\Omega}, E)$ is symmetric in $(\boldsymbol{y}, \boldsymbol{\Omega})$ about the center of each cell. The eigenfunctions are unique to within a normalization constant.

The reactivity, ρ_0, and eigenfunction, $f_0(\boldsymbol{y}, \boldsymbol{\Omega}, E)$, for the infinite periodic system satisfy:

(3.14)

$$\begin{aligned} Lf_0(\boldsymbol{y}, \boldsymbol{\Omega}, E) &= \boldsymbol{\Omega} \cdot \nabla_y f_0(\boldsymbol{y}, \boldsymbol{\Omega}, E) + \Sigma_t(\boldsymbol{y}, E) f_0(\boldsymbol{y}, \boldsymbol{\Omega}, E) \\ &\quad - \int_0^\infty \int_{4\pi} \Sigma_s(\boldsymbol{y}, \boldsymbol{\Omega}' \cdot \boldsymbol{\Omega}, E' \to E) f_0(\boldsymbol{y}, \boldsymbol{\Omega}', E') \, \mathrm{d}\Omega' \, \mathrm{d}E' \\ &\quad - (1 - \rho_0) \frac{\chi(\boldsymbol{y}, E)}{4\pi} \int_0^\infty \int_{4\pi} \nu\Sigma_f(\boldsymbol{y}, E') f_0(\boldsymbol{y}, \boldsymbol{\Omega}', E') \, \mathrm{d}\Omega' \, \mathrm{d}E' \,, \\ &= 0 \,. \end{aligned}$$

The normalization of f_0 is arbitrary, so long as the adjoint function f_0^* (defined in the next section) is normalized in the same way. In our work, we normalize f_0 such that the total fission source in a lattice cell is unity.

3.3 Solution of the First-Order Equation

Before Eq. (3.8) can be solved for Ψ_1, one must define an inner product and an adjoint operator for L. The inner product is defined as:

(3.15) $$\langle g, Lh \rangle = \int_{cell} \int_0^\infty \int_{4\pi} gLh \, \mathrm{d}\Omega \, \mathrm{d}E \, \mathrm{d}V \,,$$

and the adjoint operator L^* satisfies:

$$\langle g, Lh \rangle = \langle L^* g, h \rangle \,.$$

It is easy to show that the adjoint infinite-lattice transport operator is:

(3.16)

$$\begin{aligned} L^* f_0^*(\boldsymbol{y}, \boldsymbol{\Omega}, E) = &-\boldsymbol{\Omega} \cdot \nabla_y g(\boldsymbol{y}, \boldsymbol{\Omega}, E) + \Sigma_t(\boldsymbol{y}, E) f_0^*(\boldsymbol{y}, \boldsymbol{\Omega}, E) \\ &- \int_0^\infty \int_{4\pi} \Sigma_s(\boldsymbol{y}, \boldsymbol{\Omega}' \cdot \boldsymbol{\Omega}, E \to E') f_0^*(\boldsymbol{y}, \boldsymbol{\Omega}', E') \, \mathrm{d}\Omega' \, \mathrm{d}E' \\ &- (1 - \rho_0) \frac{\nu \Sigma_f(\boldsymbol{y}, E)}{4\pi} \int_0^\infty \int_{4\pi} \chi(\boldsymbol{y}, E') f_0^*(\boldsymbol{y}, \boldsymbol{\Omega}', E') \, \mathrm{d}\Omega' \, \mathrm{d}E' \, . \end{aligned}$$

This operator has periodic boundary conditions, as did the forward operator. The adjoint equation has the same eigenvalue as the forward equation, and the adjoint eigenfunction f_0^* satisfies:

(3.17)
$$L^* f_0^*(\boldsymbol{y}, \boldsymbol{\Omega}, E) = 0 \, .$$

We now introduce the *Fredholm Alternative Theorem* (FAT). Consider an operator M and adjoint operator M^* such that:

$$Mh = 0 \qquad \text{and} \qquad M^* h^* = 0 \, .$$

The FAT states that if there exists non-trivial solutions to the above equations, then [62]:

1. $Mh = 0$ and $M^* h^* = 0$ have the same number of linearly independent solutions,
2. $Mh = g$ has a particular solution if and only if g is orthogonal to all the solutions of $M^* h^* = 0$. Expressed another way, $\langle g, h^* \rangle = 0$,
3. The general solution to $Mh = g$ is given by:

$$h = h_{particular} + \sum_{i=1}^{N} a_i h_{homogeneous} \, ,$$

where N is the number of linearly independent non-trivial solutions to the homogeneous equation and the a_i are arbitrary constants.

In this work, $M = L$ and $M^* = L^*$, and the corresponding homogeneous solutions are $h = f_0$ and $h^* = f_0^*$. Condition 2 of the FAT gives us a solvability condition for the inhomogeneous asymptotic equations, Eqs. (3.8)-(3.10), while Condition 3 tells us the form of their solutions.

We now apply the solvability condition to Eq. (3.8) by operating on the equation by $\int_{cell}\int_0^\infty\int_{4\pi} f_0^*(\boldsymbol{y},\boldsymbol{\Omega},E)(\cdot)\mathrm{d}\Omega\,\mathrm{d}E\,\mathrm{d}V$. The left side becomes:

$$\langle f_0^*, L\Psi_1\rangle = \langle L^* f_0^*, \Psi_1\rangle = \langle 0, \Psi_1\rangle = 0\,, \tag{3.18}$$

and thus the right side must satisfy:

$$\begin{aligned} 0 = &-\int_{cell}\int_0^\infty\int_{4\pi} f_0^*(\boldsymbol{y},\boldsymbol{\Omega},E)\boldsymbol{\Omega}\cdot\nabla_z\Psi_0(\boldsymbol{y},\boldsymbol{z},\boldsymbol{\Omega},E)\,\mathrm{d}\Omega\,\mathrm{d}E\,\mathrm{d}V \\ &-\frac{\rho_1}{4\pi}\int_{cell}\int_0^\infty\int_{4\pi} f_0^*(\boldsymbol{y},\boldsymbol{\Omega},E)\chi(\boldsymbol{y},E) \\ &\quad\times\left[\int_0^\infty\int_{4\pi}\nu\Sigma_f(\boldsymbol{y},E')\Psi_0(\boldsymbol{y},\boldsymbol{z},\boldsymbol{\Omega}',E')\,\mathrm{d}\Omega'\,\mathrm{d}E'\right]\mathrm{d}\Omega\,\mathrm{d}E\,\mathrm{d}V\,. \end{aligned}$$

Introducing Eq. (3.13) yields:

$$\begin{aligned} 0 = &-\nabla_z\cdot A_0(\boldsymbol{z})\int_{cell}\int_0^\infty\int_{4\pi}\boldsymbol{\Omega} f_0^*(\boldsymbol{y},\boldsymbol{\Omega},E)f_0(\boldsymbol{y},\boldsymbol{\Omega},E)\,\mathrm{d}\Omega\,\mathrm{d}E\,\mathrm{d}V \\ &-\frac{\rho_1}{4\pi}A_0(\boldsymbol{z})\int_{cell}\int_0^\infty\int_{4\pi} f_0^*(\boldsymbol{y},\boldsymbol{\Omega},E)\chi(\boldsymbol{y},E) \\ &\quad\times\left[\int_0^\infty\int_{4\pi}\nu\Sigma_f(\boldsymbol{y},E')f_0(\boldsymbol{y},\boldsymbol{\Omega}',E')\,\mathrm{d}\Omega'\,\mathrm{d}E'\right]\mathrm{d}\Omega\,\mathrm{d}E\,\mathrm{d}V\,. \end{aligned}$$

Because $f_0^*(\boldsymbol{y},\boldsymbol{\Omega},E)$ and $f_0(\boldsymbol{y},\boldsymbol{\Omega},E)$ are symmetric functions of $(\boldsymbol{y},\boldsymbol{\Omega})$ about the center of each cell, $\boldsymbol{\Omega} f_0^*(\boldsymbol{y},\boldsymbol{\Omega},E)f_0(\boldsymbol{y},\boldsymbol{\Omega},E)$ is an antisymmetric function of $(\boldsymbol{y},\boldsymbol{\Omega})$ about the center of each cell. This implies that the first integral in the above equation is 0. Since f_0, f_0^*, χ, and $\nu\Sigma_f$ are nonnegative and not uniformly 0, it follows that:

$$\boxed{\rho_1 = 0\,.} \tag{3.19}$$

Introducing Eqs. (3.19) and (3.13) into Eq. (3.8) yields an equation for which a

nontrivial solution exists:

$$L\Psi_1(\boldsymbol{y},\boldsymbol{z},\boldsymbol{\Omega},E) = -\boldsymbol{\Omega}\cdot\nabla_z A_0(\boldsymbol{z}) f_0(\boldsymbol{y},\boldsymbol{\Omega},E)\,. \tag{3.20}$$

Equation (3.20) has a particular solution of the form:

$$\begin{aligned}\Psi_{1,particular}(\boldsymbol{y},\boldsymbol{z},\boldsymbol{\Omega},E) &= -\left[L^{-1}\boldsymbol{\Omega} f_0(\boldsymbol{y},\boldsymbol{\Omega},E)\right]\cdot\nabla_z A_0(\boldsymbol{z})\,,\\ &= -\boldsymbol{f}_1(\boldsymbol{y},\boldsymbol{\Omega},E)\cdot\nabla_z A_0(\boldsymbol{z})\,.\end{aligned}$$

The "pseudo inverse" operator L^{-1} is not unique, but with no loss of generality we make it unique by requiring that:

$$0 = \int_{cell}\int_0^\infty\int_{4\pi} f_0^*(\boldsymbol{y},\boldsymbol{\Omega},E) L^{-1}\boldsymbol{\Omega} f_0(\boldsymbol{y},\boldsymbol{\Omega},E)\,\mathrm{d}\Omega\,\mathrm{d}E\,\mathrm{d}V\,. \tag{3.21}$$

The effect of this condition is to remove the symmetric component of $L^{-1}\boldsymbol{\Omega} f_0 = f_1$, thereby guaranteeing that the function f_1 is antisymmetric in $(\boldsymbol{y},\boldsymbol{\Omega})$. One could presumably use any symmetric function in place of f_0^* to accomplish this, but in this work f_0^* is used exclusively.

Since the general homogeneous solution of Eq. (3.20) is obviously:

$$\Psi_{1,homogeneous} = f_0(\boldsymbol{y},\boldsymbol{\Omega},E) A_1(\boldsymbol{z})\,,$$

where $A_1(\boldsymbol{z})$ is unspecified, the general solution of Eq. (3.20) is (by Condition 3 of the FAT):

$$\boxed{\Psi_1(\boldsymbol{y},\boldsymbol{z},\boldsymbol{\Omega},E) = -\boldsymbol{f}_1(\boldsymbol{y},\boldsymbol{\Omega},E)\cdot\nabla_z A_0(\boldsymbol{z}) + f_0(\boldsymbol{y},\boldsymbol{\Omega},E) A_1(\boldsymbol{z})\,,} \tag{3.22}$$

where:

$$\boldsymbol{f}_1(\boldsymbol{y},\boldsymbol{\Omega},E) = L^{-1}\left(\boldsymbol{\Omega} f_0(\boldsymbol{y},\boldsymbol{\Omega},E)\right)\,. \tag{3.23}$$

Notice that the first term on the right side of Eq. (3.22) is anti-symmetric in $(\boldsymbol{y},\boldsymbol{\Omega})$, while the second term is symmetric.

3.4 Solution of the Second-Order Equation

3.4.1 Obtaining a Homogenized Diffusion Equation From the Second Order Equation

We can now derive an anisotropic diffusion equation from Eq. (3.9). In order to conserve space, we no longer explicitly write the variable dependencies of each function.

First, we introduce Eq. (3.19) into Eq. (3.9) to obtain:

$$L\Psi_2 = -\mathbf{\Omega}\cdot\nabla_z\Psi_1 - \rho_2\frac{\chi}{4\pi}\int_0^\infty\int_{4\pi}\nu\Sigma_f\Psi_0\,\mathrm{d}\Omega'\,\mathrm{d}E'\,. \tag{3.24}$$

Operating on this equation by $\int_{cell}\int_0^\infty\int_{4\pi} f_0^*(\boldsymbol{y},\mathbf{\Omega},E)(\cdot)\mathrm{d}\Omega\,\mathrm{d}E\,\mathrm{d}V$, the left side again vanishes:

$$\langle f_0^*, L\Psi_2\rangle = \langle L^* f_0^*, \Psi_2\rangle = \langle 0, \Psi_2\rangle = 0\,.$$

Therefore, the right side must also vanish:

$$\begin{aligned}0 = &-\int_{cell}\int_0^\infty\int_{4\pi} f_0^*\mathbf{\Omega}\cdot\nabla_z\Psi_1\,\mathrm{d}\Omega\,\mathrm{d}E\,\mathrm{d}V\\ &-\frac{\rho_2}{4\pi}\int_{cell}\int_0^\infty\int_{4\pi} f_0^*\chi\left[\int_0^\infty\int_{4\pi}\nu\Sigma_f\Psi_0\,\mathrm{d}\Omega'\,\mathrm{d}E'\right]\mathrm{d}\Omega\,\mathrm{d}E\,\mathrm{d}V\,.\end{aligned}$$

Introducing Eqs. (3.13) and (3.22) yields the solvability condition:

$$\begin{aligned}0 = &-\int_{cell}\int_0^\infty\int_{4\pi} f_0^*\mathbf{\Omega}\cdot\nabla_z\left[-\boldsymbol{f}_1\cdot\nabla_z A_0 + A_1 f_0\right]\mathrm{d}\Omega\,\mathrm{d}E\,\mathrm{d}V\\ &-\frac{\rho_2}{4\pi}\int_{cell}\int_0^\infty\int_{4\pi} f_0^*\chi\left[\int_0^\infty\int_{4\pi}\nu\Sigma_f f_0 A_0\,\mathrm{d}\Omega'\,\mathrm{d}E'\right]\mathrm{d}\Omega\,\mathrm{d}E\,\mathrm{d}V\,,\\ = &\nabla_z\cdot\left[\int_{cell}\int_0^\infty\int_{4\pi}\mathbf{\Omega} f_0^*\boldsymbol{f}_1\,\mathrm{d}\Omega\,\mathrm{d}E\,\mathrm{d}V\right]\cdot\nabla_z A_0\\ &-\left[\int_{cell}\int_0^\infty\int_{4\pi}\mathbf{\Omega} f_0^* f_0\,\mathrm{d}\Omega\,\mathrm{d}E\,\mathrm{d}V\right]\cdot\nabla_z A_1\\ &-\frac{\rho_2}{4\pi}\left[\int_{cell}\left(\int_0^\infty\chi F_0^*\,\mathrm{d}E\right)\left(\int_0^\infty\nu\Sigma_f F_0\,\mathrm{d}E\right)\mathrm{d}V\right]A_0\,.\end{aligned} \tag{3.25}$$

Here the scalar lattice functions are defined by:

$$F_0(\boldsymbol{y},E) = \int_{4\pi} f_0(\boldsymbol{y},\mathbf{\Omega},E)\,\mathrm{d}\Omega\,, \tag{3.26}$$

$$F_0^*(\boldsymbol{y},E)=\int_{4\pi} f_0^*(\boldsymbol{y},\boldsymbol{\Omega},E)\,\mathrm{d}\Omega\,. \tag{3.27}$$

The second integral on the right side of Eq. (3.25) is 0 because $\boldsymbol{\Omega}f_0^*f_0$ is an antisymmetric function of $(\boldsymbol{y},\boldsymbol{\Omega})$. Thus, Eq. (3.25) reduces to:

$$\begin{aligned}-\nabla_z\cdot\left[\int_{cell}\int_0^\infty\int_{4\pi}\boldsymbol{\Omega}f_0^*\boldsymbol{f}_1\,\mathrm{d}\Omega\,\mathrm{d}E\,\mathrm{d}V\right]\cdot\nabla_z A_0\\ =-\frac{\rho_2}{4\pi}\left[\int_{cell}\left(\int_0^\infty\chi F_0^*\,\mathrm{d}E\right)\left(\int_0^\infty\nu\Sigma_f F_0\,\mathrm{d}E\right)\,\mathrm{d}V\right]A_0\,.\end{aligned} \tag{3.28}$$

Multiplying the above equation by ϵ^2 and using $\epsilon^2\rho_2=\rho-\rho_0$, we obtain:

$$\begin{aligned}-\epsilon\nabla_z\cdot\left[\int_{cell}\int_0^\infty\int_{4\pi}\boldsymbol{\Omega}f_0^*\boldsymbol{f}_1\,\mathrm{d}\Omega\,\mathrm{d}E\,\mathrm{d}V\right]\cdot\epsilon\nabla_z A_0\\ =-\frac{\rho-\rho_0}{4\pi}\left[\int_{cell}\left(\int_0^\infty\chi F_0^*\,\mathrm{d}E\right)\left(\int_0^\infty\nu\Sigma_f F_0\,\mathrm{d}E\right)\,\mathrm{d}V\right]A_0\,.\end{aligned} \tag{3.29}$$

Next, we operate on Eq. (3.14) by $\int_{cell}\int_0^\infty\int_{4\pi}(\cdot)\,\mathrm{d}\Omega\,\mathrm{d}E\,\mathrm{d}V$ to obtain an expression for ρ_0:

$$\begin{aligned}&\int_{cell}\int_0^\infty\int_{4\pi}\boldsymbol{\Omega}\cdot\nabla_y f_0\,\mathrm{d}\Omega\,\mathrm{d}E\,\mathrm{d}V+\int_{cell}\int_0^\infty\int_{4\pi}\Sigma_t f_0\,\mathrm{d}\Omega\,\mathrm{d}E\,\mathrm{d}V\\ &\quad-\int_{cell}\int_0^\infty\int_{4\pi}\int_0^\infty\int_{4\pi}\Sigma_s(\boldsymbol{y},\boldsymbol{\Omega}'\cdot\boldsymbol{\Omega},E'\to E)f_0(\boldsymbol{y},\boldsymbol{\Omega}',E')\,\mathrm{d}\Omega'\,\mathrm{d}E'\,\mathrm{d}\Omega\,\mathrm{d}E\,\mathrm{d}V\\ &\quad=(1-\rho_0)\int_{cell}\int_0^\infty\int_{4\pi}\frac{\chi}{4\pi}\int_0^\infty\int_{4\pi}\nu\Sigma_f f_0\,\mathrm{d}\Omega'\,\mathrm{d}E'\,\mathrm{d}\Omega\,\mathrm{d}E\,\mathrm{d}V\,.\end{aligned} \tag{3.30}$$

The first term satisfies:

$$\int_{cell}\int_0^\infty\int_{4\pi}\boldsymbol{\Omega}\cdot\nabla_y f_0\,\mathrm{d}\Omega\,\mathrm{d}E\,\mathrm{d}V=\int_{\partial(cell)}\int_0^\infty\int_{4\pi}\boldsymbol{\Omega}\cdot\boldsymbol{n}f_0\,\mathrm{d}\Omega\,\mathrm{d}E\,\mathrm{d}S=0\,,$$

because $f_0(\boldsymbol{y},\boldsymbol{\Omega})$ is periodic. Introducing Eq. (3.27) into Eq. (3.30) and using $\Sigma_a(\boldsymbol{y},E)=\Sigma_t(\boldsymbol{y},E)-\Sigma_{s,0}(\boldsymbol{y},E)=\Sigma_t(\boldsymbol{y},E)-\int_0^\infty\int_{4\pi}\Sigma_s(\boldsymbol{y},\boldsymbol{\Omega}'\cdot\boldsymbol{\Omega},E\to E')\,\mathrm{d}\Omega'\,\mathrm{d}E'$, we obtain:

$$\int_{cell}\int_0^\infty\Sigma_a F_0\,\mathrm{d}E\,\mathrm{d}V=(1-\rho_0)\int_{cell}\int_0^\infty\nu\Sigma_f F_0\,\mathrm{d}E\,\mathrm{d}V\,,$$

or:

$$\rho_0 = 1 - \frac{\displaystyle\int_{cell}\int_0^\infty \Sigma_a F_0 \,\mathrm{d}E\,\mathrm{d}V}{\displaystyle\int_{cell}\int_0^\infty \nu\Sigma_f F_0 \,\mathrm{d}E\,\mathrm{d}V}\,. \tag{3.31}$$

Introducing Eq. (3.31) into Eq. (3.29) yields:

$$\begin{aligned}
&-\epsilon\nabla_z\cdot\left[\int_{cell}\int_0^\infty\int_{4\pi}\boldsymbol{\Omega}f_0^*\boldsymbol{f}_1\,\mathrm{d}\Omega\,\mathrm{d}E\,\mathrm{d}V\right]\cdot\epsilon\nabla_z A_0\\
&\quad=\frac{1}{4\pi}\left[1-\rho-\frac{\int_{cell}\int_0^\infty\Sigma_a F_0\,\mathrm{d}E\,\mathrm{d}V}{\int_{cell}\int_0^\infty\nu\Sigma_f F_0\,\mathrm{d}E\,\mathrm{d}V}\right]\\
&\qquad\times\left[\int_{cell}\left(\int_0^\infty\chi F_0^*\,\mathrm{d}E\right)\left(\int_0^\infty\nu\Sigma_f F_0\,\mathrm{d}E\right)\,\mathrm{d}V\right]A_0\,.
\end{aligned}$$

Multiplying both sides of the above equation by:

$$\frac{4\pi\displaystyle\int_{cell}\int_0^\infty\nu\Sigma_f F_0\,\mathrm{d}E\,\mathrm{d}V}{\displaystyle\int_{cell}\left(\int_0^\infty\chi F_0^*\,\mathrm{d}E\right)\left(\int_0^\infty\nu\Sigma_f F_0\,\mathrm{d}E\right)\,\mathrm{d}V\int_{cell}\int_0^\infty F_0\,\mathrm{d}E\,\mathrm{d}V}\,,$$

we obtain the following monoenergetic homogenized diffusion equation with an anisotropic diffusion tensor:

$$-\epsilon\nabla_z\cdot\overline{\boldsymbol{D}}\cdot\epsilon\nabla_z A_0(\boldsymbol{z})+\overline{\Sigma_a}A_0(\boldsymbol{z})=(1-\rho)\,\overline{\nu\Sigma_f}A_0(\boldsymbol{z})\,, \tag{3.32}$$

where $\overline{\Sigma_a}$ and $\overline{\nu\Sigma_f}$ are the usual flux weighted, homogenized cross sections:

$$\overline{\Sigma_a}=\frac{\displaystyle\int_{cell}\int_0^\infty\Sigma_a F_0\,\mathrm{d}E\,\mathrm{d}V}{\displaystyle\int_{cell}\int_0^\infty F_0\,\mathrm{d}E\,\mathrm{d}V}\,, \tag{3.33}$$

$$\overline{\nu\Sigma_f}=\frac{\displaystyle\int_{cell}\int_0^\infty\nu\Sigma_f F_0\,\mathrm{d}E\,\mathrm{d}V}{\displaystyle\int_{cell}\int_0^\infty F_0\,\mathrm{d}E\,\mathrm{d}V}\,, \tag{3.34}$$

and $\overline{\boldsymbol{D}}$ is the homogenized, anisotropic diffusion tensor defined by:

$$\overline{D_{ij}}=4\pi\frac{\displaystyle\int_{cell}\int_0^\infty\int_{4\pi}\Omega_i f_0^* f_{1,j}\,\mathrm{d}\Omega\,\mathrm{d}E\,\mathrm{d}V}{\displaystyle\int_{cell}\left(\int_0^\infty\chi F_0^*\,\mathrm{d}E\right)\left(\int_0^\infty\nu\Sigma_f F_0\,\mathrm{d}E\right)\,\mathrm{d}V}\frac{\displaystyle\int_{cell}\int_0^\infty\nu\Sigma_f F_0\,\mathrm{d}E\,\mathrm{d}V}{\displaystyle\int_{cell}\int_0^\infty F_0\,\mathrm{d}E\,\mathrm{d}V}\,, \tag{3.35}$$

$$i=1,2,3\qquad j=1,2,3\,.$$

3.4.2 An Expression for Ψ_2

If the solvability condition described in the previous section is satisfied, the FAT can be applied to Eq. (3.24). Therefore Eq. (3.24) has an infinite number of solutions of the form $\Psi_2 = \Psi_{2,particular} + \Psi_{2,homogeneous}$ where $\Psi_{2,particular}$ is of the form

$$\Psi_{2,particular} = L^{-1}\left(-\boldsymbol{\Omega}\cdot\nabla_z\Psi_1 - \rho_2\frac{\chi}{4\pi}\int_0^\infty\int_{4\pi}\nu\Sigma_f\Psi_0\,\mathrm{d}\Omega'\,\mathrm{d}E'\right).$$

Introducing Eqs. (3.13) and (3.22) yields:

$$\Psi_{2,particular} = L^{-1}\left(-\boldsymbol{\Omega}\cdot\nabla_z\left(-\boldsymbol{f}_1\cdot\nabla_z A_0 + f_0 A_1\right) - \rho_2\frac{\chi}{4\pi}\int_0^\infty\int_{4\pi}\nu\Sigma_f f_0 A_0\,\mathrm{d}\Omega'\,\mathrm{d}E'\right).$$

Again L is a linear operator that acts on $\boldsymbol{y}$ and $\boldsymbol{\Omega}$ but not $\boldsymbol{z}$. As before, the homogeneous equation has the same eigenfunction as $L\Psi_0 = 0$. Making use of these facts and introducing Eq. (3.23) yields:

$$\Psi_2 = \nabla_z\cdot L^{-1}\left(\boldsymbol{\Omega}\boldsymbol{f}_1\right)\cdot\nabla_z A_0 - \boldsymbol{f}_1\cdot\nabla_z A_1 - \rho_2 L^{-1}\left(\frac{\chi}{4\pi}\int_0^\infty\int_{4\pi}\nu\Sigma_f f_0\,\mathrm{d}\Omega'\,\mathrm{d}E'\right)A_0 + f_0 A_2\,. \tag{3.36}$$

As with Ψ_1, we make the particular solution unique by forcing the symmetric component of $\Psi_{2,particular}$ to vanish:

$$0 = \int_{cell}\int_0^\infty\int_{4\pi} f_0^*\Psi_{2,particular}\,\mathrm{d}\Omega\,\mathrm{d}E\,\mathrm{d}V\,. \tag{3.37}$$

3.5 Obtaining a Homogenized Diffusion Equation From the Third-Order Equation

One can now show that the amplitude function A_1 satisfies the same diffusion equation as A_0. First, we introduce Eq. (3.19) into Eq. (3.10) to obtain:

$$L\Psi_3 = -\boldsymbol{\Omega}\cdot\nabla_z\Psi_2 - \rho_2\frac{\chi}{4\pi}\int_0^\infty\int_{4\pi}\nu\Sigma_f\Psi_1\,\mathrm{d}\Omega'\,\mathrm{d}E'\,. \tag{3.38}$$

Again, we use the solvability condition to derive a diffusion equation for A_1. Operating on this equation by $\int_{cell}\int_0^\infty\int_{4\pi} f_0^*(\cdot)\mathrm{d}\Omega\,\mathrm{d}E\,\mathrm{d}V$, one again sees that the left side vanishes:

$$\langle f_0^*, L\Psi_3\rangle = \langle L^* f_0^*, \Psi_3\rangle = \langle 0, \Psi_3\rangle = 0\,.$$

Therefore, the right side must also vanish:

$$0 = -\int_{cell}\int_0^\infty\int_{4\pi} f_0^*\boldsymbol{\Omega}\cdot\nabla_z\Psi_2\,\mathrm{d}\Omega\,\mathrm{d}E\,\mathrm{d}V - \frac{\rho_2}{4\pi}\int_{cell}\int_0^\infty\int_{4\pi} f_0^*\chi\left[\int_0^\infty\int_{4\pi}\nu\Sigma_f\Psi_1\,\mathrm{d}\Omega'\,\mathrm{d}E'\right]\mathrm{d}\Omega\,\mathrm{d}E\,\mathrm{d}V\,. \tag{3.39}$$

At this point we note that each term contains a double integral over all angles $\boldsymbol{\Omega}$ and over all points $\boldsymbol{y}$ in the lattice element. Evaluating the double integral over a function that is symmetric in $(\boldsymbol{y},\boldsymbol{\Omega})$ yields a positive result if the symmetric function is non-negative and is not uniformly 0. However, if the integrand is antisymmetric in $(\boldsymbol{y},\boldsymbol{\Omega})$, the double integral will vanish.

The lattice element has been defined such that it has reflecting boundary conditions on all sides. Thus, the cross sections are symmetric about the center of the lattice element, as are the functions $f_0(\boldsymbol{y},\boldsymbol{\Omega},E)$ and $f_0^*(\boldsymbol{y},\boldsymbol{\Omega},E)$. Therefore, the functions $\boldsymbol{\Omega}f_0(\boldsymbol{y},\boldsymbol{\Omega},E)$ and $\boldsymbol{\Omega}f_0^*(\boldsymbol{y},\boldsymbol{\Omega},E)$ are antisymmetric in $(\boldsymbol{y},\boldsymbol{\Omega})$ about the center of the cell. Furthermore, as demonstrated earlier (Eqs. (3.11) and (3.12)) the operator L and its inverse L^{-1} preserve the symmetry or antisymmetry of functions on which they operate. Thus, $\boldsymbol{f}_1(\boldsymbol{y},\boldsymbol{\Omega},E)$ is antisymmetric, and $L^{-1}\left(\boldsymbol{\Omega}\boldsymbol{f}_1(\boldsymbol{y},\boldsymbol{\Omega},E)\right)$ is symmetric.

Upon inspection of Eq. (3.39), it is clear that the double integrals involving the symmetric components of Ψ_2 and the antisymmetric components of Ψ_1 will vanish. Thus, one need only consider the antisymmetric components of Ψ_2 and the symmetric components of Ψ_1.

Thus, introducing Eqs. (3.13), (3.22), and (3.36) into Eq. (3.39), we obtain:

$$
\begin{aligned}
&-\nabla_z \cdot \left[\int_{cell} \int_0^\infty \int_{4\pi} \boldsymbol{\Omega} f_0^* \boldsymbol{f}_1 \, \mathrm{d}\Omega \, \mathrm{d}E \, \mathrm{d}V \right] \cdot \nabla_z A_1 \\
&\qquad = -\frac{\rho_2}{4\pi} \left[\int_{cell} \left(\int_0^\infty \chi F_0^* \, \mathrm{d}E \right) \left(\int_0^\infty \nu\Sigma_f F_0 \, \mathrm{d}E \right) \, \mathrm{d}V \right] A_1 \, .
\end{aligned}
$$

We note the similarity between the preceding equation and Eq. (3.28), with the only difference being that $A_0(\boldsymbol{z})$ has been replaced with $A_1(\boldsymbol{z})$. Following the same procedure as in Section 3.4.1 yields the same diffusion equation for A_1 that was obtained for A_0:

$$
-\epsilon \nabla_z \cdot \overline{\boldsymbol{D}} \cdot \epsilon \nabla_z A_1(\boldsymbol{z}) + \overline{\Sigma_a} A_1(\boldsymbol{z}) = (1-\rho) \, \overline{\nu\Sigma_f} A_1(\boldsymbol{z}) \, . \tag{3.40}
$$

The coefficients in this equation are the same as those given by Eqs. (3.33)-(3.35).

3.6 Unscaling of the Diffusion Equation and Reconstruction of the Angular Flux

From Eqs. (3.5a), (3.13), and (3.22), we see that the detailed neutron flux can be reconstructed using:

$$
\begin{aligned}
\Psi(\boldsymbol{y}, \boldsymbol{z}, \boldsymbol{\Omega}, E) &= f_0(\boldsymbol{y}, \boldsymbol{\Omega}, E) A_0(\boldsymbol{z}) \\
&\quad + \epsilon \left(-\boldsymbol{f}_1(\boldsymbol{y}, \boldsymbol{\Omega}, E) \cdot \nabla_z A_0(\boldsymbol{z}) + f_0(\boldsymbol{y}, \boldsymbol{\Omega}, E) A_1(\boldsymbol{z}) \right) + O(\epsilon^2) \, .
\end{aligned}
$$

Since the error is $O(\epsilon^2)$, we can add an $O(\epsilon^2)$ term to the above equation without invalidating it. Adding $-\epsilon^2 \boldsymbol{f}_1(\boldsymbol{y}, \boldsymbol{\Omega}, E) \cdot \nabla_z A_1(\boldsymbol{z})$, we arrive at an equation in terms of the single amplitude function, $A(\boldsymbol{z}) = A_0(\boldsymbol{z}) + \epsilon A_1(\boldsymbol{z})$:

$$
\begin{aligned}
\Psi(\boldsymbol{y}, \boldsymbol{z}, \boldsymbol{\Omega}, E) &= f_0(\boldsymbol{y}, \boldsymbol{\Omega}, E) \left(A_0(\boldsymbol{z}) + \epsilon A_1(\boldsymbol{z}) \right) \\
&\quad - \epsilon \boldsymbol{f}_1(\boldsymbol{y}, \boldsymbol{\Omega}, E) \cdot \nabla_z \left(A_0(\boldsymbol{z}) + \epsilon A_1(\boldsymbol{z}) \right) + O(\epsilon^2) \\
&= f_0(\boldsymbol{y}, \boldsymbol{\Omega}, E) A(\boldsymbol{z}) - \epsilon \boldsymbol{f}_1(\boldsymbol{y}, \boldsymbol{\Omega}, E) \cdot \nabla_z A(\boldsymbol{z}) + O(\epsilon^2) \, .
\end{aligned} \tag{3.41}
$$

Next, we observe that $A(\boldsymbol{z}) = A(\epsilon\boldsymbol{x}) = \phi(\boldsymbol{x})$ and we note that $\epsilon\nabla_z A(\boldsymbol{z}) = \nabla\phi(\boldsymbol{x})$. Then, we write Eq. (3.41) in terms of the original spatial variable, $\boldsymbol{x}$, to obtain:

$$\boxed{\psi(\boldsymbol{x},\boldsymbol{\Omega},E) = f_0(\boldsymbol{x},\boldsymbol{\Omega},E)\phi(\boldsymbol{x}) - \boldsymbol{f}_1(\boldsymbol{x},\boldsymbol{\Omega},E)\cdot\nabla\phi(\boldsymbol{x}) + O(\epsilon^2)\,.} \tag{3.42}$$

By adding Eq. (3.32) to ϵ times Eq. (3.40), we obtain a single diffusion equation defining the amplitude function $\phi(\boldsymbol{x})$. In terms of the original spatial variable, $\boldsymbol{x}$, this diffusion equation is:

$$\boxed{-\nabla\cdot\overline{\boldsymbol{D}}\cdot\nabla\phi(\boldsymbol{x}) + \overline{\Sigma_a}\phi(\boldsymbol{x}) = (1-\rho)\,\overline{\nu\Sigma_f}\phi(\boldsymbol{x})\,.} \tag{3.43}$$

Also, in terms of the original spatial variables, the homogenized cross sections are defined by:

$$\boxed{\overline{\Sigma_a} = \frac{\displaystyle\int_{cell}\int_0^\infty \Sigma_a(\boldsymbol{x},E)F_0(\boldsymbol{x},E)\,\mathrm{d}E\,\mathrm{d}V}{\displaystyle\int_{cell}\int_0^\infty F_0(\boldsymbol{x},E)\,\mathrm{d}E\,\mathrm{d}V}\,,} \tag{3.44}$$

$$\boxed{\overline{\nu\Sigma_f} = \frac{\displaystyle\int_{cell}\int_0^\infty \nu\Sigma_f(\boldsymbol{x},E)F_0(\boldsymbol{x},E)\,\mathrm{d}E\,\mathrm{d}V}{\displaystyle\int_{cell}\int_0^\infty F_0(\boldsymbol{x},E)\,\mathrm{d}E\,\mathrm{d}V}\,,} \tag{3.45}$$

and the homogenized diffusion tensor, $\overline{\boldsymbol{D}}$, is defined by:

(3.46)

$$\boxed{\begin{aligned}\overline{D} = 4\pi &\left[\frac{\displaystyle\int_{cell}\int_0^\infty\int_{4\pi}\boldsymbol{\Omega}f_0^*(\boldsymbol{x},\boldsymbol{\Omega},E)\boldsymbol{f}_1(\boldsymbol{x},\boldsymbol{\Omega},E)\,\mathrm{d}\Omega\,\mathrm{d}E\,\mathrm{d}V}{\displaystyle\int_{cell}\left(\int_0^\infty\chi(\boldsymbol{x},E)F_0^*(\boldsymbol{x},E)\,\mathrm{d}E\right)\left(\int_0^\infty\nu\Sigma_f(\boldsymbol{x},E)F_0(\boldsymbol{x},E)\,\mathrm{d}E\right)\,\mathrm{d}V}\right]\\ &\times\left[\frac{\displaystyle\int_{cell}\int_0^\infty\nu\Sigma_f(\boldsymbol{x},E)F_0(\boldsymbol{x},E)\,\mathrm{d}E\,\mathrm{d}V}{\displaystyle\int_{cell}\int_0^\infty F_0(\boldsymbol{x},E)\,\mathrm{d}E\,\mathrm{d}V}\right]\,.\end{aligned}}$$

In the preceding equations, $f_0(\boldsymbol{x}, \boldsymbol{\Omega}, E)$ is the infinite, periodic lattice eigenfunction. It is obtained using any high-order transport method to solve:

$$\begin{aligned}(3.47)\qquad &\boldsymbol{\Omega}\cdot\nabla f_0(\boldsymbol{x},\boldsymbol{\Omega},E)+\Sigma_t(\boldsymbol{x},E)f_0(\boldsymbol{x},\boldsymbol{\Omega},E)\\ &\quad=\int_0^\infty\int_{4\pi}\Sigma_s(\boldsymbol{x},\boldsymbol{\Omega}'\cdot\boldsymbol{\Omega},E'\to E)f_0(\boldsymbol{x},\boldsymbol{\Omega}',E')\,\mathrm{d}\Omega'\,\mathrm{d}E'\\ &\qquad+(1-\rho_0)\,\frac{\chi(\boldsymbol{x},E)}{4\pi}\int_0^\infty\int_{4\pi}\nu\Sigma_f(\boldsymbol{x},E')f_0(\boldsymbol{x},\boldsymbol{\Omega}',E')\,\mathrm{d}\Omega'\,\mathrm{d}E'\,,\end{aligned}$$

with reflecting boundary conditions.

The vector function $\boldsymbol{f}_1(\boldsymbol{x}, \boldsymbol{\Omega})$ has, in general, 3 components. The i-th component is defined by the fixed source problem:

(3.48)

$$\begin{aligned}&\boldsymbol{\Omega}\cdot\nabla f_{1,i}(\boldsymbol{x},\boldsymbol{\Omega},E)+\Sigma_t(\boldsymbol{x},E)f_{1,i}(\boldsymbol{x},\boldsymbol{\Omega},E)\\ &\quad=\int_0^\infty\int_{4\pi}\Sigma_s(\boldsymbol{x},\boldsymbol{\Omega}'\cdot\boldsymbol{\Omega},E'\to E)f_{1,i}(\boldsymbol{x},\boldsymbol{\Omega}',E')\,\mathrm{d}\Omega'\,\mathrm{d}E'\\ &\qquad+(1-\rho_0)\,\frac{\chi(\boldsymbol{x},E)}{4\pi}\int_0^\infty\int_{4\pi}\nu\Sigma_f(\boldsymbol{x},E')f_{1,i}(\boldsymbol{x},\boldsymbol{\Omega}',E')\,\mathrm{d}\Omega'\,\mathrm{d}E'+\Omega_i f_0(\boldsymbol{x},\boldsymbol{\Omega})\,,\\ &\qquad\qquad i=1,2,3\,.\end{aligned}$$

As discussed in Section 3.3, there are an infinite number of solutions to the above equation. To make the solution unique, we require that the symmetric component of $\boldsymbol{f}_1$ be 0. This can be accomplished by requiring that $\boldsymbol{f}_1$ satisfy:

$$(3.49)\qquad 0=\int_{cell}\int_0^\infty\int_{4\pi}f_0^*(\boldsymbol{x},\boldsymbol{\Omega},E)f_{1,i}(\boldsymbol{x},\boldsymbol{\Omega},E)\,\mathrm{d}\Omega\,\mathrm{d}E\,\mathrm{d}V\,,\qquad i=1,2,3\,.$$

3.7 Relationship Between the Asymptotic, Benoist, and Deniz-Gelbard Diffusion Approximations

Hughes observed that the Asymptotic, Benoist, and Deniz-Gelbard diffusion approximations have a close relationship to one another [52]. Let us first consider the Benoist diffusion approximation. If one substitutes $R^{(0,0,0)}(\boldsymbol{x}, \boldsymbol{\Omega}, E) = f_0(\boldsymbol{x}, \boldsymbol{\Omega}, E)$

and $I_i(\boldsymbol{x}, \boldsymbol{\Omega}, E) = -f_{1,i}(\boldsymbol{x}, \boldsymbol{\Omega}, E)$, then the continuous energy forms of Eqs. (2.42) and (2.43) are exactly Eqs. (3.47) and (3.48). Thus, although the Benoist diffusion coefficient is different than ours, it is calculated using the same periodic lattice functions that arise in the asymptotic analysis.

Next, we consider the Deniz-Gelbard diffusion approximation. As with Benoist, the continuous energy forms of Eqs. (2.31) and (2.33) are exactly Eqs. (3.47) and (3.48) if one substitutes $R(\boldsymbol{x}, \boldsymbol{\Omega}, E) = f_0(\boldsymbol{x}, \boldsymbol{\Omega}, E)$ and $I_i(\boldsymbol{x}, \boldsymbol{\Omega}, E) = -f_{1,i}(\boldsymbol{x}, \boldsymbol{\Omega}, E)$. Furthermore, making these same substitutions into Eq. (2.34), noting also that $\phi_{lat} = F_0$, shows that the monoenergetic homogenized diffusion coefficient obtained by Deniz and Gelbard is exactly that obtained through the asymptotic analysis (for the case of monoenergetic neutrons), Eq. (3.46).

Finally, we compare Eq. (3.42) to Eqs. (2.38) and (2.44) and see that the flux reconstructions are performed in exactly the same manner for all three methods. From the asymptotic analysis, we now have a clear interpretation of the terms in this reconstruction. The first term is $O(1)$ and represents a rapidly varying periodic lattice function superimposed on a slowly varying amplitude function. This is exactly the form of the flux reconstruction that is typically assumed in standard reactor analysis. The second term is a correction term that is formally $O(\epsilon)$ in the asymptotic analysis, or $O(\boldsymbol{B})$ in the Benoist and Deniz-Gelbard analyses. Thus, these flux reconstructions have $O(\epsilon^2)$ or $O(\boldsymbol{B})^2$ error. Both ϵ and $\boldsymbol{B}$ are indeed small if the reactor is large and lattice elements are not large. The correction term has little effect in inner regions of the reactor, where $\nabla\phi(\boldsymbol{x})$ is small. However, in the periphery of the core, where $\nabla\phi(\boldsymbol{x})$ is not small, the correction term becomes significant.

3.8 Summary

The asymptotic derivation of an anisotropic, homogenized diffusion equation has been presented here. The asymptotic analysis begins with an unperturbed system that is an infinite, periodic lattice and then assumes that the system is perturbed to be large, but finite. The perturbation parameter ϵ is the ratio between the length scales of a single lattice element and the entire reactor, and is assumed to be small.

The asymptotic method used here is related to an earlier method by Larsen that was developed for fixed-source problems [32]. Also, although the derivation is different, the asymptotic monoenergetic diffusion approximation is exactly that obtained by Deniz and Gelbard [31, 46]. We show in the next chapter how to obtain an asymptotic multigroup diffusion tensor that is identical to the multigroup Deniz-Gelbard tensor of Eq. (2.37). Obviously, the asymptotic diffusion method can be implemented in the same manner as the Deniz-Gelbard method (see Section 2.3.2).

We note that the asymptotic method starts with the continuous-energy transport equation and ends with a *monoenergetic* homogenized diffusion equation. A *multigroup* homogenized diffusion equation is not obtained directly by any known analysis. Nevertheless, we derive a multigroup homogenized diffusion equation in Chapter IV in an indirect manner.

As of yet, we have not discussed boundary conditions for the diffusion equation. These are derived in Chapter V by applying a variational analysis to the lattice problem. We obtain conditions that are analogous to the Marshak and variational boundary conditions that are typically applied in diffusion calculations.

The standard method for reconstructing the angular flux utilizes only the leading-order asymptotic terms, while the method presented here contains an additional $O(\epsilon)$

"correction term". We show in Chapter VIII that the inclusion of this correction term significantly improves the accuracy of the pin fluxes.

CHAPTER IV

Asymptotic Diffusion Analysis of the Hypothesized Multigroup Diffusion Equation

In Chapter III we applied asymptotic analysis to the continuous energy transport equation and arrived at a monoenergetic diffusion equation (Eq. (3.43)). This is not yet a useful tool for reactor analysis, because complex energy spectra are not accurately modeled by a single energy group.

The subject of this chapter is the derivation of multigroup diffusion coefficients. We (i) begin with the *hypothesized* multigroup diffusion equation from Section 2.2.3 (Eq. (2.22)) with unspecified diffusion coefficients, (ii) apply the same asymptotic scaling used in the previous chapter, and (iii) again arrive at a monoenergetic diffusion equation. We then choose a definition of the multigroup diffusion coefficients such that this monoenergetic diffusion equation is identical to that of Chapter III. In doing this, the hypothesized multigroup diffusion equation and the continuous energy transport equation have the same asymptotic limit for large lattice systems.

4.1 Asymptotic Expansion of the Multigroup Diffusion Equation

We begin with the multigroup, homogenized diffusion equation hypothesized in Section 2.2.3:

$$-\nabla\cdot\overline{\boldsymbol{D}_g}\cdot\nabla\phi_g(\boldsymbol{x})+\overline{\Sigma_{t,g}}\phi_g(\boldsymbol{x})= \sum_{g'=1}^{G}\overline{\Sigma_{s,0,g'\to g}}\phi_{g'}(\boldsymbol{x})+(1-\rho)\,\overline{\chi_g}\sum_{g'=1}^{G}\overline{\nu\Sigma_{f,g'}}\phi_{g'}(\boldsymbol{x})\,,\qquad 1\le g\le G\,. \tag{4.1}$$

We remind the reader that the form of this equation was assumed, but is consistent with what is used in virtually all modern diffusion codes. The cross sections are chosen to be standard, flux-volume-weighted cross sections that preserve multigroup reaction rates for an infinite system. They can be written explicitly as:

$$\overline{\Sigma_{t,g}}=\frac{\displaystyle\int_{V_i}\int_{E_g}^{E_{g-1}}\Sigma_t(\boldsymbol{x},E)F_0(\boldsymbol{x},E)\,\mathrm{d}E\,\mathrm{d}V}{\displaystyle\int_{V_i}\int_{E_g}^{E_{g-1}}F_0(\boldsymbol{x},E)\,\mathrm{d}E\,\mathrm{d}V}\,, \tag{4.2}$$

$$\overline{\Sigma_{s,0,g'\to g}}=\frac{\displaystyle\int_{V_i}\int_{E_g}^{E_{g-1}}\int_{E'_g}^{E_{g'-1}}\Sigma_{s,0}(\boldsymbol{x},E'\to E)F_0(\boldsymbol{x},E')\,\mathrm{d}E'\,\mathrm{d}E\,\mathrm{d}V}{\displaystyle\int_{V_i}\int_{E_{g'}}^{E_{g'-1}}F_0(\boldsymbol{x},E')\,\mathrm{d}E'\,\mathrm{d}V}\,, \tag{4.3}$$

$$\overline{\nu\Sigma_{f,g}}=\frac{\displaystyle\int_{V_i}\int_{E_g}^{E_{g-1}}\nu\Sigma_f(\boldsymbol{x},E)F_0(\boldsymbol{x},E)\,\mathrm{d}E\,\mathrm{d}V}{\displaystyle\int_{V_i}\int_{E_g}^{E_{g-1}}F_0(\boldsymbol{x},E)\,\mathrm{d}E\,\mathrm{d}V}\,, \tag{4.4}$$

$$\overline{\chi_g}=\frac{\displaystyle\int_{V_i}\left(\int_{E_g}^{E_{g-1}}\chi(\boldsymbol{x},E)\,\mathrm{d}E\right)\left(\int_0^{\infty}\nu\Sigma_f(\boldsymbol{x},E')F_0(\boldsymbol{x},E')\,\mathrm{d}E'\right)\,\mathrm{d}V}{\displaystyle\int_{V_i}\int_0^{\infty}\nu\Sigma_f(\boldsymbol{x},E')F_0(\boldsymbol{x},E')\,\mathrm{d}E'\,\mathrm{d}V}\,. \tag{4.5}$$

At this point, the multigroup diffusion coefficient, $\overline{\boldsymbol{D}_g}$, is undefined, although we assume that it is a tensor. As a reminder, the function $F_0=\phi_{lat}$ is the scalar flux from a transport calculation for a single lattice cell in an infinite periodic medium.

We now introduce the same spatial scaling applied in Chapter III.

$$\boldsymbol{z} = \epsilon \boldsymbol{x} = \text{“slow”, non-periodic spatial variable}\,, \tag{4.6}$$

$$\phi_g(\boldsymbol{x}) = \Phi_g(\boldsymbol{z})\,. \tag{4.7}$$

Because the diffusion equation is homogenized, the “fast”, periodic spatial variable $\boldsymbol{y}$ does not appear. We again assume an asymptotic ansatz:

$$\Phi_g(\boldsymbol{z}) = \Phi_{0,g}(\boldsymbol{z}) + \epsilon^2 \Phi_{2,g}(\boldsymbol{z}) + \cdots\,, \tag{4.8a}$$

$$\rho = \rho_0 + \epsilon^2 \rho_2\,. \tag{4.8b}$$

Introducing Eqs. (4.7)-(4.8b) into Eq. (4.1) yields:

$$\begin{aligned}
&-\epsilon^2 \nabla_z \cdot \overline{\boldsymbol{D}_g} \cdot \nabla_z \left[\Phi_{0,g}(\boldsymbol{z}) + \epsilon^2 \Phi_{2,g}(\boldsymbol{z}) + \cdots\right] + \overline{\Sigma_{t,g}} \left[\Phi_{0,g}(\boldsymbol{z}) + \epsilon^2 \Phi_{2,g}(\boldsymbol{z}) + \cdots\right] \\
&\quad = \sum_{g'=1}^{G} \overline{\Sigma_{s,0,g'\to g}} \left[\Phi_{0,g'}(\boldsymbol{z}) + \epsilon^2 \Phi_{2,g'}(\boldsymbol{z}) + \cdots\right] \\
&\qquad + \left(1 - \rho_0 - \epsilon^2 \rho_2\right) \overline{\chi_g} \sum_{g'=1}^{G} \overline{\nu\Sigma_{f,g'}} \left[\Phi_{0,g'}(\boldsymbol{z}) + \epsilon^2 \Phi_{2,g'}(\boldsymbol{z}) + \cdots\right]\,, \qquad 1 \le g \le G\,.
\end{aligned}$$

Equating the coefficients of different powers of epsilon, we get:

$$\begin{aligned}
\epsilon^0: \qquad L_g \Phi_{0,g}(\boldsymbol{z}) &= \overline{\Sigma_{t,g}} \Phi_{0,g}(\boldsymbol{z}) - \sum_{g'=1}^{G} \overline{\Sigma_{s,0,g'\to g}} \Phi_{0,g'}(\boldsymbol{z}) \\
&\qquad - (1 - \rho_0) \overline{\chi_g} \sum_{g'=1}^{G} \overline{\nu\Sigma_{f,g'}} \Phi_{0,g'}(\boldsymbol{z}) \\
&= 0\,,
\end{aligned} \tag{4.9}$$

$$\epsilon^2: \qquad L_g \Phi_{2,g}(\boldsymbol{z}) = \nabla_z \cdot \overline{\boldsymbol{D}_g} \cdot \nabla_z \Phi_{0,g}(\boldsymbol{z}) - \rho_2 \overline{\chi_g} \sum_{g'=1}^{G} \overline{\nu\Sigma_{f,g'}} \Phi_{0,g'}(\boldsymbol{z})\,. \tag{4.10}$$

4.2 Solution of the Zeroth-Order Equation

We now obtain a solution for the zeroth-order Eq. (4.9). Comparing to Eq. (2.21), we see that the zeroth-order equation is just the infinite multigroup balance equation.

Therefore, the solution to Eq. (4.9) is the eigenvector defined by Eq. (2.16):

$$\overline{F_{0,g}} = \frac{1}{V_i} \int_{V_i} \int_{E_g}^{E_{g-1}} F_0(\boldsymbol{x}, E)\, \mathrm{d}E\, \mathrm{d}V\,, \qquad 1 \leq g \leq G\,. \tag{4.11}$$

Then the general solution of Eq. (4.9) is:

$$\Phi_{0,g}(\boldsymbol{z}) = \overline{F_{0,g}} A_0(\boldsymbol{z})\,, \qquad 1 \leq g \leq G\,, \tag{4.12}$$

where A_0 is an unspecified amplitude function.

The multigroup operator L_g is a $G \times G$ matrix. Its adjoint operator is simply its transpose:

$$L_g^* = L_g^T\,.$$

The adjoint operator also has an eigenvector satisfying:

$$\boxed{L_g^* \overline{F_{0,g}^*} = 0\,.} \tag{4.13}$$

At this point, we wish to emphasize that the homogenized, multigroup cross sections have been defined such that the continuous-energy eigenfunction is "preserved" in the homogenized multigroup setting. In other words:

$$L_g \overline{F_{0,g}} = 0\,,$$

where $\overline{F_{0,g}}$ is defined by Eq. (4.11). However, the special definitions of the forward-flux-weighted homogenized cross sections that makes this happen do *not* preserve the adjoint eigenfunction. Therefore, it is generally the case that:

$$\overline{F_{0,g}^*} \neq \frac{1}{V_i} \int_{V_i} \int_{E_g}^{E_{g-1}} F_0^*(\boldsymbol{x}, E)\, \mathrm{d}E\, \mathrm{d}V\,, \qquad 1 \leq g \leq G\,. \tag{4.14}$$

Thus, the eigenfunction satisfying Eq. (4.13), $\overline{F_{0,g}^*}$, can not generally be obtained from the continuous energy eigenfunction, $f_0^*(\boldsymbol{x}, \boldsymbol{\Omega}, E)$ (the solution Eq. (3.17)).

4.3 Obtaining a Homogenized Diffusion Equation From the Second Order Equation

Here we apply the FAT (see Section 3.3) to the second-order equation (Eq. (4.10)) to obtain a homogenized diffusion equation for the amplitude function A_0. The solvability condition for this system of equations is obtained by operating by $\sum_{g=1}^{G} \overline{F_{0,g}^*}(\cdot)$. The left side of Eq. (4.10) vanishes and we obtain:

$$0 = \nabla_z \cdot \left(\sum_{g=1}^{G} \overline{F_{0,g}^*}\, \overline{\boldsymbol{D}_g} \cdot \nabla_z \Phi_{0,g}(\boldsymbol{z}) \right) - \rho_2 \left(\sum_{g=1}^{G} \overline{F_{0,g}^*}\, \overline{\chi_g} \sum_{g'=1}^{G} \overline{\nu\Sigma_{f,g'}} \Phi_{0,g'}(\boldsymbol{z}) \right) .$$

Introducing Eq. (4.12) yields:

$$0 = \nabla_z \cdot \left(\sum_{g=1}^{G} \overline{F_{0,g}^*}\, \overline{\boldsymbol{D}_g}\, \overline{F_{0,g}} \right) \cdot \nabla_z A_0(\boldsymbol{z}) - \rho_2 \left(\sum_{g=1}^{G} \overline{F_{0,g}^*}\, \overline{\chi_g} \sum_{g'=1}^{G} \overline{\nu\Sigma_{f,g'}}\, \overline{F_{0,g'}} \right) A_0(\boldsymbol{z}) .$$

Multiplying the above equation by ϵ^2, using $\epsilon^2 \rho_2 = \rho - \rho_0$, and rearranging, we obtain:

(4.15)
$$-\epsilon \nabla_z \cdot \left(\sum_{g=1}^{G} \overline{F_{0,g}^*}\, \overline{\boldsymbol{D}_g}\, \overline{F_{0,g}} \right) \cdot \epsilon \nabla_z A_0(\boldsymbol{z}) = -\left(\rho - \rho_0\right) \left(\sum_{g=1}^{G} \overline{F_{0,g}^*}\, \overline{\chi_g} \sum_{g'=1}^{G} \overline{\nu\Sigma_{f,g'}}\, \overline{F_{0,g'}} \right) A_0(\boldsymbol{z}) .$$

To obtain an expression for ρ_0, we sum the equation $0 = L_g \overline{F_{0,g}}$ over all energy groups:

$$0 = \sum_{g=1}^{G} \overline{\Sigma_{t,g}}\, \overline{F_{0,g}} - \sum_{g=1}^{G} \sum_{g'=1}^{G} \overline{\Sigma_{s,0,g' \to g}}\, \overline{F_{0,g'}} - (1 - \rho_0) \sum_{g=1}^{G} \overline{\chi_g} \sum_{g'=1}^{G} \overline{\nu\Sigma_{f,g'}}\, \overline{F_{0,g'}} .$$

The fission spectrum is normalized such that $\sum_{g=1}^{G} \overline{\chi_g} = 1$. Furthermore, the absorption cross section is defined $\overline{\Sigma_{a,g}} = \overline{\Sigma_{t,g}} - \sum_{g'=1}^{G} \overline{\Sigma_{s,0,g \to g'}}$. Thus, the above equation yields:

(4.16)
$$\sum_{g=1}^{G} \overline{\Sigma_{a,g}}\, \overline{F_{0,g}} = (1 - \rho_0) \sum_{g=1}^{G} \overline{\nu\Sigma_{f,g}}\, \overline{F_{0,g}} .$$

Now we note that:

$$\sum_{g=1}^{G} \overline{\Sigma_{a,g}}\,\overline{F_{0,g}} = \sum_{g=1}^{G} \frac{\displaystyle\int_{V_i}\int_{E_g}^{E_{g-1}} \Sigma_a(\boldsymbol{x},E)F_0(\boldsymbol{x},E)\,\mathrm{d}E\,\mathrm{d}V}{\displaystyle\int_{V_i}\int_{E_g}^{E_{g-1}} F_0(\boldsymbol{x},E)\,\mathrm{d}E\,\mathrm{d}V}\overline{F_{0,g}}\,,$$

$$= \sum_{g=1}^{G} \frac{1}{V_i}\int_{V_i}\int_{E_g}^{E_{g-1}} \Sigma_a(\boldsymbol{x},E)F_0(\boldsymbol{x},E)\,\mathrm{d}E\,\mathrm{d}V\,,$$

$$= \frac{1}{V_i}\int_{V_i}\int_{0}^{\infty} \Sigma_a(\boldsymbol{x},E)F_0(\boldsymbol{x},E)\,\mathrm{d}E\,\mathrm{d}V\,,$$

and similarly:

$$\sum_{g=1}^{G} \overline{\nu\Sigma_{f,g}}\,\overline{F_{0,g}} = \frac{1}{V_i}\int_{V_i}\int_{0}^{\infty} \nu\Sigma_f(\boldsymbol{x},E)F_0(\boldsymbol{x},E)\,\mathrm{d}E\,\mathrm{d}V\,.$$

Thus, we can write Eq. (4.16) as:

$$\int_{V_i}\int_{0}^{\infty} \Sigma_a(\boldsymbol{x},E)F_0(\boldsymbol{x},E)\,\mathrm{d}E\,\mathrm{d}V$$

$$= (1-\rho_0)\int_{V_i}\int_{0}^{\infty} \nu\Sigma_f(\boldsymbol{x},E)F_0(\boldsymbol{x},E)\,\mathrm{d}E\,\mathrm{d}V\,.$$

Dividing both sides by $\int_{V_i}\int_0^\infty F_0(\boldsymbol{x},E)\,\mathrm{d}E\,\mathrm{d}V$, we obtain:

$$\overline{\Sigma_a} = (1-\rho_0)\,\overline{\nu\Sigma_f}\,.$$

Thus, the infinite lattice eigenvalue, ρ_0, is defined simply by:

$$\rho_0 = 1 - \frac{\overline{\Sigma_a}}{\overline{\nu\Sigma_f}}\,, \tag{4.17}$$

where the monoenergetic cross sections $\overline{\Sigma_a}$ and $\overline{\nu\Sigma_f}$ are the same obtained in the analysis of the continuous energy transport equation, Eqs. (3.44) and (3.45) respectively.

Introducing Eq. (4.17) into Eq. (4.15) yields:

$$-\epsilon\nabla_z\cdot\left(\sum_{g=1}^{G}\overline{F^*_{0,g}}\,\overline{\boldsymbol{D}_g}\,\overline{F_{0,g}}\right)\cdot\epsilon\nabla_z A_0(\boldsymbol{z})$$

$$= \left(1-\rho-\frac{\overline{\Sigma_a}}{\overline{\nu\Sigma_f}}\right)\left(\sum_{g=1}^{G}\overline{F^*_{0,g}}\,\overline{\chi_g}\sum_{g'=1}^{G}\overline{\nu\Sigma_{f,g'}}\,\overline{F_{0,g'}}\right)A_0(\boldsymbol{z})\,.$$

Rearranging, we obtain a familiar form of the diffusion equation:

$$-\epsilon\nabla_z\cdot\left(\frac{\sum_{g=1}^{G}\overline{F^*_{0,g}}\,\overline{\boldsymbol{D}_g}\,\overline{F_{0,g}}}{\sum_{g=1}^{G}\overline{F^*_{0,g}}\,\overline{\chi_g}\sum_{g'=1}^{G}\overline{\nu\Sigma_{f,g'}}\,\overline{F_{0,g'}}}\overline{\nu\Sigma_f}\right)\cdot\epsilon\nabla_z A_0(\boldsymbol{z})+\overline{\Sigma_a}A_0(\boldsymbol{z}) = (1-\rho)\,\overline{\nu\Sigma_f}A_0(\boldsymbol{z})\,. \tag{4.18}$$

4.4 The Multigroup Diffusion Tensor

We now unscale the diffusion equation by defining the monoenergetic scalar flux in terms of the original spatial variable:

$$\phi(\boldsymbol{x}) = A_0(\boldsymbol{z})\,.$$

Then we can write the diffusion equation as:

$$-\nabla\cdot\left(\frac{\sum_{g=1}^{G}\overline{F^*_{0,g}}\,\overline{\boldsymbol{D}_g}\,\overline{F_{0,g}}}{\sum_{g=1}^{G}\overline{F^*_{0,g}}\,\overline{\chi_g}\sum_{g'=1}^{G}\overline{\nu\Sigma_{f,g'}}\,\overline{F_{0,g'}}}\overline{\nu\Sigma_f}\right)\cdot\nabla\phi(\boldsymbol{x})+\overline{\Sigma_a}\phi(\boldsymbol{x}) = (1-\rho)\,\overline{\nu\Sigma_f}\phi(\boldsymbol{x})\,.$$

Comparing to the diffusion equation obtained from the continuous energy transport equation (Eq. (3.43)), we see that the asymptotic limit of the multigroup diffusion equation is the same if:

$$\frac{\sum_{g=1}^{G}\overline{F^*_{0,g}}\,\overline{\boldsymbol{D}_g}\,\overline{F_{0,g}}}{\sum_{g=1}^{G}\overline{F^*_{0,g}}\,\overline{\chi_g}\sum_{g'=1}^{G}\overline{\nu\Sigma_{f,g'}}\,\overline{F_{0,g'}}} = 4\pi\frac{\int_{V_i}\int_0^\infty\int_{4\pi}\boldsymbol{\Omega}f_0^*(\boldsymbol{x},\boldsymbol{\Omega},E)\boldsymbol{f}_1(\boldsymbol{x},\boldsymbol{\Omega},E)\,\mathrm{d}\Omega\,\mathrm{d}E\,\mathrm{d}V}{\int_{V_i}\left(\int_0^\infty\chi(\boldsymbol{x},E)F_0^*(\boldsymbol{x},E)\,\mathrm{d}E\right)\left(\int_0^\infty\nu\Sigma_f(\boldsymbol{x},E)F_0(\boldsymbol{x},E)\,\mathrm{d}E\right)\,\mathrm{d}V}\,.$$

There are an infinite number of choices of $\overline{\boldsymbol{D}_g}$ that will satisfy the above equation. However, the simplest way to satisfy it is by requiring for each $1 \leq g \leq G$:

$$\frac{\overline{F^*_{0,g}}\,\overline{\boldsymbol{D}_g}\,\overline{F_{0,g}}}{\displaystyle\sum_{g''=1}^{G}\overline{F^*_{0,g''}}\,\overline{\chi_{g''}}\sum_{g'=1}^{G}\overline{\nu\Sigma_{f,g'}}\,\overline{F_{0,g'}}} = 4\pi\frac{\displaystyle\int_{V_i}\int_{E_g}^{E_{g-1}}\int_{4\pi}\boldsymbol{\Omega}f_0^*(\boldsymbol{x},\boldsymbol{\Omega},E)\boldsymbol{f}_1(\boldsymbol{x},\boldsymbol{\Omega},E)\,\mathrm{d}\Omega\,\mathrm{d}E\,\mathrm{d}V}{\displaystyle\int_{V_i}\left(\int_0^\infty\chi(\boldsymbol{x},E)F_0^*(\boldsymbol{x},E)\,\mathrm{d}E\right)\left(\int_0^\infty\nu\Sigma_f(\boldsymbol{x},E)F_0(\boldsymbol{x},E)\,\mathrm{d}E\right)\,\mathrm{d}V}\,.$$

Solving for $\overline{\boldsymbol{D}_g}$ yields:

$$\boxed{\begin{aligned}\overline{\boldsymbol{D}_g} = {}& \frac{\displaystyle\sum_{g''=1}^{G}\overline{F^*_{0,g''}}\,\overline{\chi_{g''}}\sum_{g'=1}^{G}\overline{\nu\Sigma_{f,g'}}\,\overline{F_{0,g'}}}{\displaystyle\int_{V_i}\left(\int_0^\infty\chi(\boldsymbol{x},E)F_0^*(\boldsymbol{x},E)\,\mathrm{d}E\right)\left(\int_0^\infty\nu\Sigma_f(\boldsymbol{x},E)F_0(\boldsymbol{x},E)\,\mathrm{d}E\right)\,\mathrm{d}V} \\ & \times\frac{4\pi\displaystyle\int_{V_i}\int_{E_g}^{E_{g-1}}\int_{4\pi}\boldsymbol{\Omega}f_0^*(\boldsymbol{x},\boldsymbol{\Omega},E)\boldsymbol{f}_1(\boldsymbol{x},\boldsymbol{\Omega},E)\,\mathrm{d}\Omega\,\mathrm{d}E\,\mathrm{d}V}{\overline{F^*_{0,g}}\,\overline{F_{0,g}}}\,.\end{aligned}} \tag{4.19}$$

We note that the lattice function $f_{1,i}$ is antisymmetric in $(\boldsymbol{x},\Omega_i)$, but symmetric in $(\boldsymbol{x},\Omega_j)$ for $i \neq j$. Therefore:

$$\int_{V_i}\int_{E_g}^{E_{g-1}}\int_{4\pi}\boldsymbol{\Omega}f_0^*(\boldsymbol{x},\boldsymbol{\Omega},E)\boldsymbol{f}_1(\boldsymbol{x},\boldsymbol{\Omega},E)\,\mathrm{d}\Omega\,\mathrm{d}E\,\mathrm{d}V = 0\,, \qquad i \neq j\,.$$

Thus, $\overline{\boldsymbol{D}_g}$ is a diagonal tensor even for heterogeneous media. However, the tensor is in general anisotropic, i.e., $D_{11} \neq D_{22} \neq D_{33}$.

While Eq. (4.19) seems complicated, it does reduce to a familiar form for homogeneous systems. In a homogeneous medium, Eq. (3.14) simplifies to:

$$\begin{aligned}0 &= Lf_0(E)\,,\\ &= \Sigma_t(E)f_0(E) - \int_0^\infty\Sigma_{s,0}(E'\to E)f_0(E')\,\mathrm{d}E' \\ &\quad - (1-\rho_0)\chi(E)\int_0^\infty\nu\Sigma_f(E')f_0(E')\,\mathrm{d}E'\,.\end{aligned} \tag{4.20}$$

Also, Eq. (3.23) for $\boldsymbol{f}_1$

$$L\boldsymbol{f}_1(\boldsymbol{\Omega}, E) = \boldsymbol{\Omega} f_0(E)\,,$$

has an antisymmetric (in $\boldsymbol{\Omega}$) solution of the form:

$$\boldsymbol{f}_1(\boldsymbol{\Omega}, E) = \boldsymbol{\Omega} f_1(E)\,, \tag{4.21a}$$

where $f_1(E)$ satisfies:

$$\Sigma_t(E) f_1(E) - \int_0^\infty \Sigma_{s,1}(E' \to E) f_1(E')\,\mathrm{d}E' = f_0(E)\,. \tag{4.21b}$$

We recall that $\Sigma_{s,n}$ are scattering cross section moments defined by Eq. (2.7). We operate on $f_0(E)$ by $\int_{4\pi}\int_{E_g}^{E_{g-1}}(\cdot)\,\mathrm{d}E\,\mathrm{d}\Omega$ to obtain the group-integrated scalar flux:

$$\overline{F_{0,g}} = F_{0,g} = 4\pi f_{0,g} = 4\pi \int_{E_g}^{E_{g-1}} f_0(E)\,\mathrm{d}E \tag{4.22}$$

The multigroup cross sections (Eqs. (4.2)-(4.5)) simplify in a homogeneous system to:

$$\overline{\Sigma_{t,g}} = \Sigma_{t,g} = \frac{\displaystyle\int_{E_g}^{E_{g-1}} \Sigma_t(E) F_0(E)\,\mathrm{d}E}{\displaystyle\int_{E_g}^{E_{g-1}} F_0(E)\,\mathrm{d}E}\,, \tag{4.23}$$

$$\overline{\Sigma_{s,0,g'\to g}} = \Sigma_{s,0,g'\to g} = \frac{\displaystyle\int_{E_g}^{E_{g-1}}\int_{E'_g}^{E_{g'-1}} \Sigma_s(E' \to E) F_0(E')\,\mathrm{d}E'\,\mathrm{d}E}{\displaystyle\int_{E_{g'}}^{E_{g'-1}} F_0(E')\,\mathrm{d}E'}\,, \tag{4.24}$$

$$\overline{\nu\Sigma_{f,g}} = \nu\Sigma_{f,g} = \frac{\displaystyle\int_{E_g}^{E_{g-1}} \nu\Sigma_f(E) F_0(E)\,\mathrm{d}E}{\displaystyle\int_{E_g}^{E_{g-1}} F_0(E)\,\mathrm{d}E}\,, \tag{4.25}$$

$$\overline{\chi_g} = \chi_g = \int_{E_g}^{E_{g-1}} \chi(E)\,\mathrm{d}E\,. \tag{4.26}$$

Using Eqs. (4.22) and (4.25), we can rewrite the following sum:

$$\sum_{g'=1}^{G} \overline{\nu\Sigma_{f,g}}\,\overline{F_{0,g}} = \sum_{g'=1}^{G} \frac{\displaystyle\int_{E_g}^{E_{g-1}} \nu\Sigma_f(\boldsymbol{x},E)F_0(E)\,\mathrm{d}E}{F_{0,g}} F_{0,g}\,, \tag{4.27}$$
$$= \int_0^\infty \nu\Sigma_f(\boldsymbol{x},E)F_0(E)\,\mathrm{d}E\,.$$

Introducing Eqs. (4.20)-(4.27) into Eq. (4.19) and evaluating the volume integrals yields:

(4.28)
$$\overline{\boldsymbol{D}_g} = \left(\frac{\displaystyle\sum_{g''=1}^{G} \overline{F^*_{0,g''}}\,\overline{\chi_{g''}}}{V_i\displaystyle\int_0^\infty F_0^*(E)\chi(\boldsymbol{x},E)\,\mathrm{d}E}\right)\left(\frac{4\pi V_i\displaystyle\int_{E_g}^{E_{g-1}}\int_{4\pi}\boldsymbol{\Omega\Omega}f_0^*(E)f_1(E)\,\mathrm{d}\Omega\,\mathrm{d}E}{\overline{F^*_{0,g}}\left(4\pi\displaystyle\int_{E_g}^{E_{g-1}} f_0(E)\,\mathrm{d}E\right)}\right),$$
$$= \left(\frac{\displaystyle\sum_{g''=1}^{G} \overline{F^*_{0,g''}}\,\overline{\chi_{g''}}}{\displaystyle\int_0^\infty F_0^*(E)\chi(\boldsymbol{x},E)\,\mathrm{d}E}\right)\frac{4\pi}{3\overline{F^*_{0,g}}}\left(\frac{\displaystyle\int_{E_g}^{E_{g-1}} f_0^*(E)f_1(E)\,\mathrm{d}E}{\displaystyle\int_{E_g}^{E_{g-1}} f_0(E)\,\mathrm{d}E}\right)\boldsymbol{I}\,.$$

Here we have used $\int_{4\pi}\boldsymbol{\Omega\Omega}\,\mathrm{d}\Omega = (4\pi/3)\boldsymbol{I}$ where $\boldsymbol{I}$ is the 3×3 identity matrix.

We note that in a pure-scattering medium, the adjoint eigenfunction $f_0^*(E)$ satisfies:

$$0 = \Sigma_{s,0}(E)f_0^*(E) - \int_0^\infty \Sigma_{s,0}(E\to E')f_0^*(E')\,\mathrm{d}E'\,,$$

which has a constant solution that can be arbitrarily normalized. Then we may assume:

$$f_0^*(E) \approx 1\,, \tag{4.29a}$$

$$F_0^*(E) = F^*_{0,g} \approx 4\pi\,. \tag{4.29b}$$

These assumptions are accurate in a homogeneous medium in which neutrons have a high scattering probability. Introducing Eqs. (4.29) into Eq. (4.28) and recalling that the fission spectrum is probability distribution function whose sum/integral over all energies is unity, we obtain:

$$\overline{\boldsymbol{D}_g} = \left(\frac{\sum_{g''=1}^{G} \overline{\chi_{g''}}}{\int_0^\infty \chi(\boldsymbol{x}, E)\,\mathrm{d}E} \right) \frac{1}{3} \left(\frac{\int_{E_g}^{E_{g-1}} f_1(E)\,\mathrm{d}E}{\int_{E_g}^{E_{g-1}} f_0(E)\,\mathrm{d}E} \right) \boldsymbol{I}\,, \tag{4.30}$$

$$= \frac{1}{3} \left(\frac{\int_{E_g}^{E_{g-1}} f_1(E)\,\mathrm{d}E}{\int_{E_g}^{E_{g-1}} f_0(E)\,\mathrm{d}E} \right) \boldsymbol{I}\,.$$

Next, we make the following standard "diffusion" approximation:

$$\Sigma_{s,1}(E' \to E) \approx \delta(E' - E) \int_0^\infty \Sigma_{s,1}(E' \to E'')\,\mathrm{d}E''\,, \tag{4.31}$$

$$\equiv \delta(E' - E)\Sigma_{s,1}(E')\,.$$

Introducing Eq. (4.31) into Eq. (4.21b), we get:

$$\Sigma_t(E) f_1(E) - \int_0^\infty \delta(E' - E)\Sigma_{s,1}(E') f_1(E')\,\mathrm{d}E' = f_0(E)\,,$$

or:

$$\left[\Sigma_t(E) - \Sigma_{s,1}(E)\right] f_1(E) = f_0(E)\,,$$

or:

$$f_1(E) = \frac{1}{\Sigma_{tr}(E)} f_0(E)\,. \tag{4.32}$$

Introducing Eq. (4.32) into Eq. (4.30), we obtain the standard diffusion coefficient for a homogeneous medium (compare to Eq. (2.24)):

$$\overline{\boldsymbol{D}_g} = \overline{D_g}\boldsymbol{I} = \frac{1}{3} \left(\frac{\int_{E_g}^{E_{g-1}} \frac{1}{\Sigma_{tr}(E)} f_0(E)\,\mathrm{d}E}{\int_{E_g}^{E_{g-1}} f_0(E)\,\mathrm{d}E} \right) \boldsymbol{I}\,, \tag{4.33}$$

We note that for a problem with no energy-dependence, the two approximations made (Eqs. (4.29) and (4.32)) are not necessary, and Eq. (4.28) directly simplifies to the classical result:

$$\overline{D_g} = \frac{1}{3\Sigma_{tr,g}}\,.$$

4.5 Multigroup Flux Reconstruction

At this point, the flux reconstruction formulas prescribed by asymptotic analysis of the transport equation and the multigroup diffusion equation each use only the monoenergetic diffusion solution. Due to complicated energy spectra in nuclear reactors, this is not sufficiently accurate for most problems. Instead, we wish to define a flux reconstruction that uses the multigroup diffusion solution because it contains more energy spectrum information.

To do this, we begin with the flux reconstruction arising from our analysis of the multigroup diffusion equation. This is obtained by introducing Eq. (4.12) into Eq. (4.8a). In terms of the original spatial variable, we have:

$$\phi_g(\boldsymbol{x}) = \overline{F_{0,g}}\phi(\boldsymbol{x}) + O(\epsilon^2)\,, \qquad 1 \leq g \leq G\,. \tag{4.34}$$

Solving for the monoenergetic diffusion flux gives:

$$\phi(\boldsymbol{x}) = \frac{\phi_g(\boldsymbol{x})}{\overline{F_{0,g}}} + O(\epsilon^2)\,, \qquad 1 \leq g \leq G\,. \tag{4.35}$$

The continuous energy transport flux reconstruction formula (Eq. (3.42)) has $O(\epsilon^2)$ error, and so we may introduce Eq. (4.35) without any loss of accuracy. The result is an expression for the reconstructed flux that utilizes the multigroup diffusion solution:

(4.36)

$$\boxed{\psi(\boldsymbol{x},\boldsymbol{\Omega},E) = \frac{f_0(\boldsymbol{x},\boldsymbol{\Omega},E)}{\overline{F_{0,g}}}\phi_g(\boldsymbol{x}) - \frac{\boldsymbol{f}_1(\boldsymbol{x},\boldsymbol{\Omega},E)}{\overline{F_{0,g}}}\cdot\nabla\phi_g(\boldsymbol{x}) + O(\epsilon^2)\,,\;\; E_g \leq E \leq E_{g-1}\,.}$$

We note that the division by $\overline{F_{0,g}}$ makes the normalization of f_0 arbitrary. The normalization constant appears in f_0, $\boldsymbol{f}_1$, and $\overline{F_{0,g}}$, and therefore does *not* appear in the expression for the reconstructed flux. As discussed in Section 3.2, we choose to normalize f_0 such that the total fission source in a lattice cell is 1.

For homogeneous systems, we use Eqs. (4.21a), (4.22) and (4.33), to obtain:

$$\frac{\displaystyle\int_{E_g}^{E_{g-1}} f_0(\boldsymbol{x},\boldsymbol{\Omega},E)\,\mathrm{d}E}{\overline{F_{0,g}}} = \frac{\displaystyle\int_{E_g}^{E_{g-1}} f_0(\boldsymbol{x},\boldsymbol{\Omega},E)\,\mathrm{d}E}{4\pi\displaystyle\int_{E_g}^{E_{g-1}} f_0(\boldsymbol{x},\boldsymbol{\Omega},E)\,\mathrm{d}E} = \frac{1}{4\pi}\,, \qquad 1\le g\le G\,, \tag{4.37a}$$

$$\frac{\displaystyle\int_{E_g}^{E_{g-1}} \boldsymbol{f}_1(\boldsymbol{x},\boldsymbol{\Omega},E)\,\mathrm{d}E}{\overline{F_{0,g}}} = \frac{\displaystyle\int_{E_g}^{E_{g-1}} \frac{\boldsymbol{\Omega}}{\Sigma_{tr}(E)} f_0(\boldsymbol{x},\boldsymbol{\Omega},E)\,\mathrm{d}E}{4\pi\displaystyle\int_{E_g}^{E_{g-1}} f_0(\boldsymbol{x},\boldsymbol{\Omega},E)\,\mathrm{d}E} = \frac{3}{4\pi}\overline{D_g}\boldsymbol{\Omega}\,, \qquad 1\le g\le G\,. \tag{4.37b}$$

Operating on Eq. (4.36) by $\int_{E_g}^{E_{g-1}}(\cdot)\,\mathrm{d}E$ and introducing Eqs. (4.37) reveals that our flux reconstruction limits to the multigroup P_1 diffusion approximation for homogeneous media:

$$\psi_g(\boldsymbol{x},\boldsymbol{\Omega}) = \frac{1}{4\pi}\phi_g(\boldsymbol{x}) - \frac{3}{4\pi}\overline{D_g}\boldsymbol{\Omega}\cdot\nabla\phi_g(\boldsymbol{x}) + O(\epsilon^2)\,, \qquad E_g\le E\le E_{g-1}\,. \tag{4.38}$$

4.6 Equivalence of the Multigroup Asymptotic and Deniz-Gelbard Diffusion Approximations

We now repeat the procedure of Section 3.7 to show that the multigroup forms of the asymptotic and Deniz-Gelbard diffusion tensors are equivalent. We substitute $R(\boldsymbol{x},\boldsymbol{\Omega},E) = f_0(\boldsymbol{x},\boldsymbol{\Omega},E)$, $I_i(\boldsymbol{x},\boldsymbol{\Omega},E) = -f_{1,i}(\boldsymbol{x},\boldsymbol{\Omega},E)$, $\phi_{lat} = F_0$, $\overline{R_g} = \overline{F_{0,g}}$, and $\overline{R_g^*} = \overline{F_{0,g}^*}$ into the expression for the multigroup Deniz-Gelbard diffusion tensor (Eq. (2.37)). Comparing the result to Eq. (4.19), we find that the diffusion coefficients are identical. Thus, although our derivations are different, the asymptotic and Deniz-Gelbard diffusion approximations are the same.

4.7 Summary

In this chapter, we have applied our asymptotic scaling to the multigroup diffusion equation. The multigroup diffusion coefficient is defined such that the asymptotic limits of the continuous energy transport equation and the multigroup diffusion equation are equal. A method of flux reconstruction that utilizes the multigroup diffusion solution has been formulated.

In the next chapter, we discuss boundary and interface conditions for the asymptotic diffusion equation.

CHAPTER V

Boundary and Interface Conditions for the Multigroup Diffusion Equation

Boundary and interface conditions (discontinuity factors) for the asymptotic diffusion equation are discussed in this chapter. We begin with a discussion of standard boundary conditions and discontinuity factors, the latter of which are nearly always used in reactor analysis at interfaces between fuel assemblies of differing composition. Next, we propose new non-standard discontinuity factors designed to preserve angular moments of the flux at interfaces between lattices. Finally, we perform a variational analysis designed to preserve the reactor eigenvalue. The analysis results in novel boundary and interface conditions (i.e., discontinuity factors) for periodic lattice systems.

5.1 Standard Vacuum Boundary Conditions

The standard boundary conditions for the diffusion equation are typically derived by first assuming a large or semi-infinite homogeneous medium. They are not directly applicable to lattice systems for which homogenized diffusion is necessary. Nevertheless, these assumptions are generally acceptable because reactor cores are typically surrounded by a neutron reflector region. The reflector is composed of a large, (mostly) homogeneous, diffusive material.

It is customary in reactor analysis to model enough of the system beyond the reactor core such that we can assume that no neutrons enter (or re-enter) the system through the simulation boundary. The condition of no neutrons incident on the system boundary is referred to as the vacuum boundary condition.

In the case of a vacuum boundary, the exact angular flux solution is zero for incoming angles and non-zero for outgoing angles. Because the diffusion equation contains no angular information, it is generally not possible to satisfy the exact boundary condition when using diffusion. Thus, it is necessary to satisfy the boundary condition in an integral sense.

Consider the P_1 diffusion expression for the angular flux at a point x on the vacuum boundary of a system:

$$\psi(\boldsymbol{x}, \boldsymbol{\Omega}, E) \approx \frac{\phi(\boldsymbol{x}, E)}{4\pi} - \frac{3\boldsymbol{\Omega} \cdot D(E) \nabla \phi(\boldsymbol{x}, E)}{4\pi}, \qquad x \in \partial V, \tag{5.1a}$$

$$\psi(\boldsymbol{x}, \boldsymbol{\Omega}, E) = 0, \qquad x \in \partial V, \qquad \boldsymbol{n} \cdot \boldsymbol{\Omega} < 0. \tag{5.1b}$$

where $\boldsymbol{n}$ is the outward unit normal vector to the surface of the system. Suppose now that we wish to preserve the incoming partial current. We operate on Eq. (5.1a) by $\int_{\boldsymbol{n}\cdot\boldsymbol{\Omega}<0} (\boldsymbol{n} \cdot \boldsymbol{\Omega}) (\cdot) \, \mathrm{d}\Omega$ and make use of Eq. (5.1b) to obtain:

$$0 = \phi(\boldsymbol{x}, E) + 2D(E) \boldsymbol{n} \cdot \nabla \phi(\boldsymbol{x}, E), \qquad x \in \partial V. \tag{5.2}$$

This vacuum boundary condition for the diffusion equation is known as the Marshak boundary condition [7, 58, 60].

One could instead apply a variational analysis to a semi-infinite system and require that the boundary condition yield the correct neutron flux deep within the system [63, 64]. This analysis, which originated with Pomraning and has been applied to many problems of neutron and photon transport, dictates that we operate on Eq.

(5.1a) by $\int_{\boldsymbol{n}\cdot\boldsymbol{\Omega}<0}\left[(\boldsymbol{n}\cdot\boldsymbol{\Omega})+\frac{3}{2}(\boldsymbol{n}\cdot\boldsymbol{\Omega})^2\right](\cdot)\,\mathrm{d}\Omega$. Using Eq. (5.1b), we now obtain:

$$0=\phi(\boldsymbol{x},E)+\frac{17}{8}D(E)\boldsymbol{n}\cdot\nabla\phi(\boldsymbol{x},E)\,,\qquad x\in\partial V\,. \tag{5.3}$$

We note that Eqs. (5.3) and (5.2) are each of the form:

$$0=\phi(\boldsymbol{x},E)+l(E)\boldsymbol{n}\cdot\nabla\phi(\boldsymbol{x},E)\,,\qquad x\in\partial V\,, \tag{5.4}$$

which can be interpreted as follows: if one linearly extrapolates the scalar flux from a point $\boldsymbol{x}_b$ on the boundary, then the point $\boldsymbol{x}=\boldsymbol{x}_b+l\boldsymbol{n}$ is the point at which the extrapolated flux becomes 0. For this reason, l is referred to as the "extrapolation distance" or "extrapolation length". It is often referred to in units of transport mean free paths, $1/\Sigma_{tr}$. Thus, introducing the standard expression for the diffusion coefficient, $D=1/3\Sigma_{tr}$, we find that the Marshak and homogeneous variational extrapolation distances in units of transport mean free paths are:

$$l_{Mar}=\frac{2}{3}\approx 0.6667\,, \tag{5.5}$$

$$l_{HomVar}=\frac{17}{24}\approx 0.7083\,. \tag{5.6}$$

Other variational analyses by Federighi and Pomraning for one-group, planar geometry and later extended to multigroup, multidimensional geometry by Rulko et al. yields the following extrapolation length, which we will refer to as the Federighi-Pomraning extrapolation length, l_{FP} [65, 66, 67, 68]:

$$l_{FP}=\frac{1}{\sqrt{2}}\approx 0.7071\,. \tag{5.7}$$

Finally, an analysis of the so-called Milne problem shows that the *exact* extrapolation distance for a semi-infinite, planar, one-group, non-absorbing, isotropic scattering medium with no sources and no incident neutrons is:

$$l_{Milne}=0.71044609...\,. \tag{5.8}$$

This is typically referred to as the Milne extrapolation distance. Although originally derived for a very specific problem, it has proven quite accurate for a wide range of diffusive problems. We note that both of the variationally derived extrapolation lengths, l_{var} and l_{FP}, derived above are quite similar to the Milne extrapolation length, l_{Mar}. The Marshak extrapolation length, l_{Mar}, is significantly smaller than the others, and experience has shown that it is less accurate than the other extrapolation lengths.

5.2 Standard Discontinuity Factors

As mentioned in Section 2.2.2, preserving the surface-average current across every face of a lattice requires a unique definition of the diffusion coefficient on each face. Thus, the use of a single homogenized diffusion coefficient in a lattice leaves us with insufficient degrees of freedom to preserve surface-average currents on every face.

Koebke first proposed an "equivalence theory" in which heterogeneity factors define a discontinuous jump in the flux across an interface between two homogenization regions. These factors provide the additional degrees of freedom needed to preserve the currents across interfaces [21]. In this method, the heterogeneity factors and the diffusion coefficient were direction-dependent, and the factors were required to be identical on opposite sides of the homogenization region. An iterative strategy was required to solve for the direction-dependent factors.

Smith later altered the method into what he called "generalized equivalence theory", the primary difference being that the discontinuity factors (DFs) are allowed to be unique to each face, while only a single diffusion coefficient would be used [22]. This eliminated the need for iteratively obtaining the diffusion coefficient and DFs.

Smith's paper provides an illustrative example of why and how DFs are needed

for homogenized diffusion. Suppose that we know the true transport flux for the heterogeneous problem (Fig. 5.1.a). Then suppose we run a homogenized diffusion calculation for each individual lattice using the currents from the heterogeneous calculation as boundary conditions (Fig. 5.1.b). Now if we place the adjacent homog-

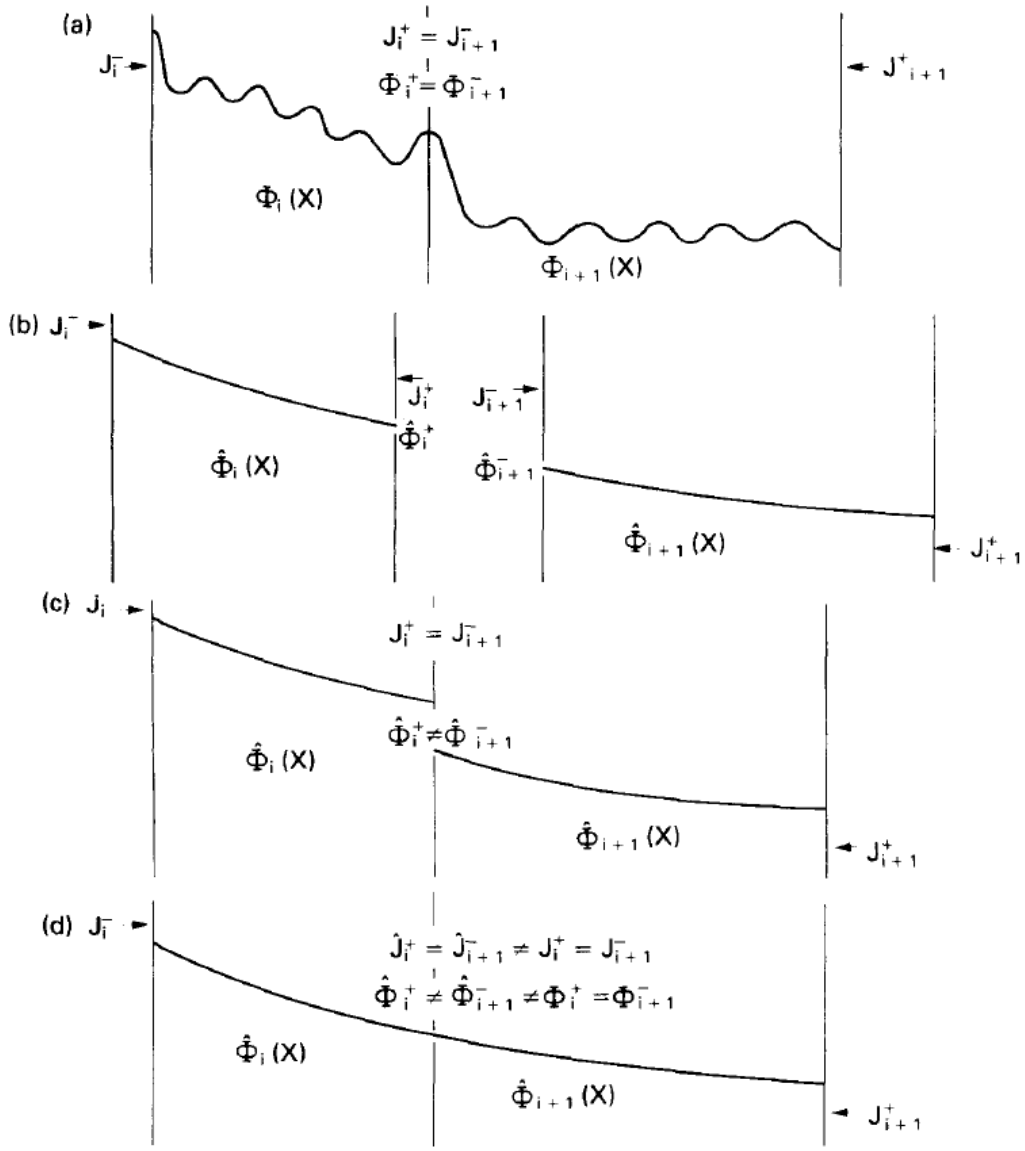

(a) Heterogeneous reactor flux.
(b) Individual homogenized nodes.
(c) Adjacent individual homogenized nodes.
(d) Conventional diffusion solution to the two-node problem.

Figure 5.1: 1-D Nodal Flux Distributions (Figure reproduced from Smith [22])

enized calculations next to each other, we would see that although the currents are exact and continuous across lattice interfaces, the diffusion fluxes are discontinuous (Fig. 5.1.c). Finally, consider what would happen if we performed a homogenized diffusion calculation for the full system, using only the boundary conditions for the outer surface of the reactor. Both the diffusion fluxes and currents would be continuous at lattice interfaces, but neither would equal the true transport values (Fig. 5.1.d).

We conclude that the homogenized diffusion solution can preserve the reaction rates and surface currents, but to do this, the homogenized diffusion solution will in general need to be discontinuous. To do this exactly, we must first solve the full core heterogeneous problem, then solve the homogenized diffusion equation using the exact surface-average currents from the heterogeneous problem as boundary conditions. The full-core homogenized diffusion calculation should then be solved with the following discontinuity condition at interfaces between lattices i and $i+1$:

$$\phi^+_{i,g} a^+_{i,g} = \phi^-_{i+1,g} a^-_{i+1,g} \,, \tag{5.9}$$

where the DFs are defined:

$$a^+_{i,g} = \frac{\phi^+_{het,i,g}}{\phi^+_{i,g}} \,, \tag{5.10}$$

$$a^-_{i+1,g} = \frac{\phi^-_{het,i+1,g}}{\phi^-_{i+1,g}} \,. \tag{5.11}$$

In the preceding equations, $\phi^+_{i,g}$ is the group-averaged, surface-averaged diffusion flux on the right surface of lattice i, $\phi^-_{i+1,g}$ is the group-averaged, surface-averaged diffusion flux on the left surface of lattice $i+1$, and $\phi^+_{het,i,g}$ and $\phi^-_{het,i+1,g}$ are the group-averaged, surface-averaged full-core transport fluxes on those same surfaces. The exact full-core transport solution is continuous, and so $\phi^+_{het,i,g} = \phi^-_{het,i+1,g}$. As

we shall see, it is necessary to approximate these functions, in which case they will no longer be equal. The condition of Eq. (5.9) simply states that the true transport fluxes are continuous across lattice interfaces, and that there is a direct relationship between the transport and diffusion surface fluxes. Equation (5.9) is illustrated by Fig. 5.2.

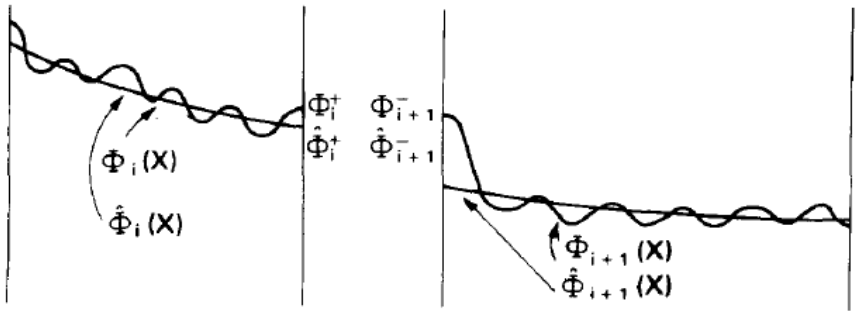

Figure 5.2: 1-D Heterogeneous and Homogeneous Flux Distributions (Figure reproduced from Smith [22])

Of course we have the same problem calculating the exact DFs that we have calculating exact homogenized cross sections: we must know the full core transport solution *a priori*. Instead, as with the homogenized cross sections, we calculate assembly discontinuity factors (ADFs) by performing a single lattice calculation with zero net current boundary conditions. The solution to the homogeneous calculation with zero net current boundary conditions is simply a constant equal to the lattice-averaged flux. Thus, the homogeneous surface-averaged flux can be replaced by the group-averaged, volume-averaged lattice flux. Therefore, Eqs. (5.10) and (5.11) become:

$$a_{i,g}^{+} = \frac{F_{0,i,g}^{+}}{\overline{F}_{0,i,g}}\,, \tag{5.12}$$

$$a_{i+1,g}^{-} = \frac{F_{0,i+1,g}^{-}}{\overline{F}_{0,i+1,g}}\,. \tag{5.13}$$

The ADFs are approximate and will not reproduce the exact transport solution, but they do offer a significant improvement over standard continuity conditions in the diffusion calculation. Unlike the full-core transport solutions $\phi^+_{het,i,g}$ and $\phi^-_{het,i+1,g}$, the lattice transport solutions are not equal at the interface, i.e., $F^+_{0,i,g} \neq F^-_{0,i+1,g}$. As we prove in the next section, the condition of Eq. (5.9) with the ADFs of Eqs. (5.12) and (5.13) has the meaning that the reconstructed surface-averaged flux is continuous across interfaces, at least in 1-D.

ADFs are based on single lattice calculations with 0 net current conditions on all boundaries. While this approximation is reasonable for neighboring fuel assemblies of similar compositions, it is not accurate when the neighboring assemblies are of very different types (e.g. between standard uranium oxide fuel and mixed-oxide fuel (MOX)) [28]. It is also not accurate at the interface between fuel assemblies and the reactor reflector.

To address this issue, one can perform a "colorset" calculation in which multiple assemblies or fractions of assemblies are modeled together. The outer boundary of the colorset will have 0 net current conditions, but homogenized diffusion calculations will be performed for the individual assemblies or quarter assemblies using the actual currents from the colorset calculation. This is expected to be more accurate because there is no material change on the outer boundary of the colorset where the 0 net current condition is applied [28]. The DFs are calculated from the surface-averaged transport and diffusion fluxes at the interface between the assemblies. For instance, to obtain DFs between uranium oxide and MOX fuel assemblies, one could model 4 quarter-assemblies in a checkerboard pattern with a reflecting boundary, then perform 4 separate homogenized diffusion calculations on each quarter assembly using the correct currents. At fuel-reflector interfaces, a 1-D analysis is typically

performed on a 2 assembly colorset.

An issue with colorset calculations is that they must be performed for every possible combination of fuel assembly types. Since reactor analysis requires on the order of 1740 state points to be simulated for every lattice or colorset [20], colorset calculations are rarely used for regular analysis. The only exception is the fuel-reflector interface, for which colorset calculations are typically performed. Based on the impracticality of colorset calculations for regular reactor analysis and on the limitations of the codes used in this research, we will restrict ourselves to using ADFs calculated from single lattice simulations, including at the fuel reflector interface.

5.3 Discontinuity Factors to Preserve Angular Moments

As mentioned in the previous section, the standard ADFs are equivalent to requiring that, in 1-D, the reconstructed scalar flux be continuous across an interface between lattice types. To see this, consider the 1-D asymptotic reconstructed flux at the interface at $x = x_i$ between lattices i and $i+1$. On the right surface of lattice i we have:

(5.14)
$$\psi(x_i, \mathbf{\Omega}, E) = \left(\frac{f^+_{0,i}(\mathbf{\Omega}, E)}{\overline{F_{0,i,g}}} \right) \phi^+_{i,g} - \left(\frac{f^+_{1,i}(\mathbf{\Omega}, E)}{\overline{F_{0,i,g}}} \right) \frac{\mathrm{d}\phi^+_{i,g}}{\mathrm{d}x} , \qquad E_g \leq E \leq E_{g-1} .$$

Similarly, on the left surface of lattice $i+1$ we have:

(5.15)
$$\psi(x_i, \mathbf{\Omega}, E) = \left(\frac{f^-_{0,i+1}(\mathbf{\Omega}, E)}{\overline{F_{0,i+1,g}}} \right) \phi^-_{i+1,g} - \left(\frac{f^-_{1,i+1}(\mathbf{\Omega}, E)}{\overline{F_{0,i+1,g}}} \right) \frac{\mathrm{d}\phi^-_{i+1,g}}{\mathrm{d}x} , \quad E_g \leq E \leq E_{g-1} .$$

We note that in the standard flux reconstruction, only the first terms on the right sides of Eqs. (5.14)-(5.15) are used.

To make the multigroup, surface-averaged scalar flux continuous, we operate on Eqs. (5.14) and (5.15) by $\int_{4\pi} \int_{E_g}^{E_{g-1}} (\cdot) \, \mathrm{d}\Omega \, \mathrm{d}E$ and set the two expressions equal to

each other:

$$\left(\frac{\int_{E_g}^{E_{g-1}} \int_{4\pi} f_{0,i}^{+}(\mathbf{\Omega}, E)\, \mathrm{d}\Omega\, \mathrm{d}E}{\overline{F_{0,i,g}}} \right) \phi_{i,g}^{+} - \left(\frac{\int_{E_g}^{E_{g-1}} \int_{4\pi} f_{1,i}^{+}(\mathbf{\Omega}, E)\, \mathrm{d}\Omega\, \mathrm{d}E}{\overline{F_{0,i,g}}} \right) \frac{\mathrm{d}\phi_{i,g}^{+}}{\mathrm{d}x} = \left(\frac{\int_{E_g}^{E_{g-1}} \int_{4\pi} f_{0,i+1}^{-}(\mathbf{\Omega}, E)\, \mathrm{d}\Omega\, \mathrm{d}E}{\overline{F_{0,i+1,g}}} \right) \phi_{i+1,g}^{-} - \left(\frac{\int_{E_g}^{E_{g-1}} \int_{4\pi} f_{1,i+1}^{-}(\mathbf{\Omega}, E)\, \mathrm{d}\Omega\, \mathrm{d}E}{\overline{F_{0,i+1,g}}} \right) \frac{\mathrm{d}\phi_{i+1,g}^{-}}{\mathrm{d}x} . \tag{5.16}$$

We now note that because the lattices are defined to be symmetric:

$$f_0(x_i, \mathbf{\Omega}, E) = f_0(x_i, \mathbf{\Omega}_r, E)\,, \tag{5.17}$$

$$f_1(x_i, \mathbf{\Omega}, E) = -f_1(x_i, \mathbf{\Omega}_r, E)\,, \tag{5.18}$$

where $\mathbf{\Omega}_r$ is the angle of reflection across the boundary corresponding to $\mathbf{\Omega}$. Therefore, the integrals of f_1 in Eq. (5.16) vanish. Then for each energy group:

$$\frac{F_{0,i,g}^{+}}{\overline{F_{0,i,g}}} \phi_{i,g}^{+} = \frac{F_{0,i+1,g}^{-}}{\overline{F_{0,i+1,g}}} \phi_{i+1,g}^{-}\,. \tag{5.19}$$

Comparing Eq. (5.19) to Eqs. (5.9), (5.12), and (5.13), we see that the standard ADFs do indeed make the 1-D reconstructed scalar flux continuous.

One might then ask, are there other angular moments of the reconstructed flux that we can or should make continuous across interfaces? We note that if the homogenized diffusion equation is solved with standard continuity of current conditions at

interfaces, then the asymptotic reconstructed current will in general be discontinuous. Thus, neutron balance is not preserved in the reconstructed solution. However, if the reconstructed solution is going to be used to calculate intra-pin reaction rates, then perhaps we should require that the reconstructed solution conserve neutrons. We will therefore propose DFs that make the multigroup reconstructed current continuous across interfaces in 1-D.

We note again that the standard flux reconstruction does not contain the f_1 term. It is the presence of this term that allows us to preserve multiple angular moments simultaneously. Furthermore, without this term, only even angular moments of the reconstructed flux can be made to be continuous.

First, we define for every energy group a current discontinuity condition with current DFs $b_{i,g}$:

$$a^+_{i,g}b^+_{i,g}J^+_{i,g} = a^+_{i,g}b^+_{i,g}D_{i,g}\frac{\mathrm{d}\phi^+_{i,g}}{\mathrm{d}x} = a^-_{i+1,g}b^-_{i+1,g}D_{i+1,g}\frac{\mathrm{d}\phi^-_{i+1,g}}{\mathrm{d}x} = a^-_{i+1,g}b^-_{i+1,g}J^-_{i+1,g}\,. \tag{5.20}$$

To make the multigroup, surface-averaged current continuous, we operate on Eqs. (5.14) and (5.15) by $\int_{4\pi}\int_{E_g}^{E_{g-1}}(\boldsymbol{n}\cdot\boldsymbol{\Omega})\,(\cdot)\,\mathrm{d}\Omega\,\mathrm{d}E$ and set the two expressions equal to each other. Here, let $\boldsymbol{n}$ be the unit normal vector to the interface directed from lattice i to lattice $i+1$. Because of the symmetry of f_0 (see Eq. (5.17)), $(\boldsymbol{n}\cdot\boldsymbol{\Omega})\,f_0$ is antisymmetric in $\boldsymbol{\Omega}$. Therefore, the integrals of f_0 in Eq. (5.16) vanish and we are left with:

$$\left(\frac{\displaystyle\int_{E_g}^{E_{g-1}}\int_{4\pi}(\boldsymbol{n}\cdot\boldsymbol{\Omega})\,f^+_{1,i}(\boldsymbol{\Omega},E)\,\mathrm{d}\Omega\,\mathrm{d}E}{\overline{F_{0,i,g}}}\right)\frac{\mathrm{d}\phi^+_{i,g}}{\mathrm{d}x} = \left(\frac{\displaystyle\int_{E_g}^{E_{g-1}}\int_{4\pi}(\boldsymbol{n}\cdot\boldsymbol{\Omega})\,f^-_{1,i+1}(\boldsymbol{\Omega},E)\,\mathrm{d}\Omega\,\mathrm{d}E}{\overline{F_{0,i+1,g}}}\right)\frac{\mathrm{d}\phi^-_{i+1,g}}{\mathrm{d}x}\,. \tag{5.21}$$

Comparing Eq. (5.21) to Eq. (5.20), we find that the current DFs should be defined:

$$b_{i,g}^{(1,+)} = \frac{1}{a_{i,g}^{+} D_{i,g}} \left(\frac{\displaystyle\int_{E_g}^{E_{g-1}} \int_{4\pi} (\boldsymbol{n} \cdot \boldsymbol{\Omega})\, f_{1,i}^{+}(\boldsymbol{\Omega}, E)\, \mathrm{d}\Omega\, \mathrm{d}E}{\overline{F_{0,i,g}}} \right), \tag{5.22}$$

$$b_{i+1,g}^{(1,-)} = \frac{1}{a_{i+1,g}^{-} D_{i+1,g}} \left(\frac{\displaystyle\int_{E_g}^{E_{g-1}} \int_{4\pi} (\boldsymbol{n} \cdot \boldsymbol{\Omega})\, f_{1,i+1}^{-}(\boldsymbol{\Omega}, E)\, \mathrm{d}\Omega\, \mathrm{d}E}{\overline{F_{0,i,g}}} \right), \tag{5.23}$$

where the superscript 1 indicates that these DFs make the reconstructed first angular moment (current) continuous across the interface.

Another useful quantity that one might want to preserve is the second angular moment of the reconstructed flux. Boundary layer analysis of a semi-infinite, homogeneous medium can be used to show that the second angular moment of the flux in such a medium is constant, even near the boundary [69]. If we then imagine two such half-spaces adjacent to each other, then because the angular flux is continuous across the interface, the second moment of the flux is constant in both half-spaces and continuous across the interface.

Although our problems are not homogeneous, we also define flux DFs $a_{i,g}^{(2)}$ to make the second angular moment of the reconstructed flux continuous across interfaces. We operate on Eqs. (5.14) and (5.15) by $\int_{4\pi} \int_{E_g}^{E_{g-1}} (\boldsymbol{n} \cdot \boldsymbol{\Omega})^2 (\cdot)\, \mathrm{d}\Omega\, \mathrm{d}E$ and set the two expressions equal to each other. As with the previous flux DFs, the integrals of f_1

vanish and we are left with:

$$\left(\frac{\int_{E_g}^{E_{g-1}}\int_{4\pi}\left(\boldsymbol{n}\cdot\boldsymbol{\Omega}\right)^2 f_{0,i}^{+}(\boldsymbol{\Omega},E)\,\mathrm{d}\Omega\,\mathrm{d}E}{\overline{F_{0,i,g}}}\right)\phi_{i,g}^{+} = \left(\frac{\int_{E_g}^{E_{g-1}}\int_{4\pi}\left(\boldsymbol{n}\cdot\boldsymbol{\Omega}\right)^2 f_{0,i+1}^{-}(\boldsymbol{\Omega},E)\,\mathrm{d}\Omega\,\mathrm{d}E}{\overline{F_{0,i+1,g}}}\right)\phi_{i+1,g}^{-}\,. \tag{5.24}$$

Thus, the flux DFs for continuity of the reconstructed second moment are defined:

$$a_{i,g}^{(2,+)} = \left(\frac{\int_{E_g}^{E_{g-1}}\int_{4\pi}\left(\boldsymbol{n}\cdot\boldsymbol{\Omega}\right)^2 f_{0,i}^{+}(\boldsymbol{\Omega},E)\,\mathrm{d}\Omega\,\mathrm{d}E}{\overline{F_{0,i,g}}}\right), \tag{5.25}$$

$$a_{i+1,g}^{(2,-)} = \left(\frac{\int_{E_g}^{E_{g-1}}\int_{4\pi}\left(\boldsymbol{n}\cdot\boldsymbol{\Omega}\right)^2 f_{0,i+1}^{-}(\boldsymbol{\Omega},E)\,\mathrm{d}\Omega\,\mathrm{d}E}{\overline{F_{0,i+1,g}}}\right), \tag{5.26}$$

where the superscript 2 indicates that these DFs make the reconstructed second angular moment continuous across the interface.

A final pair of quantities that we may want to be continuous across interfaces are the reconstructed partial currents. First, we operate on Eqs. (5.14) and (5.15) by $\int_{\boldsymbol{n}\cdot\boldsymbol{\Omega}<0}\int_{E_g}^{E_{g-1}}\left(\boldsymbol{n}\cdot\boldsymbol{\Omega}\right)(\cdot)\,\mathrm{d}\Omega\,\mathrm{d}E$ and set the two expressions equal to each other. This

equation states that the partial current into lattice i is continuous.

$$
\begin{aligned}
(5.27)\qquad & \left(\frac{\int_{E_g}^{E_{g-1}} \int_{\boldsymbol{n}\cdot\boldsymbol{\Omega}<0} (\boldsymbol{n}\cdot\boldsymbol{\Omega})\, f_{0,i}^{+}(\boldsymbol{\Omega},E)\,\mathrm{d}\Omega\,\mathrm{d}E}{\overline{F_{0,i,g}}} \right) \phi_{i,g}^{+} \\
& \qquad - \left(\frac{\int_{E_g}^{E_{g-1}} \int_{\boldsymbol{n}\cdot\boldsymbol{\Omega}<0} (\boldsymbol{n}\cdot\boldsymbol{\Omega})\, f_{1,i}^{+}(\boldsymbol{\Omega},E)\,\mathrm{d}\Omega\,\mathrm{d}E}{\overline{F_{0,i,g}}} \right) \frac{\mathrm{d}\phi_{i,g}^{+}}{\mathrm{d}x} \\
& \quad = \left(\frac{\int_{E_g}^{E_{g-1}} \int_{\boldsymbol{n}\cdot\boldsymbol{\Omega}<0} (\boldsymbol{n}\cdot\boldsymbol{\Omega})\, f_{0,i+1}^{-}(\boldsymbol{\Omega},E)\,\mathrm{d}\Omega\,\mathrm{d}E}{\overline{F_{0,i+1,g}}} \right) \phi_{i+1,g}^{-} \\
& \qquad - \left(\frac{\int_{E_g}^{E_{g-1}} \int_{\boldsymbol{n}\cdot\boldsymbol{\Omega}<0} (\boldsymbol{n}\cdot\boldsymbol{\Omega})\, f_{1,i+1}^{-}(\boldsymbol{\Omega},E)\,\mathrm{d}\Omega\,\mathrm{d}E}{\overline{F_{0,i+1,g}}} \right) \frac{\mathrm{d}\phi_{i+1,g}^{-}}{\mathrm{d}x}\,.
\end{aligned}
$$

Next, we operate on Eqs. (5.14) and (5.15) by $\int_{\boldsymbol{n}\cdot\boldsymbol{\Omega}>0} \int_{E_g}^{E_{g-1}} (\boldsymbol{n}\cdot\boldsymbol{\Omega})\,(\cdot)\,\mathrm{d}\Omega\,\mathrm{d}E$ and set the two expressions equal to each other. This equation states that the partial current into lattice $i+1$ is continuous.

$$
\begin{aligned}
(5.28)\qquad & \left(\frac{\int_{E_g}^{E_{g-1}} \int_{\boldsymbol{n}\cdot\boldsymbol{\Omega}>0} (\boldsymbol{n}\cdot\boldsymbol{\Omega})\, f_{0,i}^{+}(\boldsymbol{\Omega},E)\,\mathrm{d}\Omega\,\mathrm{d}E}{\overline{F_{0,i,g}}} \right) \phi_{i,g}^{+} \\
& \qquad - \left(\frac{\int_{E_g}^{E_{g-1}} \int_{\boldsymbol{n}\cdot\boldsymbol{\Omega}>0} (\boldsymbol{n}\cdot\boldsymbol{\Omega})\, f_{1,i}^{+}(\boldsymbol{\Omega},E)\,\mathrm{d}\Omega\,\mathrm{d}E}{\overline{F_{0,i,g}}} \right) \frac{\mathrm{d}\phi_{i,g}^{+}}{\mathrm{d}x} \\
& \quad = \left(\frac{\int_{E_g}^{E_{g-1}} \int_{\boldsymbol{n}\cdot\boldsymbol{\Omega}>0} (\boldsymbol{n}\cdot\boldsymbol{\Omega})\, f_{0,i+1}^{-}(\boldsymbol{\Omega},E)\,\mathrm{d}\Omega\,\mathrm{d}E}{\overline{F_{0,i+1,g}}} \right) \phi_{i+1,g}^{-} \\
& \qquad - \left(\frac{\int_{E_g}^{E_{g-1}} \int_{\boldsymbol{n}\cdot\boldsymbol{\Omega}>0} (\boldsymbol{n}\cdot\boldsymbol{\Omega})\, f_{1,i+1}^{-}(\boldsymbol{\Omega},E)\,\mathrm{d}\Omega\,\mathrm{d}E}{\overline{F_{0,i+1,g}}} \right) \frac{\mathrm{d}\phi_{i+1,g}^{-}}{\mathrm{d}x}\,.
\end{aligned}
$$

Now we make use of the symmetry of f_0 and anti-symmetry of f_1 (see Eqs. (5.17) and (5.18)). We subtract Eq. (5.28) from Eq. (5.27). The integrals of f_1 cancel, while the integrals of f_0 can be combined by rewriting the limits of integration in the angular integral:

$$2\left(\frac{\int_{E_g}^{E_{g-1}}\int_{\boldsymbol{n}\cdot\boldsymbol{\Omega}>0}(\boldsymbol{n}\cdot\boldsymbol{\Omega})\,f_{0,i}^{+}(\boldsymbol{\Omega},E)\,\mathrm{d}\Omega\,\mathrm{d}E}{\overline{F_{0,i,g}}}\right)\phi_{i,g}^{+}$$
$$=2\left(\frac{\int_{E_g}^{E_{g-1}}\int_{\boldsymbol{n}\cdot\boldsymbol{\Omega}>0}(\boldsymbol{n}\cdot\boldsymbol{\Omega})\,f_{0,i+1}^{-}(\boldsymbol{\Omega},E)\,\mathrm{d}\Omega\,\mathrm{d}E}{\overline{F_{0,i+1,g}}}\right)\phi_{i+1,g}^{-}.$$

Equivalently:

$$2\left(\frac{\int_{E_g}^{E_{g-1}}\int_{\boldsymbol{n}\cdot\boldsymbol{\Omega}<0}(\boldsymbol{n}\cdot\boldsymbol{\Omega})\,f_{0,i}^{+}(\boldsymbol{\Omega},E)\,\mathrm{d}\Omega\,\mathrm{d}E}{\overline{F_{0,i,g}}}\right)\phi_{i,g}^{+}$$
$$=2\left(\frac{\int_{E_g}^{E_{g-1}}\int_{\boldsymbol{n}\cdot\boldsymbol{\Omega}<0}(\boldsymbol{n}\cdot\boldsymbol{\Omega})\,f_{0,i+1}^{-}(\boldsymbol{\Omega},E)\,\mathrm{d}\Omega\,\mathrm{d}E}{\overline{F_{0,i+1,g}}}\right)\phi_{i+1,g}^{-}.$$

Therefore, the flux DFs for continuity of the reconstructed partial currents are defined:

$$a_{i,g}^{(PC,+)}=\left|\frac{\int_{E_g}^{E_{g-1}}\int_{\boldsymbol{n}\cdot\boldsymbol{\Omega}<0}(\boldsymbol{n}\cdot\boldsymbol{\Omega})\,f_{0,i}^{+}(\boldsymbol{\Omega},E)\,\mathrm{d}\Omega\,\mathrm{d}E}{\overline{F_{0,i,g}}}\right|, \tag{5.29}$$
$$=\left|\frac{\int_{E_g}^{E_{g-1}}\int_{\boldsymbol{n}\cdot\boldsymbol{\Omega}>0}(\boldsymbol{n}\cdot\boldsymbol{\Omega})\,f_{0,i}^{+}(\boldsymbol{\Omega},E)\,\mathrm{d}\Omega\,\mathrm{d}E}{\overline{F_{0,i,g}}}\right|,$$

$$a_{i+1,g}^{(PC,+)} = \left| \frac{\displaystyle\int_{E_g}^{E_{g-1}} \int_{\boldsymbol{n}\cdot\boldsymbol{\Omega}<0} (\boldsymbol{n}\cdot\boldsymbol{\Omega})\, f_{0,i+1}^{-}(\boldsymbol{\Omega},E)\,\mathrm{d}\Omega\,\mathrm{d}E}{\overline{F_{0,i+1,g}}} \right| , \tag{5.30}$$

$$= \left| \frac{\displaystyle\int_{E_g}^{E_{g-1}} \int_{\boldsymbol{n}\cdot\boldsymbol{\Omega}>0} (\boldsymbol{n}\cdot\boldsymbol{\Omega})\, f_{0,i+1}^{-}(\boldsymbol{\Omega},E)\,\mathrm{d}\Omega\,\mathrm{d}E}{\overline{F_{0,i+1,g}}} \right| ,$$

where the superscript PC indicates that these DFs make the reconstructed partial current continuous across the interface.

Both partial currents cannot be made continuous from a single set of DFs, and so we must also derive current DFs. We add Eq. (5.27) to Eq. (5.28). Now the f_0 terms cancel, leaving us with:

$$\left(\frac{\displaystyle\int_{E_g}^{E_{g-1}} \int_{4\pi} (\boldsymbol{n}\cdot\boldsymbol{\Omega})\, f_{1,i}^{+}(\boldsymbol{\Omega},E)\,\mathrm{d}\Omega\,\mathrm{d}E}{\overline{F_{0,i,g}}} \right) \frac{\mathrm{d}\phi_{i,g}^{+}}{\mathrm{d}x}$$

$$= \left(\frac{\displaystyle\int_{E_g}^{E_{g-1}} \int_{4\pi} (\boldsymbol{n}\cdot\boldsymbol{\Omega})\, f_{1,i+1}^{-}(\boldsymbol{\Omega},E)\,\mathrm{d}\Omega\,\mathrm{d}E}{\overline{F_{0,i+1,g}}} \right) \frac{\mathrm{d}\phi_{i+1,g}^{-}}{\mathrm{d}x} .$$

Then the current DFs are:

$$b_{i,g}^{(PC,+)} = \frac{1}{a_{i,g}^{+} D_{i,g}} \left(\frac{\displaystyle\int_{E_g}^{E_{g-1}} \int_{4\pi} (\boldsymbol{n}\cdot\boldsymbol{\Omega})\, f_{1,i}^{+}(\boldsymbol{\Omega},E)\,\mathrm{d}\Omega\,\mathrm{d}E}{\overline{F_{0,i,g}}} \right) , \tag{5.31}$$

$$b_{i+1,g}^{(PC,-)} = \frac{1}{a_{i+1,g}^{-} D_{i+1,g}} \left(\frac{\displaystyle\int_{E_g}^{E_{g-1}} \int_{4\pi} (\boldsymbol{n}\cdot\boldsymbol{\Omega})\, f_{1,i+1}^{-}(\boldsymbol{\Omega},E)\,\mathrm{d}\Omega\,\mathrm{d}E}{\overline{F_{0,i,g}}} \right) . \tag{5.32}$$

Thus, the current DFs are the same for the partial current as for the net current, but the flux DFs that they are paired with have changed.

The DFs in this section were derived in 1-D. If we follow the same procedure for a multi-dimensional problem, the DFs will be space-dependent because, in general, the lattice functions vary along the interface. However, the implementation of space-dependent DFs is impractical. Suppose that we wanted instead to make the surface-averaged angular moments continuous across the interface. We would follow the same procedure, but also integrate Eqs. (5.14) and (5.15) over the interface surface and divide by the surface area. Because the diffusion solution ϕ also varies along the interface, ϕ could not be separated from the surface integral, and so the equations could not be written in the form of a discontinuity condition (Eq. (5.9)).

Instead, we choose a simplified scheme: calculate DFs using surface-averaged lattice functions. The DFs will no longer exactly make the reconstructed flux moments continuous. Nevertheless, they will *approximately* make the surface-averaged reconstructed angular moments continuous. These simple multi-dimensional DFs are shown below.

Flux DFs for continuity of the reconstructed scalar flux are defined as:

$$\boxed{\begin{aligned} a_{i,g}^{(0,+)} &= \left(\frac{\dfrac{1}{A_{ij}} \displaystyle\int_{\partial V_{ij}} \int_{E_g}^{E_{g-1}} \int_{4\pi} f_{0,i}^{+}(\boldsymbol{x}, \boldsymbol{\Omega}, E) \, \mathrm{d}\Omega \, \mathrm{d}E \, \mathrm{d}S}{\overline{F_{0,i,g}}} \right), \\ a_{i+1,g}^{(0,-)} &= \left(\frac{\dfrac{1}{A_{ij}} \displaystyle\int_{\partial V_{ij}} \int_{E_g}^{E_{g-1}} \int_{4\pi} f_{0,i+1}^{-}(\boldsymbol{x}, \boldsymbol{\Omega}, E) \, \mathrm{d}\Omega \, \mathrm{d}E \, \mathrm{d}S}{\overline{F_{0,i+1,g}}} \right). \end{aligned}} \tag{5.33}$$

These DFs are equivalent to the standard ADFs typically used in reactor analysis.

Flux DFs for continuity of the second angular moment of the reconstructed flux

are defined as:

$$
\begin{aligned}
a_{i,g}^{(2,+)} &= \left(\frac{\dfrac{1}{A_{ij}} \displaystyle\int_{\partial V_{ij}} \int_{E_g}^{E_{g-1}} \int_{4\pi} (\boldsymbol{n}\cdot\boldsymbol{\Omega})^2 \, f_{0,i}^{+}(\boldsymbol{x},\boldsymbol{\Omega},E)\,\mathrm{d}\Omega\,\mathrm{d}E\,\mathrm{d}S}{\overline{F_{0,i,g}}} \right), \\
a_{i+1,g}^{(2,-)} &= \left(\frac{\dfrac{1}{A_{ij}} \displaystyle\int_{\partial V_{ij}} \int_{E_g}^{E_{g-1}} \int_{4\pi} (\boldsymbol{n}\cdot\boldsymbol{\Omega})^2 \, f_{0,i+1}^{-}(\boldsymbol{x},\boldsymbol{\Omega},E)\,\mathrm{d}\Omega\,\mathrm{d}E\,\mathrm{d}S}{\overline{F_{0,i+1,g}}} \right).
\end{aligned}
\tag{5.34}
$$

Flux DFs for continuity of the reconstructed partial currents are defined as:

$$
\begin{aligned}
a_{i,g}^{(PC,+)} &= \left| \frac{\dfrac{1}{A_{ij}} \displaystyle\int_{\partial V_{ij}} \int_{E_g}^{E_{g-1}} \int_{\boldsymbol{n}\cdot\boldsymbol{\Omega}>0} (\boldsymbol{n}\cdot\boldsymbol{\Omega}) \, f_{0,i}^{+}(\boldsymbol{x},\boldsymbol{\Omega},E)\,\mathrm{d}\Omega\,\mathrm{d}E\,\mathrm{d}S}{\overline{F_{0,i,g}}} \right|, \\
a_{i+1,g}^{(PC,-)} &= \left| \frac{\dfrac{1}{A_{ij}} \displaystyle\int_{\partial V_{ij}} \int_{E_g}^{E_{g-1}} \int_{\boldsymbol{n}\cdot\boldsymbol{\Omega}>0} (\boldsymbol{n}\cdot\boldsymbol{\Omega}) \, f_{0,i+1}^{-}(\boldsymbol{x},\boldsymbol{\Omega},E)\,\mathrm{d}\Omega\,\mathrm{d}E\,\mathrm{d}S}{\overline{F_{0,i+1,g}}} \right|.
\end{aligned}
\tag{5.35}
$$

Finally, current DFs for continuity of the reconstructed net current are defined as:

(5.36)

$$
\begin{aligned}
b_{i,g}^{(1/PC,+)} &= \frac{1}{a_{i,g}^{+} D_{i,g}} \left(\frac{\dfrac{1}{A_{ij}} \displaystyle\int_{\partial V_{ij}} \int_{E_g}^{E_{g-1}} \int_{4\pi} (\boldsymbol{n}\cdot\boldsymbol{\Omega}) \left(\boldsymbol{n}\cdot\boldsymbol{f}_{1,i}^{+}(\boldsymbol{x},\boldsymbol{\Omega},E)\right) \mathrm{d}\Omega\,\mathrm{d}E\,\mathrm{d}S}{\overline{F_{0,i,g}}} \right), \\
b_{i+1,g}^{(1/PC,-)} &= \frac{1}{a_{i+1,g}^{-} D_{i+1,g}} \left(\frac{\dfrac{1}{A_{ij}} \displaystyle\int_{\partial V_{ij}} \int_{E_g}^{E_{g-1}} \int_{4\pi} (\boldsymbol{n}\cdot\boldsymbol{\Omega}) \left(\boldsymbol{n}\cdot\boldsymbol{f}_{1,i+1}^{-}(\boldsymbol{x},\boldsymbol{\Omega},E)\right) \mathrm{d}\Omega\,\mathrm{d}E\,\mathrm{d}S}{\overline{F_{0,i,g}}} \right).
\end{aligned}
$$

where the superscript 1 indicates that the current DF is used in conjunction with $a_{i,g}^{(0)}$ or $a_{i,g}^{(2)}$, and the superscript PC indicates that the current DF is used in conjunction with $a_{i,g}^{(PC)}$.

In Eqs. (5.33)-(5.36), the right surface of lattice i, denoted by a $+$, and the left surface of lattice $i+1$, denoted by a $-$, are the same surface and represent the interface between the two lattices. The unit vector $\boldsymbol{n}$ is normal to the interface. It can be oriented in either direction, so long as the definition is consistent for all DFs. The surface area of the interface is denoted A_{ij}, while the surface itself is denoted ∂V_{ij}. If anisotropic diffusion coefficients are used, then the component of the diffusion tensor normal to the surface should be used in Eq. (5.36).

The flux DFs for continuity of the reconstructed scalar flux (Eq. (5.33)) and the reconstructed second angular moment (Eq. (5.34)) can be used alone or in conjunction with the current DFs for continuity of the reconstructed net current (Eq. (5.36)). The flux DFs for continuity of the reconstructed partial currents (Eq. (5.35)) *must* be used in conjunction with the current DFs (Eq. (5.36)).

We note that current DFs have been used in the past. Some were to be used specifically with bilinearly weighted (i.e., forward and adjoint weighted) cross sections for transient analysis [70, 71], while others were defined to preserve partial currents in the low-order (typically diffusion) calculation [23]. At present, those current DFs are used rarely, if at all. This is the first time current DFs have been defined to enforce physical conditions (e.g., continuity of the current) on the reconstructed fluxes. It is the presence of the $\boldsymbol{f}_1$ correction term in the asymptotic flux reconstruction that allows us (in 1-D) (i) to make *odd* angular moments of the reconstructed flux (e.g., the current) continuous and (ii) to make *two* angular moments of the reconstructed flux continuous simultaneously.

5.4 Variationally-Derived Boundary and Interface Conditions for the Multigroup Diffusion Equation

We now apply a variational analysis to the transport equation to obtain boundary and interface conditions for the asymptotic diffusion equation. The analysis is similar to earlier analyses [64, 68], but it differs in that our analysis is specific to lattice media and our functional is designed to estimate the reactor eigenvalue as opposed to reaction rates.

Our first step is define the functional for estimating the reactor eigenvalue. We then introduce the asymptotic expressions for the angular flux and obtain the monoenergetic asymptotic diffusion equation. The final step is to derive the appropriate boundary and interface conditions, the latter of which take the form of discontinuity conditions for the diffusion equation.

5.4.1 A Functional for Estimating the Reactor Eigenvalue

We begin by deriving a functional for estimating the reactor eigenvalue. The functional is optimal in the sense that first-order variations in the forward and adjoint fluxes will result in second-order variations in the eigenvalue.

Our notation in this section will differ from that in previous sections. First, the quantity we estimate will be the inverse of the reactor eigenvalue:

$$\lambda = 1/k = (1 - \rho)\,. \tag{5.37}$$

Second, we will split the lattice transport operator L used in Chapters III and IV into two distinct operators. The first operator, M, which we will in this chapter refer to as the *transport operator*, describes all transport processes *excluding* fission and

is defined as:

$$M\psi(\boldsymbol{x},\boldsymbol{\Omega},E) = \boldsymbol{\Omega}\cdot\nabla\psi(\boldsymbol{x},\boldsymbol{\Omega},E) + \Sigma_t(\boldsymbol{x},E)\psi(\boldsymbol{x},\boldsymbol{\Omega},E) - \int_0^\infty\int_{4\pi}\Sigma_s(\boldsymbol{x},\boldsymbol{\Omega}'\cdot\boldsymbol{\Omega},E'\to E)\psi(\boldsymbol{x},\boldsymbol{\Omega}',E')\,\mathrm{d}\Omega'\,\mathrm{d}E'\,. \tag{5.38}$$

The *fission operator*, F, is defined as:

$$F\psi(\boldsymbol{x},\boldsymbol{\Omega},E) = \frac{\chi(\boldsymbol{x},E)}{4\pi}\int_0^\infty\int_{4\pi}\nu\Sigma_f(\boldsymbol{x},E')\psi(\boldsymbol{x},\boldsymbol{\Omega}',E')\,\mathrm{d}\Omega'\,\mathrm{d}E'\,. \tag{5.39}$$

The adjoint transport and fission operators are defined as:

$$M^*\psi^*(\boldsymbol{x},\boldsymbol{\Omega},E) = -\boldsymbol{\Omega}\cdot\nabla\psi^*(\boldsymbol{x},\boldsymbol{\Omega},E) + \Sigma_t(\boldsymbol{x},E)\psi^*(\boldsymbol{x},\boldsymbol{\Omega},E) - \int_0^\infty\int_{4\pi}\Sigma_s(\boldsymbol{x},\boldsymbol{\Omega}'\cdot\boldsymbol{\Omega},E\to E')\psi^*(\boldsymbol{x},\boldsymbol{\Omega}',E')\,\mathrm{d}\Omega'\,\mathrm{d}E'\,, \tag{5.40}$$

$$F^*\psi^*(\boldsymbol{x},\boldsymbol{\Omega},E) = \frac{\nu\Sigma_f(\boldsymbol{x},E)}{4\pi}\int_0^\infty\int_{4\pi}\chi(\boldsymbol{x},E')\psi^*(\boldsymbol{x},\boldsymbol{\Omega}',E')\,\mathrm{d}\Omega'\,\mathrm{d}E'\,. \tag{5.41}$$

We define the *inner product* as:

$$\langle g, Lh\rangle = \int_V\int_0^\infty\int_{4\pi} gLh\,\mathrm{d}\Omega\,\mathrm{d}E\,\mathrm{d}V\,. \tag{5.42}$$

The transport equation with vacuum boundary conditions can now be written:

$$M\psi = \lambda F\psi\,,\qquad \boldsymbol{x}\in V\,,\qquad \boldsymbol{\Omega}\in 4\pi\,,\qquad 0\le E\le\infty\,, \tag{5.43a}$$

$$\psi(\boldsymbol{x},\boldsymbol{\Omega},E) = 0\,,\qquad \boldsymbol{x}\in\partial V\,,\qquad \boldsymbol{n}\cdot\boldsymbol{\Omega}<0\,,\qquad 0\le E\le\infty\,, \tag{5.43b}$$

where $\boldsymbol{n}$ is the outward unit normal vector at any point on the surface of the system, $\boldsymbol{x}\in\partial V$.

We now note from Eq. (5.43a) that for any function g, λ is exactly defined by:

$$\lambda = \frac{\langle g, M\psi\rangle}{\langle g, F\psi\rangle}\,. \tag{5.44}$$

We propose the following functional for estimating λ:

(5.45)
$$H[\Psi,\Psi^*,\Theta_{1,i},\Theta_{2,ij}] = \frac{\left[\begin{array}{r}\langle\Psi^*, M\Psi\rangle + \sum_i \int_{\partial V_i}\int_0^\infty\int_{\boldsymbol{n}\cdot\boldsymbol{\Omega}<0}\Theta_{1,i}\Psi\,\mathrm{d}\Omega\,\mathrm{d}E\,\mathrm{d}S \\ + \sum_{ij}\int_{\partial V_{ij}}\int_0^\infty\int_{4\pi}\Theta_{2,ij}\left(\Psi_i-\Psi_j\right)\,\mathrm{d}\Omega\,\mathrm{d}E\,\mathrm{d}S\end{array}\right]}{\langle\Psi^*, F\Psi\rangle},$$

where:

$$\partial V_i = \text{the external boundary of region } i\,,$$

$$\partial V_{ij} = \text{the interface between regions } i \text{ and } j\,,$$

$$\sum_i = \text{the sum over all regions}\,,$$

$$\sum_{ij} = \text{the sum over all interfaces}\,,$$

$$\Psi_i = \text{the flux on the region } i \text{ side of an interface between regions } i \text{ and } j\,.$$

Each region is assumed to be a periodic lattice. We note that in the interface sum, $\sum_{ij}$, each interface is considered only once, i.e., we consider ij but not ji. The functions Ψ, Ψ^*, $\Theta_{1,i}$, and $\Theta_{2,ij}$ are to-be-determined.

Now suppose that the approximate functions, denoted by capital letters, have an $O(\delta)$ error relative to exact functions, denoted by lower case letters:

(5.46a)
$$\Psi = \psi + \delta\psi\,,$$

(5.46b)
$$\Psi^* = \psi^* + \delta\psi^*\,,$$

(5.46c)
$$\Theta_{1,i} = \theta_{1,i} + \delta\theta_{1,i}\,,$$

(5.46d)
$$\Theta_{2,ij} = \theta_{2,ij} + \delta\theta_{2,ij}\,.$$

We desire that the first-order errors in these functions lead to only a second-order error in λ. Expressed mathematically, we require:

$$H[\Psi, \Psi^*, \Theta_{1,i}, \Theta_{2,ij}] = H[\psi+\delta\psi, \psi^*+\delta\psi^*, \theta_{1,i}+\delta\theta_{1,i}, \theta_{2,ij}+\delta\theta_{2,ij}] = \lambda+O(\delta^2)\,. \tag{5.47}$$

Introducing Eqs. (5.46a)-(5.46d) into Eq. (5.45), we get:

$$H[\Psi, \Psi^*, \Theta_{1,i}, \Theta_{2,ij}] = \frac{\left[\begin{array}{l} \langle(\psi^*+\delta\psi^*)\,, M\,(\psi+\delta\psi)\rangle \\ \quad + \sum_i \int_{\partial V_i} \int_0^\infty \int_{\boldsymbol{n}\cdot\boldsymbol{\Omega}<0} (\theta_{1,i}+\delta\theta_{1,i})\,(\psi+\delta\psi)\;\mathrm{d}\Omega\,\mathrm{d}E\,\mathrm{d}S \\ \quad + \sum_{ij} \int_{\partial V_{ij}} \int_0^\infty \int_{4\pi} (\theta_{2,ij}+\delta\theta_{2,ij})\,(\psi_i+\delta\psi_i-\psi_j-\delta\psi_j)\;\mathrm{d}\Omega\,\mathrm{d}E\,\mathrm{d}S \end{array}\right]}{\langle(\psi^*+\delta\psi^*)\,, F\,(\psi+\delta\psi)\rangle}\,.$$

Using the boundary condition (Eq. (5.43b)), the ψ in the boundary term vanishes. Furthermore, because the exact flux across interfaces is continuous, the ψ_i and ψ_j terms in the interface term cancel. Finally, since we expect $O(\delta^2)$ error in the functional (Eq. (5.47)), we simply neglect the $O(\delta^2)$ terms. We are left with:

$$H[\Psi, \Psi^*, \Theta_{1,i}, \Theta_{2,ij}] = \frac{\left[\begin{array}{l} \langle\psi^*, M\psi\rangle + \langle\psi^*, M\delta\psi\rangle + \langle\delta\psi^*, M\psi\rangle \\ \quad + \sum_i \int_{\partial V_i} \int_0^\infty \int_{\boldsymbol{n}\cdot\boldsymbol{\Omega}<0} \theta_{1,i}\delta\psi\;\mathrm{d}\Omega\,\mathrm{d}E\,\mathrm{d}S \\ \quad + \sum_{ij} \int_{\partial V_{ij}} \int_0^\infty \int_{4\pi} \theta_{2,ij}\,(\delta\psi_i-\delta\psi_j)\;\mathrm{d}\Omega\,\mathrm{d}E\,\mathrm{d}S \end{array}\right]}{\langle\psi^*, F\psi\rangle + \langle\psi^*, F\delta\psi\rangle + \langle\delta\psi^*, F\psi\rangle}\,.$$

Dividing the numerator and denominator by $\langle \psi^* F \psi \rangle$ and using Eq. (5.44) yields:

$$H[\Psi, \Psi^*, \Theta_{1,i}, \Theta_{2,ij}] = \lambda + \frac{\left[\begin{array}{l} \langle \psi^*, M\delta\psi \rangle + \langle \delta\psi^*, M\psi \rangle \\ \quad + \sum_i \int_{\partial V_i} \int_0^\infty \int_{\boldsymbol{n}\cdot\boldsymbol{\Omega}<0} \theta_{1,i} \delta\psi \, \mathrm{d}\Omega \, \mathrm{d}E \, \mathrm{d}S \\ \quad + \sum_{ij} \int_{\partial V_{ij}} \int_0^\infty \int_{4\pi} \theta_{2,ij} \left(\delta\psi_i - \delta\psi_j\right) \, \mathrm{d}\Omega \, \mathrm{d}E \, \mathrm{d}S \end{array}\right] / \langle \psi^*, F\psi \rangle}{1 + \left[\langle \psi^*, F\delta\psi \rangle + \langle \delta\psi^*, F\psi \rangle\right] / \langle \psi^*, F\psi \rangle} .$$

This equation is of the form $(\lambda + O(\delta)_1)/(1 + O(\delta)_2)$ and can therefore be rewritten using only the first two terms in a Taylor series expansion:

$$\begin{aligned} H[\Psi, \Psi^*, \Theta_{1,i}, \Theta_{2,ij}] &= \frac{\lambda + O(\delta)_1}{1 + O(\delta)_2} , \\ &\approx \left(\lambda + O(\delta)_1\right)\left(1 - O(\delta)_2\right) = \lambda + O(\delta)_1 - \lambda O(\delta)_2 - O(\delta)_1 O(\delta)_2 . \end{aligned}$$

Neglecting the $O(\delta^2)$ term, we have:

$$H[\Psi, \Psi^*, \Theta_{1,i}, \Theta_{2,ij}] = \lambda + \frac{\left[\begin{array}{l} \langle \psi^*, M\delta\psi \rangle + \langle \delta\psi^*, M\psi \rangle \\ \quad - \lambda \langle \psi^*, F\delta\psi \rangle - \lambda \langle \delta\psi^*, F\psi \rangle \\ \quad + \sum_i \int_{\partial V_i} \int_0^\infty \int_{\boldsymbol{n}\cdot\boldsymbol{\Omega}<0} \theta_{1,i} \delta\psi \, \mathrm{d}\Omega \, \mathrm{d}E \, \mathrm{d}S \\ \quad + \sum_{ij} \int_{\partial V_{ij}} \int_0^\infty \int_{4\pi} \theta_{2,ij} \left(\delta\psi_i - \delta\psi_j\right) \, \mathrm{d}\Omega \, \mathrm{d}E \, \mathrm{d}S \end{array}\right]}{\langle \psi^*, F\psi \rangle} .$$

Using Eq. (5.44), the red terms cancel. Comparing the preceding equation to Eq. (5.47), we find that the bracketed terms, which are all $O(\delta)$, must vanish:

$$\begin{aligned} 0 = \langle \psi^*, M\delta\psi \rangle - \lambda \langle \psi^*, F\delta\psi \rangle + \sum_i \int_{\partial V_i} \int_0^\infty \int_{\boldsymbol{n}\cdot\boldsymbol{\Omega}<0} \theta_{1,i} \delta\psi \, \mathrm{d}\Omega \, \mathrm{d}E \, \mathrm{d}S \\ + \sum_{ij} \int_{\partial V_{ij}} \int_0^\infty \int_{4\pi} \theta_{2,ij} \left(\delta\psi_i - \delta\psi_j\right) \, \mathrm{d}\Omega \, \mathrm{d}E \, \mathrm{d}S . \end{aligned} \tag{5.48}$$

We now rewrite the two inner products using the definitions of the adjoint operators (Eqs. (5.40) and (5.41)). The inner product of the fission term becomes:

$$\langle \psi^*, F\delta\psi \rangle = \langle \delta\psi, F^*\psi^* \rangle \ . \tag{5.49}$$

The inner product of the transport term becomes:

$$\begin{aligned}
\langle \psi^*, M\delta\psi \rangle &= \int_V \int_0^\infty \int_{4\pi} \left(\psi^* \mathbf{\Omega} \cdot \nabla \delta\psi + \cdots \right) \, \mathrm{d}\Omega \, \mathrm{d}E \, \mathrm{d}V \, , \\
&= \int_V \int_0^\infty \int_{4\pi} \left(\mathbf{\Omega} \cdot \nabla \left(\psi^* \delta\psi \right) - \delta\psi \mathbf{\Omega} \cdot \nabla \psi^* + \cdots \right) \, \mathrm{d}\Omega \, \mathrm{d}E \, \mathrm{d}V \, , \\
&= \left(\sum_i \int_{V_i} \int_0^\infty \int_{4\pi} \mathbf{\Omega} \cdot \nabla \left(\psi^* \delta\psi \right) \, \mathrm{d}\Omega \, \mathrm{d}E \, \mathrm{d}V \right) + \langle \delta\psi, M^*\psi^* \rangle \ .
\end{aligned}$$

The integrals in the sum over regions can each be rewritten using the divergence theorem. This leaves us with a sum of surface integrals over exterior and interior surfaces. Each exterior surface is accounted for only once, but the interior surfaces appear in two separate integrals. For instance, at the interface between regions i and j, applying the divergence theorem to each region yields two surface integrals for the surface ij. Since the error term, $\delta\psi$, could be discontinuous, we use the error term $\delta\psi_i$ in the surface integral corresponding to region i and the error term $\delta\psi_j$ in the surface integral corresponding to region j. Finally, we note that the unit normal vector $\boldsymbol{n}_{ji}$ that arises when the divergence theorem is applied to region j is the negative of the unit normal vector $\boldsymbol{n}_{ij}$ that arises when the divergence theorem is applied to region i. Therefore, the two interface surface integrals can be written as a single integral containing the difference of the two error terms, $(\delta\psi_i - \delta\psi_j)$. Then our inner product becomes:

$$\begin{aligned}
\langle \psi^*, M\delta\psi \rangle = \langle \delta\psi, M^*\psi^* \rangle &+ \sum_i \int_{\partial V_i} \int_0^\infty \int_{4\pi} \left(\boldsymbol{n} \cdot \mathbf{\Omega} \right) \psi^* \delta\psi \, \mathrm{d}\Omega \, \mathrm{d}E \, \mathrm{d}S \\
&+ \sum_{ij} \int_{\partial V_{ij}} \int_0^\infty \int_{4\pi} \left(\boldsymbol{n}_{ij} \cdot \mathbf{\Omega} \right) \psi^* \left(\delta\psi_i - \delta\psi_j \right) \, \mathrm{d}\Omega \, \mathrm{d}E \, \mathrm{d}S \, .
\end{aligned} \tag{5.50}$$

Introducing Eqs. (5.49) and (5.50) into Eq. (5.48), we obtain:

$$\begin{aligned}
0 = &\langle \delta\psi, M^*\psi^* \rangle - \lambda \langle \delta\psi, F^*\psi^* \rangle \\
&+ \sum_i \int_{\partial V_i} \int_0^\infty \int_{4\pi} (\boldsymbol{n}\cdot\boldsymbol{\Omega})\, \psi^* \delta\psi \,\mathrm{d}\Omega \,\mathrm{d}E \,\mathrm{d}S \\
&+ \sum_i \int_{\partial V_i} \int_0^\infty \int_{\boldsymbol{n}\cdot\boldsymbol{\Omega}<0} \theta_{1,i} \delta\psi \,\mathrm{d}\Omega \,\mathrm{d}E \,\mathrm{d}S \\
&+ \sum_{ij} \int_{\partial V_{ij}} \int_0^\infty \int_{4\pi} (\boldsymbol{n}_{ij}\cdot\boldsymbol{\Omega})\, \psi^* \left(\delta\psi_i - \delta\psi_j\right) \,\mathrm{d}\Omega \,\mathrm{d}E \,\mathrm{d}S \\
&+ \sum_{ij} \int_{\partial V_{ij}} \int_0^\infty \int_{4\pi} \theta_{2,ij} \left(\delta\psi_i - \delta\psi_j\right) \,\mathrm{d}\Omega \,\mathrm{d}E \,\mathrm{d}S \,.
\end{aligned}$$

It is now clear that for the $O(\delta)$ terms to vanish, the function ψ^* must satisfy the adjoint transport equation with vacuum boundary conditions (note that the adjoint boundary condition applies to outgoing angles):

$$L^*\psi^* = \lambda F^*\psi^* \,, \qquad \boldsymbol{x} \in V \,, \qquad 0 \le E \le \infty \,, \tag{5.51a}$$

$$\psi^*(\boldsymbol{x}, \boldsymbol{\Omega}, E) = 0 \,, \qquad \boldsymbol{x} \in \partial V \,, \qquad \boldsymbol{n}\cdot\boldsymbol{\Omega} > 0 \,, \qquad 0 \le E \le \infty \,. \tag{5.51b}$$

Furthermore, the following must be true:

$$\theta_{1,i} = -\left(\boldsymbol{n}\cdot\boldsymbol{\Omega}\right)\psi^*(\boldsymbol{x}, \boldsymbol{\Omega}, E) = -\left(\boldsymbol{n}\cdot\boldsymbol{\Omega}\right)\left[\psi^*(\boldsymbol{x}, \boldsymbol{\Omega}, E) + \alpha\psi^*(\boldsymbol{x}, \boldsymbol{\Omega}_r, E)\right] \,, \tag{5.52}$$

$$|\alpha| \le 1 \,,$$

$$\theta_{2,ij} = -\left(\boldsymbol{n}_{ij}\cdot\boldsymbol{\Omega}\right)\psi^*(\boldsymbol{x}, \boldsymbol{\Omega}, E) = -\frac{1}{2}\left(\boldsymbol{n}_{ij}\cdot\boldsymbol{\Omega}\right)\left[\psi_i^*(\boldsymbol{x}, \boldsymbol{\Omega}, E) + \psi_j^*(\boldsymbol{x}, \boldsymbol{\Omega}, E)\right] \,, \tag{5.53}$$

where $\boldsymbol{\Omega}_r$ is the angle of reflection across the surface. The second term in Eq. (5.52) vanishes if the exact adjoint solution is used due to the vacuum boundary condition. As we will show in Section 5.4.3, the choices $\alpha = 1$ and $\alpha = 0$ will ultimately leads to the Marshak and Federighi-Pomraning extrapolation distances respectively.

Equation (5.53) is written in this form to allow for the fact that while the exact adjoint solution ψ^* is continuous across interfaces, the trial function used in our functional estimate of λ, Ψ^*, is not. The approximate weight functions are defined using the approximate trial functions:

$$\Theta_{1,i} = -\left(\boldsymbol{n}\cdot\boldsymbol{\Omega}\right)\Psi^*(\boldsymbol{x},\boldsymbol{\Omega},E) = -\left(\boldsymbol{n}\cdot\boldsymbol{\Omega}\right)\left[\Psi^*(\boldsymbol{x},\boldsymbol{\Omega},E) + \alpha\Psi^*(\boldsymbol{x},\boldsymbol{\Omega}_r,E)\right]\,, \tag{5.54}$$

$$|\alpha| \leq 1\,,$$

$$\Theta_{2,ij} = -\left(\boldsymbol{n}_{ij}\cdot\boldsymbol{\Omega}\right)\Psi^*(\boldsymbol{x},\boldsymbol{\Omega},E) = -\frac{1}{2}\left(\boldsymbol{n}_{ij}\cdot\boldsymbol{\Omega}\right)\left[\Psi_i^*(\boldsymbol{x},\boldsymbol{\Omega},E) + \Psi_j^*(\boldsymbol{x},\boldsymbol{\Omega},E)\right]\,. \tag{5.55}$$

Introducing Eqs. (5.54) and (5.54) into Eq. (5.45) yields a functional for estimating the reactor eigenvalue:

$$H[\Psi,\Psi^*] = \frac{\left[\begin{array}{l}\langle\Psi^*, M\Psi\rangle \\ \quad -\sum_i \int_{\partial V_i}\int_0^\infty\int_{\boldsymbol{n}\cdot\boldsymbol{\Omega}<0}\left(\boldsymbol{n}\cdot\boldsymbol{\Omega}\right)\left[\Psi^* + \alpha\Psi_r^*\right]\Psi\,\mathrm{d}\Omega\,\mathrm{d}E\,\mathrm{d}S \\ \quad -\frac{1}{2}\sum_{ij}\int_{\partial V_{ij}}\int_0^\infty\int_{4\pi}\left(\boldsymbol{n}_{ij}\cdot\boldsymbol{\Omega}\right)\left[\Psi_i^* + \Psi_j^*\right]\left[\Psi_i - \Psi_j\right]\,\mathrm{d}\Omega\,\mathrm{d}E\,\mathrm{d}S\end{array}\right]}{\langle\Psi^*, F\Psi\rangle}\,, \tag{5.56}$$

where $\Psi_r^* = \Psi^*(\boldsymbol{x},\boldsymbol{\Omega}_r,E)$. Equation (5.56) can also be written in terms of the adjoint operators:

$$H[\Psi,\Psi^*] = \frac{\left[\begin{array}{l}\langle\Psi, M^*\Psi^*\rangle \\ \quad +\sum_i \int_{\partial V_i}\int_0^\infty\int_{\boldsymbol{n}\cdot\boldsymbol{\Omega}>0}\left(\boldsymbol{n}\cdot\boldsymbol{\Omega}\right)\left[\Psi + \alpha\Psi_r\right]\Psi^*\,\mathrm{d}\Omega\,\mathrm{d}E\,\mathrm{d}S \\ \quad +\frac{1}{2}\sum_{ij}\int_{\partial V_{ij}}\int_0^\infty\int_{4\pi}\left(\boldsymbol{n}_{ij}\cdot\boldsymbol{\Omega}\right)\left[\Psi_i + \Psi_j\right]\left[\Psi_i^* - \Psi_j^*\right]\,\mathrm{d}\Omega\,\mathrm{d}E\,\mathrm{d}S\end{array}\right]}{\langle\Psi, F^*\Psi^*\rangle}\,. \tag{5.57}$$

By design, the functional satisfies:

$$H[\Psi,\Psi^*] = H[\psi+\delta\psi,\psi^*+\delta\psi^*] = \lambda + O(\delta^2)\,. \tag{5.58}$$

Furthermore, introducing Eqs. (5.43a) and (5.43b) into Eq. (5.56) and Eqs. (5.51a) and (5.51b) into Eq. (5.57) reveals:

$$H[\psi, \Psi^*] = H[\Psi, \psi^*] = \lambda \,. \tag{5.59}$$

In other words, the estimate of λ is exact if either ψ or ψ^* is exact. Thus, (ψ, ψ^*) is a stationary point of H.

5.4.2 Introduction of the Asymptotic Flux Expansion Into the Functional Estimate of the Reactor Eigenvalue

We must now choose trial functions to use in our functional estimate of λ. The trial functions must satisfy Eqs. (5.46a) and (5.46b). We will use the asymptotic expressions for the forward and adjoint flux:

(5.60a)

$$\Psi(\boldsymbol{x}, \boldsymbol{\Omega}, E) = f_{0,i}(\boldsymbol{x}, \boldsymbol{\Omega}, E)\Phi_i(\boldsymbol{x}) - \boldsymbol{f}_{1,i}(\boldsymbol{x}, \boldsymbol{\Omega}, E) \cdot \nabla\Phi_i(\boldsymbol{x}) + O(\epsilon^2) \,, \qquad \boldsymbol{x} \in V_i \,,$$

(5.60b)

$$\Psi^*(\boldsymbol{x}, \boldsymbol{\Omega}, E) = f^*_{0,i}(\boldsymbol{x}, \boldsymbol{\Omega}, E)\Phi^*_i(\boldsymbol{x}) + \boldsymbol{f}^*_{1,i}(\boldsymbol{x}, \boldsymbol{\Omega}, E) \cdot \nabla\Phi^*_i(\boldsymbol{x}) + O(\epsilon^2) \,, \qquad \boldsymbol{x} \in V_i \,.$$

Although not shown explicitly, the derivation of the adjoint asymptotic flux is analogous to that of the forward asymptotic flux. Note the change in sign of the second term in Eq. (5.60b). In each region i, the lattice functions satisfy the transport equation with period boundaries:

$$M f_{0,i} = \lambda_{0,i} F f_{0,i} \,, \qquad \boldsymbol{x} \in V_i \,, \tag{5.61a}$$

$$M\boldsymbol{f}_{1,i} = \lambda_{0,i} F\boldsymbol{f}_{1,i} + \boldsymbol{\Omega} f_{0,i} \,, \qquad \boldsymbol{x} \in V_i \,, \tag{5.61b}$$

$$M^* f^*_{0,i} = \lambda_{0,i} F^* f^*_{0,i} \,, \qquad \boldsymbol{x} \in V_i \,, \tag{5.61c}$$

$$M^* \boldsymbol{f}^*_{1,i} = \lambda_{0,i} F^* \boldsymbol{f}^*_{1,i} + \boldsymbol{\Omega} f^*_{0,i} \,, \qquad \boldsymbol{x} \in V_i \,. \tag{5.61d}$$

We recall that the solutions to Eqs. (5.61b) and (5.61d) are not unique, but we make them unique by requiring:

$$0 = \langle f^*_{0,i}, \boldsymbol{f}_{1,i} \rangle \tag{5.61e}$$

$$0 = \langle f_{0,i}, \boldsymbol{f}^*_{1,i} \rangle \tag{5.61f}$$

The f_0 functions are symmetric in angle on the boundaries, while the f_1 functions are antisymmetric in angle on the boundaries:

$$f_{0,i}(\boldsymbol{x}, \boldsymbol{\Omega}, E) = f_{0,i}(\boldsymbol{x}, \boldsymbol{\Omega}_r, E) = f_{0,i,r} \,, \qquad \boldsymbol{x} \in \partial V_i \,, \tag{5.62a}$$

$$\boldsymbol{f}_{1,i}(\boldsymbol{x}, \boldsymbol{\Omega}, E) = -\boldsymbol{f}_{1,i}(\boldsymbol{x}, \boldsymbol{\Omega}_r, E) = -\boldsymbol{f}_{1,i,r} \,, \qquad \boldsymbol{x} \in \partial V_i \,, \tag{5.62b}$$

$$f^*_{0,i}(\boldsymbol{x}, \boldsymbol{\Omega}, E) = f^*_{0,i}(\boldsymbol{x}, \boldsymbol{\Omega}_r, E) = f^*_{0,i,r} \,, \qquad \boldsymbol{x} \in \partial V_i \,, \tag{5.62c}$$

$$\boldsymbol{f}^*_{1,i}(\boldsymbol{x}, \boldsymbol{\Omega}, E) = -\boldsymbol{f}^*_{1,i}(\boldsymbol{x}, \boldsymbol{\Omega}_r, E) = -\boldsymbol{f}^*_{1,i,r} \,, \qquad \boldsymbol{x} \in \partial V_i \,. \tag{5.62d}$$

Comparing Eqs. (5.60a) and (5.60b) to Eqs. (5.46a) and (5.46b), we conclude that:

$$O(\delta) = O(\epsilon^2) \,. \tag{5.63}$$

Therefore, terms of $O(\delta^2) = O(\epsilon^4)$ will be neglected. From the asymptotic analysis, we know that:

$$f_{0/1,i} = O(1) \,, \tag{5.64a}$$

$$\Phi = O(1) \,, \tag{5.64b}$$

$$\nabla^n \Phi = O(\epsilon^n)\,. \tag{5.64c}$$

We now introduce Eqs. (5.60a) and (5.60b) into Eq. (5.56) to obtain:

$$H[\Psi, \Psi^*] = H[\Phi, \Phi^*] = H_0 - \frac{B+I}{D}\,, \tag{5.65}$$

where H_0 is the functional excluding boundary and interface terms:

$$H_0 = \frac{\sum_i \left\langle \left[f^*_{0,i}\Phi^*_i + \boldsymbol{f}^*_{1,i}\cdot\nabla\Phi^*_i\right], M\left[f_{0,i}\Phi_i - \boldsymbol{f}_{1,i}\cdot\nabla\Phi_i\right]\right\rangle_i}{\sum_i \left\langle \left[f^*_{0,i}\Phi^*_i + \boldsymbol{f}^*_{1,i}\cdot\nabla\Phi^*_i\right], F\left[f_{0,i}\Phi_i - \boldsymbol{f}_{1,i}\cdot\nabla\Phi_i\right]\right\rangle_i}\,, \tag{5.66}$$

B is the boundary term:

$$\begin{aligned} B = \sum_i \int_{\partial V_i} \int_0^\infty \int_{\boldsymbol{n}\cdot\boldsymbol{\Omega}<0} (\boldsymbol{n}\cdot\boldsymbol{\Omega}) \left[f^*_{0,i}\Phi^* + \boldsymbol{f}^*_{1,i}\cdot\nabla\Phi^* + \alpha f^*_{0,i,r}\Phi^* + \alpha\boldsymbol{f}^*_{1,i,r}\cdot\nabla\Phi^*\right] \\ \times \left[f_{0,i}\Phi - \boldsymbol{f}_{1,i}\cdot\nabla\Phi\right] \mathrm{d}\Omega\,\mathrm{d}E\,\mathrm{d}S\,, \end{aligned} \tag{5.67}$$

I is the interface term:

$$\begin{aligned} I = \frac{1}{2}\sum_{ij} \int_{\partial V_{ij}} \int_0^\infty \int_{4\pi} (\boldsymbol{n}_{ij}\cdot\boldsymbol{\Omega}) \left[f^*_{0,i}\Phi^*_i + \boldsymbol{f}^*_{1,i}\cdot\nabla\Phi^*_i + f^*_{0,j}\Phi^*_j + \boldsymbol{f}^*_{1,j}\cdot\nabla\Phi^*_j\right] \\ \times \left[f_{0,i}\Phi_i - \boldsymbol{f}_{1,i}\cdot\nabla\Phi_i - f_{0,j}\Phi_j + \boldsymbol{f}_{1,j}\cdot\nabla\Phi_j\right] \mathrm{d}\Omega\,\mathrm{d}E\,\mathrm{d}S\,, \end{aligned} \tag{5.68}$$

and D is the denominator:

$$D = \left\langle \left[f^*_0\Phi^* + \boldsymbol{f}^*_1\cdot\nabla\Phi^*\right], F\left[f_0\Phi - \boldsymbol{f}_1\cdot\nabla\Phi\right]\right\rangle. \tag{5.69}$$

Note that the subscript i for an inner product $\langle\cdot\rangle_i$ indicates that the volume integral is only performed over region i rather than the full system. Thus, $\langle\cdot\rangle = \sum_i \langle\cdot\rangle_i$.

Before simplifying the above expressions, we derive some properties of the volume-angle double integrals in periodic media. We assume that the reactor is composed of 1 or more regions with a rectangular, periodic lattice structure. Each lattice

element (i,j,k) is centered at $\boldsymbol{x}_{ijk} = (x_i, y_j, z_k)$ and has dimensions $(\Delta x, \Delta y, \Delta z)$. We let the total number of lattice elements in the region be $NX \times NY \times NZ$. We now consider a volume-angle double integral in one of these periodic regions. The integral is assumed to be of the form:

$$\int_V \int_0^\infty \int_{4\pi} f(\boldsymbol{x}, \boldsymbol{\Omega}, E) A(\boldsymbol{x}) \, \mathrm{d}\Omega \, \mathrm{d}E \, \mathrm{d}V \,,$$

where f is a periodic function and A is a slowly varying, non-periodic function such that:

$$\nabla^n A = O(\epsilon^n) O(A) \,. \tag{5.70}$$

The function A will be of the general form $\nabla^n \Phi$, and so the order of A varies. We first consider the case of f being symmetric in $(\boldsymbol{x}, \boldsymbol{\Omega})$. Using a Taylor series expansion, A can be brought outside the volume integral in the following way:

$$\begin{aligned}
&\int_V \int_0^\infty \int_{4\pi} f(\boldsymbol{x}, \boldsymbol{\Omega}, E) A(\boldsymbol{x}) \, \mathrm{d}\Omega \, \mathrm{d}E \, \mathrm{d}V \\
&\quad = \sum_{i=1}^{NX} \sum_{j=1}^{NY} \sum_{i=1}^{NZ} \int_{(i-1)\Delta x}^{i\Delta x} \int_{(j-1)\Delta y}^{j\Delta y} \int_{(k-1)\Delta z}^{k\Delta z} \int_0^\infty \int_{4\pi} f(x, y, z, \boldsymbol{\Omega}, E) \\
&\qquad \times A(x, y, z) \, \mathrm{d}\Omega \, \mathrm{d}E \, \mathrm{d}x \, \mathrm{d}y \, \mathrm{d}z \,, \\
&\quad = \sum_{i=1}^{NX} \sum_{j=1}^{NY} \sum_{i=1}^{NZ} \int_{(i-1)\Delta x}^{i\Delta x} \int_{(j-1)\Delta y}^{j\Delta y} \int_{(k-1)\Delta z}^{k\Delta z} \int_0^\infty \int_{4\pi} f(x, y, z, \boldsymbol{\Omega}, E) \\
&\qquad \times \left[A(x_i, y_j, z_k) + (\boldsymbol{x} - \boldsymbol{x}_{ijk}) \cdot \nabla A(x_i, y_j, z_k) + O(\epsilon^2) O(A) \right] \mathrm{d}\Omega \, \mathrm{d}E \, \mathrm{d}x \, \mathrm{d}y \, \mathrm{d}z \,, \\
&\quad = \sum_{i=1}^{NX} \sum_{j=1}^{NY} \sum_{i=1}^{NZ} \Bigg[\left[\int_{(i-1)\Delta x}^{i\Delta x} \int_{(j-1)\Delta y}^{j\Delta y} \int_{(k-1)\Delta z}^{k\Delta z} \int_0^\infty \int_{4\pi} f(\boldsymbol{x}, \boldsymbol{\Omega}, E) \, \mathrm{d}\Omega \, \mathrm{d}E \, \mathrm{d}x \, \mathrm{d}y \, \mathrm{d}z \right] \\
&\qquad\qquad \times A(\boldsymbol{x}_{ijk}) + O(\epsilon^2) O(A) \Bigg] \,, \\
&\quad = \sum_{i=1}^{NX} \sum_{j=1}^{NY} \sum_{i=1}^{NZ} \left[\overline{f} A(\boldsymbol{x}_{ijk}) + O(\epsilon^2) O(A) \right] \,,
\end{aligned}$$

where:

$$\overline{f} = \int_{(i-1)\Delta x}^{i\Delta x} \int_{(j-1)\Delta y}^{j\Delta y} \int_{(k-1)\Delta z}^{k\Delta z} \int_0^\infty \int_{4\pi} f(\boldsymbol{x}, \boldsymbol{\Omega}, E)\, \mathrm{d}\Omega\, \mathrm{d}E\, \mathrm{d}x\, \mathrm{d}y\, \mathrm{d}z\,, \tag{5.71}$$
$$= \int_{cell} \int_0^\infty \int_{4\pi} f(\boldsymbol{x}, \boldsymbol{\Omega}, E)\, \mathrm{d}\Omega\, \mathrm{d}E\, \mathrm{d}V\,.$$

The red term $(\boldsymbol{x} - \boldsymbol{x}_{ijk})$ is an antisymmetric function of $(\boldsymbol{x}, \boldsymbol{\Omega})$. If f is symmetric in $(\boldsymbol{x}, \boldsymbol{\Omega})$, then the double integral of $f(\boldsymbol{x}, \boldsymbol{\Omega}) \times (\boldsymbol{x} - \boldsymbol{x}_{ijk})$ vanishes.

A similar Taylor series expansion can be used to show that:

$$\int_V \overline{f} A(\boldsymbol{x})\, \mathrm{d}V = \sum_{i=1}^{NX} \sum_{j=1}^{NY} \sum_{i=1}^{NZ} \left[\overline{f} A(\boldsymbol{x}_{ijk}) + O(\epsilon^2) O(A)\right]\,,$$

and therefore for symmetric functions, f_{symm}:

$$\int_V \int_0^\infty \int_{4\pi} f_{symm}(\boldsymbol{x}, \boldsymbol{\Omega}, E) A(\boldsymbol{x})\, \mathrm{d}\Omega\, \mathrm{d}E\, \mathrm{d}V = \int_V \left[\overline{f} A(\boldsymbol{x}) + O(\epsilon^2) O(A)\right]\, \mathrm{d}V\,. \tag{5.72}$$

We note that for antisymmetric functions, $f_{antisymm}$, the first term in the Taylor series expansion vanishes, and the second term involving $(\boldsymbol{x} - \boldsymbol{x}_{ijk})$ remains. Thus, for antisymmetric functions, $f_{antisymm}$:

$$\int_V \int_0^\infty \int_{4\pi} f_{antisymm}(\boldsymbol{x}, \boldsymbol{\Omega}, E) A(\boldsymbol{x})\, \mathrm{d}\Omega\, \mathrm{d}E\, \mathrm{d}V = \int_V O(\epsilon) O(A)\, \mathrm{d}V\,. \tag{5.73}$$

Next, we consider how to rewrite the following term: $M\left[f_{0,i}\Phi_i - \boldsymbol{f}_{1,i} \cdot \nabla \Phi_i\right]$. We consider the first term:

(5.74)

$$\begin{aligned} M\left(f_{0,i}\Phi_i\right) &= \boldsymbol{\Omega} \cdot \nabla \left[f_{0,i}(\boldsymbol{x}, \boldsymbol{\Omega}, E)\Phi_i(\boldsymbol{x})\right] + \Sigma_t(\boldsymbol{x}, E)\left[f_{0,i}(\boldsymbol{x}, \boldsymbol{\Omega}, E)\Phi_i(\boldsymbol{x})\right] \\ &\quad - \int_0^\infty \int_{4\pi} \Sigma_s(\boldsymbol{x}, \boldsymbol{\Omega}' \cdot \boldsymbol{\Omega}, E' \to E)\left[f_{0,i}(\boldsymbol{x}, \boldsymbol{\Omega}', E')\Phi_i(\boldsymbol{x})\right]\, \mathrm{d}\Omega'\, \mathrm{d}E'\,, \\ &= f_{0,i}\boldsymbol{\Omega} \cdot \nabla \Phi_i + \Phi_i \boldsymbol{\Omega} \cdot \nabla f_{0,i} + \Phi_i \Sigma_t f_{0,i} + \Phi_i \int_0^\infty \int_{4\pi} \Sigma_s f_{0,i}\, \mathrm{d}\Omega'\, \mathrm{d}E'\,, \\ &= f_{0,i}\boldsymbol{\Omega} \cdot \nabla \Phi_i + \Phi_i M f_{0,i}\,, \\ &= f_{0,i}\boldsymbol{\Omega} \cdot \nabla \Phi_i + \Phi_i \lambda_{0,i} F f_{0,i}\,. \end{aligned}$$

The last equation is obtained by applying Eq. (5.61a). Now we consider the second term:

(5.75)

$$\begin{aligned} M\left(\boldsymbol{f}_{1,i}\cdot\nabla\Phi_i(\boldsymbol{x})\right) &= \boldsymbol{\Omega}\cdot\nabla\left[\boldsymbol{f}_{1,i}(\boldsymbol{x},\boldsymbol{\Omega},E)\cdot\nabla\Phi_i\right]+\Sigma_t(\boldsymbol{x},E)\left[\boldsymbol{f}_{1,i}(\boldsymbol{x},\boldsymbol{\Omega},E)\cdot\nabla\Phi_i(\boldsymbol{x})\right] \\ &\quad -\int_0^\infty\int_{4\pi}\Sigma_s(\boldsymbol{x},\boldsymbol{\Omega}'\cdot\boldsymbol{\Omega},E'\to E) \\ &\qquad\qquad \times\left[\boldsymbol{f}_{1,i}(\boldsymbol{x},\boldsymbol{\Omega},E)\cdot\nabla\Phi_i(\boldsymbol{x})\right]\,\mathrm{d}\Omega'\,\mathrm{d}E'\,, \\ &= \boldsymbol{f}_{1,i}\cdot\left[\left(\boldsymbol{\Omega}\cdot\nabla\right)\nabla\Phi_i\right]+\nabla\Phi_i\cdot\left[\left(\boldsymbol{\Omega}\cdot\nabla\right)\boldsymbol{f}_{1,i}\right]+\nabla\Phi_i\cdot\left(\Sigma_t\boldsymbol{f}_{1,i}\right) \\ &\quad -\left(\nabla\Phi_i\right)\cdot\left(\int_0^\infty\int_{4\pi}\Sigma_s\boldsymbol{f}_{1,i}\,\mathrm{d}\Omega'\,\mathrm{d}E'\right)\,, \\ &= \boldsymbol{f}_{1,i}\cdot\left[\left(\boldsymbol{\Omega}\cdot\nabla\right)\nabla\Phi_i\right]+\nabla\Phi_i\cdot\left(M\boldsymbol{f}_{1,i}\right)\,, \\ &= \boldsymbol{f}_{1,i}\cdot\left[\left(\boldsymbol{\Omega}\cdot\nabla\right)\nabla\Phi_i\right]+\nabla\Phi_i\cdot\left[\lambda_{0,i}F\boldsymbol{f}_{1,i}+\boldsymbol{\Omega}f_{0,i}\right]. \end{aligned}$$

The last equation is obtained by applying Eq. (5.61b). Combining Eqs. (5.74) and (5.75) yields:

(5.76)

$$\begin{aligned} M\left[f_{0,i}\Phi_i-\boldsymbol{f}_{1,i}\cdot\nabla\Phi_i\right] &= -\boldsymbol{f}_{1,i}\cdot\left[\left(\boldsymbol{\Omega}\cdot\nabla\right)\nabla\Phi_i\right]+\Phi_i\lambda_{0,i}Ff_{0,i}-\nabla\Phi_i\cdot\lambda_{0,i}F\boldsymbol{f}_{1,i}\,, \\ &= -\boldsymbol{f}_{1,i}\cdot\left[\left(\boldsymbol{\Omega}\cdot\nabla\right)\nabla\Phi_i\right]+\lambda_{0,i}F\left[f_{0,i}\Phi_i-\boldsymbol{f}_{1,i}\cdot\nabla\Phi_i\right]\,. \end{aligned}$$

We now turn our attention to simplifying Eq. (5.66). Introducing Eq. (5.76) yields:

(5.77)
$$\begin{aligned} H_0 = &\frac{\sum_i\lambda_{0,i}\left\langle\left[f_{0,i}^*\Phi_i^*+\boldsymbol{f}_{1,i}^*\cdot\nabla\Phi_i^*\right],F\left[f_{0,i}\Phi_i-\boldsymbol{f}_{1,i}\cdot\nabla\Phi_i\right]\right\rangle_i}{\sum_i\left\langle\left[f_{0,i}^*\Phi_i^*+\boldsymbol{f}_{1,i}^*\cdot\nabla\Phi_i^*\right],F\left[f_{0,i}\Phi_i-\boldsymbol{f}_{1,i}\cdot\nabla\Phi_i\right]\right\rangle_i} \\ &-\frac{\sum_i\left\langle\left[f_{0,i}^*\Phi_i^*+\boldsymbol{f}_{1,i}^*\cdot\nabla\Phi_i^*\right],\boldsymbol{f}_{1,i}\cdot\left[\left(\boldsymbol{\Omega}\cdot\nabla\right)\nabla\Phi_i\right]\right\rangle_i}{\sum_i\left\langle\left[f_{0,i}^*\Phi_i^*+\boldsymbol{f}_{1,i}^*\cdot\nabla\Phi_i^*\right],F\left[f_{0,i}\Phi_i-\boldsymbol{f}_{1,i}\cdot\nabla\Phi_i\right]\right\rangle_i}\,. \end{aligned}$$

Consider the first term in Eq. (5.77):

$$\frac{\sum_i \lambda_{0,i} \left\langle \left[f^*_{0,i}\Phi^*_i + \boldsymbol{f}^*_{1,i}\cdot\nabla\Phi^*_i \right], F\left[f_{0,i}\Phi_i - \boldsymbol{f}_{1,i}\cdot\nabla\Phi_i \right] \right\rangle_i}{\sum_i \left\langle \left[f^*_{0,i}\Phi^*_i + \boldsymbol{f}^*_{1,i}\cdot\nabla\Phi^*_i \right], F\left[f_{0,i}\Phi_i - \boldsymbol{f}_{1,i}\cdot\nabla\Phi_i \right] \right\rangle_i}$$

$$= \frac{\sum_i \lambda_{0,i} \left\langle \begin{array}{l} f^*_{0,i}\Phi^*_i, Ff_{0,i}\Phi_i + \boldsymbol{f}^*_{1,i}\cdot\nabla\Phi^*_i, Ff_{0,i}\Phi_i \\ \quad - f^*_{0,i}\Phi^*_i, F\boldsymbol{f}_{1,i}\cdot\nabla\Phi_i - \boldsymbol{f}^*_{1,i}\cdot\nabla\Phi^*_i, F\boldsymbol{f}_{1,i}\cdot\nabla\Phi_i \end{array} \right\rangle_i}{\sum_i \left\langle \begin{array}{l} f^*_{0,i}\Phi^*_i, Ff_{0,i}\Phi_i + \boldsymbol{f}^*_{1,i}\cdot\nabla\Phi^*_i, Ff_{0,i}\Phi_i \\ \quad - f^*_{0,i}\Phi^*_i, F\boldsymbol{f}_{1,i}\cdot\nabla\Phi_i - \boldsymbol{f}^*_{1,i}\cdot\nabla\Phi^*_i, F\boldsymbol{f}_{1,i}\cdot\nabla\Phi_i \end{array} \right\rangle_i},$$

$$= \frac{\sum_i \lambda_{0,i} \left\langle \begin{array}{l} f^*_{0,i}\Phi^*_i, Ff_{0,i}\Phi_i + \boldsymbol{f}^*_{1,i}\cdot\nabla\Phi^*_i, Ff_{0,i}\Phi_i \\ \quad - f^*_{0,i}\Phi^*_i, F\boldsymbol{f}_{1,i}\cdot\nabla\Phi_i - \boldsymbol{f}^*_{1,i}\cdot\nabla\Phi^*_i, F\boldsymbol{f}_{1,i}\cdot\nabla\Phi_i \end{array} \right\rangle_i}{\sum_i \left\langle f^*_{0,i}\Phi^*_i, Ff_{0,i}\Phi_i \right\rangle_i}$$

$$\times \frac{1}{\left(1 + \dfrac{\sum_i \left\langle \begin{array}{r} \boldsymbol{f}^*_{1,i}\cdot\nabla\Phi^*_i, Ff_{0,i}\Phi_i - f^*_{0,i}\Phi^*_i, F\boldsymbol{f}_{1,i}\cdot\nabla\Phi_i \\ - \boldsymbol{f}^*_{1,i}\cdot\nabla\Phi^*_i, F\boldsymbol{f}_{1,i}\cdot\nabla\Phi_i \end{array} \right\rangle_i}{\sum_i \left\langle f^*_{0,i}\Phi^*_i, Ff_{0,i}\Phi_i \right\rangle_i} \right)}.$$

Both $f^*_{0,i}\boldsymbol{f}_{1,i}$ and $f_{0,i}\boldsymbol{f}^*_{1,i}$ are antisymmetric functions of $(\boldsymbol{x}, \boldsymbol{\Omega})$ within lattice elements. Thus, by Eqs. (5.64c) and (5.73), the terms containing these functions are $O(\epsilon^2)$. Again by Eq. (5.64c), the terms containing $\nabla\Phi^*_i\nabla\Phi_i$ are $O(\epsilon^2)$. Thus, all the red terms in the preceding equation are $O(\epsilon^2)$. Using the first two terms of of a Taylor series expansion, $1/(1+x) = 1 - x$, we can rewrite the preceding equation.

After neglecting the $O(\epsilon^4)$, we are left with:

$$
\begin{aligned}
(5.78)\qquad & \frac{\sum_i \lambda_{0,i} \left\langle \left[f^*_{0,i}\Phi^*_i + \boldsymbol{f}^*_{1,i}\cdot\nabla\Phi^*_i\right], F\left[f_{0,i}\Phi_i - \boldsymbol{f}_{1,i}\cdot\nabla\Phi_i\right]\right\rangle_i}{\sum_i \left\langle \left[f^*_{0,i}\Phi^*_i + \boldsymbol{f}^*_{1,i}\cdot\nabla\Phi^*_i\right], F\left[f_{0,i}\Phi_i - \boldsymbol{f}_{1,i}\cdot\nabla\Phi_i\right]\right\rangle_i} \\
&= \frac{\sum_i \lambda_{0,i} \left\langle f^*_{0,i}\Phi^*_i, Ff_{0,i}\Phi_i\right\rangle_i}{\sum_i \left\langle f^*_{0,i}\Phi^*_i, Ff_{0,i}\Phi_i\right\rangle_i} \\
&\quad + \frac{\sum_i \lambda_{0,i} \left\langle \begin{array}{r} \boldsymbol{f}^*_{1,i}\cdot\nabla\Phi^*_i, Ff_{0,i}\Phi_i - f^*_{0,i}\Phi^*_i, F\boldsymbol{f}_{1,i}\cdot\nabla\Phi_i \\ -\boldsymbol{f}^*_{1,i}\cdot\nabla\Phi^*_i, F\boldsymbol{f}_{1,i}\cdot\nabla\Phi_i \end{array}\right\rangle_i}{\sum_i \left\langle f^*_{0,i}\Phi^*_i, Ff_{0,i}\Phi_i\right\rangle_i} \\
&\quad - \frac{\sum_i \lambda_{0,i} \left\langle f^*_{0,i}\Phi^*_i, Ff_{0,i}\Phi_i\right\rangle_i}{\sum_i \left\langle f^*_{0,i}\Phi^*_i, Ff_{0,i}\Phi_i\right\rangle_i} \\
&\qquad \times \frac{\sum_i \lambda_{0,i} \left\langle \begin{array}{r} \boldsymbol{f}^*_{1,i}\cdot\nabla\Phi^*_i, Ff_{0,i}\Phi_i - f^*_{0,i}\Phi^*_i, F\boldsymbol{f}_{1,i}\cdot\nabla\Phi_i \\ -\boldsymbol{f}^*_{1,i}\cdot\nabla\Phi^*_i, F\boldsymbol{f}_{1,i}\cdot\nabla\Phi_i \end{array}\right\rangle_i}{\sum_i \left\langle f^*_{0,i}\Phi^*_i, Ff_{0,i}\Phi_i\right\rangle_i}.
\end{aligned}
$$

We now consider the second term in Eq. (5.77). The term $\boldsymbol{\Omega}\boldsymbol{f}^*_{1,i}\boldsymbol{f}_{1,i}$ is an antisymmetric function of $(\boldsymbol{x},\boldsymbol{\Omega})$ within lattice elements. Thus, by Eqs. (5.64c) and (5.73), the term $\left\langle \left(\boldsymbol{f}^*_{1,i}\cdot\nabla\Phi^*_i\right), \boldsymbol{f}_{1,i}\cdot\left[(\boldsymbol{\Omega}\cdot\nabla)\nabla\Phi_i\right]\right\rangle_i$ is $O(\epsilon^4)$ and can be neglected. Then the the second term in Eq. (5.77) becomes:

$$
\begin{aligned}
&\frac{\sum_i \left\langle \left[f^*_{0,i}\Phi^*_i + \boldsymbol{f}^*_{1,i}\cdot\nabla\Phi^*_i\right], \boldsymbol{f}_{1,i}\cdot\left[(\boldsymbol{\Omega}\cdot\nabla)\nabla\Phi_i\right]\right\rangle_i}{\sum_i \left\langle \left[f^*_{0,i}\Phi^*_i + \boldsymbol{f}^*_{1,i}\cdot\nabla\Phi^*_i\right], F\left[f_{0,i}\Phi_i - \boldsymbol{f}_{1,i}\cdot\nabla\Phi_i\right]\right\rangle_i} \\
&\qquad = \frac{\sum_i \left\langle \Phi^*_i f^*_{0,i}, \boldsymbol{f}_{1,i}\cdot\left[(\boldsymbol{\Omega}\cdot\nabla)\nabla\Phi_i\right]\right\rangle_i}{\sum_i \left\langle \left[f^*_{0,i}\Phi^*_i + \boldsymbol{f}^*_{1,i}\cdot\nabla\Phi^*_i\right], F\left[f_{0,i}\Phi_i - \boldsymbol{f}_{1,i}\cdot\nabla\Phi_i\right]\right\rangle_i}.
\end{aligned}
$$

Introducing Eqs. (5.71) and (5.72) yields:

$$\frac{\sum_i \left\langle \left[f^*_{0,i}\Phi^*_i + \boldsymbol{f}^*_{1,i}\cdot\nabla\Phi^*_i \right], \boldsymbol{f}_{1,i}\cdot\left[(\boldsymbol{\Omega}\cdot\nabla)\nabla\Phi_i \right] \right\rangle_i}{\sum_i \left\langle \left[f^*_{0,i}\Phi^*_i + \boldsymbol{f}^*_{1,i}\cdot\nabla\Phi^*_i \right], F\left[f_{0,i}\Phi_i - \boldsymbol{f}_{1,i}\cdot\nabla\Phi_i \right] \right\rangle_i} = \frac{\sum_i \int_{V_i} \Phi^*_i \nabla\cdot\overline{\boldsymbol{\Omega} f^*_{0,i}\boldsymbol{f}_{1,i}}\cdot\nabla\Phi_i \,\mathrm{d}V}{\sum_i \left\langle \left[f^*_{0,i}\Phi^*_i + \boldsymbol{f}^*_{1,i}\cdot\nabla\Phi^*_i \right], F\left[f_{0,i}\Phi_i - \boldsymbol{f}_{1,i}\cdot\nabla\Phi_i \right] \right\rangle_i}$$

$$= \frac{\sum_i \int_{V_i} \Phi^*_i \nabla\cdot\left(\frac{\overline{\boldsymbol{\Omega} f^*_{0,i}\boldsymbol{f}_{1,i}}}{\overline{f^*_{0,i}F f_{0,i}}}\overline{\nu\Sigma_{f,i}} \right)\cdot\nabla\Phi_i \frac{\overline{f^*_{0,i}F f_{0,i}}}{\overline{\nu\Sigma_{f,i}}} \,\mathrm{d}V}{\sum_i \left\langle \left[f^*_{0,i}\Phi^*_i + \boldsymbol{f}^*_{1,i}\cdot\nabla\Phi^*_i \right], F\left[f_{0,i}\Phi_i - \boldsymbol{f}_{1,i}\cdot\nabla\Phi_i \right] \right\rangle_i}, \tag{5.79}$$

where $\overline{\nu\Sigma_{f,i}}$ is the standard one-group, homogenized $\nu\Sigma_f$ for region i (Eq. (3.45)). Using Eqs. (5.39) and (5.71), the term in parentheses can be written:

$$\frac{\overline{\boldsymbol{\Omega} f^*_{0,i}\boldsymbol{f}_{1,i}}}{\overline{f^*_{0,i}F f_{0,i}}}\overline{\nu\Sigma_{f,i}} = 4\pi \frac{\int_{cell}\int_0^\infty\int_{4\pi} \boldsymbol{\Omega} f^*_{0,i}\boldsymbol{f}_{1,i}\,\mathrm{d}\Omega\,\mathrm{d}E\,\mathrm{d}V}{\int_{cell}\left(\int_0^\infty\int_{4\pi} f^*_{0,i}\chi\,\mathrm{d}\Omega\,\mathrm{d}E\right)\left(\int_0^\infty\int_{4\pi}\nu\Sigma_f f_{0,i}\,\mathrm{d}\Omega\,\mathrm{d}E\right)\mathrm{d}V}\overline{\nu\Sigma_{f,i}}\,. \tag{5.80}$$

Comparing to Eq. (3.46), we have:

$$\frac{\overline{\boldsymbol{\Omega} f^*_{0,i}\boldsymbol{f}_{1,i}}}{\overline{f^*_{0,i}F f_{0,i}}}\overline{\nu\Sigma_{f,i}} = \boldsymbol{D}\,. \tag{5.81}$$

Introducing Eq. (5.81) into Eq. (5.79) yields:

$$\frac{\sum_i \left\langle \left[f^*_{0,i}\Phi^*_i + \boldsymbol{f}^*_{1,i}\cdot\nabla\Phi^*_i \right], \boldsymbol{f}_{1,i}\cdot\left[(\boldsymbol{\Omega}\cdot\nabla)\nabla\Phi_i \right] \right\rangle_i}{\sum_i \left\langle \left[f^*_{0,i}\Phi^*_i + \boldsymbol{f}^*_{1,i}\cdot\nabla\Phi^*_i \right], F\left[f_{0,i}\Phi_i - \boldsymbol{f}_{1,i}\cdot\nabla\Phi_i \right] \right\rangle_i} = \frac{\sum_i \int_{V_i} \Phi^*_i \nabla\cdot\boldsymbol{D}\cdot\nabla\Phi_i \frac{\overline{f^*_{0,i}F f_{0,i}}}{\overline{\nu\Sigma_{f,i}}} \,\mathrm{d}V}{\sum_i \left\langle \left[f^*_{0,i}\Phi^*_i + \boldsymbol{f}^*_{1,i}\cdot\nabla\Phi^*_i \right], F\left[f_{0,i}\Phi_i - \boldsymbol{f}_{1,i}\cdot\nabla\Phi_i \right] \right\rangle_i}. \tag{5.82}$$

As we shall see, in order for the $O(\epsilon^2) = O(\delta)$ terms to vanish, Φ must satisfy the asymptotic, monoenergetic diffusion equation (Eq. (3.43)). Thus, we have variationally derived the asymptotic diffusion equation by assuming that the asymptotic flux

expansion is a good, i.e., $O(\delta)$, approximation to the true angular flux. Introducing Eqs. (3.43), (4.17), and (5.37) into Eq. (5.82) yields:

$$\begin{aligned}
&\frac{\sum_i \left\langle \left[f_{0,i}^* \Phi_i^* + \boldsymbol{f}_{1,i}^* \cdot \nabla \Phi_i^* \right], \boldsymbol{f}_{1,i} \cdot \left[(\boldsymbol{\Omega} \cdot \nabla) \nabla \Phi_i \right] \right\rangle_i}{\sum_i \left\langle \left[f_{0,i}^* \Phi_i^* + \boldsymbol{f}_{1,i}^* \cdot \nabla \Phi_i^* \right], F \left[f_{0,i} \Phi_i - \boldsymbol{f}_{1,i} \cdot \nabla \Phi_i \right] \right\rangle_i} \\
&\quad = \frac{\sum_i \left(\lambda \overline{\nu \Sigma_{f,i}} - \overline{\Sigma_{a,i}} \right) \int_{V_i} \Phi_i^* \Phi_i \dfrac{\overline{f_{0,i}^* F f_{0,i}}}{\overline{\nu \Sigma_{f,i}}} \, \mathrm{d}V}{\sum_i \left\langle \left[f_{0,i}^* \Phi_i^* + \boldsymbol{f}_{1,i}^* \cdot \nabla \Phi_i^* \right], F \left[f_{0,i} \Phi_i - \boldsymbol{f}_{1,i} \cdot \nabla \Phi_i \right] \right\rangle_i}, \\
&\quad = \frac{\sum_i (\lambda - \lambda_{0,i}) \int_{V_i} \Phi_i^* \Phi_i \overline{f_{0,i}^* F f_{0,i}} \, \mathrm{d}V}{\sum_i \left\langle \left[f_{0,i}^* \Phi_i^* + \boldsymbol{f}_{1,i}^* \cdot \nabla \Phi_i^* \right], F \left[f_{0,i} \Phi_i - \boldsymbol{f}_{1,i} \cdot \nabla \Phi_i \right] \right\rangle_i}.
\end{aligned}$$

From our asymptotic analysis, we know that $\lambda - \lambda_{0,i} = O(\epsilon^2)$. Then we can apply Eq. (5.72) and neglect the resulting $O(\epsilon^4)$ error term:

$$\begin{aligned}
&\frac{\sum_i \left\langle \left[f_{0,i}^* \Phi_i^* + \boldsymbol{f}_{1,i}^* \cdot \nabla \Phi_i^* \right], \boldsymbol{f}_{1,i} \cdot \left[(\boldsymbol{\Omega} \cdot \nabla) \nabla \Phi_i \right] \right\rangle_i}{\sum_i \left\langle \left[f_{0,i}^* \Phi_i^* + \boldsymbol{f}_{1,i}^* \cdot \nabla \Phi_i^* \right], F \left[f_{0,i} \Phi_i - \boldsymbol{f}_{1,i} \cdot \nabla \Phi_i \right] \right\rangle_i} \\
&\quad = \frac{\sum_i (\lambda - \lambda_{0,i}) \left\langle f_{0,i}^* \Phi_i^*, F f_{0,i} \Phi_i \right\rangle_i}{\sum_i \left\langle \left[f_{0,i}^* \Phi_i^* + \boldsymbol{f}_{1,i}^* \cdot \nabla \Phi_i^* \right], F \left[f_{0,i} \Phi_i - \boldsymbol{f}_{1,i} \cdot \nabla \Phi_i \right] \right\rangle_i}.
\end{aligned}$$

We can now treat the denominator with a Taylor series expansion as we did with the

first term in Eq. (5.77):

$$
\begin{aligned}
(5.83)\qquad & \frac{\sum_i \left\langle \left[f^*_{0,i}\Phi^*_i + \boldsymbol{f}^*_{1,i}\cdot\nabla\Phi^*_i \right], \boldsymbol{f}_{1,i}\cdot\left[(\boldsymbol{\Omega}\cdot\nabla)\nabla\Phi_i \right] \right\rangle_i}{\sum_i \left\langle \left[f^*_{0,i}\Phi^*_i + \boldsymbol{f}^*_{1,i}\cdot\nabla\Phi^*_i \right], F\left[f_{0,i}\Phi_i - \boldsymbol{f}_{1,i}\cdot\nabla\Phi_i \right] \right\rangle_i} \\
&= \frac{\sum_i (\lambda-\lambda_{0,i}) \left\langle f^*_{0,i}\Phi^*_i, Ff_{0,i}\Phi_i \right\rangle_i}{\sum_i \left\langle f^*_{0,i}\Phi^*_i, Ff_{0,i}\Phi_i \right\rangle_i} \\
&\quad \times \left(1 - \frac{\sum_i \left\langle \begin{array}{r} \boldsymbol{f}^*_{1,i}\cdot\nabla\Phi^*_i, Ff_{0,i}\Phi_i - f^*_{0,i}\Phi^*_i, F\boldsymbol{f}_{1,i}\cdot\nabla\Phi_i \\ -\boldsymbol{f}^*_{1,i}\cdot\nabla\Phi^*_i, F\boldsymbol{f}_{1,i}\cdot\nabla\Phi_i \end{array} \right\rangle_i}{\sum_i \left\langle f^*_{0,i}\Phi^*_i, Ff_{0,i}\Phi_i \right\rangle_i} \right), \\
&= \lambda - \frac{\sum_i \lambda_{0,i} \left\langle f^*_{0,i}\Phi^*_i, Ff_{0,i}\Phi_i \right\rangle_i}{\sum_i \left\langle f^*_{0,i}\Phi^*_i, Ff_{0,i}\Phi_i \right\rangle_i} \\
&\quad - \frac{\sum_i \lambda \left\langle \begin{array}{r} \boldsymbol{f}^*_{1,i}\cdot\nabla\Phi^*_i, Ff_{0,i}\Phi_i - f^*_{0,i}\Phi^*_i, F\boldsymbol{f}_{1,i}\cdot\nabla\Phi_i \\ -\boldsymbol{f}^*_{1,i}\cdot\nabla\Phi^*_i, F\boldsymbol{f}_{1,i}\cdot\nabla\Phi_i \end{array} \right\rangle_i}{\sum_i \left\langle f^*_{0,i}\Phi^*_i, Ff_{0,i}\Phi_i \right\rangle_i} \\
&\quad + \frac{\sum_i \lambda_{0,i} \left\langle f^*_{0,i}\Phi^*_i, Ff_{0,i}\Phi_i \right\rangle_i}{\sum_i \left\langle f^*_{0,i}\Phi^*_i, Ff_{0,i}\Phi_i \right\rangle_i} \\
&\qquad \times \frac{\sum_i \lambda_{0,i} \left\langle \begin{array}{r} \boldsymbol{f}^*_{1,i}\cdot\nabla\Phi^*_i, Ff_{0,i}\Phi_i - f^*_{0,i}\Phi^*_i, F\boldsymbol{f}_{1,i}\cdot\nabla\Phi_i \\ -\boldsymbol{f}^*_{1,i}\cdot\nabla\Phi^*_i, F\boldsymbol{f}_{1,i}\cdot\nabla\Phi_i \end{array} \right\rangle_i}{\sum_i \left\langle f^*_{0,i}\Phi^*_i, Ff_{0,i}\Phi_i \right\rangle_i}.
\end{aligned}
$$

We now introduce Eqs. (5.78) and (5.83) into Eq. (5.77), we obtain:

$$
H_0 = \lambda + \frac{\sum_i (\lambda_{0,i}-\lambda) \left\langle \begin{array}{r} \boldsymbol{f}^*_{1,i}\cdot\nabla\Phi^*_i, Ff_{0,i}\Phi_i - f^*_{0,i}\Phi^*_i, F\boldsymbol{f}_{1,i}\cdot\nabla\Phi_i \\ -\boldsymbol{f}^*_{1,i}\cdot\nabla\Phi^*_i, F\boldsymbol{f}_{1,i}\cdot\nabla\Phi_i \end{array} \right\rangle_i}{\sum_i \left\langle f^*_{0,i}\Phi^*_i, Ff_{0,i}\Phi_i \right\rangle_i}.
$$

However, $(\lambda_{0,i}-\lambda) = O(\epsilon^2)$ and as discussed previously, all the terms in the inner product are $O(\epsilon^2)$. Therefore, the second term in the preceding equation is $O(\epsilon^4)$

and can be neglected, leaving us simply with:

$$H_0 = \lambda \,. \tag{5.84}$$

Consider now the boundary term in Eq. (5.65) defined by Eq. (5.67). Introducing the boundary conditions for the lattice functions (Eqs. (5.62a) and (5.62b)), we obtain

(5.85)

$$\begin{aligned} B = \sum_i \int_{\partial V_i} \int_0^\infty \int_{\boldsymbol{n}\cdot\boldsymbol{\Omega}<0} & (\boldsymbol{n}\cdot\boldsymbol{\Omega}) \left[f^*_{0,i}\Phi^* + \boldsymbol{f}^*_{1,i}\cdot\nabla\Phi^* + \alpha f^*_{0,i,r}\Phi^* + \alpha \boldsymbol{f}^*_{1,i,r}\cdot\nabla\Phi^* \right] \\ & \times \left[f_{0,i}\Phi - \boldsymbol{f}_{1,i}\cdot\nabla\Phi \right] \, \mathrm{d}\Omega \, \mathrm{d}E \, \mathrm{d}S \,, \\ = \sum_i \int_{\partial V_i} \int_0^\infty \int_{\boldsymbol{n}\cdot\boldsymbol{\Omega}<0} & (\boldsymbol{n}\cdot\boldsymbol{\Omega}) \left[(1+\alpha) f^*_{0,i}\Phi^* + (1-\alpha)\boldsymbol{f}^*_{1,i}\cdot\nabla\Phi^* \right] \\ & \times \left[f_{0,i}\Phi - \boldsymbol{f}_{1,i}\cdot\nabla\Phi \right] \, \mathrm{d}\Omega \, \mathrm{d}E \, \mathrm{d}S \,. \end{aligned}$$

Next, consider the interface term defined by Eq. (5.68). Using Eqs. (5.62a)-(5.62d), we conclude that the integrals over angle of $\boldsymbol{\Omega} f^*_0 f_0$ and $\boldsymbol{\Omega}\boldsymbol{f}^*_1\boldsymbol{f}_1$ vanish. Then Eq. (5.68) becomes:

$$\begin{aligned} I = \frac{1}{2}\sum_{ij} \int_{\partial V_{ij}} \int_0^\infty \int_{4\pi} & (\boldsymbol{n}_{ij}\cdot\boldsymbol{\Omega}) \left[f^*_{0,i}\Phi^*_i + \boldsymbol{f}^*_{1,i}\cdot\nabla\Phi^*_i + f^*_{0,j}\Phi^*_j + \boldsymbol{f}^*_{1,j}\cdot\nabla\Phi^*_j \right] \\ & \times \left[f_{0,i}\Phi_i - \boldsymbol{f}_{1,i}\cdot\nabla\Phi_i - f_{0,j}\Phi_j + \boldsymbol{f}_{1,j}\cdot\nabla\Phi_j \right] \, \mathrm{d}\Omega \, \mathrm{d}E \, \mathrm{d}S \,, \\ = -\frac{1}{2}\sum_{ij} \int_{\partial V_{ij}} \int_0^\infty \int_{4\pi} & (\boldsymbol{n}_{ij}\cdot\boldsymbol{\Omega}) \left[f^*_{0,i}\Phi^*_i + f^*_{0,j}\Phi^*_j \right] \\ & \times \left[\boldsymbol{f}_{1,i}\cdot\nabla\Phi_i - \boldsymbol{f}_{1,j}\cdot\nabla\Phi_j \right] \, \mathrm{d}\Omega \, \mathrm{d}E \, \mathrm{d}S \\ + \frac{1}{2}\sum_{ij} \int_{\partial V_{ij}} \int_0^\infty \int_{4\pi} & (\boldsymbol{n}_{ij}\cdot\boldsymbol{\Omega}) \left[\boldsymbol{f}^*_{1,i}\cdot\nabla\Phi^*_i + \boldsymbol{f}^*_{1,j}\cdot\nabla\Phi^*_j \right] \\ & \times \left[f_{0,i}\Phi_i - f_{0,j}\Phi_j \right] \, \mathrm{d}\Omega \, \mathrm{d}E \, \mathrm{d}S \,. \end{aligned} \tag{5.86}$$

Finally, we introduce Eqs. (5.84), (5.85), and (5.86) into Eq. (5.65) to obtain a functional for estimating the reactor eigenvalue in terms of the asymptotic diffusion

solution:

(5.87)

$$
\begin{aligned}
H[\Psi,\Psi^*] &= H[\Phi,\Phi^*]\,, \\
&= \lambda \\
&\quad + \Bigg[-\sum_i \int_{\partial V_i} \int_0^\infty \int_{\boldsymbol{n}\cdot\boldsymbol{\Omega}<0} (\boldsymbol{n}\cdot\boldsymbol{\Omega}) \left[(1+\alpha)\, f^*_{0,i}\Phi^* + (1-\alpha)\, \boldsymbol{f}^*_{1,i}\cdot\nabla\Phi^* \right] \\
&\qquad\qquad \times \left[f_{0,i}\Phi - \boldsymbol{f}_{1,i}\cdot\nabla\Phi \right] \mathrm{d}\Omega\, \mathrm{d}E\, \mathrm{d}S \\
&\quad + \frac{1}{2}\sum_{ij} \int_{\partial V_{ij}} \int_0^\infty \int_{4\pi} (\boldsymbol{n}_{ij}\cdot\boldsymbol{\Omega}) \left[f^*_{0,i}\Phi^*_i + f^*_{0,j}\Phi^*_j \right] \\
&\qquad\qquad \times \left[\boldsymbol{f}_{1,i}\cdot\nabla\Phi_i - \boldsymbol{f}_{1,j}\cdot\nabla\Phi_j \right] \mathrm{d}\Omega\, \mathrm{d}E\, \mathrm{d}S \\
&\quad - \frac{1}{2}\sum_{ij} \int_{\partial V_{ij}} \int_0^\infty \int_{4\pi} (\boldsymbol{n}_{ij}\cdot\boldsymbol{\Omega}) \left[\boldsymbol{f}^*_{1,i}\cdot\nabla\Phi^*_i + \boldsymbol{f}^*_{1,j}\cdot\nabla\Phi^*_j \right] \\
&\qquad\qquad \times \left[f_{0,i}\Phi_i - f_{0,j}\Phi_j \right] \mathrm{d}\Omega\, \mathrm{d}E\, \mathrm{d}S \Bigg] \\
&\quad \Bigg/ \left\langle \left[f^*_0\Phi^* + \boldsymbol{f}^*_1\cdot\nabla\Phi^* \right], F\left[f_0\Phi - \boldsymbol{f}_1\cdot\nabla\Phi \right] \right\rangle .
\end{aligned}
$$

The analysis in this section can be repeated using the adjoint form of the functional

(Eq. (5.57)) as a starting point. The resulting functional is:

(5.88)

$$
\begin{aligned}
H[\Psi,\Psi^*] &= H[\Phi,\Phi^*]\,, \\
&= \lambda \\
&\quad + \Bigg[-\sum_i \int_{\partial V_i} \int_0^\infty \int_{\boldsymbol{n}\cdot\boldsymbol{\Omega}>0} (\boldsymbol{n}\cdot\boldsymbol{\Omega}) \left[(1+\alpha)\, f_{0,i}\Phi - (1-\alpha)\, \boldsymbol{f}_{1,i}\cdot\nabla\Phi \right] \\
&\qquad\qquad \times \left[f^*_{0,i}\Phi^* + \boldsymbol{f}^*_{1,i}\cdot\nabla\Phi^* \right] \mathrm{d}\Omega\, \mathrm{d}E\, \mathrm{d}S \\
&\quad + \frac{1}{2}\sum_{ij} \int_{\partial V_{ij}} \int_0^\infty \int_{4\pi} (\boldsymbol{n}_{ij}\cdot\boldsymbol{\Omega}) \left[f_{0,i}\Phi_i + f_{0,j}\Phi_j \right] \\
&\qquad\qquad \times \left[\boldsymbol{f}^*_{1,i}\cdot\nabla\Phi^*_i - \boldsymbol{f}^*_{1,j}\cdot\nabla\Phi^*_j \right] \mathrm{d}\Omega\, \mathrm{d}E\, \mathrm{d}S \\
&\quad - \frac{1}{2}\sum_{ij} \int_{\partial V_{ij}} \int_0^\infty \int_{4\pi} (\boldsymbol{n}_{ij}\cdot\boldsymbol{\Omega}) \left[\boldsymbol{f}_{1,i}\cdot\nabla\Phi_i + \boldsymbol{f}_{1,j}\cdot\nabla\Phi_j \right] \\
&\qquad\qquad \times \left[f^*_{0,i}\Phi^*_i - f^*_{0,j}\Phi^*_j \right] \mathrm{d}\Omega\, \mathrm{d}E\, \mathrm{d}S \Bigg] \\
&\quad \Big/ \left\langle \left[f_0\Phi + \boldsymbol{f}_1\cdot\nabla\Phi \right], F^* \left[f^*_0\Phi^* - \boldsymbol{f}^*_1\cdot\nabla\Phi^* \right] \right\rangle .
\end{aligned}
$$

Up to now, we have variationally derived the asymptotic diffusion equation, but we still have not obtained boundary and interface conditions for this equation. To do this, we recall that (ψ,ψ^*) is a stationary point of the functional H. Let ϕ and ϕ^* be exact solutions of the homogenized diffusion equation with appropriate boundary and interface conditions. Then we desire that $O(\delta)$ variations in ϕ and ϕ^* result in $O(\delta^2)$ variations in the functional H. In other words, we desire that (ϕ,ϕ^*) also be a stationary point of H:

$$
H[\Phi,\Phi^*] = H[\phi+\delta\phi,\phi^*+\delta\phi^*] = H[\phi,\phi^*] + O(\delta^2)\,.
$$

Thus, the boundary and interface conditions will be derived in the following sec-

tions by assuming $O(\delta)$ variations in the diffusion solutions:

$$\Phi = \phi + \delta\phi\,, \tag{5.89}$$

$$\Phi^* = \phi^* + \delta\phi^*\,. \tag{5.90}$$

We will consider $H[\phi, \Phi^*]$ and $H[\Phi, \phi^*]$ independently, and require simply that in each case the $O(\delta)$ terms that will arise in the boundary and interface terms vanish.

5.4.3 Variational Boundary Conditions

In deriving the boundary conditions for the asymptotic diffusion equation, we follow an analogous procedure to that used by Rulko et al. [68]. First, we consider the forward functional (Eq. (5.87)) with the exact forward flux, ϕ, and the approximate adjoint flux, Φ^*, defined by Eq. (5.90). Requiring that the $O(\delta)$ terms vanish yields:

$$0 = \sum_i \int_{\partial V_i} \int_0^\infty \int_{\boldsymbol{n}\cdot\boldsymbol{\Omega}<0} (\boldsymbol{n}\cdot\boldsymbol{\Omega}) \left[(1+\alpha)\, f^*_{0,i}\delta\phi^* + (1-\alpha)\, \boldsymbol{f}^*_{1,i}\cdot\nabla\delta\phi^*\right] \times \left[f_{0,i}\phi - \boldsymbol{f}_{1,i}\cdot\nabla\phi\right] \mathrm{d}\Omega\, \mathrm{d}E\, \mathrm{d}S\,.$$

Similarly, we introduce the exact adjoint flux, ϕ^*, and approximate forward flux, Φ, defined by Eq. (5.89) into the adjoint functional (Eq. (5.88)). Setting the $O(\delta)$ terms equal to 0 yields:

$$0 = \sum_i \int_{\partial V_i} \int_0^\infty \int_{\boldsymbol{n}\cdot\boldsymbol{\Omega}<0} (\boldsymbol{n}\cdot\boldsymbol{\Omega}) \left[(1+\alpha)\, f_{0,i}\delta\phi - (1-\alpha)\, \boldsymbol{f}_{1,i}\cdot\nabla\delta\phi\right] \times \left[f^*_{0,i}\phi^* + \boldsymbol{f}^*_{1,i}\cdot\nabla\phi^*\right] \mathrm{d}\Omega\, \mathrm{d}E\, \mathrm{d}S\,.$$

Then for each lattice i, the following must be true:

$$0 = \int_{\partial V_i} \int_0^\infty \int_{\boldsymbol{n}\cdot\boldsymbol{\Omega}<0} (\boldsymbol{n}\cdot\boldsymbol{\Omega}) \left[(1+\alpha)\, f^*_{0,i}\delta\phi^* + (1-\alpha)\, \boldsymbol{f}^*_{1,i}\cdot\nabla\delta\phi^*\right] \times \left[f_{0,i}\phi - \boldsymbol{f}_{1,i}\cdot\nabla\phi\right] \mathrm{d}\Omega\, \mathrm{d}E\, \mathrm{d}S\,, \tag{5.91}$$

$$0 = \int_{\partial V_i} \int_0^\infty \int_{\boldsymbol{n}\cdot\boldsymbol{\Omega}<0} (\boldsymbol{n}\cdot\boldsymbol{\Omega}) \left[(1+\alpha)\, f_{0,i}\delta\phi - (1-\alpha)\, \boldsymbol{f}_{1,i}\cdot\nabla\delta\phi\right] \times \left[f^*_{0,i}\phi^* + \boldsymbol{f}^*_{1,i}\cdot\nabla\phi^*\right] \mathrm{d}\Omega\, \mathrm{d}E\, \mathrm{d}S\,. \tag{5.92}$$

Let us first consider Eq. (5.91). The integral can be broken into four terms involving $\delta\phi^*$, $\partial/\partial x\ \delta\phi^*$, $\partial/\partial y\ \delta\phi^*$, and $\partial/\partial z\ \delta\phi^*$. Thus, we have four boundary conditions when only one is desired. To eliminate the extra conditions we make two assumptions. First, we assume that the tangential derivatives of the forward and adjoint fluxes are $O(\delta) = O(\epsilon^2)$, rather than $O(\epsilon)$. This is true for large, planar surfaces away from corners. Then:

$$\Big(\nabla - \boldsymbol{n}\,(\boldsymbol{n}\cdot\nabla)\Big)\phi \quad \text{and} \quad \Big(\nabla - \boldsymbol{n}\,(\boldsymbol{n}\cdot\nabla)\Big)\phi^* = O(\delta)\,, \tag{5.93a}$$

$$\Big(\nabla - \boldsymbol{n}\,(\boldsymbol{n}\cdot\nabla)\Big)\delta\phi \quad \text{and} \quad \Big(\nabla - \boldsymbol{n}\,(\boldsymbol{n}\cdot\nabla)\Big)\delta\phi^* = O(\delta^2)\,, \tag{5.93b}$$

Second, we assume that the monoenergetic fluxes satisfy an extrapolated boundary condition of the form:

$$0 = \phi + l_{lat,i}\boldsymbol{n}\cdot\nabla\phi\,, \qquad \boldsymbol{x}\in\partial V_i\,, \tag{5.94a}$$

$$0 = \phi^* + l_{lat,i}\boldsymbol{n}\cdot\nabla\phi^*\,, \qquad \boldsymbol{x}\in\partial V_i\,. \tag{5.94b}$$

Then one might naturally assume:

$$\delta\phi = -l_{lat,i}\boldsymbol{n}\cdot\nabla\delta\phi\,, \qquad \boldsymbol{x}\in\partial V_i\,, \tag{5.95a}$$

$$\delta\phi^* = -l_{lat,i}\boldsymbol{n}\cdot\nabla\delta\phi^*\,, \qquad \boldsymbol{x}\in\partial V_i\,. \tag{5.95b}$$

Introducing Eqs. (5.93) and (5.95b) into Eq. (5.91) yields:

$$\begin{aligned}0 = &\int_{\partial V_i}\int_0^\infty\int_{\boldsymbol{n}\cdot\boldsymbol{\Omega}<0}(\boldsymbol{n}\cdot\boldsymbol{\Omega})\left[(1+\alpha)\,f^*_{0,i}\delta\phi^* + (1-\alpha)\left(\boldsymbol{n}\cdot\boldsymbol{f}^*_{1,i}\right)\cdot(\boldsymbol{n}\cdot\nabla)\,\delta\phi^*\right]\\ &\qquad\times\left[f_{0,i}\phi - \left(\boldsymbol{n}\cdot\boldsymbol{f}_{1,i}\right)(\boldsymbol{n}\cdot\nabla)\,\phi\right]\,\mathrm{d}\Omega\,\mathrm{d}E\,\mathrm{d}S\,,\\ = &\int_{\partial V_i}\delta\phi^*\int_0^\infty\int_{\boldsymbol{n}\cdot\boldsymbol{\Omega}<0}(\boldsymbol{n}\cdot\boldsymbol{\Omega})\left[(1+\alpha)\,f^*_{0,i} - (1-\alpha)\left(\boldsymbol{n}\cdot\boldsymbol{f}^*_{1,i}\right)\frac{1}{l_{lat,i}}\right]\\ &\qquad\times\left[f_{0,i}\phi - \left(\boldsymbol{n}\cdot\boldsymbol{f}_{1,i}\right)\cdot(\boldsymbol{n}\cdot\nabla)\,\phi\right]\,\mathrm{d}\Omega\,\mathrm{d}E\,\mathrm{d}S\,.\end{aligned}$$

This equation is satisfied for any $\delta\phi^*$ if the following is true for any point on the vacuum boundary:

(5.96)

$$\begin{aligned}0 = &\left[\int_0^\infty\int_{\boldsymbol{n}\cdot\boldsymbol{\Omega}<0}(\boldsymbol{n}\cdot\boldsymbol{\Omega})\left[f^*_{0,i} - \frac{(1-\alpha)}{l_{lat,i}\,(1+\alpha)}\left(\boldsymbol{n}\cdot\boldsymbol{f}^*_{1,i}\right)\right]f_{0,i}\,\mathrm{d}\Omega\,\mathrm{d}E\right]\phi\\ &-\left[\int_0^\infty\int_{\boldsymbol{n}\cdot\boldsymbol{\Omega}<0}(\boldsymbol{n}\cdot\boldsymbol{\Omega})\left[f^*_{0,i} - \frac{(1-\alpha)}{l_{lat,i}\,(1+\alpha)}\left(\boldsymbol{n}\cdot\boldsymbol{f}^*_{1,i}\right)\right]\boldsymbol{n}\cdot\boldsymbol{f}_{1,i}\,\mathrm{d}\Omega\,\mathrm{d}E\right]\boldsymbol{n}\cdot\nabla\phi\,,\\ = \phi + &\left[-\frac{\displaystyle\int_0^\infty\int_{\boldsymbol{n}\cdot\boldsymbol{\Omega}<0}(\boldsymbol{n}\cdot\boldsymbol{\Omega})\left[f^*_{0,i} - \frac{(1-\alpha)}{l_{lat,i}\,(1+\alpha)}\left(\boldsymbol{n}\cdot\boldsymbol{f}^*_{1,i}\right)\right]\boldsymbol{n}\cdot\boldsymbol{f}_{1,i}\,\mathrm{d}\Omega\,\mathrm{d}E}{\displaystyle\int_0^\infty\int_{\boldsymbol{n}\cdot\boldsymbol{\Omega}<0}(\boldsymbol{n}\cdot\boldsymbol{\Omega})\left[f^*_{0,i} - \frac{(1-\alpha)}{l_{lat,i}\,(1+\alpha)}\left(\boldsymbol{n}\cdot\boldsymbol{f}^*_{1,i}\right)\right]f_{0,i}\,\mathrm{d}\Omega\,\mathrm{d}E}\right]\boldsymbol{n}\cdot\nabla\phi\,,\end{aligned}$$

$$\boldsymbol{x}\in\partial V_i\,.$$

Similarly, we can introducing Eqs. (5.93) and (5.95a) into Eq. (5.92) to obtain a boundary condition for the adjoint diffusion equation:

(5.97)

$$0 = \phi^* + \left[\frac{\displaystyle\int_0^\infty\int_{\boldsymbol{n}\cdot\boldsymbol{\Omega}<0}(\boldsymbol{n}\cdot\boldsymbol{\Omega})\left[f_{0,i} + \frac{(1-\alpha)}{l_{lat,i}\,(1+\alpha)}\left(\boldsymbol{n}\cdot\boldsymbol{f}_{1,i}\right)\right]\boldsymbol{n}\cdot\boldsymbol{f}^*_{1,i}\,\mathrm{d}\Omega\,\mathrm{d}E}{\displaystyle\int_0^\infty\int_{\boldsymbol{n}\cdot\boldsymbol{\Omega}<0}(\boldsymbol{n}\cdot\boldsymbol{\Omega})\left[f_{0,i} + \frac{(1-\alpha)}{l_{lat,i}\,(1+\alpha)}\left(\boldsymbol{n}\cdot\boldsymbol{f}_{1,i}\right)\right]f^*_{0,i}\,\mathrm{d}\Omega\,\mathrm{d}E}\right]\boldsymbol{n}\cdot\nabla\phi^*\,,$$

$$\boldsymbol{x}\in\partial V_i\,.$$

Note that $\boldsymbol{n}\cdot\boldsymbol{\Omega}$, $\boldsymbol{n}\cdot\boldsymbol{f}_{1,i}$, and $\boldsymbol{n}\cdot\boldsymbol{f}^*_{1,i}$ always have the same sign and so the bracketed terms in Eqs. (5.96) and (5.97) are strictly positive.

We now show how to solve for the forward multigroup extrapolation lengths. Although we do not show the derivation of the adjoint multigroup extrapolation lengths, they are obtained in a similar manner. Comparing Eq. (5.96) to Eq. (5.94a) shows that the extrapolation length is given by:

(5.98)
$$l_{lat,i}(\alpha,\boldsymbol{x}) = -\frac{\displaystyle\int_0^\infty \int_{\boldsymbol{n}\cdot\boldsymbol{\Omega}<0} (\boldsymbol{n}\cdot\boldsymbol{\Omega}) \left[f^*_{0,i} - \frac{(1-\alpha)}{l_{lat,i}\,(1+\alpha)} \left(\boldsymbol{n}\cdot\boldsymbol{f}^*_{1,i}\right)\right] \boldsymbol{n}\cdot\boldsymbol{f}_{1,i}\,\mathrm{d}\Omega\,\mathrm{d}E}{\displaystyle\int_0^\infty \int_{\boldsymbol{n}\cdot\boldsymbol{\Omega}<0} (\boldsymbol{n}\cdot\boldsymbol{\Omega}) \left[f^*_{0,i} - \frac{(1-\alpha)}{l_{lat,i}\,(1+\alpha)} \left(\boldsymbol{n}\cdot\boldsymbol{f}^*_{1,i}\right)\right] f_{0,i}\,\mathrm{d}\Omega\,\mathrm{d}E} \,.$$

This is a quadratic equation for the extrapolation length, $l_{lat,i}$. Solving for $l_{lat,i}$ yields:

(5.99a)
$$l_{lat,i}(\alpha,\boldsymbol{x}) = \frac{-b \pm \sqrt{b^2-4ac}}{2a}\,,$$

where:

(5.99b)
$$a = \int_0^\infty \int_{\boldsymbol{n}\cdot\boldsymbol{\Omega}<0} (\boldsymbol{n}\cdot\boldsymbol{\Omega})\, f^*_{0,i} f_{0,i}\,\mathrm{d}\Omega\,\mathrm{d}E\,,$$

(5.99c)
$$b = \int_0^\infty \int_{\boldsymbol{n}\cdot\boldsymbol{\Omega}<0} (\boldsymbol{n}\cdot\boldsymbol{\Omega})\, f^*_{0,i} \left(\boldsymbol{n}\cdot\boldsymbol{f}_{1,i}\right)\,\mathrm{d}\Omega\,\mathrm{d}E - \frac{(1-\alpha)}{(1+\alpha)} \int_0^\infty \int_{\boldsymbol{n}\cdot\boldsymbol{\Omega}<0} (\boldsymbol{n}\cdot\boldsymbol{\Omega}) \left(\boldsymbol{n}\cdot\boldsymbol{f}^*_{1,i}\right) f_{0,i}\,\mathrm{d}\Omega\,\mathrm{d}E\,,$$

(5.99d)
$$c = -\frac{(1-\alpha)}{(1+\alpha)} \int_0^\infty \int_{\boldsymbol{n}\cdot\boldsymbol{\Omega}<0} (\boldsymbol{n}\cdot\boldsymbol{\Omega}) \left(\boldsymbol{n}\cdot\boldsymbol{f}^*_{1,i}\right) \left(\boldsymbol{n}\cdot\boldsymbol{f}_{1,i}\right)\,\mathrm{d}\Omega\,\mathrm{d}E\,.$$

Equations (5.98) and (5.99) define an extrapolation length for the asymptotic monoenergetic diffusion equation. We desire a boundary condition for the asymptotic multigroup diffusion equation of the form:

(5.100)
$$0 = \phi_g + l_{lat,i,g}\boldsymbol{n}\cdot\nabla\phi_g\,, \qquad \boldsymbol{x}\in\partial V_i\,, \qquad 1\le g\le G\,.$$

We operate on Eq. (5.100) by $\sum_{g=1}^{G}\beta_g(\cdot)$, where β_g are to-be-determined constants:

$$0 = \sum_{g=1}^{G}\beta_g\phi_g + \sum_{g=1}^{G} l_{lat,i,g}\beta_g\boldsymbol{n}\cdot\nabla\phi_g\,, \qquad \boldsymbol{x}\in\partial V_i\,.$$

In the asymptotic limit, the multigroup flux can be expressed in terms of the monoenergetic flux (Eq. (4.34)), and doing so yields:

$$0 = \left(\sum_{g=1}^{G} \beta_g \overline{F_{0,i,g}} \right) \phi + \left(\sum_{g=1}^{G} l_{lat,i,g} \beta_g \overline{F_{0,i,g}} \right) \boldsymbol{n} \cdot \nabla \phi \,, \qquad \boldsymbol{x} \in \partial V_i \,.$$

Comparing to the monoenergetic boundary condition of Eq. (5.94a), we see that:

$$l_{lat,i} = \frac{\sum_{g=1}^{G} l_{lat,i,g} \beta_g \overline{F_{0,i,g}}}{\sum_{g=1}^{G} \beta_g \overline{F_{0,i,g}}} \,. \tag{5.101}$$

There are an infinite number of solutions for which Eqs. (5.98) and (5.101) agree. We choose the following:

$$l_{lat,i,g} \beta_g \overline{F_{0,i,g}} = - \int_{E_g}^{E_{g-1}} \int_{\boldsymbol{n}\cdot\boldsymbol{\Omega}<0} (\boldsymbol{n}\cdot\boldsymbol{\Omega}) \left[f_{0,i}^* - \frac{(1-\alpha)}{l_{lat,i}\,(1+\alpha)} \left(\boldsymbol{n} \cdot \boldsymbol{f}_{1,i}^* \right) \right] \boldsymbol{n} \cdot \boldsymbol{f}_{1,i} \, \mathrm{d}\Omega \, \mathrm{d}E \,,$$

$$\beta_g \overline{F_{0,i,g}} = \int_{E_g}^{E_{g-1}} \int_{\boldsymbol{n}\cdot\boldsymbol{\Omega}<0} (\boldsymbol{n}\cdot\boldsymbol{\Omega}) \left[f_{0,i}^* - \frac{(1-\alpha)}{l_{lat,i}\,(1+\alpha)} \left(\boldsymbol{n} \cdot \boldsymbol{f}_{1,i}^* \right) \right] f_{0,i} \, \mathrm{d}\Omega \, \mathrm{d}E \,.$$

Dividing the first equation by the second yields the multigroup extrapolation length:

$$\begin{aligned} & l_{lat,i,g}(\alpha, \boldsymbol{x}) \\ & = - \frac{\left[\int_{E_g}^{E_{g-1}} \int_{\boldsymbol{n}\cdot\boldsymbol{\Omega}<0} (\boldsymbol{n}\cdot\boldsymbol{\Omega}) \left[f_{0,i}^*(\boldsymbol{x},\boldsymbol{\Omega},E) - \frac{(1-\alpha)}{l_{lat,i}(\alpha,\boldsymbol{x})\,(1+\alpha)} \left(\boldsymbol{n} \cdot \boldsymbol{f}_{1,i}^*(\boldsymbol{x},\boldsymbol{\Omega},E) \right) \right] \times \boldsymbol{n} \cdot \boldsymbol{f}_{1,i}(\boldsymbol{x},\boldsymbol{\Omega},E) \, \mathrm{d}\Omega \, \mathrm{d}E \right]}{\left[\int_{E_g}^{E_{g-1}} \int_{\boldsymbol{n}\cdot\boldsymbol{\Omega}<0} (\boldsymbol{n}\cdot\boldsymbol{\Omega}) \left[f_{0,i}^*(\boldsymbol{x},\boldsymbol{\Omega},E) - \frac{(1-\alpha)}{l_{lat,i}(\alpha,\boldsymbol{x})\,(1+\alpha)} \left(\boldsymbol{n} \cdot \boldsymbol{f}_{1,i}^*(\boldsymbol{x},\boldsymbol{\Omega},E) \right) \right] \times f_{0,i}(\boldsymbol{x},\boldsymbol{\Omega},E) \, \mathrm{d}\Omega \, \mathrm{d}E \right]} \,. \end{aligned} \tag{5.102}$$

At first glance, Eqs. (5.98) and (5.102) seem to be complicated expressions for the extrapolation length. However, if we consider the homogeneous, monoenergetic case, then the expressions simplify greatly. In this limit, the lattice functions are:

$$f_0(\boldsymbol{x},\boldsymbol{\Omega},E) = f_0^*(\boldsymbol{x},\boldsymbol{\Omega},E) = 1 \,, \tag{5.103a}$$

(5.103b) $$\boldsymbol{f}_1(\boldsymbol{x},\boldsymbol{\Omega},E) = \boldsymbol{f}_1^*(\boldsymbol{x},\boldsymbol{\Omega},E) = \frac{\boldsymbol{\Omega}}{\Sigma_{tr}}\,.$$

Introducing these into Eqs. (5.99) yields:

(5.104a) $$a = -\pi\,,$$

(5.104b) $$b = \frac{2\pi}{3\Sigma_{tr}}\left(\frac{1-\alpha}{1+\alpha}\right)\,,$$

(5.104c) $$c = \frac{\pi}{2\Sigma_{tr}^2}\left(\frac{1-\alpha}{1+\alpha}\right)\,.$$

Introducing Eqs. (5.104) into Eq. (5.99a) yields:

$$l_{lat}(\alpha) = \frac{-\frac{2\pi}{3\Sigma_{tr}}\left(\frac{1-\alpha}{1+\alpha}\right) \pm \sqrt{\frac{4\pi^2}{9\Sigma_{tr}^2}\left(1-\frac{1-\alpha}{1+\alpha}\right) - 4(-\pi)\frac{\pi}{2\Sigma_{tr}^2}\left(\frac{1-\alpha}{1+\alpha}\right)}}{-2\pi}\,.$$

We recall that $|\alpha| \leq 1$. Then there is only one positive solution to this equation:

(5.105) $$l_{lat}(\alpha) = \frac{1}{\Sigma_{tr}}\left(\frac{1}{1+\alpha}\right)\left[\frac{2\alpha}{3} + \frac{1}{\sqrt{2}}\sqrt{1-\frac{\alpha}{3}^2}\right]\,.$$

This is exactly the result obtained by Rulko et al. [68]. As pointed out by Rulko, choosing $\alpha = 1$ yields the Marshak extrapolation length:

(5.106) $$l_{lat}(\alpha = 1) = l_{Mar} = \frac{2}{3}\Sigma_{tr}^{-1} \approx 0.6667\Sigma_{tr}^{-1}\,,$$

while choosing $\alpha = 0$ yields the Federighi-Pomraning extrapolation length:

(5.107) $$l_{lat}(\alpha = 0) = l_{FP} = \frac{1}{\sqrt{2}}\Sigma_{tr}^{-1} \approx 0.7071\Sigma_{tr}^{-1}\,.$$

The Milne extrapolation is obtained by choosing $\alpha = -0.0815$:

(5.108) $$l_{lat}(\alpha = -0.0815) = l_{Milne} = 0.7104\Sigma_{tr}^{-1}\,.$$

Thus, our variational extrapolation lengths are consistent with commonly used extrapolation lengths in the limit of a homogeneous, monoenergetic medium.

Equations (5.98), (5.99), and (5.102) define space dependent extrapolation lengths. One can define "average" extrapolation lengths for each surface by simply using surface-averaged lattice functions. The surface-averaged extrapolation lengths are not exact, but they are more practical and should be reasonably accurate for for most assemblies. These approximate surface-averaged extrapolation lengths are given by:

(5.109)

$$\boxed{\begin{aligned} &l_{lat,i,k,g}(\alpha) \\ &= -\frac{\left[\int_{E_g}^{E_{g-1}}\int_{\boldsymbol{n}\cdot\boldsymbol{\Omega}<0}(\boldsymbol{n}\cdot\boldsymbol{\Omega})\left[f^*_{0,i,k}(\boldsymbol{\Omega},E) - \frac{(1-\alpha)}{l_{lat,i,k}(\alpha)\,(1+\alpha)}\left(\boldsymbol{n}\cdot\boldsymbol{f}^*_{1,i,k}(\boldsymbol{\Omega},E)\right)\right]\times\boldsymbol{n}\cdot\boldsymbol{f}_{1,i,k}(\boldsymbol{\Omega},E)\,\mathrm{d}\Omega\,\mathrm{d}E\right]}{\left[\int_{E_g}^{E_{g-1}}\int_{\boldsymbol{n}\cdot\boldsymbol{\Omega}<0}(\boldsymbol{n}\cdot\boldsymbol{\Omega})\left[f^*_{0,i,k}(\boldsymbol{\Omega},E) - \frac{(1-\alpha)}{l_{lat,i,k}(\alpha)\,(1+\alpha)}\left(\boldsymbol{n}\cdot\boldsymbol{f}^*_{1,i,k}(\boldsymbol{\Omega},E)\right)\right]\times f_{0,i,k}(\boldsymbol{\Omega},E)\,\mathrm{d}\Omega\,\mathrm{d}E\right]}, \end{aligned}}$$

where:

(5.110a)
$$\boxed{l_{lat,i,k}(\alpha) = \frac{-b \pm \sqrt{b^2-4ac}}{2a},}$$

and:

(5.110b)
$$\boxed{a = \int_0^\infty\int_{\boldsymbol{n}\cdot\boldsymbol{\Omega}<0}(\boldsymbol{n}\cdot\boldsymbol{\Omega})\,f^*_{0,i,k}(\boldsymbol{\Omega},E)f_{0,i,k}(\boldsymbol{\Omega},E)\,\mathrm{d}\Omega\,\mathrm{d}E\,,}$$

(5.110c)
$$\boxed{\begin{aligned} b = &\int_0^\infty\int_{\boldsymbol{n}\cdot\boldsymbol{\Omega}<0}(\boldsymbol{n}\cdot\boldsymbol{\Omega})\,f^*_{0,i,k}(\boldsymbol{\Omega},E)\left(\boldsymbol{n}\cdot\boldsymbol{f}_{1,i,k}(\boldsymbol{\Omega},E)\right)\,\mathrm{d}\Omega\,\mathrm{d}E \\ &-\frac{(1-\alpha)}{(1+\alpha)}\int_0^\infty\int_{\boldsymbol{n}\cdot\boldsymbol{\Omega}<0}(\boldsymbol{n}\cdot\boldsymbol{\Omega})\left(\boldsymbol{n}\cdot\boldsymbol{f}^*_{1,i,k}(\boldsymbol{\Omega},E)\right)f_{0,i,k}(\boldsymbol{\Omega},E)\,\mathrm{d}\Omega\,\mathrm{d}E\,, \end{aligned}}$$

(5.110d)
$$\boxed{c = -\frac{(1-\alpha)}{(1+\alpha)}\int_0^\infty\int_{\boldsymbol{n}\cdot\boldsymbol{\Omega}<0}(\boldsymbol{n}\cdot\boldsymbol{\Omega})\left(\boldsymbol{n}\cdot\boldsymbol{f}^*_{1,i,k}(\boldsymbol{\Omega},E)\right)\left(\boldsymbol{n}\cdot\boldsymbol{f}_{1,i,k}(\boldsymbol{\Omega},E)\right)\,\mathrm{d}\Omega\,\mathrm{d}E\,,}$$

and:

$$\boxed{f_{n,i,k}(\mathbf{\Omega},E)=\frac{1}{A_k}\int_{A_k}f_{n,i}(\boldsymbol{x},\mathbf{\Omega},E)\,\mathrm{d}S\,,\qquad n=0,1\,,} \tag{5.111a}$$

$$\boxed{f^*_{n,i,k}(\mathbf{\Omega},E)=\frac{1}{A_k}\int_{A_k}f^*_{n,i}(\boldsymbol{x},\mathbf{\Omega},E)\,\mathrm{d}S\,,\qquad n=0,1\,,} \tag{5.111b}$$

where A_k is the area of surface k, which is a vacuum boundary of region i. We chose to use the surface-averaged lattice functions in these equations merely to simplify the implementation of the extrapolation length calculation. It would have been more accurate to instead use the surface-averaged compound functions $(f_{0,i}f^*_{0,i})_k$, $(\boldsymbol{f}_{1,i}f^*_{0,i})_k$, $(f_{0,i}\boldsymbol{f}^*_{1,i})_k$, and $(\boldsymbol{f}_{1,i}\boldsymbol{f}^*_{1,i})_k$, but we did not do this.

We note that one must first calculate the monoenergetic extrapolation distance using Eqs. (5.110) and (5.111) and insert the result into Eq. (5.109) to obtain the multigroup extrapolation extrapolation distance.

5.4.4 Variational Discontinuity Factors

To derive the variational DFs, we follow a similar procedure to that used in the previous section. First, we consider the forward functional (Eq. (5.87)) with the exact forward flux, ϕ, and the approximate adjoint flux, Φ^*, defined by Eq. (5.90). Requiring that the $O(\delta)$ terms vanish yields:

(5.112)

$$\begin{aligned}0=&\sum_{ij}\int_{\partial V_{ij}}\int_0^\infty\int_{4\pi}(\boldsymbol{n}_{ij}\cdot\mathbf{\Omega})\left[f^*_{0,i}\delta\phi^*_i+f^*_{0,j}\delta\phi^*_j\right]\left[\boldsymbol{f}_{1,i}\cdot\nabla\phi_i-\boldsymbol{f}_{1,j}\cdot\nabla\phi_j\right]\mathrm{d}\Omega\,\mathrm{d}E\,\mathrm{d}S\\&-\sum_{ij}\int_{\partial V_{ij}}\int_0^\infty\int_{4\pi}(\boldsymbol{n}_{ij}\cdot\mathbf{\Omega})\left[\boldsymbol{f}^*_{1,i}\cdot\nabla\delta\phi^*_i+\boldsymbol{f}^*_{1,j}\cdot\nabla\delta\phi^*_j\right]\left[f_{0,i}\phi_i-f_{0,j}\phi_j\right]\mathrm{d}\Omega\,\mathrm{d}E\,\mathrm{d}S\,.\end{aligned}$$

Similarly, we introduce the exact adjoint flux, ϕ^*, and approximate forward flux, Φ, defined by Eq. (5.89) into the adjoint functional (Eq. (5.88)). Setting the $O(\delta)$ terms

equal to 0 yields:

(5.113)
$$0 = \sum_{ij} \int_{\partial V_{ij}} \int_0^\infty \int_{4\pi} (\boldsymbol{n}_{ij} \cdot \boldsymbol{\Omega}) \left[f_{0,i} \delta\phi_i + f_{0,j} \delta\phi_j \right] \left[\boldsymbol{f}^*_{1,i} \cdot \nabla \phi^*_i - \boldsymbol{f}^*_{1,j} \cdot \nabla \phi^*_j \right] \mathrm{d}\Omega \, \mathrm{d}E \, \mathrm{d}S$$
$$- \sum_{ij} \int_{\partial V_{ij}} \int_0^\infty \int_{4\pi} (\boldsymbol{n}_{ij} \cdot \boldsymbol{\Omega}) \left[\boldsymbol{f}_{1,i} \cdot \nabla \delta\phi_i + \boldsymbol{f}_{1,j} \cdot \nabla \delta\phi_j \right] \left[f^*_{0,i} \phi^*_i - f^*_{0,j} \phi^*_j \right] \mathrm{d}\Omega \, \mathrm{d}E \, \mathrm{d}S \, .$$

As we did with the boundary terms, we assume that the tangential derivatives of the forward and adjoint fluxes are $O(\delta) = O(\epsilon^2)$, rather than $O(\epsilon)$. This is true for large, planar surfaces away from corners. Then:

(5.114a)
$$\Big(\nabla - \boldsymbol{n}_{ij} \left(\boldsymbol{n}_{ij} \cdot \nabla \right) \Big) \phi \quad \text{and} \quad \Big(\nabla - \boldsymbol{n}_{ij} \left(\boldsymbol{n}_{ij} \cdot \nabla \right) \Big) \phi^* = O(\delta) \, ,$$

(5.114b)
$$\Big(\nabla - \boldsymbol{n}_{ij} \left(\boldsymbol{n}_{ij} \cdot \nabla \right) \Big) \delta\phi \quad \text{and} \quad \Big(\nabla - \boldsymbol{n}_{ij} \left(\boldsymbol{n}_{ij} \cdot \nabla \right) \Big) \delta\phi^* = O(\delta^2) \, ,$$

Introducing Eqs. (5.114) into Eqs. (5.112) and (5.113) and neglecting the $O(\delta^2) = O(\epsilon^4)$ terms yields:

(5.115)
$$0 = \sum_{ij} \int_{\partial V_{ij}} \int_0^\infty \int_{4\pi} \big(\boldsymbol{n}_{ij} \cdot \boldsymbol{\Omega} \big) \Big[f^*_{0,i} \delta\phi^*_i + f^*_{0,j} \delta\phi^*_j \Big]$$
$$\times \Big[\big(\boldsymbol{n}_{ij} \cdot \boldsymbol{f}_{1,i} \big) \big(\boldsymbol{n}_{ij} \cdot \nabla \big) \phi_i - \big(\boldsymbol{n}_{ij} \cdot \boldsymbol{f}_{1,j} \big) \big(\boldsymbol{n}_{ij} \cdot \nabla \big) \phi_j \Big] \, \mathrm{d}\Omega \, \mathrm{d}E \, \mathrm{d}S$$
$$- \sum_{ij} \int_{\partial V_{ij}} \int_0^\infty \int_{4\pi} \big(\boldsymbol{n}_{ij} \cdot \boldsymbol{\Omega} \big) \Big[\big(\boldsymbol{n}_{ij} \cdot \boldsymbol{f}^*_{1,i} \big) \big(\boldsymbol{n}_{ij} \cdot \nabla \big) \delta\phi^*_i + \big(\boldsymbol{n}_{ij} \cdot \boldsymbol{f}^*_{1,j} \big) \big(\boldsymbol{n}_{ij} \cdot \nabla \big) \delta\phi^*_j \Big]$$
$$\times \Big[f_{0,i} \phi_i - f_{0,j} \phi_j \Big] \, \mathrm{d}\Omega \, \mathrm{d}E \, \mathrm{d}S \, ,$$

(5.116)

$$
\begin{aligned}
0 = \sum_{ij} \int_{\partial V_{ij}} \int_0^\infty \int_{4\pi} \big(\boldsymbol{n}_{ij} \cdot \boldsymbol{\Omega}\big) \Big[f_{0,i} \delta\phi_i + f_{0,j} \delta\phi_j \Big] \\
\times \Big[\big(\boldsymbol{n}_{ij} \cdot \boldsymbol{f}^*_{1,i}\big)\big(\boldsymbol{n}_{ij} \cdot \nabla\big)\phi^*_i - \big(\boldsymbol{n}_{ij} \cdot \boldsymbol{f}^*_{1,j}\big)\big(\boldsymbol{n}_{ij} \cdot \nabla\big)\phi^*_j \Big] \, \mathrm{d}\Omega \, \mathrm{d}E \, \mathrm{d}S \\
- \sum_{ij} \int_{\partial V_{ij}} \int_0^\infty \int_{4\pi} \big(\boldsymbol{n}_{ij} \cdot \boldsymbol{\Omega}\big) \Big[\big(\boldsymbol{n}_{ij} \cdot \boldsymbol{f}_{1,i}\big)\big(\boldsymbol{n}_{ij} \cdot \nabla\big)\delta\phi_i + \big(\boldsymbol{n}_{ij} \cdot \boldsymbol{f}_{1,j}\big)\big(\boldsymbol{n}_{ij} \cdot \nabla\big)\delta\phi_j \Big] \\
\times \Big[f^*_{0,i}\phi^*_i - f^*_{0,j}\phi^*_j \Big] \, \mathrm{d}\Omega \, \mathrm{d}E \, \mathrm{d}S \, .
\end{aligned}
$$

These equations are satisfied if for each interface ij the following four conditions are met:

(5.117a)

$$
\begin{aligned}
0 = \int_{\partial V_{ij}} \int_0^\infty \int_{4\pi} \big(\boldsymbol{n}_{ij} \cdot \boldsymbol{\Omega}\big) \Big[f^*_{0,i} \delta\phi^*_i + f^*_{0,j} \delta\phi^*_j \Big] \\
\times \Big[\big(\boldsymbol{n}_{ij} \cdot \boldsymbol{f}_{1,i}\big)\big(\boldsymbol{n}_{ij} \cdot \nabla\big)\phi_i - \big(\boldsymbol{n}_{ij} \cdot \boldsymbol{f}_{1,j}\big)\big(\boldsymbol{n}_{ij} \cdot \nabla\big)\phi_j \Big] \, \mathrm{d}\Omega \, \mathrm{d}E \, \mathrm{d}S \, ,
\end{aligned}
$$

(5.117b)

$$
\begin{aligned}
0 = \int_{\partial V_{ij}} \int_0^\infty \int_{4\pi} \big(\boldsymbol{n}_{ij} \cdot \boldsymbol{\Omega}\big) \Big[\big(\boldsymbol{n}_{ij} \cdot \boldsymbol{f}^*_{1,i}\big)\big(\boldsymbol{n}_{ij} \cdot \nabla\big)\delta\phi^*_i + \big(\boldsymbol{n}_{ij} \cdot \boldsymbol{f}^*_{1,j}\big)\big(\boldsymbol{n}_{ij} \cdot \nabla\big)\delta\phi^*_j \Big] \\
\times \Big[f_{0,i}\phi_i - f_{0,j}\phi_j \Big] \, \mathrm{d}\Omega \, \mathrm{d}E \, \mathrm{d}S \, ,
\end{aligned}
$$

(5.117c)

$$
\begin{aligned}
0 = \int_{\partial V_{ij}} \int_0^\infty \int_{4\pi} \big(\boldsymbol{n}_{ij} \cdot \boldsymbol{\Omega}\big) \Big[f_{0,i} \delta\phi_i + f_{0,j} \delta\phi_j \Big] \\
\times \Big[\big(\boldsymbol{n}_{ij} \cdot \boldsymbol{f}^*_{1,i}\big)\big(\boldsymbol{n}_{ij} \cdot \nabla\big)\phi^*_i - \big(\boldsymbol{n}_{ij} \cdot \boldsymbol{f}^*_{1,j}\big)\big(\boldsymbol{n}_{ij} \cdot \nabla\big)\phi^*_j \Big] \, \mathrm{d}\Omega \, \mathrm{d}E \, \mathrm{d}S \, ,
\end{aligned}
$$

(5.117d)

$$
\begin{aligned}
0 = \int_{\partial V_{ij}} \int_0^\infty \int_{4\pi} \big(\boldsymbol{n}_{ij} \cdot \boldsymbol{\Omega}\big) \Big[\big(\boldsymbol{n}_{ij} \cdot \boldsymbol{f}_{1,i}\big)\big(\boldsymbol{n}_{ij} \cdot \nabla\big)\delta\phi_i + \big(\boldsymbol{n}_{ij} \cdot \boldsymbol{f}_{1,j}\big)\big(\boldsymbol{n}_{ij} \cdot \nabla\big)\delta\phi_j \Big] \\
\times \Big[f^*_{0,i}\phi^*_i - f^*_{0,j}\phi^*_j \Big] \, \mathrm{d}\Omega \, \mathrm{d}E \, \mathrm{d}S \, .
\end{aligned}
$$

At this point, we assume that the diffusion fluxes and surface-normal currents are discontinuous at lattice interfaces in the manner discussed in previous sections:

$$a_i(\boldsymbol{x})\phi_i(\boldsymbol{x}) = a_j(\boldsymbol{x})\phi_j(\boldsymbol{x})\,, \qquad \boldsymbol{x} \in \partial V_{ij}\,, \tag{5.118a}$$

$$a_i(\boldsymbol{x})b_i(\boldsymbol{x})D_{i,nn}\boldsymbol{n}_{ij}\cdot\nabla\phi_i(\boldsymbol{x}) = a_j(\boldsymbol{x})b_j(\boldsymbol{x})D_{j,nn}\boldsymbol{n}_{ij}\cdot\nabla\phi_j(\boldsymbol{x})\,, \qquad \boldsymbol{x} \in \partial V_{ij}\,, \tag{5.118b}$$

$$c_i(\boldsymbol{x})\phi_i^*(\boldsymbol{x}) = c_j(\boldsymbol{x})\phi_j^*(\boldsymbol{x})\,, \qquad \boldsymbol{x} \in \partial V_{ij}\,, \tag{5.118c}$$

$$c_i(\boldsymbol{x})d_i(\boldsymbol{x})D_{i,nn}\boldsymbol{n}_{ij}\cdot\nabla\phi_i^*(\boldsymbol{x}) = c_j(\boldsymbol{x})d_j(\boldsymbol{x})D_{j,nn}\boldsymbol{n}_{ij}\cdot\nabla\phi_j^*(\boldsymbol{x})\,, \qquad \boldsymbol{x} \in \partial V_{ij}\,, \tag{5.118d}$$

where $D_{i,nn}$ is the normal component of the diffusion coefficient for region i and the DFs a, b, c, and d are to-be-determined. We then assume that the variations in the diffusion solutions have the same discontinuities:

$$a_i(\boldsymbol{x})\delta\phi_i(\boldsymbol{x}) = a_j(\boldsymbol{x})\delta\phi_j(\boldsymbol{x})\,, \qquad \boldsymbol{x} \in \partial V_{ij}\,, \tag{5.119a}$$

$$a_i(\boldsymbol{x})b_i(\boldsymbol{x})D_{i,nn}\boldsymbol{n}_{ij}\cdot\nabla\delta\phi_i(\boldsymbol{x}) = a_j(\boldsymbol{x})b_j(\boldsymbol{x})D_{j,nn}\boldsymbol{n}_{ij}\cdot\nabla\delta\phi_j(\boldsymbol{x})\,, \qquad \boldsymbol{x} \in \partial V_{ij}\,, \tag{5.119b}$$

$$c_i(\boldsymbol{x})\delta\phi_i^*(\boldsymbol{x}) = c_j(\boldsymbol{x})\delta\phi_j^*(\boldsymbol{x})\,, \qquad \boldsymbol{x} \in \partial V_{ij}\,, \tag{5.119c}$$

$$c_i(\boldsymbol{x})d_i(\boldsymbol{x})D_{i,nn}\boldsymbol{n}_{ij}\cdot\nabla\delta\phi_i^*(\boldsymbol{x}) = c_j(\boldsymbol{x})d_j(\boldsymbol{x})D_{j,nn}\boldsymbol{n}_{ij}\cdot\nabla\delta\phi_j^*(\boldsymbol{x})\,, \qquad \boldsymbol{x} \in \partial V_{ij}\,. \tag{5.119d}$$

Introducing Eqs. (5.118) and (5.119) into Eq. (5.117), we obtain:

(5.120a)

$$0 = \int_{\partial V_{ij}} \delta\phi_i^* \big(\boldsymbol{n}_{ij} \cdot \nabla\big) \phi_i \Bigg[\int_0^\infty \int_{4\pi} \big(\boldsymbol{n}_{ij} \cdot \boldsymbol{\Omega}\big) \Bigg[f_{0,i}^* \big(\boldsymbol{n}_{ij} \cdot \boldsymbol{f}_{1,i}\big) - f_{0,i}^* \big(\boldsymbol{n}_{ij} \cdot \boldsymbol{f}_{1,j}\big) \frac{a_i b_i D_{i,nn}}{a_j b_j D_{j,nn}} + f_{0,j}^* \big(\boldsymbol{n}_{ij} \cdot \boldsymbol{f}_{1,i}\big) \frac{c_i}{c_j} - f_{0,j}^* \big(\boldsymbol{n}_{ij} \cdot \boldsymbol{f}_{1,j}\big) \frac{a_i b_i D_{i,nn}}{a_j b_j D_{j,nn}} \frac{c_i}{c_j} \Bigg] \mathrm{d}\Omega \, \mathrm{d}E \Bigg] \mathrm{d}S \,,$$

(5.120b)

$$0 = \int_{\partial V_{ij}} \big(\boldsymbol{n}_{ij} \cdot \nabla\big) \delta\phi_i^* \phi_i \Bigg[\int_0^\infty \int_{4\pi} \big(\boldsymbol{n}_{ij} \cdot \boldsymbol{\Omega}\big) \Bigg[\big(\boldsymbol{n}_{ij} \cdot \boldsymbol{f}_{1,i}^*\big) f_{0,i} - \big(\boldsymbol{n}_{ij} \cdot \boldsymbol{f}_{1,i}^*\big) f_{0,j} \frac{a_i}{a_j} + \big(\boldsymbol{n}_{ij} \cdot \boldsymbol{f}_{1,j}^*\big) f_{0,i} \frac{c_i d_i D_{i,nn}}{c_j d_j D_{j,nn}} - \big(\boldsymbol{n}_{ij} \cdot \boldsymbol{f}_{1,j}^*\big) f_{0,j} \frac{a_i}{a_j} \frac{c_i d_i D_{i,nn}}{c_j d_j D_{j,nn}} \Bigg] \mathrm{d}\Omega \, \mathrm{d}E \Bigg] \mathrm{d}S \,,$$

(5.120c)

$$0 = \int_{\partial V_{ij}} \delta\phi_i \big(\boldsymbol{n}_{ij} \cdot \nabla\big) \phi_i^* \Bigg[\int_0^\infty \int_{4\pi} \big(\boldsymbol{n}_{ij} \cdot \boldsymbol{\Omega}\big) \Bigg[\big(\boldsymbol{n}_{ij} \cdot \boldsymbol{f}_{1,i}^*\big) f_{0,i} - \big(\boldsymbol{n}_{ij} \cdot \boldsymbol{f}_{1,j}^*\big) f_{0,i} \frac{c_i d_i D_{i,nn}}{c_j d_j D_{j,nn}} + \big(\boldsymbol{n}_{ij} \cdot \boldsymbol{f}_{1,i}^*\big) f_{0,j} \frac{a_i}{a_j} - \big(\boldsymbol{n}_{ij} \cdot \boldsymbol{f}_{1,j}^*\big) f_{0,j} \frac{a_i}{a_j} \frac{c_i d_i D_{i,nn}}{c_j d_j D_{j,nn}} \Bigg] \mathrm{d}\Omega \, \mathrm{d}E \Bigg] \mathrm{d}S \,,$$

(5.120d)

$$0 = \int_{\partial V_{ij}} (\boldsymbol{n}_{ij} \cdot \nabla) \delta\phi_i \phi_i^* \Bigg[\int_0^\infty \int_{4\pi} (\boldsymbol{n}_{ij} \cdot \boldsymbol{\Omega}) \Bigg[f_{0,i}^*(\boldsymbol{n}_{ij} \cdot \boldsymbol{f}_{1,i}) - f_{0,j}^*(\boldsymbol{n}_{ij} \cdot \boldsymbol{f}_{1,i}) \frac{c_i}{c_j} + f_{0,i}^*(\boldsymbol{n}_{ij} \cdot \boldsymbol{f}_{1,j}) \frac{a_i b_i D_{i,nn}}{a_j b_j D_{j,nn}} - f_{0,j}^*(\boldsymbol{n}_{ij} \cdot \boldsymbol{f}_{1,j}) \frac{a_i b_i D_{i,nn}}{a_j b_j D_{j,nn}} \frac{c_i}{c_j} \Bigg] \mathrm{d}\Omega \, \mathrm{d}E \Bigg] \mathrm{d}S \,.$$

Equations (5.120) are satisfied for any $\delta\phi$ and $\delta\phi^*$ if the following are true:

(5.121a)

$$0 = \int_0^\infty \int_{4\pi} (\boldsymbol{n}_{ij} \cdot \boldsymbol{\Omega}) \Bigg[f_{0,i}^*(\boldsymbol{n}_{ij} \cdot \boldsymbol{f}_{1,i}) - f_{0,i}^*(\boldsymbol{n}_{ij} \cdot \boldsymbol{f}_{1,j}) \frac{a_i b_i D_{i,nn}}{a_j b_j D_{j,nn}} + f_{0,j}^*(\boldsymbol{n}_{ij} \cdot \boldsymbol{f}_{1,i}) \frac{c_i}{c_j} - f_{0,j}^*(\boldsymbol{n}_{ij} \cdot \boldsymbol{f}_{1,j}) \frac{a_i b_i D_{i,nn}}{a_j b_j D_{j,nn}} \frac{c_i}{c_j} \Bigg] \mathrm{d}\Omega \, \mathrm{d}E \,, \qquad \boldsymbol{x} \in \partial V_{ij} \,,$$

(5.121b)

$$0 = \int_0^\infty \int_{4\pi} (\boldsymbol{n}_{ij} \cdot \boldsymbol{\Omega}) \Bigg[(\boldsymbol{n}_{ij} \cdot \boldsymbol{f}_{1,i}^*) f_{0,i} - (\boldsymbol{n}_{ij} \cdot \boldsymbol{f}_{1,i}^*) f_{0,j} \frac{a_i}{a_j} + (\boldsymbol{n}_{ij} \cdot \boldsymbol{f}_{1,j}^*) f_{0,i} \frac{c_i d_i D_{i,nn}}{c_j d_j D_{j,nn}} - (\boldsymbol{n}_{ij} \cdot \boldsymbol{f}_{1,j}^*) f_{0,j} \frac{a_i}{a_j} \frac{c_i d_i D_{i,nn}}{c_j d_j D_{j,nn}} \Bigg] \mathrm{d}\Omega \, \mathrm{d}E \,, \qquad \boldsymbol{x} \in \partial V_{ij} \,,$$

(5.121c)

$$0 = \int_0^\infty \int_{4\pi} (\boldsymbol{n}_{ij} \cdot \boldsymbol{\Omega}) \Bigg[(\boldsymbol{n}_{ij} \cdot \boldsymbol{f}_{1,i}^*) f_{0,i} + (\boldsymbol{n}_{ij} \cdot \boldsymbol{f}_{1,i}^*) f_{0,j} \frac{a_i}{a_j} - (\boldsymbol{n}_{ij} \cdot \boldsymbol{f}_{1,j}^*) f_{0,i} \frac{c_i d_i D_{i,nn}}{c_j d_j D_{j,nn}} - (\boldsymbol{n}_{ij} \cdot \boldsymbol{f}_{1,j}^*) f_{0,j} \frac{a_i}{a_j} \frac{c_i d_i D_{i,nn}}{c_j d_j D_{j,nn}} \Bigg] \mathrm{d}\Omega \, \mathrm{d}E \,, \qquad \boldsymbol{x} \in \partial V_{ij} \,,$$

(5.121d)

$$0 = \int_0^\infty \int_{4\pi} (\boldsymbol{n}_{ij} \cdot \boldsymbol{\Omega}) \Bigg[f_{0,i}^*(\boldsymbol{n}_{ij} \cdot \boldsymbol{f}_{1,i}) + f_{0,i}^*(\boldsymbol{n}_{ij} \cdot \boldsymbol{f}_{1,j}) \frac{a_i b_i D_{i,nn}}{a_j b_j D_{j,nn}} - f_{0,j}^*(\boldsymbol{n}_{ij} \cdot \boldsymbol{f}_{1,i}) \frac{c_i}{c_j} - f_{0,j}^*(\boldsymbol{n}_{ij} \cdot \boldsymbol{f}_{1,j}) \frac{a_i b_i D_{i,nn}}{a_j b_j D_{j,nn}} \frac{c_i}{c_j} \Bigg] \mathrm{d}\Omega \, \mathrm{d}E \,, \qquad \boldsymbol{x} \in \partial V_{ij} \,,$$

We add Eqs. (5.121a) and (5.121d) and divide by 2 to obtain:

$$0 = \int_0^\infty \int_{4\pi} \big(\boldsymbol{n}_{ij}\cdot\boldsymbol{\Omega}\big)\left[f^*_{0,i}\big(\boldsymbol{n}_{ij}\cdot\boldsymbol{f}_{1,i}\big) - f^*_{0,j}\big(\boldsymbol{n}_{ij}\cdot\boldsymbol{f}_{1,j}\big)\frac{a_i b_i D_{i,nn}}{a_j b_j D_{j,nn}}\frac{c_i}{c_j}\right]\mathrm{d}\Omega\,\mathrm{d}E\,, \qquad \boldsymbol{x}\in\partial V_{ij}\,,$$

or:

$$\frac{a_i b_i D_{i,nn}}{a_j b_j D_{j,nn}}\frac{c_i}{c_j} = \frac{\displaystyle\int_0^\infty \int_{4\pi} \big(\boldsymbol{n}_{ij}\cdot\boldsymbol{\Omega}\big) f^*_{0,i}\big(\boldsymbol{n}_{ij}\cdot\boldsymbol{f}_{1,i}\big)\,\mathrm{d}\Omega\,\mathrm{d}E}{\displaystyle\int_0^\infty \int_{4\pi} \big(\boldsymbol{n}_{ij}\cdot\boldsymbol{\Omega}\big) f^*_{0,j}\big(\boldsymbol{n}_{ij}\cdot\boldsymbol{f}_{1,j}\big)\,\mathrm{d}\Omega\,\mathrm{d}E}\,, \qquad \boldsymbol{x}\in\partial V_{ij}\,. \tag{5.122a}$$

Subtracting Eq. (5.121a) from Eq. (5.121d) and dividing by 2, we get:

$$0 = \int_0^\infty \int_{4\pi} \big(\boldsymbol{n}_{ij}\cdot\boldsymbol{\Omega}\big)\left[f^*_{0,i}\big(\boldsymbol{n}_{ij}\cdot\boldsymbol{f}_{1,j}\big)\frac{a_i b_i D_{i,nn}}{a_j b_j D_{j,nn}} - f^*_{0,j}\big(\boldsymbol{n}_{ij}\cdot\boldsymbol{f}_{1,i}\big)\frac{c_i}{c_j}\right]\mathrm{d}\Omega\,\mathrm{d}E\,, \qquad \boldsymbol{x}\in\partial V_{ij}\,,$$

or:

$$\frac{a_i b_i D_{i,nn}}{a_j b_j D_{j,nn}}\frac{c_j}{c_i} = \frac{\displaystyle\int_0^\infty \int_{4\pi} \big(\boldsymbol{n}_{ij}\cdot\boldsymbol{\Omega}\big) f^*_{0,j}\big(\boldsymbol{n}_{ij}\cdot\boldsymbol{f}_{1,i}\big)\,\mathrm{d}\Omega\,\mathrm{d}E}{\displaystyle\int_0^\infty \int_{4\pi} \big(\boldsymbol{n}_{ij}\cdot\boldsymbol{\Omega}\big) f^*_{0,i}\big(\boldsymbol{n}_{ij}\cdot\boldsymbol{f}_{1,j}\big)\,\mathrm{d}\Omega\,\mathrm{d}E}\,, \qquad \boldsymbol{x}\in\partial V_{ij}\,. \tag{5.122b}$$

Adding Eqs. (5.121b) and (5.121c) and dividing by 2, we have:

$$0 = \int_0^\infty \int_{4\pi} \big(\boldsymbol{n}_{ij}\cdot\boldsymbol{\Omega}\big)\left[\big(\boldsymbol{n}_{ij}\cdot\boldsymbol{f}^*_{1,i}\big) f_{0,i} - \big(\boldsymbol{n}_{ij}\cdot\boldsymbol{f}^*_{1,j}\big) f_{0,j}\frac{a_i}{a_j}\frac{c_i d_i D_{i,nn}}{c_j d_j D_{j,nn}}\right]\mathrm{d}\Omega\,\mathrm{d}E\,, \qquad \boldsymbol{x}\in\partial V_{ij}\,,$$

or:

$$\frac{a_i}{a_j}\frac{c_i d_i D_{i,nn}}{c_j d_j D_{j,nn}} = \frac{\displaystyle\int_0^\infty \int_{4\pi} \big(\boldsymbol{n}_{ij}\cdot\boldsymbol{\Omega}\big)\big(\boldsymbol{n}_{ij}\cdot\boldsymbol{f}^*_{1,i}\big) f_{0,i}\,\mathrm{d}\Omega\,\mathrm{d}E}{\displaystyle\int_0^\infty \int_{4\pi} \big(\boldsymbol{n}_{ij}\cdot\boldsymbol{\Omega}\big)\big(\boldsymbol{n}_{ij}\cdot\boldsymbol{f}^*_{1,j}\big) f_{0,j}\,\mathrm{d}\Omega\,\mathrm{d}E}\,, \qquad \boldsymbol{x}\in\partial V_{ij}\,. \tag{5.122c}$$

We subtract Eq. (5.121b) from Eq. (5.121c) and divide by 2 to find:

$$0 = \int_0^\infty \int_{4\pi} \big(\boldsymbol{n}_{ij}\cdot\boldsymbol{\Omega}\big)\left[\big(\boldsymbol{n}_{ij}\cdot\boldsymbol{f}^*_{1,i}\big) f_{0,j}\frac{a_i}{a_j} - \big(\boldsymbol{n}_{ij}\cdot\boldsymbol{f}^*_{1,j}\big) f_{0,i}\frac{c_i d_i D_{i,nn}}{c_j d_j D_{j,nn}}\right]\mathrm{d}\Omega\,\mathrm{d}E\,, \qquad \boldsymbol{x}\in\partial V_{ij}\,,$$

or:

$$\frac{a_j}{a_i}\frac{c_i d_i D_{i,nn}}{c_j d_j D_{j,nn}} = \frac{\displaystyle\int_0^\infty \int_{4\pi} \big(\boldsymbol{n}_{ij}\cdot\boldsymbol{\Omega}\big)\big(\boldsymbol{n}_{ij}\cdot\boldsymbol{f}^*_{1,i}\big) f_{0,j}\,\mathrm{d}\Omega\,\mathrm{d}E}{\displaystyle\int_0^\infty \int_{4\pi} \big(\boldsymbol{n}_{ij}\cdot\boldsymbol{\Omega}\big)\big(\boldsymbol{n}_{ij}\cdot\boldsymbol{f}^*_{1,j}\big) f_{0,i}\,\mathrm{d}\Omega\,\mathrm{d}E}\,, \qquad \boldsymbol{x}\in\partial V_{ij}\,. \tag{5.122d}$$

We now solve for the forward DFs a and b. (The adjoint DFs c and d are not needed in our work, but can be obtained in an analogous fashion.) We divide Eq. (5.122c) by Eq. (5.122d) to obtain:

$$\frac{a_i^2}{a_j^2} = \left[\frac{\displaystyle\int_0^\infty \int_{4\pi} \big(\boldsymbol{n}_{ij}\cdot\boldsymbol{\Omega}\big)\big(\boldsymbol{n}_{ij}\cdot\boldsymbol{f}_{1,i}^*\big) f_{0,i}\,\mathrm{d}\Omega\,\mathrm{d}E}{\displaystyle\int_0^\infty \int_{4\pi} \big(\boldsymbol{n}_{ij}\cdot\boldsymbol{\Omega}\big)\big(\boldsymbol{n}_{ij}\cdot\boldsymbol{f}_{1,i}^*\big) f_{0,j}\,\mathrm{d}\Omega\,\mathrm{d}E}\right] \times \left[\frac{\displaystyle\int_0^\infty \int_{4\pi} \big(\boldsymbol{n}_{ij}\cdot\boldsymbol{\Omega}\big)\big(\boldsymbol{n}_{ij}\cdot\boldsymbol{f}_{1,j}^*\big) f_{0,i}\,\mathrm{d}\Omega\,\mathrm{d}E}{\displaystyle\int_0^\infty \int_{4\pi} \big(\boldsymbol{n}_{ij}\cdot\boldsymbol{\Omega}\big)\big(\boldsymbol{n}_{ij}\cdot\boldsymbol{f}_{1,j}^*\big) f_{0,j}\,\mathrm{d}\Omega\,\mathrm{d}E}\right], \qquad \boldsymbol{x}\in\partial V_{ij}\,. \tag{5.123a}$$

Next, we multiply Eqs. (5.122a) and (5.122b):

$$\frac{a_i^2 b_i^2 D_{i,nn}^2}{a_j^2 b_j^2 D_{j,nn}^2} = \left[\frac{\displaystyle\int_0^\infty \int_{4\pi} \big(\boldsymbol{n}_{ij}\cdot\boldsymbol{\Omega}\big) f_{0,i}^*\big(\boldsymbol{n}_{ij}\cdot\boldsymbol{f}_{1,i}\big)\,\mathrm{d}\Omega\,\mathrm{d}E}{\displaystyle\int_0^\infty \int_{4\pi} \big(\boldsymbol{n}_{ij}\cdot\boldsymbol{\Omega}\big) f_{0,i}^*\big(\boldsymbol{n}_{ij}\cdot\boldsymbol{f}_{1,j}\big)\,\mathrm{d}\Omega\,\mathrm{d}E}\right] \times \left[\frac{\displaystyle\int_0^\infty \int_{4\pi} \big(\boldsymbol{n}_{ij}\cdot\boldsymbol{\Omega}\big) f_{0,j}^*\big(\boldsymbol{n}_{ij}\cdot\boldsymbol{f}_{1,i}\big)\,\mathrm{d}\Omega\,\mathrm{d}E}{\displaystyle\int_0^\infty \int_{4\pi} \big(\boldsymbol{n}_{ij}\cdot\boldsymbol{\Omega}\big) f_{0,j}^*\big(\boldsymbol{n}_{ij}\cdot\boldsymbol{f}_{1,j}\big)\,\mathrm{d}\Omega\,\mathrm{d}E}\right], \qquad \boldsymbol{x}\in\partial V_{ij}\,. \tag{5.123b}$$

Equations (5.123) have an infinite number of solutions. We choose to satisfy them in the following way:

$$a_i(\boldsymbol{x}) = \left[\left(\int_0^\infty \int_{4\pi} \big(\boldsymbol{n}_{ij}\cdot\boldsymbol{\Omega}\big)\big(\boldsymbol{n}_{ij}\cdot\boldsymbol{f}_{1,i}^*\big) f_{0,i}\,\mathrm{d}\Omega\,\mathrm{d}E\right) \times \left(\int_0^\infty \int_{4\pi} \big(\boldsymbol{n}_{ij}\cdot\boldsymbol{\Omega}\big)\big(\boldsymbol{n}_{ij}\cdot\boldsymbol{f}_{1,j}^*\big) f_{0,i}\,\mathrm{d}\Omega\,\mathrm{d}E\right)\right]^{1/2}, \qquad \boldsymbol{x}\in\partial V_{ij}\,, \tag{5.124a}$$

$$a_j(\boldsymbol{x}) = \left[\left(\int_0^\infty \int_{4\pi} \big(\boldsymbol{n}_{ij}\cdot\boldsymbol{\Omega}\big)\big(\boldsymbol{n}_{ij}\cdot\boldsymbol{f}_{1,i}^*\big) f_{0,j}\,\mathrm{d}\Omega\,\mathrm{d}E\right) \times \left(\int_0^\infty \int_{4\pi} \big(\boldsymbol{n}_{ij}\cdot\boldsymbol{\Omega}\big)\big(\boldsymbol{n}_{ij}\cdot\boldsymbol{f}_{1,j}^*\big) f_{0,j}\,\mathrm{d}\Omega\,\mathrm{d}E\right)\right]^{1/2}, \qquad \boldsymbol{x}\in\partial V_{ij}\,. \tag{5.124b}$$

(5.125a)

$$b_i(\boldsymbol{x}) = \frac{1}{a_i D_{i,nn}} \Bigg[\left(\int_0^\infty \int_{4\pi} \big(\boldsymbol{n}_{ij} \cdot \boldsymbol{\Omega}\big) f_{0,i}^*\big(\boldsymbol{n}_{ij} \cdot \boldsymbol{f}_{1,i}\big) \, \mathrm{d}\Omega \, \mathrm{d}E \right) \times \left(\int_0^\infty \int_{4\pi} \big(\boldsymbol{n}_{ij} \cdot \boldsymbol{\Omega}\big) f_{0,j}^*\big(\boldsymbol{n}_{ij} \cdot \boldsymbol{f}_{1,i}\big) \, \mathrm{d}\Omega \, \mathrm{d}E \right) \Bigg]^{1/2}, \qquad \boldsymbol{x} \in \partial V_{ij} \,,$$

(5.125b)

$$b_j(\boldsymbol{x}) = \frac{1}{a_j D_{j,nn}} \Bigg[\left(\int_0^\infty \int_{4\pi} \big(\boldsymbol{n}_{ij} \cdot \boldsymbol{\Omega}\big) f_{0,i}^*\big(\boldsymbol{n}_{ij} \cdot \boldsymbol{f}_{1,j}\big) \, \mathrm{d}\Omega \, \mathrm{d}E \right) \times \left(\int_0^\infty \int_{4\pi} \big(\boldsymbol{n}_{ij} \cdot \boldsymbol{\Omega}\big) f_{0,j}^*\big(\boldsymbol{n}_{ij} \cdot \boldsymbol{f}_{1,j}\big) \, \mathrm{d}\Omega \, \mathrm{d}E \right) \Bigg]^{1/2}, \qquad \boldsymbol{x} \in \partial V_{ij} \,.$$

These DFs are specified for the monoenergetic diffusion equation. However, we desire interface conditions for the multigroup diffusion equation of the form:

(5.126a) $$a_{i,g}\phi_{i,g}(\boldsymbol{x}) = a_{j,g}\phi_{j,g}(\boldsymbol{x}) \,, \qquad \boldsymbol{x} \in \partial V_{ij} \,,$$

(5.126b) $$a_{i,g} b_{i,g} D_{i,g,nn}\big(\boldsymbol{n}_{ij} \cdot \nabla\big)\phi_{i,g}(\boldsymbol{x}) = a_{j,g} b_{j,g} D_{j,g,nn}\big(\boldsymbol{n}_{ij} \cdot \nabla\big)\phi_{j,g}(\boldsymbol{x}) \,, \qquad \boldsymbol{x} \in \partial V_{ij} \,.$$

We operate on Eq. (5.126a) by $\sum_{g=1}^{G}(\cdot)$:

$$\sum_{g=1}^{G} a_{i,g}\phi_{i,g}(\boldsymbol{x}) = \sum_{g=1}^{G} a_{j,g}\phi_{j,g}(\boldsymbol{x}) \,, \qquad \boldsymbol{x} \in \partial V_{ij} \,.$$

In the asymptotic limit, the multigroup flux can be expressed in terms of the monoenergetic flux (Eq. (4.34)). Making this substitution in the previous equation yields:

$$\left(\sum_{g=1}^{G} a_{i,g} \overline{F_{0,i,g}} \right) \phi_i(\boldsymbol{x}) = \left(\sum_{g=1}^{G} a_{j,g} \overline{F_{0,j,g}} \right) \phi_j(\boldsymbol{x}) \,, \qquad \boldsymbol{x} \in \partial V_{ij} \,.$$

Comparing to the monoenergetic flux discontinuity condition of Eq. (5.118a), we see that in each region adjacent to the interface:

(5.127) $$a_i = \sum_{g=1}^{G} a_{i,g} \overline{F_{0,i,g}} \,, \qquad \boldsymbol{x} \in \partial V_{ij} \,.$$

Similarly:

$$a_i b_i D_{i,nn} = \sum_{g=1}^{G} a_{i,g} b_{i,g} D_{i,g,nn} \overline{F_{0,i,g}}\,, \qquad \boldsymbol{x} \in \partial V_{ij}\,. \tag{5.128}$$

Unfortunately, because of the complicated structure of Eqs. (5.124) and (5.125), the integrals cannot simply be split into G terms as we did with the extrapolation lengths. Instead, we must multiply and divide each DF expression by a function that mirrors the physics of the true DF as closely as possible. We choose to multiply and divide the flux DF in region i (Eq. (5.124a)) by:

$$\int_0^\infty \int_{4\pi} (\boldsymbol{n}_{ij} \cdot \boldsymbol{\Omega}) \sqrt{(\boldsymbol{n}_{ij} \cdot \boldsymbol{f}^*_{1,i})(\boldsymbol{n}_{ij} \cdot \boldsymbol{f}^*_{1,j})} f_{0,i}\, \mathrm{d}\Omega\, \mathrm{d}E\,,$$

and obtain:

$$\begin{aligned} a_i(\boldsymbol{x}) = &\left[\left(\int_0^\infty \int_{4\pi} (\boldsymbol{n}_{ij} \cdot \boldsymbol{\Omega})(\boldsymbol{n}_{ij} \cdot \boldsymbol{f}^*_{1,i}) f_{0,i}\, \mathrm{d}\Omega\, \mathrm{d}E \right) \right. \\ &\left. \times \left(\int_0^\infty \int_{4\pi} (\boldsymbol{n}_{ij} \cdot \boldsymbol{\Omega})(\boldsymbol{n}_{ij} \cdot \boldsymbol{f}^*_{1,j}) f_{0,i}\, \mathrm{d}\Omega\, \mathrm{d}E \right) \right]^{1/2} \\ &\times \left[\frac{\displaystyle\int_0^\infty \int_{4\pi} (\boldsymbol{n}_{ij} \cdot \boldsymbol{\Omega}) \sqrt{(\boldsymbol{n}_{ij} \cdot \boldsymbol{f}^*_{1,i})(\boldsymbol{n}_{ij} \cdot \boldsymbol{f}^*_{1,j})} f_{0,i}\, \mathrm{d}\Omega\, \mathrm{d}E}{\displaystyle\int_0^\infty \int_{4\pi} (\boldsymbol{n}_{ij} \cdot \boldsymbol{\Omega}) \sqrt{(\boldsymbol{n}_{ij} \cdot \boldsymbol{f}^*_{1,i})(\boldsymbol{n}_{ij} \cdot \boldsymbol{f}^*_{1,j})} f_{0,i}\, \mathrm{d}\Omega\, \mathrm{d}E} \right], \qquad \boldsymbol{x} \in \partial V_{ij}\,. \end{aligned}$$

Comparing to Eq. (5.127), we see group dependent DFs can be obtained by splitting the numerator of the second bracketed term into G integrals:

(5.129)

$$\begin{aligned} a_{i,g}(\boldsymbol{x}) = &\frac{1}{\overline{F_{0,i,g}}} \left[\left(\int_0^\infty \int_{4\pi} (\boldsymbol{n}_{ij} \cdot \boldsymbol{\Omega})(\boldsymbol{n}_{ij} \cdot \boldsymbol{f}^*_{1,i}) f_{0,i}\, \mathrm{d}\Omega\, \mathrm{d}E \right) \right. \\ &\left. \times \left(\int_0^\infty \int_{4\pi} (\boldsymbol{n}_{ij} \cdot \boldsymbol{\Omega})(\boldsymbol{n}_{ij} \cdot \boldsymbol{f}^*_{1,j}) f_{0,i}\, \mathrm{d}\Omega\, \mathrm{d}E \right) \right]^{1/2} \\ &\times \left[\frac{\displaystyle\int_{E_g}^{E_{g-1}} \int_{4\pi} (\boldsymbol{n}_{ij} \cdot \boldsymbol{\Omega}) \sqrt{(\boldsymbol{n}_{ij} \cdot \boldsymbol{f}^*_{1,i})(\boldsymbol{n}_{ij} \cdot \boldsymbol{f}^*_{1,j})} f_{0,i}\, \mathrm{d}\Omega\, \mathrm{d}E}{\displaystyle\int_0^\infty \int_{4\pi} (\boldsymbol{n}_{ij} \cdot \boldsymbol{\Omega}) \sqrt{(\boldsymbol{n}_{ij} \cdot \boldsymbol{f}^*_{1,i})(\boldsymbol{n}_{ij} \cdot \boldsymbol{f}^*_{1,j})} f_{0,i}\, \mathrm{d}\Omega\, \mathrm{d}E} \right], \qquad \boldsymbol{x} \in \partial V_{ij}\,. \end{aligned}$$

We obtain the current DF in region i by multiplying and dividing Eq. (5.125a) by:

$$\int_0^\infty \int_{4\pi} \big(\boldsymbol{n}_{ij} \cdot \boldsymbol{\Omega}\big) \sqrt{f^*_{0,i} f^*_{0,j}} \big(\boldsymbol{n}_{ij} \cdot \boldsymbol{f}_{1,i}\big) \, \mathrm{d}\Omega \, \mathrm{d}E \,,$$

and obtain:

$$a_i(\boldsymbol{x}) b_i(\boldsymbol{x}) D_{i,nn} = \left[\left(\int_0^\infty \int_{4\pi} \big(\boldsymbol{n}_{ij} \cdot \boldsymbol{\Omega}\big) f^*_{0,i} \big(\boldsymbol{n}_{ij} \cdot \boldsymbol{f}_{1,i}\big) \, \mathrm{d}\Omega \, \mathrm{d}E \right) \times \left(\int_0^\infty \int_{4\pi} \big(\boldsymbol{n}_{ij} \cdot \boldsymbol{\Omega}\big) f^*_{0,j} \big(\boldsymbol{n}_{ij} \cdot \boldsymbol{f}_{1,i}\big) \, \mathrm{d}\Omega \, \mathrm{d}E \right) \right]^{1/2} \times \left[\frac{\displaystyle\int_0^\infty \int_{4\pi} \big(\boldsymbol{n}_{ij} \cdot \boldsymbol{\Omega}\big) \sqrt{f^*_{0,i} f^*_{0,j}} \big(\boldsymbol{n}_{ij} \cdot \boldsymbol{f}_{1,i}\big) \, \mathrm{d}\Omega \, \mathrm{d}E}{\displaystyle\int_0^\infty \int_{4\pi} \big(\boldsymbol{n}_{ij} \cdot \boldsymbol{\Omega}\big) \sqrt{f^*_{0,i} f^*_{0,j}} \big(\boldsymbol{n}_{ij} \cdot \boldsymbol{f}_{1,i}\big) \, \mathrm{d}\Omega \, \mathrm{d}E} \right] , \qquad \boldsymbol{x} \in \partial V_{ij} \,.$$

Equation (5.128) can now be satisfied by splitting the numerator of the second bracketed term into G integrals:

(5.130)

$$b_{i,g}(\boldsymbol{x}) = \frac{1}{a_{i,g}(\boldsymbol{x}) D_{i,g,nn} \overline{F_{0,i,g}}} \left[\left(\int_0^\infty \int_{4\pi} \big(\boldsymbol{n}_{ij} \cdot \boldsymbol{\Omega}\big) f^*_{0,i} \big(\boldsymbol{n}_{ij} \cdot \boldsymbol{f}_{1,i}\big) \, \mathrm{d}\Omega \, \mathrm{d}E \right) \times \left(\int_0^\infty \int_{4\pi} \big(\boldsymbol{n}_{ij} \cdot \boldsymbol{\Omega}\big) f^*_{0,j} \big(\boldsymbol{n}_{ij} \cdot \boldsymbol{f}_{1,i}\big) \, \mathrm{d}\Omega \, \mathrm{d}E \right) \right]^{1/2} \times \left[\frac{\displaystyle\int_{E_g}^{E_{g-1}} \int_{4\pi} \big(\boldsymbol{n}_{ij} \cdot \boldsymbol{\Omega}\big) \sqrt{f^*_{0,i} f^*_{0,j}} \big(\boldsymbol{n}_{ij} \cdot \boldsymbol{f}_{1,i}\big) \, \mathrm{d}\Omega \, \mathrm{d}E}{\displaystyle\int_0^\infty \int_{4\pi} \big(\boldsymbol{n}_{ij} \cdot \boldsymbol{\Omega}\big) \sqrt{f^*_{0,i} f^*_{0,j}} \big(\boldsymbol{n}_{ij} \cdot \boldsymbol{f}_{1,i}\big) \, \mathrm{d}\Omega \, \mathrm{d}E} \right] , \qquad \boldsymbol{x} \in \partial V_{ij} \,.$$

In the case of a single energy group, these DFs will optimally estimate the reactor multiplication factor as stipulated by our variational analysis. However, our multigroup treatment is *approximate*. Because numerators of the second bracketed terms in Eqs. (5.129) and (5.130) only approximate the operand of the square root, the exact energy information required to optimally estimate the reactor eigenvalue is lost. Nevertheless, we expect these approximate multigroup DFs to perform well.

A final issue with our DFs is that they, like the variational extrapolation lengths, are space-dependent. Nodal diffusion methods solve coupled 1-D equations for transverse-integrated fluxes. In other words, DFs cannot be space-dependent when nodal diffusion methods are applied. Since in commercial reactor design these methods are nearly universally used, we now propose "surface-averaged" variational DFs. As we did with the variational extrapolation lengths, we simply use surface-averaged lattice functions in place of the space-dependent functions. The surface-averaged DFs become:

$$
\begin{aligned}
a_{i,g} = \frac{1}{\overline{\overline{F_{0,i,g}}}} & \left[\left(\int_0^\infty \int_{4\pi} \left(\boldsymbol{n}_{ij} \cdot \boldsymbol{\Omega}\right) \left(\boldsymbol{n}_{ij} \cdot \boldsymbol{f}^*_{1,i,k}\right) f_{0,i,k} \, \mathrm{d}\Omega \, \mathrm{d}E \right) \right. \\
& \left. \times \left(\int_0^\infty \int_{4\pi} \left(\boldsymbol{n}_{ij} \cdot \boldsymbol{\Omega}\right) \left(\boldsymbol{n}_{ij} \cdot \boldsymbol{f}^*_{1,j,k}\right) f_{0,i,k} \, \mathrm{d}\Omega \, \mathrm{d}E \right) \right]^{1/2} \\
& \times \left[\frac{\displaystyle\int_{E_g}^{E_{g-1}} \int_{4\pi} \left(\boldsymbol{n}_{ij} \cdot \boldsymbol{\Omega}\right) \sqrt{\left(\boldsymbol{n}_{ij} \cdot \boldsymbol{f}^*_{1,i,k}\right) \left(\boldsymbol{n}_{ij} \cdot \boldsymbol{f}^*_{1,j,k}\right)} f_{0,i,k} \, \mathrm{d}\Omega \, \mathrm{d}E}{\displaystyle\int_0^\infty \int_{4\pi} \left(\boldsymbol{n}_{ij} \cdot \boldsymbol{\Omega}\right) \sqrt{\left(\boldsymbol{n}_{ij} \cdot \boldsymbol{f}^*_{1,i,k}\right) \left(\boldsymbol{n}_{ij} \cdot \boldsymbol{f}^*_{1,j,k}\right)} f_{0,i,k} \, \mathrm{d}\Omega \, \mathrm{d}E} \right], \\
a_{j,g} = \frac{1}{\overline{\overline{F_{0,j,g}}}} & \left[\left(\int_0^\infty \int_{4\pi} \left(\boldsymbol{n}_{ij} \cdot \boldsymbol{\Omega}\right) \left(\boldsymbol{n}_{ij} \cdot \boldsymbol{f}^*_{1,i,k}\right) f_{0,j,k} \, \mathrm{d}\Omega \, \mathrm{d}E \right) \right. \\
& \left. \times \left(\int_0^\infty \int_{4\pi} \left(\boldsymbol{n}_{ij} \cdot \boldsymbol{\Omega}\right) \left(\boldsymbol{n}_{ij} \cdot \boldsymbol{f}^*_{1,j,k}\right) f_{0,j,k} \, \mathrm{d}\Omega \, \mathrm{d}E \right) \right]^{1/2} \\
& \times \left[\frac{\displaystyle\int_{E_g}^{E_{g-1}} \int_{4\pi} \left(\boldsymbol{n}_{ij} \cdot \boldsymbol{\Omega}\right) \sqrt{\left(\boldsymbol{n}_{ij} \cdot \boldsymbol{f}^*_{1,i,k}\right) \left(\boldsymbol{n}_{ij} \cdot \boldsymbol{f}^*_{1,j,k}\right)} f_{0,j,k} \, \mathrm{d}\Omega \, \mathrm{d}E}{\displaystyle\int_0^\infty \int_{4\pi} \left(\boldsymbol{n}_{ij} \cdot \boldsymbol{\Omega}\right) \sqrt{\left(\boldsymbol{n}_{ij} \cdot \boldsymbol{f}^*_{1,i,k}\right) \left(\boldsymbol{n}_{ij} \cdot \boldsymbol{f}^*_{1,j,k}\right)} f_{0,j,k} \, \mathrm{d}\Omega \, \mathrm{d}E} \right],
\end{aligned}
\tag{5.131}
$$

and:

$$
\begin{aligned}
b_{i,g} = \frac{1}{a_{i,g} D_{i,g,nn} \overline{F_{0,i,g}}} \Bigg[& \left(\int_0^\infty \int_{4\pi} \left(\boldsymbol{n}_{ij} \cdot \boldsymbol{\Omega}\right) f^*_{0,i,k}\left(\boldsymbol{n}_{ij} \cdot \boldsymbol{f}_{1,i,k}\right) \mathrm{d}\Omega \, \mathrm{d}E \right) \\
& \times \left(\int_0^\infty \int_{4\pi} \left(\boldsymbol{n}_{ij} \cdot \boldsymbol{\Omega}\right) f^*_{0,j,k}\left(\boldsymbol{n}_{ij} \cdot \boldsymbol{f}_{1,i,k}\right) \mathrm{d}\Omega \, \mathrm{d}E \right) \Bigg]^{1/2} \\
& \times \left[\frac{\displaystyle\int_{E_g}^{E_{g-1}} \int_{4\pi} \left(\boldsymbol{n}_{ij} \cdot \boldsymbol{\Omega}\right) \sqrt{f^*_{0,i,k} f^*_{0,j,k}}\left(\boldsymbol{n}_{ij} \cdot \boldsymbol{f}_{1,i,k}\right) \mathrm{d}\Omega \, \mathrm{d}E}{\displaystyle\int_0^\infty \int_{4\pi} \left(\boldsymbol{n}_{ij} \cdot \boldsymbol{\Omega}\right) \sqrt{f^*_{0,i,k} f^*_{0,j,k}}\left(\boldsymbol{n}_{ij} \cdot \boldsymbol{f}_{1,i,k}\right) \mathrm{d}\Omega \, \mathrm{d}E} \right] , \\
b_{j,g} = \frac{1}{a_{j,g} D_{j,g,nn} \overline{F_{0,j,g}}} \Bigg[& \left(\int_0^\infty \int_{4\pi} \left(\boldsymbol{n}_{ij} \cdot \boldsymbol{\Omega}\right) f^*_{0,i,k}\left(\boldsymbol{n}_{ij} \cdot \boldsymbol{f}_{1,j,k}\right) \mathrm{d}\Omega \, \mathrm{d}E \right) \\
& \times \left(\int_0^\infty \int_{4\pi} \left(\boldsymbol{n}_{ij} \cdot \boldsymbol{\Omega}\right) f^*_{0,j,k}\left(\boldsymbol{n}_{ij} \cdot \boldsymbol{f}_{1,j,k}\right) \mathrm{d}\Omega \, \mathrm{d}E \right) \Bigg]^{1/2} \\
& \times \left[\frac{\displaystyle\int_{E_g}^{E_{g-1}} \int_{4\pi} \left(\boldsymbol{n}_{ij} \cdot \boldsymbol{\Omega}\right) \sqrt{f^*_{0,i,k} f^*_{0,j,k}}\left(\boldsymbol{n}_{ij} \cdot \boldsymbol{f}_{1,j,k}\right) \mathrm{d}\Omega \, \mathrm{d}E}{\displaystyle\int_0^\infty \int_{4\pi} \left(\boldsymbol{n}_{ij} \cdot \boldsymbol{\Omega}\right) \sqrt{f^*_{0,i,k} f^*_{0,j,k}}\left(\boldsymbol{n}_{ij} \cdot \boldsymbol{f}_{1,j,k}\right) \mathrm{d}\Omega \, \mathrm{d}E} \right] .
\end{aligned}
\tag{5.132}
$$

The surface-averaged lattice functions are defined by Eqs. (5.111), where the surface k is now the interface between regions i and j.

We conclude this section by noting some properties of the variational DFs. First, when calculating either the flux or current DF for region i, only the forward lattice function from that region is used. In this sense, the variational DFs are similar to the more traditional DFs. However, the adjoint lattice functions from both sides of the interface, i.e., from both region i and region j, are used to weight the forward function.

Second, these DFs simplify greatly if the surface-averaged adjoint lattice functions are well approximated by the constant-in-energy functions:

$$
f^*_{0,i}(\boldsymbol{x}, \boldsymbol{\Omega}, E) = 1 \, , \tag{5.133a}
$$

$$f^*_{0,j}(\boldsymbol{x},\boldsymbol{\Omega},E) = 1\,, \tag{5.133b}$$

$$\boldsymbol{f}^*_{1,i}(\boldsymbol{x},\boldsymbol{\Omega},E) = C_i\boldsymbol{\Omega}\,, \tag{5.133c}$$

$$\boldsymbol{f}^*_{1,j}(\boldsymbol{x},\boldsymbol{\Omega},E) = C_j\boldsymbol{\Omega}\,, \tag{5.133d}$$

We note that these expressions are exact for homogeneous, monoenergetic systems, in which case $C_i = 1/\Sigma_{tr,i}$. Introducing Eqs. (5.133) into Eqs. (5.131), we obtain:

$$\begin{aligned} a_{i,g} = \frac{\sqrt{C_iC_j}}{\overline{F_{0,i,g}}} &\left[\left(\int_0^\infty \int_{4\pi} \left(\boldsymbol{n}_{ij}\cdot\boldsymbol{\Omega}\right)\left(\boldsymbol{n}_{ij}\cdot\boldsymbol{\Omega}\right) f_{0,i,k}\,\mathrm{d}\Omega\,\mathrm{d}E \right) \right. \\ &\left. \times \left(\int_0^\infty \int_{4\pi} \left(\boldsymbol{n}_{ij}\cdot\boldsymbol{\Omega}\right)\left(\boldsymbol{n}_{ij}\cdot\boldsymbol{\Omega}\right) f_{0,i,k}\,\mathrm{d}\Omega\,\mathrm{d}E \right) \right]^{1/2} \\ \times &\left[\frac{\displaystyle\int_{E_g}^{E_{g-1}} \int_{4\pi} \left(\boldsymbol{n}_{ij}\cdot\boldsymbol{\Omega}\right)\sqrt{\left(\boldsymbol{n}_{ij}\cdot\boldsymbol{\Omega}\right)\left(\boldsymbol{n}_{ij}\cdot\boldsymbol{\Omega}\right)} f_{0,i,k}\,\mathrm{d}\Omega\,\mathrm{d}E}{\displaystyle\int_0^\infty \int_{4\pi} \left(\boldsymbol{n}_{ij}\cdot\boldsymbol{\Omega}\right)\sqrt{\left(\boldsymbol{n}_{ij}\cdot\boldsymbol{\Omega}\right)\left(\boldsymbol{n}_{ij}\cdot\boldsymbol{\Omega}\right)} f_{0,i,k}\,\mathrm{d}\Omega\,\mathrm{d}E} \right], \\ = \frac{\sqrt{C_iC_j}}{\overline{F_{0,i,g}}} &\left[\int_0^\infty \int_{4\pi} \left(\boldsymbol{n}_{ij}\cdot\boldsymbol{\Omega}\right)^2 f_{0,i,k}\,\mathrm{d}\Omega\,\mathrm{d}E \right] \left[\frac{\displaystyle\int_{E_g}^{E_{g-1}} \int_{4\pi} \left(\boldsymbol{n}_{ij}\cdot\boldsymbol{\Omega}\right)^2 f_{0,i,k}\,\mathrm{d}\Omega\,\mathrm{d}E}{\displaystyle\int_0^\infty \int_{4\pi} \left(\boldsymbol{n}_{ij}\cdot\boldsymbol{\Omega}\right)^2 f_{0,i,k}\,\mathrm{d}\Omega\,\mathrm{d}E} \right]. \end{aligned}$$

Since the factor $\sqrt{C_iC_j}$ appears in both a_i and a_j, it can be canceled out of each DF. We are left with the following definition of the flux DF for region i:

$$a_{i,g} = \frac{\displaystyle\int_{E_g}^{E_{g-1}} \int_{4\pi} \left(\boldsymbol{n}_{ij}\cdot\boldsymbol{\Omega}\right)^2 f_{0,i,k}\,\mathrm{d}\Omega\,\mathrm{d}E}{\overline{F_{0,i,g}}}\,. \tag{5.134}$$

Introducing Eqs. (5.133) into Eqs. (5.132), and simplifying in a similar manner yields the following current DF for region j:

$$b_{i,g} = \frac{1}{a_{i,g}D_{i,g,nn}} \frac{\displaystyle\int_{E_g}^{E_{g-1}} \int_{4\pi} \left(\boldsymbol{n}_{ij}\cdot\boldsymbol{\Omega}\right)\left(\boldsymbol{n}_{ij}\cdot\boldsymbol{f}_{1,j,k}\right)\mathrm{d}\Omega\,\mathrm{d}E}{\overline{F_{0,i,g}}}\,. \tag{5.135}$$

Comparing Eqs. (5.134) and (5.135) to Eqs. (5.34) and (5.36) reveals that the simplified variational DFs are identical to the previously-derived DFs for continuity of the second angular moment of the reconstructed flux and continuity of the reconstructed current. This gives credence to those heuristic DFs and suggests that they should be used in cases when not enough information is available to calculate the variational DFs.

5.5 Summary

This chapter began with a discussion of standard boundary and interface conditions. We then presented a series of DFs designed to make certain angular moments of the reconstructed flux continuous across interfaces between lattices (Eqs. (5.33)-(5.36)). These DFs were heuristic and only exact for 1-D problems. Nevertheless, we expect them to be reasonably effective for multi-dimensional problems.

The standard flux reconstruction contains only the leading order term of the asymptotic solution (written in monoenergetic form here for simplicity):

$$\psi(\boldsymbol{x}, \boldsymbol{\Omega}) = f_0(\boldsymbol{x}, \boldsymbol{\Omega})\phi(\boldsymbol{x})\,, \tag{5.136}$$

where f_0 is symmetric in angle on lattice boundaries. This single term means that we can assign only one DF, while the fact that f_0 is symmetric in angle on boundaries means that only even angular moments of the reconstructed flux can be made continuous. In contrast, the asymptotic flux reconstruction also contains an $O(\epsilon)$ term:

$$\psi(\boldsymbol{x}, \boldsymbol{\Omega}) = f_0(\boldsymbol{x}, \boldsymbol{\Omega})\phi(\boldsymbol{x}) - \boldsymbol{f}_1 \cdot \nabla\phi(\boldsymbol{x})\,, \tag{5.137}$$

where $\boldsymbol{f}_1$ is antisymmetric in angle on lattice boundaries. The antisymmetry of $\boldsymbol{f}_1$ enables us to preserve odd angular moments (e.g., current) of the reconstructed

flux, and the inclusion of the second term allows us to assign two DFs, allowing two angular moments of the reconstructed flux to be continuous at an interface.

Thus, unlike standard DFs, we allow both the homogenized flux *and* current to be discontinuous. However, the reconstructed flux and currents are continuous, with the right choice of discontinuity factors. The standard flux discontinuity condition at the interface between lattices i and j to be used in the homogenized diffusion calculation is:

$$\boxed{a_{i,g}\phi_{i,g}(\boldsymbol{x}) = a_{j,g}\phi_{j,g}(\boldsymbol{x})\,, \qquad \boldsymbol{x} \in \partial V_{ij}\,,} \tag{5.138}$$

while the current discontinuity condition is:

$$\boxed{a_{i,g}b_{i,g}D_{i,g,nn}\big(\boldsymbol{n}_{ij}\cdot\nabla\big)\phi_{i,g}(\boldsymbol{x}) = a_{j,g}b_{j,g}D_{j,g,nn}\big(\boldsymbol{n}_{ij}\cdot\nabla\big)\phi_{j,g}(\boldsymbol{x})\,, \qquad \boldsymbol{x} \in \partial V_{ij}\,.} \tag{5.139}$$

We also variationally derived boundary and interface conditions specifically for lattice problems. The functional is chosen to optimally estimate the reactor eigenvalue, and the trial functions used in the estimate are the forward and adjoint asymptotic reconstructed fluxes.

The multigroup vacuum boundary condition is of the form:

$$\boxed{0 = \phi_g(\boldsymbol{x}) + l_{lat,i,g}\boldsymbol{n}\cdot\nabla\phi_g(\boldsymbol{x})\,, \qquad \boldsymbol{x} \in \partial V_i\,, \qquad 1 \le g \le G\,.} \tag{5.140}$$

The variational extrapolation distance is given by Eqs. (5.109)-(5.111). The extrapolation length depends on a parameter, α, which can be varied arbitrarily between -1 and 1. It is not ideal that there is no known prescription for choosing the optimal value of α. For consistency with standard Federighi-Pomraning or Milne homogeneous extrapolation lengths, the choices $\alpha = 0$ or $\alpha = -0.0815$ should be used.

The variational DFs are given by Eqs. (5.131) and (5.132) and specify both a flux and current discontinuity. It is important to note that while the variational DFs *do*

use adjoint flux information from neighboring lattices, they do *not* require colorset calculations. The functions f_0 and $\boldsymbol{f}_1$ are calculated from single lattice calculations without knowledge of neighboring lattices, and that information can be used to quickly calculate variational DFs when any two different assemblies are adjoined to each other.

We remark that for the case of a homogeneous "lattice" with no periodic space-dependence, f_0 and $\boldsymbol{f}_1$ simplify to:

$$f_0 = \frac{1}{4\pi}\,, \tag{5.141a}$$

$$\boldsymbol{f}_1 = \frac{1}{4\pi}\frac{\boldsymbol{\Omega}}{\Sigma_{tr}}\,. \tag{5.141b}$$

Thus, Eqs. (5.136) and (5.137) become:

$$\psi(\boldsymbol{x},\boldsymbol{\Omega}) = \frac{1}{4\pi}\phi(\boldsymbol{x})\,, \tag{5.142a}$$

$$\psi(\boldsymbol{x},\boldsymbol{\Omega}) = \frac{1}{4\pi}\left[\phi(\boldsymbol{x}) - \frac{1}{\Sigma_{tr}}\boldsymbol{\Omega}\cdot\nabla\phi(\boldsymbol{x})\right]\,. \tag{5.142b}$$

Therefore, the asymptotic representation (Eq. (5.137)) of ψ is analogous to the classical P_1 approximation (5.142b). Imposing discontinuity factors that make the reconstructed scalar flux and current continuous at an interface is analogous to the requirement in the classical P_1 approximation that the scalar flux and current should be continuous at an interface.

Finally, we note that the variational analysis applied in this chapter does not apply to reflector (non-multiplying) regions. Thus, the variational DFs cannot be applied to the fuel-reflector interface. This issue is addressed in Section 6.3.1.

CHAPTER VI

Implementation of the Asymptotic Diffusion Theory

This chapter is meant to prepare the reader for the numerical results chapters that follow (Chapters VII-XI) by explaining the notation, procedures, and codes used in obtaining and presenting the results. We suggest that after completing this chapter, readers familiarize themselves with the materials and numerical test problems defined in Appendices B and C.

We begin this chapter by introducing notation that is used in the presentation of numerical results. Then we derive the finite difference diffusion equations with flux and current discontinuity factors, the latter of which are a novel feature of our method. Next, we outline a numerical procedure for performing asymptotic homogenized diffusion calculations. Finally, we describe the codes used to perform our numerical simulations.

6.1 Notation Used in the Presentation of Numerical Results

Here, we present notation used to distinguish between various diffusion coefficients, extrapolation lengths, and discontinuity factors in this chapter as well as our numerical results chapters (Chapters VII-XI). Tables 6.1, 6.2, 6.3 and 6.4 contain defintions of the symbols for the diffuson coefficients, flux reconstruction methods, extrapolation lengths, and discontinuity factors respectively.

Table 6.1: Diffusion Coefficient Notation

Symbol	Description	Definition
$\boldsymbol{D}_a$	Asymptotic diffusion coefficient. This is equivalent to the Deniz-Gelbard diffusion coefficient.	Eq. (4.19)
$\boldsymbol{D}_{bci}$	Benoist diffusion coefficient with the correction term (the second term) included. The i indicates which definition of a lattice cell is used. In general there are multiple symmetric definitions of a lattice and each yields a different value of D_{bc}.	Eq. (2.47)
$\boldsymbol{D}_{bu}$	Benoist diffusion coefficient without the correction term (the second term) included.	Eq. (2.47)
D_s	Standard diffusion coefficient.	Eq. (2.24)

Table 6.2: Flux Reconstruction Method Notation

Symbol	Description	Definition
O(1)	Standard flux reconstruction, i.e., flux reconstruction with only the leading order asymptotic term.	Eq. (2.23)
O(eps)	Asymptotic flux reconstruction with the $O(\epsilon)$ correction term.	Eq. (4.36)

Table 6.3: Extrapolation Length Notation

Symbol	Description	Definition
l_{Mar}	Marshak extrapolation length for a homogeneous medium.	Eq. (5.5)
l_{HomVar}	Variational extrapolation length for a homogeneous medium	Eq. (5.6)
$l_{LatVar}(\alpha)$	Variational extrapolation length for the asymptotic, lattice system. $\lvert\alpha\rvert \leq 1$.	Eqs. (5.109)-(5.111)

Table 6.4: Discontinuity Factor Notation

Symbol	Description	Definition
$NoDF$	No discontinuity factor used.	N/A
a_0	Discontinuity factor for making the reconstructed scalar flux continuous across an interface. This is equivalent to standard assembly discontinuity factors.	Eq. (5.33)
$a_0 b_{01}$	Discontinuity factors for making the reconstructed scalar flux and net current continuous across an interface.	Eqs. (5.33), (5.36)
a_2	Discontinuity factor for making the reconstructed second angular moment continuous across an interface.	Eq. (5.34)
$a_2 b_{21}$	Discontinuity factors for making the reconstructed second angular moment and net current continuous across an interface.	Eqs. (5.34), (5.36)
ab_{PC}	Discontinuity factors for making the reconstructed partial currents continuous across an interface.	Eqs. (5.35), (5.36)
ab_{Var}	Variational discontinuity factors for the asymptotic, lattice system.	Eqs. (5.131), (5.132)

6.2 Finite-Difference Diffusion Equations with Flux and Current Discontinuity Factors

The concept of current discontinuity factors introduced in Chapter V is non-standard, and so we now derive finite-difference diffusion equations that include these factors. For simplicity, we consider the monoenergetic diffusion equation in 1-D:

$$-\frac{\mathrm{d}}{\mathrm{d}x}\overline{D}(x)\frac{\mathrm{d}\phi}{\mathrm{d}x}(x)+\overline{\Sigma_a}(x)\phi(x)=\frac{1}{k}\overline{\nu\Sigma_f}(x)\phi(x)\,, \tag{6.1a}$$

or:

$$\frac{\mathrm{d}}{\mathrm{d}x}J(x)+\overline{\Sigma_a}(x)\phi(x)=\frac{1}{k}\overline{\nu\Sigma_f}(x)\phi(x)\,, \tag{6.1b}$$

where:

$$J(x)=-\overline{D}(x)\frac{\mathrm{d}\phi}{\mathrm{d}x}(x)\,. \tag{6.2}$$

The extension of this 1-D, monoenergetic derivation to the derivation of multi-dimensional, multigroup finite-difference diffusion equations is trivial. The cross sections and diffusion coefficient are homogenized, but in general there are multiple homogenization regions. Therefore, the cross sections and diffusion coefficients are histogram functions of x.

Operating on Eq. (6.1b) by $\int_{x_{i-1/2}}^{x_{i+1/2}}(\cdot)\,\mathrm{d}x$ (i.e., integrating the balance equation over each mesh cell) yields the following *exact* equation:

$$J^l_{i+1/2}-J^r_{i-1/2}+h_i\Sigma_{a,i}\phi_i=\frac{h_i}{k}\nu\Sigma_{f,i}\phi_i\,, \tag{6.3}$$

We then discretize Eq. (6.2) in space to obtain *approximate* expressions for the surface currents [72]:

$$J^l_{i+1/2}=-\frac{2D_i}{h_i}\left(\phi^l_{i+1/2}-\phi_i\right)\,, \tag{6.4a}$$

$$J^r_{i+1/2} = -\frac{2D_{i+1}}{h_{i+1}}\left(\phi_{i+1} - \phi^r_{i+1/2}\right)\,, \tag{6.4b}$$

In Eqs. (6.3) and (6.4), i is the index of the spatial mesh cell and h_i is the width of that cell. The superscripts l and r signify that a quantity is calculated from the left or right side of an interface. The distinction is necessary because we allow the flux and current to be discontinuous across interfaces. As discussed in the previous chapter, the flux and current discontinuity conditions are written:

$$a^l_{i+1/2}\phi^l_{i+1/2} = a^r_{i+1/2}\phi^r_{i+1/2}\,, \tag{6.5a}$$

$$a^l_{i+1/2}b^l_{i+1/2}J^l_{i+1/2} = a^r_{i+1/2}b^r_{i+1/2}J^r_{i+1/2}\,. \tag{6.5b}$$

Introducing Eqs. (6.4) into Eq. (6.5b), we obtain:

$$a^l_{i+1/2}b^l_{i+1/2}\frac{2D_i}{h_i}\left(\phi^l_{i+1/2} - \phi_i\right) = a^r_{i+1/2}b^r_{i+1/2}\frac{2D_{i+1}}{h_{i+1}}\left(\phi_i - \phi^r_{i+1/2}\right)\,. \tag{6.6}$$

We now use Eq. (6.5a) to eliminate $\phi^r_{i+1/2}$ from Eq. (6.6):

$$a^l_{i+1/2}b^l_{i+1/2}\frac{2D_i}{h_i}\left(\phi^l_{i+1/2} - \phi_i\right) = a^r_{i+1/2}b^r_{i+1/2}\frac{2D_{i+1}}{h_{i+1}}\left(\phi_{i+1} - \frac{a^l_{i+1/2}}{a^r_{i+1/2}}\phi^l_{i+1/2}\right)\,.$$

Solving for $\phi^l_{i+1/2}$ yields:

$$\phi^l_{i+1/2} = \frac{\left[\dfrac{a^l_{i+1/2}b^l_{i+1/2}D_i}{h_i}\phi_i + \dfrac{a^r_{i+1/2}b^r_{i+1/2}D_{i+1}}{h_{i+1}}\phi_{i+1}\right]}{\left[\dfrac{a^l_{i+1/2}b^l_{i+1/2}D_i}{h_i} + \dfrac{a^l_{i+1/2}b^r_{i+1/2}D_{i+1}}{h_{i+1}}\right]}\,. \tag{6.7a}$$

Similarly, we use Eq. (6.5a) to eliminate $\phi^l_{i+1/2}$ from Eq. (6.6):

$$a^l_{i+1/2}b^l_{i+1/2}\frac{2D_i}{h_i}\left(\frac{a^r_{i+1/2}}{a^l_{i+1/2}}\phi^r_{i+1/2} - \phi_i\right) = a^r_{i+1/2}b^r_{i+1/2}\frac{2D_{i+1}}{h_{i+1}}\left(\phi_{i+1} - \phi^r_{i+1/2}\right)\,.$$

Solving for $\phi^r_{i+1/2}$ yields:

$$\phi^r_{i+1/2} = \frac{\left[\dfrac{a^l_{i+1/2}b^l_{i+1/2}D_i}{h_i}\phi_i + \dfrac{a^r_{i+1/2}b^r_{i+1/2}D_{i+1}}{h_{i+1}}\phi_{i+1}\right]}{\left[\dfrac{a^r_{i+1/2}b^l_{i+1/2}D_i}{h_i} + \dfrac{a^r_{i+1/2}b^r_{i+1/2}D_{i+1}}{h_{i+1}}\right]}\,. \tag{6.7b}$$

Introducing Eq. (6.7a) into Eq. (6.4a), we obtain:

$$J^l_{i+1/2} = -\frac{2D_i}{h_i}\left[\frac{\left(\frac{a^l_{i+1/2}b^l_{i+1/2}D_i}{h_i}\phi_i + \frac{a^r_{i+1/2}b^r_{i+1/2}D_{i+1}}{h_{i+1}}\phi_{i+1}\right)}{\left(\frac{a^l_{i+1/2}b^l_{i+1/2}D_i}{h_i} + \frac{a^l_{i+1/2}b^r_{i+1/2}D_{i+1}}{h_{i+1}}\right)} - \frac{\left(\frac{a^l_{i+1/2}b^l_{i+1/2}D_i}{h_i}\phi_i + \frac{a^l_{i+1/2}b^r_{i+1/2}D_{i+1}}{h_{i+1}}\phi_i\right)}{\left(\frac{a^l_{i+1/2}b^l_{i+1/2}D_i}{h_i} + \frac{a^l_{i+1/2}b^r_{i+1/2}D_{i+1}}{h_{i+1}}\right)}\right],$$

The red terms cancel, and so the expression for the current becomes:

$$J^l_{i+1/2} = -\frac{\left[\frac{2D_iD_{i+1}b^r_{i+1/2}}{h_ih_{i+1}}\right]\left[a^r_{i+1/2}\phi_{i+1} - a^l_{i+1/2}\phi_i\right]}{\left[\frac{a^l_{i+1/2}b^l_{i+1/2}D_i}{h_i} + \frac{a^l_{i+1/2}b^r_{i+1/2}D_{i+1}}{h_{i+1}}\right]}. \tag{6.8a}$$

Introducing Eq. (6.7b) into Eq. (6.4b) and simplifying in a similar manner, we obtain:

$$J^r_{i+1/2} = -\frac{\left[\frac{2D_iD_{i+1}b^l_{i+1/2}}{h_ih_{i+1}}\right]\left[a^r_{i+1/2}\phi_{i+1} - a^l_{i+1/2}\phi_i\right]}{\left[\frac{a^r_{i+1/2}b^l_{i+1/2}D_i}{h_i} + \frac{a^r_{i+1/2}b^r_{i+1/2}D_{i+1}}{h_{i+1}}\right]}. \tag{6.8b}$$

If we consider the conventional case of a discontinuous flux and continuous current, then $b = 1/a$ and Eqs. (6.8) simplify to:

$$J^l_{i+1/2} = J^r_{i+1/2} = -\frac{2D_iD_{i+1}}{h_ih_{i+1}}\frac{\left[a^r_{i+1/2}\phi_{i+1} - a^l_{i+1/2}\phi_i\right]}{\left[\frac{a^r_{i+1/2}D_i}{h_i} + \frac{a^l_{i+1/2}D_{i+1}}{h_{i+1}}\right]}. \tag{6.9}$$

This is the standard expression for the interface current equation with flux discontinuity factors only (Smith's Eq. (13), [22]).

Equations (6.8) can be rewritten as:

$$J^l_{i+1/2} = -\frac{2b^r_{i+1/2}\left[a^r_{i+1/2}\phi_{i+1} - a^l_{i+1/2}\phi_i\right]}{\left[\frac{a^l_{i+1/2}b^l_{i+1/2}h_{i+1}}{D_{i+1}} + \frac{a^l_{i+1/2}b^r_{i+1/2}h_i}{D_i}\right]}, \tag{6.10a}$$

$$J^r_{i+1/2} = -\frac{2b^l_{i+1/2}\left[a^r_{i+1/2}\phi_{i+1} - a^l_{i+1/2}\phi_i\right]}{\left[\dfrac{a^r_{i+1/2}b^l_{i+1/2}h_{i+1}}{D_{i+1}} + \dfrac{a^r_{i+1/2}b^r_{i+1/2}h_i}{D_i}\right]}\,. \tag{6.10b}$$

We define interface diffusion coefficients by:

$$\boxed{D^l_{i+1/2} = \frac{h_i + h_{i+1}}{\left[\dfrac{a^l_{i+1/2}b^l_{i+1/2}h_{i+1}}{D_{i+1}} + \dfrac{a^l_{i+1/2}b^r_{i+1/2}h_i}{D_i}\right]}\,,} \tag{6.11a}$$

$$\boxed{D^r_{i+1/2} = \frac{h_i + h_{i+1}}{\left[\dfrac{a^r_{i+1/2}b^l_{i+1/2}h_{i+1}}{D_{i+1}} + \dfrac{a^r_{i+1/2}b^r_{i+1/2}h_i}{D_i}\right]}\,,} \tag{6.11b}$$

and the average mesh size for the adjacent regions by:

$$\boxed{h_{i+1/2} = \frac{1}{2}\Big(h_i + h_{i+1}\Big)\,,} \tag{6.11c}$$

Then Eqs. (6.10) can be written:

$$J^l_{i+1/2} = -\frac{b^r_{i+1/2}D^l_{i+1/2}}{h_{i+1/2}}\left[a^r_{i+1/2}\phi_{i+1} - a^l_{i+1/2}\phi_i\right]\,, \tag{6.12a}$$

$$J^r_{i+1/2} = -\frac{b^l_{i+1/2}D^r_{i+1/2}}{h_{i+1/2}}\left[a^r_{i+1/2}\phi_{i+1} - a^l_{i+1/2}\phi_i\right]\,. \tag{6.12b}$$

Introducing Eqs. (6.12) into Eq. (6.3), we obtain the finite-difference diffusion equation with both flux and current discontinuity factors:

(6.13)

$$\boxed{\begin{aligned} &-\frac{a^r_{i+1/2}b^r_{i+1/2}D^l_{i+1/2}}{h_{i+1/2}}\phi_{i+1} - \frac{a^l_{i-1/2}b^l_{i-1/2}D^r_{i-1/2}}{h_{i-1/2}}\phi_{i-1} \\ &\quad + \left(\frac{a^l_{i+1/2}b^r_{i+1/2}D^l_{i+1/2}}{h_{i+1/2}} + \frac{a^r_{i-1/2}b^l_{i-1/2}D^r_{i-1/2}}{h_{i-1/2}} + h_i\Sigma_{a,i}\right)\phi_i = \frac{h_i}{k}\nu\Sigma_{f,i}\phi_i\,. \end{aligned}}$$

6.3 Procedure for Performing Asymptotic Homogenized Diffusion Calculations

The procedures for performing standard, Deniz-Gelbard, and Benoist diffusion calculations are outlined in Sections 2.2.4, 2.3.2, and 2.3.3 repsectively. The procedure for solving the asymptotic homogenized diffusion equation is essentially the same as the Deniz-Gelbard procedure. We present this procedure here in more detail, and include the changes involved in using variational boundary and interface conditions. The primary differences between the asymptotic procedure and the standard procedure of Section 2.2.4 are: (i) multiple lattice calculations must be performed, (ii) the homogenized diffusion coefficient and discontinuity factors used in the diffusion equation are rigorously derived specifically for lattice systems, and (iii) an $O(\epsilon)$ correction term is included when performing flux reconstruction. The asymptotic homogenized diffusion procedure is:

1. Perform a series of lattice calculations for each homogenization region i using transport theory. The lattice transport equations are:

$$\boxed{\begin{aligned} L_i f_{0,i} &= 0\,, \qquad \text{(6.14a)} \\ L_i \boldsymbol{f}_{1,i} &= \boldsymbol{\Omega} f_0\,, \qquad \text{(6.14b)} \\ L_i^* f_{0,i}^* &= 0\,, \qquad \text{(6.14c)} \\ L_i^* \boldsymbol{f}_{1,i}^* &= \boldsymbol{\Omega} f_0^*\,, \qquad \text{(6.14d)} \end{aligned}}$$

   where the forward and adjoint transport operators are defined by Eqs. (3.14)

and (3.16), which are rewritten here for convenience:

(6.15a)

$$
\begin{aligned}
&L_i g_i(\boldsymbol{x},\boldsymbol{\Omega},E) \\
&\quad = \boldsymbol{\Omega}\cdot\nabla g_i(\boldsymbol{x},\boldsymbol{\Omega},E) + \Sigma_t(\boldsymbol{x},E) g_i(\boldsymbol{x},\boldsymbol{\Omega},E) \\
&\qquad - \int_0^\infty \int_{4\pi} \Sigma_s(\boldsymbol{x},\boldsymbol{\Omega}'\cdot\boldsymbol{\Omega},E'\to E) g_i(\boldsymbol{x},\boldsymbol{\Omega}',E')\,\mathrm{d}\Omega'\,\mathrm{d}E' \\
&\qquad - (1-\rho_0)\,\frac{\chi(\boldsymbol{x},E)}{4\pi} \int_0^\infty \int_{4\pi} \nu\Sigma_f(\boldsymbol{x},E') g_i(\boldsymbol{x},\boldsymbol{\Omega}',E')\,\mathrm{d}\Omega'\,\mathrm{d}E'\,, \\
&\qquad\qquad \boldsymbol{x}\in V_i\,,
\end{aligned}
$$

(6.15b)

$$
\begin{aligned}
&L_i^* g_i^*(\boldsymbol{x},\boldsymbol{\Omega},E) \\
&\quad = -\boldsymbol{\Omega}\cdot\nabla g(\boldsymbol{x},\boldsymbol{\Omega},E) + \Sigma_t(\boldsymbol{x},E) g_i^*(\boldsymbol{x},\boldsymbol{\Omega},E) \\
&\qquad - \int_0^\infty \int_{4\pi} \Sigma_s(\boldsymbol{x},\boldsymbol{\Omega}'\cdot\boldsymbol{\Omega},E\to E') g_i^*(\boldsymbol{x},\boldsymbol{\Omega}',E')\,\mathrm{d}\Omega'\,\mathrm{d}E' \\
&\qquad - (1-\rho_0)\,\frac{\nu\Sigma_f(\boldsymbol{x},E)}{4\pi} \int_0^\infty \int_{4\pi} \chi(\boldsymbol{x},E') g_i^*(\boldsymbol{x},\boldsymbol{\Omega}',E')\,\mathrm{d}\Omega'\,\mathrm{d}E'\,, \\
&\qquad\qquad \boldsymbol{x}\in V_i\,.
\end{aligned}
$$

We note that Eq. (6.14d) should only be solved if the variational boundary conditions or discontinuity factors are desired, as the function $\boldsymbol{f}_{1,i}^*$ is not used for any other purpose. Of course, if we desired only the standard diffusion coefficient, then only Eq. (6.14a) would be solved. We recall that the solutions to Eqs. (6.14b) and (6.14d) are not unique. We make the forward solution unique by requiring that Eq. (3.49) be satisfied. Thus, we require that each of the components of the forward function $\boldsymbol{f}_1$ satisfy:

$$
0 = \int_{cell}\int_0^\infty \int_{4\pi} f_0^*(\boldsymbol{x},\boldsymbol{\Omega},E) f_{1,i}(\boldsymbol{x},\boldsymbol{\Omega},E)\,\mathrm{d}\Omega\,\mathrm{d}E\,\mathrm{d}V\,, \qquad i=1,2,3\,. \tag{6.16}
$$

Similarly, we require that the adjoint solution satisfy:

$$
0 = \int_{cell}\int_0^\infty \int_{4\pi} f_0(\boldsymbol{x},\boldsymbol{\Omega},E) f_{1,i}^*(\boldsymbol{x},\boldsymbol{\Omega},E)\,\mathrm{d}\Omega\,\mathrm{d}E\,\mathrm{d}V\,, \qquad i=1,2,3\,. \tag{6.17}
$$

We note that since each pin is assumed to be symmetric, then f_0 and f_0^* in each pin type i are symmetric functions of $(\boldsymbol{x}, \boldsymbol{\Omega})$. Therefore, Eqs. (6.16) and (6.17) ensure that $\boldsymbol{f}_1$ and $\boldsymbol{f}_1^*$ are antisymmetric functions of $(\boldsymbol{x}, \boldsymbol{\Omega})$.

The standard fixed-source iteration scheme must be modified slightly in order to solve for $\boldsymbol{f}_1$ and $\boldsymbol{f}_1^*$. Consider for now only the forward function. Since $\boldsymbol{f}_1$ is a vector function, the three components of this function, $f_{1,i}$, must be obtained via three distinct fixed-source calculations. Furthermore, we must enforce the condition of Eq. (6.16) during each outer iteration. The inner iterations of each fixed-source calculation are carried out as usual to calculate the fluxes in each energy group based on the in-scattering source from the previous outer iteration k. Let $f_{1,i}^{(k+1/2)}(\boldsymbol{x}, \boldsymbol{\Omega}, E)$ be the estimate of the solution after the inner iterations are completed for every energy group. Then the estimate is updated by the following equation:

(6.18a)

$$f_{1,i}^{(k+1)}(\boldsymbol{x}, \boldsymbol{\Omega}, E) = f_{1,i}^{(k+1/2)}(\boldsymbol{x}, \boldsymbol{\Omega}, E) - A_i^{(k+1/2)} f_0(\boldsymbol{x}, \boldsymbol{\Omega}, E) \qquad i = 1, 2, 3\,,$$

where:

(6.18b)

$$A_i^{(k+1/2)} = \frac{\displaystyle\int_{cell}\int_0^\infty\int_{4\pi} f_0^*(\boldsymbol{x}, \boldsymbol{\Omega}, E) f_{1,i}^{(k+1/2)}(\boldsymbol{x}, \boldsymbol{\Omega}, E)\,\mathrm{d}\Omega\,\mathrm{d}E\,\mathrm{d}V}{\displaystyle\int_{cell}\int_0^\infty\int_{4\pi} f_0^*(\boldsymbol{x}, \boldsymbol{\Omega}, E) f_0(\boldsymbol{x}, \boldsymbol{\Omega}, E)\,\mathrm{d}\Omega\,\mathrm{d}E\,\mathrm{d}V} \qquad i = 1, 2, 3\,,$$

The in-scattering sources are updated for the next outer iteration as usual using $f_{1,i}^{(k+1)}$. Operating on Eq. (6.18a) by $\int_{cell}\int_0^\infty\int_{4\pi} f_0^*(\cdot)\,\mathrm{d}\Omega\,\mathrm{d}E\,\mathrm{d}V$ reveals that at the end of each outer iteration, the solution estimate $f_{1,i}^{(k+1)}$ satisfies Eq. (6.16). An analogous iteration procedure is used to calculate $\boldsymbol{f}_{1,i}^*$.

2. The lattice functions from Step 1 are used to generate multigroup homogenized

cross sections defined by Eqs. (4.2)-(4.5), where the scalar lattice function F_0 is the integral of f_0 over all angles. We note that when using deterministic methods such as MOC or S_N, the lattice calculations are performed with a fine energy group, rather than continuous energy, structure. The equations are also discretized in space and angle. Thus, integrals over space, angle, and energy are replaced by sums over discrete regions, angles, and fine energy groups. The sums over regions are weighted by region volumes, while the angle sums are weighted according to the specific quadrature set used. The sums over fine energy group are not weighted, as the weighting is accounted for in the definition of the fine-group cross sections and fluxes. Thus, the following transformations should be made to the cross section definitions:

$$\int_V f(\boldsymbol{x},\boldsymbol{\Omega},E)\mathrm{d}V \Longrightarrow \sum_{i\in V} f(\boldsymbol{x}_i,\boldsymbol{\Omega},E)V_i\,, \tag{6.19a}$$

$$\int_{4\pi} f(\boldsymbol{x},\boldsymbol{\Omega},E)\mathrm{d}V \Longrightarrow \sum_{n\in N} f(\boldsymbol{x},\boldsymbol{\Omega}_n,E)w_n\,, \tag{6.19b}$$

$$\int_{E_g}^{E_{g-1}} f(\boldsymbol{x},\boldsymbol{\Omega},E)\mathrm{d}V \Longrightarrow \sum_{h\in g} f_h(\boldsymbol{x},\boldsymbol{\Omega})\,, \tag{6.19c}$$

where i is a fine region within the volume of integration, n is one of N discrete angles in a quadrature set and w_n are the corresponding weights, h is the index of a fine energy group lying within the coarse energy group g.

3. We now calculate the multigroup homogeneous lattice functions in lattice i. The forward function $\overline{F_{0,i,g}}$ is calculated by solving Eq. (4.11) after applying the integral transformations of Eqs. (6.19). The adjoint function $\overline{F_{0,i,g}}^*$ is calculated by solving Eq. (4.13). L_g^* is the mathematical adjoint (i.e., transpose) of the

infinite homogeneous multigroup equation, written explicitly as:

(6.20)

$$L_g^* F_{0,i,g}^* = \overline{\Sigma_{t,i,g}} F_{0,i,g}^* - \sum_{g'=1}^{G} \overline{\Sigma_{s,i,0,g\to g'}} F_{0,i,g'}^* - (1-\rho_0)\,\overline{\nu\Sigma_{f,i,g}} \sum_{g'=1}^{G} \overline{\chi_{i,g'}} F_{0,i,g'}^* \,,$$
$$1 \le g \le G\,.$$

This system of equations can be solved via a homogenized diffusion solver using reflecting boundaries on all sides or via a linear solver, though outer iterations must still be performed to converge the eigenvalue $(1-\rho_0)$.

4. The asymptotic diffusion tensor is calculated from Eq. (4.19) after applying the integral transformations of Eqs. (6.19). This equation makes use of the lattice functions from Step 1 and the homogenized parameters from Steps 2 and 3.

5. We calculate the extrapolation lengths, l, and discontinuity factors, a and b. The variational extrapolation lengths for lattice systems are defined by Eqs. (5.109)-(5.111). Discontinuity factors that make certain angular moments of the reconstructed flux continuous across interfaces between lattices are defined by Eqs. (5.33)-(5.36). Variational discontinuity factors are defined by Eqs. (5.131) and (5.132). In all of these equations, the integrals must be converted to sums using Eqs. (6.19). The current discontinuity factors all make use of the homogenized diffusion coefficient, and so *must* be calculated after Step 4.

6. Next, we perform a diffusion calculation using the asymptotic homogenized parameters, i.e., solve Eq. (2.22), which we rewrite below:

(6.21)

$$-\nabla\cdot\overline{\boldsymbol{D}_g}(\boldsymbol{x})\cdot\nabla\phi_g(\boldsymbol{x}) + \overline{\Sigma_{t,g}}(\boldsymbol{x})\phi_g(\boldsymbol{x}) =$$
$$\sum_{g'=1}^{G} \overline{\Sigma_{s,0,g'\to g}}(\boldsymbol{x})\phi_{g'}(\boldsymbol{x}) + (1-\rho)\,\overline{\chi_g}(\boldsymbol{x}) \sum_{g'=1}^{G} \overline{\nu\Sigma_{f,g'}}(\boldsymbol{x})\phi_{g'}(\boldsymbol{x})\,, \quad 1 \le g \le G\,.$$

The homogenized parameters are hisotgram functions, i.e., they are constant within each homogenization region. Typically this equation is solved using a nodal diffusion method [24, 25, 27]. However, in our work we use fine-mesh finite-difference diffusion. The monoenergetic, 1-D finite difference equations were derived in Section 6.2. The multigroup, multi-dimensional finite-difference diffusion equations with a diagonal diffusion tensor are:

(6.22)
$$\boxed{\begin{aligned}&\frac{J^-_{x,i+1/2,j,k} - J^+_{x,i-1/2,j,k}}{h_{x,i}} + \frac{J^-_{y,i,j+1/2,k} - J^+_{y,i,j-1/2,k}}{h_{y,i}} + \frac{J^-_{z,i,j,k+1/2} - J^+_{z,i,j,k-1/2}}{h_{z,i}} \\ &\qquad + \left[\Sigma_{t,i,j,k,g} - \Sigma_{s,i,j,k,g\to g}\right]\phi_{i,j,k,g} \\ &\quad = \sum_{g=1,g'\neq g}^{G} \Sigma_{s,i,j,k,g'\to g}\phi_{i,j,k,g'} + \frac{\chi_{i,j,k,g}}{k}\sum_{g'=1}^{G}\nu\Sigma_{f,i,j,k,g'}\phi_{i,j,k,g'}\,.\end{aligned}}$$

The subscripts i, j, and k are the x, y, and z index of the mesh cell. The superscripts $-$ and $+$ indicate that a quantity is calculated on the lower or upper side of an interface. h_x, h_y, and h_z are the mesh cell widths in the x, y, and z directions. The interior surface currents are defined by Eqs. (6.11) and (6.12), except that now the current is direction-dependent and so the diagonal component of the diffusion tensor and cell width corresponding to that direction should be used in the equations. The finite-difference vacuum boundary conditions are of the standard form [72]:

(6.23)
$$\boxed{J_{x,1/2,j,k,g} = \frac{2D_{xx,1/2,j,k,g}}{(2l_{x,1,g} + h_{x,1})\,h_{x,1}}\,,}$$

as are the finite-difference reflecting (0 net current) boundary conditions:

(6.24)
$$\boxed{J_{x,1/2,j,k,g} = 0\,.}$$

Equations (6.23) and (6.24) specify boundary conditions for the x^- face of the system, but extension to the other faces is straight-forward.

7. Then the continuous energy or fine energy group pin fluxes are reconstructed using Eq. (4.36), which we rewrite below:

$$\boxed{\psi(\boldsymbol{x},\boldsymbol{\Omega},E) = \frac{f_0(\boldsymbol{x},\boldsymbol{\Omega},E)}{\overline{F_{0,g}}}\phi_g(\boldsymbol{x}) - \frac{\boldsymbol{f}_1(\boldsymbol{x},\boldsymbol{\Omega},E)}{\overline{F_{0,g}}}\cdot\nabla\phi_g(\boldsymbol{x}) + O(\epsilon^2)\,, \quad E_g \le E \le E_{g-1}\,.} \tag{6.25}$$

We note that the flux reconstruction at a point $\boldsymbol{x}$ requires knowledge of the lattice functions *and* diffusion solution at that point. In other words, either the lattice and diffusion calculations must be performed on the same spatial mesh, or else the diffusion solution must be interpolated in some way such that the diffusion solution is known at the location of each transport mesh cell. If fine-mesh diffusion is used, then the interpolation is straightforward between the cells of the fine diffusion mesh. If nodal methods are used, which solve coupled 1-D diffusion equations in all directions on a coarse mesh, other schemes can be used to calculate the intra-nodal flux [73, 74]. We avoid these complications by only performing flux reconstruction for problems in wich the spatial meshes of the transport and diffusion calculations are the same.

6.3.1 Treatment of Non-Multiplying Regions

The asymptotic diffusion method presented in this thesis is derived specifically for multiplying (i.e., containing fissile material) lattice systems. The appropriate treatment of non-multiplying regions, e.g. the reactor reflector, is still unknown. Becker generated diffusion coefficients designed to match a diffusion solution to an analytic solution for deep-penetration problems [75]. These diffusion coefficients were effectively used to generate weight-windows for variance reduction in Monte Carlo simulations of radiation shielding problems. However, our preliminary results indicated that these using these diffusion coefficients in reflector regions yielded significantly

less accurate solutions than standard diffusion coefficients for reactor simulations. Furthermore, one must still perform an energy group collapse to the desired coarse group structure before the necessary analytic solutions can be obtained. Therefore, this method does not eliminate the need for a colorset calculation in the reflector region. The generation of coarse group diffusion coefficients in the reflector is still a topic of interest, but in this thesis we limit ourselves to a more traditional treatment of the reflector diffusion coefficients and an approximate treatment of reflector discontinuity factors.

Coarse group reflector diffusion coefficients are generated using a traditional *colorset* technique. A single fuel assembly and reflector assembly are modeled together with reflecting boundaries on all sides. The modeling of the assemblies together yields an accurate energy spectrum in the reflector. The coarse group cross sections and diffusion coefficients for the reflector are calculated from the standard definitions, Eqs. (4.2)-(4.5) and (2.24)-(2.25) respectively, using the scalar fluxes from the reflector region. This procedure for calculating group-collapsed, homogenized reflector parameters is standard. Our numerical results have shown that the reflector cross sections are insensitive to the fuel assembly that it borders, and so we use only one set of coarse group parameters for all reflector assemblies, regardless of what type fuel assembly it borders.

The calculation of discontinuity factors for the reflector region is not well understood at this point. The standard method is to perform transport and homogenized diffusion calculations for the fuel-reflector colorset (possibly using only a 1-D simulation) and use the surface-flux information to generate discontinuity factors [22]. This method is simple and accurate when only the standard lattice function f_0 is needed. However, our discontinuity factors require the non-standard lattice function

$\boldsymbol{f}_1$ as well as the adjoint functions f_0^* and $\boldsymbol{f}_1^*$. The functions $\boldsymbol{f}_1$ and $\boldsymbol{f}_1^*$ arise specifically from the asymptotic analysis, which assumes a uniform, periodic lattice. We do not believe that calculating these functions from a colorset calculation, in which the system is certainly not a uniform periodic lattice, is mathematically justifiable. Furthermore, neither the ability to extract the necessary surface fluxes and currents nor the ability to run diffusion calculations with a specified current boundary condition (as is necessary at the interface for the colorset calculations) have been implemented in the codes we use. For these reasons, we do not use colorset calculations to generate reflector discontinuity factors.

Instead, we make use of the fact that for a homogeneous medium in region i, either multiplying or non-multiplying, the lattice functions satisfy:

$$\frac{\int_{E_g}^{E_{g-1}} f_{0,i}(\boldsymbol{x},\boldsymbol{\Omega},E)\,\mathrm{d}E}{\overline{F_{0,i,g}}} = \frac{1}{4\pi}\,, \qquad \boldsymbol{x}\in V_i\,, \tag{6.26a}$$

$$\frac{\int_{E_g}^{E_{g-1}} \boldsymbol{f}_{1,i}(\boldsymbol{x},\boldsymbol{\Omega},E)\,\mathrm{d}E}{\overline{F_{0,i,g}}} = \frac{\boldsymbol{\Omega}}{4\pi\Sigma_{tr,i,g}} = \frac{3D_{i,g}\boldsymbol{\Omega}}{4\pi}\,, \qquad \boldsymbol{x}\in V_i\,. \tag{6.26b}$$

Introducing Eqs. (6.26) into the definitions of the discontinuity factors for preserving angular moments of the reconstructed flux, Eqs. (5.33)-(5.36) yields the homogeneous discontinuity factors in Table 6.5.

Table 6.5: Discontinuity Factor Values for Homogeneous Assemblies

DF Type	a	b
a_0	1.0	1.0
a_0b_{01}	1.0	1.0
a_2	0.3333...	3.0
a_2b_{21}	0.3333...	3.0
ab_{PC}	0.5	2.0

The homogeneous variational extrapolation length, l_{HomVar} defined by Eq. (5.6), is used for all vacuum boundaries of the reflector regions. The variational discontinuity

factors, ab_{Var}, cannot be calculated at the fuel-reflector interface because the energy dependence of $\boldsymbol{f}_1$ is unknown, as are the adjoint functions f_0^* and $\boldsymbol{f}_1^*$. As discussed at the end of Section 5.4.4, the discontinuity factors for making the second angular moment and current of the reconstructed flux continuous, a_2b_{21}, should be used in place of the variational discontinuity factors in the event that insufficient information is available for calculating ab_{Var}. Thus, in all our simulations of reactor cores with variational discontinuity factors, we use a_2b_{21} discontinuity factors on all fuel-reflector interfaces. Note that the a_2b_{21} factors are used on *both* the fuel side *and* the reflector side of the interface.

6.4 Codes Used to Obtain Numerical Results

6.4.1 Codes Used to Perform One-Dimensional Simulations

A series of test codes have been written to perform asymptotic homogenized diffusion calculations in 1-D. Two planar geometry S_N codes, "1d_transport" and "f1_calculator", are used to perform the lattice calculations (Section 6.3, Step 1). Steps 2, 4, and 5 of the asymptotic homogenization procedure are carried about by two separate calls to the code "d_calculator". The 1-D code "homogenized_diffusion" performs homogenized diffusion calculations, including the calculation of the homogeneous, multigroup adjoint flux (Section 6.3, Step 3), and the full core homogenized diffusion calculation (Section 6.3, Step 6).

6.4.2 Codes Used to Perform Multi-Dimensional Simulations

We aspire to have the asymptotic diffusion method applied to realistic reactor analysis problems, and so the calculation of asymptotic homogenized parameters has been implemented in the MOC code MPACT [14, 76]. MPACT can now perform lattice calculations for every lattice type defined for a reactor core, or a subset of

those lattices. The lattice calculations can be performed in parallel, serial, or as completely distinct MPACT runs. The code both performs all the necessary lattice calculations *and* generates the homogenized parameters in a single run, thereby minimizing the effort of the user (Section 6.3, Steps 1-5). *All* of the diffusion coefficients and discontinuity factors discussed in this thesis can be calculated by MPACT *in the same run*, thereby reducing the number of calculations needed. Only the variational extrapolation lengths are calculated by the code, because the standard boundary conditions are trivially calculated from the diffusion coefficient.

The storage of multiple space-dependent angular lattice functions is a unique requirement of the asymptotic homogenization method; typically only a single scalar flux is needed. As a result, the method has a *very* large memory footprint, and it is not always practical or even possible to simulate all the lattice types in a single run. Thus it may be impossible to calculate the variational discontinuity factors ab_{Var} in a single run, as they depend on flux information from all possible neighboring lattices. MPACT deals with this issue by editing the surface-average angle-dependent lattice functions to files for every boundary surface. After all the individual lattice runs have been completed, the user simply takes an existing input file from one of these individuall runs, adds a flag to signal *not* to perform the lattice calculations, and updates the list of lattice types to include all lattices for which the ab_{Var} are desired. MPACT will read in the boundary flux information and calculate ab_{Var} without performing additional lattice calculations.

Once the homogenized parameters are known, the homogenized diffusion calculation is performed using the Diffusion for Immediate Results (DiffIR) test code. The general structure of the code is modeled after MPACT, and it makes use of some of MPACT's basic utility modules. This is a fine-mesh finite-difference diffusion code,

rather than a nodal diffusion code. Although nodal diffusion methods are more efficient and more frequently used for full core reactor analysis, the fine-mesh finite-difference method can achieve arbitrarily low *numerical* errors by simply reducing the mesh spacing. Our goal in this thesis is to demonstrate the accuracy of the asymptotic homogenization method, and not compare its efficiency to the transport methods. Therefore reducing numerical errors is a higher priority than decreasing simulation times. Thus, we use fine-mesh finite difference diffusion exclusively for our numerical simulations.

6.4.3 Codes Used to Perform Flux Reconstruction

As noted in Section 6.3, to reconstruct the heterogeneous flux at a point $\boldsymbol{x}$, we must know both the lattice functions and homogeneous diffusion flux at that point. Thus, we must either solve the lattice transport equations and diffusion equation on the same mesh, or we must perform a flux reconstruction of sorts on the diffusion solution itself to obtain the flux at the desired points. As the intent of this thesis is only to demonstrate the effectiveness of the asymptotic diffusion method, we choose the first and simpler of these choices and only perform flux reconstruction for problems in which the transport and diffusion meshes are the same.

For 1-D problems, flux reconstruction is performed manually using Microsoft Excel. Flux reconstruction for multi-dimensional test problems is done using the research code MPACT to DiffIR Post-Processor (MDPP).

The MDPP user input file specifies spatial mesh information and fine and coarse energy group structures. Although the diffusion and transport spatial meshes must be the same, the indexing of mesh cells for DiffIR and MPACT is not the same. A mapping from the MPACT mesh to the DiffIR mesh is specified in the input file. The user can input a flag to request that the reactor multiplication factor k and pin

powers be calculated from the reconstructed flux. If so, material cross sections and system boundary conditions are read from the input file so that reaction rates can be calculated and neutron leakage can be estimated.

After reading the user input file, the diffusion and transport fluxes are read from the DiffIR and MPACT output files. A different MPACT output file is read for every assembly type. If needed for calculating k and/or pin powers, the heterogeneous material maps are read from the MPACT output files.

Once all the information is collected, the reconstructed fluxes are calculated from Eq. (7) with and without the $O(\epsilon)$ correction term. If desired, the power, fission source rate, and absorption rate in each pin and the whole core are calculated from the reconstructed fluxes with and without the correction term. If the reactor multiplication factor k is desired, then the leakage rates out of all vacuum boundaries are estimated and k is calculated from:

$$k = \frac{TotalFissionRate}{TotalAbsorptionRate + TotalLeakageRate} . \tag{6.27}$$

It is believed that the leakage estimates for vacuum boundaries are inaccurate, and so we only present "reconstructed" values of k for problems with reflecting (0 net leakage) boundaries.

CHAPTER VII

Numerical Results: Comparison of Diffusion Coefficients

In this chapter, we demonstrate that the asymptotic diffusion coefficient yields more accurate solutions than the standard and Benoist diffusion coefficients for lattice systems. Furthermore, we show that the asymptotic diffusion coefficient is anisotropic for multi-dimensional problems, and that this is particularly important for problems with optically-thin channels.

In order to isolate the effects of changing the diffusion coefficient, in most cases we show results for only a single boundary condition or set of discontinuity factors. The extrapolation lengths l_{HomVar} and $l_{LatVar}(\alpha = 0.0)$ (Eqs. (5.6) and (5.109)-(5.111)) are used for vacuum boundaries on homogeneous and lattice regions respectively. These extrapolation lengths are consistent if the "lattice" is homogeneous (see Section 5.4.3). Furthermore, when using the standard diffusion coefficient, l_{HomVar} is used for the extrapolation length regardless of whether or not the region is homogeneous or a lattice, because this is standard procedure. All the current DFs, b, defined in this thesis depend on the diffusion coefficient (Eqs. (5.36) and (5.132)). In order to prevent this dependency from interfering with the comparison of diffusion coefficients, we present results obtained using only flux DFs. Specifically, we use the a_2 DFs exclusively in this chapter.

7.1 Comparison of Homogenized Diffusion Methods for a 1-D Uniform Lattice (Problem 1)

Initially, we consider the case of a 1-D, uniform periodic lattice. The test problem is the ZPPR core studied by Gelbard (Problem 1, Section C.1) [31]. This is a uniformly periodic problem with alternating uranium oxide (UO) and uranium plutonium (UP) fuel types. Several reactor sizes are modeled. There are two possible definitions of a symmetric periodic lattice cell. As noted in Section 2.3.3, the "corrected" Benoist diffusion coefficient is therefore double-valued. Let D_{bc1} be the corrected Benoist diffusion coefficient for a cell defined from the center of one UO cell to the center of the next UO cell, and let D_{bc2} be the corrected Benoist diffusion coefficient for a cell defined from the center of one UP cell to the center of the next UP cell. See Fig. C.1 for a graphical representation of the cell definitions. Since the problem is one-dimensional, only the component of the anisotropic diffusion tensors corresponding to diffusion in this single dimension are used.

The numerical values of the various diffusion coefficients are listed in Table 7.1. These diffusion coefficients do not exactly match those obtained by Gelbard, although they are similar [31]. We believe that the difference is due to the fact that Gelbard used a different quadrature set with fewer angles and a different mesh size (mesh information is not stated in his paper). Furthermore, Gelbard approximated the problem as a fixed source problem, while in our work the true eigenvalue problem is simulated. As expected, the corrected Benoist diffusion coefficients are double-valued, and the uncorrected Benoist diffusion coefficient lies between the two corrected values. The asymptotic diffusion coefficient is significantly smaller than the Benoist coefficients, which are all slightly smaller than the standard diffusion coefficient.

Table 7.2 shows the absolute error in the eigenvalue for the various diffusion

Table 7.1: Fuel Assembly Diffusion Coefficients for the ZPPR Test Problem[1]

D_s	D_{bu}	D_{bc1}	D_{bc2}	D_a
2.77274	2.75859	2.76517	2.74739	2.68003

[1] All D's measured in cm.

coefficients. As might be expected, the errors are large when the finite system is thin. This occurs because all of the approximations assume either a small buckling or a small perturbation from an infinite, periodic lattice problem. It can be seen that the asymptotic diffusion approximation has the lowest error in all cases. This is expected, since the asymptotic diffusion approximation is the same obtained by Deniz and Gelbard, which they obtained by attempting to preserve the eigenvalue. The standard homogenized diffusion approximation yields an eigenvalue that is less accurate than the other methods.

Table 7.2: Absolute Error in k for the ZPPR Test Problem with Various Diffusion Coefficients[1]

Number of UO Fuel Plates	Reference k	D_s (l_{HomVar})	D_{bu} $(l_{LatVar})^2$	D_{bc1} $(l_{LatVar})^2$	D_{bc2} $(l_{LatVar})^2$	D_a $(l_{LatVar})^2$
5	0.21617	-3035	-2957	-2983	-2913	-2642
11	0.32904	-1216	-1155	-1177	-1118	-890
25	0.40796	-250	-228	-237	-212	-120
45	0.43272	-69	-61	-64	-55	-18
75	0.44169	-27	-20	-21	-18	-3

[1] All errors in pcm.

[2] l_{LatVar} is calculated with $\alpha = 0.0$.

Figure 7.1 depicts the diffusion-calculated neutron scalar fluxes divided by the transport-calculated neutron scalar fluxes for the various methods. All fluxes are normalized such that the average scalar flux is unity. As one moves away from the center of the reactor, if the ratio of the diffusion flux to the transport flux increases, then the diffusion approximation underestimates the reactor buckling (the diffusion flux is too high in the outer regions of the reactor). Conversely, if the ratio of the diffusion flux to the transport flux decreases as one moves away from the center of

the core, then the diffusion approximation overestimates the reactor buckling. The left edge of the plot corresponds to the outer edge of the reactor, while the right edge of the plot corresponds to the mid-plane of the reactor.

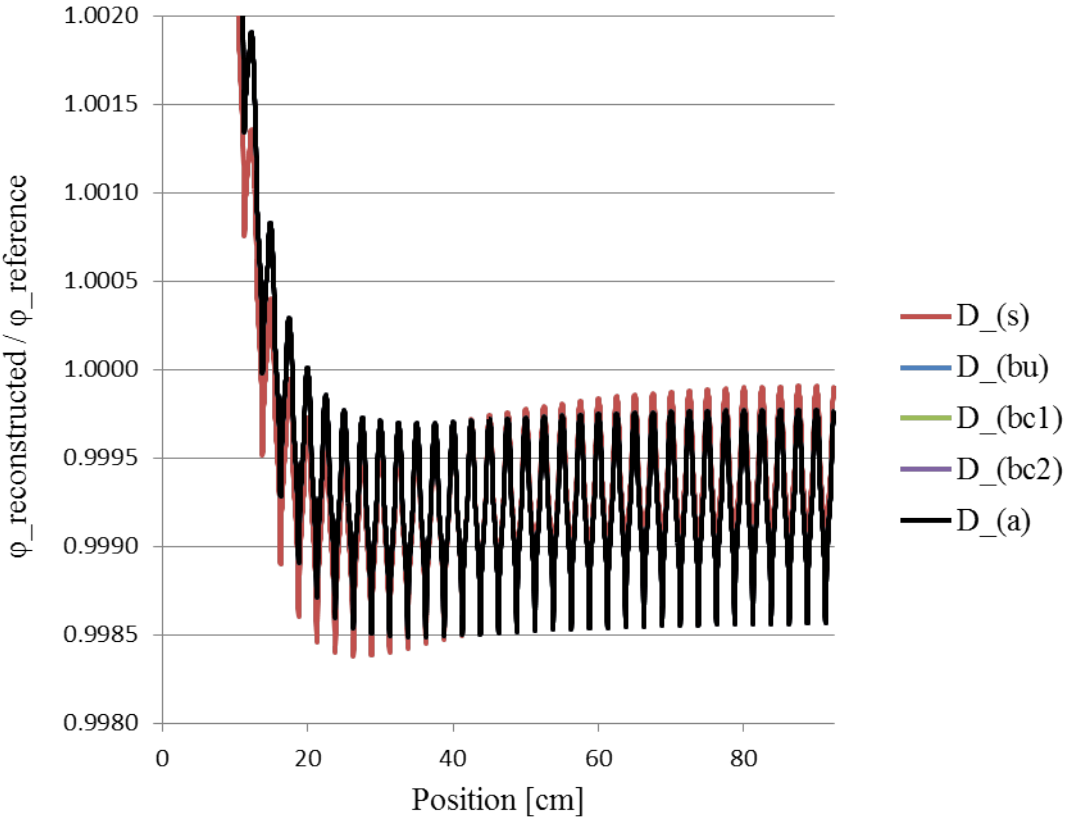

Figure 7.1: Ratio of Reconstructed Fluxes to Reference Fluxes for the ZPPR Test Problem with the Various Diffusion Coefficients. Results shown are for asymptotic flux reconstruction and $l_{LatVar}(\alpha = 0.0)$. (The Benoist and asymptotic scalar fluxes are nearly identical, and cannot be distinguished in the plot.)

In Fig. 7.1, the asymptotic and Benoist solutions nearly match the exact reactor buckling. The standard solution overestimates the reactor buckling, though some of this error can be attributed to the use of a different extrapolation length. The errors become large near the periphery of the reactor for all methods because no diffusion method can accurately capture the strong transport effects that occur near boundaries.

7.2 Comparison of Homogenized Diffusion Methods for a 1-D Non-Uniform Lattice (Problem 3)

We now proceed to the 1-D MOX LWR Benchmark (Problem 3, Section C.3), which is a reactor with a non-periodic loading of *nearly* periodic assemblies. In this case, the homogenization cells are assemblies, rather than pins. We do not consider the "corrected" Benoist diffusion coefficients for this problem, though we do present results for the "uncorrected" Benoist diffusion coefficient, which is uniquely defined for any definition of the cell. Again, only the component of the diffusion tensor corresponding to the single spatial dimension is used.

The diffusion coefficients for each of the fuel assemblies are listed in Table 7.3. Since the reflector assemblies are homogeneous, no homogenization is necessary, and we do not show the diffusion coefficients for these assemblies. For this problem, D_s and D_a are very similar, while D_{bu} is slightly larger than both for all assembly types.

Table 7.3: Fuel Assembly Diffusion Coefficients for the 1-D MOX LWR Benchmark[1]

Assembly	D_s	D_{bu}	D_a
A	1.58387	1.58448	1.58382
B	1.66182	1.67241	1.66245
C	1.58524	1.58585	1.58518
M	1.70393	1.70447	1.70372

[1] All D's measured in cm.

In Table 7.4, we find the absolute errors in the reactor multiplication factor for each diffusion coefficient. In this case, the system is large and the solution is relatively flat. Therefore, leakage effects are small and small changes in the diffusion coefficient have minimal effect on the solution. Thus, the various diffusion coefficients yield nearly identical values of k.

The ratios of the reconstructed fluxes to the reference transport fluxes are shown

Table 7.4: Absolute Error in k for the 1-D MOX LWR Benchmark with Various Diffusion Coefficients[1]

Reference k	D_s	D_{bu}	D_a
1.21221	-8	-9	-8

[1] All errors in pcm. Results shown are for a_2 DFs.

in Figure 7.2. Not surprisingly since D_a and D_s are so similar for every assembly type in this reactor, the asymptotic and standard reconstructed fluxes are so similar that they are indistinguishable from each other. Each of these are more accurate than the Benoist reconstructed flux, which has slightly larger errors in the center and periphery of the core.

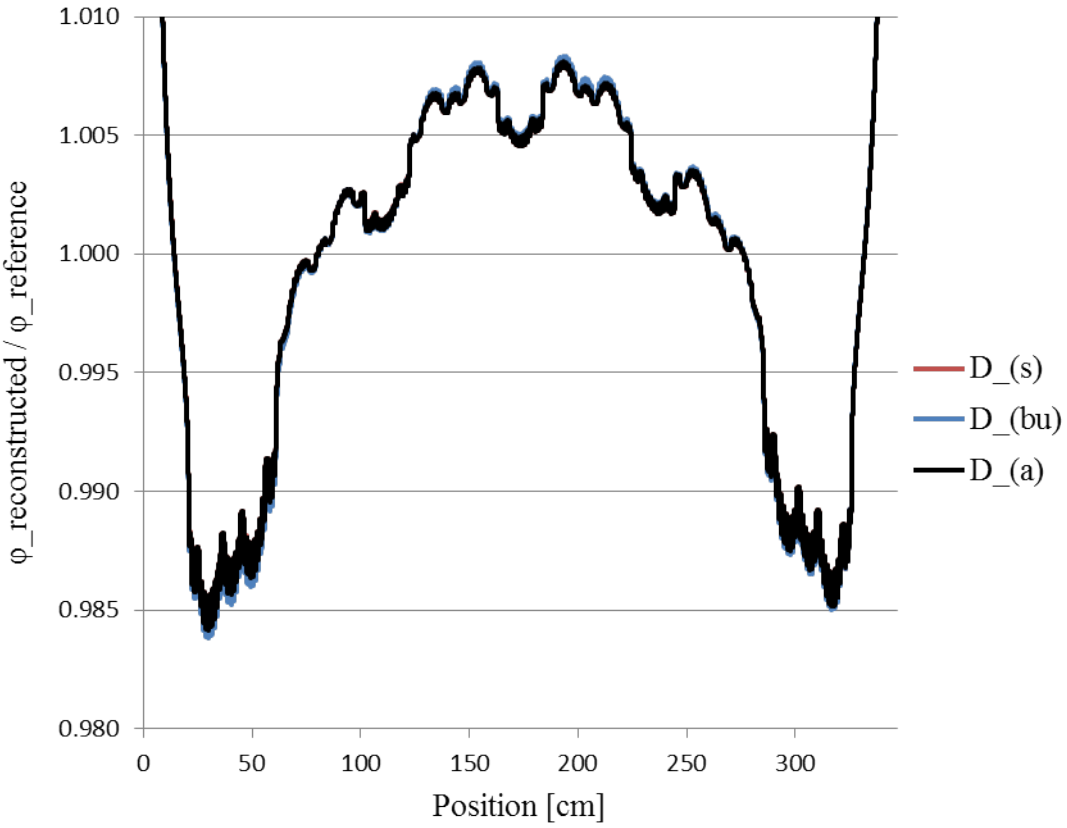

Figure 7.2: Ratio of Reconstructed Fluxes to Reference Fluxes for the 1D MOX LWR Benchmark with the Various Diffusion Coefficients. Results shown are for asymptotic flux reconstruction and a_2. (The standard and asymptotic scalar fluxes are nearly identical, and cannot be distinguished in the plot.)

7.3 Comparison of Homogenized Diffusion Methods for a 2-D Core with Two Assembly Types (Problem 8)

Next, we consider a more realistic multi-dimensional LWR problem. The system consists of a line of UO2 assemblies with 2 enrichments with a reflector assembly on one side (Problem 8, Section C.8). The geometry of each assembly is modeled in great detail, and the fine group cross sections have a 47 energy group structure. The assemblies are grouped together such that when the reflecting boundary condition at the center of the reactor is taken into account, there are 4 assemblies of each type clustered together. Thus, the assembly structure is periodic over the width of four assemblies, while each individual assembly is *nearly* periodic. The diffusion calculation uses 2, 5, and 10 energy group structures defined in Tables B.17-B.19 respectively. The "corrected" Benoist diffusion coefficients are not used in this problem.

The 2, 5, and 10 group diffusion coefficients for the LWR fuel assemblies are listed in Tables 7.5-7.7. The reflector assembly diffusion coefficients are not shown because the reflector is already homogeneous. Although this is a 2-D problem, we show the axial (zz component) Benoist and asymptotic diffusion coefficients. We see that for all energy group structures: (i) $\boldsymbol{D}_{bu}$ and $\boldsymbol{D}_a$ are anisotropic as expected, (ii) the differences between the transverse (xx and yy components) and axial (zz component) diffusion coefficients is greatest at lower energies (higher group numbers), (iii) the differences between D_s, $\boldsymbol{D}_{bu}$, and $\boldsymbol{D}_a$ are all greatest at lower energies. The reason the differences are greater at lower energies is because the cross sections are larger at these energies. When cross sections are small, regions are optically-thin and homogenized cross sections and diffusion coefficients are well approximated by simple volume-averaged quantities. When regions are optically-thick, transport effects are stronger, and as a result diffusion is more anisotropic and the standard flux-volume-

weighted diffusion coefficient is less accurate.

Table 7.5: Fuel Assembly Diffusion Coefficients for the Two Assembly Type LWR Test Problem[1] (2 Energy Groups)

	2.1% UO2				
Energy Group	D_s	$\boldsymbol{D}_{bu}$		$\boldsymbol{D}_a$	
		xx, yy	zz	xx, yy	zz
1	9.16196E-01	9.24025E-01	9.24434E-01	9.23111E-01	9.22948E-01
2	3.12724E-01	3.24683E-01	3.35369E-01	3.33754E-01	3.42150E-01
	2.6% UO2				
Energy Group	D_s	$\boldsymbol{D}_{bu}$		$\boldsymbol{D}_a$	
		xx, yy	zz	xx, yy	zz
1	9.17352E-01	9.25959E-01	9.25536E-01	9.25183E-01	9.25011E-01
2	3.14230E-01	3.24829E-01	3.35325E-01	3.34752E-01	3.41766E-01

[1] All D's measured in cm.

Table 7.6: Fuel Assembly Diffusion Coefficients for the Two Assembly Type LWR Test Problem[1] (5 Energy Groups)

	2.1% UO2				
Energy Group	D_s	$\boldsymbol{D}_{bu}$		$\boldsymbol{D}_a$	
		xx, yy	zz	xx, yy	zz
1	1.07276E+00	1.08201E+00	1.07999E+00	1.07535E+00	1.07399E+00
2	4.27276E-01	4.30531E-01	4.37725E-01	4.43754E-01	4.46548E-01
3	4.32216E-01	4.36528E-01	4.49742E-01	4.68979E-01	4.77114E-01
4	3.79258E-01	3.91145E-01	3.99594E-01	3.96461E-01	4.04748E-01
5	2.46175E-01	2.58206E-01	2.71131E-01	2.69245E-01	2.77694E-01
	2.6% UO2				
Energy Group	D_s	$\boldsymbol{D}_{bu}$		$\boldsymbol{D}_a$	
		xx, yy	zz	xx, yy	zz
1	1.07306E+00	1.08327E+00	1.08028E+00	1.07633E+00	1.07502E+00
2	4.26431E-01	4.29859E-01	4.36706E-01	4.42634E-01	4.45268E-01
3	4.31237E-01	4.35624E-01	4.48509E-01	4.67859E-01	4.75752E-01
4	3.78900E-01	3.90134E-01	3.98301E-01	3.95867E-01	4.03253E-01
5	2.43492E-01	2.53395E-01	2.66439E-01	2.66093E-01	2.72656E-01

[1] All D's measured in cm.

Table 7.8 shows the absolute error in the eigenvalues calculated from each diffusion coefficient. We see that for this moderately large reactor, the estimates of the eigenvalue are similar for all diffusion coefficients.

The reference assembly powers are shown in Fig. 7.3. Figures 7.4-7.6 depict the relative errors in the assembly powers for the 2, 5, and 10 group diffusion calculations. Because the assembly types are loaded contiguously (they are grouped such that four

Table 7.7: Fuel Assembly Diffusion Coefficients for the Two Assembly Type LWR Test Problem[1] (10 Energy Groups)

	2.1% UO2				
Energy Group	D_s	$\boldsymbol{D}_{bu}$		$\boldsymbol{D}_a$	
		xx, yy	zz	xx, yy	zz
1	1.84626E+00	1.86909E+00	1.86226E+00	1.87115E+00	1.86398E+00
2	7.58577E-01	7.62313E-01	7.62239E-01	7.62625E-01	7.63779E-01
3	4.27276E-01	4.30531E-01	4.37725E-01	4.43763E-01	4.46557E-01
4	2.81839E-01	2.47098E-01	2.91604E-01	2.35656E-01	2.75468E-01
5	4.32550E-01	4.35978E-01	4.48051E-01	4.44865E-01	4.46666E-01
6	4.50974E-01	4.60671E-01	4.70551E-01	4.62148E-01	4.70166E-01
7	4.43812E-01	4.54474E-01	4.63473E-01	4.54980E-01	4.63580E-01
8	4.28265E-01	4.37877E-01	4.45867E-01	4.40081E-01	4.47196E-01
9	3.63488E-01	3.75755E-01	3.84122E-01	3.79500E-01	3.87736E-01
10	2.46175E-01	2.58206E-01	2.71131E-01	2.67976E-01	2.76385E-01
	2.6% UO2				
Energy Group	D_s	$\boldsymbol{D}_{bu}$		$\boldsymbol{D}_a$	
		xx, yy	zz	xx, yy	zz
1	1.84629E+00	1.87063E+00	1.86229E+00	1.87097E+00	1.86395E+00
2	7.58667E-01	7.63136E-01	7.62326E-01	7.62673E-01	7.63824E-01
3	4.26431E-01	4.29859E-01	4.36706E-01	4.42643E-01	4.45277E-01
4	2.81643E-01	2.46700E-01	2.91461E-01	2.35314E-01	2.75383E-01
5	4.31050E-01	4.34344E-01	4.46161E-01	4.42965E-01	4.44480E-01
6	4.50213E-01	4.60142E-01	4.69571E-01	4.61360E-01	4.69122E-01
7	4.43101E-01	4.54034E-01	4.62550E-01	4.54283E-01	4.62639E-01
8	4.25795E-01	4.35262E-01	4.42686E-01	4.37524E-01	4.43965E-01
9	3.62280E-01	3.73691E-01	3.81831E-01	3.78057E-01	3.85245E-01
10	2.43492E-01	2.53395E-01	2.66439E-01	2.64862E-01	2.71394E-01

[1] All D's measured in cm.

Table 7.8: Absolute Error in k for the Two Assembly Type LWR Test Problem with Various Diffusion Coefficients[1].

Number of Coarse Groups	D_s	$\boldsymbol{D}_{bu}$	$\boldsymbol{D}_a$
2	16	-2	0
5	-6	-23	-22
10	15	-7	-1

[1] All errors in pcm. Results shown are for a_2 DFs. The reference value of k from an MOC calculation is 1.08819.

assemblies of the same kind are adjacent to each other), this is a nearly periodic problem. In other words, the assumptions of the asymptotic analysis are met, and the D_a yields slightly more accurate assembly powers than the D_{bu}, which in turn yields significantly more accurate assembly powers than D_s. The results are less accurate for the 5 coarse energy group structure, presumably because the definition

of the 5 coarse groups is not optimal.

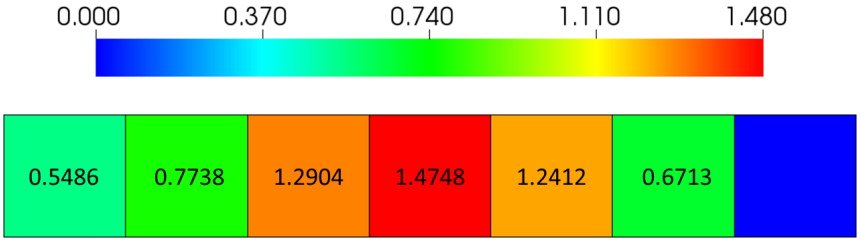

Figure 7.3: Reference Assembly Powers for the Two Assembly Type LWR Test Problem. Numbers indicate normalized power in each assembly.

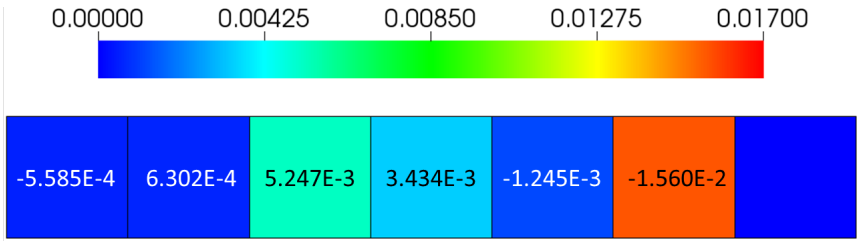

(a) $\boldsymbol{D}_a$

(b) $\boldsymbol{D}_{bu}$

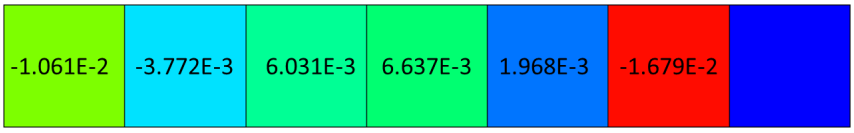

(c) D_s

Figure 7.4: Errors in Assembly Powers for the Two Assembly Type LWR Test Problem with Various Diffusion Coefficients (2 Energy Groups). Numbers indicate relative error values in each assembly. Colors indicate the magnitude of the errors. Results shown are for a_2.

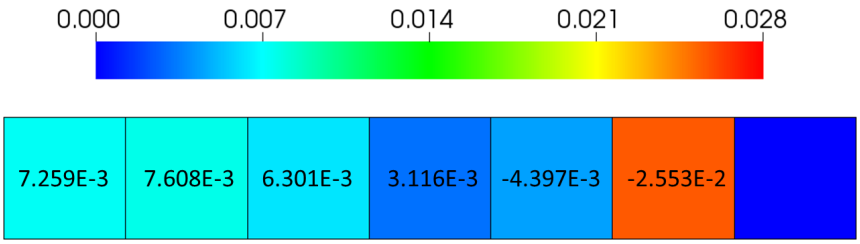

(a) $\boldsymbol{D}_a$

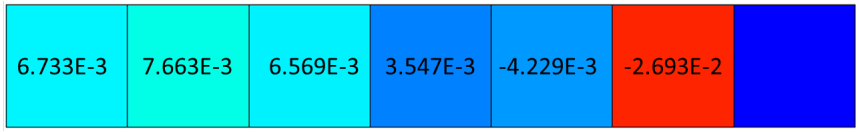

(b) $\boldsymbol{D}_{bu}$

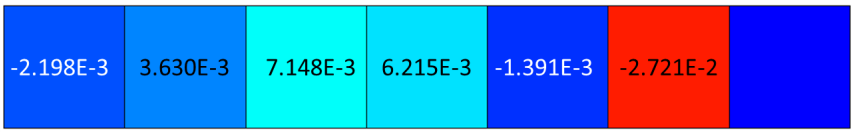

(c) D_s

Figure 7.5: Errors in Assembly Powers for the Two Assembly Type LWR Test Problem with Various Diffusion Coefficients (5 Energy Groups). Numbers indicate relative error values in each assembly. Colors indicate the magnitude of the errors. Results shown are for a_2.

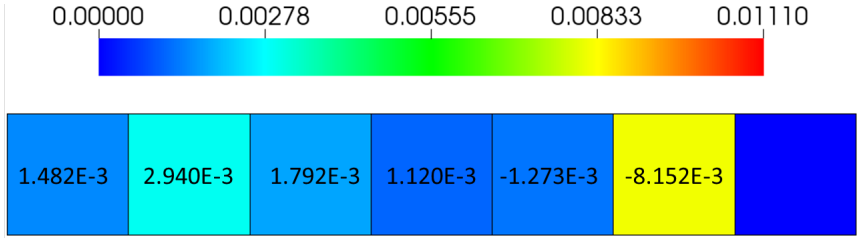

(a) $\boldsymbol{D}_a$

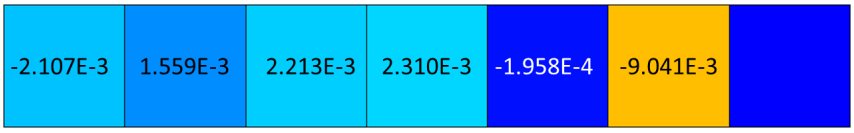

(b) $\boldsymbol{D}_{bu}$

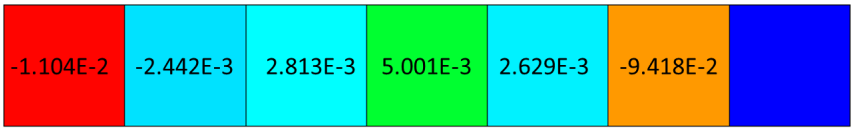

(c) D_s

Figure 7.6: Errors in Assembly Powers for the Two Assembly Type LWR Test Problem with Various Diffusion Coefficients (10 Energy Groups). Numbers indicate relative error values in each assembly. Colors indicate the magnitude of the errors. Results shown are for a_2.

7.4 Comparison of Homogenized Diffusion Methods for a 2-D Very High Temperature Reactor (Problem 4)

We conclude our comparison of diffusion coefficients by studying a reactor with long, optically-thin channels. The presence of these streaming channels makes anisotropic diffusion effects more significant. The test problem is a 2-D approximation of an annular VHTR (Problem 4, Section C.4). The "corrected" Benoist diffusion coefficients are not used in this problem.

Table 7.9 lists the diffusion coefficients for the VHTR fuel assembly. The reflector assembly diffusion coefficients are not shown because the reflector is already homogeneous. Due to the optically-thin streaming channels, neutrons diffuse more readily in the axial direction. The standard diffusion coefficient, which is a scalar, does not capture these anisotropic effects. On the other hand, the asymptotic and Benoist diffusion coefficients are tensors, and the axial components of the diffusion tensors are (correctly) much larger than the radial components.

Table 7.9: Fuel Assembly Diffusion Coefficients for the VHTR Test Problem[1]

Energy Group	D_s	$\boldsymbol{D}_{bu}$		$\boldsymbol{D}_a$	
		(radial)	(axial)	(radial)	(axial)
1	3.51778	3.52311	3.80527	3.53384	3.80465
2	1.68569	1.67185	2.07103	1.67449	2.07116
3	1.40853	1.39541	1.82700	1.39274	1.83234
4	1.37739	1.36503	1.80241	1.35762	1.80149

[1] All D's measured in cm.

The absolute errors in the reactor multiplication factor for each diffusion coefficient are shown in Table 7.10. The asymptotic diffusion coefficient yields the best estimate of the reactor multiplication factor, while the standard, isotropic diffusion coefficient yields the worst estimate by a considerable margin.

The reference assembly powers are shown in Fig. 7.7. The fuel assemblies are divided into 5 cm axial segments so that axial trends can be observed. The rel-

Table 7.10: Absolute Error in k for the VHTR Test Problem with Various Diffusion Coefficients[1]

D_s	$\boldsymbol{D}_{bu}$	$\boldsymbol{D}_a$
404	212	203

[1] All errors in pcm. Results shown are for a_2 DFs. The reference value of k from an MOC calculation is 1.15947.

ative errors in the assembly powers are plotted in Fig. 7.8. It is clear that the standard, isotropic diffusion coefficient is inadequate for modeling problems in which anisotropic diffusion effects are strong. The asymptotic and Benoist diffusion coefficients, which are anisotropic, yield similarly accurate powers, and each are significantly more accurate than the standard diffusion coefficient.

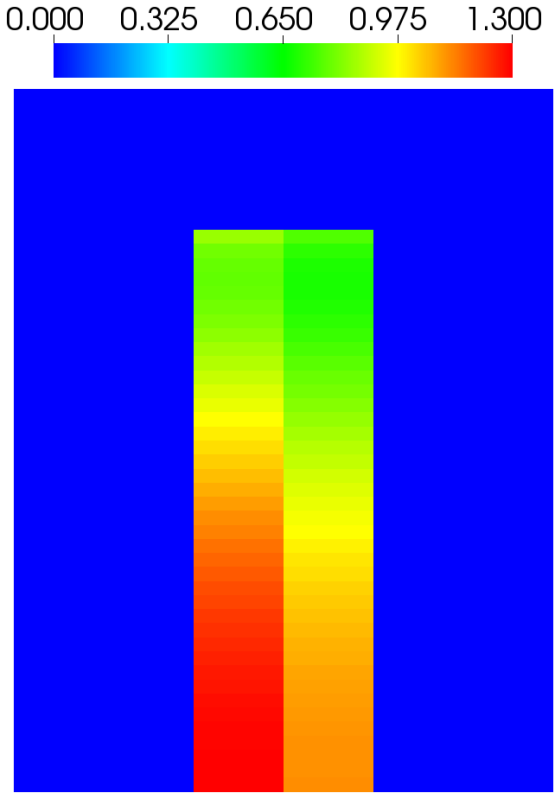

Figure 7.7: Reference Assembly Powers for the VHTR Test Problem

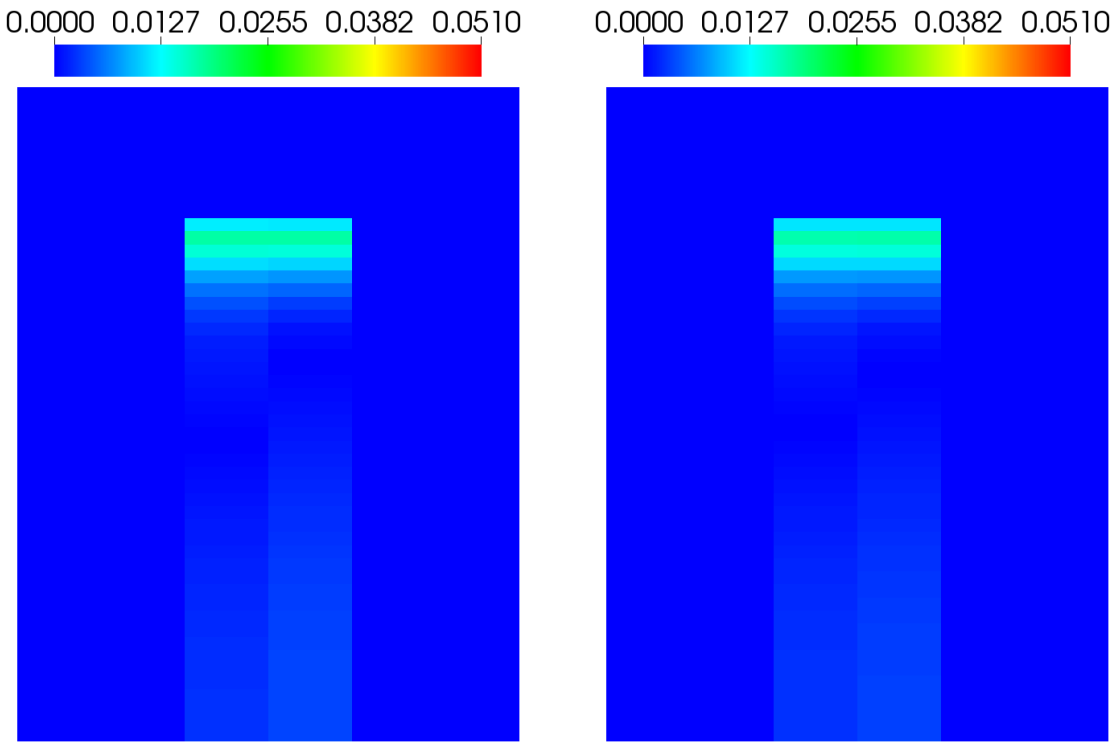

(a) $\boldsymbol{D}_a$ (b) $\boldsymbol{D}_{bu}$

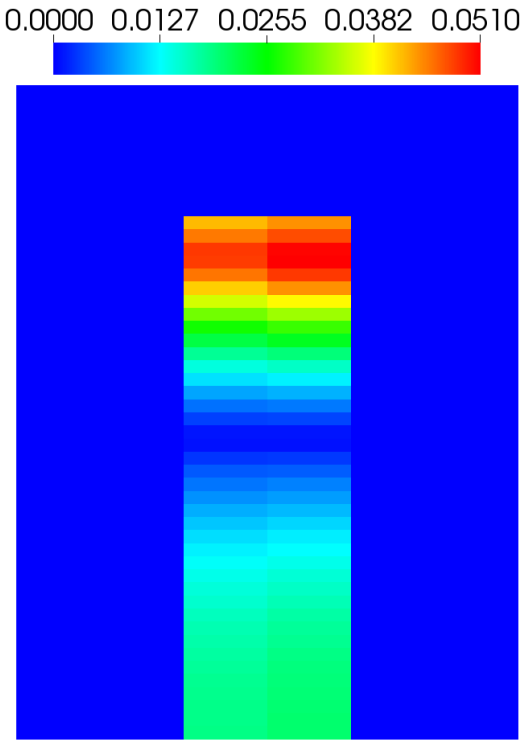

(c) D_s

Figure 7.8: Errors in Assembly Powers for the VHTR Test Problem with Various Diffusion Coefficients. Results shown are for a_2.

7.5 Summary

In periodic or nearly-periodic lattice systems in which the leakage is moderate to large, the use of the asymptotic diffusion coefficient often leads to more accurate reactor eigenvalues compared to the Benoist and standard diffusion coefficients. This is expected because the Deniz-Gelbard diffusion coefficient, which is identical to the asymptotic diffusion coefficient, is designed to preserve the eigenvalue of the system with $O(B^2) = O(\epsilon^2)$ error, while the Benoist diffusion coefficient is designed to preserve the leakage in a cell with $O(B^2)$ error. The asymptotic and Benoist diffusion coefficients tend to yield similarly accurate flux distributions and assembly powers, with both typically outperforming the standard diffusion coefficient.

For large systems in which the diffusion solution is slowly-varying (i.e., where leakage is small), the changes in the diffusion coefficient have a small effect on the solution. Thus, in large systems, the asymptotic, Benoist, and standard diffusion coefficients yield comparable results.

However, in large reactors containing optically-thin channels through which neutrons stream long distances, anisotropic diffusion effects become critically important. For these reactors, the asymptotic and Benoist diffusion tensors yield vastly superior solutions compared to the standard, isotropic diffusion coefficient.

We note that the development of Small Modular Reactors (SMRs) has drawn signigicant global interest in recent years, and the Department of Energy Office of Nuclear Energy has formed a Small Modular Reactor Licensing Technical Support program to expedite the design and deployment of these reactors [77]. Due to their relatively small size, these reactors have larger buckling (i.e., greater leakage and greater curvature in the diffusion solution) compared to standard LWRs. As a result,

we believe the choice of an accurate diffusion coefficient is particularly important for these reactors. Because the asymptotic diffusion coefficient is more accurate for small-size, large-leakage reactors compared to the standard diffusion coefficient, it could be particularly useful for designing of SMRs.

CHAPTER VIII

Numerical Results: Comparison of Reconstructed Fluxes

We now present numerical test results that demonstrate that the asymptotic flux reconstruction (Eq. (4.38)) is superior to the standard flux reconstruction (Eq. (2.23)) for a wide range of problems.

An important point needs to be emphasized about the asymptotic flux reconstruction. From the 1-D, monoenergetic asymptotic flux reconstruction, one obtains the scalar flux estimate:

$$\phi_{rec}(x) = F_0(x)\phi(x) - F_1(x)\frac{\mathrm{d}\phi}{\mathrm{d}x}(x) + O(\epsilon^2)\,, \tag{8.1}$$

where

$$F_n(x) = \int_{-1}^{1} f_n(x,\mu)\,\mathrm{d}\mu\,, \qquad n = 0, 1\,, \tag{8.2}$$

are periodic functions. In the P_1 approximation, we replace f_1 by μ/Σ_{tr}, and then F_1 is uniformly 0. Thus, both the P_1 approximation and the standard flux reconstruction leave us with only one term in the scalar flux reconstruction. However, in the asymptotic method, the pointwise values of $F_1(x)$ (defined in Eq. (8.2)) are not zero. Thus, the asymptotic reconstruction of the scalar flux contains an additional term that is roughly periodic over short distances, and that acts as an $O(\epsilon)$ "correction" to the standard flux reconstruction. Furthermore, the magnitude of the correction

term increases with $\mathrm{d}\phi/\mathrm{d}x$. Therefore, we expect that the correction term will be relatively unimportant in regions where $\mathrm{d}\phi/\mathrm{d}x$ is small (typically, near the center of the reactor), but more significant in regions where $\mathrm{d}\phi/\mathrm{d}x$ is large (typically, near the periphery of the reactor).

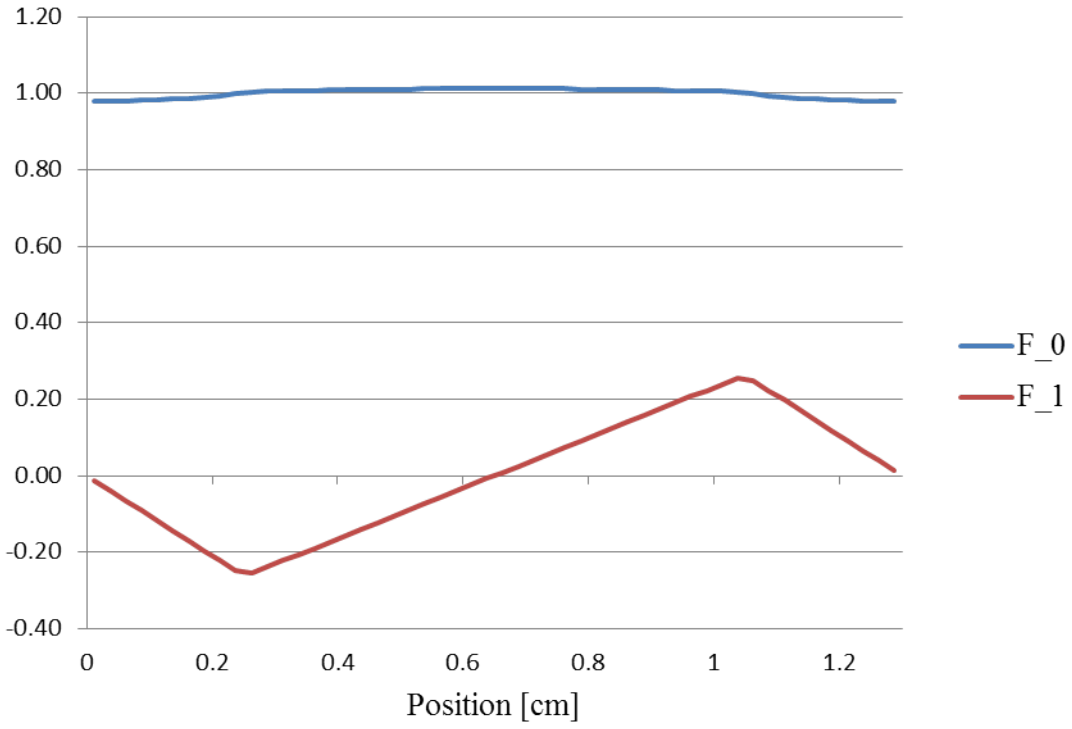

Figure 8.1: Scalar Lattice Functions for a Typical Fuel Pin

The scalar lattice functions F_0 and F_1 are plotted for a typical fuel pin (the fuel-centered pin of Problem 2, Section C.2) in Fig. 8.1. The function F_0 is familiar, and is peaked in the fuel for this monoenergetic problem. The function F_1 is non-standard, and we observe the following: (i) F_1 is zero on the cell boundaries because f_1 is antisymmetric in angle at these locations, (ii) the derivative of F_1 changes sign at interfaces between multiplying and non-multiplying regions (in this case, on the fuel boundaries), (iii) the magnitude of F_1 is smaller than that of F_0, and (iv) the volume average of F_1 is 0, as required. Based on the shape of F_1, we see that the

correction term in Eq. (8.1) will tend to redistribute neutrons from one side of a cell to the other.

In this chapter, except where noted, we used the asymptotic diffusion coefficient, $\boldsymbol{D}_a$. For bare problems (problems without reflector assemblies) we use the lattice variational extrapolation lengths, $l_{LatVar}(\alpha)$. The boundary condition results (Chapter IX) indicate that in 1-D, a value of $\alpha = 0.0$ is good for a wide range of problems, while in 2-D, a value of $\alpha = 0.8$ performs well for many problems. Thus, the numerical results for 1-D and 2-D problems without reflector assemblies presented in these chapters use the extrapolation lengths $l_{LatVar}(\alpha = 0.0)$ and $l_{LatVar}(\alpha = 0.8)$ respectively. For reflected problems, the standard homogeneous variational extrapolation lengths, l_{HomVar}, are used. In problems containing multiple assembly types, we use variational discontinuity factors, ab_{Var}, because they tend to yield accurate eigenvalues for many problems (see Chapter X).

8.1 Flux Reconstruction for a 1-D Uniform Lattice (Problem 1)

We first consider the simple case of a uniform lattice in planar geometry. We study the ZPPR test problem (Problem 1, Section C.1). Figure 8.2 depicts the reconstructed flux, with and without the $O(\epsilon)$ correction term, divided by the reference S_N solution for the ZPPR lattice with 75 uranium oxide plates. The fluxes are normalized such that average scalar flux is unity.

If the reconstructed flux were exact, then the ratio of the reconstructed flux to the reference flux would be uniformly equal to unity. Instead we see that there is an oscillating error with the period of the lattice. The standard flux reconstruction and the asymptotic flux reconstruction agree near the center of the reactor, where $\mathrm{d}\phi/\mathrm{d}x$ is small. However, when standard flux reconstruction is performed (i.e., if we use

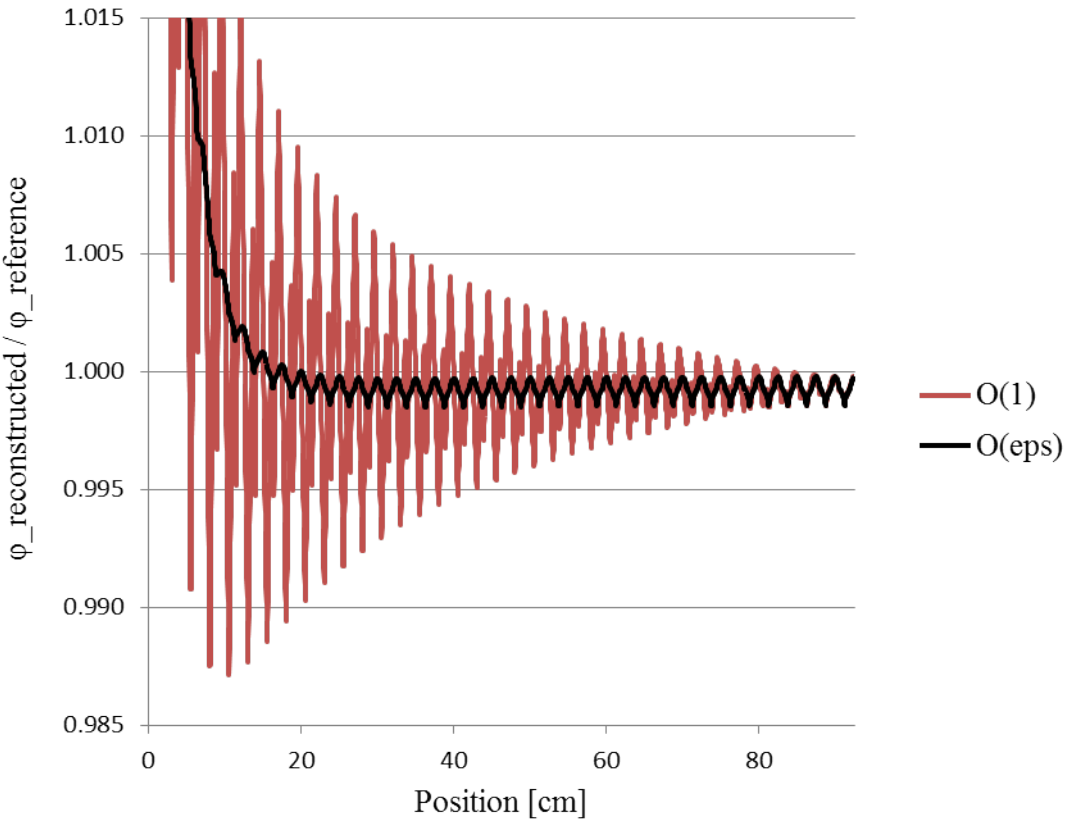

Figure 8.2: Comparison of Flux Reconstruction Methods with the Asymptotic Diffusion Coefficient for the ZPPR Test Problem. The case shown is the ZPPR core with 75 uranium oxide fuel plates (74 uranium plutonium fuel plates). The right edge of the plot corresponds to the mid-plane of the reactor. Results shown are for $\boldsymbol{D}_a$ and $l_{LatVar}(\alpha = 0.0)$.

only the $O(1)$ term from the asymptotic analysis), the amplitude of the oscillating error grows significantly as we move towards the outer regions of the reactor, where $\mathrm{d}\phi/\mathrm{d}x$ is large. On the other hand, the magnitude of the oscillating error grows only marginally, if at all, when we include the $O(\epsilon)$ correction term that arises from the asymptotic analysis.

8.2 Flux Reconstruction for a 1-D Non-Uniform Lattice (Problem 3)

Next, we consider a planar geometry reactor core in which the lattice is no longer uniform. The one-group MOX LWR benchmark designed by Joo (Problem 3, Section C.3) is not strictly periodic, but is composed of several *nearly* periodic assemblies.

Thus, neither the core nor the individual assemblies are periodic in this problem.

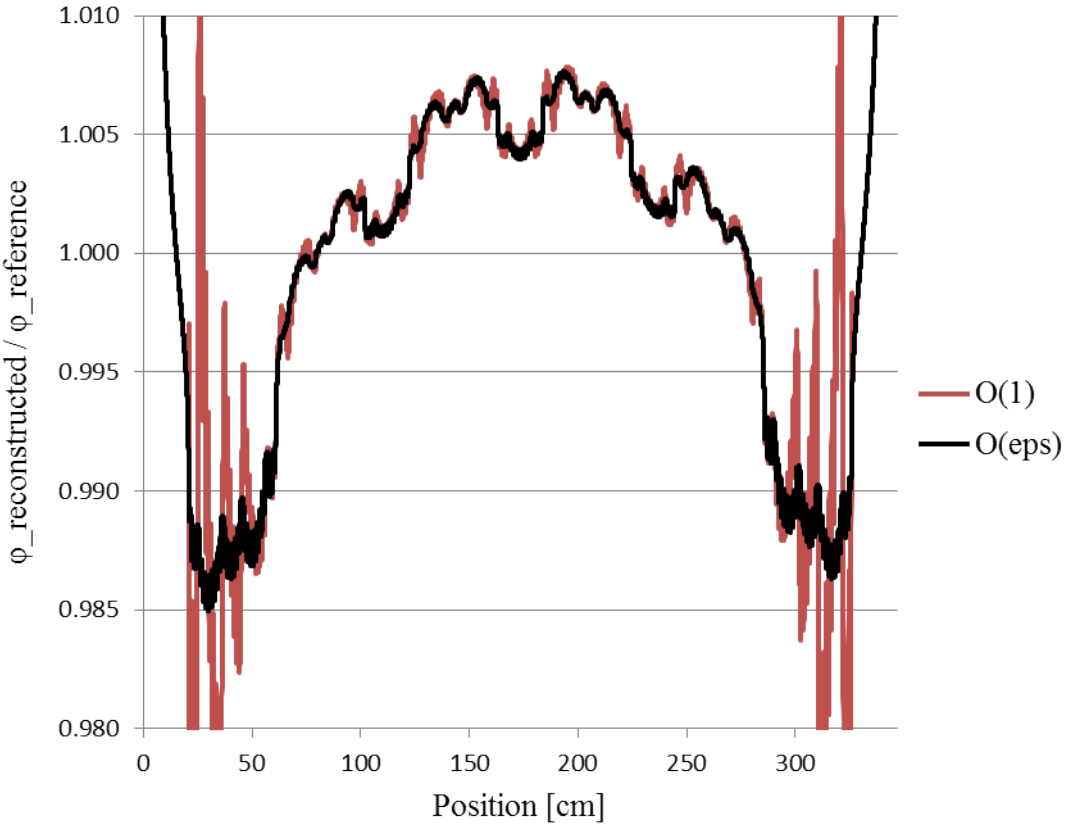

Figure 8.3: Comparison of Flux Reconstruction Methods with the Asymptotic Diffusion Coefficient for the 1-D MOX LWR Benchmark. Results shown are for $\boldsymbol{D}_a$ and ab_{Var}.

Again, we consider the ratio of the reconstructed fluxes to the reference fluxes (Fig. 8.3). In this problem, the fluxes are normalized such that the integral of the scalar flux over the active core volume is 1 neutron/(cm^2 s). Despite the fact that the periodic lattice assumption has been violated, the $O(\epsilon)$ correction term from the asymptotic analysis still reduces the error in the flux reconstruction, particularly in the outer regions of the core. We note that the largest "spikes" in the error of the standard flux reconstruction occur at the locations of water holes and burnable absorber (UO2-Gd) pins. In other words, the largest errors in the standard reconstruction occur where the periodicity of the lattice is broken. However,

the asymptotic flux reconstruction with the correction term nearly eliminates the spikes. Thus, *for nearly-periodic systems, the asymptotic flux reconstruction yields the greatest improvements where the assumption of a uniform lattice is broken.*

8.3 Flux Reconstruction for a 2-D Uniform Pin Lattice (Problem 5: Bare UO2 Configuration)

We turn our attention to uniform lattices in multi-dimensional geometries. The problem we consider is the six-assembly test problem in the bare, UO2 configuration (Problem 5, Section C.5) which is a uniform lattice of UO2 fuel pins. The diffusion energy group structure is the same as the reference MOC energy group structure (7 groups).

The absolute value of the relative error in the coarse group fluxes relative to the reference MOC fluxes are shown in Figs. (8.4)-(8.10). As was the case in 1-D, the standard flux reconstruction contains periodic errors that grow as we approach the exterior of the core. The differences between the standard and asymptotic flux reconstructions is relatively small in the fast groups (fine groups 1-4) in which material regions are optically-thin. In the thermal groups (fine groups 5-7), the material regions are optically-thick, the true fluxes vary more strongly, and the asymptotic flux reconstruction is more capable of capturing these variations. Thus, the improvement of the asymptotic flux reconstruction over the standard flux reconstruction is greater for the thermal groups.

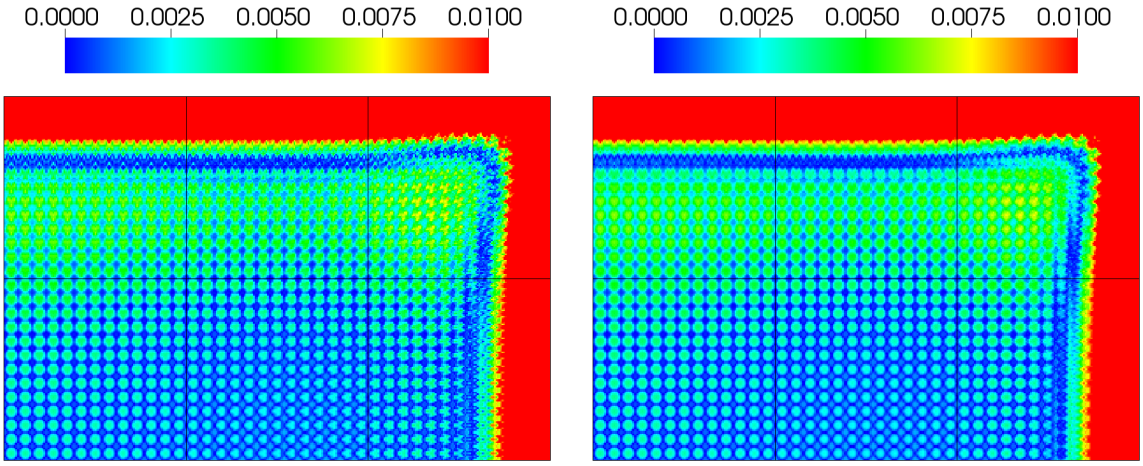

(a) O(1) (b) O(eps)

Figure 8.4: Absolute Value of Relative Error in Reconstructed Scalar Flux for the Bare, Six-Assembly UO2 Core: Fine Group 1. Results shown are for $\boldsymbol{D}_a$ and $l_{LatVar}(\alpha = 0.8)$. (Note that the scale does not extend to the maximum error in either plot.)

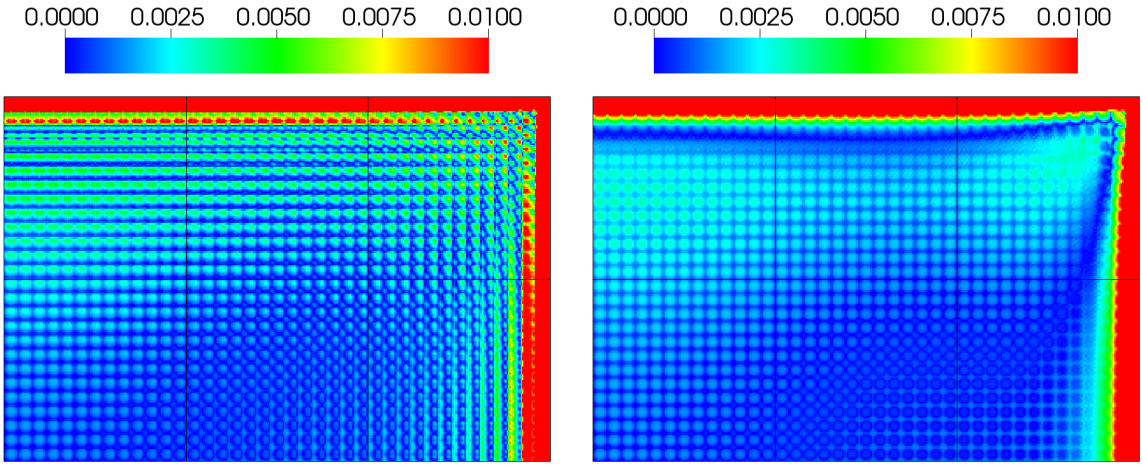

(a) O(1) (b) O(eps)

Figure 8.5: Absolute Value of Relative Error in Reconstructed Scalar Flux for the Bare, Six-Assembly UO2 Core: Fine Group 2. Results shown are for $\boldsymbol{D}_a$ and $l_{LatVar}(\alpha = 0.8)$. (Note that the scale does not extend to the maximum error in either plot.)

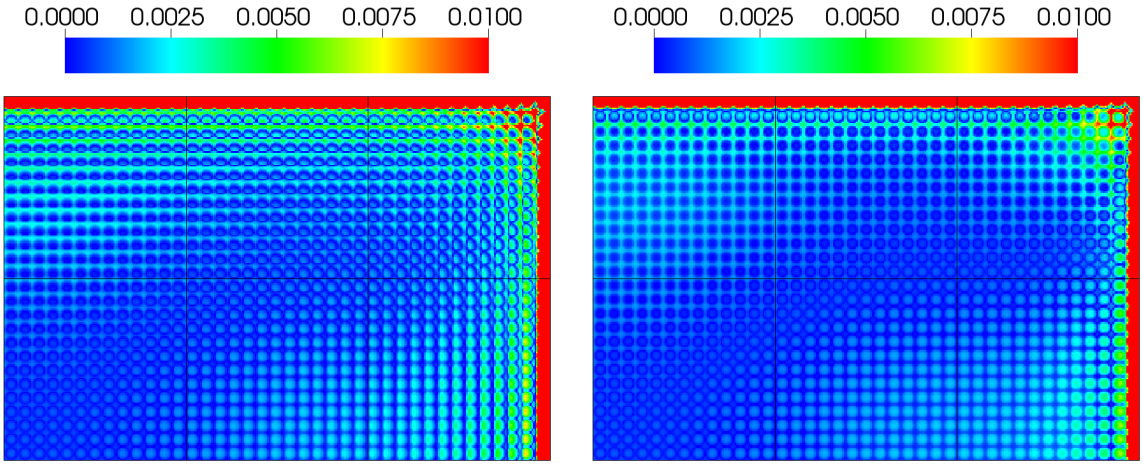

(a) O(1) (b) O(eps)

Figure 8.6: Absolute Value of Relative Error in Reconstructed Scalar Flux for the Bare, Six-Assembly UO2 Core: Fine Group 3. Results shown are for $\boldsymbol{D}_a$ and $l_{LatVar}(\alpha = 0.8)$. (Note that the scale does not extend to the maximum error in either plot.)

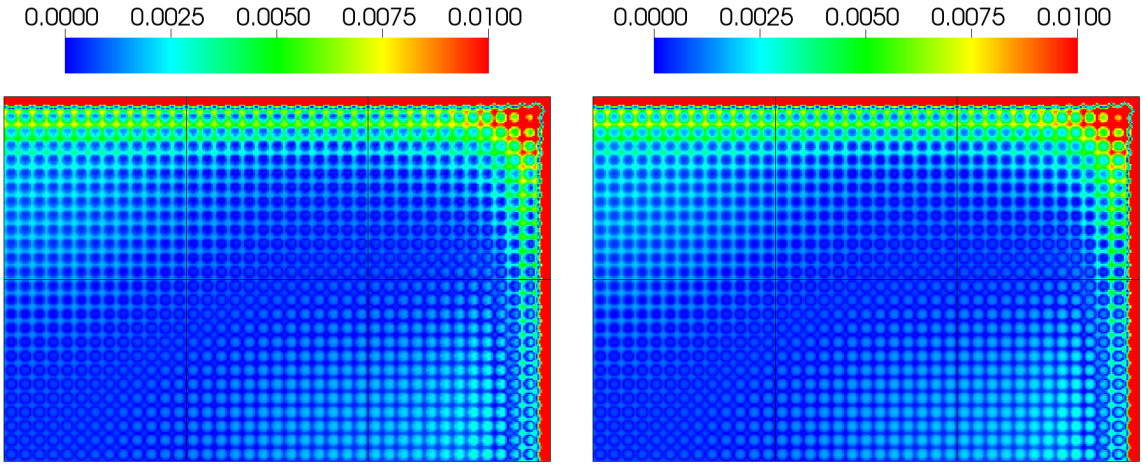

(a) O(1) (b) O(eps)

Figure 8.7: Absolute Value of Relative Error in Reconstructed Scalar Flux for the Bare, Six-Assembly UO2 Core: Fine Group 4. Results shown are for $\boldsymbol{D}_a$ and $l_{LatVar}(\alpha = 0.8)$. (Note that the scale does not extend to the maximum error in either plot.)

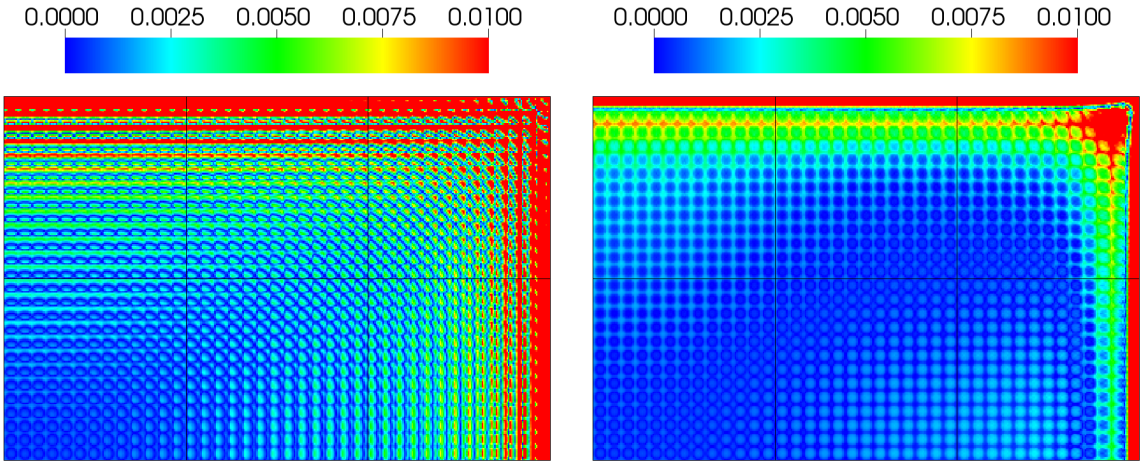

(a) O(1) (b) O(eps)

Figure 8.8: Absolute Value of Relative Error in Reconstructed Scalar Flux for the Bare, Six-Assembly UO2 Core: Fine Group 5. Results shown are for $\boldsymbol{D}_a$ and $l_{LatVar}(\alpha = 0.8)$. (Note that the scale does not extend to the maximum error in either plot.)

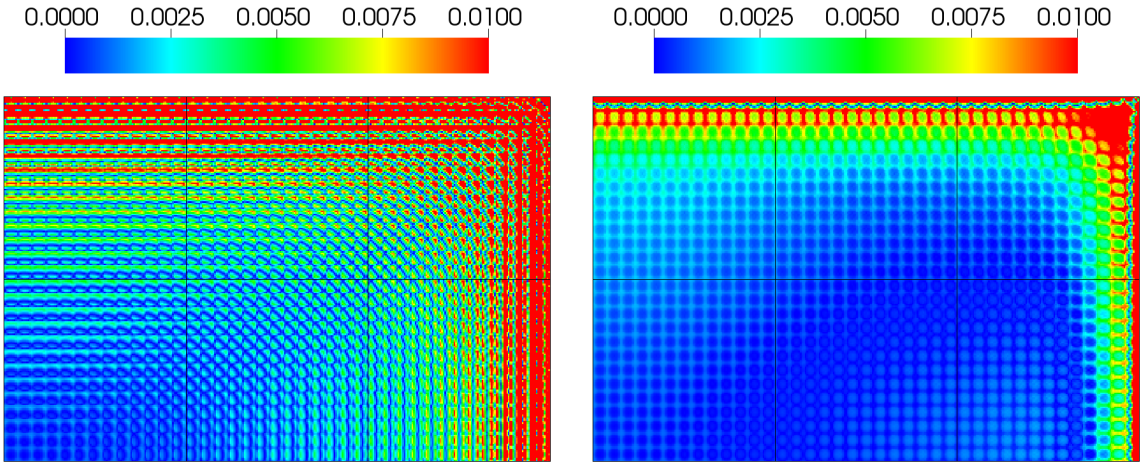

(a) O(1) (b) O(eps)

Figure 8.9: Absolute Value of Relative Error in Reconstructed Scalar Flux for the Bare, Six-Assembly UO2 Core: Fine Group 6. Results shown are for $\boldsymbol{D}_a$ and $l_{LatVar}(\alpha = 0.8)$. (Note that the scale does not extend to the maximum error in either plot.)

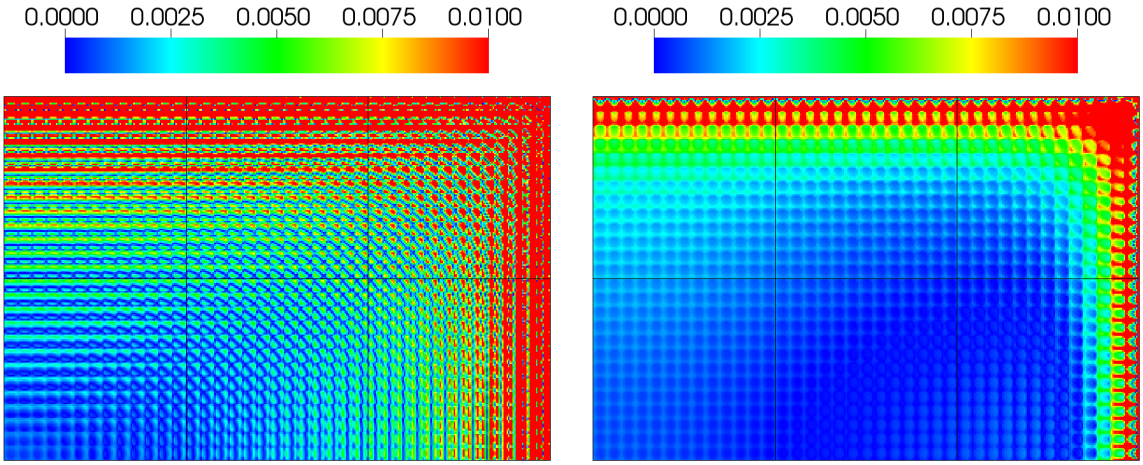

(a) O(1) (b) O(eps)

Figure 8.10: Absolute Value of Relative Error in Reconstructed Scalar Flux for the Bare, Six-Assembly UO2 Core: Fine Group 7. Results shown are for $\boldsymbol{D}_a$ and $l_{LatVar}(\alpha = 0.8)$. (Note that the scale does not extend to the maximum error in either plot.)

8.4 Flux Reconstruction for a 2-D Uniform Assembly Lattice (Problem 5: Bare MOX Configuration)

Next, we consider a problem that has assembly-level periodicity, rather than pin-level periodicity. The test problem is the six-assembly core in the bare, MOX configuration (Problem 5, Section C.5), which is a uniform lattice of MOX assemblies. The diffusion energy group structure is the same as the reference MOC energy group structure (7 groups).

The absolute value of the relative error in the coarse group fluxes relative to the reference MOC fluxes are shown in Figs. (8.11)-(8.17). It is apparent from these results that the asymptotic flux reconstruction is a *significant* improvement over the standard flux reconstruction, even though the core is not periodic at a pin level. In fact, it seems that the improvement is larger for the uniform assembly lattice than for the uniform pin lattice because the standard reconstruction is so poor where the pin periodicity is broken. As was observed in Section 8.2, for nearly-periodic systems, the asymptotic reconstructed flux is most effective where the periodicity of the lattice

is broken. In this case, we see that the largest errors in the standard reconstructed flux occur in the vicinity of guide tubes and fission chambers (i.e., non-fuel pins).

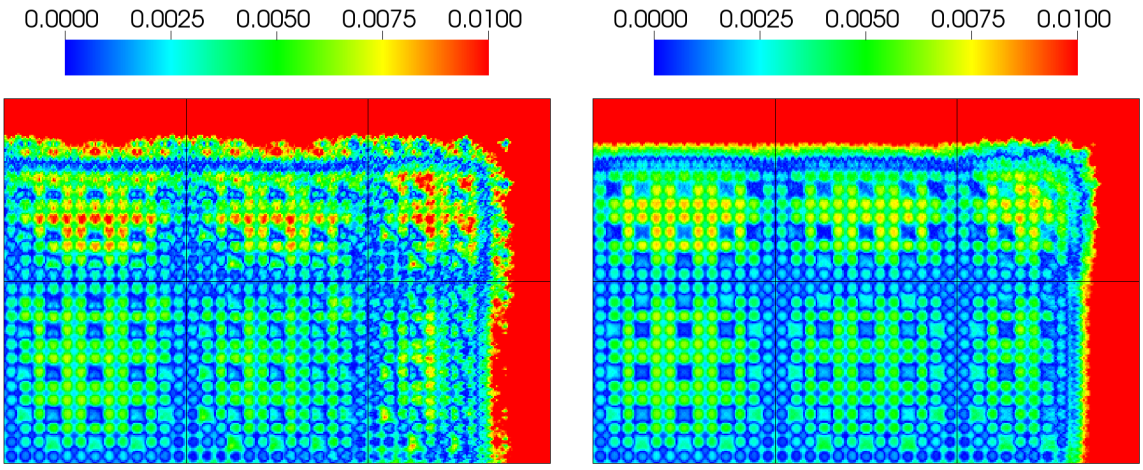

(a) O(1) (b) O(eps)

Figure 8.11: Absolute Value of Relative Error in Reconstructed Scalar Flux for the Bare, Six-Assembly MOX Core: Fine Group 1. Results shown are for $\boldsymbol{D}_a$ and $l_{LatVar}(\alpha = 0.8)$. (Note that the scale does not extend to the maximum error in either plot.)

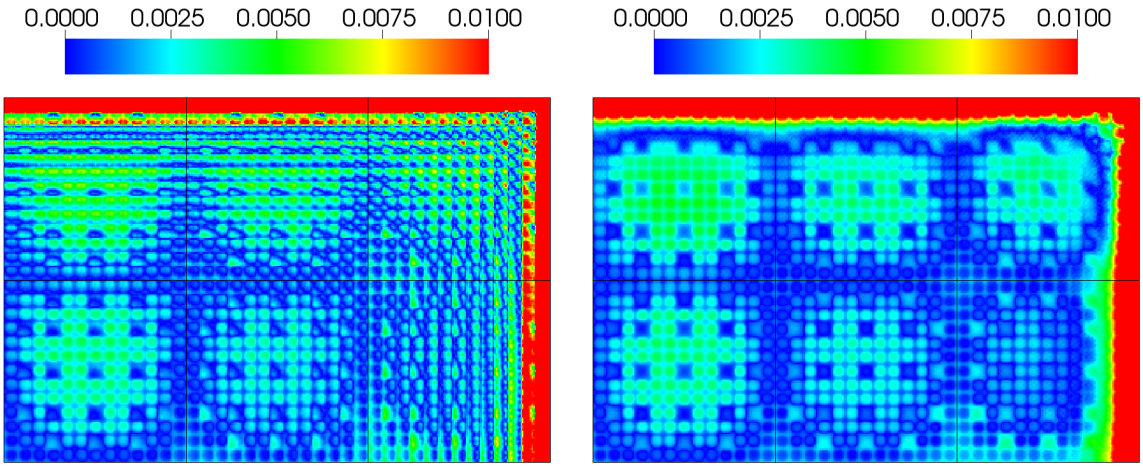

(a) O(1) (b) O(eps)

Figure 8.12: Absolute Value of Relative Error in Reconstructed Scalar Flux for the Bare, Six-Assembly MOX Core: Fine Group 2. Results shown are for $\boldsymbol{D}_a$ and $l_{LatVar}(\alpha = 0.8)$. (Note that the scale does not extend to the maximum error in either plot.)

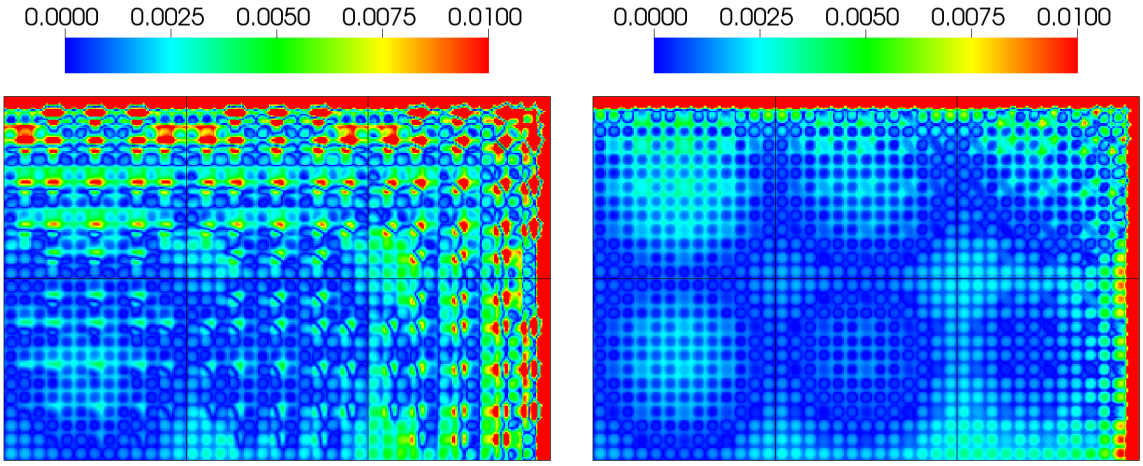

(a) O(1) (b) O(eps)

Figure 8.13: Absolute Value of Relative Error in Reconstructed Scalar Flux for the Bare, Six-Assembly MOX Core: Fine Group 3. Results shown are for $\boldsymbol{D}_a$ and $l_{LatVar}(\alpha = 0.8)$. (Note that the scale does not extend to the maximum error in either plot.)

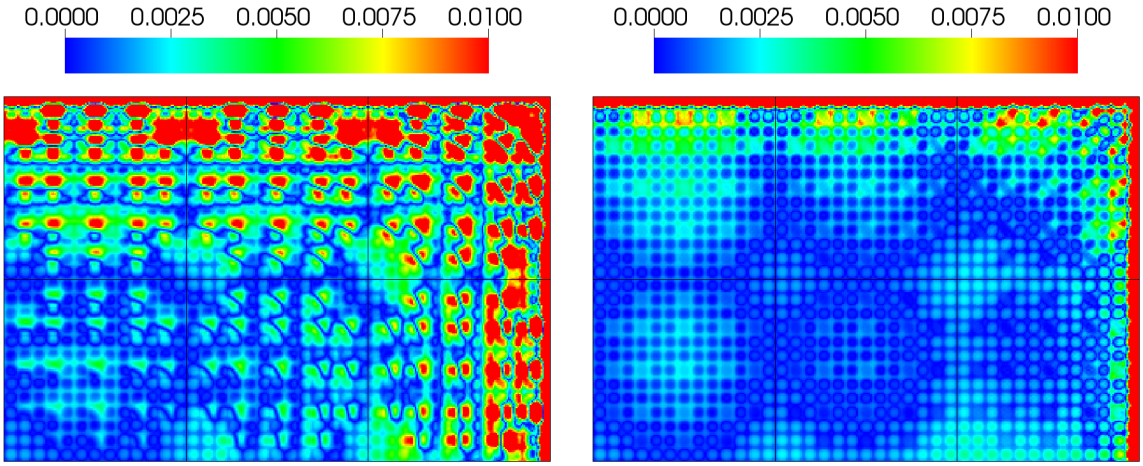

(a) O(1) (b) O(eps)

Figure 8.14: Absolute Value of Relative Error in Reconstructed Scalar Flux for the Bare, Six-Assembly MOX Core: Fine Group 4. Results shown are for $\boldsymbol{D}_a$ and $l_{LatVar}(\alpha = 0.8)$. (Note that the scale does not extend to the maximum error in either plot.)

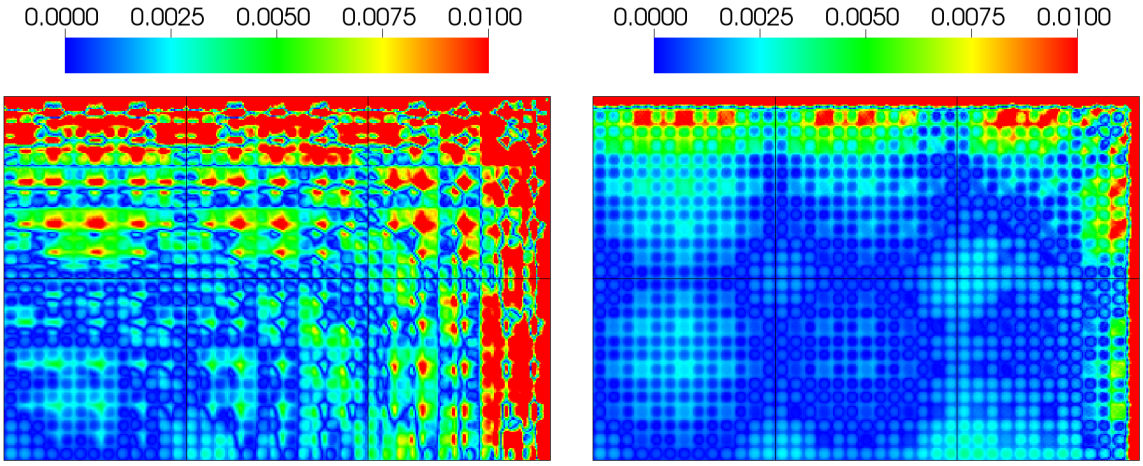

(a) O(1) (b) O(eps)

Figure 8.15: Absolute Value of Relative Error in Reconstructed Scalar Flux for the Bare, Six-Assembly MOX Core: Fine Group 5. Results shown are for $\boldsymbol{D}_a$ and $l_{LatVar}(\alpha = 0.8)$. (Note that the scale does not extend to the maximum error in either plot.)

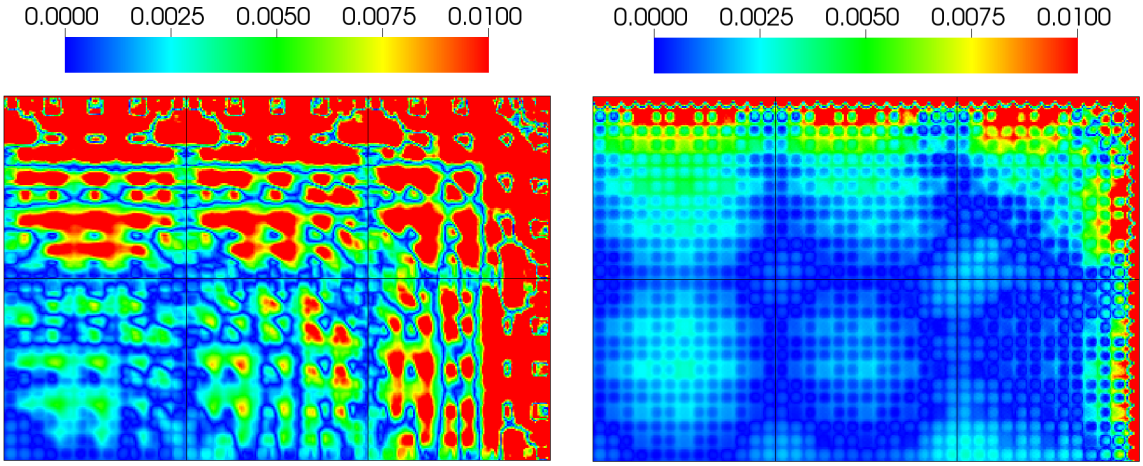

(a) O(1) (b) O(eps)

Figure 8.16: Absolute Value of Relative Error in Reconstructed Scalar Flux for the Bare, Six-Assembly MOX Core: Fine Group 6. Results shown are for $\boldsymbol{D}_a$ and $l_{LatVar}(\alpha = 0.8)$. (Note that the scale does not extend to the maximum error in either plot.)

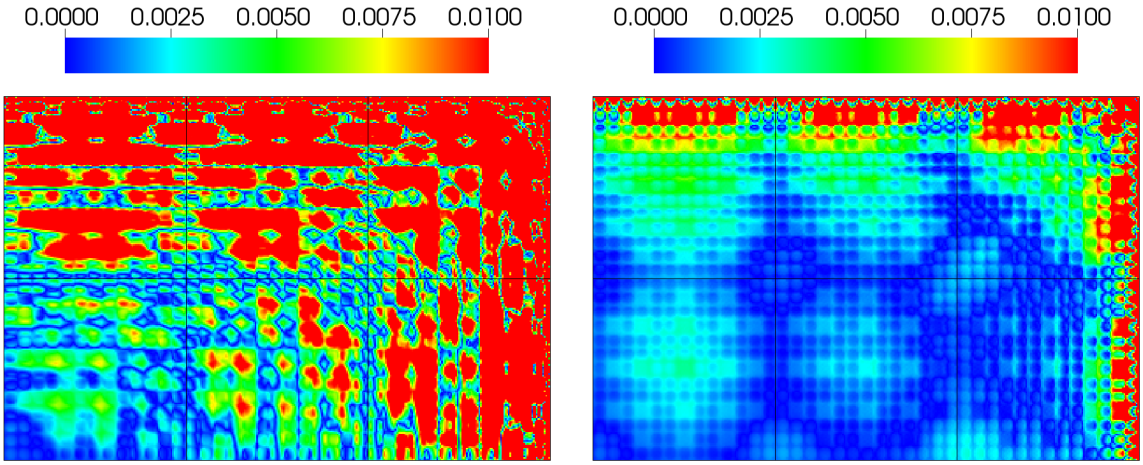

(a) O(1) (b) O(eps)

Figure 8.17: Absolute Value of Relative Error in Reconstructed Scalar Flux for the Bare, Six-Assembly MOX Core: Fine Group 7. Results shown are for $\boldsymbol{D}_a$ and $l_{LatVar}(\alpha = 0.8)$. (Note that the scale does not extend to the maximum error in either plot.)

8.5 Flux Reconstruction for a 2-D Non-Uniform Lattice (Problem 6)

Next, we consider a problem in which the core has neither pin nor assembly periodicity. The test problem is a four-assembly colorset with a checkerboard loading of UO2 and MOX assemblies (Problem 6, Section C.6). Both the diffusion and reference MOC calculations have a 7 group energy structure.

Figures 8.18-8.24 show the absolute value of the relative error in the reconstructed scalar fluxes for the four-assembly colorset. There is some small improvement when the asymptotic flux reconstruction is used, particularly for groups 6 and 7. However, the difference between the standard and asymptotic flux reconstructions is considerably smaller for this non-periodic system than it was for the periodic systems. This is not surprising since the assumptions of the asymptotic analysis have been violated.

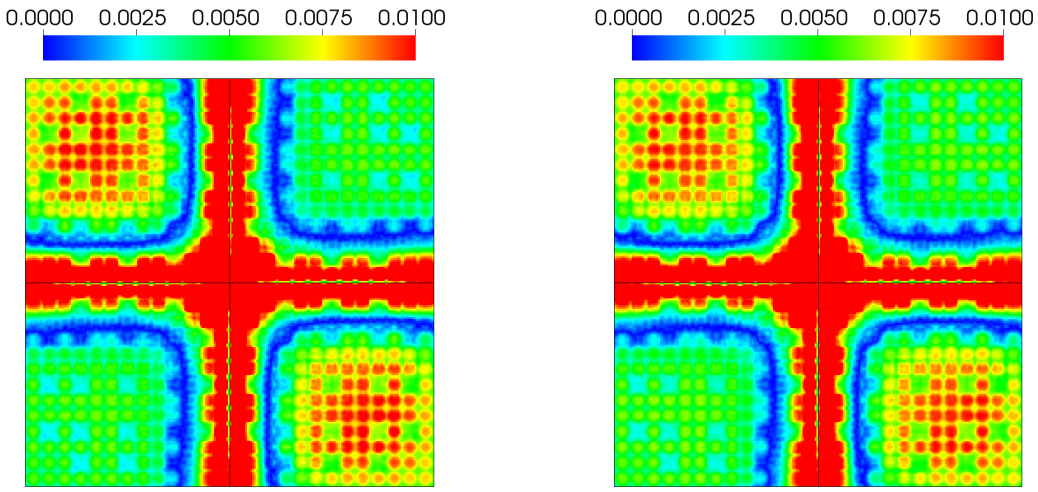

(a) O(1) (b) O(eps)

Figure 8.18: Absolute Value of Relative Error in Reconstructed Scalar Flux for the Four-Assembly Colorset: Fine Group 1. Results shown are for $\boldsymbol{D}_a$ and ab_{Var}. (Note that the scale does not extend to the maximum error in either plot.)

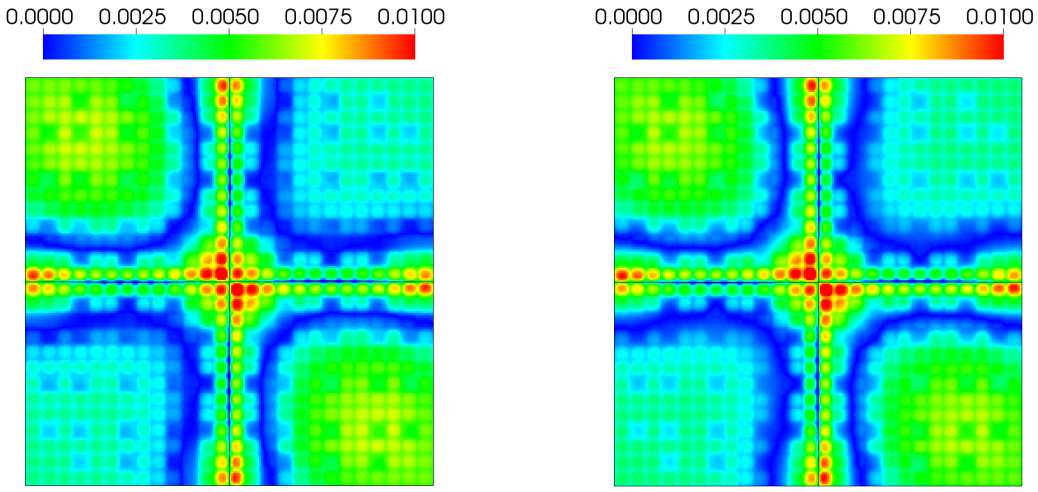

(a) O(1) (b) O(eps)

Figure 8.19: Absolute Value of Relative Error in Reconstructed Scalar Flux for the Four-Assembly Colorset: Fine Group 2. Results shown are for $\boldsymbol{D}_a$ and ab_{Var}. (Note that the scale does not extend to the maximum error in either plot.)

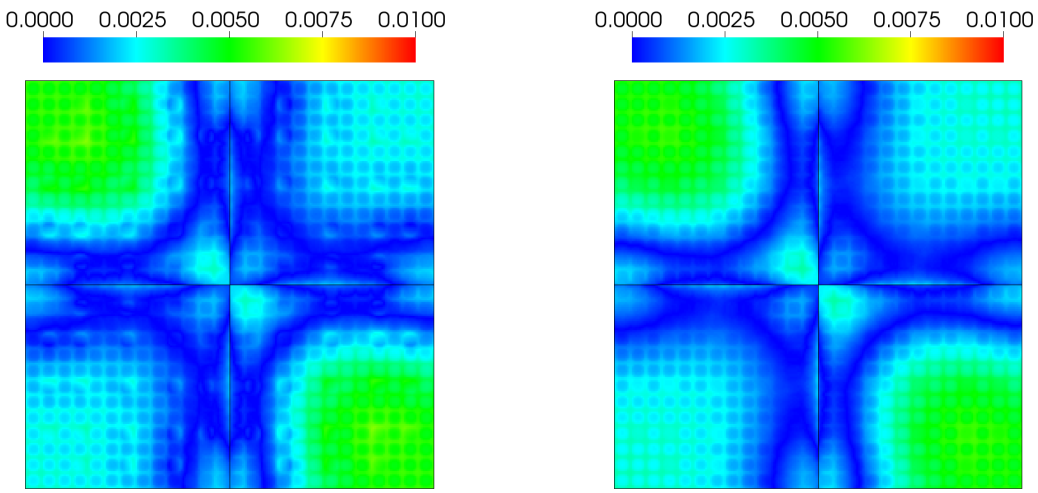

(a) O(1) (b) O(eps)

Figure 8.20: Absolute Value of Relative Error in Reconstructed Scalar Flux for the Four-Assembly Colorset: Fine Group 3. Results shown are for $\boldsymbol{D}_a$ and ab_{Var}.

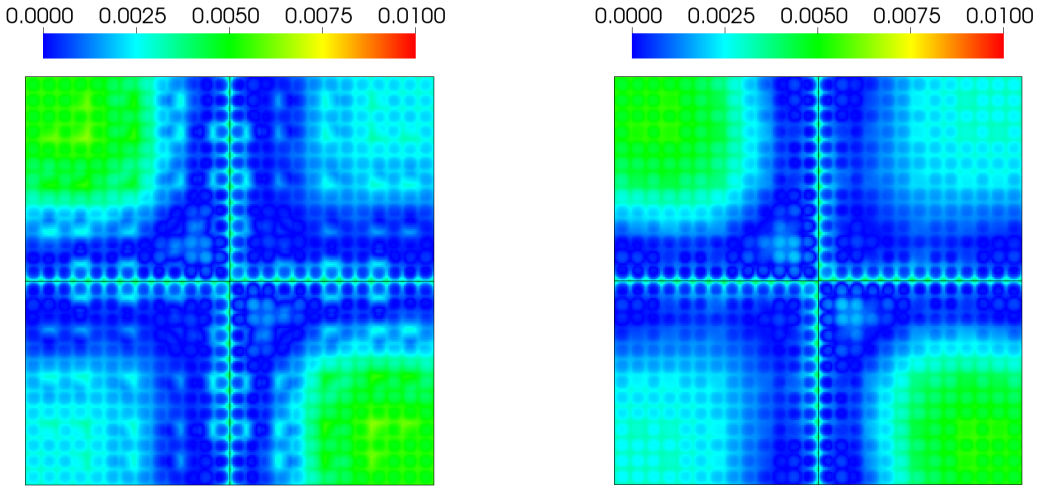

(a) O(1) (b) O(eps)

Figure 8.21: Absolute Value of Relative Error in Reconstructed Scalar Flux for the Four-Assembly Colorset: Fine Group 4. Results shown are for $\boldsymbol{D}_a$ and ab_{Var}.

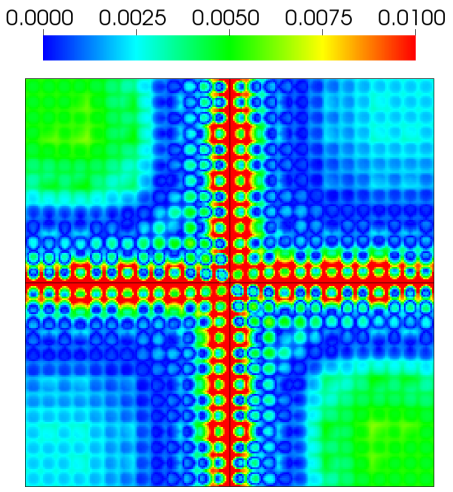

(a) O(1)

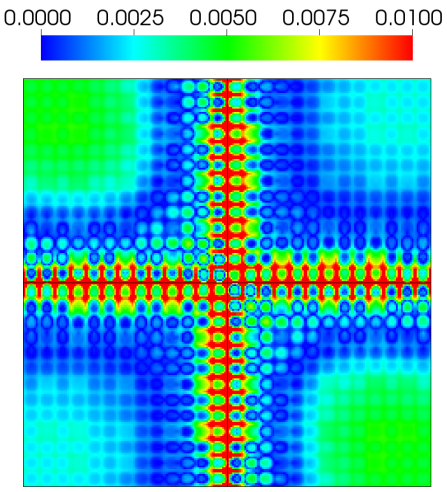

(b) O(eps)

Figure 8.22: Absolute Value of Relative Error in Reconstructed Scalar Flux for the Four-Assembly Colorset: Fine Group 5. Results shown are for $\boldsymbol{D}_a$ and ab_{Var}. (Note that the scale does not extend to the maximum error in either plot.)

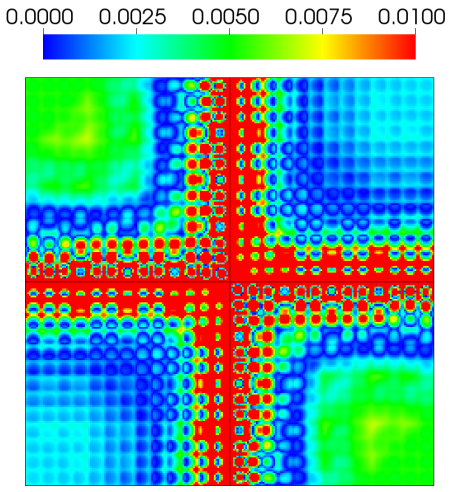

(a) O(1)

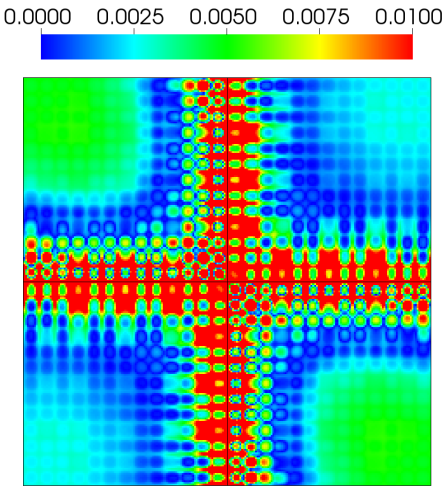

(b) O(eps)

Figure 8.23: Absolute Value of Relative Error in Reconstructed Scalar Flux for the Four-Assembly Colorset: Fine Group 6. Results shown are for $\boldsymbol{D}_a$ and ab_{Var}. (Note that the scale does not extend to the maximum error in either plot.)

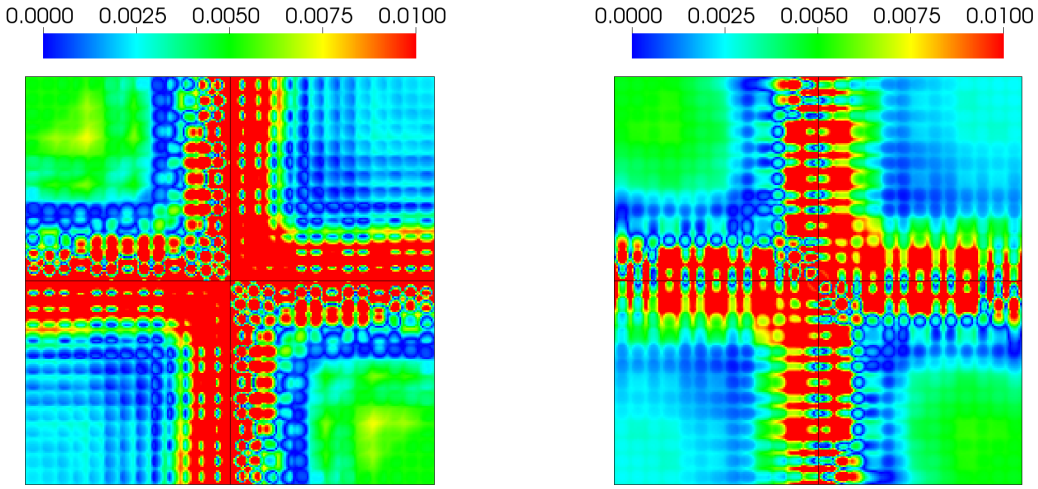

(a) O(1) (b) O(eps)

Figure 8.24: Absolute Value of Relative Error in Reconstructed Scalar Flux for the Four-Assembly Colorset: Fine Group 7. Results shown are for $\boldsymbol{D}_a$ and ab_{Var}. (Note that the scale does not extend to the maximum error in either plot.)

8.6 Flux Reconstruction with the Standard Diffusion Coefficient (Problems 1 and 5)

We now consider what happens if one performs asymptotic flux reconstruction using the standard, rather than asymptotic, diffusion coefficient. This may happen if a diffusion code with direction-dependent diffusion coefficients is not available. Since we use the standard diffusion coefficient, we also use the standard homogeneous variational extrapolation length, l_{HomVar}.

First, we consider the ZPPR test problem (Problem 1, Section C.1). As in Section 8.1, we plot the reconstructed flux divided by the reference S_N solution for the ZPPR lattice with 75 uranium oxide plates, except that now the diffusion solution is obtained using the standard diffusion coefficient rather than the asymptotic diffusion coefficient (Fig. 8.25). Even though the "wrong" diffusion coefficient has been used to obtain the asymptotic solution, the correction term is still effective at reducing errors, particularly in the outer regions of the core.

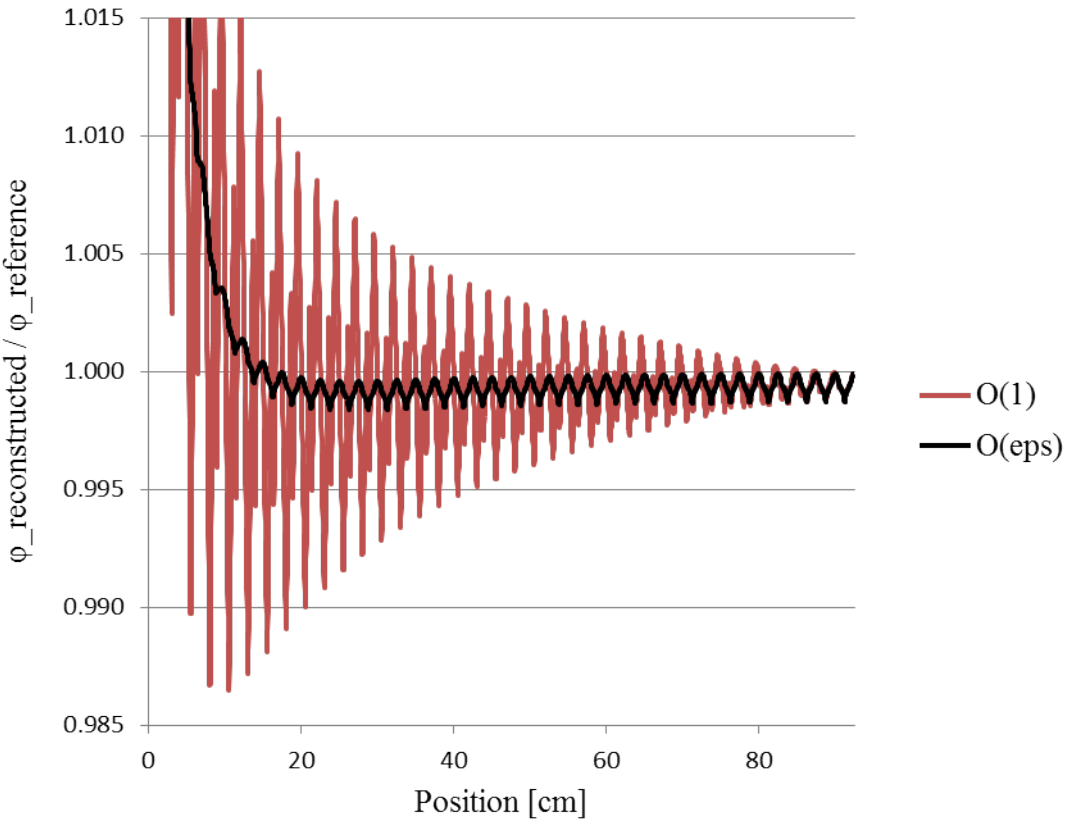

Figure 8.25: Comparison of Flux Reconstruction Methods with the Standard Diffusion Coefficient for the ZPPR Test Problem. The case shown is the ZPPR core with 75 uranium oxide fuel plates (74 uranium plutonium fuel plates). The right edge of the plot corresponds to the mid-plane of the reactor. Results shown are for D_s and l_{HomVar}.

Second, we consider the six assembly test problem in the bare, MOX Configuration (Problem 5, Section C.5). The diffusion energy group structure is the same as the reference MOC energy group structure (7 groups). Figure 8.26 depicts the absolute value of the relative error in the group 7 asymptotic and standard reconstructed fluxes. Comparing to the group 7 reconstructed fluxes using $\boldsymbol{D}_a$ (Fig. 8.17), we see that similar improvements are obtained when the D_s is used. The behavior observed for the groups 1-6 when using $\boldsymbol{D}_a$ (Figs. 8.11-8.16) is also observed when using D_s , so we do not present plots for groups 1-6 here.

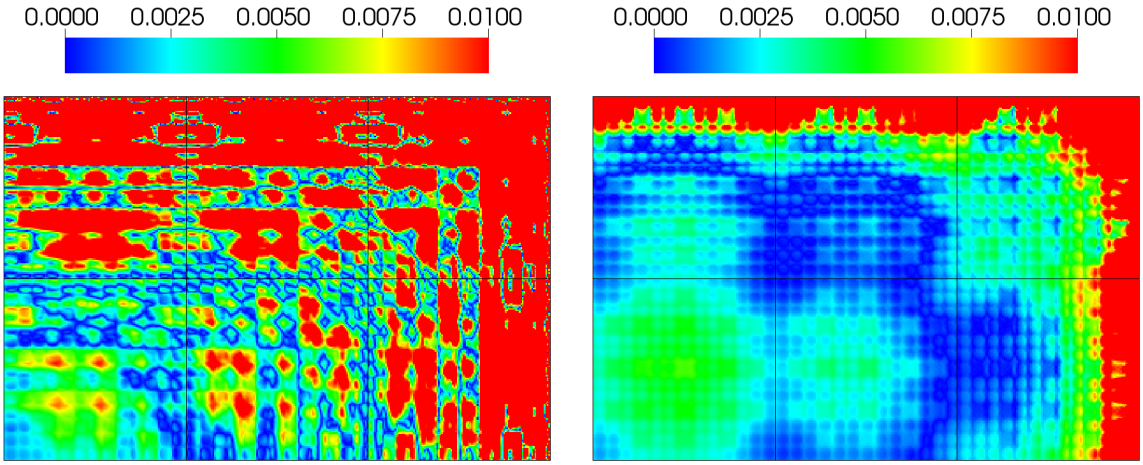

(a) O(1) (b) O(eps)

Figure 8.26: Absolute Value of Relative Error in Reconstructed Scalar Flux for the Bare, Six Assembly MOX Core: Fine Group 7, Standard Diffusion Coefficient. Results shown are for D_s and l_{HomVar}. (Note that the scale does not extend to the maximum error in either plot.)

8.7 Coarse Group Flux Reconstruction (Problem 5: Bare MOX Configuration)

Thus far, we have only considered problems in which the diffusion energy group structure is the same as the reference group structure. In practical applications, diffusion calculations are often performed on a coarser energy grid. One might then ask: is the asymptotic flux reconstruction still effective when the diffusion solution used in the flux reconstruction has a coarse energy group structure?

We consider once again the six assembly test problem in the bare, MOX Configuration (Problem 5, Section C.5). This time, the diffusion energy group structure has only 2 groups (defined in Table B.15). The flux reconstruction is performed for the seven fine groups, and then the fine groups are summed to yield the two coarse group reconstructed fluxes. The absolute value of the relative error in the coarse group fluxes relative to the reference MOC fluxes are shown in Figs. (8.27) and (8.28). We see that the asymptotic reconstructed flux is more accurate than the standard reconstructed flux. The errors in the standard flux reconstruction are

smaller than the asymptotic errors in some places, but higher in others due to the periodic nature of the error when the correction term is not included. However, the improvements in the reconstructed fluxes are less pronounced than when diffusion and transport energy grids are the same.

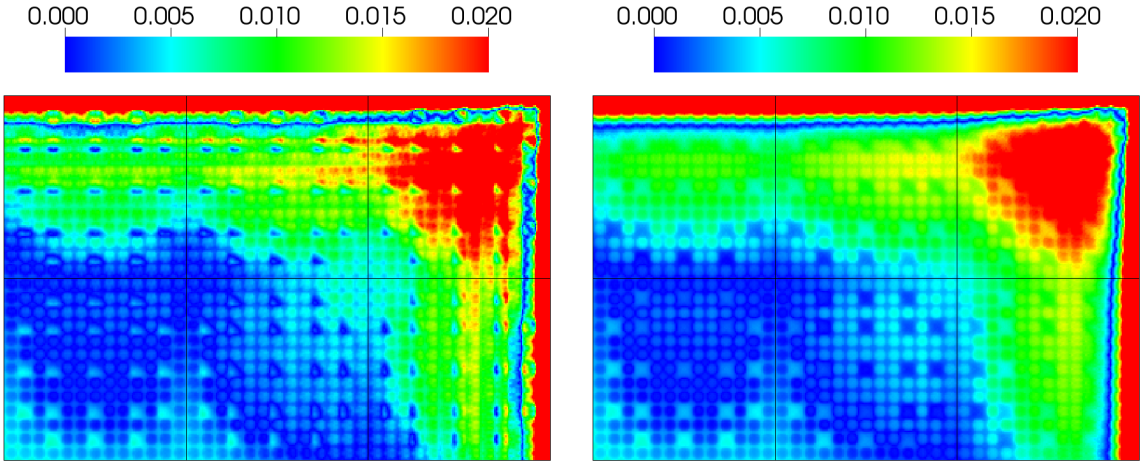

(a) O(1) (b) O(eps)

Figure 8.27: Absolute Value of Relative Error in Reconstructed Scalar Flux: Coarse Group 1. Coarse group 1 fluxes are the sum of fine groups 1-4. Results shown are for $\boldsymbol{D}_a$ and $l_{LatVar}(\alpha = 0.8)$. (Note that the scale does not extend to the maximum error in either plot.)

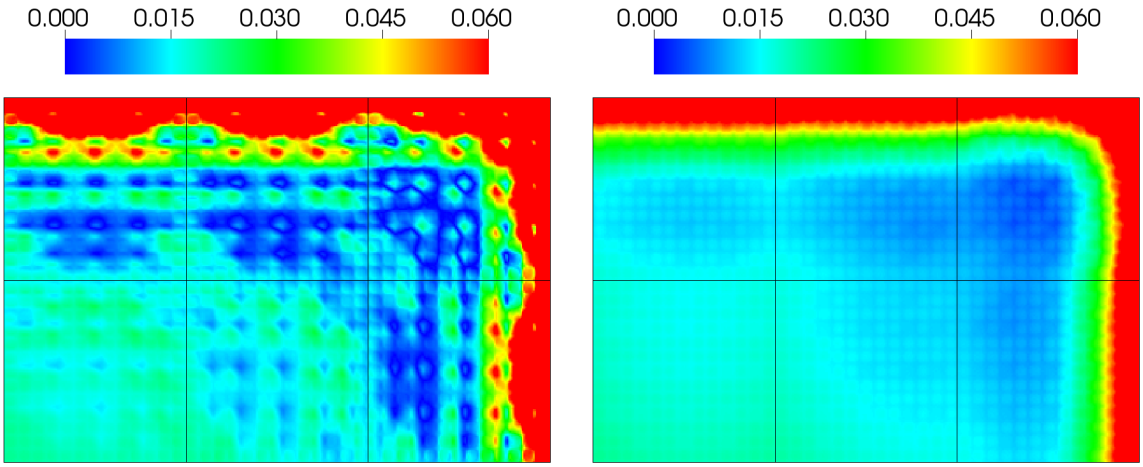

(a) O(1) (b) O(eps)

Figure 8.28: Absolute Value of Relative Error in Reconstructed Scalar Flux: Coarse Group 2. Coarse group 2 fluxes are the sum of fine groups 5-7. Results shown are for $\boldsymbol{D}_a$ and $l_{LatVar}(\alpha = 0.8)$. (Note that the scale does not extend to the maximum error in either plot.)

8.8 Calculation of k and Assembly Powers from Reconstructed Fluxes (Problem 6)

Finally, we calculate the reactor eigenvalue k and assembly powers from the reconstructed fluxes and compare the results to the values obtained directly from the diffusion calculation. The reactor eigenvalue and assembly powers are calculated from the reconstructed fluxes using the procedure described in Section 6.4.3. The test problem is the four-assembly colorset with UO2 and MOX assemblies (Problem 6, Section C.6). Results are obtained for 2 and 7 energy group structures in the diffusion calculation. The 2 group structure is defined in Table B.15.

The absolute errors in the eigenvalue relative to the reference MOC solution are presented in Table 8.1 for seven-group diffusion calculations and in Table 8.2 for two-group diffusion calculations. The seven-group results indicate that calculating k

Table 8.1: Absolute Errors in k Calculated From Diffusion Calculations Compared to Absolute Errors in k Calculated From Reconstructed Fluxes (7 Energy Groups)[1]

Discontinuity Factor	Diffusion Calculation	Standard $O(1)$ Flux	Asymptotic $O(\epsilon)$ Flux
$NoDF$	30	-79	-26
a_0	64	-24	18
$a_0 b_{01}$	-124	-58	-15
a_2	48	-44	0
$a_2 b_{21}$	-151	-80	-35
ab_{PC}	-146	-76	-32
ab_{Var}	-151	-80	-35

[1] All errors shown in pcm. Results shown are for $\boldsymbol{D}_a$. The reference value of k from an MOC calculation is 1.27454.

from asymptotic reconstructed fluxes is always more accurate than calculating k from standard reconstructed fluxes. With most discontinuity factors, values of k calculated from standard reconstructed fluxes are more accurate than values of k obtained directly from the diffusion calculation. The values of k calculated from asymptotic reconstructed fluxes are more accurate than diffusion calculation values for all dis-

continuity factors. From the two-group results, we see again that the asymptotic

Table 8.2: Absolute Errors in k Calculated From Diffusion Calculations Compared to Absolute Errors in k Calculated From Reconstructed Fluxes (2 Energy Groups)[1]

Discontinuity Factor	Diffusion Calculation	Standard $O(1)$ Flux	Asymptotic $O(\epsilon)$ Flux
$NoDF$	-468	-518	-479
a_0	-342	-384	-353
$a_0 b_{01}$	-339	-384	-352
a_2	-368	-412	-378
$a_2 b_{21}$	-363	-412	-378
ab_{PC}	-358	-406	-373
ab_{Var}	-192	-292	-262

[1] All errors shown in pcm. Results shown are for $\boldsymbol{D}_a$. The reference value of k from an MOC calculation is 1.27454.

reconstruction yields more accurate values of k than the standard reconstruction for all discontinuity factor types. However, the values of k obtained directly from the diffusion calculation are always the most accurate. We recall that the coarse-group, homogenized cross sections are defined in such a way that reaction rates are preserved within homogenization regions in the diffusion calculation. It is therefore not surprising that the diffusion calculation would yield more accurate estimates of k which, in the absence of leakage, is a ratio of reaction rates.

Figure. 8.29 shows the reference assembly powers for this problem. The relative errors in assembly powers are shown in Figure 8.30 and 8.31 for the 7 and 2 energy group diffusion calculations respectively. The same trends are observed for the assembly powers that were observed for k: (i) calculating assembly powers from the asymptotic reconstructed flux is always more accurate than calculation them from the standard reconstructed flux (though only slightly), and (ii) the assembly powers obtained directly from the diffusion calculation are less accurate than assembly powers calculated from reconstructed fluxes when the diffusion calculation uses the fine energy group structure, but more accurate when the diffusion calculation uses a

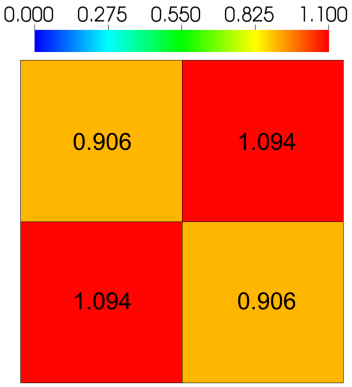

Figure 8.29: Reference Assembly Powers for the Four Assembly Type LWR Test Problem. Numbers indicate normalized power in each assembly.

coarse energy group structure.

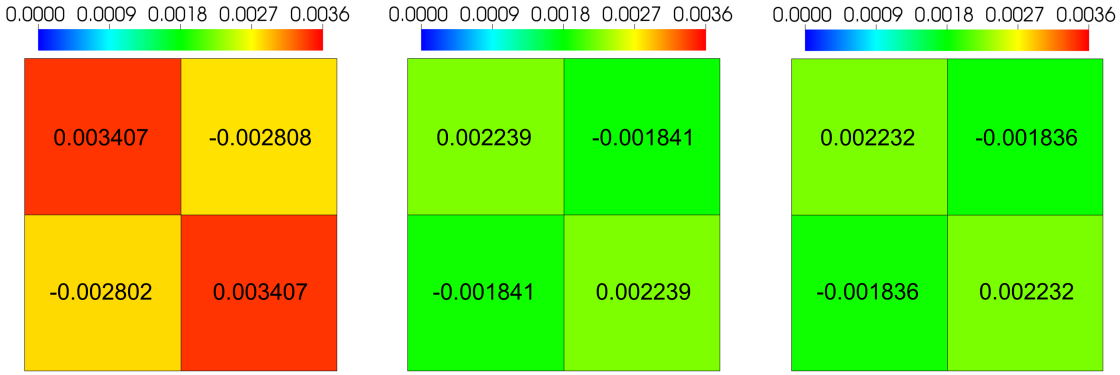

(a) Diffusion Calculation (b) O(1) (c) O(eps)

Figure 8.30: Errors in Assembly Powers Calculated From Diffusion Calculations Compared to Absolute Errors in Assembly Powers Calculated From Reconstructed Fluxes (7 Energy Groups). Numbers indicate relative error values in each assembly. Colors indicate the magnitude of the errors. Results shown are for $\boldsymbol{D}_a$ and ab_{Var}.

8.9 Summary

The numerical results presented in this chapter have shown that asymptotic flux reconstruction is superior to standard flux reconstruction for many problems. We conclude from these results that:

1. In regions where the diffusion solution is slowly varying (i.e., where $\nabla\phi$ is small), the $O(\epsilon)$ correction term is small and the asymptotic and standard reconstructed fluxes are similar.

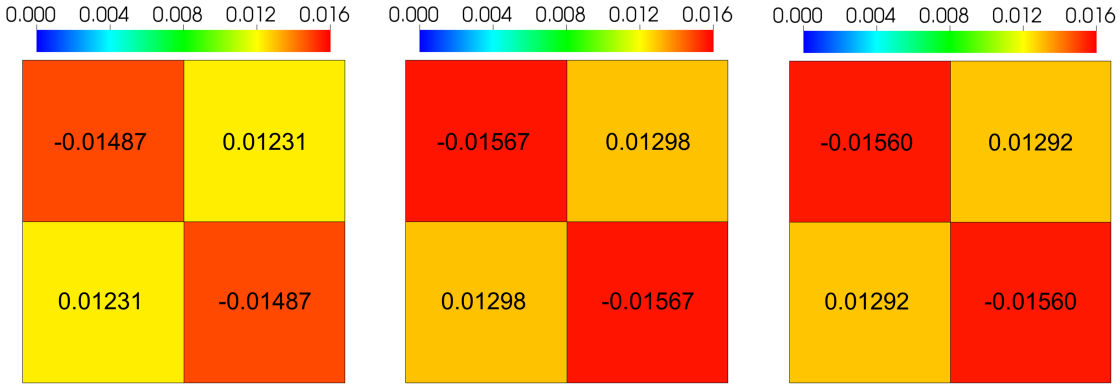

(a) Diffusion Calculation (b) O(1) (c) O(eps)

Figure 8.31: Errors in Assembly Powers Calculated From Diffusion Calculations Compared to Absolute Errors in Assembly Powers Calculated From Reconstructed Fluxes (2 Energy Groups). Numbers indicate relative error values in each assembly. Colors indicate the magnitude of the errors. Results shown are for $\boldsymbol{D}_a$ and ab_{Var}.

2. Conversely, when the diffusion solution is rapidly varying (i.e., where $\nabla\phi$ is large), the $O(\epsilon)$ correction term is large. As a result, the standard reconstructed flux has large, nearly-periodic errors, while asymptotic flux reconstruction nearly eliminates these errors.

3. In energy-dependent problems, the largest improvements of the asymptotic reconstruction over the standard reconstruction occur in energy groups in which the cross sections are large. The larger cross sections mean regions are optically-thick, and the variations in the true flux are stronger. The standard flux reconstruction, which does not include the correction term, is unable to model the stronger variations.

4. The asymptotic flux reconstruction is very effective for periodic and nearly-periodic systems. For nearly-periodic system, the asymptotic flux reconstruction is particularly effective in the regions where the periodicity of the lattice is broken.

5. For systems that are not nearly-periodic, the assumptions of the asymptotic analysis are violated, and, in the worst case, the asymptotic solution becomes

no better than the standard solution. Importantly, in all the problems we have studied, the asymptotic solution is never worse than the standard solution.

6. Asymptotic flux reconstruction is still effective if the standard diffusion coefficient is used to obtain the diffusion solution instead of the asymptotic diffusion coefficient.

7. Asymptotic flux reconstruction can be used effectively with coarse- as well as fine-group diffusion calculations, though the improvements over the standard flux reconstruction are smaller for coarse-group diffusion.

8. The reconstructed fluxes can be used to calculate assembly powers and reactor multiplication factors. The asymptotic reconstructed flux will almost always yield more accurate estimates of these quantities compared to the standard reconstructed flux. However, these quantities can also be obtained directly from the diffusion solution, and this is often more accurate because the homogenized parameters are designed to preserve these integral quantities in the diffusion calculation.

CHAPTER IX

Numerical Results: Comparison of Boundary Conditions

This chapter contains numerical results demonstrating the effectiveness of the variationally-derived vacuum boundary conditions for the asymptotic diffusion equation. We note that practical nuclear reactor cores are not bare; they are surrounded by reflector and shielding materials. Therefore, vacuum boundary conditions for a multiplying lattice medium have limited applications. They may have potential for accident analysis of LWR cores in which some or all of the water reflector boils away. Nevertheless, we study vacuum boundary conditions for lattice systems for completeness of the theory.

In Chapter V we variationally derived extrapolation lengths for lattice systems. The functional used in the variational analysis optimally estimates the reactor multiplication factor, and so the variational extrapolation lengths should yield accurate estimates of this quantity. The exact lattice variational extrapolation lengths are space-dependent, and thus are impractical for reactor analysis. We therefore defined approximate, space-independent extrapolation lengths. We recall that the lattice variational extrapolation lengths depend on a parameter α, and there is no known systematic way to choose the optimal value of this parameter. The extrapolation lengths $l_{LatVar}(\alpha = 1.0)$ and $l_{LatVar}(\alpha = 0.0)$ simplify to the familiar ex-

trapolation lengths l_{Mar} and l_{FP}, while the standard extrapolation lengths l_{HomVar} and l_{Milne} correspond to lattice extrapolation lengths between $l_{LatVar}(\alpha = 0.0)$ and $l_{LatVar}(\alpha = -0.1)$. We study lattice extrapolation lengths with $-0.5 \leq \alpha \leq 1.0$ at intervals of 0.1.

9.1 Comparison of Boundary Conditions for a 1-D Uniform Lattice (Problem 1)

First, we study the ZPPR test problem with 75 uranium oxide fuel plates (Problem 1, Section C.1). In 1-D, no approximations are necessary to make the extrapolation lengths space-independent. Thus, we expect the lattice variational extrapolation lengths to yield accurate results for this 1-D uniform lattice.

The values of the extrapolation lengths are listed in Table 9.1. We see that l_{LatVar} increases monotonically with α.

Table 9.1: Extrapolation Lengths for the ZPPR Test Problem

	Extrapolation Length [cm]
l_{Mar}	5.36007
l_{HomVar}	5.69507
$l_{LatVar}(\alpha = 1.0)$	5.58719
$l_{LatVar}(\alpha = 0.9)$	5.61996
$l_{LatVar}(\alpha = 0.8)$	5.65241
$l_{LatVar}(\alpha = 0.7)$	5.68461
$l_{LatVar}(\alpha = 0.6)$	5.71661
$l_{LatVar}(\alpha = 0.5)$	5.74846
$l_{LatVar}(\alpha = 0.4)$	5.78024
$l_{LatVar}(\alpha = 0.3)$	5.81198
$l_{LatVar}(\alpha = 0.2)$	5.84374
$l_{LatVar}(\alpha = 0.1)$	5.87558
$l_{LatVar}(\alpha = 0.0)$	5.90753
$l_{LatVar}(\alpha = -0.1)$	5.93966
$l_{LatVar}(\alpha = -0.2)$	5.97202
$l_{LatVar}(\alpha = -0.3)$	6.00466
$l_{LatVar}(\alpha = -0.4)$	6.03763
$l_{LatVar}(\alpha = -0.5)$	6.07101

Absolute errors in k for various extrapolation lengths are presented in Table 9.2. This system is reasonably large, so all the extrapolation lengths yield accu-

rate estimates of k. As expected, the variational extrapolation lengths l_{HomVar} and $l_{LatVar}(-0.1 < \alpha < 0.0)$, are more accurate than the Marshak extrapolation lengths, l_{Mar} and $l_{LatVar}(\alpha = 1.0)$ respectively. The lattice extrapolation lengths each outperform their homogeneous counterparts. The error in k decreases monotonically as α increases, even beyond $l_{LatVar}(\alpha = -0.1)$. This is consistent with the findings of Rulko et al., who demonstrated that the extrapolation length that yields the exact eigenvalue is consistently greater than the Milne extrapolation length (corresponding to $\alpha = -0.0815$ in a lattice system) [68].

Table 9.2: Absolute Error in k for the ZPPR Test Problem with Various Extrapolation Lengths[1]

	Error [pcm]
l_{Mar}	-9
l_{HomVar}	-6
$l_{LatVar}(\alpha = 1.0)$	-7
$l_{LatVar}(\alpha = 0.9)$	-6
$l_{LatVar}(\alpha = 0.8)$	-6
$l_{LatVar}(\alpha = 0.7)$	-6
$l_{LatVar}(\alpha = 0.6)$	-5
$l_{LatVar}(\alpha = 0.5)$	-5
$l_{LatVar}(\alpha = 0.4)$	-5
$l_{LatVar}(\alpha = 0.3)$	-4
$l_{LatVar}(\alpha = 0.2)$	-4
$l_{LatVar}(\alpha = 0.1)$	-3
$l_{LatVar}(\alpha = 0.0)$	-3
$l_{LatVar}(\alpha = -0.1)$	-3
$l_{LatVar}(\alpha = -0.2)$	-2
$l_{LatVar}(\alpha = -0.3)$	-2
$l_{LatVar}(\alpha = -0.4)$	-2
$l_{LatVar}(\alpha = -0.5)$	-1

[1] Results shown are for $\boldsymbol{D}_a$. The reference value of k from an S_N calculation is 0.44169.

The ratios of the reconstructed fluxes to the reference transport fluxes for select extrapolation lengths are shown in Figure 9.1. As with the eigenvalues, the variational extrapolation lengths are more accurate than the Marshak extrapolation lengths, and the lattice extrapolation lengths are more accurate than their homogeneous counterparts. Neglecting the outer regions of the core where "boundary layer"

effects render all diffusion solutions inaccurate, the $l_{LatVar}(\alpha = 0.0)$ is the flattest, indicating that this extrapolation length yields a solution that most closely matches the true curvature of the global solution.

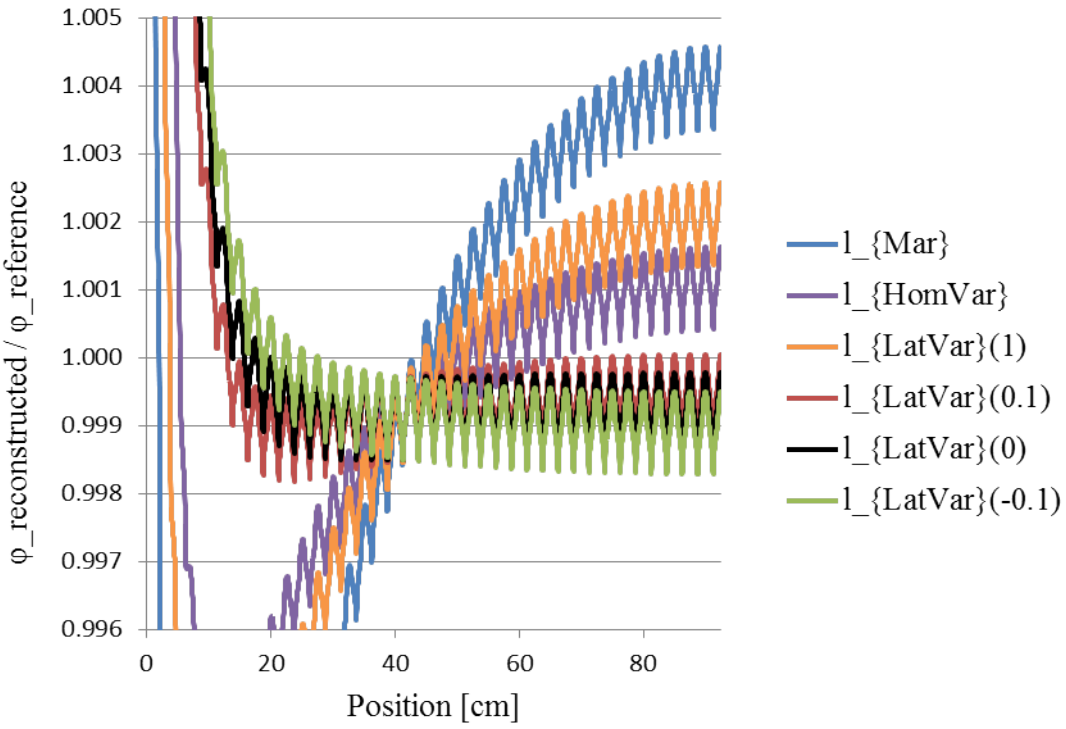

Figure 9.1: Ratio of Reconstructed Fluxes to Reference Fluxes for the ZPPR Test Problem with Various Extrapolation Lengths. Results shown are for asymptotic flux reconstruction and $\boldsymbol{D}_a$.

9.2 Comparison of Boundary Conditions for a 2-D Uniform Pin Lattice (Problem 5: Bare UO2 Configuration)

Next, we consider a multi-dimensional uniform lattice. The test problem is the six-assembly bare core with UO2 fuel pins (Problem 5, Section C.5). Because the variational analysis of Chapter V leads to space-dependent extrapolation lengths for multi-dimensional problems, but for implementation reasons we use approximate, space-independent extrapolation lengths, we expect the performance of the variational extrapolation lengths to be worse for this multidimensional problem. The diffusion calculations for this problem were performed using 2-group (defined by

Table B.15) and 7-group energy structures.

Tables 9.3 and 9.4 present the extrapolation lengths for 2 and 7 energy group structures respectively. For every energy group l_{LatVar} increases monotonically with α. However, the rate at which l_{LatVar} increases varies from one group to another. We note that with multigroup problems, it is possible for the homogeneous extrapolation lengths to be longer than the lattice extrapolation lengths for some groups and shorter for others.

Table 9.3: 2-Group Extrapolation Lengths for the Bare, Six-Assembly UO2 Core[1]

Extrapolation Length	Group 1	Group 2
l_{Mar}	2.10958	0.875119
l_{HomVar}	2.24143	0.929814
$l_{LatVar}(\alpha = 1.0)$	2.13522	0.820342
$l_{LatVar}(\alpha = 0.9)$	2.19505	0.829190
$l_{LatVar}(\alpha = 0.8)$	2.24905	0.837908
$l_{LatVar}(\alpha = 0.7)$	2.29861	0.846607
$l_{LatVar}(\alpha = 0.6)$	2.34471	0.855377
$l_{LatVar}(\alpha = 0.5)$	2.38807	0.864297
$l_{LatVar}(\alpha = 0.4)$	2.42925	0.873445
$l_{LatVar}(\alpha = 0.3)$	2.46869	0.882898
$l_{LatVar}(\alpha = 0.2)$	2.50674	0.892741
$l_{LatVar}(\alpha = 0.1)$	2.54371	0.903064
$l_{LatVar}(\alpha = 0.0)$	2.57987	0.913972
$l_{LatVar}(\alpha = -0.1)$	2.61545	0.925591
$l_{LatVar}(\alpha = -0.2)$	2.65068	0.938068
$l_{LatVar}(\alpha = -0.3)$	2.68578	0.951591
$l_{LatVar}(\alpha = -0.4)$	2.72098	0.966394
$l_{LatVar}(\alpha = -0.5)$	2.75651	0.982782

[1] All extrapolation lengths in cm.

The absolute errors in k for this problem are listed in Table 9.5. For the case of 7-group diffusion, the error in k again decreases monotonically as α increases, even beyond $\alpha = -0.1$ (which roughly corresponds to the traditional variational and Milne extrapolation lengths). However, for the 2-group case, there is an optimal extrapolation length corresponding to $\alpha = 0.4$, which does not correspond to any traditional extrapolation length. There is no systematic way to arrive at this optimal

Table 9.4: 7-Group Extrapolation Lengths for the Bare, Six-Assembly UO2 Core[1]

Extrapolation Length	Group 1	Group 2	Group 3	Group 4	Group 5	Group 6	Group 7
l_{Mar}	3.92995	1.81844	1.25552	1.15366	1.37146	0.891172	0.495458
l_{HomVar}	4.17557	1.93209	1.33399	1.22577	1.45717	0.946871	0.526424
$l_{LatVar}(\alpha = 1.0)$	3.96269	1.83509	1.25598	1.15443	1.35820	0.863587	0.444247
$l_{LatVar}(\alpha = 0.9)$	4.01769	1.84772	1.26235	1.16011	1.36586	0.866933	0.445256
$l_{LatVar}(\alpha = 0.8)$	4.06330	1.85954	1.26852	1.16564	1.37322	0.870252	0.446284
$l_{LatVar}(\alpha = 0.7)$	4.10214	1.87074	1.27457	1.17110	1.38039	0.873584	0.447343
$l_{LatVar}(\alpha = 0.6)$	4.13593	1.88149	1.28057	1.17654	1.38745	0.876961	0.448447
$l_{LatVar}(\alpha = 0.5)$	4.16582	1.89188	1.28655	1.18200	1.39445	0.880413	0.449607
$l_{LatVar}(\alpha = 0.4)$	4.19266	1.90202	1.29257	1.18752	1.40145	0.883972	0.450839
$l_{LatVar}(\alpha = 0.3)$	4.21704	1.91198	1.29868	1.19316	1.40849	0.887667	0.452158
$l_{LatVar}(\alpha = 0.2)$	4.23943	1.92183	1.30491	1.19894	1.41563	0.891532	0.453583
$l_{LatVar}(\alpha = 0.1)$	4.26019	1.93163	1.31131	1.20491	1.42290	0.895605	0.455138
$l_{LatVar}(\alpha = 0.0)$	4.27959	1.94144	1.31792	1.21112	1.43037	0.899931	0.456852
$l_{LatVar}(\alpha = -0.1)$	4.29788	1.95133	1.32480	1.21762	1.43808	0.904561	0.458763
$l_{LatVar}(\alpha = -0.2)$	4.31524	1.96134	1.33201	1.22448	1.44610	0.909560	0.460920
$l_{LatVar}(\alpha = -0.3)$	4.33184	1.97154	1.33961	1.23176	1.45449	0.915006	0.463390
$l_{LatVar}(\alpha = -0.4)$	4.34783	1.98201	1.34770	1.23957	1.46333	0.921001	0.466266
$l_{LatVar}(\alpha = -0.5)$	4.36334	1.99283	1.35637	1.24801	1.47273	0.927679	0.469680

[1] All extrapolation lengths in cm.

value, which is different for different problems and different energy group structures. It is only found by comparing the diffusion solution to an already known transport solution. This makes choosing a value of α problematic, as the transport solution is generally not available.

Figure 9.2 shows the reference assembly powers for this problem. The relative errors in the assembly powers for the 2 and 7 energy group structures are presented in Figs. 9.3 and 9.4 respectively.

In the 2-group case, the lattice "Marshak" extrapolation length ($\alpha = 1.0$) is more accurate than the standard Marshak extrapolation length. The optimal lattice variational extrapolation length is in the vicinity of $\alpha = 0.7$ or $\alpha = 0.8$. Thus, the extrapolation lengths that are optimal for estimating k are different than those that are optimal for estimating assembly powers. The assembly powers become progressively worse for $\alpha < 0.7$. The traditional variational extrapolation length

Table 9.5: Absolute Error in k for the Bare, Six-Assembly UO2 Core with Various Extrapolation Lengths[1]

Extrapolation Length	2 Energy Groups	7 Energy Groups
l_{Mar}	-166	-242
l_{HomVar}	-88	-157
$l_{LatVar}(\alpha = 1.0)$	-157	-237
$l_{LatVar}(\alpha = 0.9)$	-124	-225
$l_{LatVar}(\alpha = 0.8)$	-95	-214
$l_{LatVar}(\alpha = 0.7)$	-67	-204
$l_{LatVar}(\alpha = 0.6)$	-42	-195
$l_{LatVar}(\alpha = 0.5)$	-18	-186
$l_{LatVar}(\alpha = 0.4)$	4	-179
$l_{LatVar}(\alpha = 0.3)$	26	-171
$l_{LatVar}(\alpha = 0.2)$	47	-164
$l_{LatVar}(\alpha = 0.1)$	68	-157
$l_{LatVar}(\alpha = 0.0)$	88	-150
$l_{LatVar}(\alpha = -0.1)$	107	-143
$l_{LatVar}(\alpha = -0.2)$	127	-137
$l_{LatVar}(\alpha = -0.3)$	147	-130
$l_{LatVar}(\alpha = -0.4)$	167	-123
$l_{LatVar}(\alpha = -0.5)$	187	-116

[1] All errors in pcm. Results shown are for $\boldsymbol{D}_a$. The reference value of k from an MOC calculation is 1.19605.

yields more accurate assembly powers than all other extrapolation lengths tested here.

In the 7-group case, the lattice "Marshak" and standard Marshak extrapolation lengths yield nearly identical assembly powers. Once again, the optimal lattice variational extrapolation length is in the vicinity of $\alpha = 0.7$ or $\alpha = 0.8$, which is different than the optimal extrapolation length for estimating k. Unlike the ZPPR and 2-group cases, and contrary to conventional wisdom, the homogeneous variational extrapolation length is *worse* than the standard Marshak extrapolation length. Thus, the inconsistencies in the effectiveness of the extrapolation lengths for this multi-dimensional problem extend to conventional extrapolation lengths as well as the lattice variational extrapolation lengths.

Unfortunately, it seems that there is not a systematic method for selecting an

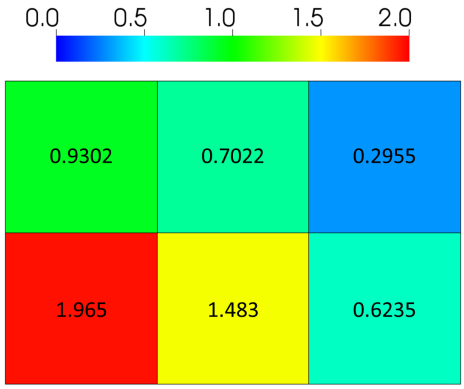

Figure 9.2: Reference Assembly Powers for the Bare, Six-Assembly UO2 Core. Numbers indicate normalized power in each assembly.

extrapolation length that optimally estimates both the reactor multiplication factor *and* the assembly powers. Evidently, space-independent extrapolation lengths are not capable of fully modeling multi-dimensional systems in which there are space-dependent boundary effects.

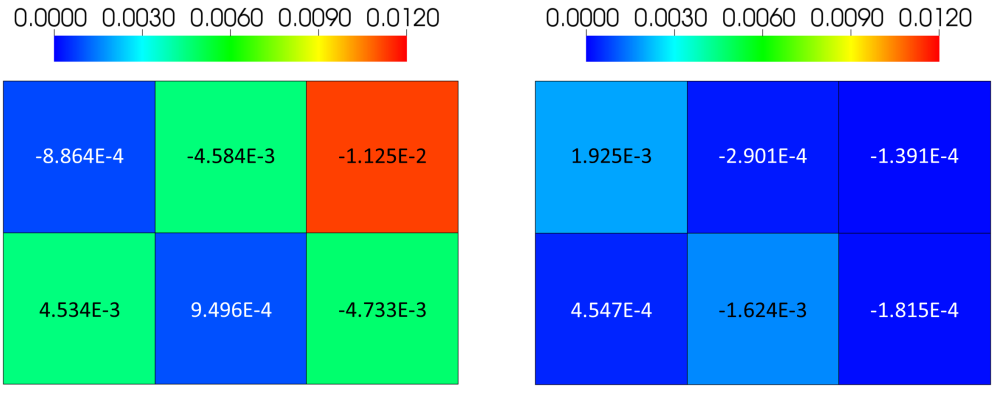

(a) l_{Mar}

(b) l_{HomVar}

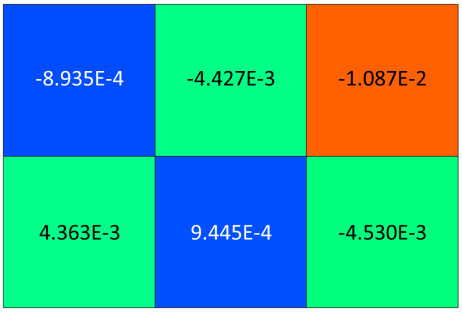

(c) $l_{LatVar}(\alpha = 1.0)$

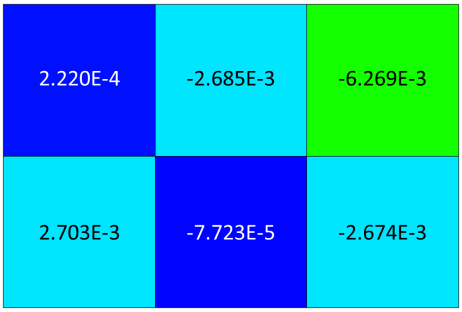

(d) $l_{LatVar}(\alpha = 0.9)$

(e) $l_{LatVar}(\alpha = 0.8)$

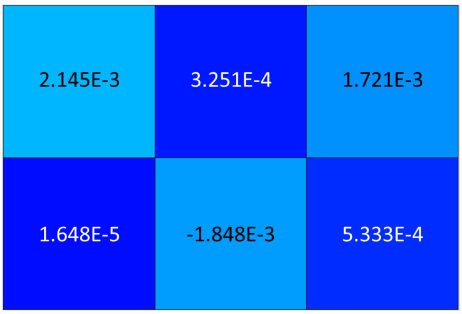

(f) $l_{LatVar}(\alpha = 0.7)$

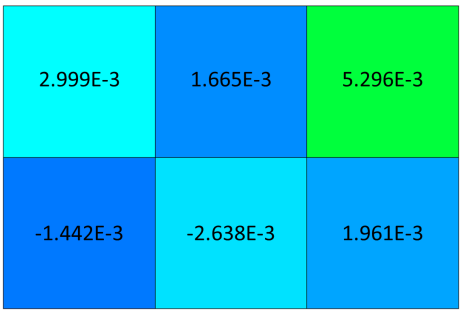

(g) $l_{LatVar}(\alpha = 0.6)$

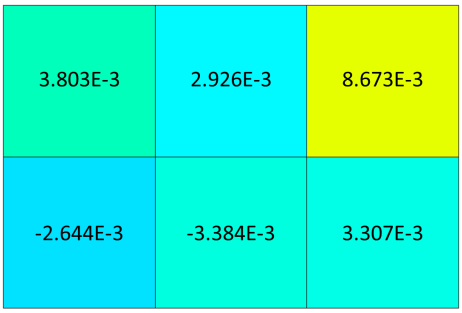

(h) $l_{LatVar}(\alpha = 0.5)$

Figure 9.3: Errors in Assembly Powers for the Bare, Six-Assembly UO2 Core with Various Extrapolation Lengths (2 Energy Groups). Numbers indicate relative error values in each assembly. Colors indicate the magnitude of the errors. Results shown are for $\boldsymbol{D}_a$.

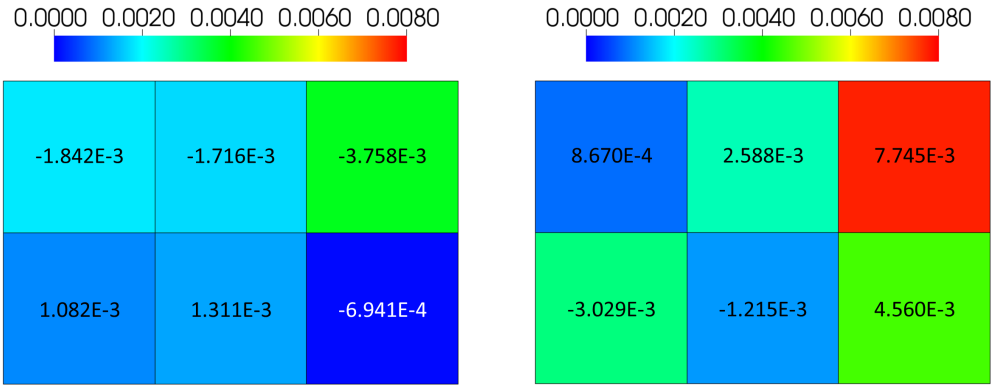

(a) l_{Mar}

(b) l_{HomVar}

(c) $l_{LatVar}(\alpha = 1.0)$

(d) $l_{LatVar}(\alpha = 0.9)$

(e) $l_{LatVar}(\alpha = 0.8)$

(f) $l_{LatVar}(\alpha = 0.7)$

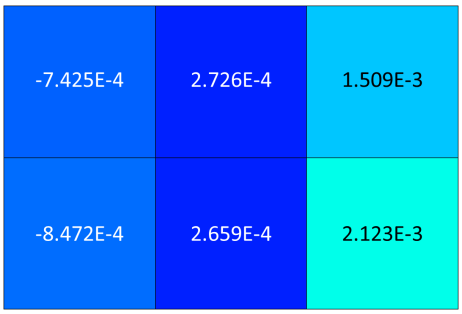

(g) $l_{LatVar}(\alpha = 0.6)$

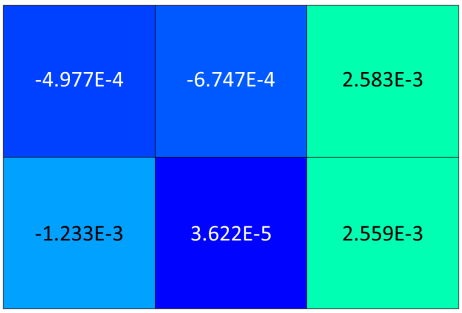

(h) $l_{LatVar}(\alpha = 0.5)$

Figure 9.4: Errors in Assembly Powers for the Bare, Six-Assembly UO2 Core with Various Extrapolation Lengths (7 Energy Groups). Numbers indicate relative error values in each assembly. Colors indicate the magnitude of the errors. Results shown are for $\boldsymbol{D}_a$.

9.3 Summary

In this chapter, we analyzed the effectiveness of variationally-derived vacuum boundary conditions for lattice systems. Vacuum boundaries are particularly challenging for the any diffusion method because the flux is strongly anisotropic near the vacuum boundary. The addition of a reflector around reactor cores renders boundary conditions for lattice systems irrelevant, and improves the performance of diffusion methods. However, it introduces the need for interface conditions (i.e., DFs), and these are discussed in Chapter X.

We have seen that the lattice variational boundary conditions are effective for 1-D problems. The lattice variational extrapolation lengths $l_{LatVar}(\alpha = 1.0)$ and $l_{LatVar}(\alpha = 0.0)$ yield more accurate fluxes than the standard extrapolation lengths l_{Mar} and l_{HomVar} for 1-D problems. Estimates of the reactor multiplication factor improve steadily as the extrapolation length increases, even beyond $l_{LatVar}(\alpha = 0.0)$. This is consistent with the findings of Rulko et al. who found that extrapolation lengths that give the exact reactor multiplication factor are consistently longer than the Milne extrapolation length [68].

Unfortunately, for multidimensional, multigroup problems, the results are less clear. The optimal extrapolation length for estimating the reactor multiplication factor varies with the diffusion energy group structure, while the optimal extrapolation length for estimating assembly powers is roughly between $l_{LatVar}(\alpha = 0.7)$ and $l_{LatVar}(\alpha = 0.8)$, which does not correspond to any standard extrapolation length. Thus, there appears to be no systematic way to choose an optimal value of α for multidimensional problems.

We note that the standard extrapolation lengths also do not perform well for

multidimensional problems. In particular, l_{HomVar}, which is widely believed to be more accurate than l_{Mar}, is in fact less accurate for some multi-dimensional lattice problems.

It seems that because multi-dimensional lattice problems have space-dependent boundary effects along the boundary of the system, space-independent extrapolation lengths lead to unpredictable errors in diffusion solutions. Space-dependent extrapolation lengths have not been determined to be practical, and reactor analysts have made do with space-independent extrapolation lengths. We recall that the space-independent extrapolation lengths used in this chapter are calculated using the surface-averaged lattice functions $f_{0,i,k}$, $f^*_{0,i,k}$, $\boldsymbol{f}_{1,i,k}$, and $\boldsymbol{f}^*_{1,i,k}$. It would have been more accurate to use the surface-averaged compound lattice functions $(f_{0,i}f^*_{0,i})_k$, $(\boldsymbol{f}_{1,i}f^*_{0,i})_k$, $(f_{0,i}\boldsymbol{f}^*_{1,i})_k$, and $(\boldsymbol{f}_{1,i}\boldsymbol{f}^*_{1,i})_k$. It is possible that doing this would reduce some errors in the multi-dimensional problems. However, the optimal value of α would most likely still be problem-dependent.

At present, there is no known systematic method for choosing an optimal extrapolation length. For 1-D problems, the lattice variational extrapolation lengths with $-0.1 \leq \alpha \leq 0.0$ seem to yield consistent, accurate results. For multi-dimensional problems, we are forced to choose between an accurate flux solution and an accurate estimate of the reactor multiplication factor. Even after making this choice, the optimal value of α varies from one problem to another. For the time being, it is recommended to continue using the traditional homogeneous variational or Milne extrapolation lengths. Fortunately, nuclear reactor cores are virtually never designed without a reflector surrounding the core, and so the question of how to choose an optimal boundary condition for such a problem is, for now, merely academic.

CHAPTER X

Numerical Results: Comparison of Discontinuity Factors

In this chapter, we present numerical results demonstrating the effectiveness of various discontinuity factors for a wide range of problems. We isolate the effects of changing the discontinuity factor by presenting results only for the asymptotic diffusion coefficient. At vacuum boundaries for lattice regions in 1-D problems, we use the extrapolation length $l_{LatVar}(\alpha = 0.0)$ because it yields the most accurate results (see Section 9.1). No bare, multi-dimensional lattices are studied in this chapter. The extrapolation length l_{HomVar} is applied to vacuum boundaries on homogeneous regions. The DFs are material- and group-dependent, and to reduce the volume of data presented, we show the values of the DFs only for one-group problems.

We recall from Chapter V that DFs were defined to make specified angular moments of the asymptotic reconstructed flux continuous across an interface. These moments included the scalar flux, current, and second angular moment (which boundary layer analysis shows must be constant in a large, homogeneous medium). The DFs that make the scalar flux continuous are equivalent to the standard assembly discontinuity factors (ADFs) used frequently in reactor analysis. Discontinuity factors were also derived variationally. The functional defined in the variational analysis was designed to optimally estimate the reactor eigenvalue, and so the variational disconti-

nuity factors should yield good estimates of this quantity. However, approximations were made in order to define multigroup, space-independent discontinuity factors. These approximations reduce the accuracy of the DFs. Finally, we recall that the asymptotic DFs allow the flux *and* current to be discontinuous in the homogenized diffusion calculation, while typical reactor analysis uses only flux DFs.

10.1 Comparison of Discontinuity Factors for a 1-D, Two Pin Type Test (Problem 2: Configurations 1 and 2)

Our first test is a 1-D problem with two adjacent uniform lattice regions (Problem 2, Section C.2). In this section we consider Configurations 1 and 2, which consist of fuel-centered pins in the left half of the problem and moderator-centered pins in the right half. Configuration 1 has reflecting boundaries on all sides, while Configuration 2 has a reflecting left boundary and vacuum right boundary.

The pins consist of the same materials and thicknesses; the definition of a cell is merely shifted such that the fuel is in the center of the pin for the left assembly, and the moderator is in the center of the pin for the right assembly. Thus, the homogenized parameters are identical in each assembly. If both boundaries are reflecting, then the diffusion solution is a constant, and current DFs have no effect. Therefore, no current DFs are used for Configuration 1. Furthermore, since the Configuration 1 solution is constant, the eigenvalue $k = \overline{\nu\Sigma_f}/\overline{\Sigma_a}$ is the same for all DFs, and they so the eigenvalues are not presented.

The DFs for this problem are presented in Table 10.1. Although the magnitudes of the non-standard DFs (a_2, b_{21}, ab_{PC}, and ab_{Var}) are very different than the magnitudes of the standard DF (a_0), the ratios of the DFs on each side of the interface are close to unity for all DFs. Since it is the ratio of the DFs across an interface that determines the magnitude of the discontinuity in the diffusion solution, each

Table 10.1: Discontinuity Factors for the 1-D DF Test Problem

Discontinuity Factor	Fuel-Centered		Moderator-Centered		Ratio[1]	
	a	b [2]	a	b [2]	a	b
$NoDF$	1.00000	1.00000	1.00000	1.00000	1.00000	1.00000
a_0	0.979417	1.02102	1.01184	0.988295	0.967956	1.03311
$a_0 b_{01}$	0.979417	1.04607	1.01184	0.997880	0.967956	1.04829
a_2	0.328268	3.04629	0.333096	3.00214	0.985506	1.01471
$a_2 b_{21}$	0.328268	3.12105	0.333096	3.03126	0.985506	1.02962
ab_{PC}	0.491972	2.08252	0.501639	2.01280	0.980729	1.03464
ab_{Var} [3]	0.100069	5.07833	0.101540	4.93225	0.985513	1.02962

[1] Fuel-centered divided by moderator-centered.
[2] $b = 1/a$ if there is no current discontinuity.
[3] Variational DF for one pin type assuming its neighbor is the other pin type.

set of DFs will yield diffusion solutions that are different, but not radically so. The ab_{Var} DFs have the nearly same a and b ratios across the interface as the $a_2 b_{21}$ DFs. This was predicted in Section 5.4.4, where it was shown that for 1-D, monoenergetic problems, the $a_2 b_{21}$ and ab_{Var} DFs are equivalent. The slight difference in the a ratios across the interface is likely due to numerical errors in the calculation of the lattice functions.

The reference S_N scalar flux and the reconstructed scalar fluxes (*not* the ratio of the reconstructed fluxes to the reference solution) for Configuration 1 are plotted in Fig. 10.1. Applying flux reconstruction to the problem is equivalent to multiplying the lattice solution by the constant diffusion solution. However, the lattice solution for the moderator-centered pins is shifted half the width of a pin cell compared to the fuel-centered pins, so there is a discontinuity in the reconstructed flux at the interface. The standard ADFs (a_0) force the reconstructed flux to be continuous, but this is an overcorrection for this problem. The non-standard a_2 DFs nearly perfectly match the reference solution except within roughly a quarter-pin-width of the interface. It was shown in Section 5.4.4 that for 1-D, monoenergetic problems, $a_2 b_{21}$ (or in this case, a_2 since the current is 0 everywhere) and ab_{Var} are equivalent,

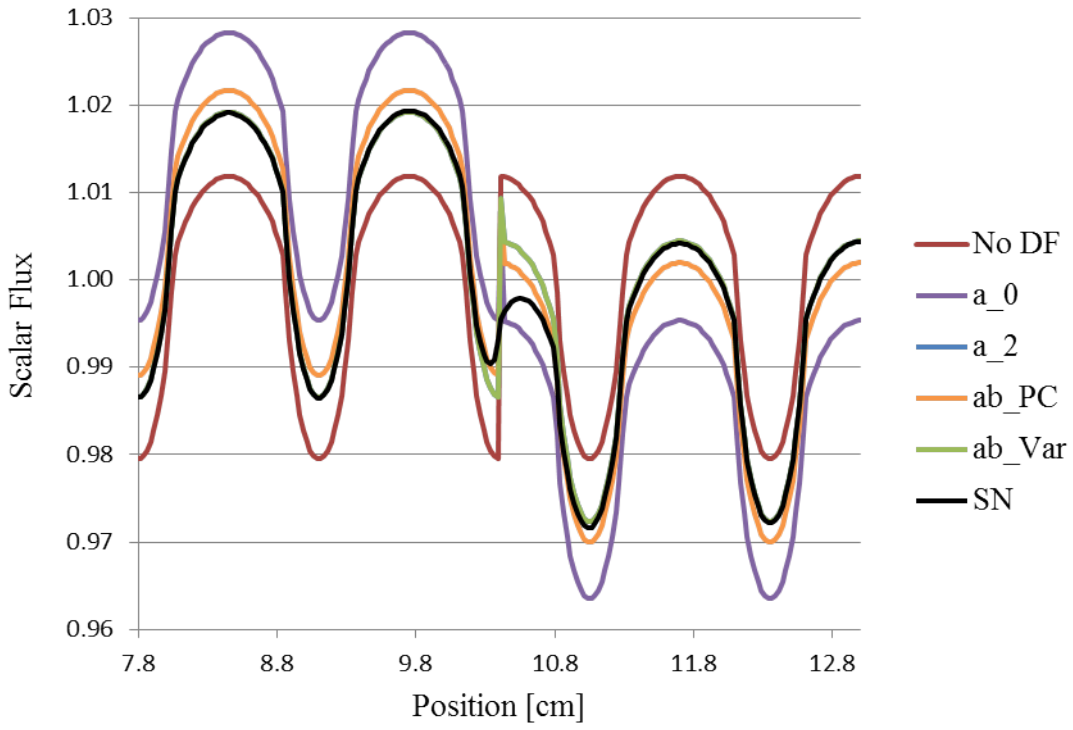

Figure 10.1: Reconstructed Scalar Flux for the 1-D DF Test Problem (Configuration 1) with Various Discontinuity Factors. Results shown are for asymptotic flux reconstruction and $\boldsymbol{D}_a$. The a_2 and ab_{Var} fluxes are nearly identical to the reference S_N flux, and are difficult to distinguish from the S_N flux except near the interface at 10.4 cm.

and this is confirmed in Fig. 10.1 (the a_2 solution lies beneath the ab_{Var} solution). Finally, the ab_{PC} DFs perform similarly to the a_2 and ab_{Var} DFs, though they are slightly less accurate.

Viewing the Configuration 1 results in another way, we present the ratio of the reconstructed fluxes to the reference solution in Fig. 10.2. Not using DFs results in underprediction of the flux in the left assembly and overprediction in the right assembly. The standard ADFs overcorrect and the situation is reversed. Discontinuity factors for continuity of the partial current (ab_{PC}) are significantly more accurate than $NoDF$ and a_0. The a_2 and ab_{Var} solutions are superior to all other DFs, and the ratios of the reconstructed fluxes to the reference flux are nearly uniformly unity, except in the immediate vicinity of the interface.

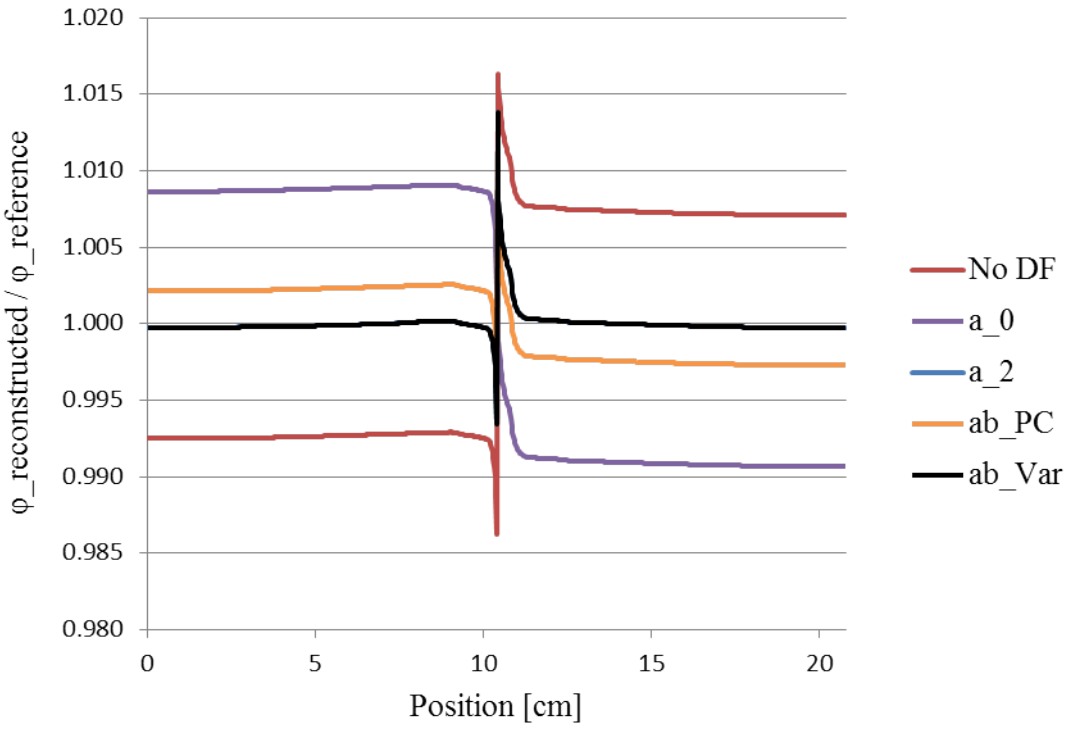

Figure 10.2: Ratio of Reconstructed Fluxes to Reference Fluxes for the 1-D DF Test Problem (Configuration 1) with Various Discontinuity Factors. Results shown are for asymptotic flux reconstruction and $\boldsymbol{D}_a$. The a_2 and ab_{Var} fluxes are identical.

Table 10.2: Absolute Error in k for the 1-D DF Test Problem (Configuration 2) with Various Discontinuity Factors[1]

Discontinuity Factor	Error [pcm]
$NoDF$	-18
a_0	2
$a_0 b_{01}$	11
a_2	-10
$a_2 b_{21}$	-1
ab_{PC}	2
ab_{Var}	-1

[1] Results shown are for $\boldsymbol{D}_a$. The reference value of k from an S_N calculation is 1.71105.

We now turn our attention to Configuration 2. Absolute errors in k for Configuration 2 are listed in Table 10.2. The results indicate that not using any DFs yields the least accurate estimate of k, while the $a_2 b_{21}$ and ab_{Var} DFs (which are the same for 1-D, monoenergetic problems) yield the most accurate estimate of k, though only

by a slim margin.

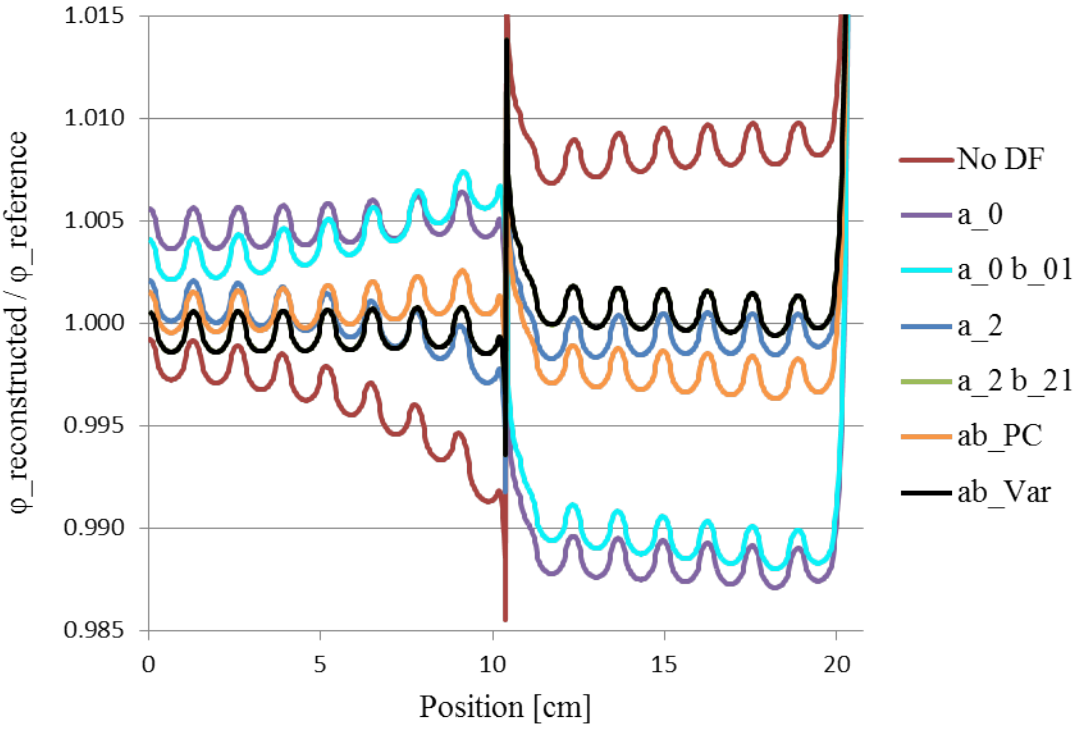

Figure 10.3: Ratio of Reconstructed Fluxes to Reference Fluxes for the 1-D DF Test Problem (Configuration 2) with Various Discontinuity Factors. Results shown are for asymptotic flux reconstruction and $\boldsymbol{D}_a$. The a_2b_{21} and ab_{Var} fluxes are identical.

Because of the vacuum boundary condition, the diffusion solution does have a gradient, and current DFs will now have an effect. Figure 10.3 depicts the ratio of the reconstructed scalar fluxes to the reference scalar flux for this configuration. As before, not using any DFs results in a large discontinuity in the reconstructed flux at the interface, and standard ADFs overcorrect for the problem. The ab_{PC} DFs offer a significant improvement over the standard a_0 DFs, but are still slightly less accurate than the a_2 DFs. In this case, the use of current DFs (a_0b_{01}, a_2b_{21}) yields a slight improvement compared to only using flux DFs (a_0, a_2). Again, ab_{Var} and a_2b_{21} are identical, and these are the most accurate DFs.

10.2 Comparison of Discontinuity Factors for a 2-D, Two Assembly Type Tests

Next, we consider multi-dimensional lattice cores with multiple assembly types. The numerical results indicate that the non-standard asymptotic discontinuity factors can yield accurate results for multi-dimensional problems. Not surprisingly, they may not perform as well when neighboring assemblies have significantly different energy spectra. In these cases, it may be necessary to generate DFs using colorset calculations.

10.2.1 Contiguous Loading of Like Assembly Types (Problem 8)

We first consider an LWR core in which assembly composition changes occur only every four assemblies (Problem 8, Section C.8). Since the materials are periodic across groups of four assemblies, the asymptotic discontinuity factors for periodic systems perform quite well. The diffusion calculation uses the 2, 5, and 10 energy group structures defined in Tables B.17-B.19 respectively.

Table 10.3 lists the absolute errors in k for this problem. The errors are all so small that it is difficult to say how much better one set of DFs is than another. Nevertheless, we can see that: (i) not using any DFs results in the largest error, (ii) flux and current DFs used together yields smaller errors than flux DFs alone, (iii) the lattice variational DFs do not give the most accurate estimates of k, but are still accurate.

The reference assembly powers for this problem are shown in Fig. 7.3. Relative errors for each set of DFs for the 2, 5, and 10 group diffusion calculations are shown in Figs. 10.4-10.6. For each energy group structure: (i) not using any DFs results in the largest errors, (ii) the DFs for continuity of the second moment always yield lower maximum errors and lower errors in the peak power assembly (4th assembly from

Table 10.3: Absolute Error in k for the Two Assembly Type LWR Test Problem with Various Discontinuity Factors[1]

Discontinuity Factor	2 Energy Groups	5 Energy Groups	10 Energy Groups
$NoDF$	-6	-26	-11
a_0	-3	-23	-7
$a_0 b_{01}$	-1	-18	-4
a_2	-2	-23	-7
$a_2 b_{21}$	-1	-18	-4
ab_{PC}	-1	-19	-5
ab_{Var}	-3	-19	-5

[1] All errors in pcm. Results shown are for $\boldsymbol{D}_a$. The reference value of k from an MOC calculation is 1.08819.

the left) than the DFs for continuity of the scalar flux, (iii) using flux and current DFs results in lower maximum errors and lower errors in the peak power assembly than the flux DFs alone, and (iv) the variational DFs give the lowest maximum error and lowest error in the peak power assembly compared to all other DFs.

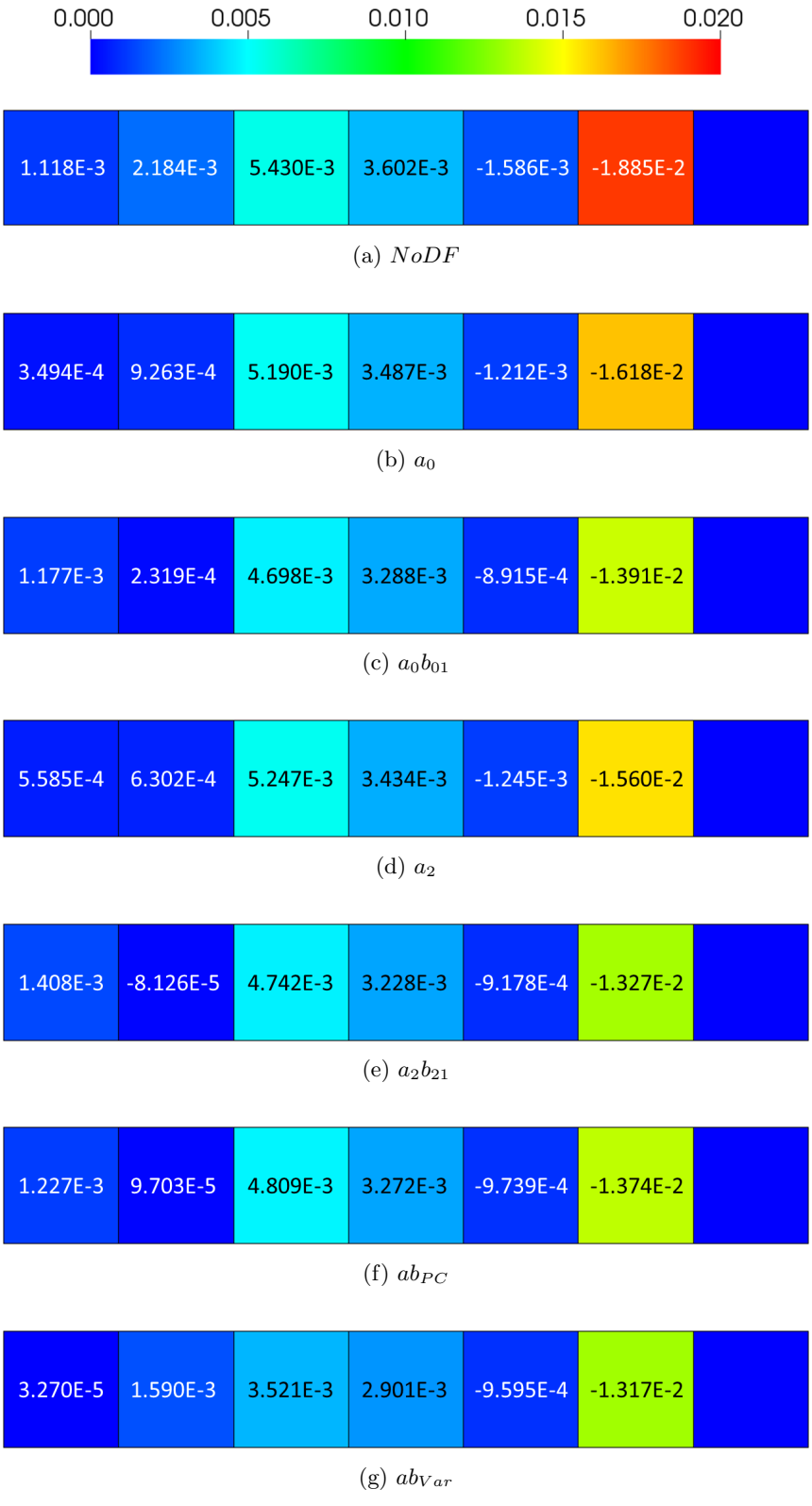

(a) $NoDF$

(b) a_0

(c) $a_0 b_{01}$

(d) a_2

(e) $a_2 b_{21}$

(f) ab_{PC}

(g) ab_{Var}

Figure 10.4: Errors in Assembly Powers for the Two Assembly Type LWR Test Problem with Various Discontinuity Factors (2 Energy Groups). Numbers indicate relative error values in each assembly. Colors indicate the magnitude of the errors. Results shown are for $\boldsymbol{D}_a$.

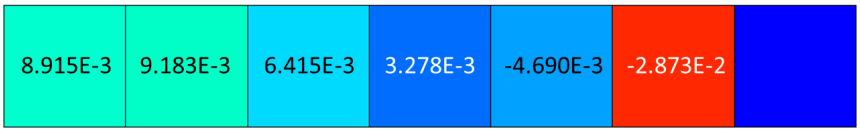

(a) $NoDF$

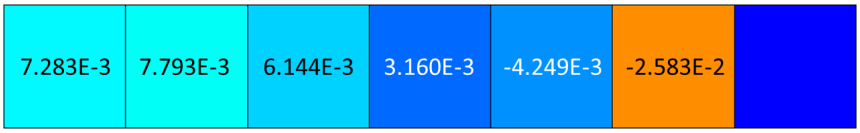

(b) a_0

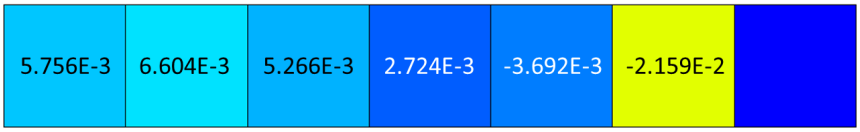

(c) $a_0 b_{01}$

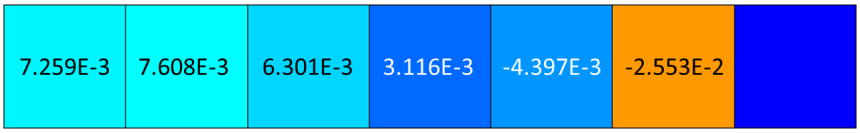

(d) a_2

(e) $a_2 b_{21}$

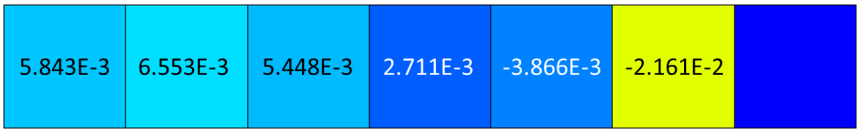

(f) ab_{PC}

(g) ab_{Var}

Figure 10.5: Errors in Assembly Powers for the Two Assembly Type LWR Test Problem with Various Discontinuity Factors (5 Energy Groups). Numbers indicate relative error values in each assembly. Colors indicate the magnitude of the errors. Results shown are for $\boldsymbol{D}_a$.

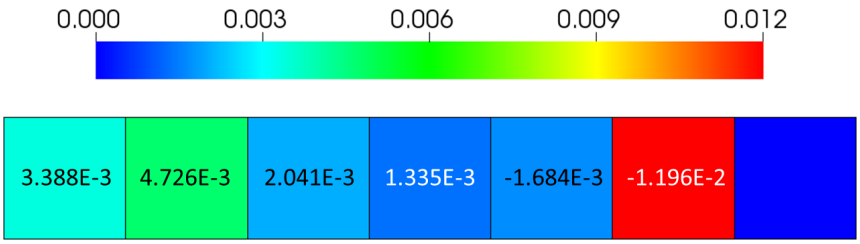

(a) $NoDF$

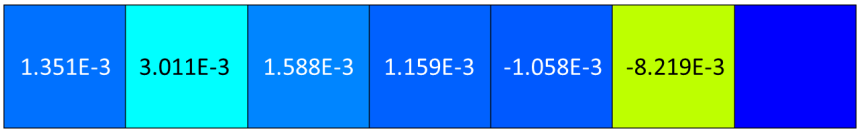

(b) a_0

(c) $a_0 b_{01}$

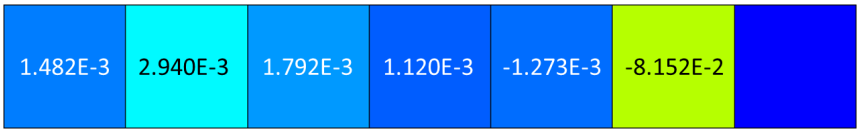

(d) a_2

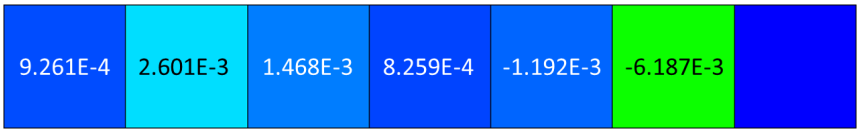

(e) $a_2 b_{21}$

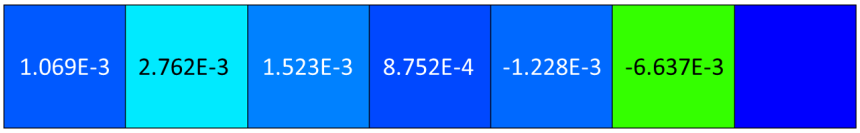

(f) ab_{PC}

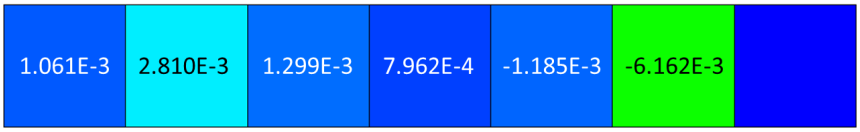

(g) ab_{Var}

Figure 10.6: Errors in Assembly Powers for the Two Assembly Type LWR Test Problem with Various Discontinuity Factors (10 Energy Groups). Numbers indicate relative error values in each assembly. Colors indicate the magnitude of the errors. Results shown are for $\boldsymbol{D}_a$.

10.2.2 Checkerboard Loading of Assembly Types (Problem 6)

Next, we consider a 4 assembly MOX-UO2 colorset in which, when reflecting boundaries are taken into account, assemblies are loaded in a checkerboard pattern with like assemblies forming 2×2 blocks. Thus, the system is periodic over only 2 lattices, whereas in the last problem the system was periodic over 4 lattices. Also, the assemblies are more dissimilar (containing MOX and UO2 instead of different enrichments of UO2). Therefore, we expect the DFs to be less accurate than in the previous problem, and that calculating DFs from colorset calculations would likely be more accurate. The diffusion calculations are performed with 2-group (defined by Table B.15) and 7-group energy structures.

Table 10.4: Absolute Error in k for the Four-Assembly Colorset with Various Discontinuity Factors[1]

Discontinuity Factor	2 Energy Groups	7 Energy Groups
$NoDF$	-468	30
a_0	-342	64
$a_0 b_{01}$	-339	-124
a_2	-368	48
$a_2 b_{21}$	-363	-151
ab_{PC}	-358	-146
ab_{Var}	-192	-151

[1] All errors shown in pcm. Results shown are for $\boldsymbol{D}_a$. The reference value of k from an MOC calculation is 1.27454.

The absolute errors in k are listed in Table 10.4. We see that for 7 groups: (i) using no DFs yields the best solution and (ii) using flux and current DFs decreases the accuracy of the estimate of k relative to using only flux DFs. Since the exact transport physics have 7 energy groups, this is an indication that DFs are not needed when no group-condensation is performed. When group condensation *is* performed (down to 2 groups): (i) not using DFs results in the worst estimate of k, (ii) using flux and current DFs yields slightly more accurate estimates of k compared to using only flux DFs, (iii) DFs for continuity of the second angular moment perform slightly

worse than DFs for continuity of the zeroth angular moment (scalar flux), and (iv) the variational DFs yield a significantly better estimate of k compared to all other DFs.

The reference assembly powers are presented in Fig. 8.29. Relative errors in the assembly powers are shown for 2- and 7-group diffusion in Figs. 10.7 and 10.8 respectively. Analysis of the assembly powers leads us to different conclusions than the analysis of the reactor eigenvalues.

First, consider the 2-group assembly powers. The flux and current DFs together yield slightly better k values and assembly powers. However, the a_2 and $a_2 b_{21}$ DFs give more accurate powers than a_0 and $a_0 b_{01}$, whereas they gave less accurate estimates of k. Furthermore, the ab_{Var} DFs, which led to the best estimate of k, lead to significantly less accurate estimates of the assembly powers than the other DFs.

Next, consider the 7-group assembly powers. Using no DFs gives considerably less accurate assembly powers than using any of the DFs we tested, despite the fact that using no DFs gave the best value of k. The a_0 and $a_0 b_{01}$ DFs give more accurate powers than a_2 and $a_2 b_{21}$, whereas they gave less accurate estimates of k.

Unfortunately, as we saw with the extrapolation lengths (see Chapter IX), it seems as though we must choose obtaining *either* the best estimate of k *or* the most accurate assembly powers when we select DFs. The differences between these results and those of Section 10.2.1 are: (i) fewer assemblies of the same type are loaded contiguously, thereby violating the assumptions of the asymptotic analysis to a greater degree, and (ii) the assemblies are less similar, being composed of MOX and UO2 rather than different enrichments of UO2. As a result of these differences, the DFs perform inconsistently for this problem, and choosing an optimal DF may not be possible without comparing to a reference solution, which is impractical. It

is highly likely that DFs calculated from colorset calculations would outperform the DFs studied in this thesis, which use only data from single assembly calculations.

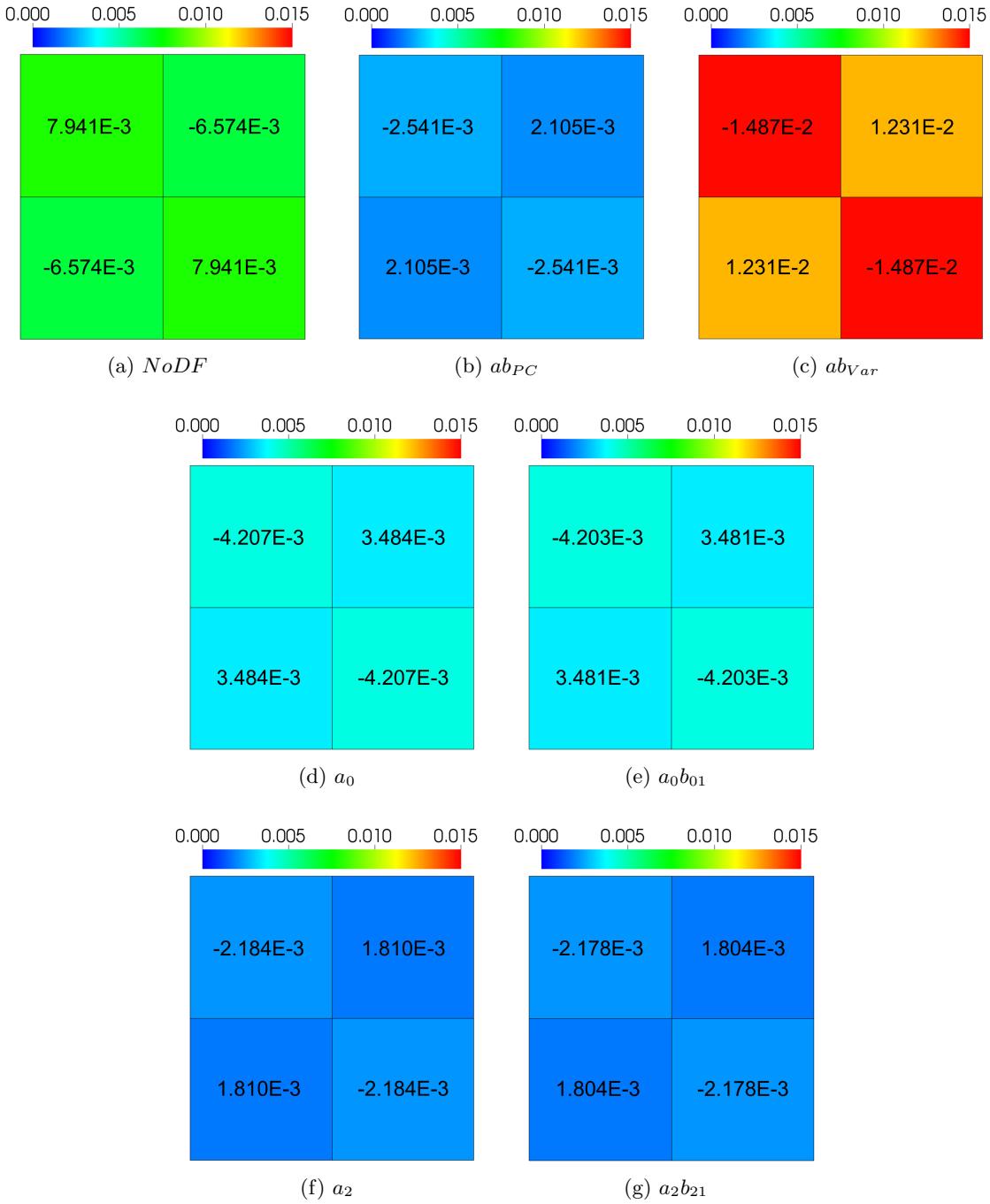

(a) $NoDF$ (b) ab_{PC} (c) ab_{Var}

(d) a_0 (e) $a_0 b_{01}$

(f) a_2 (g) $a_2 b_{21}$

Figure 10.7: Errors in Assembly Powers for the Four-Assembly Colorset with Various Discontinuity Factors (2 Energy Groups). Numbers indicate relative error values in each assembly. Colors indicate the magnitude of the errors. Results shown are for $\boldsymbol{D}_a$.

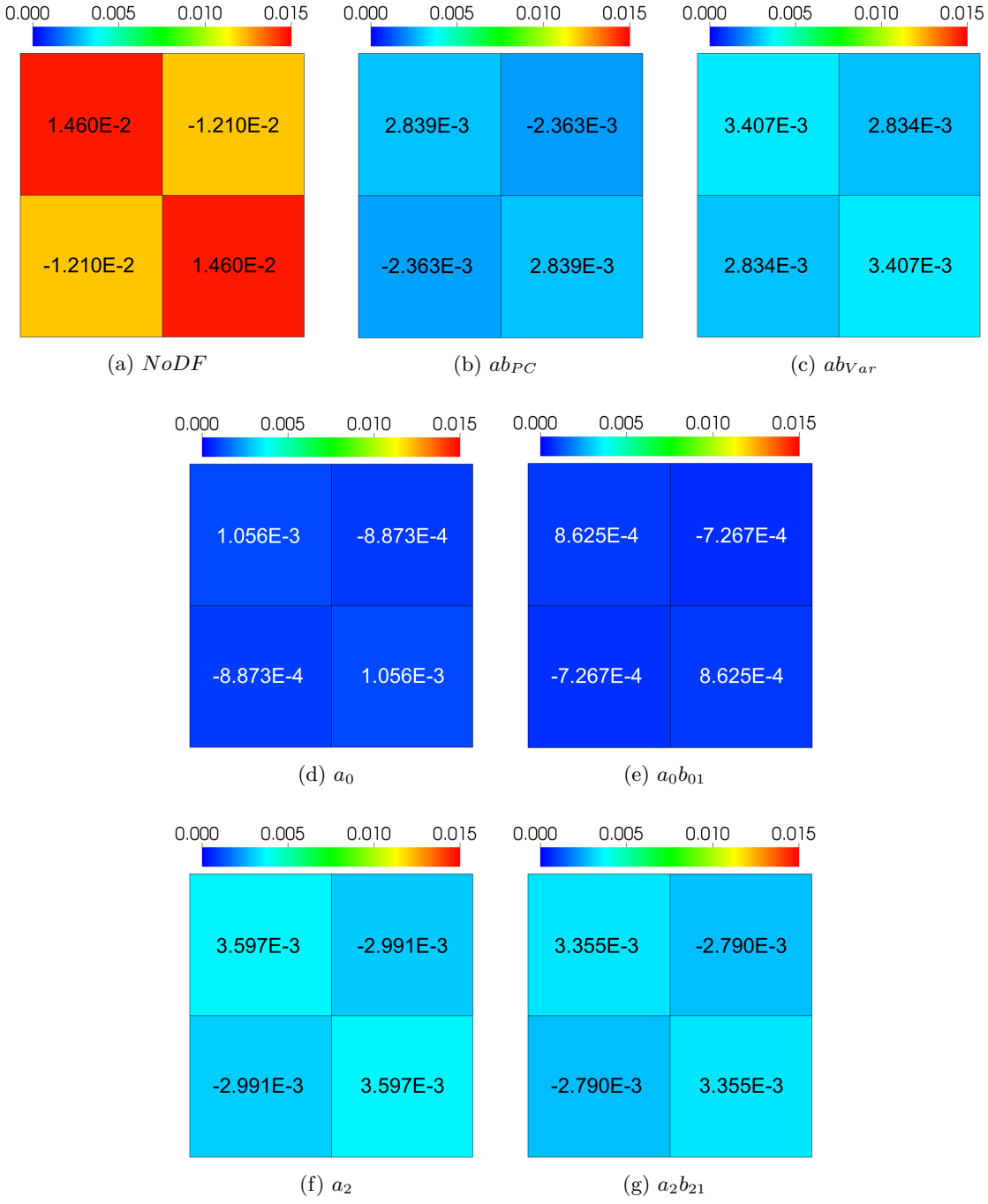

(a) $NoDF$ (b) ab_{PC} (c) ab_{Var}

(d) a_0 (e) $a_0 b_{01}$

(f) a_2 (g) $a_2 b_{21}$

Figure 10.8: Errors in Assembly Powers for the Four-Assembly Colorset with Various Discontinuity Factors (7 Energy Groups). Numbers indicate relative error values in each assembly. Colors indicate the magnitude of the errors. Results shown are for $\boldsymbol{D}_a$.

10.3 Effectiveness of Discontinuity Factors at Fuel-Reflector Interfaces

The fuel-reflector interface DFs proposed in Section 6.3.1 are heuristic. They assume that the lattice functions for a homogeneous multiplying lattice can be applied to a homogeneous reflector. In reality, strong changes in the energy spectrum in the vicinity of the fuel-reflector interface mean that neither the fuel nor the homogeneous reflector lattice functions are similar enough to the true angular flux at the interface to yield accurate discontinuity factors. This is why colorset calculations (consisting of a fuel assembly adjacent to a reflector assembly) are typically used to obtain energy spectra at the interface, which can then be used to generate accurate discontinuity factors. Because the heuristic fuel-reflector DFs avoid the colorset calculation, they are not expected to yield consistently accurate results at fuel-reflector interfaces. The numerical results in this section will confirm that this is indeed the case. However, we also demonstrate that the inconsistencies cannot be wholly attributed to the changes in energy spectrum, as the DF performance varies even for monoenergetic problems.

10.3.1 1D LWR Assembly with Reflector (Problem 2: Configuration 3)

We return to the 1-D, 2 region DF test (Problem 2, Section C.2). In this section, we consider Configuration 3, which has fuel-centered pins in the left region and a homogeneous reflector in the right region. The left boundary is reflecting and the right boundary is a vacuum.

Table 10.5 lists the absolute errors in k for this system. Not using any DFs yields the least accurate estimate of k. The a_2b_{21}, ab_{PC}, and ab_{Var} DFs are all similarly accurate, but the a_0b_{01} DFs are the most accurate by 5 pcm.

The ratio of the reconstructed fluxes to the reference solution is shown in Fig.

Table 10.5: Absolute Error in k for the 1-D DF Test Problem (Configuration 3) with Various Discontinuity Factors[1]

Discontinuity Factor	Error [pcm]
$NoDF$	-56
a_0	-35
$a_0 b_{01}$	-10
a_2	-40
$a_2 b_{21}$	-16
ab_{PC}	-15
ab_{Var}	-16

[1] Results shown are for $\boldsymbol{D}_a$. The reference value of k from an S_N calculation is 1.69716.

10.9. Comparing to Configuration 2 (Fig. 10.3), which has moderator-centered fuel pins in the right assembly instead of a homogeneous reflector, we find several notable differences. Unlike for Configuration 2: (i) the difference between a_0 and a_2 is small, (ii) the differences between using flux and current DFs together and only using flux DFs is large, with the flux and current DFs being significantly more accurate, (iii) the ab_{PC} and ab_{Var} DFs are similar, and (iv) the $a_0 b_{01}$ DFs are the most accurate. This last point is particularly interesting because the $a_0 b_{01}$ DFs were among the least accurate for Configuration 2. We conclude that even for monoenergetic problems, DF behavior is unpredictable at fuel-reflector interfaces.

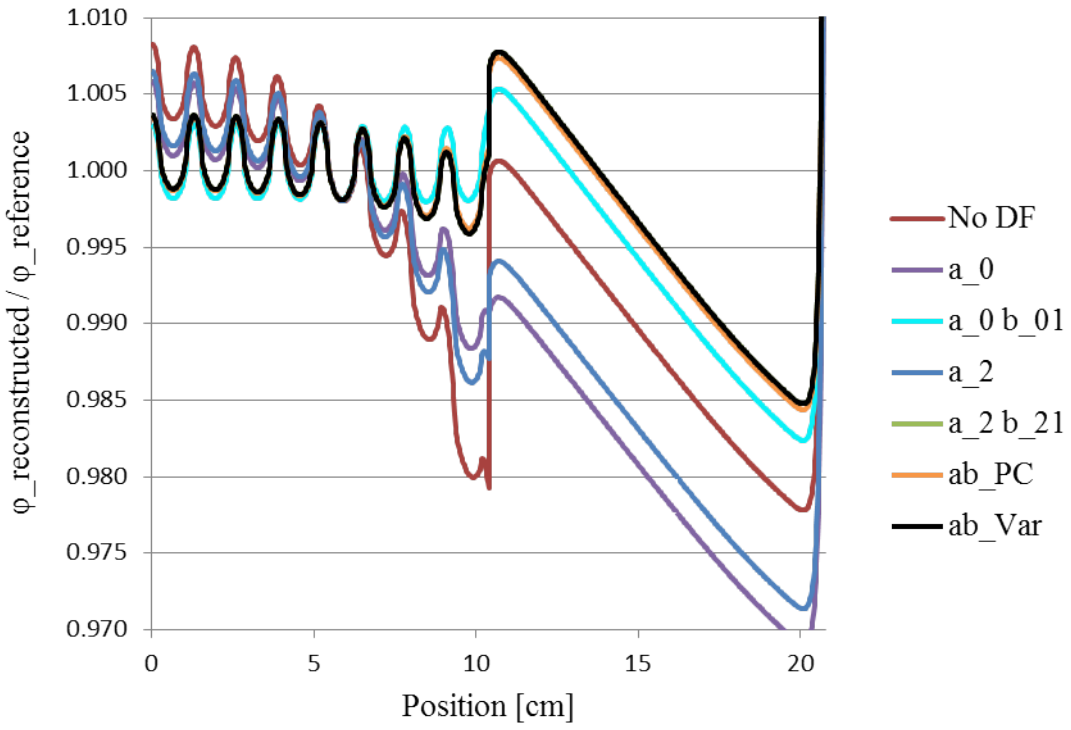

Figure 10.9: Reconstructed Scalar Flux for the 1-D DF Test Problem (Configuration 3) with Various Discontinuity Factors. Results shown are for asymptotic flux reconstruction and $\boldsymbol{D}_a$. The a_2b_{21} and ab_{Var} fluxes are identical.

10.3.2 MOX-Reflector Interface (Problem 5: Reflected MOX Configuration)

We now consider the six-assembly MOX core with a reflector (Problem 5, Section C.5. All of the fuel assemblies have the same composition, so no DFs are applied within the core; they are applied only at the fuel-reflector interface.

The absolute eigenvalue errors for this problem are shown in Table 10.6. The results show that for this problem, not using any DFs will yield a more accurate estimate of k than any of the DFs tested.

Figure 10.11 shows the relative errors in the assembly powers for this problem. As with k, using no DFs yields considerably more accurate solutions than any of the DFs. Thus, for this problem, it is best not to use any DFs at the fuel-reflector interface. However, as we shall see, this is not the case for every fuel-reflector interface.

Table 10.6: Absolute Error in k for the Reflected, Six-Assembly MOX Core with Fuel-Reflector Discontinuity Factors[1]

Discontinuity Factor	Error [pcm]
$NoDF$	-208
a_0	-255
$a_0 b_{01}$	-284
a_2	-259
$a_2 b_{21}$	-290
ab_{PC}	-290

[1] Results shown are for $\boldsymbol{D}_a$. The reference value of k from an MOC calculation is 1.11665.

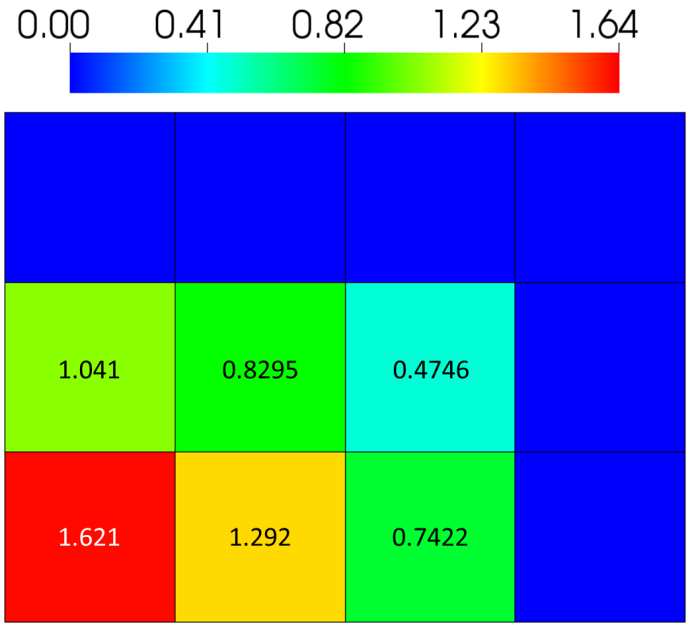

Figure 10.10: Reference Assembly Powers for the Reflected, Six-Assembly MOX Core. Numbers indicate normalized power in each assembly.

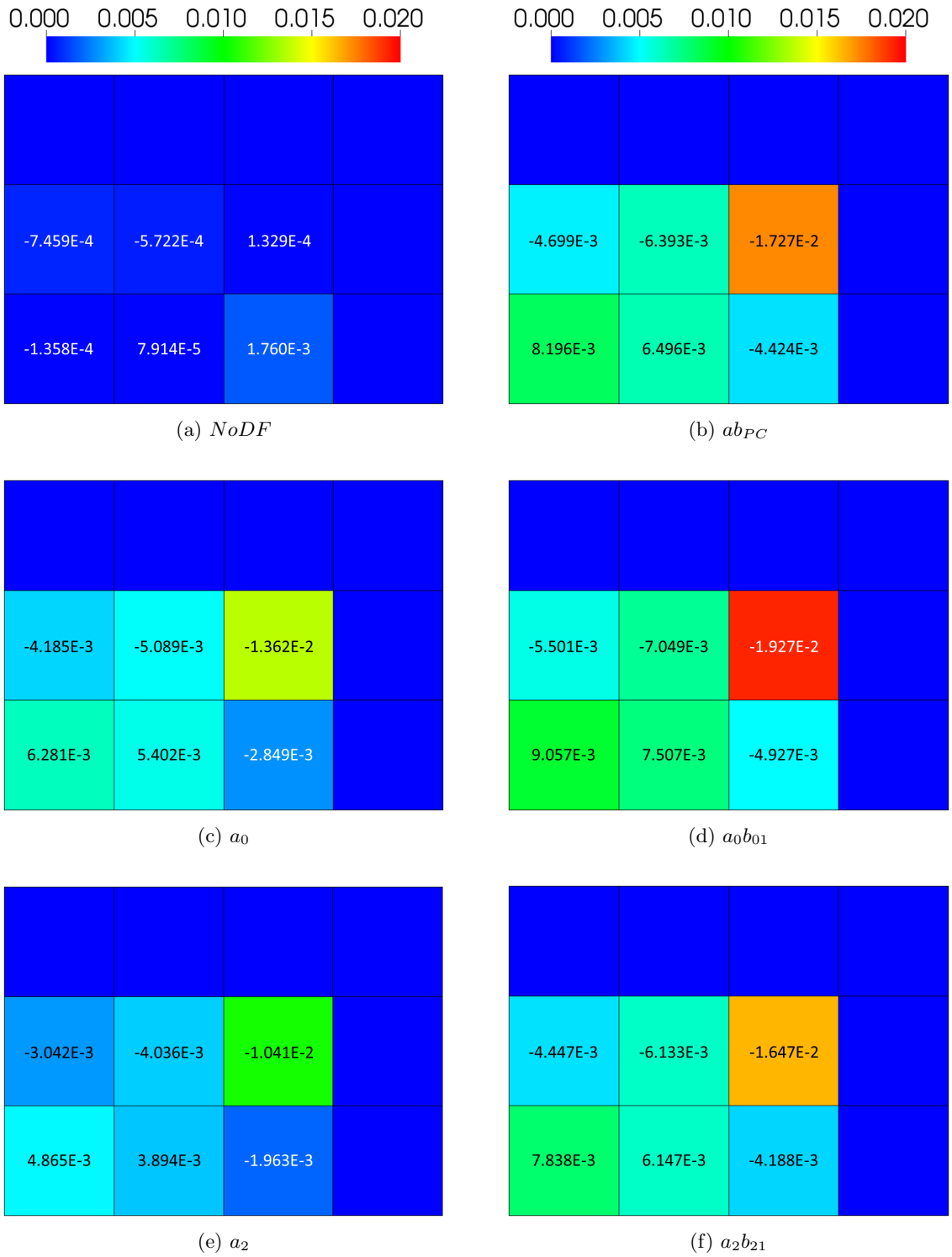

(a) $NoDF$ (b) ab_{PC}

(c) a_0 (d) $a_0 b_{01}$

(e) a_2 (f) $a_2 b_{21}$

Figure 10.11: Errors in Assembly Powers for the Reflected, Six-Assembly MOX Core with Fuel-Reflector Discontinuity Factors. Results shown are for $\boldsymbol{D}_a$.

10.3.3 47-Group LWR Fuel-Reflector Interface (Problem 8)

Next, we consider again the LWR core studied in Section 10.2.1. In this problem, assembly composition changes occur only every several assemblies (see the definition of Problem 8, Section C.8). In Section 10.2.1, DFs were applied to the interface between the 2.1% UO2 and 2.6% UO2 fuel *and* the fuel-reflector interface. In this section, DFs are only applied to the fuel-fuel interface and *not* to the fuel-reflector interface. We then compare the results to those of Section 10.2.1 and draw conclusions about the effectiveness of the fuel-reflector DFs.

The absolute errors in k for this problem are listed in Table 10.7. Compared to the results with the fuel-reflector DFs (Table 10.3), each estimate of k without the fuel-reflector DFs is worse, though only be a few pcm.

Table 10.7: Absolute Error in k for the Two Assembly Type LWR Test Problem without Reflector Discontinuity Factors[1]

Extrapolation Length	2 Energy Groups	5 Energy Groups	10 Energy Groups
a_0	-5	-25	-10
$a_0 b_{01}$	-5	-25	-9
a_2	-5	-25	-9
$a_2 b_{21}$	-5	-25	-10
ab_{PC}	-5	-25	-9
ab_{Var}	-8	-25	-9

[1] All errors in pcm. Results shown are for $\boldsymbol{D}_a$. The reference value of k from an MOC calculation is 1.08819.

The relative errors in the assembly powers for the 2 group case are shown in Fig. 10.12 (we note that the "$NoDF$" case remains unchanged, and is not depicted in this plot). Comparing to Fig. 10.4, we see that in all cases, using fuel-reflector DFs reduces assembly power errors, particularly in the outermost fuel assembly. The results for the 5 and 10 group diffusion calculations (not shown) are similar. Thus, for this problem, it is beneficial to use DFs at the fuel-reflector interface. This is

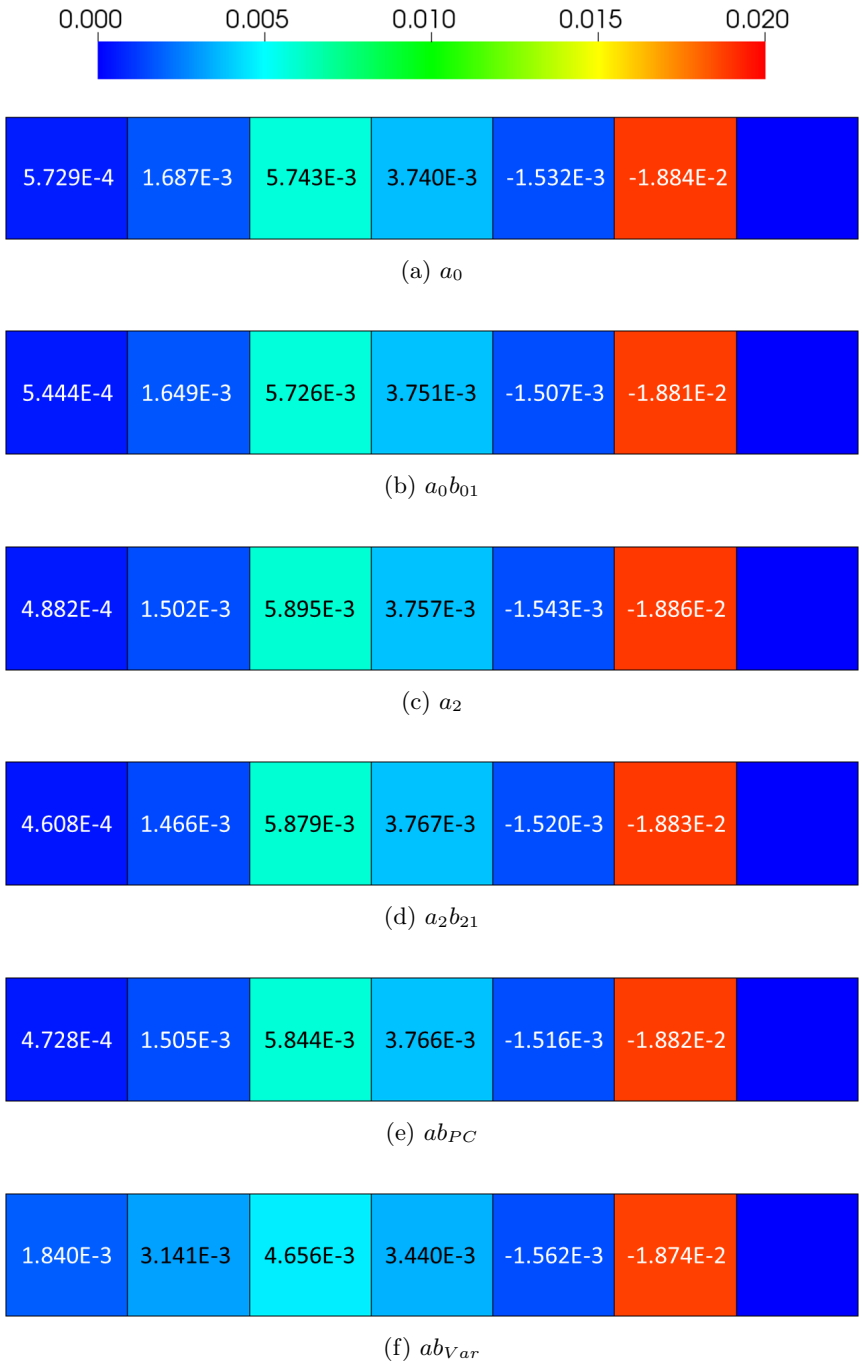

(a) a_0

(b) $a_0 b_{01}$

(c) a_2

(d) $a_2 b_{21}$

(e) ab_{PC}

(f) ab_{Var}

Figure 10.12: Errors in Assembly Powers for the Two Assembly Type LWR Test Problem without Reflector Discontinuity Factors (2 Energy Groups). Numbers indicate relative error values in each assembly. Colors indicate the magnitude of the errors. Results shown are for $\boldsymbol{D}_a$.

not the case for all problems (see Section 10.3.2), and we conclude that the DFs proposed in this thesis, which are calculated from single assembly calculations, are only sometimes effective at fuel-reflector interfaces. At this time, it is not known how

to systematically determine *a priori* which problems our fuel-reflector DFs should be applied to, and which ones colorset DFs should be applied to.

10.4 Dependence of the Variationally-Derived Discontinuity Factors on the Type of Neighboring Assembly

The variationally-derived DFs (Eqs. (5.131) and (5.132)) for a particular assembly are weighted by the adjoint lattice functions for that assembly and the adjoint lattice functions of its neighbor. To see this, we consider the 1-D MOX LWR Benchmark (Problem 3, Section C.3), which contains four types of fuel assemblies. The ab_{Var} DFs for this problem are listed in Table 10.8. We see that the variationally-derived DFs for a particular assembly type do depend on the neighboring assembly type.

Table 10.8: Variational Discontinuity Factors for the Two Assembly Type LWR Test Problem

	a_{Var}			
Assembly Type	Neighbor Assembly Type[1]			
	A	B	C	M
A	-	0.816955	0.792737	-
B	0.813414	-	0.813764	0.843648
C	0.792736	0.817307	-	-
M	-	0.847294	-	-
	b_{Var}			
Assembly Type	Neighbor Assembly Type[1]			
	A	B	C	M
A	-	0.611076	0.631114	-
B	0.621514	-	0.621246	0.599231
C	0.631115	0.610813	-	-
M	-	0.589196	-	-

[1] Some assembly types are never adjacent in this problem, and these DFs are not calculated. DFs for an assembly neighboring an assembly with the same type are also not calculated, as these are irrelevant.

10.5 Summary

The numerical results presented in this chapter have shown that the asymptotic DFs can yield more accurate solutions than using no DFs or using standard ADFs (a_0) for a limited range of problems. When the conditions of the asymptotic theory

are largely satisfied, i.e., when the system is periodic over reasonably large volumes and fuel assemblies are similar in composition (e.g., different enrichments of the same fuel type), then the DFs introduced in this thesis perform well. In particular, if these conditions are met, then:

1. Using flux and current DFs together often improves the accuracy of k, reconstructed fluxes, and assembly powers compared to using only flux DFs.
2. The DFs that make the second angular moment of the reconstructed flux continuous (a_2) are often more accurate than the standard ADFs (a_0), which make the reconstructed scalar flux continuous.
3. The variational DFs for lattice systems (ab_{Var}), the DFs for continuity of the reconstructed partial currents (ab_{PC}), and the DFs for continuity of the first and second angular moments (a_2b_{21}) are typically the most accurate DFs.

Unfortunately, when the conditions of the asymptotic theory are not largely satisfied, i.e., when the system is not periodic or periodic only over small volumes, or when adjacent assemblies are dissimilar, the DFs introduced in this thesis perform inconsistently. For these problems:

1. Using no DFs is sometimes better than using any, and sometimes worse.
2. Using flux and current DFs together is sometimes better than using flux DFs only, and sometimes worse.
3. The DFs that make the second angular moment of the reconstructed flux continuous (a_2) are sometimes better and sometimes worse than the standard ADFs (a_0), which make the reconstructed scalar flux continuous.
4. The DFs that yield the best value of k often yield the least accurate assembly powers, and vice versa.

To summarize: for problems in which the conditions of the asymptotic theory are not satisfied, the most accurate DFs varies from one problem to another, and there is no method at this time to determine *a priori* which DFs are best for a specific problem.

Examples of interfaces between dissimilar assemblies include MOX-UO2 interfaces, fuel-reflector interfaces, and interfaces between assemblies with strong neutron absorbers and assemblies without them. When the assemblies have very different compositions, the energy spectrum at the interface is very different than the energy spectrum predicted by single assembly lattice calculations. As a result, DFs calculated from single assembly data may not accurately predict energy-dependent behavior. In these cases, DFs obtained from colorset calculations, which yield a more accurate energy spectrum at the interface, will almost certainly lead to more accurate solutions.

However, as observed in Section 10.3.1, the inaccuracy of the energy spectra in single lattice calculations is not the sole cause of inconsistent DF performance. In monoenergetic problems, dissimilar assemblies can still have very different surface-averaged lattice functions at an interface, in which case the reconstructed flux will have a large discontinuity. Discontinuity factors can overcorrect this problem, and in some cases the solution with DFs can be less accurate than the solution without them. Calculating DFs from colorset calculations would likely be an improvement for monoenergetic problems as well. Unfortunately, colorset calculations are expensive, and must be performed for every combination of adjacent assemblies in a nuclear reactor, which is prohibitively expensive.

We note that the poor performance of DFs has been observed before by Cheng et al. [57]. Their work showed that for PWRs, the use of ADFs could increase

the error in assembly powers compared to using no DFs. They observed that for a reactor with a checkerboard loading of rodded and unrodded assemblies, the ADFs underpredicted powers in rodded assemblies and overpredicted powers in unrodded assemblies, while the opposite was true with no DFs. Thus, they concluded that ADFs overcorrected for the errors when using no DFs.

Finally, we note that the variational analysis used to derive the ab_{Var} DFs in Chapter V is not unique. This analysis was designed to optimally estimate the reactor multiplication factor, and indeed it does tend to yield good estimates of k when the assumptions of the asymptotic analysis are met. However, it may be the case that a different variational analysis (e.g., one designed to optimally estimate leakage rates), could lead to more accurate DFs. Furthermore, several approximations had to be made to define multigroup, space-independent variational DFs. These approximations no doubt have reduced the accuracy of the DFs, particularly for multigroup, multi-dimensional problems. It is likely that because multi-dimensional problems typically have space-dependent effects at interfaces, using space-dependent DFs would yield more accurate solutions. However, the use of space-dependent DFs is impractical, particularly for nodal diffusion methods.

CHAPTER XI

Numerical Results: Challenge Problems

This chapter contains numerical results for two challenging test problems in 2-D and 3-D. Whereas in Chapters VII-X we considered the various aspects of the asymptotic diffusion method piece-by-piece, in this chapter we consider the diffusion coefficients and discontinuity factors together. The asymptotic homogenized diffusion method is compared to the standard and Benoist homogenized diffusion methods.

As in previous chapters, we do not use current DFs for the standard and Benoist methods, because these depend on the diffusion coefficient. We limit our results to 2-group diffusion calculations, as this is the most commonly used group structure for analysis of LWRs. Only the "uncorrected" Benoist diffusion coefficient, which is uniquely defined for every lattice, is used in this chapter.

11.1 Comparison of Homogenized Diffusion Methods for the C5G7 Extended Benchmark (Problem 7)

We now consider the well-known C5G7 "Benchmark on Deterministic Transport Calculations Without Spatial Homogenisation - MOX Fuel Assembly 3-D Extension Case" (Problem 7, Section C.7) [78]. This 3-D problem consists of 4 assemblies (2 UO2 and 2 MOX) surrounded by a reflector. There are 3 configurations of the problem with control rods withdrawn or inserted to varying degrees. The C5G7

benchmark has been studied extensively, and detailed Monte Carlo reference solutions are available [78]. The 2-group energy structure is defined by Table B.15.

This is a small reactor and has many features that are difficult for the asymptotic method to model accurately (e.g., rodded and unrodded regions, checkerboard loading of MOX and UO2 assemblies, fuel-reflector interfaces). Based on the results of VII-X, the asymptotic method is not expected to offer a significant improvement over the standard and Benoist methods. Nevertheless, we demonstrate that even though the assumptions of the asymptotic analysis are violated to a great degree, the asymptotic method still performs comparably to the other methods.

In general, the standard diffusion coefficient yields the most accurate estimates of the reactor eigenvalue. The asymptotic diffusion coefficient tends to yield only slightly less accurate eigenvalues than the standard diffusion coefficient, but significantly more accurate assembly powers. The Benoist diffusion coefficient is typically less accurate than the each of the other diffusion coefficients for eigenvalues, and slightly less accurate than the asymptotic diffusion coefficient for assembly powers.

11.1.1 C5G7 Extended Benchmark: Unrodded Configuration

First, we consider the Unrodded Configuration, in which control rods are fully withdrawn from the fuel assemblies, though still present in the upper reflector region.

The reactor multiplication factor is listed for each combination of diffusion coefficient and DF in Table 11.1. Comparing the diffusion coefficients to each other, we see that D_s is slightly more accurate than $\boldsymbol{D}_a$, though only by ≈ 20 pcm. $\boldsymbol{D}_{bu}$ is significantly less accurate than the other diffusion coefficients.

Now comparing the discontinuity factors, we see that all the DFs yield more accurate estimates of k than not using any DFs. The a_0 DFs are slightly more accurate than the a_2 DFs. Current DFs improve the estimate of k when fuel-reflector

DFs are used, though they make it less accurate if no fuel-reflector DFs are used. Using fuel-reflector DFs improves the estimate of k when current DFs are used. The ab_{Var} DFs yield considerably more accurate estimates of k than the other DFs, which is expected because the variational analysis was designed to optimally estimate the reactor multiplication factor.

Table 11.1: Absolute Error in k for the C5G7 Benchmark (Unrodded Configuration)[1]

	With Fuel-Reflector DFs		
Discontinuity Factor	D_s	$\boldsymbol{D}_{bu}$	$\boldsymbol{D}_a$
$NoDF$	-362	-454	-382
a_0	-286	-374	-299
$a_0 b_{01}$	-	-	-282
a_2	-294	-383	-308
$a_2 b_{21}$	-	-	-289
ab_{PC}	-	-	-297
ab_{Var}	-	-	-122
	Without Fuel-Reflector DFs		
Discontinuity Factor	D_s	$\boldsymbol{D}_{bu}$	$\boldsymbol{D}_a$
a_0	-276	-364	-289
$a_0 b_{01}$	-	-	-321
a_2	-293	-382	-307
$a_2 b_{21}$	-	-	-338
ab_{PC}	-	-	-334
ab_{Var}	-	-	-170

[1] All errors in pcm. The reference value of k from an MC calculation is 1.14308 ± 0.00003.

The reference assembly powers for the Unrodded Configuration are shown in Fig. 11.1.

Relative errors in the assembly powers for the standard, Benoist, and asymptotic diffusion coefficients are shown in Figs. 11.2, 11.3, and 11.4 respectively. First comparing the various diffusion coefficients to each other, we see that the asymptotic and Benoist diffusion coefficients yield similarly accurate assembly powers. The standard diffusion coefficient is the least accurate.

Next, comparing the DFs to each other, we see that using no DFs is more accurate

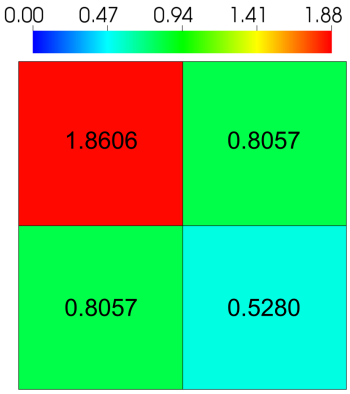

(a) $NoDF$

Figure 11.1: Reference Assembly Powers for the C5G7 Extended Benchmark (Unrodded Configuration). Numbers indicate normalized power in each assembly.

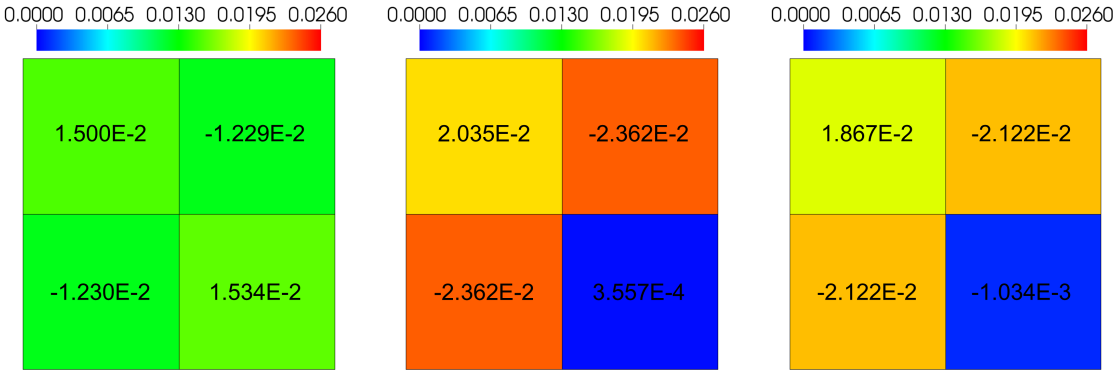

(a) $NoDF$ (b) a_0 (c) a_2

Figure 11.2: Errors in Assembly Powers for the C5G7 Extended Benchmark with the Standard Diffusion Coefficient (Unrodded Configuration, 2 Energy Groups). Numbers indicate relative error values in each assembly. Colors indicate the magnitude of the errors.

than using any DFs, and the variational DFs are the least accurate. As in Chapter X, this is the reverse behavior observed for the reactor multiplication factor. The a_2 DFs are more accurate than the a_0 DFs for all diffusion coefficients, and using current and flux DFs together is more accurate than using only flux DFs.

Figure 11.5 shows the relative errors in the assembly powers when DFs are applied between fuel assemblies, but not at the fuel-reflector interface. Comparing to Figure 11.4, which shows the relative errors in the assembly powers when DFs are applied at the fuel-reflector interface, we see that the fuel-reflector DFs improve the solution

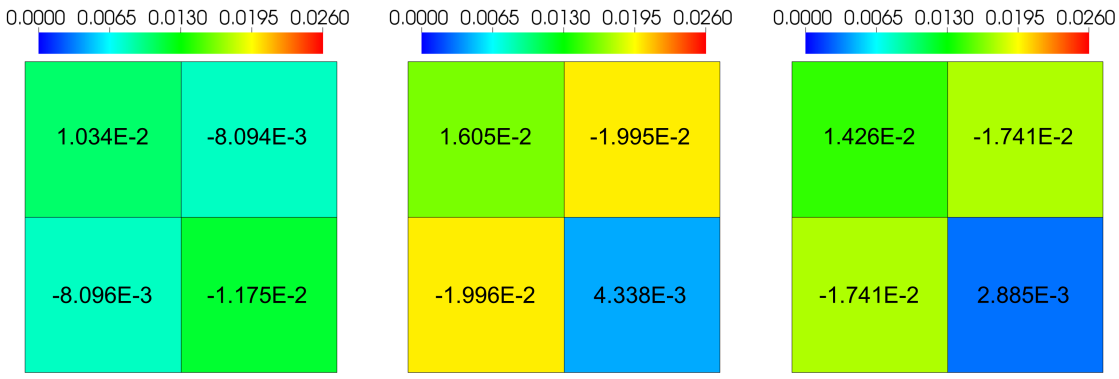

(a) $NoDF$ (b) a_0 (c) a_2

Figure 11.3: Errors in Assembly Powers for the C5G7 Extended Benchmark with the Benoist Diffusion Coefficient (Unrodded Configuration, 2 Energy Groups). Numbers indicate relative error values in each assembly. Colors indicate the magnitude of the errors.

when current DFs are used, but decrease the accuracy of the solution when only flux DFs are used. The inconsistent behavior for fuel-reflector DFs was observed in Section 10.3.

(a) $NoDF$ (b) a_0 (c) a_2

(d) ab_{PC} (e) a_0b_{01} (f) a_2b_{21}

(g) ab_{Var}

Figure 11.4: Errors in Assembly Powers for the C5G7 Extended Benchmark with the Asymptotic Diffusion Coefficient (Unrodded Configuration, 2 Energy Groups). Numbers indicate relative error values in each assembly. Colors indicate the magnitude of the errors.

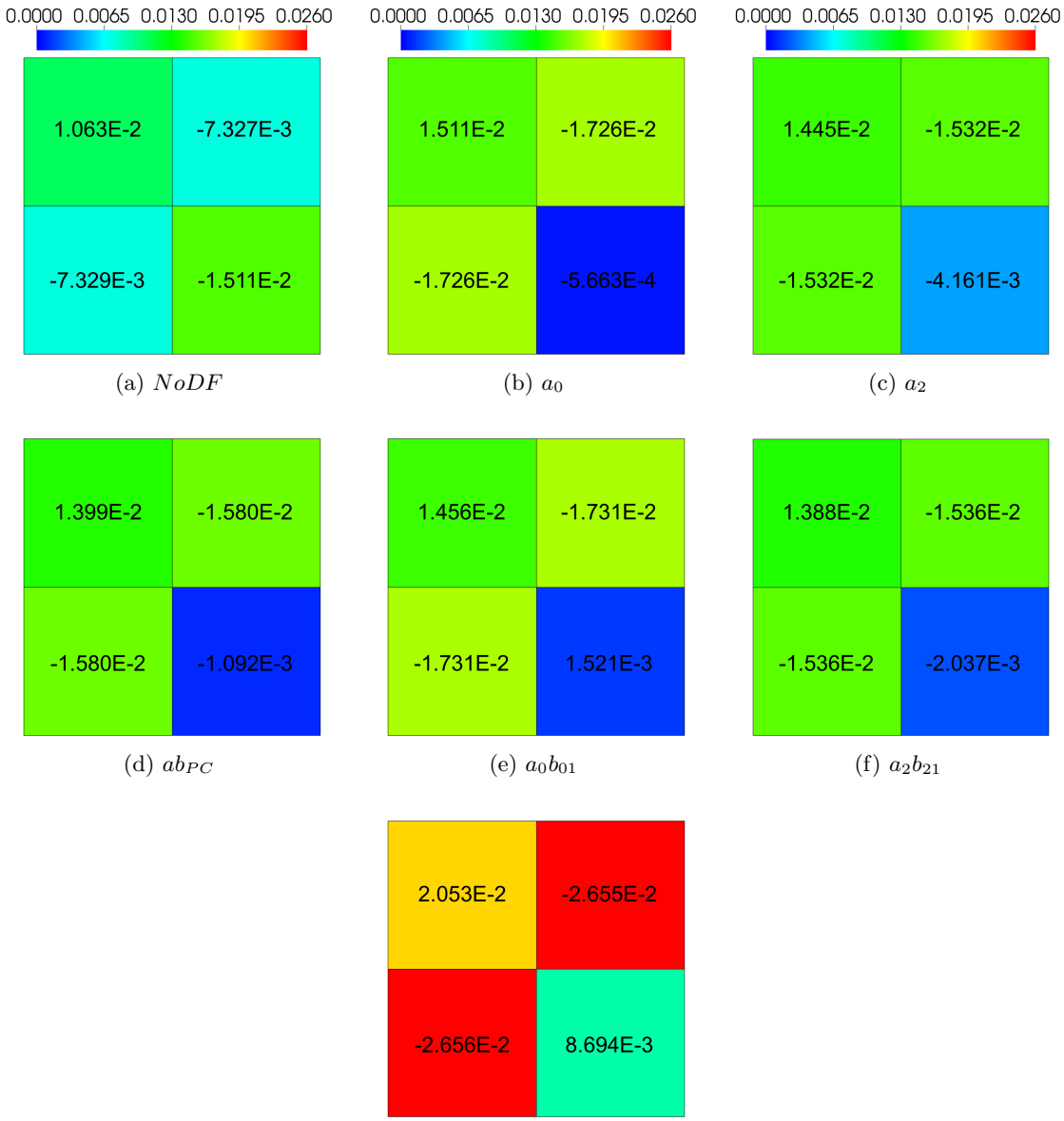

(a) $NoDF$ (b) a_0 (c) a_2

(d) ab_{PC} (e) a_0b_{01} (f) a_2b_{21}

(g) ab_{Var}

Figure 11.5: Errors in Assembly Powers for the C5G7 Extended Benchmark with the Asymptotic Diffusion Coefficient and without Reflector Discontinuity Factors (Unrodded Configuration, 2 Energy Groups). Numbers indicate relative error values in each assembly. Colors indicate the magnitude of the errors.

11.1.2 C5G7 Extended Benchmark: Rodded A Configuration

We turn our attention to the Rodded A Configuration, which has partially inserted control rods in the inner UO2 assembly.

Table 11.2 lists the absolute errors in the reactor multiplication factors for this problem. Again, the Benoist diffusion coefficient is the least accurate, while the standard diffusion coefficient is the most accurate by a margin of < 25 pcm.

Using no DFs yields the least accurate estimates of k, while the variational DFs once again give the most accurate estimates of k. The exceptional performance of the variational DFs is due to the fact that the variational analysis optimally estimates $\lambda = 1/k$. As with the Unrodded Configuration, the a_2 DFs are slightly less accurate than the a_0 DFs, and using flux and current DFs together is more accurate than using only flux DFs. Finally, the fuel-reflector DFs increase the accuracy of current DFs, but decrease the accuracy of flux DFs.

Table 11.2: Absolute Error in k for the C5G7 Benchmark (Rodded A Configuration)[1]

	With Fuel-Reflector DFs		
Discontinuity Factor	D_s	$\boldsymbol{D}_{bu}$	$\boldsymbol{D}_a$
$NoDF$	-306	-405	-330
a_0	-245	-340	-263
$a_0 b_{01}$	-	-	-247
a_2	-250	-346	-270
$a_2 b_{21}$	-	-	-250
ab_{PC}	-	-	-258
ab_{Var}	-	-	-77
	Without Fuel-Reflector DFs		
Discontinuity Factor	D_s	$\boldsymbol{D}_{bu}$	$\boldsymbol{D}_a$
a_0	-234	-328	-251
$a_0 b_{01}$	-	-	-287
a_2	-247	-342	-266
$a_2 b_{21}$	-	-	-300
ab_{PC}	-	-	-298
ab_{Var}	-	-	-126

[1] All errors in pcm. The reference value of k from an MC calculation is 1.12806 ± 0.00003.

The reference assembly powers for the Rodded A Configuration are shown in Fig. 11.6.

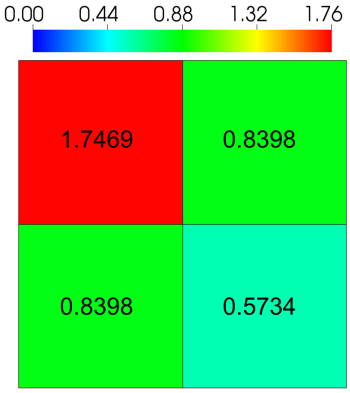

(a) *NoDF*

Figure 11.6: Reference Assembly Powers for the C5G7 Extended Benchmark (Rodded A Configuration). Numbers indicate normalized power in each assembly.

Figures 11.7-11.9 show the relative errors in the assembly powers for this configuration. Comparing the diffusion coefficients, we find that $\boldsymbol{D}_a$ is slightly more accurate than $\boldsymbol{D}_{bu}$, and both are significantly more accurate than D_s.

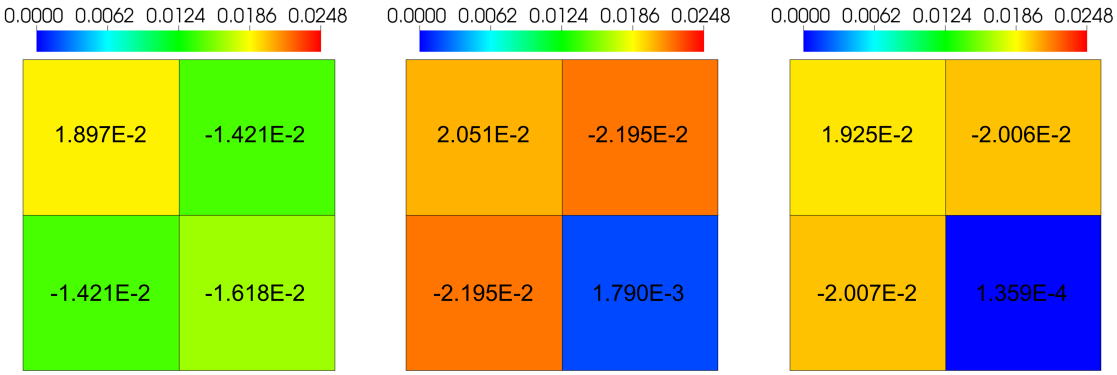

(a) *NoDF* (b) a_0 (c) a_2

Figure 11.7: Errors in Assembly Powers for the C5G7 Extended Benchmark with the Standard Diffusion Coefficient (Rodded A Configuration, 2 Energy Groups). Numbers indicate relative error values in each assembly. Colors indicate the magnitude of the errors.

Now comparing the DFs to each other, we observe the same trends seen for the Unrodded Configuration: (i) using no DF is more accurate than using any DFs, (ii) the ab_{Var} DFs are the least accurate, (iii) the a_2 DFs are more accurate than the

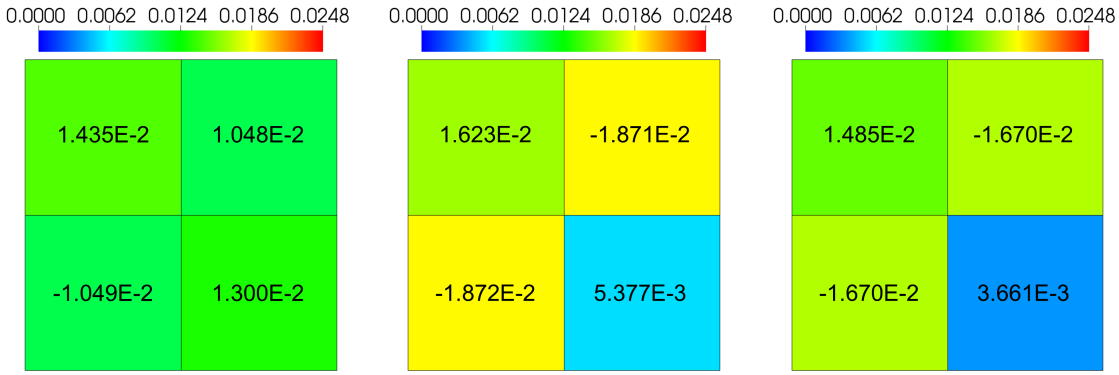

(a) $NoDF$ (b) a_0 (c) a_2

Figure 11.8: Errors in Assembly Powers for the C5G7 Extended Benchmark with the Benoist Diffusion Coefficient (Rodded A Configuration, 2 Energy Groups). Numbers indicate relative error values in each assembly. Colors indicate the magnitude of the errors.

a_0 DFs, and (iv) using current and flux DFs together is more accurate than using only flux DFs. Thus, as has been observed for several other test problems, the DFs that yield the most accurate estimate of k yield the worst estimate of the assembly powers and vice versa.

We do not present results without fuel-reflector DFs, as the trends for this configuration are identical to those for the Unrodded Configuration: fuel-reflector DFs improve the solution when flux and current DFs are used, but not when only flux DFs are used.

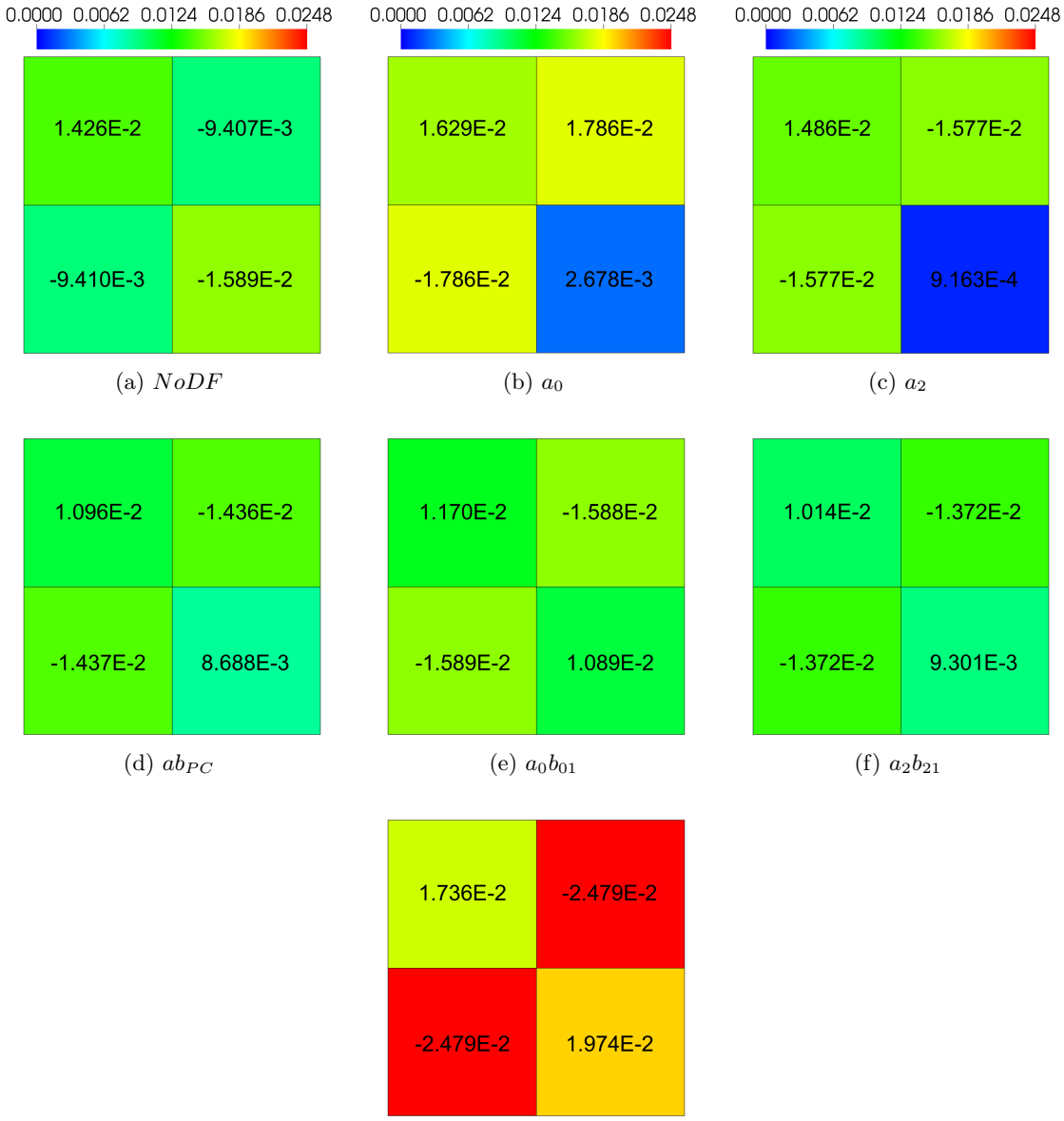

(a) $NoDF$ (b) a_0 (c) a_2

(d) ab_{PC} (e) a_0b_{01} (f) a_2b_{21}

(g) ab_{Var}

Figure 11.9: Errors in Assembly Powers for the C5G7 Extended Benchmark with the Asymptotic Diffusion Coefficient (Rodded A Configuration, 2 Energy Groups). Numbers indicate relative error values in each assembly. Colors indicate the magnitude of the errors.

11.1.3 C5G7 Extended Benchmark: Rodded B Configuration

Next, we study the Rodded B Configuration, which contains partially inserted control rods in the inner UO2 assembly and in both MOX assemblies.

The absolute errors in the reactor multiplication factor are listed in Table 11.3. The trends are similar to the other two configurations. The asymptotic diffusion coefficient is slightly less accurate than the standard diffusion coefficient, but significantly more accurate than the Benoist diffusion coefficient.

Using any set of DFs yields more accurate estimates of k compared to not using any DFs. The ab_{Var} DFs yield the most accurate estimate of k by a wide margin because the variational analysis is designed to optimally estimate $\lambda = 1/k$. Unlike with the other two configurations, the a_2 DFs are more accurate than the a_0 DFs for the Rodded B case, although the differences between the a_0 and a_2 DFs are small for all configurations.

Table 11.3: Absolute Error in k for the C5G7 Benchmark (Rodded B Configuration)[1]

	With Fuel-Reflector DFs		
Discontinuity Factor	D_s	$\boldsymbol{D}_{bu}$	$\boldsymbol{D}_a$
$NoDF$	-208	-296	-224
a_0	-176	-261	-187
a_0b_{01}	-	-	-162
a_2	-173	-258	-185
a_2b_{21}	-	-	-156
ab_{PC}	-	-	-168
ab_{Var}	-	-	12
	Without Fuel-Reflector DFs		
Discontinuity Factor	D_s	$\boldsymbol{D}_{bu}$	$\boldsymbol{D}_a$
a_0	-176	-261	-167
a_0b_{01}	-	-	-203
a_2	-173	-258	-177
a_2b_{21}	-	-	-210
ab_{PC}	-	-	-210
ab_{Var}	-	-	-42

[1] All errors in pcm. The reference value of k from an MC calculation is 1.07777 ± 0.00003.

The reference assembly powers for the Rodded B Configuration are shown in Fig. 11.10.

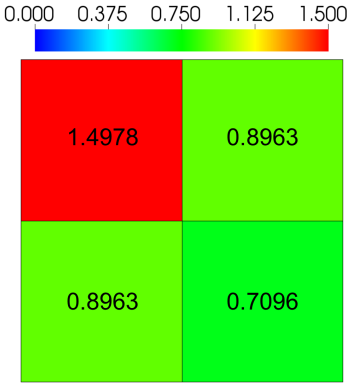

(a) *NoDF*

Figure 11.10: Reference Assembly Powers for the C5G7 Extended Benchmark (Rodded B Configuration). Numbers indicate normalized power in each assembly.

Figures 11.11-11.13 show the relative errors in the assembly powers using the standard, Benoist, and asymptotic diffusion coefficients. Comparing the diffusion coefficients, we see that the asymptotic diffusion coefficient yields the most accurate assembly powers, while the standard diffusion coefficient yields the least accurate assembly powers.

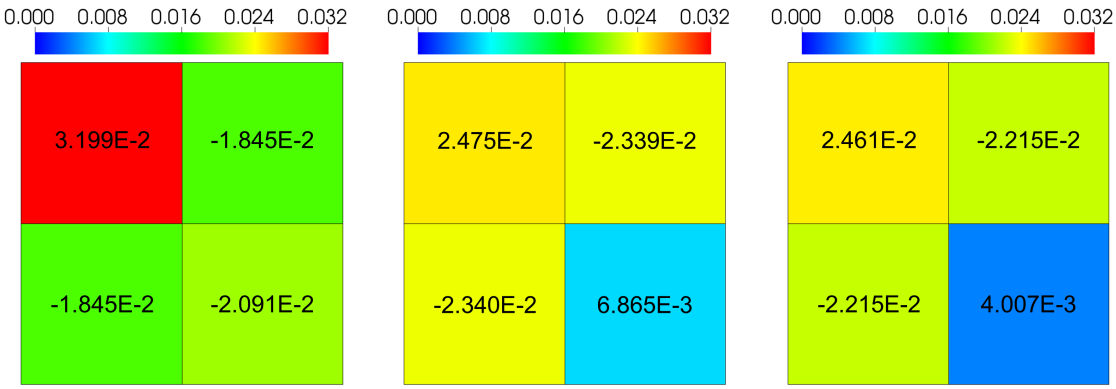

(a) *NoDF* (b) a_0 (c) a_2

Figure 11.11: Errors in Assembly Powers for the C5G7 Extended Benchmark with the Standard Diffusion Coefficient (Rodded B Configuration, 2 Energy Groups). Numbers indicate relative error values in each assembly. Colors indicate the magnitude of the errors.

Next, we compare the DFs for this configuration. The a_2 DFs are more accurate

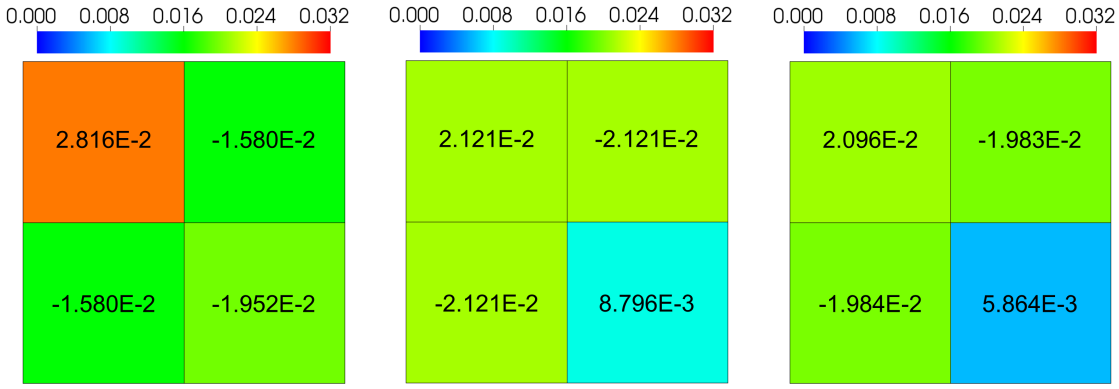

(a) $NoDF$ (b) a_0 (c) a_2

Figure 11.12: Errors in Assembly Powers for the C5G7 Extended Benchmark with the Benoist Diffusion Coefficient (Rodded B Configuration, 2 Energy Groups). Numbers indicate relative error values in each assembly. Colors indicate the magnitude of the errors.

than the a_0 DFs, and using current and flux DFs together is more accurate than using only flux DFs. Unlike with the Unrodded and Rodded A Configurations, not using any DFs is less accurate than all but the ab_{Var} DFs.

We do not present results without fuel-reflector DFs, as the trends for this configuration are identical to those for the Unrodded Configuration: fuel-reflector DFs improve the solution when flux and current DFs are used, but not when only flux DFs are used.

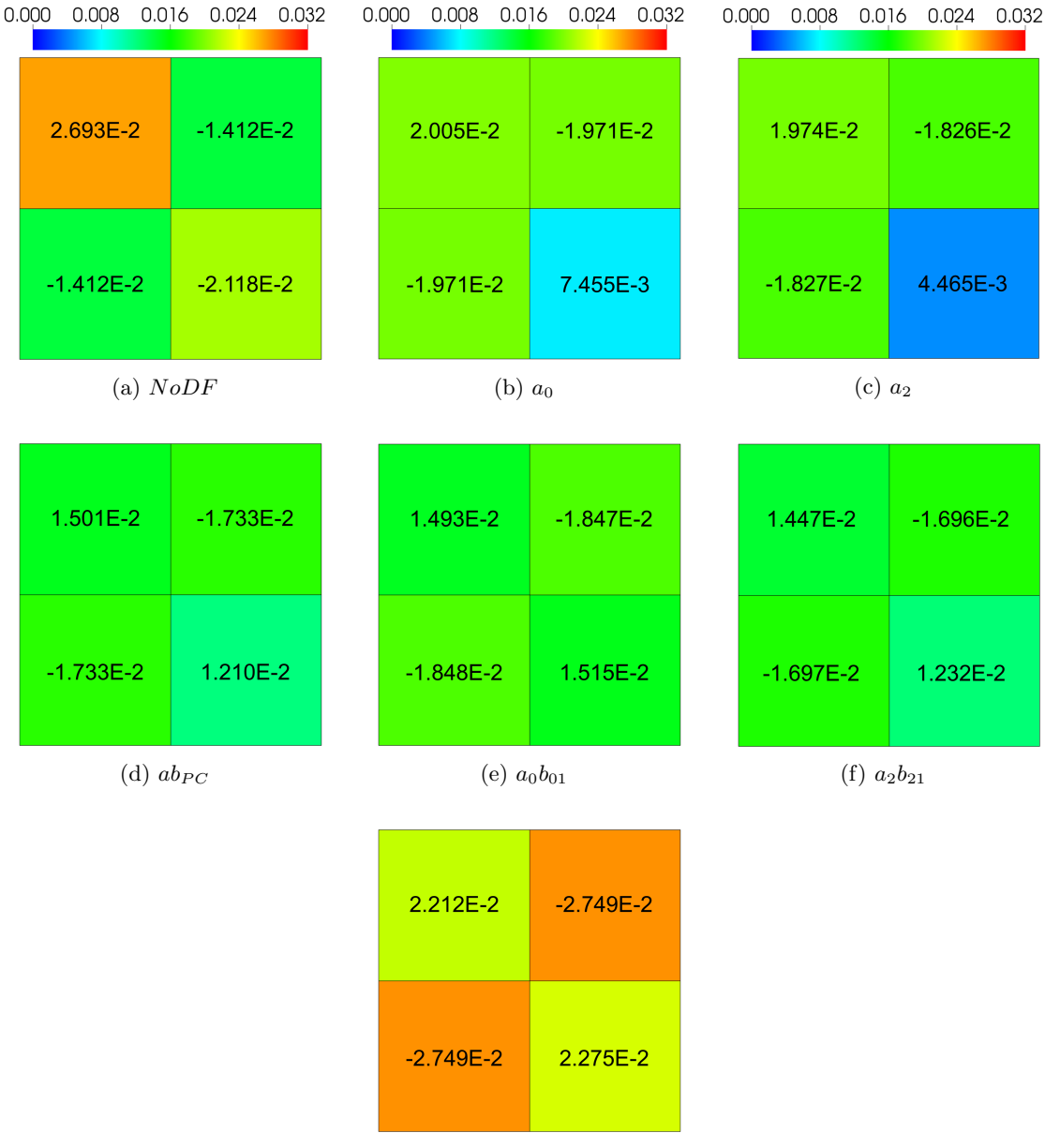

(a) $NoDF$ (b) a_0 (c) a_2

(d) ab_{PC} (e) a_0b_{01} (f) a_2b_{21}

(g) ab_{Var}

Figure 11.13: Errors in Assembly Powers for the C5G7 Extended Benchmark with the Asymptotic Diffusion Coefficient (Rodded B Configuration, 2 Energy Groups). Numbers indicate relative error values in each assembly. Colors indicate the magnitude of the errors.

11.2 Comparison of Homogenized Diffusion Methods for a 2-D Full-Core Light Water Reactor (Problem 9)

In this section, we consider a realistic, full-core LWR test problem (Problem 9, Section C.9). This reactor is a 17×17 array of fuel and reflector assemblies. The fuel assemblies can contain any of three different enrichments of UO2, and may have various numbers of Pyrex burnable absorber pins or control rods. The reference solution is obtained via an MPACT MOC calculation.

Although this reactor is large, the majority of assemblies are loaded in a checkerboard pattern, so the reactor is not periodic. As a result, the asymptotic method performs similarly to the standard and Benoist diffusion methods, though it is slightly better for some configurations.

11.2.1 Full-Core LWR: No Pyrex Configuration

The first configuration, "No Pyrex", contains no burnable absorbers and no rodded assemblies. As a result, the fuel assemblies are all similar, and the asymptotic DFs perform well.

Table 11.4 presents absolute errors in k for this configuration. Overall, there is very little variation in the eigenvalues for the various diffusion coefficients and discontinuity factors. The asymptotic and Benoist diffusion coefficients yield essentially identical eigenvalues, which are roughly 10 pcm less accurate than those obtained using the standard diffusion coefficient.

The DFs have little effect on the reactor multiplication factor. Nevertheless, the results indicate that: (i) not using DFs is worse than using DFs, (ii) a_2 DFs are more accurate than a_0 DFs, (iii) flux and current DFs together are more accurate than flux DFs alone, (iv) using DFs at fuel-reflector interfaces is more accurate than not using DFs at these interfaces, and (v) the ab_{Var} DFs do *not* yield the most

accurate estimates of the reactor multiplication factor. This last observation is not consistent with the idea that the ab_{Var} DFs should yield the best value of k because the functional in the variational analysis optimally estimates this quantity. However, the estimates of k for this configuration are all so similar that this is likely just an anomalous result.

Table 11.4: Absolute Error in k for the Full-Core LWR Problem (No Pyrex Configuration)[1]

	With Fuel-Reflector DFs		
Discontinuity Factor	D_s	$\boldsymbol{D}_{bu}$	$\boldsymbol{D}_a$
$NoDF$	-36	-47	-46
a_0	-29	-40	-40
a_0b_{01}	-	-	-33
a_2	-27	-38	-37
a_2b_{21}	-	-	-30
ab_{PC}	-	-	-31
ab_{Var}	-	-	-38
	Without Fuel-Reflector DFs		
Discontinuity Factor	D_s	$\boldsymbol{D}_{bu}$	$\boldsymbol{D}_a$
a_0	-34	-45	-45
a_0b_{01}	-	-	-43
a_2	-33	-44	-43
a_2b_{21}	-	-	-41
ab_{PC}	-	-	-42
ab_{Var}	-	-	-50

[1] All errors in pcm. The reference value of k from an MOC calculation is 1.08409.

The reference assembly powers for the No Pyrex Configuration are shown in Fig. 11.14. Relative errors in the assembly powers for the standard, Benoist, and asymptotic diffusion coefficients are shown in Figs. 11.15, 11.16, and 11.17 respectively. First we see that for a given set of DFs, the asymptotic diffusion coefficient yields smaller maximum errors in the assembly powers. However, the asymptotic diffusion coefficient gives larger errors in the center of the core than the standard coefficient, and the Benoist diffusion coefficient gives still larger errors in this region.

Next, comparing the DFs to each other, we see that using no DFs is less accurate

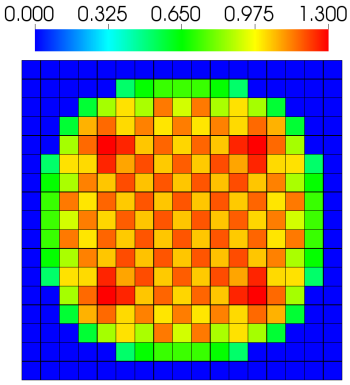

(a) $NoDF$

Figure 11.14: Reference Assembly Powers for the Full-Core LWR Problem (No Pyrex Configuration). Numbers indicate normalized power in each assembly.

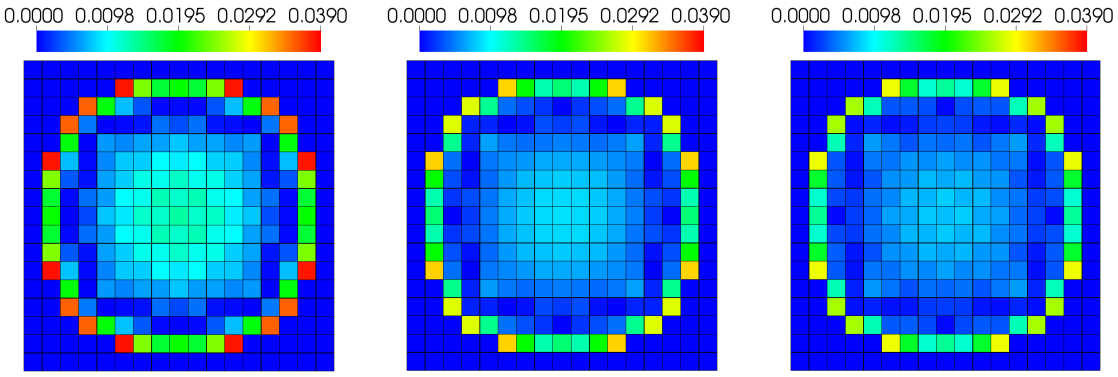

(a) $NoDF$ (Max Error 0.03826) (b) a_0 (Max Error 0.03100) (c) a_2 (Max Error 0.02863)

Figure 11.15: Absolute Values of Relative Errors in Assembly Powers for the Full-Core LWR Problem with the Standard Diffusion Coefficient (No Pyrex Configuration, 2 Energy Groups).

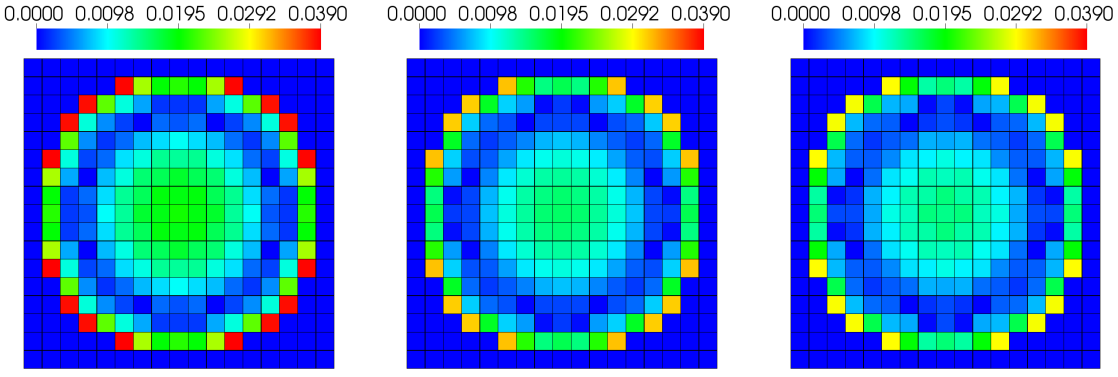

(a) $NoDF$ (Max Error 0.03894) (b) a_0 (Max Error 0.03164) (c) a_2 (Max Error 0.02924)

Figure 11.16: Absolute Values of Relative Errors in Assembly Powers for the Full-Core LWR Problem with the Benoist Diffusion Coefficient (No Pyrex Configuration, 2 Energy Groups).

than using any set of DFs, and the variational DFs are the least accurate. The a_2 DFs are more accurate than the a_0 DFs for all diffusion coefficients, and using current and flux DFs together is more accurate than using only flux DFs. The $a_2 b_{21}$ DFs are arguable the most accurate, though the $a_0 b_{01}$, ab_{PC} and ab_{Var} DFs are also accurate.

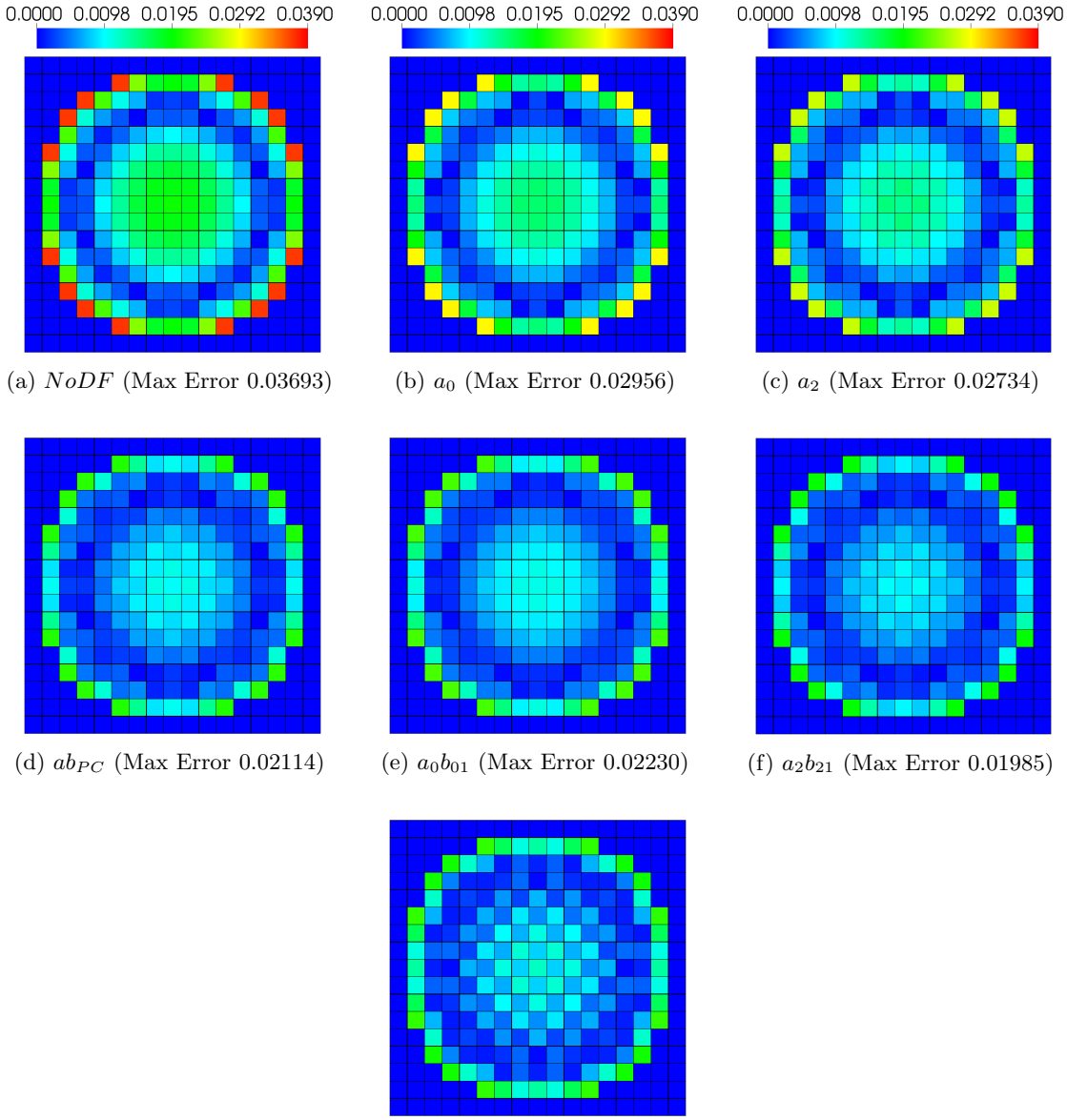

(a) $NoDF$ (Max Error 0.03693) (b) a_0 (Max Error 0.02956) (c) a_2 (Max Error 0.02734)

(d) ab_{PC} (Max Error 0.02114) (e) $a_0 b_{01}$ (Max Error 0.02230) (f) $a_2 b_{21}$ (Max Error 0.01985)

(g) ab_{Var} (Max Error 0.02144)

Figure 11.17: Absolute Values of Relative Errors in Assembly Powers for the Full-Core LWR Problem with the Asymptotic Diffusion Coefficient (No Pyrex Configuration, 2 Energy Groups).

Figure 11.18 shows the relative errors in the assembly powers when DFs are applied between fuel assemblies, but not at the fuel-reflector interface. Comparing to Figure 11.17, which shows the relative errors in the assembly powers when DFs are applied at the fuel-reflector interface, we see that the fuel-reflector DFs improve the solution for all DF types.

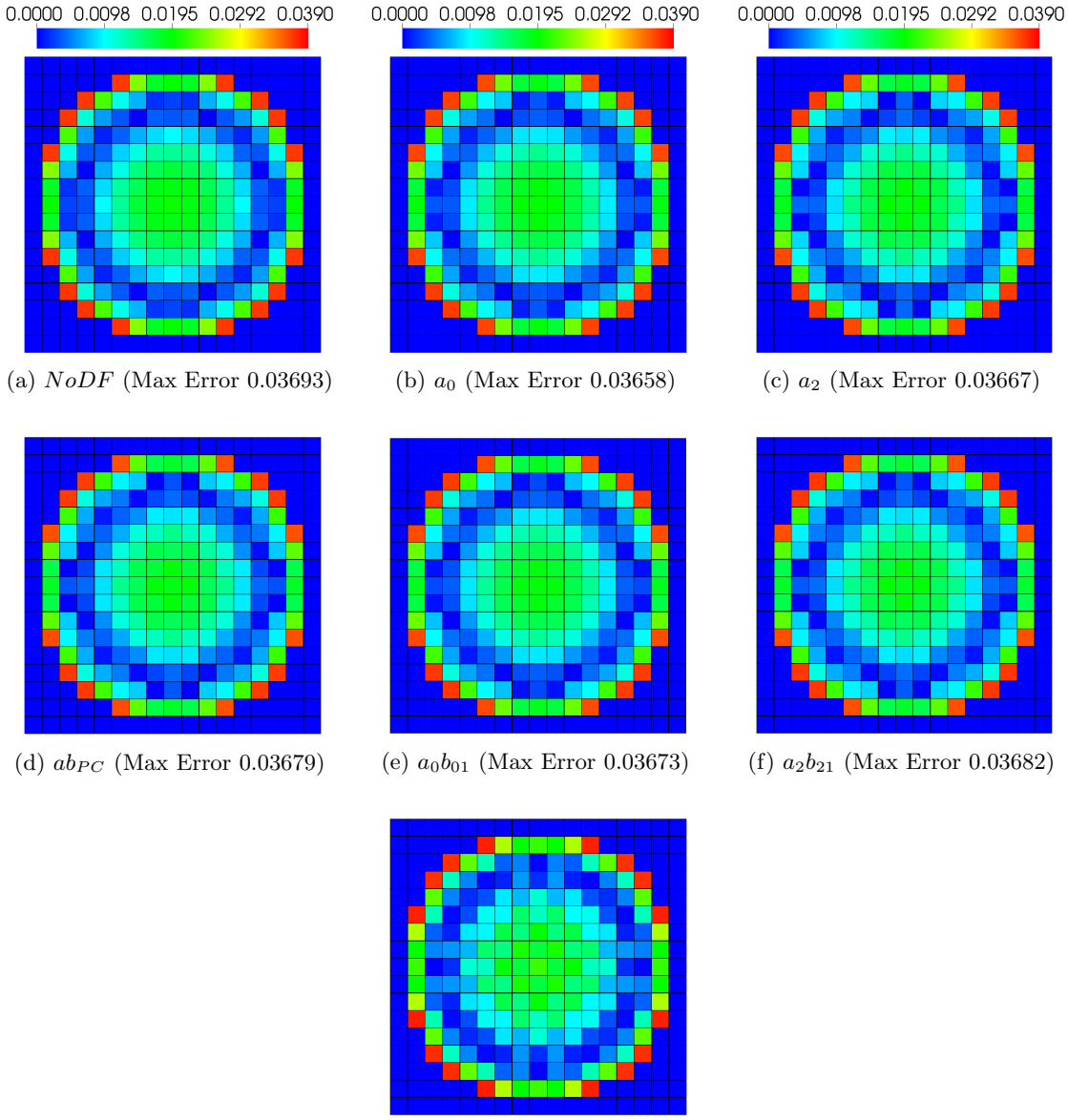

(a) $NoDF$ (Max Error 0.03693) (b) a_0 (Max Error 0.03658) (c) a_2 (Max Error 0.03667)

(d) ab_{PC} (Max Error 0.03679) (e) a_0b_{01} (Max Error 0.03673) (f) a_2b_{21} (Max Error 0.03682)

(g) ab_{Var} (Max Error 0.03781)

Figure 11.18: Absolute Values of Relative Errors in Assembly Powers for the Full-Core LWR Problem with the Asymptotic Diffusion Coefficient and without Reflector Discontinuity Factors (No Pyrex Configuration, 2 Energy Groups).

11.2.2 Full-Core LWR: Unrodded Configuration

Next, we consider the "Unrodded" Configuration, which contains assemblies with Pyrex burnable absorbers, but no assemblies with control rods inserted. Because of the checkerboard loading of assemblies with and without burnable absorbers, the asymptotic DFs are not as accurate as in the "No Pyrex" case, but they still yield an improved solution.

The absolute errors in the reactor multiplication factor for this configuration are shown in Table 11.5. The results indicate that for this configuration, the standard diffusion coefficient yields slightly more accurate values of k than the Benoist diffusion coefficient, which yields slightly more accurate values of k than the asymptotic diffusion coefficient.

The DF results indicate: (i) not using discontinuity factors is less accurate than using any set of DFs, (ii) the a_0 DFs are slightly more accurate than the a_2 DFs (unlike the No Pyrex case), (iii) using flux and current DFs together is more accurate than using only flux DFs, (iv) using DFs at the fuel-reflector interface is slightly more accurate than not doing so, and (v) the ab_{Var} DFs yield the most accurate estimate of k, as expected due to the definition of the functional in the variational analysis.

The reference assembly powers for the Unrodded Configuration are shown in Fig. 11.19. Figures 11.20, 11.21, and 11.22 show the relative errors in the assembly powers for the standard, Benoist, and asymptotic diffusion coefficients respectively. Each of the three diffusion coefficients yield similarly accurate results for this configuration.

Table 11.5: Absolute Error in k for the Full-Core LWR Problem (Unrodded Configuration)[1]

	With Fuel-Reflector DFs		
Discontinuity Factor	D_s	$\boldsymbol{D}_{bu}$	$\boldsymbol{D}_a$
$NoDF$	-269	-281	-291
a_0	-143	-154	-162
a_0b_{01}	-	-	-122
a_2	-149	-160	-168
a_2b_{21}	-	-	-128
ab_{PC}	-	-	-127
ab_{Var}	-	-	-114
	Without Fuel-Reflector DFs		
Discontinuity Factor	D_s	$\boldsymbol{D}_{bu}$	$\boldsymbol{D}_a$
a_0	-148	-159	-167
a_0b_{01}	-	-	-137
a_2	-158	-170	-178
a_2b_{21}	-	-	-147
ab_{PC}	-	-	-144
ab_{Var}	-	-	-133

[1] All errors in pcm. The reference value of k from an MOC calculation is 1.00211.

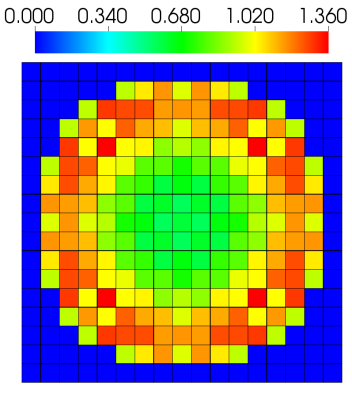

(a) $NoDF$

Figure 11.19: Reference Assembly Powers for the Full-Core LWR Problem (Unrodded Configuration). Numbers indicate normalized power in each assembly.

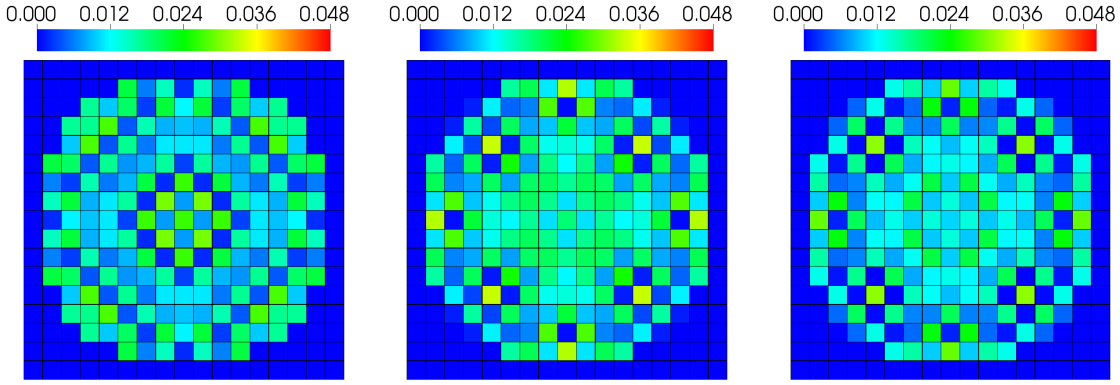

(a) $NoDF$ (Max Error 0.02955) (b) a_0 (Max Error 0.03336) (c) a_2 (Max Error 0.03063)

Figure 11.20: Absolute Values of Relative Errors in Assembly Powers for the Full-Core LWR Problem with the Standard Diffusion Coefficient (Unrodded Configuration, 2 Energy Groups).

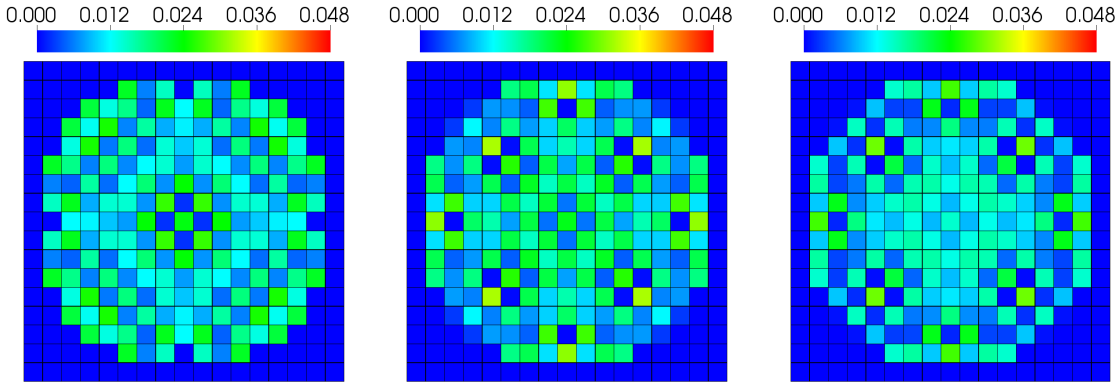

(a) $NoDF$ (Max Error 0.02650) (b) a_0 (Max Error 0.03199) (c) a_2 (Max Error 0.02925)

Figure 11.21: Absolute Values of Relative Errors in Assembly Powers for the Full-Core LWR Problem with the Benoist Diffusion Coefficient (Unrodded Configuration, 2 Energy Groups).

We compare the various DFs to each other and find that the a_2 DFs are more accurate than the a_0 DFs. Unlike the No Pyrex Configuration, in the Unrodded Configuration, the flux and current DFs together yield less accurate results than using only flux DFs. Using no DFs gives lower maximum errors than using any DFs, and the ab_{Var} DFs are among the least accurate.

The poor performance of the DFs is likely a result of the checkerboard loading of assemblies with burnable absorbers. As observed in Section 10.2.2, checkerboard loading of unlike assemblies violates the assumptions of the asymptotic and varia-

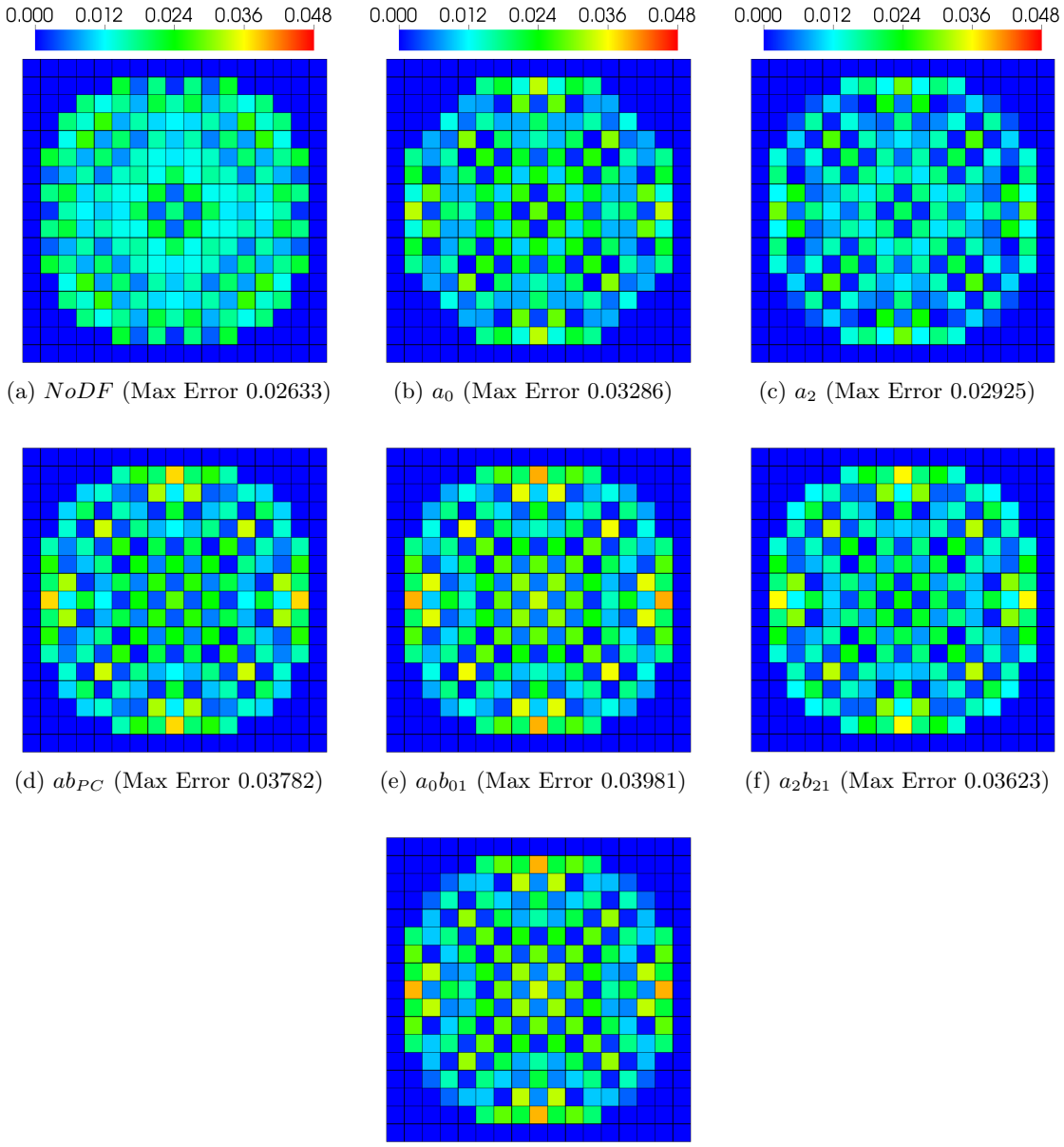

(a) $NoDF$ (Max Error 0.02633) (b) a_0 (Max Error 0.03286) (c) a_2 (Max Error 0.02925)

(d) ab_{PC} (Max Error 0.03782) (e) a_0b_{01} (Max Error 0.03981) (f) a_2b_{21} (Max Error 0.03623)

(g) ab_{Var} (Max Error 0.03961)

Figure 11.22: Absolute Values of Relative Errors in Assembly Powers for the Full-Core LWR Problem with the Asymptotic Diffusion Coefficient (Unrodded Configuration, 2 Energy Groups).

tional analyses, and leads to poor DF performance. The poor performance was also observed by Cheng, who showed that for a checkerboard loading of rodded assemblies, standard ADFs (a_0) tend to underpredict assembly powers in rodded nodes and overpredict powers in unrodded nodes [57]. When no DFs are used, the opposite is true. Thus, the standard ADFs overcorrect for errors when no DFs are used.

Although our assemblies contain a checkerboard loading of burnable absorbers, rather than control rods, the situation is similar, and the DFs overcorrect for errors occurring when no DFs are used. To see this, we plot the relative errors using no DFs and ADFs (a_0 DFs) in Fig. 11.23. Unlike the other figures in this chapter, the color scale indicates relative errors, as opposed to magnitudes of the relative errors. In other words, the color scale indicates when the error is negative or positive. This allows us to see where assembly powers are overpredicted, and where they are underpredicted. The figure indicates that not using DFs yields powers that are too low in most unrodded assemblies, and too high in most rodded assemblies. The opposite is true for the standard ADFs, as expected.

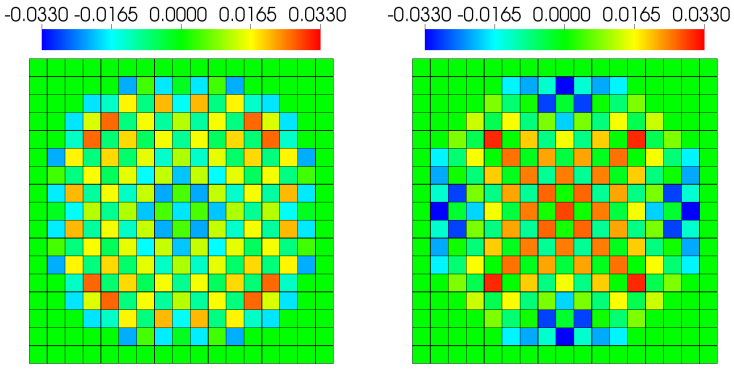

(a) $NoDF$ (b) a_0

Figure 11.23: Relative Errors in Assembly Powers for the Full-Core LWR Problem with the Asymptotic Diffusion Coefficient (Unrodded Configuration, 2 Energy Groups). The unrodded and rodded assemblies are loaded (with few exceptions) in a checkerboard pattern, with the central assembly being unrodded.

Figure 11.24 shows the relative errors in the assembly powers when DFs are applied between fuel assemblies, but not at the fuel-reflector interface. Comparing to Figure 11.22, which shows the relative errors in the assembly powers when DFs are applied at the fuel-reflector interface, we see that the fuel-reflector DFs improve the solution when current DFs are used, but decrease the accuracy of the solution when only flux DFs are used. The inconsistent behavior for fuel-reflector DFs was observed

in Section 10.3.

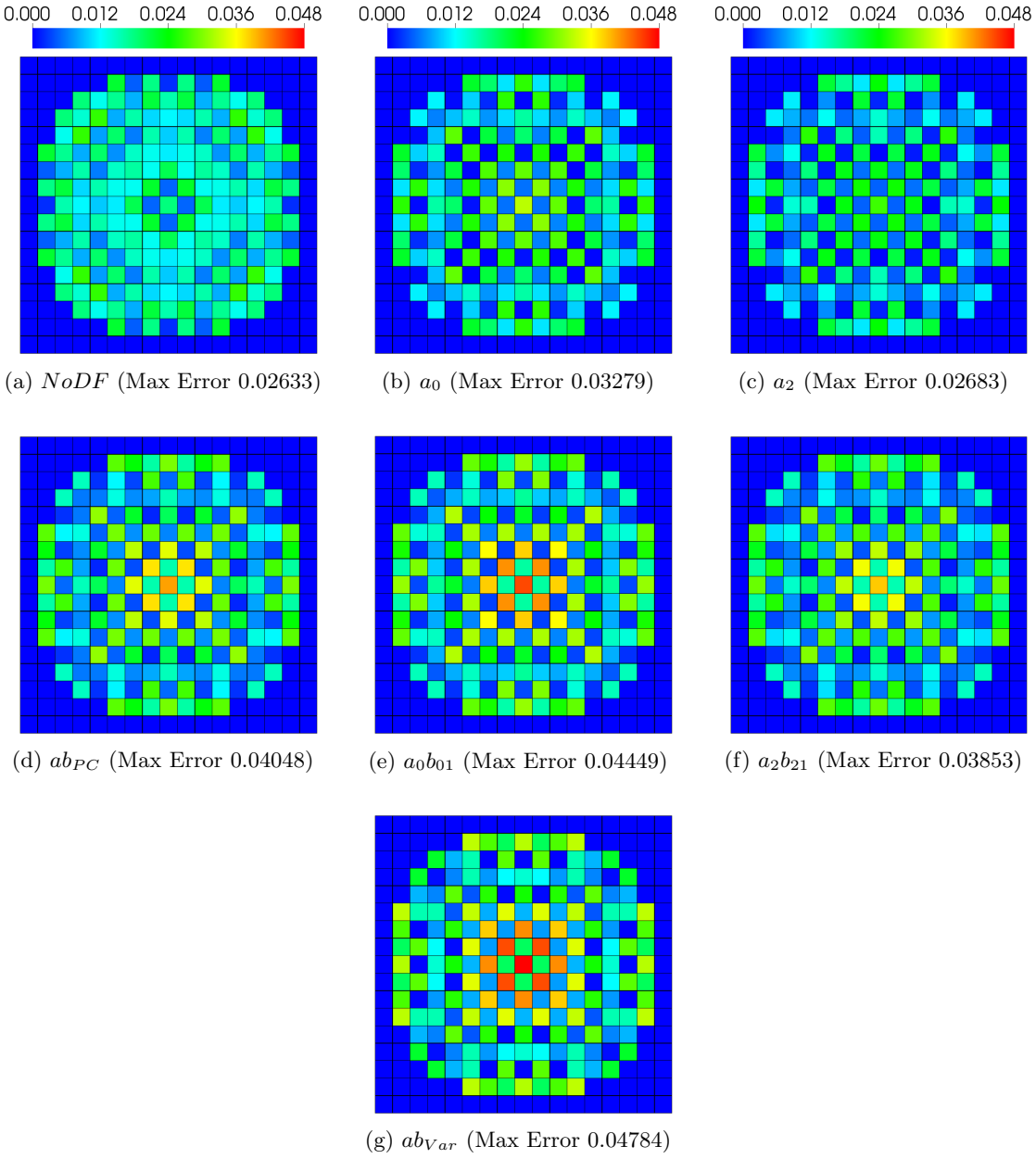

(a) $NoDF$ (Max Error 0.02633) (b) a_0 (Max Error 0.03279) (c) a_2 (Max Error 0.02683)

(d) ab_{PC} (Max Error 0.04048) (e) a_0b_{01} (Max Error 0.04449) (f) a_2b_{21} (Max Error 0.03853)

(g) ab_{Var} (Max Error 0.04784)

Figure 11.24: Absolute Values of Relative Errors in Assembly Powers for the Full-Core LWR Problem with the Asymptotic Diffusion Coefficient and without Reflector Discontinuity Factors (Unrodded Configuration, 2 Energy Groups).

11.2.3 Full-Core LWR: Rodded Configuration

The final configuration, "Rodded", contains both burnable absorbers and 3 asymmetrically loaded rodded assemblies. The presence of the control rods makes the power distribution in the core asymmetric, and introduces large flux gradients.

Table 11.6 lists the absolute errors in the reactor multiplication factor for this configuration. For the Rodded Configuration, as with the Unrodded Configuration, the standard diffusion coefficient yields slightly more accurate values of k than the Benoist diffusion coefficient, which yields slightly more accurate values of k than the asymptotic diffusion coefficient.

Comparing the DF results, we find the same trends observed for the Unrodded Configuration: (i) not using discontinuity factors is less accurate than using any set of DFs, (ii) the a_0 DFs are slightly more accurate than the a_2 DFs, (iii) using flux and current DFs together is more accurate than using only flux DFs, (iv) using DFs at the fuel-reflector interface is slightly more accurate than not doing so, and (v) the ab_{Var} DFs yield the most accurate estimate of k.

The reference assembly powers for the Rodded Configuration are shown in Fig. 11.25.

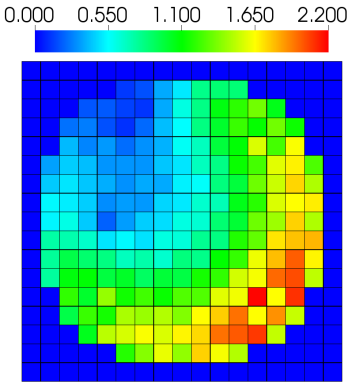

(a) $NoDF$

Figure 11.25: Reference Assembly Powers for the Full-Core LWR Problem (Rodded Configuration). Numbers indicate normalized power in each assembly.

Table 11.6: Absolute Error in k for the Full-Core LWR Problem (Rodded Configuration)[1]

	With Fuel-Reflector DFs		
Discontinuity Factor	D_s	$\boldsymbol{D}_{bu}$	$\boldsymbol{D}_a$
$NoDF$	-267	-280	-290
a_0	-140	-152	-161
$a_0 b_{01}$	-	-	-120
a_2	-147	-158	-167
$a_2 b_{21}$	-	-	-126
ab_{PC}	-	-	-125
ab_{Var}	-	-	-113
	Without Fuel-Reflector DFs		
Discontinuity Factor	D_s	$\boldsymbol{D}_{bu}$	$\boldsymbol{D}_a$
a_0	-146	-158	-167
$a_0 b_{01}$	-	-	-136
a_2	-157	-168	-177
$a_2 b_{21}$	-	-	-146
ab_{PC}	-	-	-143
ab_{Var}	-	-	-133

[1] All errors in pcm. The reference value of k from an MOC calculation is 1.00106.

Relative errors in the assembly powers for the standard, Benoist, and asymptotic diffusion coefficients are shown in Figs. 11.26, 11.27, and 11.28 respectively. By comparing the various diffusion coefficients, we find that the asymptotic diffusion coefficient yields the smallest maximum assembly power error, but has larger errors in many assemblies than the other diffusion coefficients. The standard and Benoist diffusion coefficients yield similar assembly powers.

We now compare the results for different DFs. The use of DFs improves the accuracy of the assembly powers compared to not using any. The a_2 DFs are more accurate than the a_0 DFs for all diffusion coefficients. Like the Unrodded Configuration, and unlike the No Pyrex Configuration, using current and flux DFs together is less accurate than using only flux DFs. The poor performance of the current DFs is likely a consequence of the reactor not being periodic or nearly-periodic. As a result, the asymptotic and variational analyses do not apply, and DF performance is

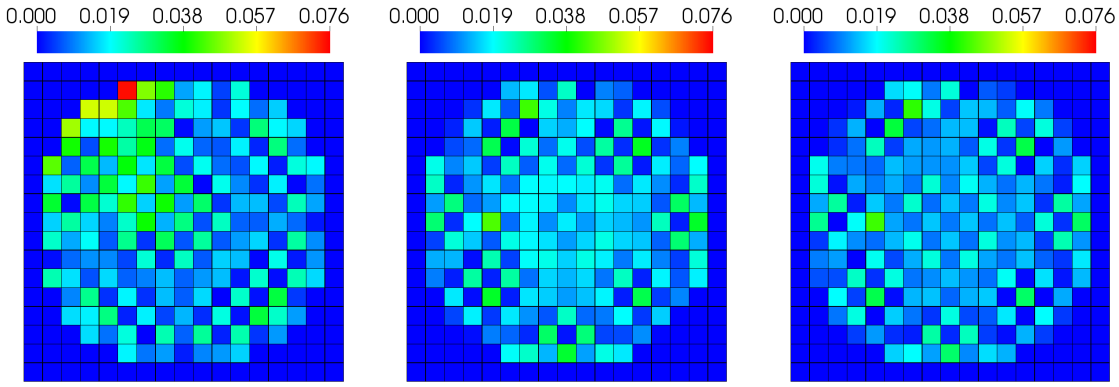

(a) $NoDF$ (Max Error 0.07500) (b) a_0 (Max Error 0.04378) (c) a_2 (Max Error 0.04263)

Figure 11.26: Absolute Values of Relative Errors in Assembly Powers for the Full-Core LWR Problem with the Standard Diffusion Coefficient (Rodded Configuration, 2 Energy Groups).

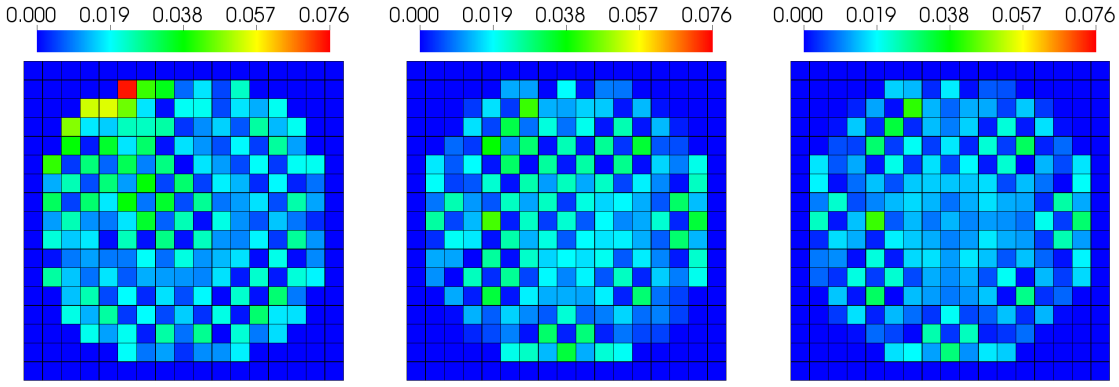

(a) $NoDF$ (Max Error 0.07444) (b) a_0 (Max Error 0.04334) (c) a_2 (Max Error 0.04222)

Figure 11.27: Absolute Values of Relative Errors in Assembly Powers for the Full-Core LWR Problem with the Benoist Diffusion Coefficient (Rodded Configuration, 2 Energy Groups).

inconsistent. As with many other of our test problems, the DFs that give the most accurate values of k and the DFs that give the most accurate assembly powers are not the same.

We do not present results without DFs at fuel-reflector interfaces, as the behavior is the same for this configuration as it was for the No Pyrex Configuration: using DFs at fuel-reflector interfaces yields more accurate assembly powers compared to not doing so.

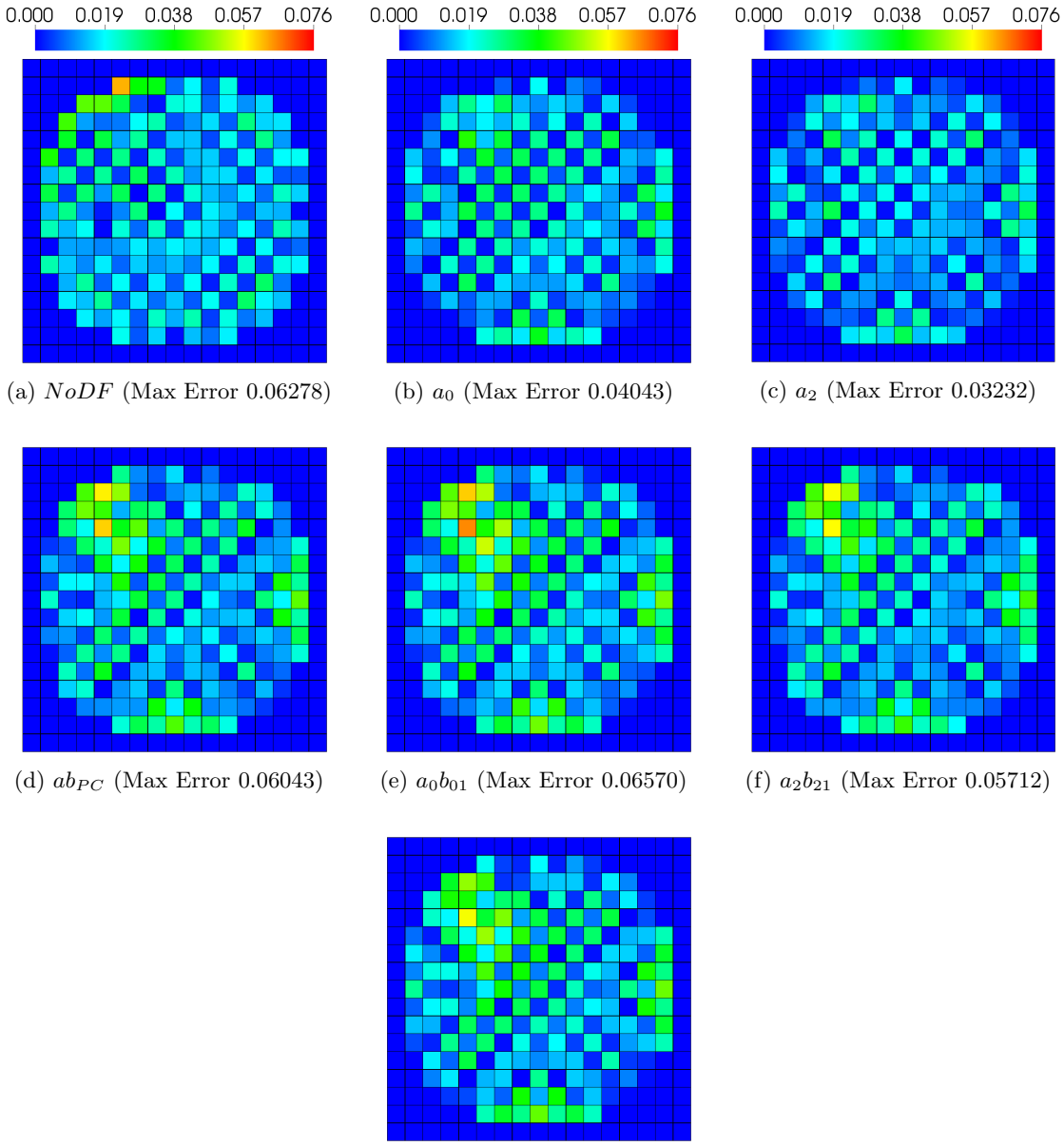

(a) $NoDF$ (Max Error 0.06278) (b) a_0 (Max Error 0.04043) (c) a_2 (Max Error 0.03232)

(d) ab_{PC} (Max Error 0.06043) (e) a_0b_{01} (Max Error 0.06570) (f) a_2b_{21} (Max Error 0.05712)

(g) ab_{Var} (Max Error 0.05620)

Figure 11.28: Absolute Values of Relative Errors in Assembly Powers for the Full-Core LWR Problem with the Asymptotic Diffusion Coefficient (Rodded Configuration, 2 Energy Groups).

11.3 Summary

In this chapter, we presented numerical results for two challenging LWR (specifically, PWR) test problems. The C5G7 benchmark reactor is small, non-periodic, and contains drastic changes in material leading to energy spectra that are very different from those predicted by single assembly lattice calculations. As a result, the

assumptions of the asymptotic analysis are violated to a great degree. Nevertheless, the asymptotic method is still similar in accuracy to the other methods.

The full-core LWR test problem is large, and the unrodded assemblies without burnable absorbers are all similar in composition. However, the Unrodded and Rodded Configurations contain a checkerboard loading of assemblies with burnable absorbers, and this makes the system non-periodic. The No Pyrex Configuration also contains a checkerboard loading of assemblies with different enrichments, although there are no burnable absorbers. Nevertheless, the asymptotic diffusion method yields similar results to the standard and Benoist diffusion methods.

For both problems, the standard diffusion coefficient tends to yield slightly more accurate estimates of the reactor multiplication factor than the other diffusion coefficients, while the asymptotic diffusion coefficient tends to yield the smallest maximum errors in assembly power. For most configurations, the a_2 DFs are more accurate than the a_0 DFs, and flux and current DFs together are more accurate than flux DFs alone. However, this is not true for all configurations, particularly for the full-core LWR. Finally, although using no DF almost always yields the least accurate estimate of the reactor multiplication factor, it does sometimes yield the most accurate assembly powers. This is consistent with the results of Cheng, who showed that DFs can overcorrect for errors in pressurized LWR cores with checkerboard loadings of rodded assemblies. Conversely, the ab_{Var} DFs typically give the best estimates of the reactor multiplication factor, but are often among the least accurate DFs in terms of assembly power. This is because the functional in the variational analysis optimally estimates the reactor multiplication factor. Other variational analyses could be applied to optimally estimate assembly-averaged reaction rates or surface-averaged leakage rates, and these may lead to DFs that give more accurate assembly powers.

We conclude that the asymptotic method can be safely applied to any problem, regardless of whether or not it is periodic or nearly-periodic. In the worst case, the asymptotic diffusion method will perform similarly to traditional diffusion methodologies. If the problem is nearly periodic, or if it contains strongly anisotropic diffusion behavior, the asymptotic method will likely yield more accurate solutions.

CHAPTER XII

Conclusions and Future Work

In this final chapter, we summarize our theoretical and numerical results and discuss ongoing and future work related to the asymptotic, homogenized diffusion approximation presented in this thesis.

12.1 Summary of the Asymptotic, Homogenized Diffusion Method

Over the past half-century or more, reactor analysts have developed a methodology for simulating nuclear reactor cores based largely on engineering approximations. The multigroup approximation, homogenized cross sections and, to a greater extent, homogenized diffusion coefficients, and assembly discontinuity factors (as opposed to exact, reactor discontinuity factors) are all obtained via engineering approximations. Despite this, reactor analysts have found great success linking these approximations and using them to design several generations of nuclear reactors.

In this thesis, we have derived an alternative methodology based on rigorous mathematical analysis of the Boltzmann neutron transport equation. The resulting asymptotic, homogenized, anisotropic, multigroup diffusion approximation is remarkably similar to standard homogenized, multigroup diffusion approximation typically used for reactor analysis. This gives a theoretical justification to the standard methodology developed over the past several decades. Nevertheless, there are

key differences between the asymptotic method and the standard method, and these are discussed below.

Because the asymptotic method is rigorously derived, it is straightforward to identify where improvements can be made. This is less clear for the standard method, because it is not always obvious how an additional mathematical or engineering approximation can be applied to a method based on intuition and experience.

The asymptotic analysis begins by considering the Boltzmann neutron transport equation in the limit of a large, spatially periodic (lattice) medium (Chapter III). The solvability conditions for the second- and third-order asymptotic equations lead to a homogenized, monoenergetic diffusion equation. Monoenergetic diffusion is not useful for reactor analysis because energy-dependent effects can have a large effect on the solution. Unfortunately, there is no known asymptotic analysis of the continuous energy transport equation that leads to a multigroup diffusion equation.

Instead, we apply the same asymptotic scaling to a hypothesized form of the homogenized, multigroup diffusion equation (Chapter IV). The analysis again leads to a monoenergetic diffusion equation, but we choose definitions of the multigroup diffusion coefficients that make this monoenergetic diffusion equation the same as that obtained from analysis of the continuous energy transport equation. Thus, *the homogenized, multigroup diffusion equation with these asymptotic diffusion coefficients and the continuous energy transport equation have the same asymptotic limit for large lattice systems.*

The asymptotic, homogenized, multigroup diffusion equation is nearly identical to the standard multigroup diffusion equation. The key difference is that the standard diffusion coefficient is ambiguously defined, while the asymptotic diffusion coefficient is an unambiguously defined tensor. Furthermore, the asymptotic analysis gives an

expression for reconstructing the angular flux using the lattice transport and full-core diffusion solutions. The leading-order term of this asymptotic expansion of the angular flux is identical to the standard flux reconstruction. However, the expansion contains an additional, formally small correction term that can improve the accuracy of the angular flux, particularly in regions where the gradient of the diffusion solution is large.

Typically, discontinuity factors are applied at interfaces between lattice regions of different types. Exact, reactor discontinuity factors can be defined that preserve surface-averaged currents across these interfaces, but the exact definitions require knowledge of the full-core transport solution, which makes them impractical. Instead, approximate assembly discontinuity factors are defined that use transport solutions for individual assemblies. These assembly discontinuity factors make the reconstructed scalar flux continuous across an interface, as one might expect based on physical intuition.

Because the asymptotic reconstructed flux contains an additional term, we have an additional degree of freedom to make *two* angular moments of the reconstructed flux continuous across interfaces, rather than just one. We defined several (heuristic) discontinuity factors that make various combinations of angular moments of the reconstructed flux continuous across interfaces in Chapter V.

We also variationally derived boundary and interface conditions specifically for lattice systems in Chapter V. The functional in the variational analysis optimally estimates the reactor multiplication factor (or rather, its inverse). As a result, our boundary and interface conditions are expected to give good estimates of the reactor multiplication factor.

Standard vacuum boundary conditions for the homogenized diffusion equation are

obtained using variational analysis of a truly homogeneous half-space. This is not appropriate for a lattice system. Our variationally-derived extrapolated boundary conditions for vacuum boundaries should yield more accurate eigenvalues for lattice systems, though they may not yield better fluxes or assembly powers. The variational extrapolation lengths depend on a parameter $-1 \leq \alpha \leq 1$ that can be tuned to obtain better results. Unfortunately, there is no known systematic method for choosing the optimal value of α.

The variationally-derived discontinuity factors define a flux and current discontinuity in the diffusion solution, and should yield more accurate estimates of the reactor multiplication factor than both the standard assembly discontinuity factors and our heuristic ones. The variational discontinuity factors are weighted with adjoint lattice functions from both sides of the interface. Thus, the variational discontinuity factors use information from neighboring assemblies, yet they avoid the use of colorset calculations.

We note that our exact variational extrapolation lengths are monoenergetic and space-dependent. Approximations were made to obtain multigroup, surface-averaged quantities. It is clear that these approximations can be improved, and in some cases avoided, and that doing this would improve the performance of the asymptotic boundary and interface conditions.

12.2 Summary of Numerical Results

We now summarize the numerical results presented in this thesis. First, we note the following about the asymptotic diffusion coefficient:

1. The asymptotic diffusion coefficient is an anisotropic tensor.

2. For light water reactors, the tensor is most anisotropic in thermal energy groups.

In fast energy groups, regions are optically thinner, and diffusion coefficients are well-approximated by simple volume-averaged (isotropic) quantities.

3. In problems containing long, optically-thin channels through which neutrons can stream long distances, the component of the tensor describing diffusion parallel to the channels is significantly larger than the components corresponding to diffusion perpendicular to the channels.

When the assumptions of the asymptotic analysis are met, the asymptotic diffusion method outperforms the standard and Benoist diffusion methods (Chapters VII and VIII). In particular:

1. The asymptotic diffusion coefficient yields more accurate estimates of the reactor multiplication factor, scalar fluxes, and assembly powers than the other diffusion coefficients.

2. The asymptotic reconstructed flux with the first-order correction term is more accurate than the standard reconstructed flux, which includes only the leading-order asymptotic term. The improvement is small in regions where the diffusion solution is slowly varying, but significant where the gradient of the diffusion solution is large.

3. The asymptotic and Benoist diffusion coefficients are significantly more accurate than the standard diffusion coefficient for problems containing strongly anisotropic diffusion behavior, such as reactors with long, optically-thin channels. Thus, the method is expected to perform well for Very High Temperature Reactors. It may also perform well for Boiling Water Reactors.

When the assumptions of the asymptotic analysis are violated, even to an extreme degree, the asymptotic diffusion method performs comparably to the standard and

Benoist diffusion methods. Thus, the asymptotic method is "safe" to use for any problem.

In this thesis, we studied the effectiveness of non-standard vacuum boundary extrapolation lengths and discontinuity factors (Chapters IX and X). The non-standard extrapolation lengths and discontinuity factors clearly outperformed standard extrapolation lengths and discontinuity factors in 1-D, but results were often less clear for multi-dimensional problems. We recall that the exact extrapolation lengths and discontinuity factors derived in Chapter V were all space-dependent for multi-dimensional problems, but to make them more practical, we made approximations to obtain surface-averaged quantities. Since our non-standard boundary and interface conditions perform well in 1-D, where these approximations are not necessary, we conclude that using space-dependent extrapolation lengths and discontinuity factors will yield more accurate results in problems in which space-dependent behavior occurs on boundaries and interfaces.

Our boundary condition results (Chapter IX) have shown that the variational extrapolation lengths for vacuum boundaries can yield more accurate solutions than standard extrapolation lengths (e.g., Marshak or Milne), but the value of α that gives the most accurate reactor multiplication factor is often different than the value of α that gives the most accurate scalar fluxes or assembly powers. At this time, it is not known how to systematically choose an optimal value of α.

Numerical tests have shown that our non-standard discontinuity factors perform well for problems in which lattice composition changes only every several assemblies. For these problems:

1. Discontinuity factors that make the second moment of the reconstructed flux continuous across interfaces typically yield more accurate reactor multiplication

factors, scalar fluxes, and assembly powers than the standard assembly discontinuity factors, which make the zeroth moment (scalar flux) of the reconstructed flux continuous across interfaces. This is true when using either one or two sets of discontinuity factors.

2. Using two sets of discontinuity factors to make two angular moments of the reconstructed flux continuous across interfaces often yields better reactor multiplication factors, scalar fluxes, and assembly powers than using only a single set of discontinuity factors.

3. The variational discontinuity factors are typically among the most accurate discontinuity factors.

However, when assemblies of different types are loaded in a checkerboard pattern, as is typically the case, or if assembly compositions are drastically different (e.g. MOX and UO2 assemblies, or assemblies with and without strong neutron absorbers) the discontinuity factor results are more erratic:

1. Using no discontinuity factors is sometimes better than using any discontinuity factors, either standard or non-standard.

2. The variational discontinuity factors are typically the most accurate in terms of the reactor multiplication factor.

3. Often the discontinuity factors that yield the best estimate of the reactor multiplication factor yield the worst assembly powers, and vice versa.

We note also that our treatment of discontinuity factors at fuel-reflector interfaces is heuristic, and their performance varies greatly from one problem to the next. We conclude that for neighboring assemblies of drastically different composition, and at fuel-reflector interfaces, colorset calculations should be more accurate than

discontinuity factors calculated from single-assembly calculations.

12.3 Ongoing and Future Work

We end this thesis with a discussion of ongoing and future work related to the asymptotic diffusion method. There are numerous ways to improve the implementation of the method, including: (i) using nodal diffusion in place of finite-difference diffusion, and (ii) reducing the memory usage in the lattice calculations, as this is usually a limiting factor in how finely the system can be discretized, and how many processors can be used when using domain-replicated parallelism.

The variational analysis to obtain boundary and interface conditions is not unique. Our variational analysis makes use of a functional that optimally estimates the reactor multiplication factor, but it is likely that optimally estimating assembly-averaged reaction rates or surface-averaged leakage rates across interfaces would yield more accurate assembly powers. This should be attempted in the future. An effort should also be made to develop a systematic method for choosing the optimal value of α in the calculation of the variational extrapolation lengths.

In our work, we have assumed that changes in the lattice composition occur abruptly (e.g., at the interfaces between pins or assemblies of different types), and the lattice is otherwise perfectly periodic. In reality, burnup of the fuel leads to gradual changes in composition from one pin to the next. Some preliminary work has been performed for nearly-periodic lattices with slowly varying composition. This could be useful for depletion calculations.

Our treatment of non-multiplying regions (e.g., reflector assemblies) has combined standard practice (for calculation of homogenized, multigroup parameters) and heuristic approximations (for calculation of discontinuity factors at the fuel-reflector

interface). In the future, a more rigorous mathematical treatment should be applied to non-multiplying regions.

Finally, the asymptotic analysis can be extended to include more terms in the asymptotic expansion. This is the subject of another Ph.D. thesis currently in progress. Using more asymptotic terms leads to the inclusion of more transport effects in the low-order model (e.g. simplified P_2 instead of diffusion), and also further improves the accuracy of the reconstructed flux. Thus, it is probable that including more asymptotic terms will allow the asymptotic method to be successfully applied to a wider range of problems. For example, it may be that the curious phenomenon observed by Cheng [57] and us - that it does not seem possible to simultaneously optimize the accuracy of k and the assembly powers - is an inherent limitation of the homogenized diffusion model of the Boltzmann transport equation. If so, including more (higher-order) transport terms in the homogenized diffusion model could ameliorate this strange inconsistency.

We conclude this thesis with a list of scenarios for which the use of the asymptotic, homogenized, multigroup diffusion method should be unambiguously advantageous:

1. Modeling problems that are spatially periodic, or nearly-periodic with infrequent changes in assembly composition.
2. Modeling problems containing optically-thin channels, such as Very High Temperature Reactors.
3. Modeling any problem with the 2D/1D method [18, 19], which uses transport physics in the radial directions, and diffusion physics in the axial direction. Since diffusion behavior is typically different in the radial and axial directions, using the axial component of the asymptotic diffusion tensor should provide a significant gain in accuracy.

APPENDICES

APPENDIX A

Glossary

The symbols and acronyms used througout this dissertation are defined here. They are divided into three sections: Greek symbols, Latin symbols, and abbreviations. The symbols are listed alphabetically within each section.

A.1 Acronyms

ADF Assembly Discontinuity Factors.

BWR Boiling Water Reactor.

CASL Consortium for Advanced Simulation of Light water reactors.

DF Discontinuity Factors.

DiffIR Diffusion for Immediate Results (code).

FAT Fredholm Alternative Theorem.

LWR Light Water Reactor.

MC Monte Carlo (transport method).

MOC Method Of Characteristics (transport method).

MOX Mixed Oxide (fuel type).

MPACT Michigan PArallel Characteristics based Transport tool (code).

BWR Pressurized Water Reactor.

VHTR Very High Temperature Reactor.

A.2 Greek Symbols

ϵ Asymptotic scaling parameter. It is formally defined as the ratio of the length scale of a single periodic lattice element to the length scale of the full system.

λ Inverse of the reactor eigenvalue. $\lambda = 1/k$.

ν Average number of neutrons born per fission. It is a function of the incident neutron energy, and it is typically lumped together with Σ_f.

ρ Reactivity. $(1-\rho) = 1/k$. Subscripts indicate order in the asymptotic expansion of the reactivity for large lattice systems.

Σ_a Macroscopic absorption cross section. Typically, Σ_a is a function of space and incident neutron energy. It is the probability per unit distance traveled that a neutron at a point in phase space will undergo an absorption interaction. An overbar indicates that the cross section has been homogenized.

Σ_f Macroscopic fission cross section. Typically, Σ_f is a function of space and incident neutron energy. It is the probability per unit distance traveled that a neutron at a point in phase space will initiate a fission. Σ_f and ν are typically lumped together as they both depend on the incident neutron energy. An overbar indicates that the cross section has been homogenized.

Σ_s Macroscopic differential scattering cross section. Typically, Σ_s is a function of space, cosine of the scattering angle, and incident and outgoing neutron energy. It is the probability per unit distance traveled that a neutron at a point in phase space at an incident energy will undergo a scattering interaction into an outgoing energy with a given scattering angle. An additional subscript n indicates that this is the n-th scattering cross section moment with respect to the cosine of the scattering angle. An overbar indicates that the cross section has been homogenized.

Σ_t Macroscopic total cross section. Typically, Σ_t is a function of space and incident neutron energy. It is the probability per unit distance traveled that a neutron at a point in phase space will undergo an interaction of any kind. An overbar indicates that the cross section has been homogenized.

Σ_{tr} Macroscopic transport cross section. Typically, Σ_{tr} is a function of space and incident neutron energy. It is related to the standard diffusion coefficient by $D = 1/3\Sigma_{tr}$. In one group, it is related to the total cross section by $\Sigma_{tr} = \Sigma_t - \Sigma_{s,1}$. An overbar indicates that the cross section has been homogenized.

ϕ Scalar neutron flux. In general, ϕ is a function of space and energy. It is the integral of ψ over all angles. An $*$ indicates an adjoint scalar flux. Typically in this document, no subscript indicates that the scalar flux comes from a homogenized diffusion calculation, a *lat* subscript indicates that the scalar flux comes from a lattice calculation, a *rec* subscript indicates a reconstructed scalar flux, and a *het* subscript indicates that the scalar flux comes from a transport calculation for the true heterogeneous problem.

χ Fission spectrum. Normalized energy spectrum of neutrons born from fission.

Ψ 1. Angular neutron flux as a function of the asymptotic length scales. It is equal to the angular neutron flux, though it is written as a function of the asymptotic spatial variables, $\boldsymbol{y}$ and $\boldsymbol{z}$. Numerical subscripts indicate a component of the asymptotic expansion of the flux as in: $\Psi = \Psi_0 + \epsilon\Psi_1 + \cdots$.

2. Approximate trial function used in variational estimate of reactor eigenvalue.

ψ Angular neutron flux. In general, ψ is a function of space, angle, and energy. It is directly related to the neutron density at a point in phase space. An $*$ indicates an adjoint angular flux. A b in the subscript indicates a boundary condition.

$\boldsymbol{\Omega}$ Angle vector. Its components are the x, y, and z cosines of a neutron's direction of flight.

A.3 Latin Symbols

A_i 1. Amplitude function. This is the amplitude of the i-th component of the asymptotic expansion of Ψ or Φ. It is a function only of the slow spatial variable, $\boldsymbol{z}$.

2. Area. The subscript indicates that this is the surface area of surface i.

a Coefficient of the quadratic term in the quadratic equation for the extrapolation length l_{lat}.

a_0 Discontinuity factor for making the reconstructed scalar flux continuous across an interface. This is equivalent to standard assembly discontinuity factors.

$a_0 b_{01}$ Discontinuity factors for making the reconstructed scalar flux and net current continuous across an interface.

a_2 Discontinuity factor for making the reconstructed second angular moment continuous across an interface.

$a_2 b_{21}$ Discontinuity factors for making the reconstructed second angular moment and net current continuous across an interface.

ab_{PC} Discontinuity factors for making the reconstructed partial currents continuous across an interface.

ab_{Var} Variational discontinuity factors for the asymptotic, lattice system.

$a_{i,g}$ Flux discontinuity factor. Flux discontinuity factors are defined for every face of every lattice i and for every energy group g. The ratio of flux discontinuity factors at the interface between lattices i and $i+1$ defines a discontinuity in the homogenized diffusion flux at the interface.

B The boundary term in the functional for estimating λ.

$\boldsymbol{B}^2$ Buckling. This a measure of the curvature of the neutron flux.

$\mathrm{B_N}$ Buckling (transport) method.

b Coefficient of the linear term in the quadratic equation for the extrapolation length l_{lat}.

$b_{i,g}$ Current discontinuity factor. Current discontinuity factors are defined for every face of every lattice i and for every energy group g. The ratio of current discontinuity factors at the interface between lattices i and $i+1$ defines a discontinuity in the homogenized diffusion current at the interface.

c Constant coefficient in the quadratic equation for the extrapolation length l_{lat}.

$c_{i,g}$ Adjoint flux discontinuity factor. Flux discontinuity factors are defined for every face of every lattice i and for every energy group g. The ratio of flux discontinuity factors at the interface between lattices i and $i+1$ defines a discontinuity in the homogenized diffusion flux at the interface.

D 1. Diffusion coefficient. It is typically a function of space, energy, and time. The diffusion coefficient relates the scalar flux, ϕ, to the neutron current, $\boldsymbol{J}$ through Fick's Law: $\boldsymbol{J} = -D\nabla\phi$. A bold $\boldsymbol{D}$ indicates that the diffusion coefficient is a tensor, while an overbar indicates the diffusion coefficient has been homogenized. In the numerical results chapters, it is assumed that the diffusion coefficient is homogenized, with or without the overbar.

2. Denominator in the functional for estimating λ.

$\boldsymbol{D}_a$ Asymptotic diffuson coefficient. Equivalent to the Deniz-Gelbard diffusion coefficient.

$\boldsymbol{D}_b$ Benoist diffuson coefficient. The Benoist diffusion coefficient may have an additional subscript u, $c1$, or $c2$. A u indicates that the coefficient is uncorrected, i.e., does not include the "correction" term. $c1$ and $c2$ denote the two possible values of the diffusion coefficient when the "correction" term is included.

D_s Standard diffuson coefficient.

$d_{i,g}$ Adjoint current discontinuity factor. Current discontinuity factors are defined for every face of every lattice i and for every energy group g. The ratio of current discontinuity factors at the interface between lattices i and $i+1$ defines a discontinuity in the homogenized diffusion current at the interface.

E Energy.

F Fission operator.

f Periodic lattice flux. This is the angular flux for an infinite periodic lattice. In the Benoist and Deniz-Gelbard analyses, f has no subscript, and is periodic and complex. Its real and imaginary components are denoted by R and I respectively.

f_0 Infinite lattice eigenfunction. This is the solution to the zeroth order asymptotic equation. It is the angular flux for an infinite periodic medium. It is a function of the fast spatial variable ($\boldsymbol{y}$), angle, and energy. An $*$ indicates an adjoint flux. A subscript i indicates that the lattice function applies to the periodic lattice in region i. A subscript k indicates that the lattice function is averaged over a surface k. A capital F indicates that the function has been integrated over angle, i.e., it is a scalar flux. Note that $F_0 = \phi_{lat}$. The group-integrated, cell-averaged lattice flux is defined $\overline{F_{0,g}} = \frac{1}{V_{cell}} \int_{cell} \int_{E_g}^{E_{g-1}} F_0(\boldsymbol{x}, E)\, \mathrm{d}E\, \mathrm{d}V$.

f_1 First order lattice function. This is the angular flux solution to the first order asymptotic equation. It is a function of the fast spatial variable ($\boldsymbol{y}$), angle, and energy. An $*$ indicates an adjoint flux. A subscript i indicates that the lattice function applies to the periodic lattice in region i. A subscript k indicates that the lattice function is averaged over a surface k. A capital F indicates that the function has been integrated over angle, i.e., it is a scalar flux.

H Functional for estimating λ.

H_0 Functional for estimating λ excluding boundary and interface terms.

I 1. The imaginary component of f. It is closely related to the function f_1. An $*$ indicates an adjoint flux.

2. The interface term in the functional for estimating λ.

$\boldsymbol{J}$ Neutron current. It is a vector, and the components are the number of neutrons crossing a surface perpindicular to the x, y, or z axis per unit area per unit time. It is the first angular moment of ψ.

k 1. Reactor eigenvalue/multiplication factor. It is equal to the number of neutrons in one generation divided by the number of neutrons in the preceding generation.

2. Outer iteration index.

L Continuous energy infinite lattice operator. This operator is the continuous energy Boltzmann transport operator applied to an infinite, periodic lattice.

L_{MG} Multigroup infinite lattice operator for all energy groups. This operator is the multigroup diffusion operator for an infinite, homogenized lattice system. The rows of this operator are the individual group operators L_g.

L_g Multigroup infinite lattice operator for group g. This operator is the multigroup diffusion operator for an infinite, homogenized lattice system.

l Extrapolation length or extrapolation distance. This is the distance, often in units of transport mean free paths, from the system boundary at which the linear extrapolation of the flux on the surface would be 0. The subscripts Mar, $HomVar$, FP, $Milne$, and as denote the Marshak, homogeneous variational, Federighi-Pomraning, Milne, and asymptotic variational extrapolation distances respectively. The asymptotic extrapolation length depends continuously on a parameter α that is allowed to vary between -1 and 1.

M Transport operator. This operator is the Boltzmann transport operator, excluding the fission operator.

$\boldsymbol{n}$ Unit normal vector. Typically appears in surface integrals, in which case it is the outward unit normal vector to the surface of integration. A subscript ij indicates that the vector is oriented from region i into region j.

P_n Legendre polynomial of order n.

$\mathrm{P_N}$ Spherical Harmonics (transport) method.

R The real component of f. It is exactly equal to the function f_0. An $*$ indicates an adjoint flux.

$\mathrm{S_N}$ Discrete Ordinates (transport) method.

V	Volume. A subscript i indicates that this is the volume of region i. ∂V indicates the surface of volume V.
$\boldsymbol{x}$	Position vector. Its components are the x, y, and z coordinates of a neutron's position.
Y_n^m	Spherical harmonics functions. An overbar denotes the complex conjugate.
$\boldsymbol{y}$	Periodic spatial variable. This is the "fast", periodic spatial scale. Its components are the x, y, and z coordinates of a neutron's position within a periodic lattice element.
$\boldsymbol{z}$	Slow spatial variable. This is the "slow", non-periodic spatial variable defined by $\boldsymbol{z} = \epsilon\boldsymbol{x}$. Its components are the x, y, and z coordinates of a neutron's position within the global coordinate system.

APPENDIX B

Material Compositions and Cross Sections

This appendix contains the material compositions and cross sections for the numerical test problems presented in this thesis.

B.1 One-Group Zero Power Plutonium Reactor Materials

The Zero-Power Plutonium Reactor (ZPPR) cross sections are taken directly from a paper by Gelbard, so that we can compare our diffusion coefficients to those that he calculated [31]. The ZPPR was a plate-fuel reactor located at Argonne National Laboratory-West (now Idaho National Laboratory). The fuel plates are made of uranium-oxide and a uranium-plutonium mixture, and are separated by layers of sodium coolant. The one-group cross sections for these materials are shown in Table B.1.

Table B.1: ZPPR One-Group Macroscopic Cross Sections

	Σ_t [cm^{-1}]	Σ_s [cm^{-1}]	Σ_a [cm^{-1}]	$\nu\Sigma_f$ [cm^{-1}]
Uranium Oxide	0.1815510	0.1178900	0.0636610	0.00998
Sodium	0.0452915	0.0267661	0.0185254	0.00000
Uranium Plutonium	0.2526480	0.0860426	0.1666054	0.18500

B.2 One-Group Disontinuity Factor Test Materials

A 2-assembly test problem with only two materials, MOX fuel and light water moderator, is used to test the effectiveness of various disontinuity factors. The MOX

and light water cross sections are the thermal group cross sections from the UO2 Fuel and Moderator respectively in the C5G7 "Benchmark on Deterministic Transport Calculation without Spatial Homogenisation" [79, 78]. The one-group cross sections for these materials are shown in Table B.2.

Table B.2: Two-Assembly Discontinuity Factor Test Macroscopic Cross Sections

	Σ_t [cm^{-1}]	Σ_s [cm^{-1}]	Σ_a [cm^{-1}]	$\nu\Sigma_f$ [cm^{-1}]
UO2 Fuel (Fuel)	5.706100E-01	2.878300E-01	2.827800E-01	5.257105E-01
Water (Mod)	3.305700E+00	3.268461E+00	3.723900E-01	0.000000E+00

B.3 One-Group 1-D Mixed-Oxide Light Water Reactor Materials

A one-group numerical test problem designed by Joo contains 5 different fuel assembly types and a reflector assembly [80]. The assemblies are made of 4 different fuel types (uranium-oxide (UO2), less-enriched uranium-oxide (UO2-l), uranium-oxide with gadalinium burnable poison (UO2-Gd), and mixed-oxide (MOX)), and water coolant at three different densities in the reflector (H2O-Refl), fuel pins (H2O-Fuel), and water holes (H2O-WH). One-group cross sections for the 7 materials used in the numerical test problem are shown in Table B.3.

Table B.3: 1-D MOX LWR One-Group Macroscopic Cross Sections

	Σ_t [cm^{-1}]	Σ_s [cm^{-1}]	Σ_a [cm^{-1}]	$\nu\Sigma_f$ [cm^{-1}]
UO2	3.32734E-1	2.74910E-1	5.78256E-2	7.97840E-2
UO2-l	3.33356E-1	2.75534E-1	5.78218E-2	7.96455E-2
UO2-Gd	8.58463E-2	4.32728E-2	4.25733E-2	1.85589E-3
MOX	2.82548E-1	2.14888E-1	6.76607E-2	8.64238E-2
H2O-Refl	7.85602E-2	7.77942E-2	7.65957E-4	0.00000E+00
H2O-Fuel	1.74713E-1	1.73779E-1	9.33242E-4	0.00000E+00
H2O-WH	9.01554E-2	8.96296E-2	5.25823E-4	0.00000E+00

B.4 Four-Group Very High Temperature Reactor Materials

Four group microscopic cross sections for a Very High Temperature Reactor (VHTR) were generated by Lee using the Dragon code [81, 44]. The microscopic

cross sections were converted to macroscopic cross sections by choosing contrived yet realistic material densities for a typical VHTR. The materials were then mixed into "Fuel", "Graphite", and "Helium" The resulting four-group cross sections for the VHTR test problem can be found in Tables B.4-B.6.

Table B.4: VHTR Four-Group Macroscopic Cross Sections: Fuel

	Σ_t [cm^{-1}]	Σ_a [cm^{-1}]	$\nu\Sigma_f$ [cm^{-1}]	χ
Group 1	1.43957E-01	4.23706E-04	8.35455E-04	6.28884E-01
Group 2	3.07381E-01	2.75031E-04	2.53093E-04	3.70865E-01
Group 3	3.75228E-01	8.02039E-03	3.43677E-03	2.51311E-04
Group 4	3.84996E-01	1.58497E-02	3.09495E-02	0.00000E+00

Scattering Block

Σ_s	Group 1	Group 2	Group 3	Group 4
to Group 1	1.16616E-01	0.00000E+00	0.00000E+00	0.00000E+00
to Group 2	2.69145E-02	2.97515E-01	0.00000E+00	0.00000E+00
to Group 3	2.53164E-06	9.59051E-03	3.61600E-01	1.33131E-03
to Group 4	4.95502E-14	0.00000E+00	5.60739E-03	3.67815E-01

Table B.5: VHTR Four-Group Macroscopic Cross Sections: Graphite

	Σ_t [cm^{-1}]	Σ_a [cm^{-1}]	$\nu\Sigma_f$ [cm^{-1}]	χ
Group 1	1.71975E-01	8.59168E-05	0.00000E+00	0.00000E+00
Group 2	3.58275E-01	1.00948E-07	0.00000E+00	0.00000E+00
Group 3	4.16605E-01	1.01368E-05	0.00000E+00	0.00000E+00
Group 4	4.25085E-01	1.24089E-04	0.00000E+00	0.00000E+00

Scattering Block

Σ_s	Group 1	Group 2	Group 3	Group 4
to Group 1	1.39980E-01	0.00000E+00	0.00000E+00	0.00000E+00
to Group 2	3.19100E-02	3.46750E-01	0.00000E+00	0.00000E+00
to Group 3	1.32632E-07	1.15257E-02	4.09943E-01	1.46501E-03
to Group 4	0.00000E+00	0.00000E+00	6.65206E-03	4.23496E-01

B.5 Seven-Group C5G7 Materials

Seven-group cross section are taken from the C5G7 "Benchmark on Deterministic Transport Calculation without Spatial Homogenisation" [79, 78]. The C5G7 cross sections are presented in Tables B.7-B.14.

Table B.6: VHTR Four-Group Macroscopic Cross Sections: Helium

	Σ_t [cm^{-1}]	Σ_a [cm^{-1}]	$\nu\Sigma_f$ [cm^{-1}]	χ
Group 1	2.54671E-03	0.00000E+00	0.00000E+00	0.00000E+00
Group 2	9.45922E-04	0.00000E+00	0.00000E+00	0.00000E+00
Group 3	4.44827E-04	0.00000E+00	0.00000E+00	0.00000E+00
Group 4	4.54900E-04	0.00000E+00	0.00000E+00	0.00000E+00

Scattering Block

Σ_s	Group 1	Group 2	Group 3	Group 4
to Group 1	1.51556E-03	0.00000E+00	0.00000E+00	0.00000E+00
to Group 2	1.03114E-03	9.11925E-04	0.00000E+00	0.00000E+00
to Group 3	0.00000E+00	3.39971E-05	4.25993E-04	9.53444E-08
to Group 4	0.00000E+00	0.00000E+00	1.88341E-05	4.54804E-04

Table B.7: C5G7 UO2 Fuel-Clad Macroscopic Cross Sections

	Σ_{tr} [cm^{-1}]	Σ_a [cm^{-1}]	$\nu\Sigma_f$ [cm^{-1}]	χ
Group 1	1.77949E-01	8.02480E-03	2.005998E-02	5.8791E-01
Group 2	3.29805E-01	3.71740E-03	2.027303E-03	4.1176E-01
Group 3	4.80388E-01	2.67690E-02	1.570599E-02	3.3906E-04
Group 4	5.54367E-01	9.62360E-02	4.518301E-02	1.1761E-07
Group 5	3.11801E-01	3.00200E-02	4.334208E-02	0.0000E+00
Group 6	3.95168E-01	1.11260E-01	2.020901E-01	0.0000E+00
Group 7	5.64406E-01	2.82780E-01	5.257105E-01	0.0000E+00

Scattering Block

Σ_s	Group 1	Group 2	Group 3	Group 4	Group 5	Group 6	Group 7
to Group 1	1.27537E-01	0.00000E+00	0.00000E+00	0.00000E+00	0.00000E+00	0.00000E+00	0.00000E+00
to Group 2	4.23780E-02	3.24456E-01	0.00000E+00	0.00000E+00	0.00000E+00	0.00000E+00	0.00000E+00
to Group 3	9.43740E-06	1.63140E-03	4.50940E-01	0.00000E+00	0.00000E+00	0.00000E+00	0.00000E+00
to Group 4	5.51630E-09	3.14270E-09	2.67920E-03	4.52565E-01	1.25250E-04	0.00000E+00	0.00000E+00
to Group 5	0.00000E+00	0.00000E+00	0.00000E+00	5.56640E-03	2.71401E-01	1.29680E-03	0.00000E+00
to Group 6	0.00000E+00	0.00000E+00	0.00000E+00	0.00000E+00	1.02550E-02	2.65802E-01	8.54580E-03
to Group 7	0.00000E+00	0.00000E+00	0.00000E+00	0.00000E+00	1.00210E-08	1.68090E-02	2.73080E-01

Table B.8: C5G7 4.3% MOX Fuel-Clad Macroscopic Cross Sections

	Σ_{tr} [cm^{-1}]	Σ_a [cm^{-1}]	$\nu\Sigma_f$ [cm^{-1}]	χ
Group 1	1.78731E-01	8.43390E-03	2.175300E-02	5.8791E-01
Group 2	3.30849E-01	3.75770E-03	2.535103E-03	4.1176E-01
Group 3	4.83772E-01	2.79700E-02	1.626799E-02	3.3906E-04
Group 4	5.66922E-01	1.04210E-01	6.547410E-02	1.1761E-07
Group 5	4.26227E-01	1.39940E-01	3.072409E-02	0.0000E+00
Group 6	6.78997E-01	4.09180E-01	6.666510E-01	0.0000E+00
Group 7	6.82852E-01	4.09350E-01	7.139904E-01	0.0000E+00

Scattering Block

Σ_s	Group 1	Group 2	Group 3	Group 4	Group 5	Group 6	Group 7
to Group 1	1.28876E-01	0.00000E+00	0.00000E+00	0.00000E+00	0.00000E+00	0.00000E+00	0.00000E+00
to Group 2	4.14130E-02	3.25452E-01	0.00000E+00	0.00000E+00	0.00000E+00	0.00000E+00	0.00000E+00
to Group 3	8.22900E-06	1.63950E-03	4.53188E-01	0.00000E+00	0.00000E+00	0.00000E+00	0.00000E+00
to Group 4	5.04050E-09	1.59820E-09	2.61420E-03	4.57173E-01	1.60460E-04	0.00000E+00	0.00000E+00
to Group 5	0.00000E+00	0.00000E+00	0.00000E+00	5.53940E-03	2.76814E-01	2.00510E-03	0.00000E+00
to Group 6	0.00000E+00	0.00000E+00	0.00000E+00	0.00000E+00	9.31270E-03	2.52962E-01	8.49480E-03
to Group 7	0.00000E+00	0.00000E+00	0.00000E+00	0.00000E+00	9.16560E-09	1.48500E-02	2.65007E-01

Table B.9: C5G7 7.0% MOX Fuel-Clad Macroscopic Cross Sections

	Σ_{tr} [cm^{-1}]	Σ_a [cm^{-1}]	$\nu\Sigma_f$ [cm^{-1}]	χ
Group 1	1.81323E-01	9.06570E-03	2.381395E-02	5.8791E-01
Group 2	3.34368E-01	4.29670E-03	3.858689E-03	4.1176E-01
Group 3	4.93785E-01	3.28810E-02	2.413400E-02	3.3906E-04
Group 4	5.91216E-01	1.22030E-01	9.436622E-02	1.1761E-07
Group 5	4.74198E-01	1.82980E-01	4.576988E-02	0.0000E+00
Group 6	8.33601E-01	5.68460E-01	9.281814E-01	0.0000E+00
Group 7	8.53603E-01	5.85210E-01	1.043200E+00	0.0000E+00

Scattering Block

Σ_s	Group 1	Group 2	Group 3	Group 4	Group 5	Group 6	Group 7
to Group 1	1.30457E-01	0.00000E+00	0.00000E+00	0.00000E+00	0.00000E+00	0.00000E+00	0.00000E+00
to Group 2	4.17920E-02	3.28428E-01	0.00000E+00	0.00000E+00	0.00000E+00	0.00000E+00	0.00000E+00
to Group 3	8.51050E-06	1.64360E-03	4.58371E-01	0.00000E+00	0.00000E+00	0.00000E+00	0.00000E+00
to Group 4	5.13290E-09	2.20170E-09	2.53310E-03	4.63709E-01	1.76190E-04	0.00000E+00	0.00000E+00
to Group 5	0.00000E+00	0.00000E+00	0.00000E+00	5.47660E-03	2.82313E-01	2.27600E-03	0.00000E+00
to Group 6	0.00000E+00	0.00000E+00	0.00000E+00	0.00000E+00	8.72890E-03	2.49751E-01	8.86450E-03
to Group 7	0.00000E+00	0.00000E+00	0.00000E+00	0.00000E+00	9.00160E-09	1.31140E-02	2.59529E-01

Table B.10: C5G7 8.7% MOX Fuel-Clad Macroscopic Cross Sections

	Σ_{tr} [cm^{-1}]	Σ_a [cm^{-1}]	$\nu\Sigma_f$ [cm^{-1}]	χ
Group 1	1.83045E-01	9.48620E-03	2.518600E-02	5.8791E-01
Group 2	3.36705E-01	4.65560E-03	4.739509E-03	4.1176E-01
Group 3	5.00507E-01	3.62400E-02	2.947805E-02	3.3906E-04
Group 4	6.06174E-01	1.32720E-01	1.122500E-01	1.1761E-07
Group 5	5.02754E-01	2.08400E-01	5.530301E-02	0.0000E+00
Group 6	9.21028E-01	6.58700E-01	1.074999E+00	0.0000E+00
Group 7	9.55231E-01	6.90170E-01	1.239298E+00	0.0000E+00

Scattering Block

Σ_s	Group 1	Group 2	Group 3	Group 4	Group 5	Group 6	Group 7
to Group 1	1.31504E-01	0.00000E+00	0.00000E+00	0.00000E+00	0.00000E+00	0.00000E+00	0.00000E+00
to Group 2	4.20460E-02	3.30403E-01	0.00000E+00	0.00000E+00	0.00000E+00	0.00000E+00	0.00000E+00
to Group 3	8.69720E-06	1.64630E-03	4.61792E-01	0.00000E+00	0.00000E+00	0.00000E+00	0.00000E+00
to Group 4	5.19380E-09	2.60060E-09	2.47490E-03	4.68021E-01	1.85970E-04	0.00000E+00	0.00000E+00
to Group 5	0.00000E+00	0.00000E+00	0.00000E+00	5.43300E-03	2.85771E-01	2.39160E-03	0.00000E+00
to Group 6	0.00000E+00	0.00000E+00	0.00000E+00	0.00000E+00	8.39730E-03	2.47614E-01	8.96810E-03
to Group 7	0.00000E+00	0.00000E+00	0.00000E+00	0.00000E+00	8.92800E-09	1.23220E-02	2.56093E-01

Table B.11: C5G7 Fission Chamber Macroscopic Cross Sections

	Σ_{tr} [cm^{-1}]	Σ_a [cm^{-1}]	$\nu\Sigma_f$ [cm^{-1}]	χ
Group 1	1.26032E-01	5.1132E-04	1.323401E-08	5.8791E-01
Group 2	2.93160E-01	7.5813E-05	1.434500E-08	4.1176E-01
Group 3	2.84250E-01	3.1643E-04	1.128599E-06	3.3906E-04
Group 4	2.81020E-01	1.1675E-03	1.276299E-05	1.1761E-07
Group 5	3.34460E-01	3.3977E-03	3.538502E-07	0.0000E+00
Group 6	5.65640E-01	9.1886E-03	1.740099E-06	0.0000E+00
Group 7	1.17214E+00	2.3244E-02	5.063302E-06	0.0000E+00

Scattering Block

Σ_s	Group 1	Group 2	Group 3	Group 4	Group 5	Group 6	Group 7
to Group 1	6.61659E-02	0.00000E+00	0.00000E+00	0.00000E+00	0.00000E+00	0.00000E+00	0.00000E+00
to Group 2	5.90700E-02	2.40377E-01	0.00000E+00	0.00000E+00	0.00000E+00	0.00000E+00	0.00000E+00
to Group 3	2.83340E-04	5.24350E-02	1.83425E-01	0.00000E+00	0.00000E+00	0.00000E+00	0.00000E+00
to Group 4	1.46220E-06	2.49900E-04	9.22880E-02	7.90769E-02	3.73400E-05	0.00000E+00	0.00000E+00
to Group 5	2.06420E-08	1.92390E-05	6.93650E-03	1.69990E-01	9.97570E-02	9.17420E-04	0.00000E+00
to Group 6	0.00000E+00	2.98750E-06	1.07900E-03	2.58600E-02	2.06790E-01	3.16774E-01	4.97930E-02
to Group 7	0.00000E+00	4.21400E-07	2.05430E-04	4.92560E-03	2.44780E-02	2.38760E-01	1.09910E+00

Table B.12: C5G7 Guide Tube Macroscopic Cross Sections

	Σ_{tr} [cm^{-1}]	Σ_a [cm^{-1}]	$\nu\Sigma_f$ [cm^{-1}]	χ
Group 1	1.26032E-01	5.1132E-04	0.000000E+00	0.0000E+00
Group 2	2.93160E-01	7.5801E-05	0.000000E+00	0.0000E+00
Group 3	2.84240E-01	3.1572E-04	0.000000E+00	0.0000E+00
Group 4	2.80960E-01	1.1582E-03	0.000000E+00	0.0000E+00
Group 5	3.34440E-01	3.3975E-03	0.000000E+00	0.0000E+00
Group 6	5.65640E-01	9.1878E-03	0.000000E+00	0.0000E+00
Group 7	1.17215E+00	2.3242E-02	0.000000E+00	0.0000E+00

Scattering Block

Σ_s	Group 1	Group 2	Group 3	Group 4	Group 5	Group 6	Group 7
to Group 1	6.61659E-02	0.00000E+00	0.00000E+00	0.00000E+00	0.00000E+00	0.00000E+00	0.00000E+00
to Group 2	5.90700E-02	2.40377E-01	0.00000E+00	0.00000E+00	0.00000E+00	0.00000E+00	0.00000E+00
to Group 3	2.83340E-04	5.24350E-02	1.83297E-01	0.00000E+00	0.00000E+00	0.00000E+00	0.00000E+00
to Group 4	1.46220E-06	2.49900E-04	9.23970E-02	7.88511E-02	3.73330E-05	0.00000E+00	0.00000E+00
to Group 5	2.06420E-08	1.92390E-05	6.94460E-03	1.70140E-01	9.97372E-02	9.17260E-04	0.00000E+00
to Group 6	0.00000E+00	2.98750E-06	1.08030E-03	2.58810E-02	2.06790E-01	3.16765E-01	4.97920E-02
to Group 7	0.00000E+00	4.21400E-07	2.05670E-04	4.92970E-03	2.44780E-02	2.38770E-01	1.09912E+00

Table B.13: C5G7 Moderator Macroscopic Cross Sections

	Σ_{tr} [cm^{-1}]	Σ_a [cm^{-1}]	$\nu\Sigma_f$ [cm^{-1}]	χ
Group 1	1.59206E-01	6.01050E-04	0.000000E+00	0.0000E+00
Group 2	4.12970E-01	1.57930E-05	0.000000E+00	0.0000E+00
Group 3	5.90310E-01	3.37160E-04	0.000000E+00	0.0000E+00
Group 4	5.84350E-01	1.94060E-03	0.000000E+00	0.0000E+00
Group 5	7.18000E-01	5.74160E-03	0.000000E+00	0.0000E+00
Group 6	1.25445E+00	1.50010E-02	0.000000E+00	0.0000E+00
Group 7	2.65038E+00	3.72390E-02	0.000000E+00	0.0000E+00

Scattering Block

Σ_s	Group 1	Group 2	Group 3	Group 4	Group 5	Group 6	Group 7
to Group 1	4.44777E-02	0.00000E+00	0.00000E+00	0.00000E+00	0.00000E+00	0.00000E+00	0.00000E+00
to Group 2	1.13400E-01	2.82334E-01	0.00000E+00	0.00000E+00	0.00000E+00	0.00000E+00	0.00000E+00
to Group 3	7.23470E-04	1.29940E-01	3.45256E-01	0.00000E+00	0.00000E+00	0.00000E+00	0.00000E+00
to Group 4	3.74990E-06	6.23400E-04	2.24570E-01	9.10284E-02	7.14370E-05	0.00000E+00	0.00000E+00
to Group 5	5.31840E-08	4.80020E-05	1.69990E-02	4.15510E-01	1.39138E-01	2.21570E-03	0.00000E+00
to Group 6	0.00000E+00	7.44860E-06	2.64430E-03	6.37320E-02	5.11820E-01	6.99913E-01	1.32440E-01
to Group 7	0.00000E+00	1.04550E-06	5.03440E-04	1.21390E-02	6.12290E-02	5.37320E-01	2.48070E+00

Table B.14: C5G7 Control Rod Macroscopic Cross Sections

	Σ_{tr} [cm^{-1}]	Σ_a [cm^{-1}]	$\nu\Sigma_f$ [cm^{-1}]	χ
Group 1	2.16768E-01	1.70490E-03	0.000000E+00	0.0000E+00
Group 2	4.80098E-01	8.36224E-03	0.000000E+00	0.0000E+00
Group 3	8.86369E-01	8.37901E-02	0.000000E+00	0.0000E+00
Group 4	9.70009E-01	3.97797E-01	0.000000E+00	0.0000E+00
Group 5	9.10481E-01	6.98763E-01	0.000000E+00	0.0000E+00
Group 6	1.13775E+00	9.29508E-01	0.000000E+00	0.0000E+00
Group 7	1.84049E+00	1.17836E+00	0.000000E+00	0.0000E+00

Scattering Block

Σ_s	Group 1	Group 2	Group 3	Group 4	Group 5	Group 6	Group 7
to Group 1	1.70563E-01	0.00000E+00	0.00000E+00	0.00000E+00	0.00000E+00	0.00000E+00	0.00000E+00
to Group 2	4.44012E-02	4.71050E-01	0.00000E+00	0.00000E+00	0.00000E+00	0.00000E+00	0.00000E+00
to Group 3	9.83670E-05	6.85480E-04	8.01859E-01	0.00000E+00	0.00000E+00	0.00000E+00	0.00000E+00
to Group 4	1.27786E-07	3.91395E-10	7.20132E-04	5.70752E-01	6.55562E-05	0.00000E+00	0.00000E+00
to Group 5	0.00000E+00	0.00000E+00	0.00000E+00	1.46015E-03	2.07838E-01	1.02427E-03	0.00000E+00
to Group 6	0.00000E+00	0.00000E+00	0.00000E+00	0.00000E+00	3.81486E-03	2.02465E-01	3.53043E-03
to Group 7	0.00000E+00	0.00000E+00	0.00000E+00	0.00000E+00	3.69760E-09	4.75290E-03	6.58597E-01

The diffusion calculations are performed with and without an energy group collapse (2 and 7 energy groups repsectively). The 2 energy group struture is shown in Table B.15.

Table B.15: 2 Coarse Group Structure for C5G7 Test Problems

Coarse Group Number	Fine Group Number(s)
1	1 - 4
2	5 - 7

B.6 Forty-Seven Group Light Water Reactor Materials

The HELIOS 47-group neutron cross section library is used to model our most realistic Light Water Reactor (LWR) test problems [82]. The LWR material compositons come from an MPACT validation test for a 2-D LWR [83], and are similar to the materials defined for the CASL Advanced Modeling Applications Core Physics Benchmark Progression Problem 5 [16]. The material compositions are shown in Table B.16. The density of the oxygen in the gap was increased to avoid numerical issues related to division by small numbers in the calculation of $\boldsymbol{f}_1$.

Table B.16: 1-D MOX LWR One-Group Macroscopic Cross Sections

Material	Isotope ID [ZZZAAA[1]]	Atom Density [(barn-cm)$^{-1}$]		Material	Isotope ID [ZZZAAA[1]]	Atom Density [(barn-cm)$^{-1}$]
UO2 2.1%	8001[3]	4.57432E-02		UO2 2.6%	8001[3]	4.57458E-02
	92234	4.01947E-06			92234	5.06459E-06
	92235	4.86473E-04			92235	6.02296E-04
	92236	2.22949E-06			92236	2.75807E-06
	92238	2.23863E-02			92238	2.22702E-02
UO2 3.1%	8001[3]	6.12818E-06		AIC	47107	2.36159E-02
	92234	7.18116E-04		Control	47109	2.19403E-02
	92235	3.28928E-06		Rod	48000[2]	2.73220E-03
	92236	2.21541E-02			49113	3.44262E-04
	92238	4.57484E-02			49115	7.68050E-03
PYREX	8016	4.53216E-02		Coolant	1001	4.41460E-02
Burnable	5010	9.22829E-04			5010	9.54117E-06
Absorber	5011	3.71450E-03			5011	3.83265E-05
	13027	5.02189E-04			8016	2.20790E-02
	14000[2]	1.81883E-02				
	11023	2.41648E-03				
Gap	8016	1.00000E-07		Clad	40002[4]	4.32487E-02
SS-304	26001[5]	8.82784E-02				

[1] ZZZ is the 3 digit atomic number with leading 0's omitted. AAA is the 3 digit atomic mass.
[2] An AAA value of 000 indicates the natural isotopic mixture for that element.
[3] Oxygen-16 in uranium oxide.
[4] Zircaloy-2.
[5] Stainless steel 304.

The LWR diffusion calculations are performed with 3 coarse group structures (2, 5, and 10 energy groups repsectively). The 2, 5, and 10 coarse energy group strutures are shown in Tables B.17, B.18, and B.19 respectively.

Table B.17: 2 Coarse Group Structure for 47 Fine Group LWR Test Problems

Coarse Group Number	Fine Group Number(s)
1	1 - 24
2	25 - 47

Table B.18: 5 Coarse Group Structure for 47 Fine Group LWR Test Problems

Coarse Group Number	Fine Group Number(s)
1	1 - 10
2	11 - 18
3	19 - 24
4	25 - 40
5	41 - 47

Table B.19: 10 Coarse Group Structure for 47 Fine Group LWR Test Problems

Coarse Group Number	Fine Group Numbers
1	1 - 4
2	5 - 10
3	11 - 18
4	19
5	20 - 22
6	23 - 24
7	25 - 27
8	28 - 31
9	32 - 40
10	41 - 47

APPENDIX C

Numerical Test Problem Definitions

This appendix contains the material and geometry specifications of the numerical test problems studied in this dissertation. It also contains the space, angle, and energy discretizations used for each test problem. The problems are numbered roughly in order of increasing complexity.

C.1 Problem 1. One-Group, One-Dimensional Zero Power Plutonium Reactor

We investigate the Zero Power Plutonium Reactor (ZPPR) problem studied by Gelbard [31]. The ZPPR was a plate-fuel reactor located at Argonne National Laboratory-West (now Idaho National Laboratory). The fuel plates are made of uranium-oxide and a uranium-plutonium mixture, and are separated by layers of sodium coolant. This problem is modeled in 1-D planar geometry. The macroscopic cross sections are defined in Table B.1. The thicknesses of the ZPPR regions are shown in Table C.1.

Table C.1: ZPPR Region thicknesses

	Thickness [cm]
Uranium Oxide (UO)	1.000
Sodium (Na)	0.625
Uranium Plutonium (UP)	0.250

We model problems cores with 5, 11, 25, 45, and 75 uranium oxide fuel plates with

4, 10, 24, 44, and 74 uranium fuel plates respectively. In order to make the system boundary line up with the boundary of a symmetric cell, the outermost uranium oxide plates are only half the usual width. Vacuum boundaries are applied to each surface of the core. Since the core is symmetric, we model only half of the system.

The S_N calculations are performed using the S_{32} Guass-Legendre quadrature set. The mesh cell thickness for both the S_N and diffusion calculations is $\Delta x = 0.03125$cm. There are two definitions of a lattice cell that yield reflecting boundary conditions. Therefore, the Benoist diffusion coefficients with the correction term included are double-valued. We let D_{bc1} be the diffusion coefficient when the cell is defined from the center of a uranium oxide fuel plate to the center of the next uranium oxide fuel plate, and D_{bc2} be the diffusion coefficient when the cell is defined from the center of a uranium-plutonium fuel plate to the center of the next uranium-plutonium fuel plate (see Fig. C.1).

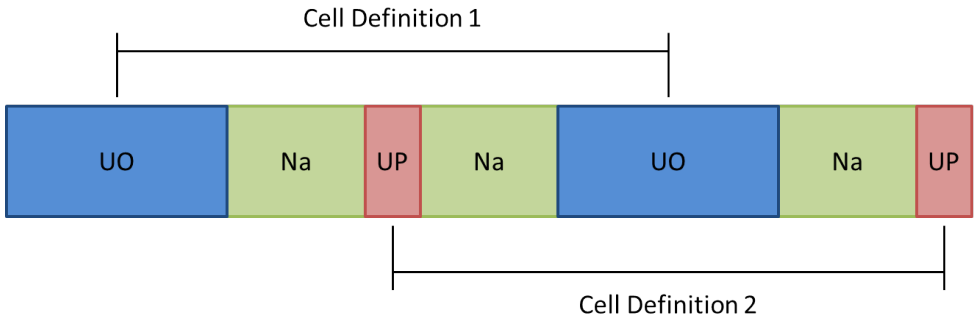

Figure C.1: ZPPR Test Geometry. There are two ways to define a symmetric lattice.

C.2 Problem 2. One-Group, One-Dimensional Two-Assembly Discontinuity Factor Test

This 1-D, planar geometry, two-assembly problem is designed to test discontinuity factors for lattice systems. Macroscopic cross sections for this problem are shown in Table B.2. There are three pin types for this problem (see Fig. C.2). The thicknesses

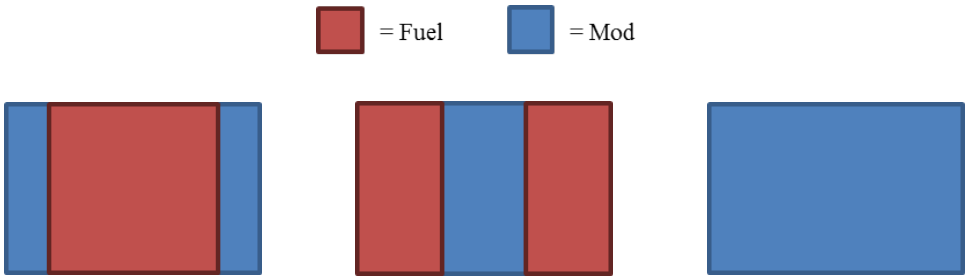

(a) Fuel-Centered Pin (b) Moderator-Centered Pin (c) Reflector Pin

Figure C.2: Two-Assembly Discontinuity Factor Test Pin Definitions

of each pin is 1.26 cm. The thicknesses of each region are presented in Table C.2.

Table C.2: Two-Assembly Discontinuity Factor Test Region thicknesses

	Thickness [cm]
UO2 Fuel (Fuel)	0.84
Water (Mod)	0.42
Reflector	1.26

There are three possible configurations for the problem. All involve two assembly regions with 8 pins in each region. The configurations are:

1. Fuel-centered pins in the left assembly, moderator-centered pins in the right assembly. Both sides of the problem have reflecting boundary conditions. Because the homogenized cross sections are the same in both assemblies and the boundaries are reflecting, the homogeneous solution is constant.
2. Fuel-centered pins in the left assembly, moderator-centered pins in the right assembly. A reflecting boundary condition is applied on the left side of the system and a vacuum boundary is applied on the right side.
3. Fuel-centered pins in the left assembly, reflector pins in the right assembly. A reflecting boundary condition is applied on the left side of the system and a vacuum boundary is applied on the right side.

The S_N calculations are solved using the S_{32} Guass-Legendre quadrature set. The mesh cell thickness for both the S_N and diffusion calculations is $\Delta x = 0.021$cm.

C.3 Problem 3. One-Group, One-Dimensional MOX LWR

A one-group, 1-D numerical test problem designed by Joo contains 4 different fuel assembly types and a reflector assembly [80]. The assemblies are made of 4 different fuel types (uranium-oxide (UO2), less-enriched uranium-oxide (UO2-l), uranium-oxide with gadalinium burnable poison (UO2-Gd), and mixed-oxide (MOX)), and water coolant at three different densities in the reflector (H2O-Refl), fuel pins (H2O-Fuel), and water holes (H2O-WH). Macroscopic cross sections for the 7 materials used in the numerical test problem are shown in Table B.3.

Six pin types are defined for this problem in Table C.3. Each pin is 1.275 cm wide and is subdivided into 3 equally-sized regions. Five assembly types are defined for this problem in Fig. C.3. Each assembly consists of 16 pins. The 1-D core contains 15 fuel assemblies flanked by reflector assemblies on each side. Figure C.4 shows the core assembly map.

Table C.3: 1-D MOX LWR Pin Definitions

Pin Type	Region 1	Region 2	Region 3
Thickness	0.425 cm	0.425 cm	0.425 cm
UO2 Pin	H2O-Fuel	UO2	H2O-Fuel
UO2-l Pin	H2O-Fuel	UO2-l	H2O-Fuel
UO2-Gd Pin	H2O-Fuel	UO2-Gd	H2O-Fuel
MOX Pin	H2O-Fuel	MOX	H2O-Fuel
Water Hole (WH) Pin	H2O-WH	H2O-WH	H2O-WH
Reflector (Refl) Pin	H2O-Refl	H2O-Refl	H2O-Refl

The S_N calculations are solved using the S_{32} Guass-Legendre quadrature set. For both S_N and diffusion calculations, each material region (one-third of a pin-cell) is divided into 17 spatial mesh cells. The uncorrected Benoist diffusion coefficients, D_{bc}, are *not* used in this problem.

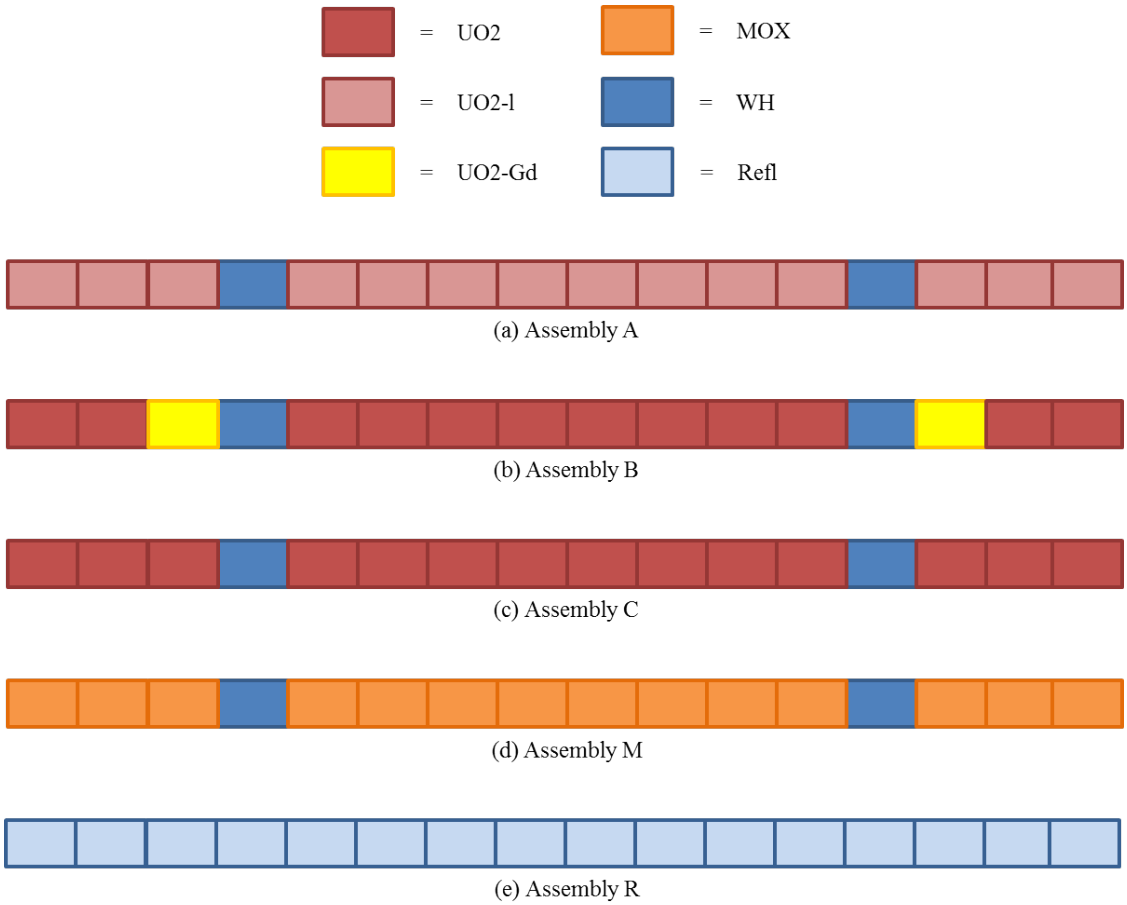

Figure C.3: 1-D MOX LWR Assembly Definitions

Figure C.4: 1-D MOX LWR Core Definition

C.4 Problem 4. Four-Group, Two-Dimensional Very High Temperature Reactor

This problem is a 2-D approximation to the 3-D VHTR in the technical report by Lee et al. [84]. The pin pitches are taken directly from the report, and the fuel and coolant widths are adjusted to preserve their volume fractions within individual pin cells.

The four-group VHTR cross sections are given in Tables B.4-B.6. Pin specifica-

tions are given in Table C.4.

Table C.4: VHTR Pin Specifications

Pin Pitch [cm]	1.8796
Fuel Width [cm]	1.4958
Helium Width [cm]	1.5564
Active Fuel Height [cm]	200
Top Reflector Thickness [cm]	50

Each fuel assembly contains 17 pins: 9 fuel pins separated by 8 helium coolant channels (see Fig. C.5). Graphite surrounds both the fuel and helium regions. For the purposes of calculating axial assembly power distributions, the assemblies are divided into 5 cm axial segments. Reflector assemblies are the same size as the fuel assemblies, but are composed entirely of graphite.

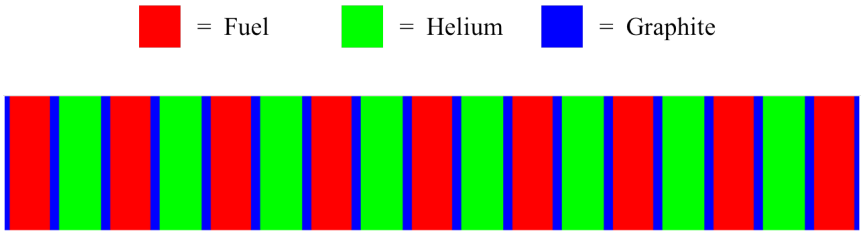

Figure C.5: VHTR Fuel Assembly Definition

The reactor is composed of 2 fuel assemblies surrounded by 2 reflector assemblies on each side. The active fuel height (in only the half of the reactor that we model) is 200 cm, while the top reflector has a thickness of 50 cm. The VHTR core is annular and the reflecting boundary condition on the left side represents the center of the annulaus. Our simplified core is axially symmetric, so the bottom boundary is also reflecting. The top and right boundaries are vacuum boundaries. A diagram of our 2-D VHTR core is shown in Fig. C.6.

The run parameters for the MOC and diffusion calculations are shown in Tables C.5 and C.6. The diffusion calculations have a large spectral radius, so tighter convergence criteria are used to prevent false convergence.

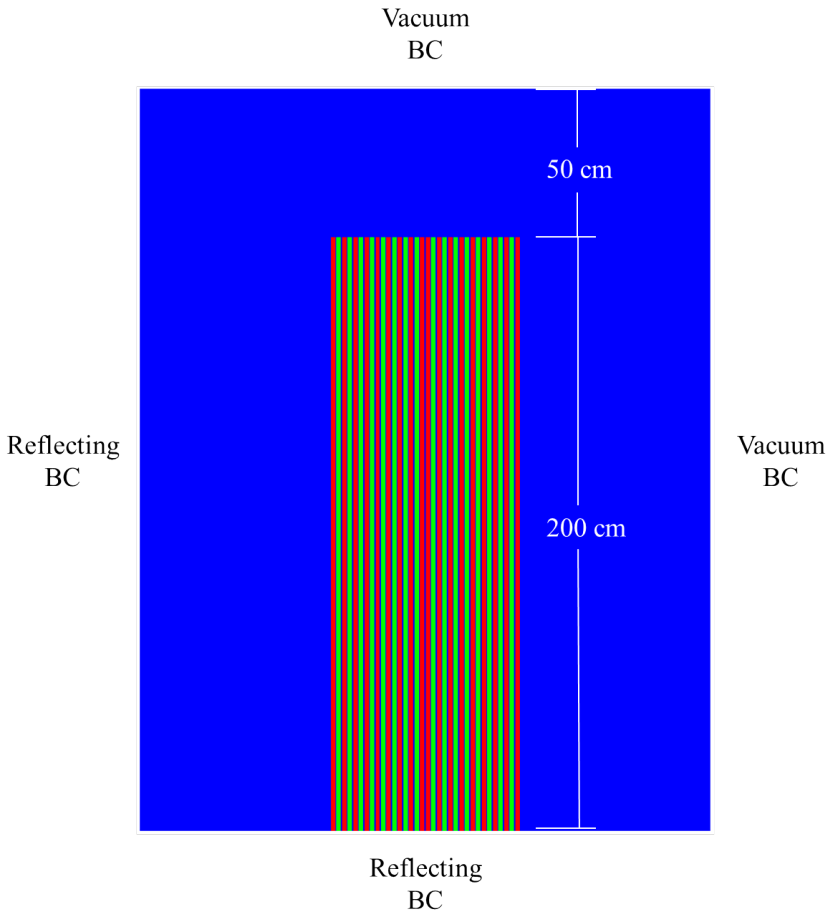

Figure C.6: VHTR Core

Table C.5: MOC Run Parameters for VHTR Test Problem

Quadrature Type	Chebyshev-Gauss
Azimuthal Angles Per Octant	32
Polar Angles Per Octant	16
Ray Spacing [cm]	0.03
k Convergence Tolerance	1.E-07
ϕ Convergence Tolerance	1.E-07

Table C.6: Diffusion Run Parameters for VHTR Test Problem

x Mesh Spacing [cm]	0.62653
y Mesh Spacing [cm]	0.50000
k Convergence Tolerance	1.E-08
ϕ Convergence Tolerance	1.E-08

No group collapse is performed for this problem (i.e., the diffusion calculation is performed with 4 energy groups).

C.5 Problem 5. Seven-Group, Two-Dimensional Six-Assembly Quarter-Core

We now consider a six-assembly problem in 2-D. We consider multiple cores, but each is composed of only a single assembly type. Both bare and reflected cores are modeled.

This problem uses the C5G7 macroscopic cross sections defined by Tables B.7-B.14. In order to simplify flux reconstruction, we define a geometry with *no* curvilinear surfaces. Each pin cell is a 9×9 array of square mesh cells, with the 45 central cells representing a pin, and the 36 outer cells representing a moderator. The pin specifications are defined by Fig. C.7 and Table C.7.

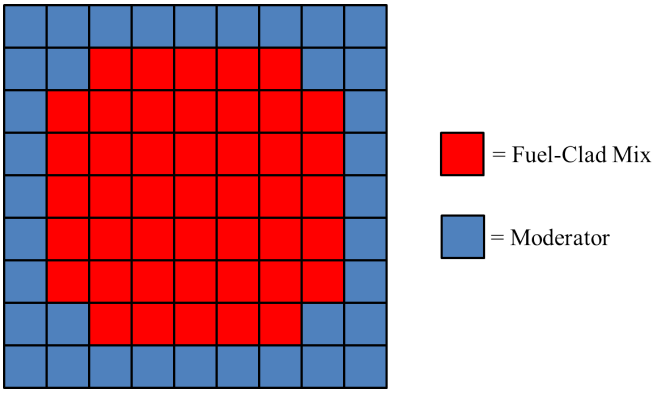

Figure C.7: 9×9 Rectilinear Pin

Table C.7: 9×9 Rectilinear Pin Specifications

Pin Pitch [cm]	1.26
Pin Mesh	9×9
Mesh Cell Width [cm]	0.14
Fuel Mesh Cells Per Pin	45
Moderator Mesh Cells Per Pin	36

Each assembly in this problem is a 13×13 array of pins. The smaller 13×13 assemblies are used instead of 17×17 assemblies to save memory. Two assembly types are studied in this test. The first is a uniform lattice of UO2 pins (Fig. C.8),

and the second is a MOX assembly with multiple MOX enrichments, guide tubes, and a fission chamber (Fig. C.9). Reflector assemblies are the same size as the fuel assemblies, but are composed only of the "Moderator" material.

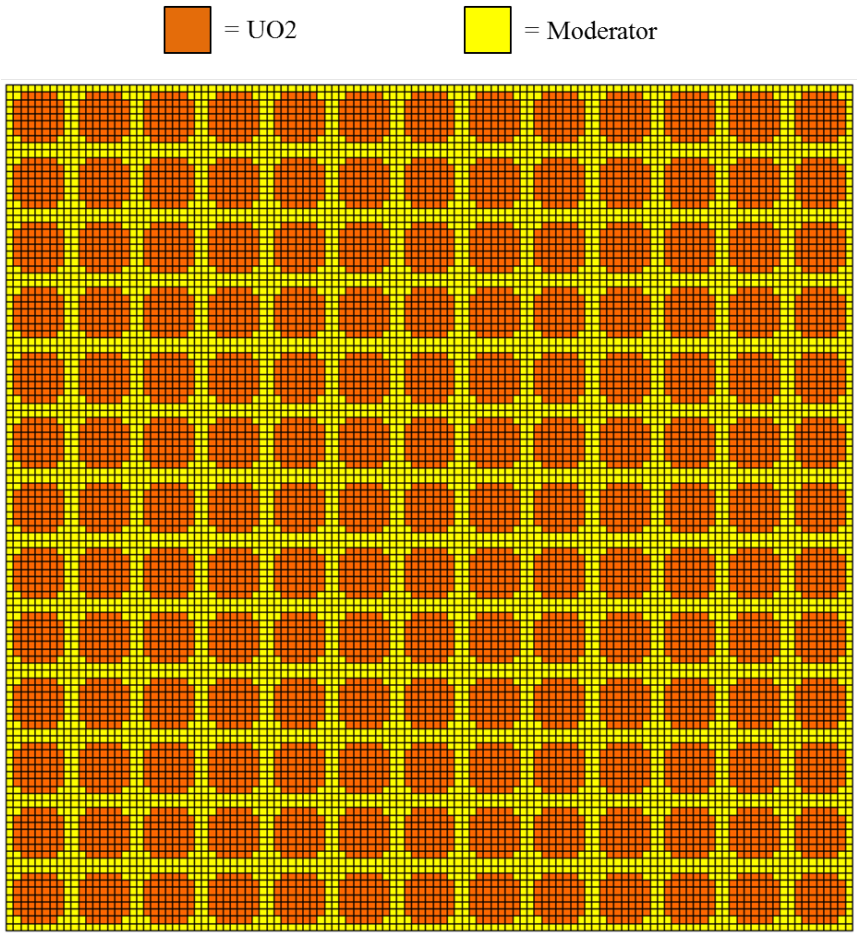

Figure C.8: 13×13 Uniform UO2 Assembly

The core is composed of six assemblies in a 3×2 array. All the assemblies are the same type, and the core may be bare or surrounded by reflector assemblies. The bare core is identical to the reflected core (Fig. C.10) except that the reflector assemblies are removed. The left and bottom boundaries are reflecting, while the right and top boundaries are vacuum.

The run parameters for the MOC and diffusion calculations are shown in Tables C.8 and C.9. The diffusion calculations have a large spectral radius, so tighter

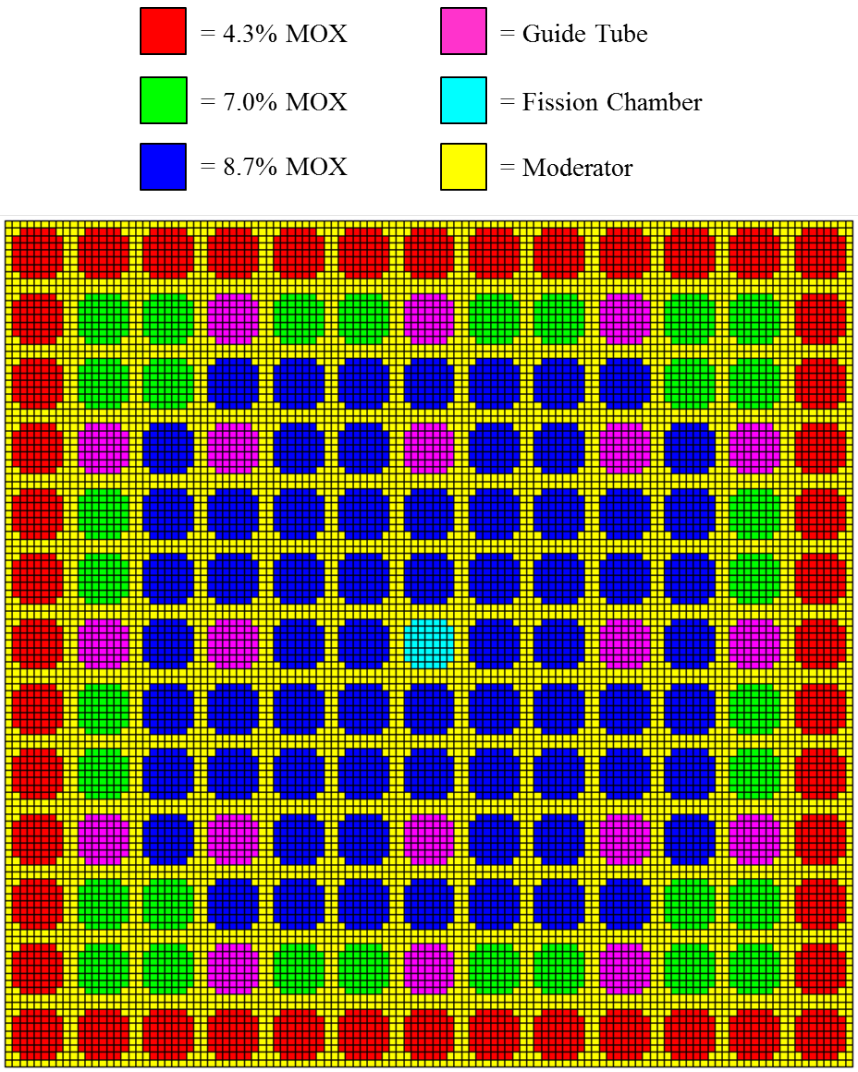

Figure C.9: 13 × 13 MOX Assembly

convergence criteria are used to prevent false convergence.

Table C.8: MOC Run Parameters for Six-Assembly Test Problem

Quadrature Type	Chebyshev-Gauss
Azimuthal Angles Per Octant	16
Polar Angles Per Octant	8
Ray Spacing [cm]	0.03
k Convergence Tolerance	1.E-06
ϕ Convergence Tolerance	1.E-06

No group collapse is performed for the reflected configuration of this problem (i.e., the diffusion calculation is performed with 7 energy groups). Diffusion calculations for the bare configuration of this problem were performed using 2 and 7 energy group

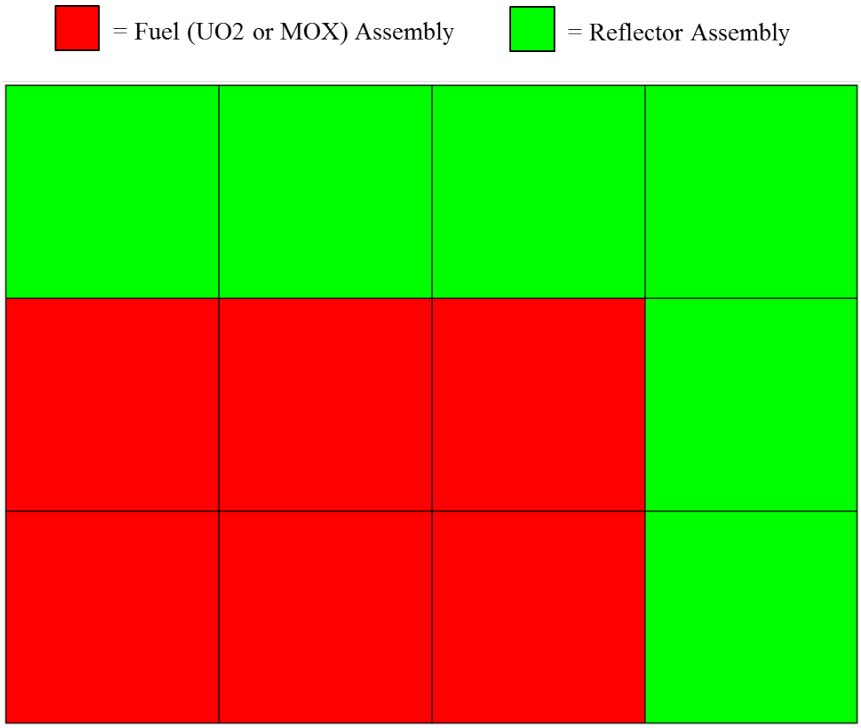

Figure C.10: Six-Assembly Test Core

Table C.9: Diffusion Run Parameters for Six-Assembly Test Problem

x Mesh Spacing [cm]	0.14
y Mesh Spacing [cm]	0.14
k Convergence Tolerance	1.E-07
ϕ Convergence Tolerance	1.E-07[1]

[1] 7 group calculations terminated prior to flux convergence, after 20000 iterations.

structures. The 2-group structure is defined by Table B.15.

C.6 Problem 6. Seven-Group, Two-Dimensional Four-Assembly Colorset

This problem is a four-assembly colorset with a checkerboard loading of two types of assemblies. This problem uses the C5G7 macroscopic cross sections defined by Tables B.7-B.14. In order to simplify flux reconstruction, we define a geometry with *no* curvilinear surfaces. Each pin cell is a 9×9 array of square mesh cells, with the 45 central cells representing a pin, and the 36 outer cells representing a moderator. The pin specifications are defined by Fig. C.7 and Table C.7 in the Section C.5. Although

the benchmark refers to the inner region as “Fuel-Clad Mix”, it may consist of any of the materials defined by Tables B.7-B.14. Thus, Fuel-Clad Mix can be: “UO2”, “4.3% MOX”, “7.0% MOX”, “8.7% MOX”, “Fission Chamber”, or “Guide Tube”.

The colorset consists of unrodded UO2 and MOX assemblies whose configurations are taken from the C5G7 “Benchmark on Deterministic Transport Calculation without Spatial Homogenisation” [79, 78]. The unrodded UO2 and MOX assemblies are shown in Figs. C.11 and C.12.

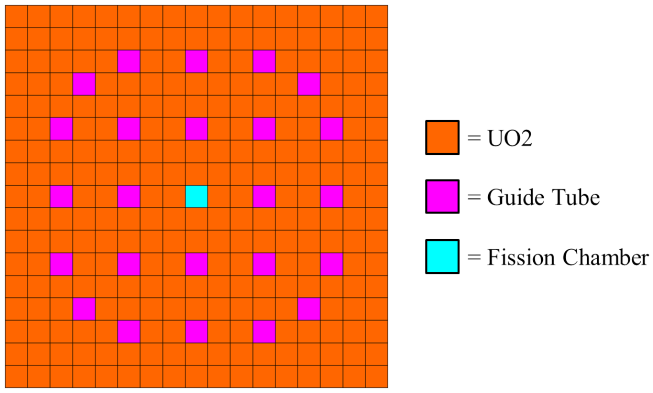

Figure C.11: C5G7 Unrodded UO2 Assembly

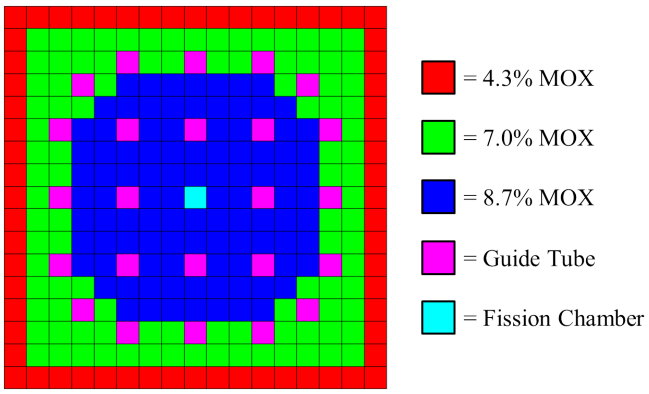

Figure C.12: C5G7 Unrodded MOX Assembly

The four-assembly colorset core consists of two UO2 assemblies and two MOX assemblies with a checkerboard loading (see Fig. C.13). All core boundaries are reflecting.

The run parameters for the MOC and diffusion calculations are shown in Tables

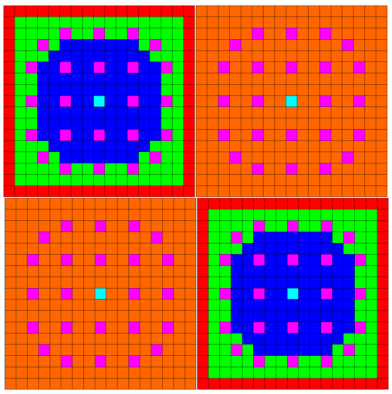

Figure C.13: Four-Assembly Colorset Configuration

C.10 and C.11. The diffusion calculations have a large spectral radius, so tighter convergence criteria are used to prevent false convergence.

Table C.10: MOC Run Parameters for Four-Assembly Colorset Test

Quadrature Type	Chebyshev-Gauss
Azimuthal Angles Per Octant	16
Polar Angles Per Octant	8
Ray Spacing [cm]	0.03
k Convergence Tolerance	1.E-08
ϕ Convergence Tolerance	1.E-08

Table C.11: Diffusion Run Parameters for Four-Assembly Colorset Test

x Mesh Spacing [cm]	0.14
y Mesh Spacing [cm]	0.14
k Convergence Tolerance	1.E-08 (for 7 Groups) or 1.E-10 (for 2 Groups)
ϕ Convergence Tolerance	1.E-08 (for 7 Groups) or 1.E-10 (for 2 Groups)

Diffusion calculations were performed using 2 and 7 energy group structures. The 2-group structure is defined by Table B.15.

C.7 Problem 7. Seven-Group, Three-Dimensional C5G7 Benchmarks

This is the C5G7 "Benchmark on Deterministic Transport Calculation without Spatial Homogenisation" [79, 78]. This problem uses the C5G7 macroscopic cross sections defined by Tables B.7-B.14. Four assemblies (two uranium-oxide and two mixed-oxide) are surrounded by a water reflector and control rods may be inserted

depending on the specific benchmark configuration.

The benchmark defines simplified fuel pins such that each pin contains only two regions: a homogenized "Fuel-Clad Mix" in the center, and a water "Moderator" surrounding the central region (see Fig. C.14). Table C.12 lists measurments and MOC mesh information for the fuel pins. Although the benchmark refers to the inner region as "Fuel-Clad Mix", it may consist of any of the materials defined by Tables B.7-B.14. Thus, Fuel-Clad Mix can be: "UO2", "4.3% MOX", "7.0% MOX", "8.7% MOX", "Fission Chamber", "Guide Tube", or "Control Rod". "Homogeneous Moderator" pins (composed entirely of the "Moderator" material) are also defined for this problem, and the MOC mesh for these pins is a 5×5 rectilinear grid.

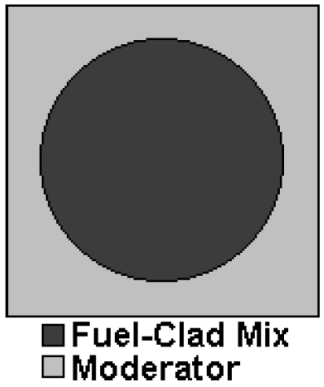

Figure C.14: C5G7 Benchmark Fuel Pin (Figure reproduced from official benchmark definition [78])

Table C.12: C5G7 Benchmark Fuel Pin Specifications

	Material	Outer Radius [cm]	Radial Mesh Rings	Mesh Cells Per Ring
Fuel-Clad Mix	*various*	0.54	6	8, 8, 8, 8, 8, 8
Moderator	Moderator	0.62	3	8, 8, 8
Outer Pin[1]	Moderator	1.2600[2]	N/A	8

[1] This is the region of the pin outside the outermost mesh ring and inside the pin boundaries.
[2] Total pin width.

The C5G7 core contains both uranium-oxide (UO2) and mixed-oxide (MOX) assemblies, and each assembly may be rodded or unrodded. The unrodded assemblies

have the same pin compositions as the assemblies of Problem 6 (Section C.6), but the pin geometries are now defined by Fig. C.14 and Table C.12. The unrodded assemblies are shown in Figs. C.11 and C.12. Rodded assemblies are shown in Figs. C.15 and C.16. In addition to the homogeneous reflector assemblies (consisting entirely of homogeneous moderator pins), rodded reflector assemblies are also defined, and these are located above the fuel assemblies (see Fig. C.17).

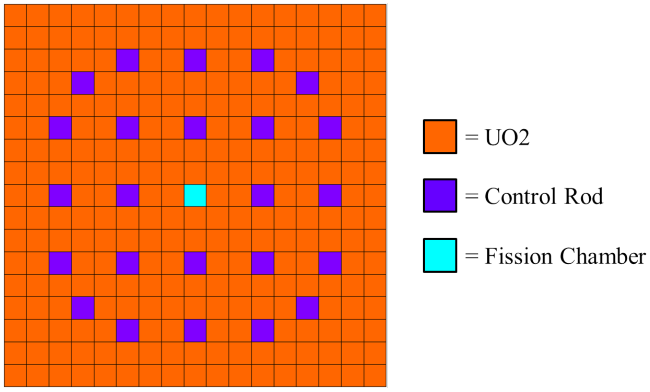

Figure C.15: C5G7 Rodded UO2 Assembly

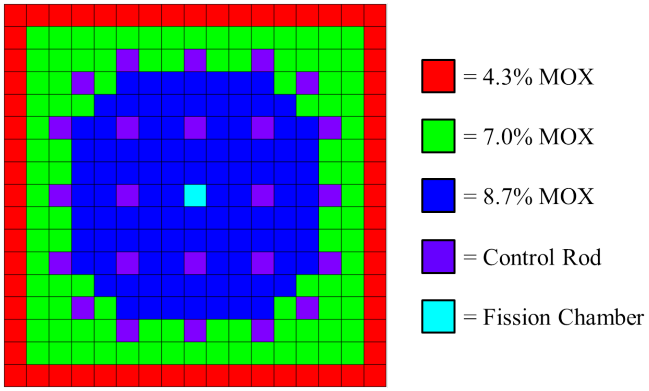

Figure C.16: C5G7 Rodded MOX Assembly

We consider only the extended C5G7 Benchmark, which has three configurations: (i) "Unrodded", (ii) "Rodded A", and (iii) "Rodded B". The core dimensions are shown in Fig. C.18. The active fuel region is divided axially into thirds. In the Unrodded configuration, the control rods are fully withdrawn such that only the reflector assemblies above the core are rodded (see Fig. C.19). In the Rodded A

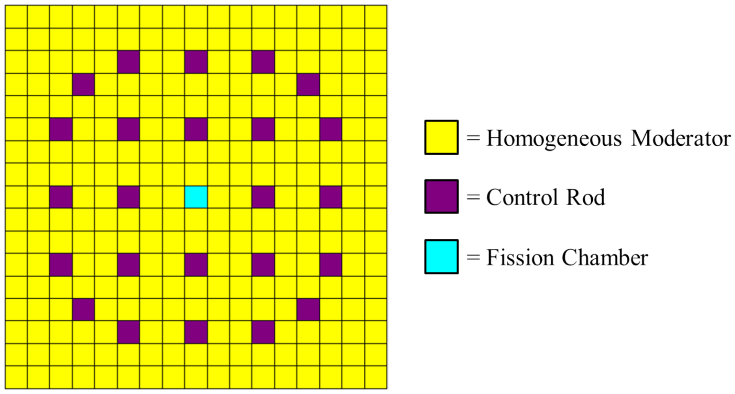

Figure C.17: C5G7 Rodded Reflector Assembly

configuration, control rods are inserted one-third into the core in the inner UO2 assembly only (see Fig. C.20). In the Rodded B configuration, control rods are inserted two-thirds into the the core in the inner UO2 assembly and one-third into the core in each of the MOX assemblies (see Fig. C.21). The boundary conditions for the C5G7 core are shown in Figs. C.18-C.21.

The run parameters for the MOC and diffusion calculations are shown in Tables C.13 and C.14. The diffusion calculations have a large spectral radius, so tighter convergence criteria are used to prevent false convergence.

Table C.13: MOC Run Parameters for C5G7 Benchmark

Quadrature Type	Chebyshev-Gauss
Azimuthal Angles Per Octant	16
Polar Angles Per Octant	8
Ray Spacing [cm]	0.03
k Convergence Tolerance	1.E-07
ϕ Convergence Tolerance	1.E-06

Table C.14: Diffusion Run Parameters for C5G7 Benchmark

x Mesh Spacing [cm]	0.42
y Mesh Spacing [cm]	0.42
z Mesh Spacing [cm]	1.19
k Convergence Tolerance	1.E-08
ϕ Convergence Tolerance	1.E-07

Diffusion calculations were performed using 2 and 7 energy group structures. The

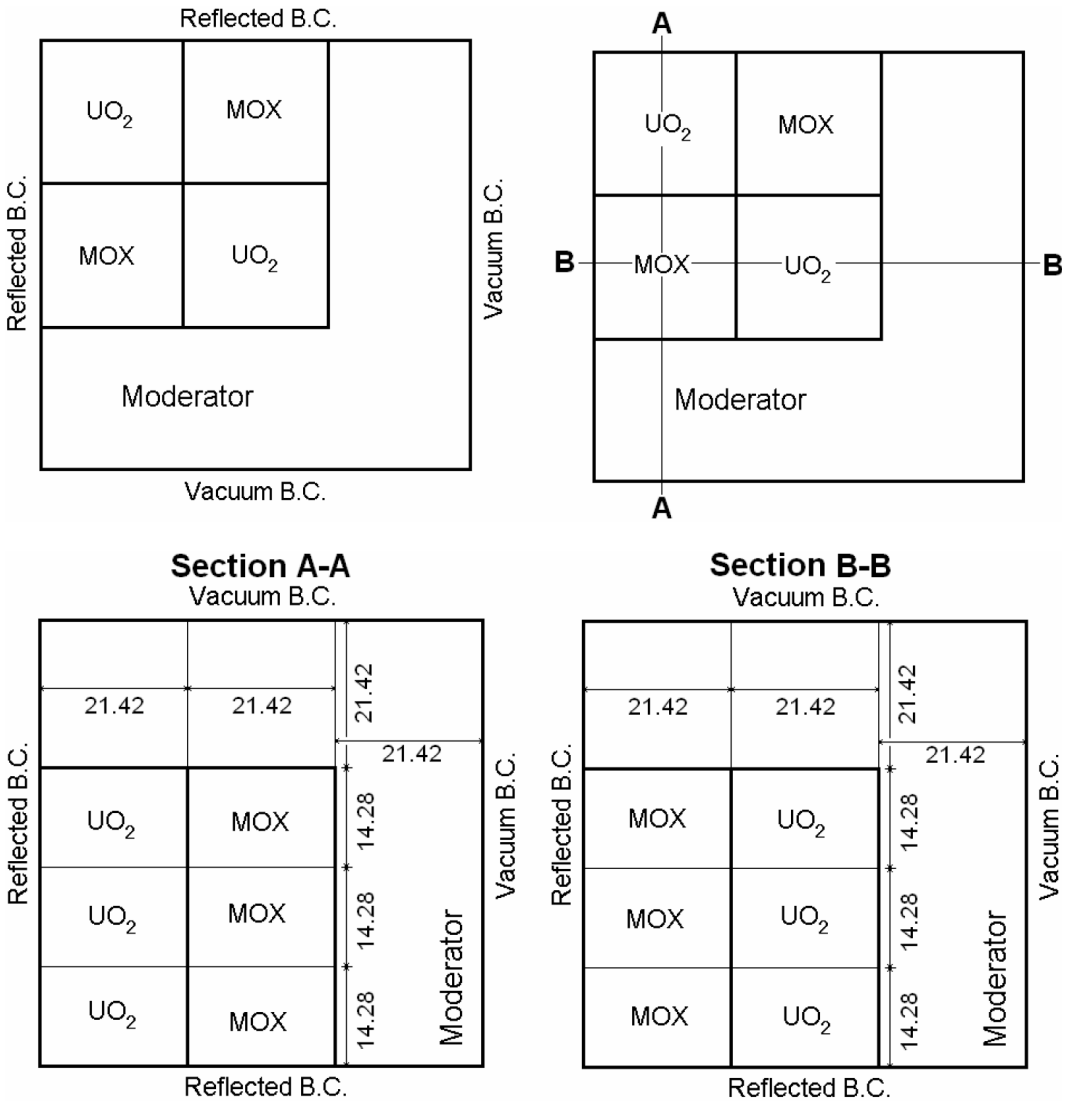

Figure C.18: C5G7 Core Dimensions (Figure reproduced from official benchmark definition [78])

2-group structure is defined by Table B.15. The rodded reflector assembly cross sections were group-collapsed using a 2-D (*not* 3-D) fuel-reflector colorset calculation with an unrodded MOX assembly (Fig. C.22). The 2-D colorset geometry is not equivalent to the 3-D geometry in which the rodded reflector assembly is located above, instead of to the side, of the fuel assembly. However, we only need an approximate energy spectrum to perform the group-collapse, and this colorset yields an accurate spectrum, particularly when compared to the alternative of assuming a constant cross section. The homogeneous reflector assembly cross sections were

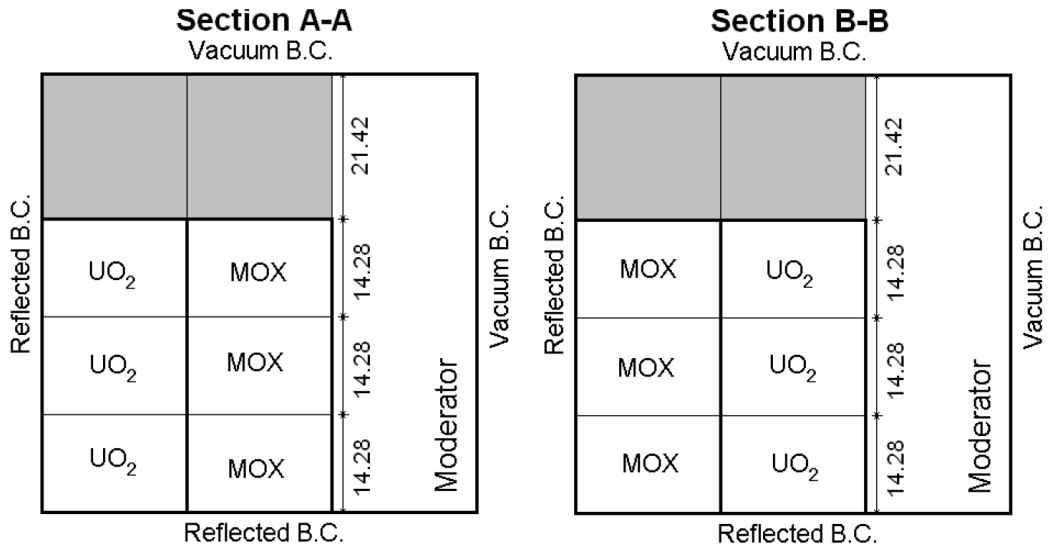

Shaded regions denote control rod locations.

Figure C.19: C5G7 Core: Unrodded Configuration (Figure reproduced from official benchmark definition [78])

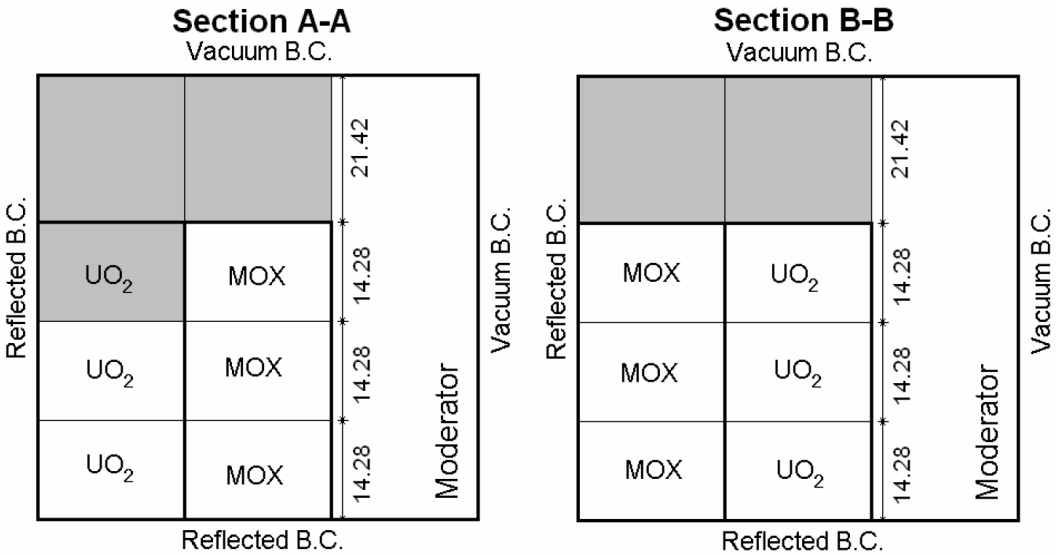

Shaded regions denote control rod locations.

Figure C.20: C5G7 Core: Rodded A Configuration (Figure reproduced from official benchmark definition [78])

also group-collapsed using a 2-D fuel-reflector colorset calculation with an unrodded MOX assembly.

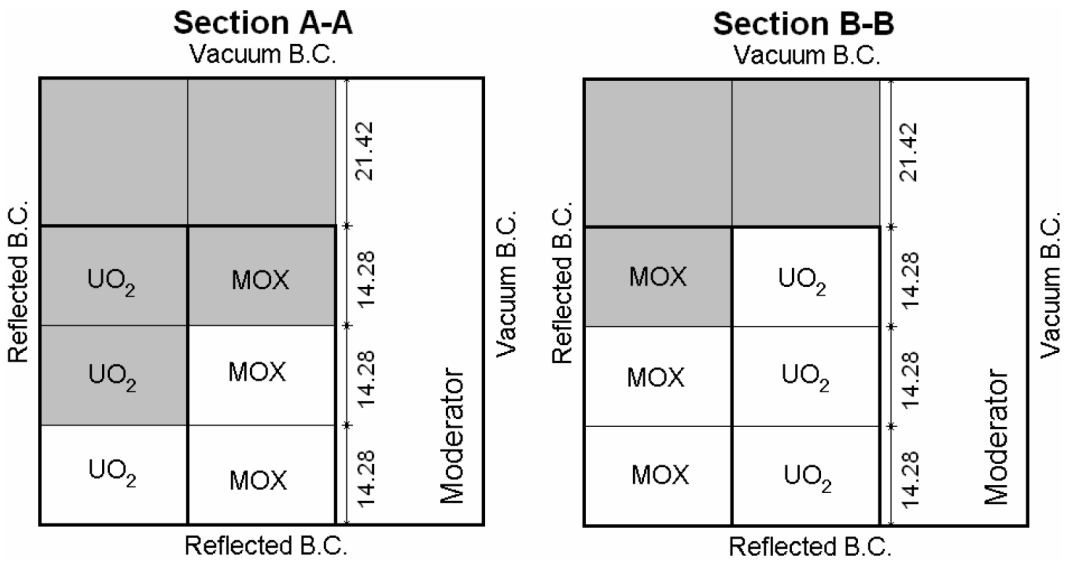

Shaded regions denote control rod locations.

Figure C.21: C5G7 Core: Rodded B Configuration (Figure reproduced from official benchmark definition [78])

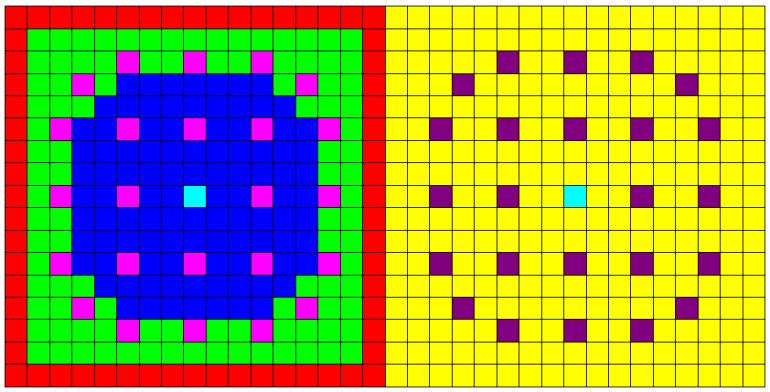

Figure C.22: Fuel-Reflector Colorset for C5G7 Rodded Reflector Assembly. An Unrodded MOX Assembly (Left) is Adjoined to a Rodded Reflector Assembly (Right).

C.8 Problem 8. Forty-Seven-Group, Two-Dimensional Two Assembly Type LWR Test

This problem contains six 2-D fuel assemblies in a line with a reflector assembly on the right side. Two different assembly types are used. This problem uses the 47-group material mixtures defined by Table B.16. The assemblies contain 17×17 pins, with 264 being fuel and 25 being guide tubes. The fuel pin and guide tube geometries and MOC spatial meshes are defined by Figs. (C.23) and (C.24) and Tables (C.15)

and (C.16).

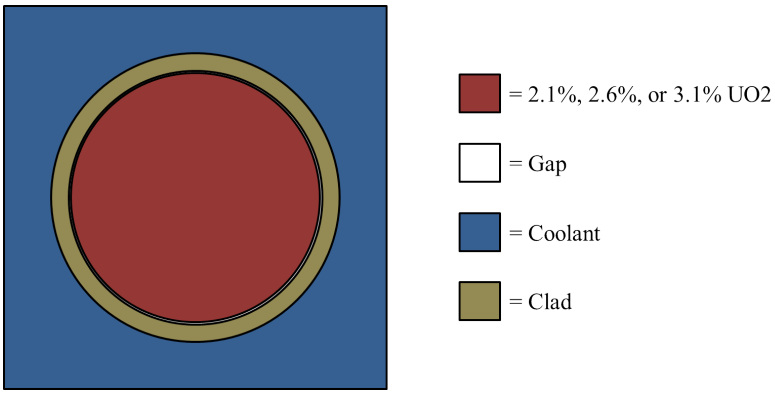

Figure C.23: LWR Fuel Pin

Table C.15: LWR Fuel Pin Specifications

	Material	Outer Radius [cm]	Radial Mesh Rings	Mesh Cells Per Ring
Fuel	UO2	0.4096	3	4, 8, 8
Gap	Gap	0.4180	1	8
Clad	Clad	0.4750	1	8
Coolant	Coolant	0.6200	2	8, 8
Outer Pin[1]	Coolant	1.2600[2]	N/A	8

[1] This is the region of the pin outside the outermost mesh ring and inside the pin boundaries.
[2] Total pin width.

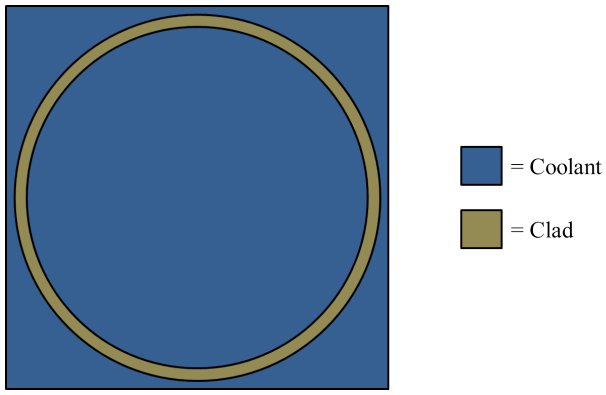

Figure C.24: LWR Guide Tube

The unrodded fuel assemblies are shown in Fig. (C.25). In this problem, the fuel assemblies can use either 2.1% or 2.6% fuel. Each reflector assembly is the same size

Table C.16: LWR Guide Tube Specifications

	Material	Outer Radius [cm]	Radial Mesh Rings	Mesh Cells Per Ring
Inner Coolant	Coolant	0.5610	3	4, 8, 8
Guide Tube	Clad	0.6020	1	8
Outer Pin[1]	Coolant	1.2600[2]	N/A	8

[1] This is the region of the pin outside the outermost mesh ring and inside the pin boundaries.
[2] Total pin width.

as a fuel assembly and is composed entiredly of the "Coolant" material. The MOC spatial mesh for each reflector *pin* is a 4×4 grid.

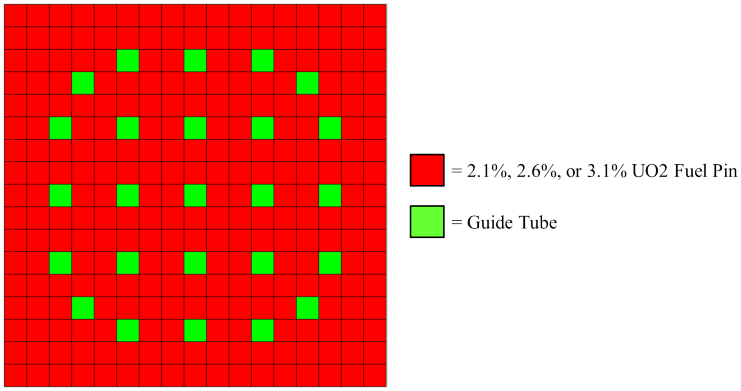

Figure C.25: LWR Unrodded Fuel Assembly

The core is composed of six fuel assemblies in a row with a reflector assembly on the right side (Fig. C.26). The right boundary is a vacuum, while all other boundaries are reflecting.

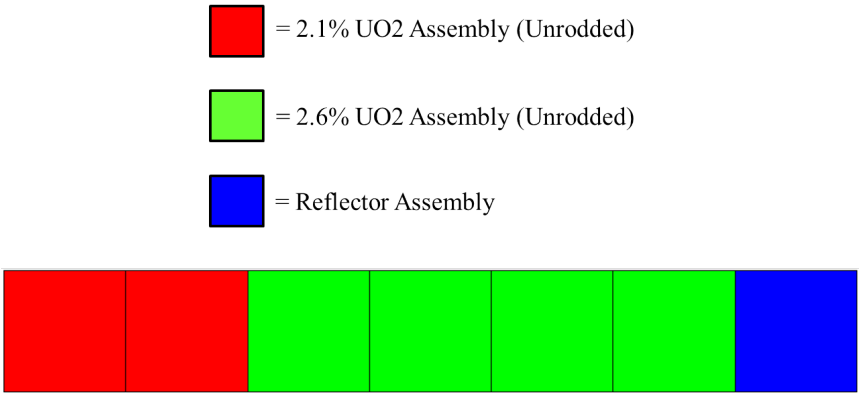

Figure C.26: Two Assembly Type LWR Test Core

The run parameters for the MOC and diffusion calculations are shown in Tables C.17 and C.18. The diffusion calculations have a large spectral radius, so tighter convergence criteria are used to prevent false convergence.

Table C.17: MOC Run Parameters for Two Assembly Type LWR Test

Quadrature Type	Chebyshev-Yamamoto
Azimuthal Angles Per Octant	16
Polar Angles Per Octant	3
Ray Spacing [cm]	0.05
k Convergence Tolerance	1.E-06
ϕ Convergence Tolerance	1.E-06

Table C.18: Diffusion Run Parameters for Two Assembly Type LWR Test

x Mesh Spacing [cm]	0.42
y Mesh Spacing [cm]	0.42
k Convergence Tolerance	1.E-08
ϕ Convergence Tolerance	1.E-07

Diffusion calculations were performed using 2, 5, and 10 coarse energy group structures (Tables B.17-B.19). The reflector assembly cross sections were group-collapsed using a fuel-reflector colorset calculation with a 3.1% enriched fuel assembly containing 0 Pyrex rods. The 3.1% fuel assembly was used because the reflector was originally homogenized with the next problem (Section C.9) in mind, and because in our earlier tests, the reflector cross sections were not sensitive to the fuel type of neighboring assemblies.

C.9 Problem 9. Forty-Seven Group, Two-Dimensional Full-Core Light Water Reactor

This problem is a full LWR core based on CASL Advanced Modeling Applications Core Physics Benchmark Progression Problem 5 [16]. It uses the 47-group material mixtures defined by Table B.16. The assemblies contain 17×17 pins, with 264 being fuel and the remaining 25 being a combination of guide tubes, Pyrex burnable absorbers, and control rods. The core is a 17×17 array of assemblies.

The fuel pin and guide tube geometries and MOC spatial meshes are defined by Figs. (C.23) and (C.24) and Tables (C.15) and (C.16) in the previous section. The Pyrex burnable absorber and control rod geometries and MOC spatial meshes are defined by Figs. (C.27) and (C.28) and Tables (C.19) and (C.20).

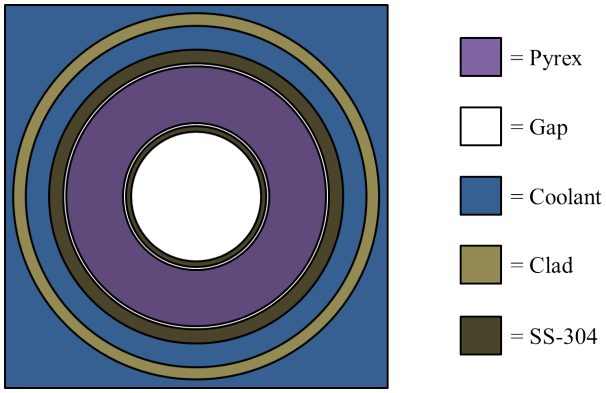

Figure C.27: LWR PYREX Burnable Absorber

Table C.19: LWR PYREX Burnable Absorber Specifications

	Material	Outer Radius [cm]	Radial Mesh Rings	Mesh Cells Per Ring
Inner Void	Gap	0.214	1	8
Inner Clad	SS-304	0.230	1	8
Inner Gap	Gap	0.241	1	8
Pyrex	Pyrex	0.427	1	8
Outer Gap	Gap	0.437	1	8
Outer Clad	SS-304	0.484	1	8
Coolant	Coolant	0.561	1	8
Guide Tube	Clad	0.602	1	8
Outer Pin[1]	Coolant	1.260[2]	N/A	8

[1] This is the region of the pin outside the outermost mesh ring and inside the pin boundaries.
[2] Total pin width.

The unrodded fuel assemblies are shown in Fig. (C.25) in the previous section. In this problem, the fuel assemblies can use either 2.1%, 2.6%, or 3.1% fuel. Fuel assemblies may also be rodded (Fig. C.29), or contain 8, 12, 16, 20, or 24 Pyrex burnable absorber rods (Figs. C.30-C.34). The reflector assembly is the same size as a fuel assembly and is composed entiredly of the "Coolant" material. The MOC

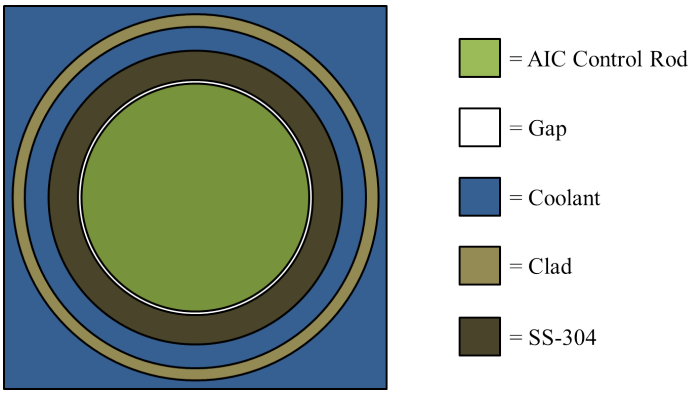

Figure C.28: LWR Control Rod

Table C.20: LWR Control Rod Specifications

	Material	Outer Radius [cm]	Radial Mesh Rings	Mesh Cells Per Ring
Control Rod	AIC	0.382	3	8, 8, 8
Gap	Gap	0.386	1	8
Clad	SS-304	0.484	1	8
Coolant	Coolant	0.561	1	8
Guide Tube	Clad	0.602	1	8
Outer Pin[1]	Coolant	1.2600[2]	N/A	8

[1] This is the region of the pin outside the outermost mesh ring and inside the pin boundaries.
[2] Total pin width.

spatial mesh for each reflector *pin* is a 4×4 grid.

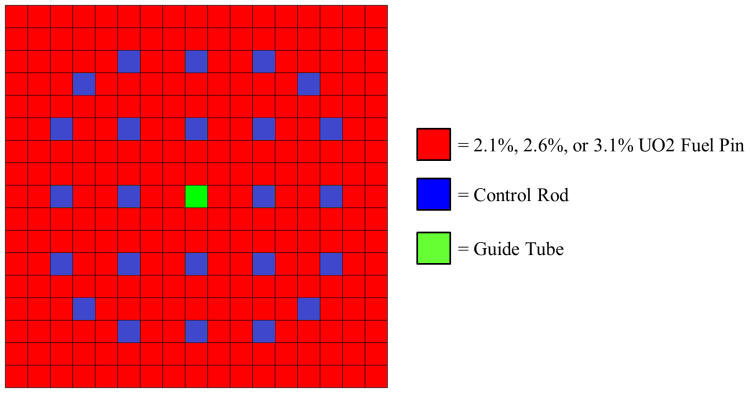

Figure C.29: LWR Rodded Fuel Assembly

Three core configurations are considered for this problem. The core loading pattern is taken directly from CASL Advanced Modeling Applications Core Physics

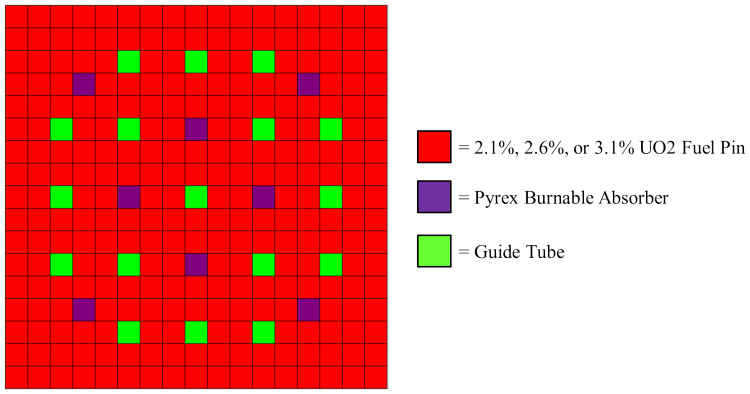

Figure C.30: LWR Fuel Assembly with 8 Pyrex Burnable Absorber Rods

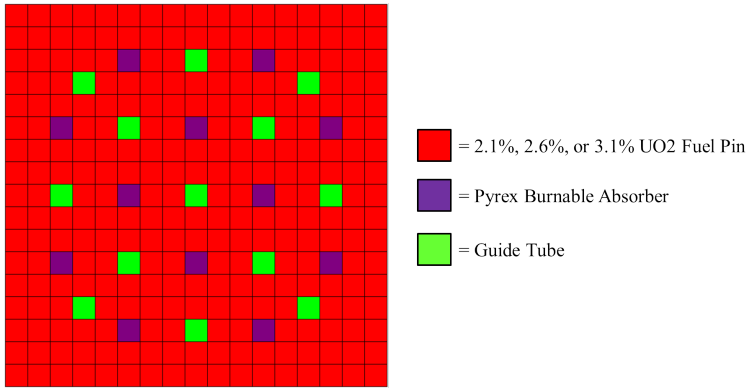

Figure C.31: LWR Fuel Assembly with 12 Pyrex Burnable Absorber Rods

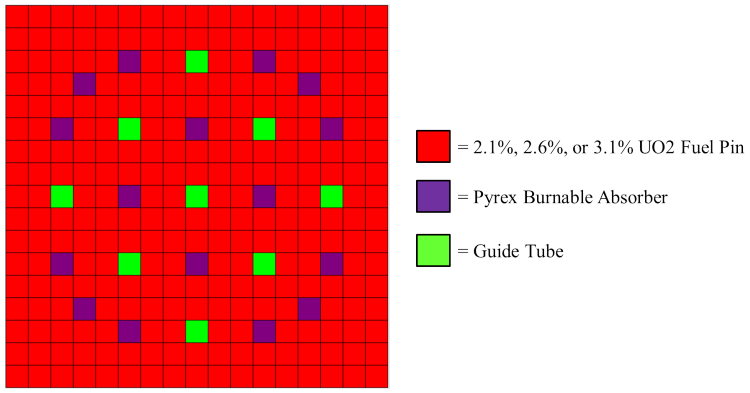

Figure C.32: LWR Fuel Assembly with 16 Pyrex Burnable Absorber Rods

Benchmark Progression Problem 5 [16]. The first configuration ("No Pyrex") contains only fuel assemblies without burnable absorbers (Fig. C.35). The second configuration ("Unrodded") is an unrodded core with burnable absorbers (Fig. C.36). This configuration is identical to the CASL problem. The third configuration ("Rodded")

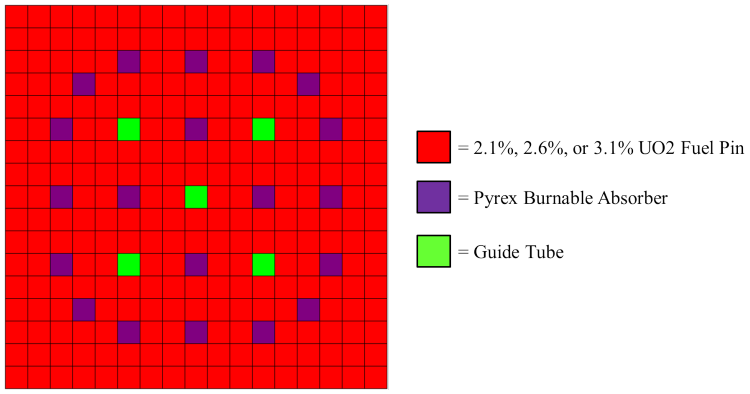

Figure C.33: LWR Fuel Assembly with 20 Pyrex Burnable Absorber Rods

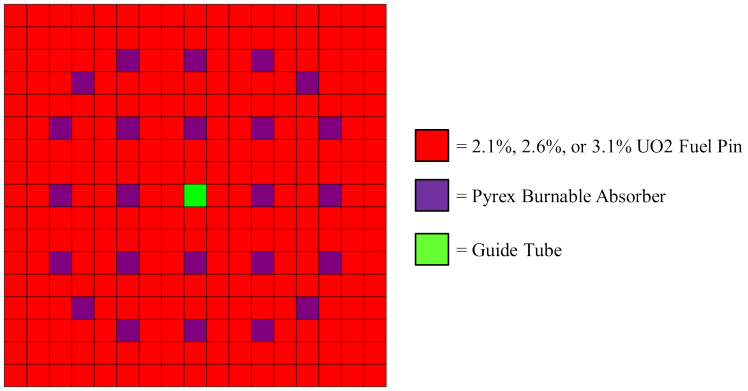

Figure C.34: LWR Fuel Assembly with 24 Pyrex Burnable Absorber Rods

contains burnable absorbers and 3 asymmetrically located rodded assemblies (Fig. C.37). The "Rodded" and "Unrodded" reference solutions were obtained using reflecting boundary conditions on all sides, but the reflector assemblies are sufficiently thick that this should have negligible effect. The "No Pyrex" reference solution was obtained using vacuum boundary conditions on all sides.

The run parameters for the MOC and diffusion calculations are shown in Tables C.21 and C.22. The diffusion calculations have a large spectral radius, so tighter convergence criteria are used to prevent false convergence.

Diffusion calculations were performed using 2, 5, and 10 coarse energy group structures (Tables B.17-B.19). The reflector assembly cross sections were group-collapsed using a fuel-reflector colorset calculation with a 3.1% enriched fuel assembly

containing 0 Pyrex rods.

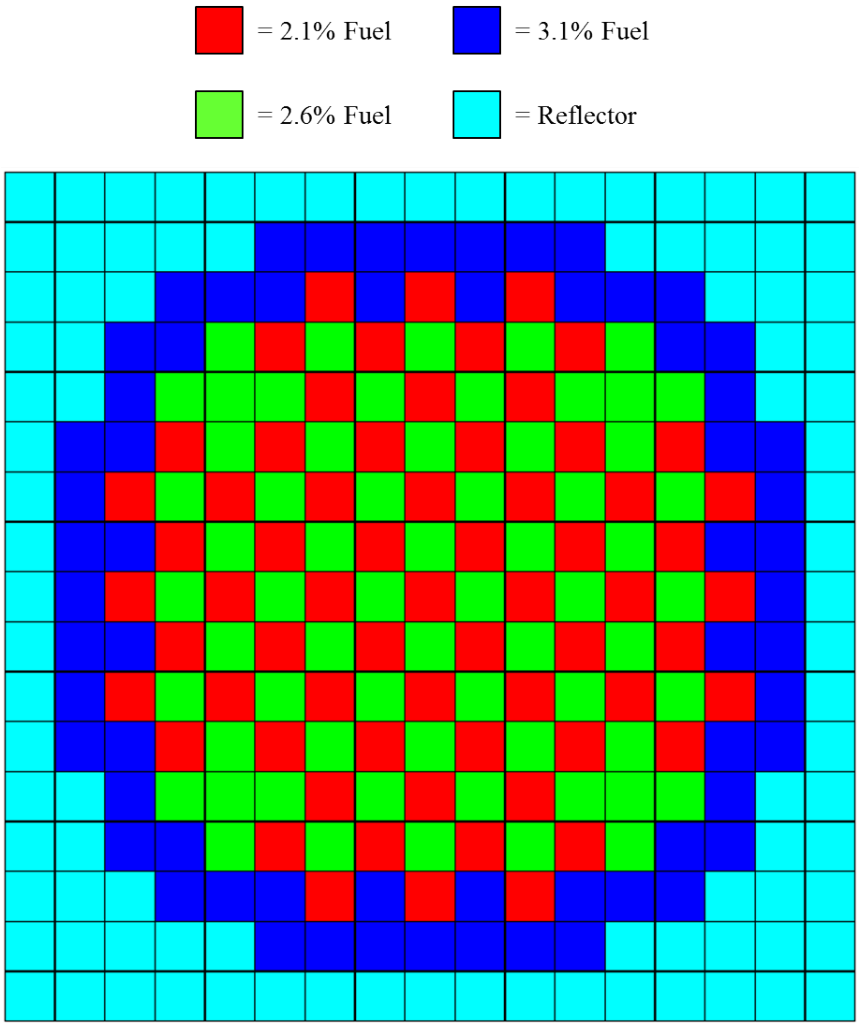

Figure C.35: LWR Core: No Pyrex Configuration

Table C.21: MOC Run Parameters for Full-Core LWR Test

Quadrature Type	Chebyshev-Yamamoto
Azimuthal Angles Per Octant	16
Polar Angles Per Octant	3
Ray Spacing [cm]	0.05
k Convergence Tolerance	1.E-06
ϕ Convergence Tolerance	1.E-06

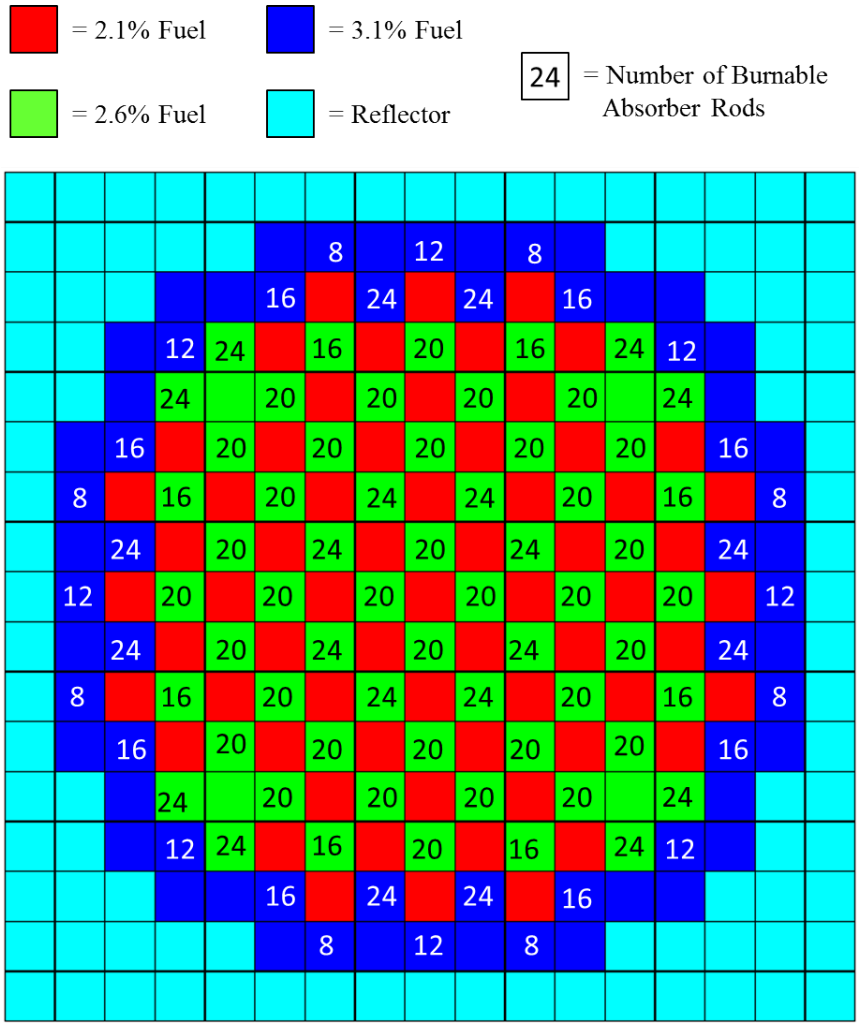

Figure C.36: LWR Core: Unrodded Configuration

Table C.22: Diffusion Run Parameters for Full-Core LWR Test

x Mesh Spacing [cm]	0.63
y Mesh Spacing [cm]	0.63
k Convergence Tolerance	1.E-08
ϕ Convergence Tolerance	1.E-07[1]

[1] 5 and 10 group "Rodded" calculations terminated prior to flux convergence, after 100000 iterations.

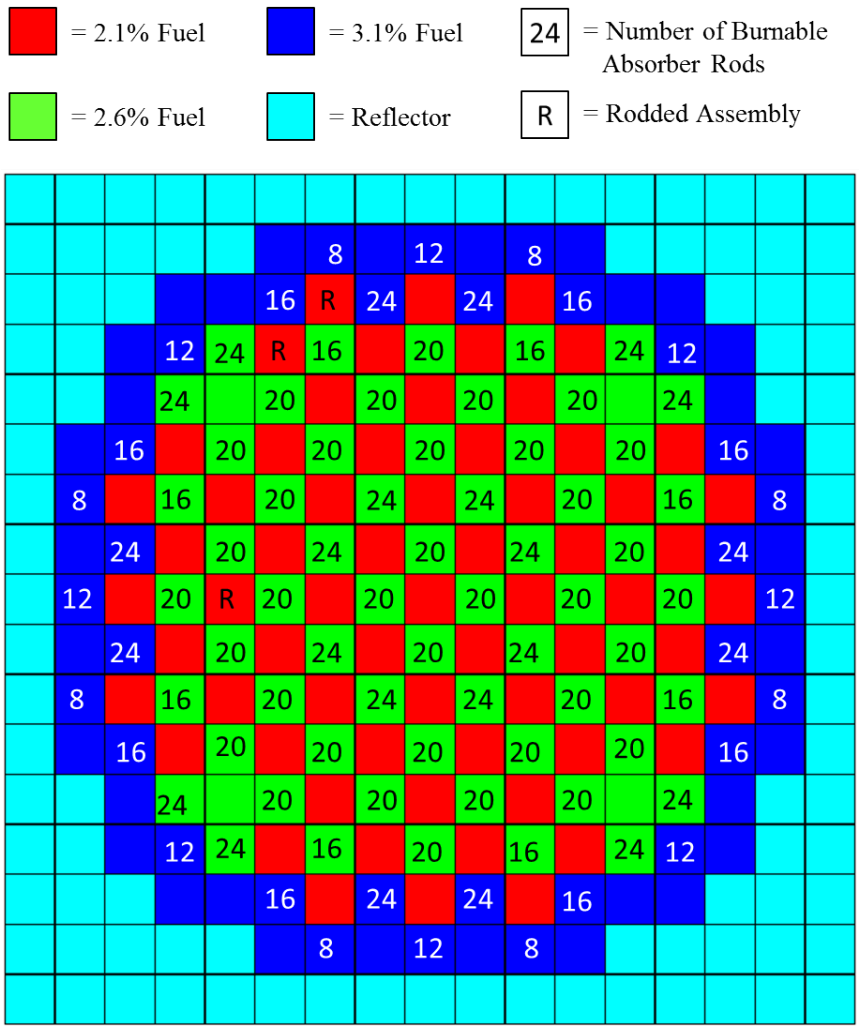

Figure C.37: LWR Core: Rodded Configuration

BIBLIOGRAPHY

BIBLIOGRAPHY

[1] J. J. DUDERSTADT and L. J. HAMILTON, *Nuclear Reactor Analysis*, John Wiley & Sons, Inc., New York, NY, USA (1976).

[2] "Acceptance criteria for emergency core cooling systems for light-water nuclear power reactors," Title 10 *Code of Federal Regulations* Part 50, Section 46, Paragraph (b) (2013).

[3] N. E. TODREAS and M. S. KAZIMI, *Nuclear Systems I: Thermal Hydraulic Fundamentals*, Hemisphere Publishing Corporation, USA (1990).

[4] "Nuclear Fuel Safety Criteria Technical Review - Second Edition," Tech. Rep. NEA Report 7072, Organisation for Economic Co-operation and Development Nuclear Energy Agency, France (2012).

[5] D. TESTA, *The Westinghouse Pressurized Water Reactor Nuclear Power Plant*, Westinghouse Electric Company LLC, Pittsburgh, PA, USA (2006).

[6] N. Z. CHO, "Fundamentals and Recent Developments of Reactor Physics Methods," *Nuclear Engineering and Technology*, **37**, 1, 25–78 (2005).

[7] E. E. LEWIS and W. F. MILLER, *Computational Methods of Neutron Transport*, American Nuclear Society, La Grange Park, Il, USA (1993).

[8] T. M. SUTTON, T. J. DONOVAN, T. H. TRUMBULL, P. S. DOBREFF, E. CARO, D. P. GRIESHEIMER, L. J. TYBURSKI, D. C. CARPENTER, and H. JOO, "The MC21 Monte Carlo Transport Code," in "Proceedings of Joint International Topical Meeting on Mathematics & Computation and Supercomputing in Nuclear Applications (M&C + SNA 2007)," Monterey, CA, USA (April 2007).

[9] D. J. KELLY, T. M. SUTTON, and S. C. WILSON, "MC21 Analysis of the Nuclear Energy Agency Monte Carlo Performance Benchmark Problem," in "Proceedings of Advances in Reactor Physics Linking Research, Industry, and Education (PHYSOR 2012)," Knoxville, TN, USA (April 2012).

[10] D. J. KELLY, B. A. AVILES, and B. R. HERMAN, "MC21 Analysis of the MIT PWR Benchmark: Hot Zero Power Results," in "Proceedings of International Conference on Mathematics and Computational Methods Applied to Nuclear Science and Engineering (M&C 2013)," Sun Valley, ID, USA (May 2013).

[11] "Consortium for Advanced Simulation of Light Water Reactors," http://www.casl.gov, (Accessed September 21, 2012).

[12] J. C. WAGNER, D. E. PEPLOW, S. W. MOSHER, and M. E. THOMAS, "Review of Hybrid (Deterministic/Monte Carlo) Radiation Transport Codes and Application at Oak Ridge National Laboratory," in "Proceedings of the Joint International Conference on Supercomputing in Nuclear Applications plus Monte-Carlo 2010 (SNA + MC 2010)," Tokyo, Japan (October 2010).

[13] J. C. WAGNER, S. W. MOSHER, T. M. EVANS, D. E. PEPLOW, and J. A. TURNER, "Hybrid and Parallel Domain-Decomposition Methods Development to Enable Monte Carlo for Reactor Analyses," *Progress in Nuclear Science and Technology*, **2**, 815–820 (2011).

[14] B. KOCHUNAS, B. COLLINS, D. JABAAY, T. J. DOWNAR, and W. R. MARTIN, "Overview of Development and Design of MPACT: Michigan Parallel Characteristics Transport Code," in "Proceedings of International Conference on Mathematics and Computational Methods Applied to Nuclear Science and Engineering (M&C 2013)," Sun Valley, ID, USA (May 2013).

[15] B. KOCHUNAS, T. J. DOWNAR, and Z. LIU, "Parallel 3-D Method of Characteristics in MPACT," in "Proceedings of International Conference on Mathematics and Computational Methods Applied to Nuclear Science and Engineering (M&C 2013)," Sun Valley, ID, USA (May 2013).

[16] A. T. GODFREY, "VERA Core Physics Benchmark Progression Problem Specifications," Tech. Rep. CASL Technical Report: CASL-U-2012-0131-002, Consortium for Advanced Simulation of LWRs, Oak Ridge, TN, USA (2013).

[17] T. M. EVANS, G. G. DAVIDSON, and R. N. SLAYBAUGH, "Three-Dimensional Full Core Power Calculations for Pressurized Water Reactors," in "Proceedings of the 2010 Scientific Discovery through Advanced Computing Conference (SciDAC 2010)," Chattanooga, TN, USA (July 2010).

[18] B. W. KELLEY and E. W. LARSEN, "2D/1D Approximations to the 3D Neutron Transport Equation. I: Theory," in "Proceedings of International Conference on Mathematics and Computational Methods Applied to Nuclear Science and Engineering (M&C 2013)," Sun Valley, ID, USA (May 2013).

[19] B. W. KELLEY and E. W. LARSEN, "2D/1D Approximations to the 3D Neutron Transport Equation. II: Numerical Results," in "Proceedings of International Conference on Mathematics and Computational Methods Applied to Nuclear Science and Engineering (M&C 2013)," Sun Valley, ID, USA (May 2013).

[20] K. SMITH, "Reactor Core Methods," in "Proceedings of Nuclear Mathematical & Computational Sciences: A Century in Review, A Centuray Anew (M&C 2003)," Gatlinburg, TN, USA (April 2003).

[21] K. KOEBKE, "Advances in Homogenization and Dehomogenization," in "Proceedings of the International Topical Meeting on Advances in Mathematical Methods for the Solution of Nuclear Engineering Problems (M&C 1981)," Munich, Germany (April 1981).

[22] K. S. SMITH, "Assembly Homogenization Techniques for Light Water Reactor Analysis," *Prog. Nucl. Energ.*, **17**, 3, 303–335 (1986).

[23] R. SANCHEZ, "Assembly homogenization techniques for core calculations," *Prog. Nucl. Energ.*, **51**, 1, 14–31 (2009).

[24] F. B. H. FINNEMANN, F. BENNEWITZ, and M. R. WAGNER, "Interface Current Techniques for Multidimensional Reactor Calculations," *Atomkernenergie*, **30**, 123–128 (1977).

[25] K. SMITH, *An analytic nodal method for solving the two-group, multi-dimensional, static and transient neutron diffusion equations*, Ph.D. thesis, Massachusetts Institute of Technology, Cambridge, MA, USA (1979).

[26] J. M. NOH and N. Z. CHO, "A New Approach of Analytic Basis Function Expansion to Neutron Diffusion Calculations," *Nucl. Sci. Eng.*, **116**, 165 (1994).

[27] Y. I. KIM, Y. J. KIM, S. J. KIM, and T. K. KIM, "A Semi-Analytic Multigroup Nodal Method," *Annals of Nuclear Energy*, **26**, 699–708 (1999).

[28] M. KNIGHT, P. BRYCE, and S. HALL, "WIMS/PANTHER Analysis of UO2/MOX Cores Using Embedded Supercells," in "Proceedings of Advances in Reactor Physics Linking Research, Industry, and Education (PHYSOR 2012)," Knoxville, TN, USA (April 2012).

[29] P. BENOIST, "Théorie du Coefficient de Diffusion des Neutrons Dans un Réseau Comportant des Cavités," Tech. Rep. CEA-R-2278, Centre d'Etudes Nucléaires de Saclay, France (1964).

[30] P. BENOIST, "Streaming Effects and Collision Probabilities in Lattices," *Nucl. Sci. Eng.*, **34**, 285–307 (1968).

[31] E. M. GELBARD, "Anisotropic Neutron Diffusion in Lattices of the Zero-Power Plutonium Reactor Experiments," *Nucl. Sci. Eng.*, **54**, 327–340 (1974).

[32] E. W. LARSEN, "Neutron Transport and Diffusion in Inhomogeneous Media. I," *J. Math. Phys.*, **16**, 1421–1427 (1975).

[33] E. W. LARSEN, "Neutron Transport and Diffusion in Inhomogeneous Media. II," *Nucl. Sci. Eng.*, **60**, 357–368 (1976).

[34] T. IIJIMA and K. SHIRAKATA, "Proposal of Method to Estimate Criticality Correction for Anisotropic Diffusion in Plate Lattice Fast Assembly," *J. Nucl. Sci. Technol.*, **14**, 9, 682–684 (1977).

[35] E. W. LARSEN and T. J. TRAHAN, "2-D Anisotropic Diffusion in Optically Thin Channels," *Trans. Am. Nucl. Soc.*, **101**, 387–389 (2009).

[36] B. KELLEY, "Application of 3-D Anisotropic Diffusion Coefficients to a VHTR Assembly," in "Proceedings of the 2010 American Nuclear Society Student Conference," Ann Arbor, MI, USA (April 2010).

[37] T. J. TRAHAN and E. W. LARSEN, "3-D Anisotropic Neutron Diffusion in Optically Thick Media with Optically Thin Channels," in "Proceedings of International Conference on Mathematics and Computational Methods Applied to Nuclear Science and Engineering (M&C 2011)," Rio de Janeiro, RJ, Brazil (May 2011).

[38] J. LEPPÄNEN, *Serpent - a Continuous-energy Monte Carlo Reactor Physics Burnup Calculation Code, User's Manual*, VTT Technical Research Centre of Finland (March 6, 2013).

[39] R. J. J. STAMM'LER and M. J. ABBATE, *Methods of Steady-State Reactor Physics in Nuclear Design*, Academic Press Limited, London, England (1983).

[40] M. L. ADAMS, "Course Notes for NUEN 301: Nuclear Reactor Theory, Texas A&M University," (2006).

[41] J. LEPPÄNEN, *Development of a New Monte Carlo Reactor Physics Code*, Ph.D. thesis, Helsinki University of Technology, Espoo, Finland (2007).

[42] J. C. LEE, "Course Notes for NERS 561: Nuclear Core Design and Analysis I, University of Michigan," (2009).

[43] H. G. JOO, "Course Notes for NERS 561: Nuclear Core Design and Analysis I, University of Michigan," (2011).

[44] G. MARLEAU, A. HÉBERT, and R. ROY, "A User Guide for Dragon," Tech. Rep. IGE-174 Rev. 4 (September 1998).

[45] R. J. ZERR, M. OUISLOUMEN, and Y. AZMY, "Effect of Direction-Dependent Diffusion Coefficients on the Accuracy of the Diffusion Model for LWR Cores," in "Proceedings of the International Conference on the Physics of Reactors (PHYSOR 2008)," Interlaken, Switzerland (Septemeber 2008).

[46] V. DENIZ, "Study of the Kinetics of Thermalized Neutron Populations in Multiplying or Nonmultiplying Heterogeneous Media," *Nucl. Sci. Eng.*, **28**, 397–403 (1967).

[47] H. ZHANG, RIZWAN-UDDIN, and J. J. DORNING, "A Multiple-Scales Systematic Theory for the Simultaneous Homogenization of Lattice Cells and Fuel Assemblies," *Transport Theory and Statistical Physics*, **26**, 7, 765–811 (1997).

[48] G. J. HABETLER and B. J. MATKOWSKY, "Uniform asymptotic expansions in transport theory with small mean free paths, and the diffusion approximation," *J. Math. Phys.*, **16**, 4, 846–854 (1975).

[49] G. C. PAPANICOLAOU, "Asymptotic Analysis of Transport Processes," *Bulletin of the American Mathematical Society*, **81**, 2, 330–392 (1975).

[50] A. BENSOUSSAN, J. L. LIONS, and G. C. PAPANICOLAOU, "Homogenization of Transport Equations," *Publications of the Research Institute for Mathematical Sciences, Kyoto University*, **15**, 1, 53–157 (1979).

[51] L. DUMAS and F. GOLSE, "Homogenization of Transport Equations," *J. Appl. Math.*, **60**, 4, 1447–1470 (2000).

[52] R. P. HUGHES, "A Unified Derivation of the Various Definitions of Lattice Cell Diffusion Coefficients," *Nucl. Sci. Eng.*, **67**, 85–90 (1978).

[53] E. W. LARSEN and R. P. HUGHES, "Homogenized Diffusion Approximations to the Neutron Transport Equation," *Nucl. Sci. Eng.*, **73**, 274–285 (1980).

[54] T. TAKEDA and T. SEKIYA, "Comparison of the Anisotropic Diffusion Coefficients Based on the Benoist and Deniz Formulas," *J. Nucl. Sci. Technol.*, **9**, 11, 682–685 (1972).

[55] T. KOBAYASHI, A. SUGAWARA, Y. SEKI, T. HOJUYAMA, H. YOKOBORI, and M. SASAKI, "A Numerical Study on Application of Benoist's Anisotropic Diffusion Coefficients," *J. Nucl. Sci. Technol.*, **12**, 7, 456–459 (1975).

[56] T. J. TRAHAN and E. W. LARSEN, "An Asymptotic Homogenized Diffusion Approximation. II. Numerical Comparisons," in "Proceedings of Advances in Reactor Physics Linking Research, Industry, and Education (PHYSOR 2012)," Knoxville, TN, USA (April 2012).

[57] A. Y. CHENG, A. F. HENRY, and C. L. HOXIE, "A Method for Determining Equivalent Homogenized Parameters," in "Proceedings of the International Topical Meeting on Advances in Mathematical Methods for the Solution of Nuclear Engineering Problems (M&C 1981)," Munich, Germany (April 1981).

[58] G. C. POMRANING, *The Equations of Radiation Hydrodynamics*, Dover Publications, Inc., Mineola, NY, USA (1973).

[59] E. W. LARSEN, "Course Notes for NERS 644: Transport Theory, University of Michigan," (2008).

[60] E. W. LARSEN, "Course Notes for NERS 543: Numerical Reactor Theory II, University of Michigan," (2008).

[61] B. S. COLLINS, *Multiscale Methods for Nuclear Reactor Analysis*, Ph.D. thesis, University of Michigan, Ann Arbor, MI, USA (2011).

[62] A. G. RAMM, "A Simple Proof of the Fredholm Alternative and a Characterization of the Fredholm Operators," *American Mathematical Monthly*, **108**, 9, 855–860 (2001).

[63] F. MALVAGI and G. C. POMRANING, "Initial and Boundary Conditions for Diffusive Linear Transport Problems," *J. Math. Phys.*, **32**, 3, 805–820 (1991).

[64] E. W. LARSEN, "Course Notes for NERS 644: Transport Theory, University of Michigan," (1993).

[65] F. D. FEDERIGHI, "Vacuum Boundary Conditions for the Spherical Harmonics Method," *Nukleonik*, **6**, 277 (1964).

[66] G. C. POMRANING, "Variational Boundary Conditions for the Spherical Harmonics Approximation to the Neutron Transport Equation," *Ann. Phys.*, **27**, 193 (1964).

[67] G. C. POMRANING, "An Improved Free-Surface Boundary Condition for the P-3 Approximation," *Nucl. Sci. Eng.*, **18**, 528 (1964).

[68] R. P. RULKO, D. TOMASEVIC, and E. W. LARSEN, "Variational P1 Approximations of General-Geometry Multigroup Transport Problems," *Nucl. Sci. Eng.*, **121**, 393–404 (1995).

[69] S. R. JOHNSON and E. W. LARSEN, "Diffusion Boundary Conditions in Flatland Geometry," *Trans. Am. Nucl. Soc.*, **105**, 446–448 (2011).

[70] F. A. TARANTINO, *The Development of Cross Sections from Bilinear Variational Theory for use in Few-Group Transient Analysis*, Ph.D. thesis, Massachusetts Institute of Technology, Cambridge, MA, USA (1990).

[71] M. L. ZERKLE, *Development of a Polynomial Nodal Method with Flux and Current Discontinuity Factors*, Ph.D. thesis, Massachusetts Institute of Technology, Cambridge, MA, USA (1992).

[72] J. E. MOREL, "Course Notes for NUEN 430: Computer Applications in Nuclear Engineering, Texas A&M University," (2006).

[73] K. R. REMPE, K. S. SMITH, and A. F. HENRY, "Simulate-3 Pin Power Reconstruction: Methodology and Benchmarking," *Nucl. Sci. Eng.*, **334-342**, 103 (1989).

[74] Z. GAO, Y. XU, and T. DOWNAR, "Critical Node Treatment in the Analytic Function Expansion Method for Pin Power Reconstruction," in "International Conference on Mathematics and Computational Methods Applied to Nuclear Science and Engineering (M&C 1981)," Sun Valley, ID, USA (May 2013), p. 103.

[75] T. L. BECKER, *Hybrid Monte Carlo/Deterministic Methods for Radiation Shielding Problems*, Ph.D. thesis, University of Michigan, Ann Arbor, MI, USA (2009).

[76] University of Michigan, Ann Arbor, *MPACT User Manual* (March 21, 2013).

[77] "Small Modular Nuclear Reactors," http://www.energy.gov/ne/nuclear-reactor-technologies/small-modular-nuclear-reactors, (Accessed December 18, 2013).

[78] "Benchmark on Deterministic Transport Calculations Without Spatial Homogenisation - MOX Fuel Assembly 3-D Extension Case," Tech. Rep. NEA/NSC/DOC(2005)16 (2005).

[79] "Benchmark on Deterministic Transport Calculations Without Spatial Homogenisation - A 2-D/3-D MOX Fuel Assembly Benchmark," Tech. Rep. NEA/NSC/DOC(2003)16 (2003).

[80] H. G. JOO, Soeul National University, Personal Communication (2011).

[81] C. H. LEE, Argonne National Laboratory, Personal Communication (2010).

[82] Studsvik Scandpower, *HELIOS Methods (version 1.10)* (January 23, 2008).

[83] "Core Validation Test," Unpublished (2013).

[84] L. C. H., Z. ZHONG, T. A. TAIWO, W. S. YANG, M. A. SMITH, and G. PALMIOTTI, "Status of Reactor Physics Activities on Cross Section Generation and Functionalization for the Prismatic Very High Temperature Reactor, and Development of Spatially-Heterogeneous Codes," Tech. Rep. ANL-GenIV-075 (2006).